

## ENHANCEMENT OF CONVECTIVE HEAT TRANSFER IN LAMINAR AND TURBULENT FLOWS WITH NANOFLUIDS

Bürvan Apaçođlu<sup>a</sup>, Ođuz Kirez<sup>b</sup>

Department of Mechanical Engineering

<sup>a</sup>TOBB University of Economics and Technology, bapacoglu@etu.edu.tr

<sup>b</sup>Middle East Technical University, oguzkirez@gmail.com

Sadık Kakaç<sup>c</sup>, Almla Güvenç Yazıcıođlu<sup>d</sup>

Department of Mechanical Engineering

<sup>c</sup>TOBB University of Economics and Technology, sadikakac@yahoo.com

<sup>d</sup>Middle East Technical University, agyazi@gmail.com

### Abstract

Nanofluids are considered to offer important advantages over conventional heat transfer fluids. Over a decade ago, researchers focused on measuring and modeling the effective thermal conductivity and viscosity of nanofluids. Recently important theoretical and experimental research on convective heat transfer appeared in the open literature on the enhancement of heat transfer using suspensions of nanometer-sized solid particles, metallic or nonmetallic, in base heat transfer fluids. The purpose of this article is to investigate the enhancement of convective heat transfer with nanofluids in laminar and turbulent flow regimes by using the thermophysical nanofluid properties estimated by the effective medium theory. The energy equation for the hydrodynamically fully-developed nanofluid flow in a tube is solved under constant wall temperature boundary condition for various values of volume fraction of nanoparticles, nanofluid Peclet numbers and particle diameters. The effects of the volume fraction, nanoparticle diameter, fluid Peclet number are shown in graphical forms and they are compared to observe differences between laminar and turbulent nanofluid flow in a tube.

### KEYWORDS

Nanofluids, heat transfer enhancement, forced convection, laminar flow, turbulent flow.

### INTRODUCTION

Heat transfer with nanofluids draws attention because of its promising advantages. In thermal systems, it is desired to improve thermal characteristics of the system to provide adequate heat transfer with less energy consumption. The size and operating costs can be reduced by using thermally more effective working fluids. The studies performed until today show that thermal efficiency of energy systems can be increased by using nanofluids instead of conventional working fluids. Nanofluids are newly described engineered fluids that are produced by the dispersion of nanometer sized solid particles with a relatively high thermal conductivity into a base fluid to increase the thermal conductivity of the fluid. Higher thermal conductivity of the nanofluid considerably increases the convective heat transfer coefficient. Since it comes into attention as a result of developments in nanotechnology, which enable the production of nanoparticles, there are gaps in literature about its research concerning the theory behind it and its applications.

Nanofluids were first investigated by Masuda et al. [1] and Choi [2]. Nanofluids have some advantages over ordinary suspensions prepared with larger particles. Experimental studies show that the thermal conductivity enhancements obtained with nanofluids exceed the enhancements obtained by using conventional suspensions, which contain particles in the dimensions of millimeters and micrometers [3]. In addition, because of the small size of nanoparticles; some problems such as clogging of channels, erosion on the channel walls, and sedimentation are eliminated with the use of nanofluids in engineered systems.

For the forced convection of nanofluids, the general trend observed as a result of experimental studies performed in literature is that the heat transfer coefficient enhancement by nanofluids exceeds the associated enhancement obtained in thermal conductivity [4]. This further enhancement indicates the presence of additional heat transfer enhancement mechanisms.

General dimensionless parameters such as Peclet number and Reynolds number can be utilized in the analysis of nanofluid flows since solid particles in the fluid have sizes on the order of nanometers and they fluidize easily [5]. Therefore, correlations derived in literature for pure fluids may be used for nanofluids. The effect of nanoparticles is taken into account only through the substitution of thermophysical properties of nanofluids into associated correlations. Alternatively, energy equation can be solved numerically by using nanofluid thermophysical properties to investigate heat transfer characteristics of nanofluids.

The aim of this study is to numerically analyze hydrodynamically fully-developed laminar and turbulent convective heat transfer of nanofluids flowing in a tube under constant wall temperature boundary condition. Enhancement in heat transfer coefficient is analyzed to observe the effectiveness of the use of nanofluids in thermal systems instead of conventional pure fluids. The models and formulations used in the analyses are described in the following sections.

## NANOFLUID PROPERTIES

### Conductivity Model

In the analyses, the enhancement of the nanofluid thermal conductivity must be used to investigate the its effect. For predicting the thermal conductivity, various conductivity models are available. Effective Medium Theory (EMT) is an approximation that describes the macroscopic properties of a medium based on the properties and the relative fractions of its components. Maxwell [6] developed this theory over 100 years ago and stated a simple equation that can be used to evaluate thermal conductivity of nanofluids ( $k_{nf}$ ) which include spherical and well-dispersed nanoparticles:

$$k_{nf} = \frac{k_p + 2k_f + 2(k_p - k_f)\phi}{k_p + 2k_f - (k_p - k_f)\phi} k_f . \quad (1)$$

Here,  $k_p$  and  $k_f$  are the thermal conductivity of the nanoparticle and base fluid, respectively.  $\phi$  is the particle volume fraction.

Maxwell model only considers the volume fraction of the nanoparticles. As seen from the expression, the effect of the size and shape of the particles was not included in the analysis. It should be noted that the interaction between the particles was also neglected in this expression.

Maxwell model has been extended by Hamilton and Crosser [7] by introducing a shape factor,  $n$ , that is a parameter determined experimentally for the nanoparticles.

$$k_{nf} = \frac{k_p + (n-1)k_f - (n-1)\phi(k_f - k_p)}{k_p + (n-1)k_f + \phi(k_f - k_p)} k_f . \quad (2)$$

The empirical shape factor,  $n$ , is defined as  $3/\psi$ . Here  $\psi$  denotes the sphericity of the nanoparticles, the ratio of the surface area of a sphere with a volume equal to that of the particle to the surface area of the particle. Therefore,  $n=3$  for a sphere and in that case eq. (2) becomes identical to the eq. (1).

Brownian motion is described as the random movement of nanoparticles in the continuous medium and it affects the thermal conductivity of the nanofluid since this movement makes a contribution to the heat transport in the nanofluid. At elevated temperatures, Brownian motion dominates and the effect of Brownian motion is introduced as an additional term in thermal conductivity of nanofluids expression by Koo and Kleinstreuer [8] as:

$$k_{nf} = k_{static} + k_{Brownian} . \quad (3)$$

Here,  $k_{static}$  can be evaluated by the Hamilton-Crosser model. The additional term,  $k_{Brownian}$ , that arises because of the Brownian motion of the particles can be computed by the expression proposed as follows [8]:

$$k_{\text{Brownian}} = 5 \times 10^4 \beta \phi \rho_f c_{p,f} \sqrt{\frac{\kappa_B T}{\rho_p d_p}} f. \quad (4)$$

Here,  $\kappa_B$  is Boltzmann constant and equal to  $1.3807 \times 10^{-23}$  J/K.  $T$  is temperature of the medium.  $\rho_f$ ,  $c_{p,f}$ ,  $\rho_p$  and  $d_p$  denote density of the fluid, specific heat of the fluid, density of the particles and diameter of the particles, respectively. For  $\text{Al}_2\text{O}_3$  nanoparticles  $f$  is assumed to be 1 because of the lack in experimental data.  $\beta$  is also a parameter that differs according to the type of the nanoparticles. It is defined as follows for  $\text{Al}_2\text{O}_3$  nanoparticles [8]:

$$\beta = 0.0017(100\phi)^{-0.0841}, \quad \phi > 1\%. \quad (5)$$

### Evaluation of Other Thermophysical Properties

Thermophysical properties of the nanofluid such as density, viscosity and specific heat also change with the volume fraction of nanoparticles. Density and specific heat of the nanofluid can be estimated by utilizing the well-known mixing-cup formulations that are generally used for the fluids consisting of two different types of substances:

$$\rho_{nf} = \phi \rho_p + (1 - \phi) \rho_f, \quad (6)$$

$$(\rho c_p)_{nf} = \phi (\rho c_p)_p + (1 - \phi) (\rho c_p)_f. \quad (7)$$

An expression for determining the dynamic viscosity of dilute suspensions ( $\mu_{nf}$ ) that contain spherical particles is stated in eq. (8) in terms of volume fraction and viscosity of the nanofluid ( $\mu_f$ ). Note that the interactions between the particles are neglected in this model.

$$\mu_{nf} = (1 + 2.5\phi) \mu_f. \quad (8)$$

Expressions in eqs. (2)–(8) are used in nanofluid flow simulations to calculate the thermophysical properties of the nanofluid.

## FORMULATION OF THE PROBLEM

### Governing Equations for Nanofluid Flow

The current problem focuses on the effect of heat transfer enhancement in incompressible laminar and turbulent nanofluid flows in a pipe under constant wall temperature boundary condition. The schematic representation of the problem is shown in Fig. 1.

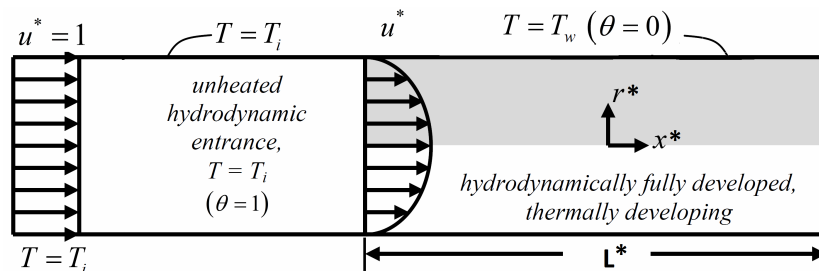


Fig. 1. Schematic of the problem

The governing energy equation with axial convection term for the prescribed system is as follows:

$$\rho c_p \left( \frac{\partial T}{\partial t} + V \cdot \nabla T \right) = \nabla \cdot (\rho c_p D \nabla T) + \dot{q} + \Phi. \quad (9)$$

Here, total diffusivity is  $D = (\alpha + \varepsilon_h)$  and  $V$ ,  $\dot{q}$  and  $\Phi$  show velocity field, heat generation and viscous dissipation, respectively. For hydrodynamically fully-developed and steady-state flow in the x-direction, when axial conduction and viscous dissipation terms are neglected, the energy equation simplifies to:

$$u_x \frac{\partial T}{\partial x} = \frac{1}{r} \frac{\partial}{\partial r} \left[ Dr \frac{\partial T}{\partial r} \right]. \quad (10)$$

Heat transfer increases due to time varying fluctuations in turbulent flow caused by small eddies. Eddy diffusivity of heat ( $\varepsilon_h$ ) is described to include this effect. This term is zero for laminar flow since it does not contain turbulent structures and fluctuations. The energy equation is rearranged and simplified by making use of dimensionless parameters stated below:

$$x^* = \frac{x}{r_0}, \quad r^* = \frac{r}{r_0}, \quad k^* = \frac{k_{nf,T}}{k_{nf,b}}, \quad u^* = \frac{u_x}{u_m}, \quad Pe_{nf} = \frac{u_m d}{\alpha_{nf,b}}, \quad \theta = \frac{T - T_w}{T_i - T_w}. \quad (11)$$

Here  $T_i$  and  $T_w$  are inlet and wall temperatures, respectively.  $r_0$  is the tube radius and  $u_m$  is the mean velocity. The subscript  $T$  indicates that the nanofluid thermal conductivity should be calculated at the local temperature, whereas subscript  $b$  corresponds to the bulk temperature.  $\alpha_{nf}$  is the thermal diffusivity of the nanofluid which can be computed with using nanofluid properties estimated by eqs. (2)-(8). Non-dimensional form of the general energy equation is obtained as follows:

$$\frac{Pe_{nf}}{2} u^* \frac{\partial \theta}{\partial x^*} = \frac{1}{r^*} \frac{\partial}{\partial r^*} \left[ r^* k^* \left( 1 + \frac{\varepsilon_h}{\alpha_{nf}} \right) \frac{\partial \theta}{\partial r^*} \right]. \quad (12)$$

For laminar nanofluid flow analyses, this equation reduces to:

$$\frac{Pe_{nf}}{2} u^* \frac{\partial \theta}{\partial x^*} = \frac{1}{r^*} \frac{\partial}{\partial r^*} \left[ r^* k^* \frac{\partial \theta}{\partial r^*} \right]. \quad (13)$$

The boundary conditions are given in Table 1.

Boundary Condition	Centerline	Inlet	Wall
Constant $T_w$	$\frac{\partial \theta}{\partial r^*} = 0$ at $r^* = 0$	$\theta = 1$ at $x^* = 0$	$\theta = 0$ at $r^* = 1$

In pursuit of numerical solution of the problem; to validate the results and to observe the changes in heat transfer characteristics of the flow, it is convenient to calculate Nusselt number of the flow. Nusselt number can be calculated numerically by making use of non-dimensional parameters:

$$Nu = \frac{2}{\theta_w - \theta_b} \left( \frac{\partial \theta}{\partial r^*} \right)_{r^*=1}, \quad (14)$$

where subscripts  $w$  and  $b$  denote wall and bulk temperatures. Note that the Nusselt number given above is local and expressions that are used to evaluate Nusselt number change in the axial direction. The partial differential term  $(\partial\theta/\partial r^*)$  is calculated numerically by using finite difference formulation. Dimensionless bulk temperature,  $\theta_b$ , is determined by calculating the following expression numerically.

$$\theta_b = \frac{\int_0^1 \theta(x^*, r^*) u^* r^* dr^*}{\int_0^1 u^* r^* dr^*}. \quad (15)$$

Then,  $\theta_b$  can be converted to  $T_b$  and it can be used to evaluate heat transfer coefficient of a definite nanofluid flow system, which means the flow and geometry parameters such as inlet and wall temperature values, diameter of the tube and volume fraction of the nanoparticles are known. If the length of the tube is long enough to enable nanofluid be thermally fully-developed, Nusselt numbers and heat transfer coefficients at the tube exit will be similar for different cases. Therefore, the average Nusselt number ( $\overline{Nu}$ ) and average heat transfer coefficient ( $\overline{h}$ ) given below are used for comparison purposes in both laminar and turbulent flow analyses.

$$\overline{h} = \frac{(\rho c_p)_{nf} u_m A (T_{b,in} - T_{b,out})}{\pi DL (T_w - T_b)_{LM}}, \quad (16)$$

$$\overline{Nu} = \frac{\overline{h} d}{k_{nf}}. \quad (17)$$

Here  $(T_w - T_b)_{LM}$  shows logarithmic mean temperature. Thermophysical properties of the nanofluid in eq. (16) and eq. (17) are evaluated at the bulk mean temperature which is the arithmetic mean of inlet and outlet bulk temperatures. Note that  $A$  denotes the cross-sectional area of the tube.

In the numerical analyses, thermophysical properties of water are not assumed to be constant. Temperature dependent conductivity, density, viscosity and specific heat values of water are evaluated by using 6<sup>th</sup> order polynomial regressions. Since temperature values should be known to calculate thermophysical properties, a representative problem is defined as follows: In laminar flow simulations,  $T_i = 25$  °C,  $T_w = 100$  °C,  $D = 6$  mm,  $L = 1$  m are used, while in turbulent flow simulations,  $T_i = 25$  °C,  $T_w = 100$  °C,  $D = 20$  mm,  $L = 1$  m are used. These parameters are used in the simulations in which thermal conductivity and heat transfer coefficient of the nanofluid are computed.  $Al_2O_3$ /water nanofluid is used and particles are assumed to be spherical and to have uniform sizes. Thermophysical properties of alumina are taken as  $k_p = 46$  W/(m·K),  $\rho_p = 3700$  kg/m<sup>3</sup>,  $(c_p)_p = 880$  J/(kg·K).

The flow is assumed to be hydrodynamically fully-developed and hence parabolic velocity profile on x-direction ( $u_x$ ) is described to evaluate the convection term given on the left hand side of the energy equation in laminar flow, below, and in dimensionless form in eq. (19):

$$u_x = 2u_m \left( 1 - \frac{r^2}{r_0^2} \right), \quad (18)$$

$$u^* = 2 \left( 1 - \frac{r^2}{r_0^2} \right). \quad (19)$$

Then, non-dimensional energy equation for laminar flow becomes:

$$Pe(1-r^{*2})\frac{\partial\theta}{\partial x^*} = \frac{1}{r^*}\frac{\partial}{\partial r^*}\left[r^*k^*\frac{\partial\theta}{\partial r^*}\right] \quad (20)$$

Turbulent flow has three regions; laminar, buffer and turbulent zones. These three regions have different velocity profiles. A solution obtained by Von Karman [9] can be implemented to solve the energy equation.

$$u^+ = \begin{cases} y^+ & 0 < y^+ < 5 \\ -3.05 + 5 \ln y^+ & 5 \leq y^+ \leq 30 \\ 5.5 + 2.5 \ln y^+ & 30 \leq y^+ \end{cases}, \quad (21)$$

where

$$y^+ = (r_o - r)\frac{\sqrt{\tau_w / \rho}}{\nu}, \quad (22)$$

$$u^+ = \frac{u_x}{\sqrt{\tau_w / \rho}}. \quad (23)$$

Here  $y^+$  is the non-dimensional wall distance,  $\nu$  is kinematic viscosity and  $u^+$  is the ratio of flow velocity to the friction velocity ( $\sqrt{\tau_w / \rho}$ ). Friction factor to calculate the wall shear stress ( $\tau_w$ ) in these non-dimensional terms is obtained by Filonenko [10]. In addition, friction factor for conventional flows can be used to calculate friction factor of nanofluids, although there are also specific expressions for it [11].

There are different eddy diffusivity of momentum expressions in literature. However, this variable is very sensitive to dimensionless radial location and it must be carefully implemented. Corcoran [12] empirically obtained data for eddy diffusivity of momentum, which varies with radial location. Tabulated data for different Reynolds numbers provided in the reference are used in this work. Once eddy diffusivity of momentum is obtained, eddy diffusivity of heat can be readily calculated from eq. (24).

$$\frac{\varepsilon_h}{\alpha_{nf}} = \frac{\varepsilon_m}{\nu_{nf}} \frac{Pr_{nf}}{Pr_{t,nf}}. \quad (24)$$

Here  $Pr_{t,nf}$  is the turbulent Prandtl number of the nanofluid. It is assumed to be constant and equal to 0.9, as in the study of Launder and Spalding [13].

## METHODOLOGY

The method of research involves computational heat transfer analyses for laminar and turbulent flows in the tube and comparison between laminar and turbulent nanofluid flow results. The enhancement ratios of the heat transfer coefficients are determined in order to observe the effectiveness of the nanofluid use in thermal systems. The procedure of the solution is summarized in the following sections.

### Discretization of the Energy Equation for Laminar Flow

Finite difference method is used to obtain the discretized form of the energy equation. Second order backward and central differencing schemes are applied to the convective term and the radial conduction term in the energy equation, respectively. Coefficients in the discretized equation form a tridiagonal matrix and it can be effectively solved by using the Thomas algorithm.

$$\theta_{i-1,j} = a_{i,j}\theta_{i,j-1} + b_{i,j}\theta_{i,j} + c_{i,j}\theta_{i,j+1}, \quad (25)$$

$$a_{i,j} = \frac{1}{\lambda} \left( \frac{\Delta r^*}{r_j^*} k_{i,j}^* + \frac{k_{i,j+1}^* - k_{i,j-1}^*}{2} - 2k_{i,j}^* \right), \quad (26)$$

$$b_{i,j} = \left( \frac{\lambda + 4k_{i,j}^*}{\lambda} \right), \quad (27)$$

$$c_{i,j} = \frac{1}{\lambda} \left( -\frac{\Delta r^*}{r_j^*} k_{i,j}^* - \frac{k_{i,j+1}^* - k_{i,j-1}^*}{2} - 2k_{i,j}^* \right). \quad (28)$$

$$\lambda = 2Pe_i (1 - r_j^{*2}) \frac{\Delta r^{*2}}{\Delta x^*} \quad (29)$$

Therefore an implicit solution on r-direction with marching steps on the x-axis is obtained.

### Discretization of the Energy Equation for Turbulent Flow

As in the laminar flow analysis, backward finite difference for the convective term and central finite difference for the radial conduction term is used to discretize the energy equation. Fully implicit scheme is implemented to compose a coefficient matrix and rearranged with boundary conditions.

$$a_{i,j} \theta_{i-1,j} + b_{i,j} \theta_{i,j-1} + c_{i,j} \theta_{i,j} + d_{i,j} \theta_{i,j+1} = 0, \quad (30)$$

$$a_{i,j} = -\lambda, \quad b_{i,j} = -(D^* r)_{i,j}, \quad c_{i,j} = \lambda + 2(D^* r)_{i,j}, \quad d_{i,j} = -(D^* r)_{i,j+1}, \quad (31)$$

$$\lambda = Pe_i u_j r_j^* \frac{(\Delta r^*)^2}{\Delta x^*}, \quad (32)$$

$$D_i^* = \left( k_{i,j}^* \left( 1 + \frac{\varepsilon_h}{\alpha_{nf}} \right)_{i,j} \right). \quad (33)$$

The solution is obtained by solving the equations iteratively. First, an initial guess of the temperature values for each node is made and the matrix is solved according to these values. Then, the temperature values are replaced by the calculated ones. In this way, temperature dependent variables are calculated with high accuracy.

### Verification of the Code and Grid Sensitivity

The code is verified by making use of the fully-developed Nusselt number values given in literature. To verify laminar flow analyses, pure water ( $\phi = 0$ ) flow is analyzed by the program and local Nusselt number values are obtained with different grid structures. The representative problem is used in this analysis except the length of the pipe, which is assumed to be  $L = 40$  m to obtain thermally fully-developed condition at the exit. Peclet number of the flow is defined as 8000 that approximately corresponds to a Reynolds number of 2000 and it is close to the upper limit of laminar flow. Grid parameters obtained with this Peclet number can yield more accurate results for the analyses with smaller Peclet numbers.

At the exit of the tube, it is observed that Nusselt number obtained with all grids converges to the same asymptotic value, that is the fully-developed Nusselt number. Fully-developed Nusselt number obtained computationally is very close to the one derived analytically in literature ( $Nu_{fd} = 3.66$ , Ref. 14) with an error of 0.009%. This error is acceptable since this difference may originate from the constant thermophysical

properties of water assumption in the analytical derivation. Also the residual of  $Nu_{fd}$  is obtained to be below  $10^{-4}$  with the grid parameters  $\Delta x^* = 0.03333$ ,  $\Delta r^* = 0.0025$ . Therefore, these parameters will be used in further nanofluid flow simulations.

In order to verify the turbulent simulations, analyses are made with pure water at different Reynolds numbers. Computed Nusselt numbers are compared to the ones obtained by Gnielinski correlation [15]. Good agreement between the correlation and numerical results are observed with a maximum difference of 2.96%.

## RESULTS

### Laminar Nanofluid Flow Analyses

In laminar nanofluid flow simulations; effects of Peclet number, volume fraction, and particle diameter on convective heat transfer are investigated. To understand the effect of nanoparticles, it is convenient to use enhancement in average heat transfer coefficient to visualize the results of the simulations. The ratio of average heat transfer coefficient of the nanofluid to the one for the pure water can interpret the results in a more perceptible manner.

As clearly seen in Fig. 3 and Fig. 4, enhancement does not change considerably with the inlet Peclet number for laminar nanofluid flow in a tube. It increases with volume fraction as expected (Fig. 3), but it decreases with particle diameter because of the degradation in Brownian motion of the particles (Fig. 4).

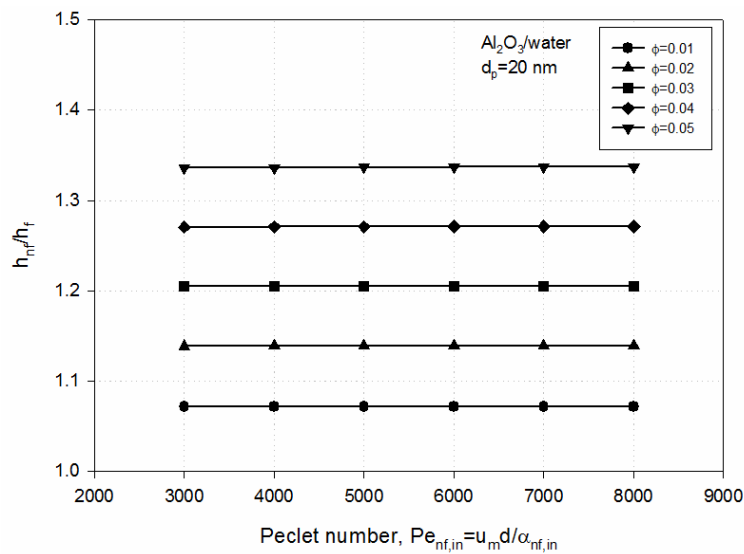


Fig. 3. Enhancement in average heat transfer coefficient at different inlet Peclet numbers (constant particle diameter)

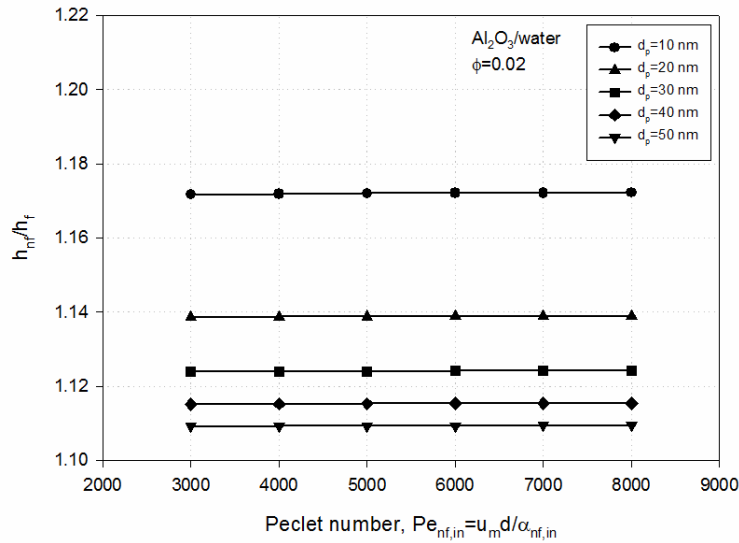


Fig. 4. Enhancement in average heat transfer coefficient at different inlet Peclet numbers (constant volume fraction)

Fig. 5 shows the particle diameter dependency of the enhancement in average heat transfer coefficient. Enhancement decreases exponentially with an increase in the diameter of the nanoparticles as expected, since the effect of Brownian motion on thermal conductivity of the nanofluid decreases as proposed in eq. (4). Change in particle diameter has more impact on the heat transfer enhancement at higher volume fractions.

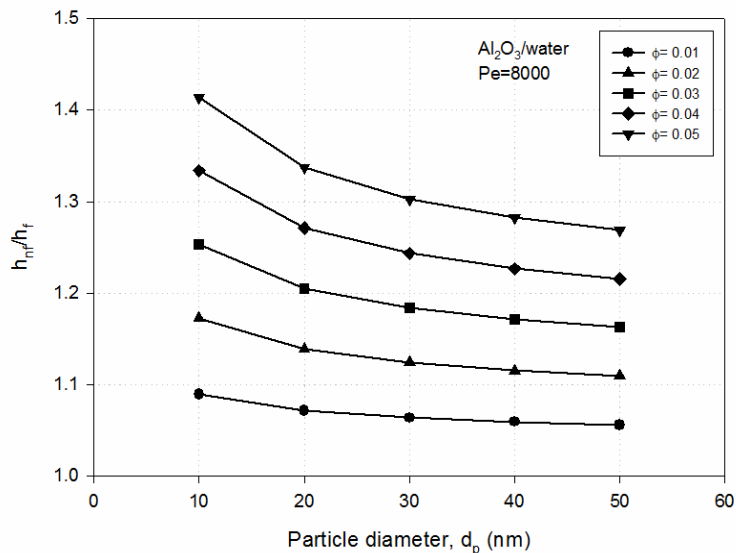


Fig. 5. Enhancement in average heat transfer coefficient at different particle diameters (constant Peclet number)

### Turbulent Nanofluid Flow Analyses

In turbulent nanofluid flow analyses; effects of Reynolds number, volume fraction, and particle diameter are investigated. As in the laminar flow analyses, average heat transfer coefficient ratios of the nanofluid to pure water are represented for three different cases in this section.

When Fig. 6 is observed, heat transfer enhancement decreases slightly with increasing Reynolds number for constant volume fraction. On the other hand, heat transfer enhancement significantly increases with increasing volume fraction at constant Reynolds number. This can be explained with the thermal conductivity enhancement in the nanofluid.

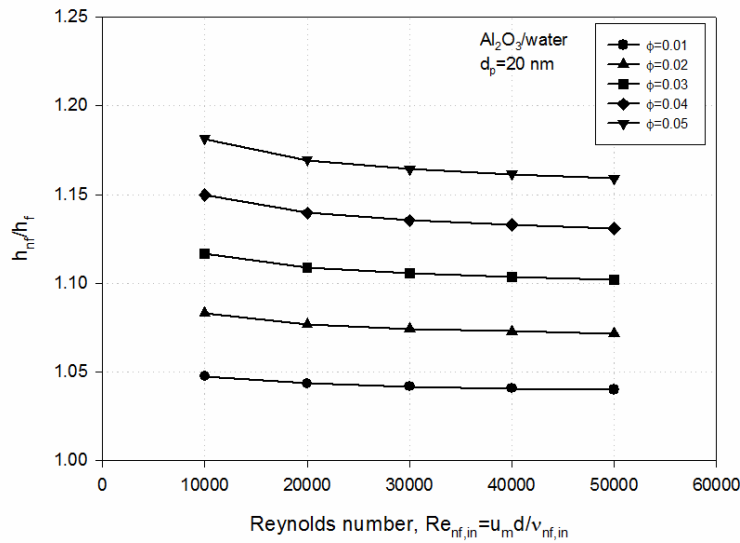


Fig. 6. Enhancement in average heat transfer coefficients at different inlet Reynolds numbers (constant particle diameter)

Fig. 7 presents the variation of enhancement ratio with Reynolds number at different particle diameters. Again, it represents Koo & Kleinstreuer [8] model because particle diameter increment decreases heat transfer enhancement. Similar to Fig. 7, an increase in Reynolds number has a slight negative effect in heat transfer enhancement with nanofluids.

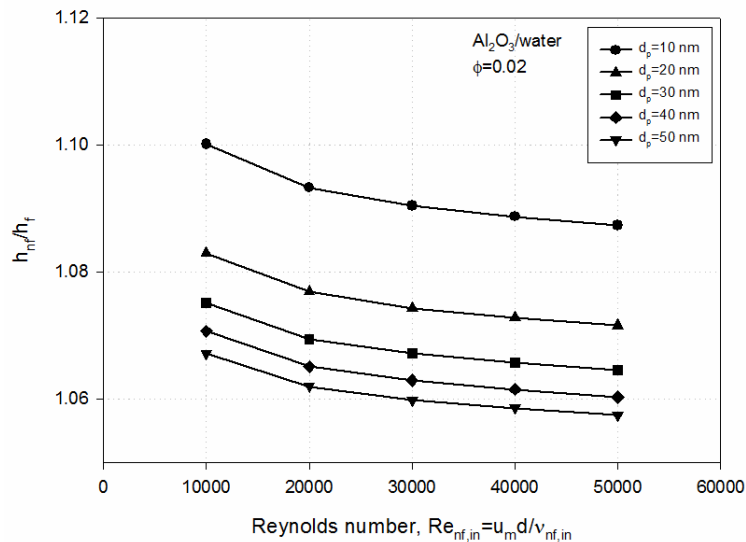


Fig. 7. Enhancement in average heat transfer coefficient at different inlet Reynolds numbers (constant volume fraction)

In Fig. 8, the variation of enhancement ratio with particle diameter is given for different particle volume fraction values. As it can be seen, the heat transfer enhancement is inversely proportional to the increase in

particle size. In other words, smaller particle sizes provide larger enhancement due to effect of Brownian motion in Koo & Kleinstreuer model [8].

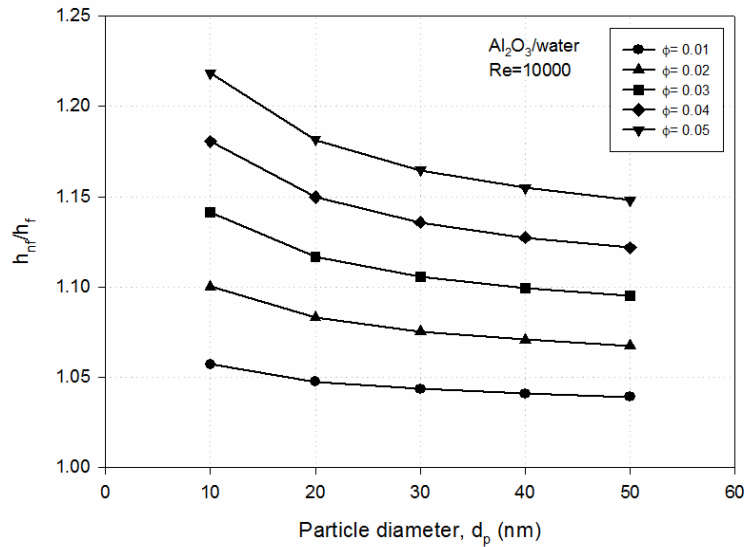


Fig. 8. Enhancement in average heat transfer coefficients at different particle diameters (constant inlet Reynolds number)

A combined plot of average heat transfer coefficient variation with Peclet number for laminar and turbulent flow regimes is presented in Fig. 9. Heat transfer coefficient increases with increasing Peclet number but enhancement ratio remains almost constant for the laminar flow (Fig. 3) because of the increase in heat transfer coefficient of the pure fluid at the same time. For the turbulent flow (Fig. 6), enhancement ratio decreases since pure water heat transfer characteristics are also enhanced by the eddy diffusivity with increasing Peclet numbers and it has more influence on heat transfer mechanism than the effect of nanoparticle conductivity.

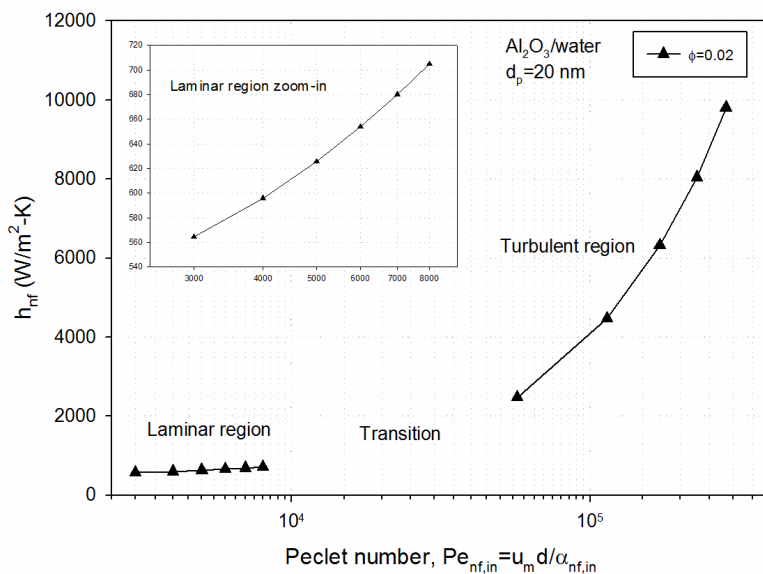


Fig. 9. Average heat transfer coefficient at different flow regimes with respect to inlet Peclet numbers (constant particle diameter and volume fraction)

## CONCLUSION

Convective heat transfer enhancement with nanofluids is investigated in laminar and turbulent flow regimes under the constant wall temperature boundary condition. The effects of particle volume fraction, particle diameter, Peclet and Reynolds numbers on heat transfer enhancement are analyzed. Temperature dependency of thermal conductivity of water and conductivity enhancement due to Brownian motion are considered. In the simulations, nanofluid Peclet and Reynolds numbers are changed by changing mean velocity term, i.e., Reynolds number is increased by increasing mean velocity for constant volume fraction, particle diameter and tube diameter.

As a result of the simulations, a considerable increase in enhancement is observed with increasing particle volume fractions both for laminar and turbulent flows, since it increases thermal conductivity of the nanofluid. Lower heat transfer enhancements are obtained with increasing particle diameters, because of the attenuation in Brownian motion of the nanoparticles. Particle diameter has a significant effect on enhancement especially in small particle diameter ranges.

Effect of flow velocity (Peclet and Reynolds numbers) on enhancement requires special concern by virtue of the difference in trends observed in laminar and turbulent flow simulations. Although enhancement ratio remains the same with increasing Peclet numbers for laminar flow, it decreases with increasing Reynolds numbers for the turbulent one. The reason of this may be the drop in bulk mean temperature of the flow, since the mass flow rate is very high at higher Reynolds numbers and heat is removed with a smaller bulk temperature. This may cause a decrease in nanofluid thermal conductivity resulting in a decrease in the enhancement ratio. Because laminar flow Peclet number ranges between 3000–8000, which causes relatively low difference in mean velocity, it may not be observed in laminar flow regime. Another explanation of this case may be already enhanced heat transfer characteristics of the flow because of the eddies which also exist in pure water flow.

It can be concluded that particle diameter decrement and volume fraction increment affect heat transfer coefficient positively. However, one should be careful about aggregation of nanoparticles [16], which is not in the scope of this work.

## Acknowledgements

The authors wish to thank the Scientific and Technological Research Council of Turkey (TUBITAK) for financial support.

## Nomenclature

$c_p$	specific heat capacity, J/(kg·K)	$\varepsilon_h$	eddy diffusivity of heat, m <sup>2</sup> /s
$d$	tube diameter, m	$\varepsilon_m$	eddy diffusivity of momentum, m <sup>2</sup> /s
$D$	total diffusivity, m <sup>2</sup> /s	$\theta$	dimensionless temperature
$d_p$	nanoparticle diameter, m	$\mu$	dynamic viscosity, Pa·s
$f$	friction factor	$\nu$	kinematic viscosity, m <sup>2</sup> /s
$h$	heat transfer coefficient, W/(m <sup>2</sup> ·K)	$\rho$	density, kg/m <sup>3</sup>
$k$	thermal conductivity, W/(m·K)	$\phi$	particle volume fraction
$L$	tube length, m	$\tau_w$	wall shear stress
$Nu$	Nusselt number, $hd/k$		
$Pe$	Peclet number, $u_m d/\alpha$	<b>Subscripts</b>	
$Pr$	Prandtl number, $\nu/\alpha$	$b$	bulk
$r$	radius, m	$eff$	effective
$r_0$	tube radius, m	$f$	base fluid
$Re$	Reynolds number, $\rho u_m d/\mu$	$fd$	fully developed
$T$	temperature, K	$i$	inlet
$u_m$	mean flow velocity, m/s	$nf$	nanofluid
$u_x$	axial flow velocity, m/s	$o$	outlet
		$p$	nanoparticle
		$t$	turbulent
<b>Greek letters</b>		$w$	wall
$\alpha$	thermal diffusivity, m <sup>2</sup> /s	$x$	local

### References

1. Masuda H., Ebata A., Teramae K., Hishinuma N. Alteration of thermal conductivity and viscosity of liquid by dispersing ultra-fine particles (dispersion of  $\gamma$ -Al<sub>2</sub>O<sub>3</sub>, SiO<sub>2</sub>, and TiO<sub>2</sub> ultra-fine particles) // *Netsu Bussei*. 1993. Vol. 4. Pp. 227–233.
2. Choi S.U.S. Enhancing thermal conductivity of fluids with nanoparticles, in: D.A. Siginer, H.P. Wang (eds) // *Developments and Applications of Non-Newtonian Flows*, New York. 1995. FED-Vol. 231, MD-Vol. 66. Pp. 99–105.
3. Eastman J., Choi S.U.S., Li S., Thompson L., Lee S. Enhanced thermal conductivity through the development of nanofluids // *Proceedings of the Symposium on "Nanophase and Nanocomposite Materials II"*, Materials Research Society, Boston, MA, 1997. Pp. 3–11.
4. Li Q., Xuan Y. Convective heat transfer and flow characteristics of Cu-water nanofluid // *Science in China Series E: Technological Sciences*. 2002. Vol. 45 (4). Pp. 408–416.
5. Maïga S.E.B., Nguyen C.T., Galanis N., Roy G. Heat transfer behaviours of nanofluids in a uniformly heated tube // *Superlattices and Microstructures*. 2004. Vol. 35 (3-6), Pp. 543–557.
6. Maxwell J. C., *A Treatise on Electricity and Magnetism*, Clarendon Press, Oxford, 1873.
7. Hamilton R. L., Crosser O. K. Thermal conductivity of heterogeneous two-component systems // *Ind. Eng. Chem. Fund.* 1962. Vol. 1(3). Pp. 187–191.
8. Koo J., Kleinstreuer C. A new thermal conductivity model for nanofluids // *J. Nanopart. Res.* 2004. Vol. 6(6). Pp. 577–588.
9. von Karman T. The Analogy between Fluid Friction and Heat Transfer // *Trans. ASME*. 1939. Vol. 61. Pp. 705–710.
10. Filonenko G.K.. Hydraulic Resistance in Pipes (in Russian) // *Teploenergetika*. 1954. Vol. 1 (4). Pp. 40–44.
11. Duangthongsuk W., Wongwises S. An experimental study on the heat transfer performance and pressure drop of TiO<sub>2</sub>-water nanofluids flowing under a turbulent flow regime // *Int.J. of Heat and Mass Transfer*. 2009. Vol. 53. Pp. 334–344.
12. Corcoran, W. H., Opfell J. B., Sage B. H. *Momentum Transfer in Fluids*, Academic Press Inc. Publishers, New York, 1956.
13. B.E. Launder, D.B. Spalding. *Lectures in Mathematical Models of Turbulence*, Academic Press, London, 1972.
14. Kakaç S., Yener Y., *Convective Heat Transfer*, 2nd edition, CRC Press, 1994.
15. Gnielinski V. New equations for heat and mass transfer in turbulent pipe and channel flow // *International Chemical Engineering*. 1976. Vol. 16. Pp. 359–68.
16. Xuan Y, Li Q, Hu W. Aggregation structure and thermal conductivity of nanofluids // *AIChE J.* 2003. Vol. 49 (4). Pp. 1038–1043.

## DEVELOPMENT OF CHEMICAL HEAT PUMP FOR RECOVERY OF WASTE HEAT AT MIDDLE TEMPERATURES OF 200~400°C

Yukitaka Kato, Rui Takahashi, Toshiya Sekiguchi, Naoya Hirao, Junichi Ryu

Research Laboratory for Nuclear Reactors

Tokyo Institute of Technology

2-12-1-N1-22, Ookayama, Meguro-ku, Tokyo 152-8550, Japan

Tel/Fax +81 3 5734 2967; E-mail: yukitaka@nr.titech.ac.jp

### Abstract

Chemical heat storage materials which can store waste heat at medium-temperature around 200~400°C was discussed. The performances of materials were evaluated thermodynamically and experimentally. Waste heats around 200~400°C are emitted as exhaust gases from internal combustion engine, co-generation, high-temperature process and solar systems. Amount of exhaust gas emission is quite large, and needed to utilize well for energy efficiency improvement. Waste heat storage function for medium-temperature heat becomes important for an efficient operation of high-temperature processes. Magnesium oxide/water (MgO/H<sub>2</sub>O) chemical heat pump is a candidate for medium-temperature heat storage. On the other hand, MgO/H<sub>2</sub>O system still needs relatively higher decomposition (dehydration) temperature of around 350°C. Chemical reaction systems for the chemical heat pump were surveyed thermodynamically. A mixed hydroxide, Mg<sub>α</sub>Co<sub>1-α</sub>(OH)<sub>2</sub>, which was mixed with magnesium hydroxide, Mg(OH)<sub>2</sub>, and cobalt hydroxide, Co(OH)<sub>2</sub>, was one of candidates of the middle heat storage material at lower than 300°C. The material performance was demonstrated by thermo-balance and packed bed analysis. It was shown that mixed material technology was useful for chemical heat pumps for the medium-temperature heat utilization.

### KEYWORDS

Chemical heat pump, waste heat recovery, magnesium oxide, cobalt oxide, water, middle temperature, internal combustion engine

### INTRODUCTION

Waste heats around 200~400°C, which are defined as medium-temperatures in this paper, are emitted as exhaust gases from internal combustion engine, co-generation, high-temperature process and solar systems. Amount of exhaust gas emission is quite large, and needed to utilize well for energy efficiency improvement.

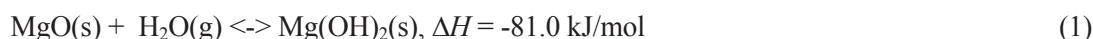
Waste heat recoveries from high-temperature processes are well developed for heat at over 400°C by steam and gas turbines, and also at less 100°C by sensible and latent heat storage technologies. On the other hand, medium-temperature heat has not been utilized well. Efficient utilization of the medium-temperature heat would be one of important way for an improvement of energy efficiency of high-temperature processes.

Vehicle is one of key high-temperature systems. Number of vehicle production is still increasing in the world. Impact of vehicle usage on carbon dioxide emission is important subject for global warming phenomena. Energy conversion efficiency from fuel to driving work in vehicle is around 20% in enthalpy-base, and rest 80% of energy is emitted as exhaust heats via exhaust gas and radiator coolant as shown in Fig. 1 [1]. Although huge efforts have already made for the improvement of engine efficiency, the efficiency has already attained at almost mechanical upper-limitation. On the other hand, vehicle still has room for energy efficiency improvement at heat management. Thermal energy storage (TES) technologies are possible to contribute on fuel efficiency by utilization of excess heat emitted as an exhaust gas from a muffler and an effluent coolant from an engine jacket cooler.

Fuel cell or battery vehicles are expected for the next generation automobile. The vehicles lack thermal energy sources for cabin air-conditioning. The lack induces a depression of total energy efficiency for the vehicles. Preliminary TES at a stationary plant with high-efficiency and by charging TES material into vehicle is useful for cabin air-conditioning. TES technologies application on vehicle has big-potential for effective fuel consumption and CO<sub>2</sub> emission reduction. Medium-temperature heat recovery is important for not only vehicle, but also cogeneration engines, solar power system and high-temperature processes. For heat

process in practical use, an influence of instable thermal operations on a reduction of total energy efficiency is not negligible. For a cogeneration engine in practical use, a mismatch between heat output from engine and heat demand generates plenty amount of waste heat to atmosphere. Then, waste heat storage function for medium-temperature heat becomes important for an efficient operation of high-temperature processes. Then, feasibilities of TES technology using chemical reaction for the middle temperature were discussed in this paper.

Chemical heat pump has possibility to establish the thermal hybrid system by chemical heat storage of medium-temperature heats. However, there were small candidates which could be operated at medium-temperature range except magnesium oxide/water (MgO/H<sub>2</sub>O) chemical heat pump [2].



On the other hand, although MgO/H<sub>2</sub>O system has high reactivity, the reaction system is needed relatively higher decomposition (dehydration) temperature of around 350°C. Chemical reaction systems for the chemical heat pump for heats at lower-temperature less than 300°C were surveyed thermodynamically. Ryu had proposed new heat storage material methodology by mixing of metal hydroxides for heat recovery under 300°C [3]. The material is required to be used in a reactor bed for practical application. Then, the thermal performances of materials developed by using the methodology were discussed experimentally in a packed bed reactor in this study.

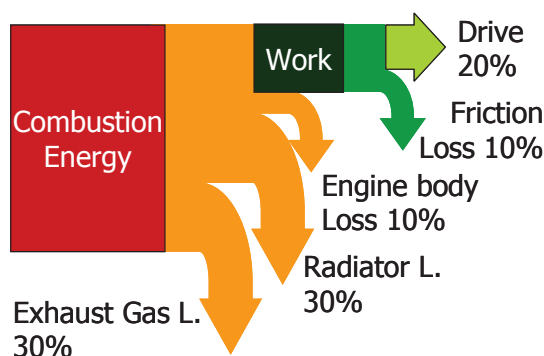


Fig. 1 Enthalpy balance of a vehicle driven by internal combustion engine [1].

## PROPOSAL OF A HYBRID SYSTEM WITH A CHEMICAL HEAT PUMP AND A HIGH-TEMPERATURE PROCESS

An electric hybrid system (EHS), which combines an internal combustion engine (ICE) with an electrical battery and a power controller as shown in Fig. 2, has good energy saving performance. Upon braking, the EHS kinetically converts surplus work into electricity, which is stored in the electrical battery. The stored electricity is used to start the vehicle or to assist during a period of low-efficient operation of the ICE. Such a method is particularly effective for vehicles used for city driving or commuting. Total efficiency is double compared to a conventional ICE vehicle. The authors are proposing a thermal hybrid system (THS) that combines an ICE with a thermal battery and a thermal power controller for efficient use of exhaust heat from ICE as shown in Fig. 1 in comparison with the EHS. The thermal battery in THS is used for heat storage of surplus exhaust heat from ICE. The stored heat in the thermal battery is supplied to heat output side for tasks such as cold start, catalyst heating for exhaust gas reduction and vehicle cabin heating. The THS is expected to contribute to load leveling of ICE operation, improvement of fuel consumption efficiency, and reduction of CO<sub>2</sub> emission. The THS concept can also be applied to the cogeneration engine and solar thermal power systems. To realize the THS, medium-temperature heat storage capability is required in the system. Heat storage of waste heat is possible by

using sensible and latent heat storage. However, from the standpoint of heat quality (exergy) recovery, these storage methods are insufficient for the storage of medium-temperature heat because of upper limitation of heat storage temperature and temporal diffusivity of stored heat. Heat storage for medium-temperature may be accomplished by means of a chemical heat pump, which enables longer term heat storage, higher energy storage density, and a wider variety of operation temperature ranges by selecting the reaction conditions, as compared to sensible and latent heat storage methods.

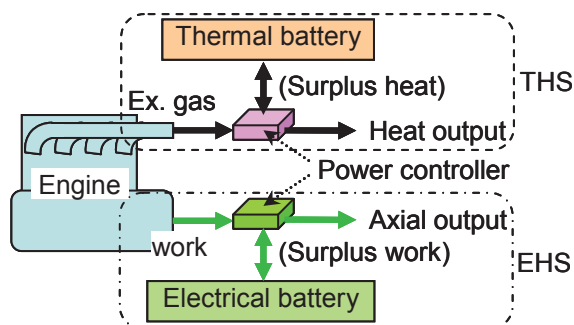


Fig. 2 Concept of electricity and thermal hybrid systems for an internal combustion engine.

## MIXED HYDROXIDES OF HEAT STORAGE MATERIALS FOR MEDIUM-TEMPERATURE CHEMICAL HEAT PUMPS

The chemical heat pump may be useful in managing medium-temperature heat. However, there have been few previous studies on chemical heat pumps for this temperature range [2]. The temperature applicability of a chemical heat pump depends on the chemical reaction in the heat pump.

The authors attempted to thermodynamically survey chemical reaction systems for the chemical heat pump. The candidate reactions for the medium-temperature heat pump are required to have high-reaction selectivity for the main reaction, lower risk on flammability and toxicity, and compressibility and compactness of reactants. Based on our survey, metal oxide/water reaction systems were selected as the most promising candidate. The reaction of metal oxide with divalent cation is written as follows:



The thermodynamic relationship between the water vapor pressure ( $P_{\text{H}_2\text{O}}$  [Pa]) and the reaction temperature ( $T$  [K]) is given as follows:

$$P_{\text{H}_2\text{O}} = P_0 \exp\left(\frac{-\Delta G}{RT}\right) = P_0 \exp\left(\frac{-\Delta H}{R} \frac{1}{T} + \frac{\Delta S}{R}\right) \quad (2)$$

Where

$$P_0 = 1.013 \times 10^5 \text{ Pa} \quad (3)$$

and  $\Delta G$  [J mol<sup>-1</sup>] and  $\Delta S$  [J mol<sup>-1</sup> K<sup>-1</sup>] are the Gibbs free energy change and entropy change for the reaction, respectively, and  $R$  [J mol<sup>-1</sup> K<sup>-1</sup>] is the gas constant.

The plots of Eq. 2 for some metal oxide/water vapor reaction systems, which are defined as reaction equilibrium lines, are shown in Fig. 3 [4]. The temperature under  $P_{\text{H}_2\text{O}}$  at atmospheric pressure is defined as the dehydration temperature. At the temperature region around the dehydration temperature, both hydration and dehydration tend to be reversible, and a chemical heat pump operation using the reaction could be established.

From the thermodynamic survey of reaction systems using the equilibrium lines, nickel oxide, cobalt oxide, and other metal oxides appear to have potential as new reaction systems for the chemical heat pump at medium

temperature. However, those oxides have generally low reactivity with water vapor. On the other hand, magnesium oxide, MgO, has high reactivity, although magnesium hydroxide, Mg(OH)<sub>2</sub>, has a higher decomposition (dehydration) temperature of around 350°C

As such, the authors proposed the mixed hydroxide candidates containing magnesium hydroxide for use in the medium-temperature chemical heat pump [3].

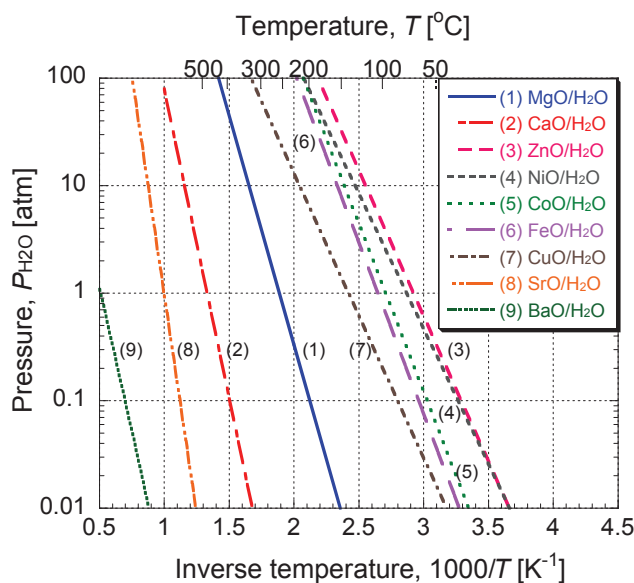


Fig. 3 Reaction equilibria of some metal oxide/water reaction systems.

## DIFFERENTIAL REACTIVITY STUDY USING THERMO-BALANCE

Mixed hydroxides of cobalt hydroxide, Co(OH)<sub>2</sub>, and Mg(OH)<sub>2</sub> on the atomic level, Mg<sub>α</sub>Co<sub>1-α</sub>(OH)<sub>2</sub>, were prepared by a co-precipitation method as new chemical heat storage materials. Here, α denotes the molar fraction of magnesium ion to total metal cation in a mixed hydroxide.

The differential reactivity of the hydroxide materials was investigated using a thermo-balance. The thermal decomposition curves of the mixed hydroxide, Mg<sub>0.5</sub>Co<sub>0.5</sub>(OH)<sub>2</sub>, and a physical mixture of Mg(OH)<sub>2</sub> - Co(OH)<sub>2</sub> (prepared from authentic hydroxide powders) are shown in Fig. 4 for a rate of temperature increase of 5 °C·min<sup>-1</sup> and in Argon flow. The ordinate shows the mass change during decomposition. The physical mixture has a two-step dehydration curve because the hydroxides decomposed independently. On the other hand, the mixed hydroxide has a single-step dehydration curve. This indicates that the mixed hydroxide forms a new phase, such as a solid solution, and has a unique thermochemical property.

Fig. 5 shows the effect of α on the decomposition curve of Mg<sub>α</sub>Co<sub>1-α</sub>(OH)<sub>2</sub>. The ordinate, x, shows the reacted fraction. The fully hydrated and dehydrated states are shown by x = 100% and 0%, respectively. The decomposition curves shifted to lower temperatures with decreasing α. The decomposition temperature decreased from 320°C for Mg(OH)<sub>2</sub> to around 190°C for Mg<sub>0.25</sub>Co<sub>0.75</sub>(OH)<sub>2</sub>. Pure Co(OH)<sub>2</sub> showed different profile for the decomposition. It was thought that pure Co(OH)<sub>2</sub> would contain not only CoO and also Co<sub>2</sub>O<sub>3</sub> in crystal. The results between α = 1.0 ~ 0.25 show that the decomposition temperature of Mg(OH)<sub>2</sub> can be reduced by the addition of cation in the hydroxide. The mixed hydroxide can expand operation heat storage temperature by changing the composition of the added cation in its. These results also show that Co(OH)<sub>2</sub> enhanced the reduction of the decomposition (= heat storage) temperature of the mixed hydroxide. The mixed hydroxides are expected to realize new medium-temperature chemical heat pump.

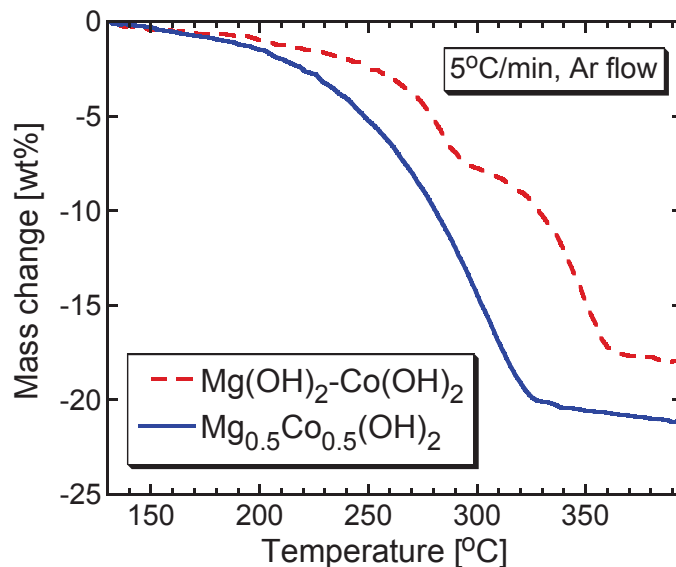


Fig. 4 Thermal decomposition (dehydration) curves of Mg<sub>0.5</sub>Co<sub>0.5</sub>(OH)<sub>2</sub> mixed hydroxide and a Mg(OH)<sub>2</sub> - Co(OH)<sub>2</sub> mixture.

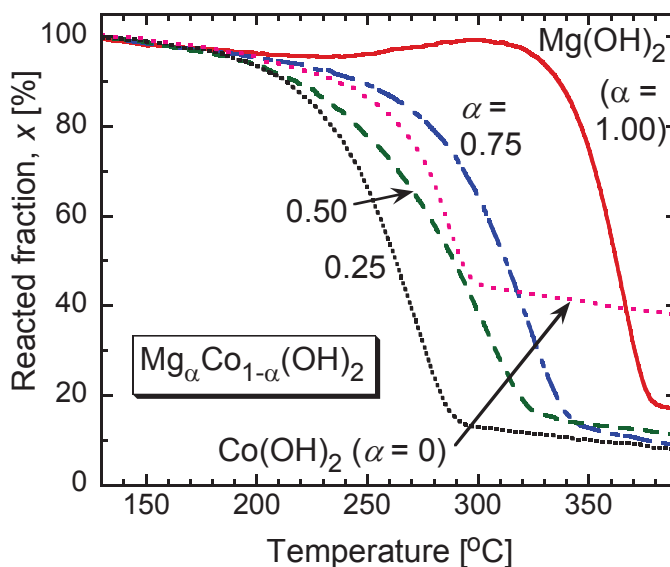


Fig. 5 Effect of  $\alpha$  on the thermal decomposition curves of mixed hydroxides of Mg <sub>$\alpha$</sub> Co<sub>1- $\alpha$</sub> (OH)<sub>2</sub>.

The hydration reactivity of Mg<sub>0.5</sub>Co<sub>0.5</sub>(OH)<sub>2</sub> and simple Mg(OH)<sub>2</sub> and under the same dehydration and hydration conditions is shown in Fig. 6. Both hydroxides were charged independently into the balance in hydroxide states and were dehydrated (decomposed) at 280°C under an Argon flow. These hydroxides were then hydrated at 110°C at a vapor pressure of 58 kPa and dehydrated again under the same conditions as the first dehydration. Simple Mg(OH)<sub>2</sub> was only slightly decomposed at 280°C, and a small amount of MgO was generated. Then, the amount of reacted fraction at hydration,  $\Delta x_h$ , was 3%. Simple Mg(OH)<sub>2</sub> is not applicable as a heat pump material at 280°C. On the other hand, Mg<sub>0.5</sub>Co<sub>0.5</sub>(OH)<sub>2</sub> was well dehydrated at 280°C, and a mixed metal oxide was generated. As a result, the amount of reacted fraction at hydration,  $\Delta x_h$ , reached 43%. Mg<sub>0.5</sub>Co<sub>0.5</sub>(OH)<sub>2</sub> is demonstrated to be applicable to heat storage operation in the chemical heat pump at approximately 280°C. After hydration, the vapor supply was stopped. Saturated water adsorbed physically on

the material was then desorbed from the material, and the reacted fraction was decreased and reached a water desorbed equilibrium state. The amount of physically adsorbed water was derived from the change between after-hydration state and the water desorbed equilibrium state. After the water desorption, the reaction temperature was increased to the dehydration temperature, and the chemical dehydration of  $\text{Mg}(\text{OH})_2$  was measured. The saturated reacted fraction of the second dehydration was similar to that of the first dehydration. Then, it was expected that the dehydration would have reproduce ability in cyclic operation.

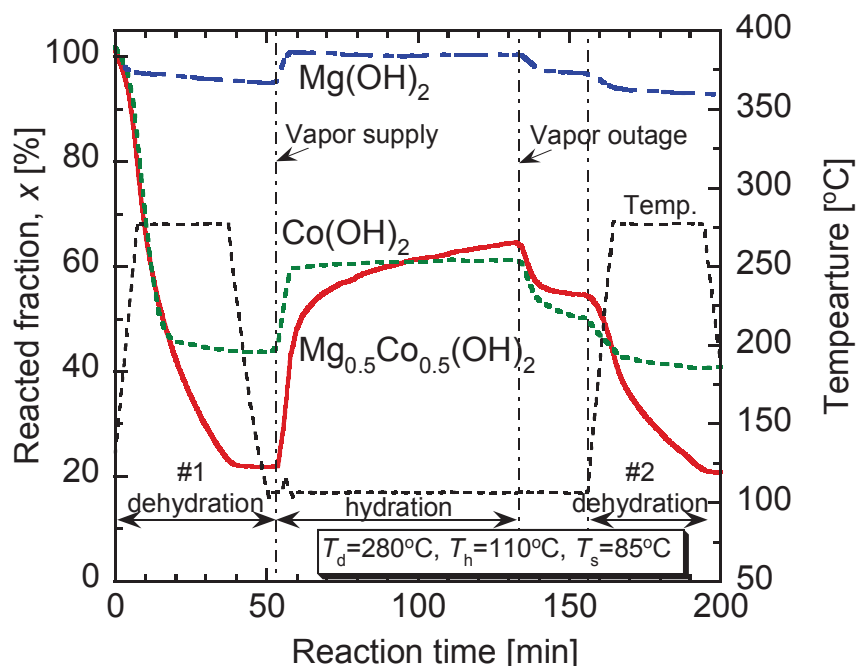


Fig. 6 Hydration reactivity of  $\text{Mg}_{0.5}\text{Co}_{0.5}(\text{OH})_2$  mixed hydroxide and simple  $\text{Mg}(\text{OH})_2$  under the same dehydration and hydration conditions.

The hydration heat of  $\text{Mg}_{0.5}\text{Co}_{0.5}(\text{OH})_2$ , which corresponds to the heat storage capacity of the material, was estimated from the results shown in Fig. 6. It was assumed that the hydration heat consisted of physical water sorption and chemical hydration. The amount of physical adsorbed water was derived from the physical water desorption at the second dehydration. The amount of chemical hydration was derived by subtracting a fraction of the physical adsorbed water from the total reacted fraction amount of hydration. It was also assumed that the chemical hydration enthalpy is directly proportional to the mixing ratio between enthalpies of pure  $\text{Mg}(\text{OH})_2$  and pure  $\text{Co}(\text{OH})_2$ . The heat storage capacity of  $\text{Mg}_{0.5}\text{Co}_{0.5}(\text{OH})_2$  was estimated to be  $358 \text{ kJ} (\text{kg-Mg}_{0.5}\text{Co}_{0.5}(\text{OH})_2)^{-1}$  under the operation condition of Fig. 6.

Mixed material of  $\text{Mg}_{0.5}\text{Ni}_{0.5}(\text{OH})_2$  had been synthesized by the same procedure and discussed in previous study [5]. The material has higher hydration reactivity than pure  $\text{Mg}(\text{OH})_2$  at lower than  $300^\circ\text{C}$ . It was reported that  $\text{Mg}_{0.5}\text{Ni}_{0.5}(\text{OH})_2$  had the amount of reacted fraction at hydration,  $\Delta x_h$ , reached 26%, and was estimated the heat storage capacity of  $170 \text{ kJ} (\text{kg-Mg}_{0.5}\text{Ni}_{0.5}(\text{OH})_2)^{-1}$  under the same operation condition of Fig. 6. It was expected that  $\text{Mg}_\alpha\text{Co}_{1-\alpha}(\text{OH})_2$  had higher heat storage capability at middle temperature in comparison with  $\text{Mg}_\alpha\text{Ni}_{1-\alpha}(\text{OH})_2$  under some extent of reaction condition.

## INTEGRAL REACTIVITY STUDY USING A PACKED BED REACTOR

The integral reactivity of the developed mixed hydroxide was investigated using a packed bed reactor. The hydration reactivity under higher vapor pressures, at which the thermo-balance was not able to measure the reactivity, was primarily investigated. The experimental apparatus shown in Fig. 7 was used for the thermal

evaluation of the chemical heat pump ability. The apparatus consists of a packed bed reactor and a water reservoir. The reactor was made from SUS304 steel and had an inner diameter of 11.6 mm and a length of 100 mm. As reactant, 10.0 g of  $\text{Mg}_{0.5}\text{Co}_{0.5}(\text{OH})_2$  was charged into the reactor. The bed temperature,  $T_b$ , was monitored by a thermocouple positioned in the center of the bed. The hydroxide material,  $\text{Mg}_{0.5}\text{Co}_{0.5}(\text{OH})_2$ , was dehydrated at 330°C by joule heating using a ribbon heater wrapped around the reactor under 5–10 kPa with a vacuum pump operation. In a previous thermo-balance study, it was shown that dehydration proceeded at approximately 280°C. However, in order to ensure completion of the dehydration, the reactant was dehydrated at higher temperature. After the dehydration process, the bed was cooled to the initial bed temperature which was 40°C higher than one of steam temperature for hydration. When the bed reached a stable state at the initial temperature, joule heating was discontinued, and water vapor at the target pressure was supplied to the reactor. The change in the bed temperature,  $T_b$ , was then monitored during the hydration period.

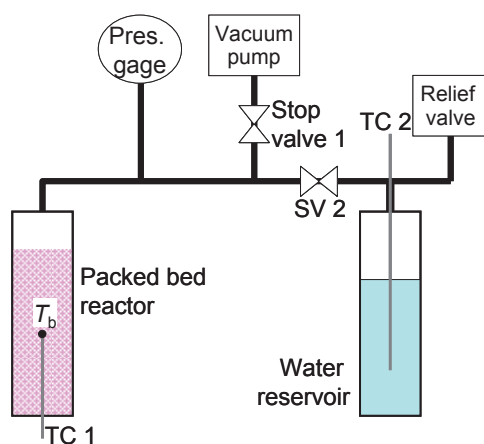


Fig. 7 Experimental packed bed apparatus for evaluation of chemical heat pump capacity.

The effect of hydration pressure on the temporal profile of the bed temperature is shown in Fig. 8. Vapor temperatures of 85, 12, 160°C, which corresponding to steam pressures ( $P_s$ ) of 57.8, 198, and 618 kPa, respectively, were introduced into the reactor during three runs. At a vapor pressure of 618 kPa, the reactor bed temperature reached 245°C and the temperature decreased gradually. At  $P_s$  of 57.8, 198, the bed temperatures kept constant values. It means that hydration heat from reactant and heat dispersion from bed to atmosphere was balanced during the hydration period.

Fig. 9 shows a relationship between the maximum attained temperature for hydration and reaction equilibrium. Attained maximum temperatures were located between equilibrium lines of  $\text{Mg}(\text{OH})_2/\text{MgO}$  and  $\text{Ca}(\text{OH})_2/\text{CaO}$ . It was possible to assume that the maximum temperature is apparent equilibrium temperature of the hydration of  $\text{Mg}_{0.5}\text{Co}_{0.5}(\text{OH})_2$ , the inverse of the maximum temperature tended to show monotonous change to pressure in logarithm. It was concluded that the apparent hydration temperature was controllable by select of hydration steam pressure. Hydration temperature over 300°C which was higher than dehydration temperature in thermo-balance measurement was expected to be capable at steam pressure over 1.0 MPa. It was expected that  $\text{Mg}_{0.5}\text{Co}_{0.5}(\text{OH})_2$  chemical heat pump would realize heat transformation operation, in which hydration temperature was higher than dehydration temperature, by selecting operation condition. Pure  $\text{Mg}(\text{OH})_2$  requires around 350°C for dehydration, then it is hard to realize heat transformation operation [6]. The mixed hydroxide showed new possibility of chemical heat pump for utilization of waste heat at medium temperature.

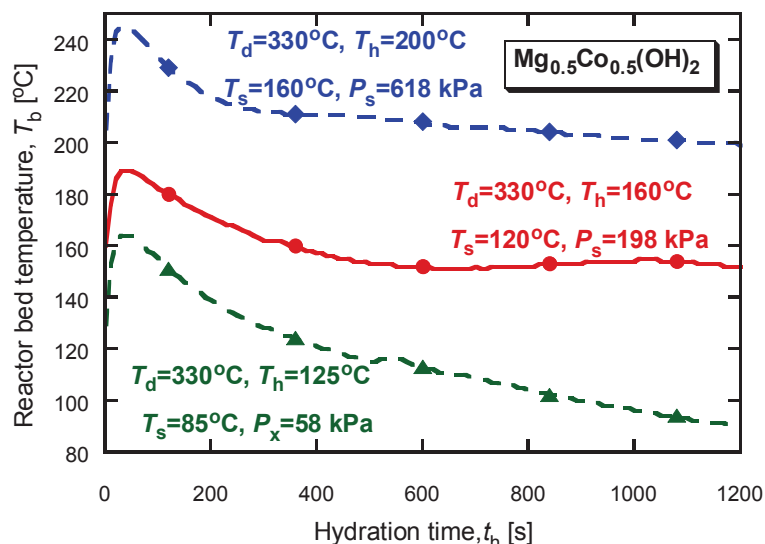


Fig. 8 Effect of hydration pressure on the temporal profile of the bed temperature.

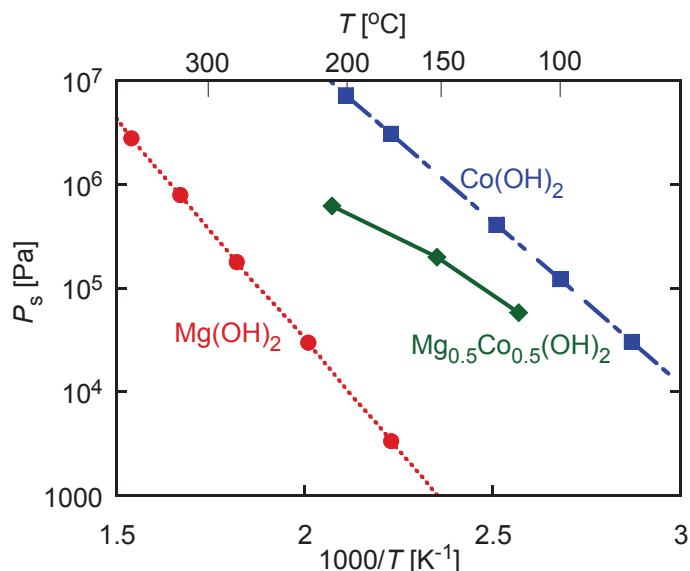


Fig. 9 Relationship between the maximum attained temperature for hydration and reaction equilibrium.

## CONCLUSIONS

Mixed hydroxides of chemical heat storage materials, which can store medium-temperature waste heat at approximately 200~300°C, were newly developed. The mixed hydroxide performance was demonstrated in a packed bed reactor.

Waste heats of approximately 200~300°C are emitted as exhaust gases from internal combustion engines.  $\text{Mg}_\alpha\text{Co}_{1-\alpha}(\text{OH})_2$ , which are mixed hydroxides of magnesium hydroxide,  $\text{Mg}(\text{OH})_2$ , and cobalt hydroxide,  $\text{Co}(\text{OH})_2$ , are candidate mixed hydroxide materials for medium-temperature heat storage. It was demonstrated that the mixed hydroxide was capable of storing heat at 200~300°C. The mixed hydroxide expands the operation temperature for heat storage by changing the composition of the mixed hydroxide. The mixed hydroxide was dehydrated, that is, the hydroxide was capable of storing heat at 200~300°C, at which simple  $\text{Mg}(\text{OH})_2$  could not be dehydrated, i.e., could not store heat. The chemical heat output performance of the

mixed hydroxide was demonstrated in a packed bed reactor. The heat capacity of  $\text{Mg}_{0.5}\text{Co}_{0.5}(\text{OH})_2$  was estimated to be  $358 \text{ kJ}\cdot(\text{kg}\cdot\text{Mg}_{0.5}\text{Co}_{0.5}(\text{OH})_2)^{-1}$  from a thermo-balance measurement which was higher than one of  $\text{Mg}_{0.5}\text{Ni}_{0.5}(\text{OH})_2$  which was synthesized by the same procedure. It was expected that  $\text{Mg}_{0.5}\text{Co}_{0.5}(\text{OH})_2$  chemical heat pump would realize heat transformation operation, which hydration temperature was higher than dehydration temperature, by selecting operation condition.

The use of mixed hydroxide revealed the possibility of using medium-temperature heat in a chemical heat pump and demonstrated the feasibility of a hybrid system combining a medium-temperature chemical heat pump and a high-temperature process for efficient primary energy use.

### Acknowledgements

The present study was supported in part by a Grant-in-Aid for Scientific Research (#20360428) from the Ministry of Education, Science, Sports, and Culture of Japan.

### Nomenclature

$T$	Temperature [K] or [ $^{\circ}\text{C}$ ]
$t$	Reaction time [s]
$P$	Pressure [Pa]
$P_0$	Standard pressure ( $1.013 \times 10^5$ kPa)
$R$	Gas constant ( $= 8.13 \text{ J mol}^{-1} \text{ K}^{-1}$ )
$x$	Reacted fraction [-]

### Greek

$\alpha$	Molar fraction of magnesium ion to total metal ion in a mixed hydroxide [-]
$\Delta G$	Gibbs free energy change [ $\text{J mol}^{-1}$ ]
$\Delta S$	Entropy change [ $\text{J mol}^{-1} \text{ K}^{-1}$ ]

### Subscript

H <sub>2</sub> O	water
h	hydration
s	water vapor

### References

1. K. Suzuki, Map 11: Technology Road Map for Thermal Energy Management in Vehicles, *HONEBUTO Energy Road Map (Honebuto no Energy Road Map)*, pp. 105-113, H. Kameyama and Y. Kato ed., Kagaku-Kogyo-Sha, Tokyo, Japan (2005)
2. Y. Kato, N. Yamashita, K. Kobayashi and Y. Yoshizawa, Kinetic study of the hydration of magnesium oxide for a chemical heat pump, *Applied Thermal Engineering*, 16, pp. 853-862 (1996).
3. J. Ryu, R. Takahashi, N. Hirao and Y. Kato, Effect of Transition Metal Mixing on Reactivities of Magnesium Oxide for Chemical Heat Pump, *J. Chem. Eng. Japan*, 40, pp. 1281-1286 (2007).
4. Chemical Society of Japan, Chemical Handbook, Basics II, 287, Maruzen, Tokyo, Japan (2004).
5. Y. Kato, R. Takahashi, T. Sekiguchi, J. Ryu; "Study on medium-temperature chemical heat storage using mixed hydroxides", *J. Intn'l J of Refrigeration*, 32(4), pp. 661-666 (2009).
6. Y. Kato, T. Oshima and Y. Yoshizawa, Thermal Performance of a Packed Bed Reactor for a High-Temperature Chemical Heat Pump, *Int. J. Energy Research*, 25, pp. 577-589 (2001).

## OPTIMISATION OF ADSORPTION DYNAMICS IN ADSORPTIVE HEAT TRANSFORMERS: EXPERIMENT AND MODELING

**Yuriy I. Aristov**

Laboratory of Energy Accumulating Processes and Materials  
Boreskov Institute of Catalysis, Siberian Branch of the Russian Academy of Sciences  
Pr. Lavrentieva 5, Novosibirsk, 630090, Russia  
Tel/Fax: +7 383 330 95 73; E-mail: aristov@catalysis.ru

### Abstract

An "adsorbent-heat exchanger" (Ad-HEX) unit is a core of any adsorptive heat transformer (AHT), and its efficient performance is of prime importance. In this lecture, we present recent advances in understanding and trends in studying the adsorption dynamics. Dynamic experiments have been performed in laboratory Ad-HEX units which closely imitate the conditions of isobaric stages of AHT when desorption (adsorption) is initiated by a fast jump (drop) of the temperature of a heat exchanger wall which is in thermal contact with the adsorbent layer (Large Temperature Jump Method, LTJM). All results concern configuration of Ad-HEX with one, two or four layers of loose adsorbent grains. Water, methanol and ammonia are used as adsorbates. Mathematical model of coupled heat and mass transfer during isobaric adsorption process developed in the Moscow State University (for monolayer configuration) has been used for detailed dynamical analysis and extracting the heat and mass transfer coefficients. Finally, several recommendations followed from the LTJM study have been checked with a prototype of adsorptive chiller in ITAE-CNR. These tests clearly demonstrated that dynamic performance of AHT can be significantly improved by a proper management of AHT cycle (reallocation of relative durations of isobaric adsorption and desorption phases, optimization of the cycle time and the conversion degree, etc.). The most important findings and general regularities that have been revealed as result of the LTJM application for systematic studying the adsorption dynamics of water, methanol and ammonia in AHT systems are summarized, illustrated and discussed in the paper.

### KEYWORDS

Adsorptive heat transformers, adsorption dynamics, Linear Driving Force model, diffusivity, coupled heat and mass transfer, Large Temperature Jump method, optimal adsorbent.

### INTRODUCTION

Adsorption technology has already become a key tool that is used pervasively in industry for well-established applications, such as gas separation and purification. Impressive progress has recently been made in a relatively new, although quite close to practice, application of adsorbents for heat transformation that includes cooling, heat pumping and heat storage. The current-state-of-the art in this specific application was presented in the recent book [1] and reviews (see e.g. [2–8]).

For analyzing dynamic behaviour of the adsorbent, it is obligatory to consider the adsorbent and heat exchanger (Ad-HEX) as an integrated unit and to study adsorption dynamics under real operating conditions of AHT [9]. This dynamics strongly affects the AHT performance and determines its specific power and compactness. Current methodologies as well as a novel experimental approach (the LTJM) for dynamic characterization and optimization of the Ad-HEX units was described in [10]. The LTJM closely imitates conditions of isobaric stages of AHT when desorption (adsorption) is initiated by a fast jump (drop) of the temperature of a heat exchanger wall which is in thermal contact with the adsorbent. This method provides a simple and efficient tool to investigate the effect of the adsorbent nature, its grain size, cycle boundary conditions, non-adsorbable gas, heating rate, shape of adsorption isobar, configuration of the "adsorbent-heat exchanger" system, etc. on the ad- and desorption dynamics under isobaric stages of AHT [10]. This dynamic study has been performed for promising adsorbents of water, namely, Fuji silica RD, FAM-Z02 and SWS-1L (silica modified by calcium chloride). Based on the results obtained demands to an adsorbent optimal for AHT from the dynamic point of view have been suggested.

A basic three temperature (3T) AHT cycle consists of two isosters and two isobars (Fig. 1 *a*) and is uniquely characterized by a set of the three boundary temperatures ( $T_e$ ,  $T_c$ ,  $T_{HS}$ ) where  $T_e$  is the evaporator

temperature,  $T_c$  is the condenser temperature and  $T_{HS}$  is the temperature of the external heat source. The uptake (release) temporal evolution  $q(t)$  *uniquely* characterizes the main dynamic features of isobaric stages “4→1” and “2→3” of AHT. These stages make the capital contribution to the Coefficient Of Performance (COP) and the Specific Cooling Power (SCP), while the isosteric stages “1→2” and “3→4” are short and less significant as a rule.

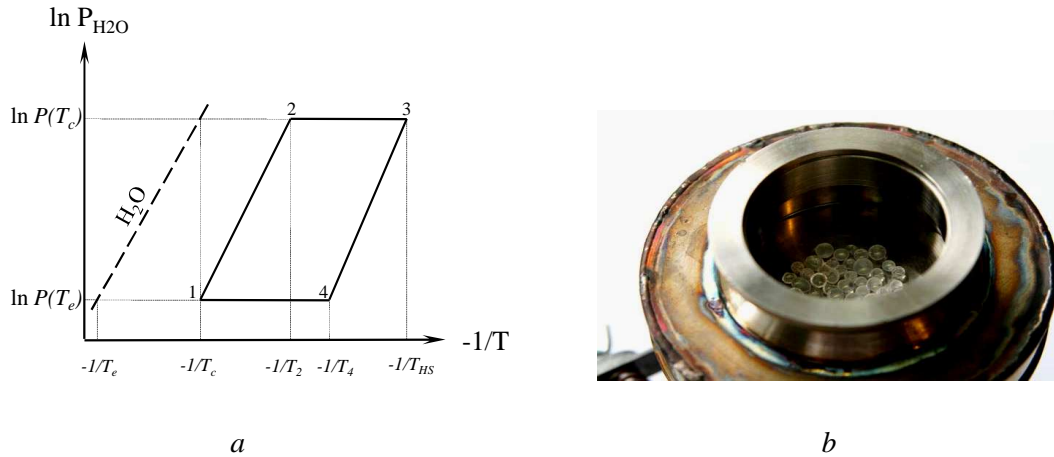


Fig. 1. Basic 3T cycle of AHP in the Clapeyron diagram (a), and the measuring cell with loose silica grains on the metal support exposed to temperature jump/drop (b)

At the moment two main concepts of Ad-HEX configuration can be clearly differentiated: a) n-layers of loose adsorbent grains contacted with HEX fins [11], and b) the fins surface coated with a consolidated sorbent layer [12]. Although the coating approach looks very encouraging [12], so far there is no experimental data which demonstrate that it is certainly superior to the loose grain concept. Moreover, recent experimental data obtained by the LTG method [13] demonstrated that quite acceptable values of the Specific Cooling Power (SCP) of 1–2 kW/(kg adsorbent) can be, in principle, obtained for multi-layers configuration of loose grains [10]. In our opinion, the choice between “loose grains” and “coated surface” concepts is still open and needs more theoretical and experimental analysis.

Here we focus on the adsorption dynamics for the loose grain configuration (Fig. 1 b) which is very simple in realization and ensures good intergrain vapour transport [14]. On the other hand, it is considered to suffer from a poor heat transfer both in the adsorbent layer and between the adsorbent grains and the HEX surface. Because of this, the layer should not be too thick and its optimization is strictly necessary as discussed below. It is worthy to mention that the loose grain configuration has been successfully realized in several prototypes [15–17] as well as commercial units [18, 19] of adsorption chillers.

Dynamic experiments have been performed in a laboratory Ad-HEX unit by LTJM. For a monolayer configuration, a mathematical model of coupled heat and mass transfer, developed in the Moscow State University [20], has been used to study the effect of the adsorption isobar shape on the sorption dynamics. For multi-layers configuration a novel approach has recently been realized in ITAE-CNR to extract the heat and mass transfer coefficients [21]. The system of partial differential equations was solved by using the COMSOL Multiphysics simulation environment. Finally, several recommendations followed from the LTG study have been checked with prototypes of adsorptive chiller in ITAE-CNR and of the University of Warwick [22–24]. These tests clearly demonstrated that dynamic performance of AHT can be significantly improved by a proper reallocation of durations of isobaric adsorption and desorption phases.

The aim of this lecture is to highlight the most important findings and general regularities that have been revealed as result of the LTJM systematic application for studying the adsorption dynamics of water, methanol and ammonia in AHT systems.

## ADSORPTION DYNAMICS IN MODEL AD-HEX UNITS

Adsorption (desorption) during isobaric stages of AHT cycle is initiated by a fast cooling (heating) of metal surface of heat exchanger. Hence, a study of the adsorption dynamics has to be performed under

similar conditions in order to make its appropriate characterization. Principle drawbacks of the common procedure (experimental determination of the necessary heat and mass transfer parameters → mathematical modeling of the adsorption dynamics) are discussed in [9]. The Large Temperature Jump method [13] was intently developed to avoid or, at least, to reduce these obstacles and to get dynamic information more appropriate to real AHT. Detailed experimental procedure can be found elsewhere [13, 26]. Adsorption was initiated by the temperature drop from  $T_4$  down to  $T_1$  ( $T_4 \rightarrow T_1$ ) at almost constant pressure  $P(T_c)$  (Fig. 1 a). Desorption was initiated by the temperature jump from  $T_2$  down to  $T_3 = T_{HS}$  ( $T_2 \rightarrow T_3$ ) at almost constant pressure  $P(T_c)$  (Fig. 1 a).

Since the first presentation [13], the LTGM has been systematically applied for loose grain configuration to investigate how the dynamics of water, methanol and ammonia adsorption is affected by adsorbent nature [10,25], its grain size [26,27], cycle boundary conditions [26–28], presence of a non-adsorbable gas [25, 29,30], heating rate [10], adsorption uptake [27], shape of adsorption isobar [31], adsorption driving temperature [28] and the number of the adsorbent layers  $n$  [10, 27]. Here we summarize and illustrate the main experimental findings and general regularities of adsorption dynamics which have been revealed so far as well as discuss some recommendations which could improve the dynamics of real AHT units.

The main experimental findings on AHT adsorption dynamics are as follows:

- the initial stage of ad-/desorption process follows exponential kinetics [9, 10, 13, 27, 28, 31];
- a concave adsorption isobar is profitable for desorption, while convex - for adsorption [20];
- the isobaric adsorption stage of AHT cycle is slower than the isobaric desorption stage [10, 26, 27];
- the adsorbent grain size has a dominant effect on the adsorption dynamics [26, 27];
- the instant driving force for isobaric ad-/desorption is the temperature difference between the plate and the grains,  $DTD = T_3 - T_g$  or  $T_g - T_1$  [26–28].

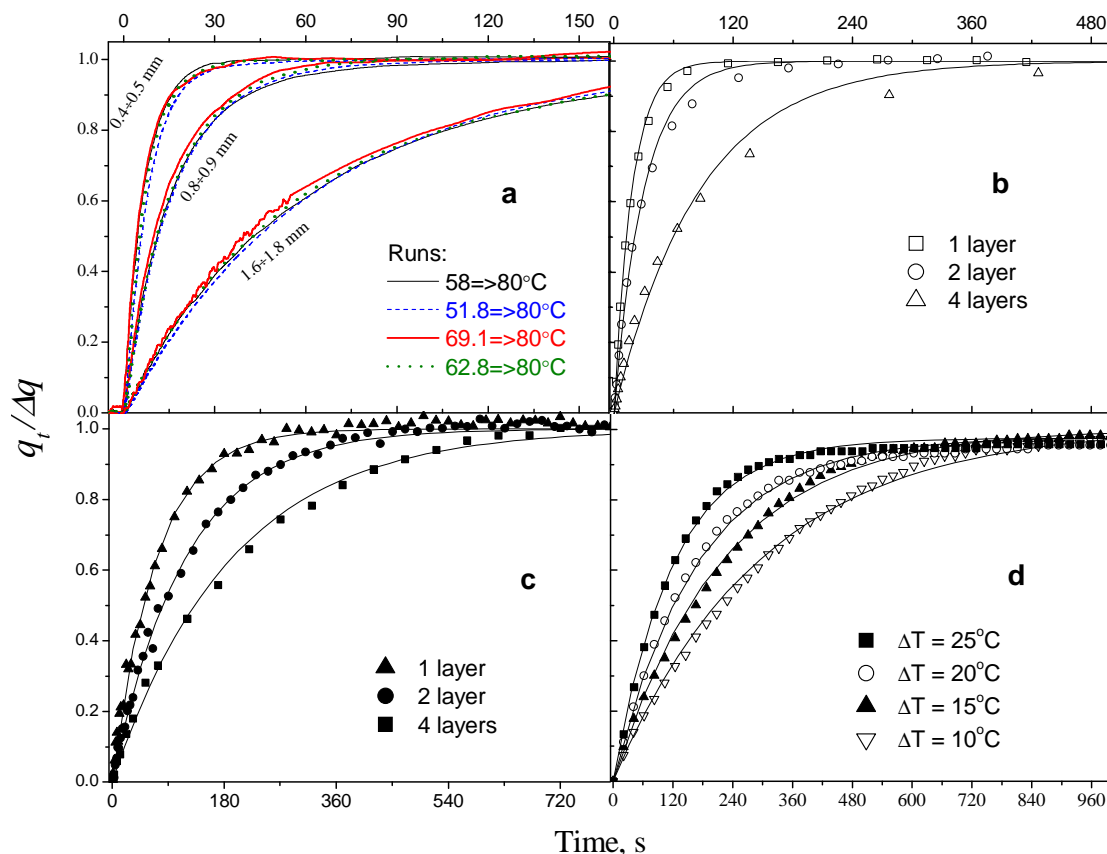


Fig. 2. Dimensionless uptake/release curves of the *water* desorption from silica Fuji RD at three grain size and boundary temperatures (a) [26]; the *water* adsorption on silica Fuji (0.4–0.5 mm) at various  $n$  (b) [32]; the *methanol* adsorption on LiCl/silica at various  $n$  (c) [27], the *ammonia* adsorption on the monolayer of BaCl<sub>2</sub>/vermiculite at  $P = 5.8$  bar and various DTD  $\Delta T$  (d) [28]. Lines – exponential fits

**Exponential kinetics.** It is really amazing that quite complex and coupled process of adsorption, heat and mass transfer ultimately results in exponential dependence of the sorption uptake (release)  $q$  on time  $t$  (Fig. 2)

$$q(t) = q(0) \pm \Delta q \exp(-t/\tau). \quad (1)$$

This simple equation describes the ad-/desorption dynamics by a *single* characteristic time  $\tau$  that permits stupendous simplification of the analysis, easy quantitative comparison of various adsorbents, boundary conditions, Ad-HEX configurations, etc. Eq. (1) is quite universal: it is valid for all tested adsorbents (eight materials) and adsorbates as well as various boundary conditions up to 80–100, 65–100 and 50–100% of the final conversion for  $n = 1, 2$  and  $4$ , correspondingly [22, 25–29]. The evolution of the tail can be slower than exponential, so that for any adsorbent and boundary conditions, a ratio of the characteristic times  $\tau_{0.9}/\tau_{0.8}$  is typically 1.3–1.7 [10, 27, 29].

**Recommendation 1.** That prompts to restrict the duration of AHT isobaric stages by time  $\tau_{0.8}$  (for  $n = 1$ ) or even lesser (for  $n > 1$ ). This would allow avoiding a dramatic drop of the cycle SCP at longer times at the expense of a just little reduction of the cycle COP.

**Shape of the adsorption isobar.** Effect of the shape of equilibrium adsorption isobar on dynamics of isobaric water has been studied in [31]. Composite sorbent SWS-1L was used for these tests as its water adsorption isobars have segments with both convex and concave shapes. From those experiments the conclusion has been drawn that under the same boundary conditions desorption is faster than adsorption for a concave isobar segment and vice versa for a convex one. The authors proposed that the most challenging shape of adsorption isobar is a step-like isobar, because it ensures a maximal average DTD between the grains and HEX fins during isobaric sorption stages. The effect of the isobar shape on the dynamics of isobaric water ad-/desorption stages of AHT cycles has been investigated by its mathematical modeling (see below and in [33]).

**Adsorption vs. desorption time.** If compare the characteristic times of adsorption and desorption for all tested cycles [22, 26, 27], the desorption runs (2–4, Fig. 1 *a*) are faster than appropriate adsorption runs (4–1) by a factor of 2.2–3.5. In our opinion, this is due to higher average temperature and vapor pressure during the desorption stage (Fig. 1 *a*). A concave shape of the sorption isobar is also profitable for desorption process [31]. This substantial difference in the durations of ad- and desorption isobaric phases helps to come to the conclusion [22] that commonly settled equal durations ( $t_{\text{des}} = t_{\text{ads}}$ ) do not result in optimal AHT performance.

**Recommendation 2.** The duration of isobaric adsorption phase should be prolong at the expense of shortening the isobaric desorption phase. This allows more complete adsorption stage, thus increasing the amount of adsorbate changed, the cycle COP and SCP. The first confirmation of this idea has just been obtained in [22].

**Effect of the boundary conditions.** Another (and somewhat unexpected) finding is that the cycle boundary conditions just weakly affect the dimensionless uptake curves (Fig. 2 *a*). Because of this insignificant effect of the boundary conditions, the specific cooling power mostly depends on the grain size, which dictates the characteristic time  $\tau$ , as well as the amount of water  $\Delta q$  exchanged in the cycle.

**Effect of adsorbent grain size.** For any adsorbent, both adsorption and desorption become faster for smaller grains (Fig. 2 and 3). For a monolayer configuration there are two regions:

- for large grains ( $2R_g = 0.8\text{--}0.9$  and  $1.6\text{--}1.8$  mm), the characteristic time strongly depends on the grain size both for ad- and desorption runs (Fig. 3 *b*):  $\tau \sim R_g^2$ . For these grains the characteristic time does not depend on the rate of heating the metal support. This regime is adsorbent-sensitive;
- for small grains ( $0.2\text{--}0.25$  and  $0.4\text{--}0.5$  mm size), the sorption process is fast and its time becomes comparable with the time of metal plate heating. In this limit, the time  $\tau$  is not adsorbent-specific, but rather reflects the fin heating scenario. As a result, the dependence  $\tau(R_g)$  almost vanishes (Fig. 3 *b*).

A crossover between the two limiting modes nominally corresponds to the silica grains of app. 0.55 mm size which can be considered as an upper limit of the optimal grain size for particular adsorbent and configuration.

The heat balance at short adsorption time can be written as

$$\frac{\Delta H m \Delta q}{\tau} = \alpha S \Delta T_{\max}, \quad (2)$$

where  $m$  – adsorbent mass,  $\Delta H$  – adsorption heat,  $\Delta q$  – uptake change (g/g),  $\tau$  – exponential sorption time,  $\alpha$  – heat transfer coefficient,  $S$  – heat transfer area,  $\Delta T_{\max}$  – maximal DTD. Hence, the characteristic sorption time

$$\tau = \frac{\Delta H m \Delta q}{\alpha S \Delta T_{\max}} = \left( \frac{\Delta H \Delta q}{\Delta T_{\max}} \right) \left( \frac{m}{\alpha S} \right) \quad (3)$$

depends on the thermodynamic parameters ( $\Delta H$ ,  $\Delta q$  and  $\Delta T_{\max} = T_3 - T_2$  or  $T_4 - T_1$ ) which can be taken from the cycle diagram (Fig. 1 *a*) and the parameters of Ad-HEX ( $\alpha$ ,  $S$  and  $m$ ) which affect the adsorption dynamics. In our experiments,  $m = \text{const}$  and  $S \sim 1/R_g$ . As  $\tau \sim R_g^2$ , hence, the heat transfer coefficient  $\alpha \sim 1/R_g$ . It is reasonable, as the heat conduction through the thin gap between the grain and the plate filled with a stagnant vapor substantially contributes to the heat transfer. The average gap thickness can be estimated as  $d_{\text{av}} \approx R_g/2$ , that gives  $\alpha = \lambda/d_{\text{av}} \approx 2\lambda/R_g = 0.04/R_g \sim 1/R_g$ , where  $\lambda = 0.019$  W/(m·K) is the thermal conductivity of water vapor at  $T = 35$  °C and  $P = 10$  mbar.

Thus, the size of the loose adsorbent grains is a very powerful instrument to manage the dynamics of isobaric stages of water ad-/desorption in AHTs.

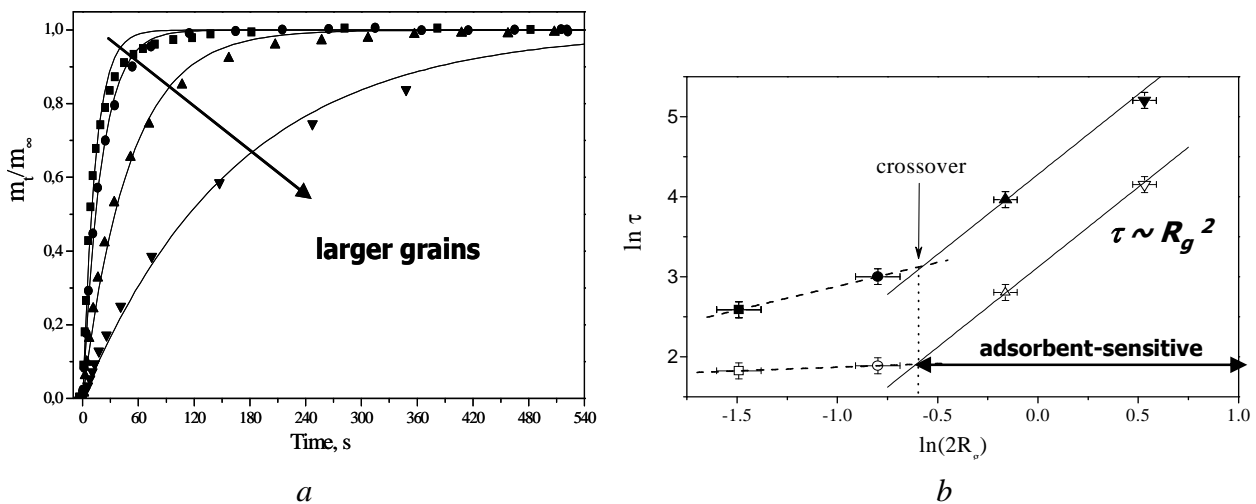


Fig. 3. *a* – The uptake curves for a monolayer of loose silica grains of different size. Solid lines – exponential approximation; *b* – exponential time  $\tau$  vs. grain size  $2R_g$  in logarithmical scale, solid lines – linear approximation  $\ln \tau = \ln \tau_0 + 2p \ln R_g$ . Adsorption run  $50 \geq 30$  °C (solid symbols) and desorption run  $58 \Rightarrow 80$  °C (open symbols). Grain size: 0.2–0.25 mm (■), 0.4–0.5 mm (●), 0.8–0.9 mm (▲), 1.6–1.8 mm (▼)

**Effect of the number of adsorbent layers.** One can expect that for the monolayer configuration the COP is not optimal because the mass of adsorbent housed in the monolayer is small as compared with the inert masses of AC unit. Because of this, more realistic are configurations with the number  $n$  of loose grains layers more than one. On the other hand, the whole layer should not be too thick and optimization of the  $n$ -number is strictly necessary. We have made LTJ measurements and analyze the dynamics of water ad-/desorption for multilayer configuration " $n$ -layers of loose grains of a silica Fuji RD" with  $n = 2$  and 4. This case reflects a realistic situation of compact heat exchanger of a finned flat-tube type in which 2–4 adsorbent grains are housed in a 1–2 mm gap between the fins [22]. We have selected for the measurements only one boundary set typical for cycles driven by low temperature heat: adsorption run  $50 \geq 30$  °C and desorption run

58  $\Rightarrow$  80 °C. The grains of Fuji silica type RD of four sizes are tested as fractions 0.2–0.25, 0.4–0.5, 0.8–0.9, and 1.6–1.8 mm. The dry sample weight was maintained constant, so that the diameter  $D \sim R_g^{-0.5}$  of the circle covered by the grains and the heat transfer surface  $S = \pi D^2/4 \sim R_g^{-1}$  are reduced accordingly (Fig. 4).

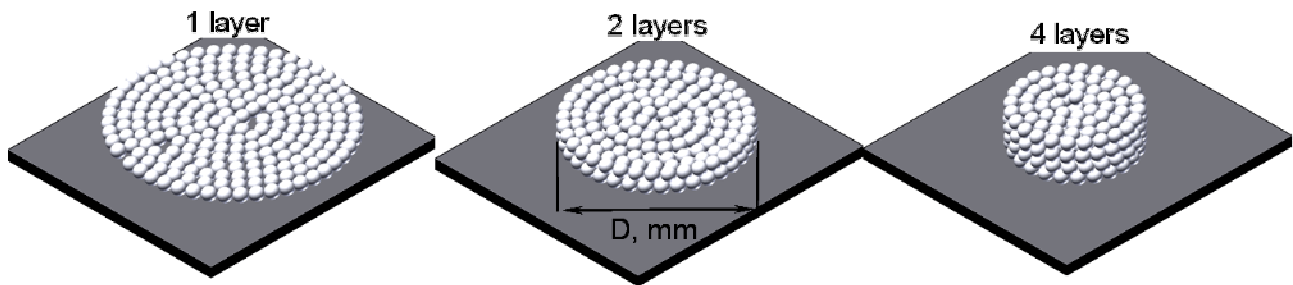


Fig. 4. Schematics of the loose grains configurations with  $n = 1, 2$  and  $4$

For all experimental runs, a gradual slowing down of the evolution of the *dimensionless* uptake with increasing  $n$  is observed (Fig. 2 *b*). This Figure demonstrates faster setting of water sorption equilibrium for thinner layer of Fuji silica RD. However, if plot the temporal evolution of the *absolute* water uptake, the adsorption rate at very short adsorption time ( $< 10$  s) is the same for  $n = 1, 2$  and  $4$  (Fig. 5 *a*), which corresponds to the same initial power of heat transfer between the plate and the adsorbent (app. 8 kW/kg). At longer time, the power is reducing according to the decrease in the temperature difference between the plate and the adsorbent layer. This difference is approaching to zero at equilibrium which has reached faster for layer that exchanges smaller mass of water – 0.012 g at  $n = 1$  as compared with 0.024 and 0.048 g for  $n = 2$  and  $4$ , respectively. It is similar to the case of monolayer configuration of adsorbents with different water exchange (Fig. 5 *b*) [25].

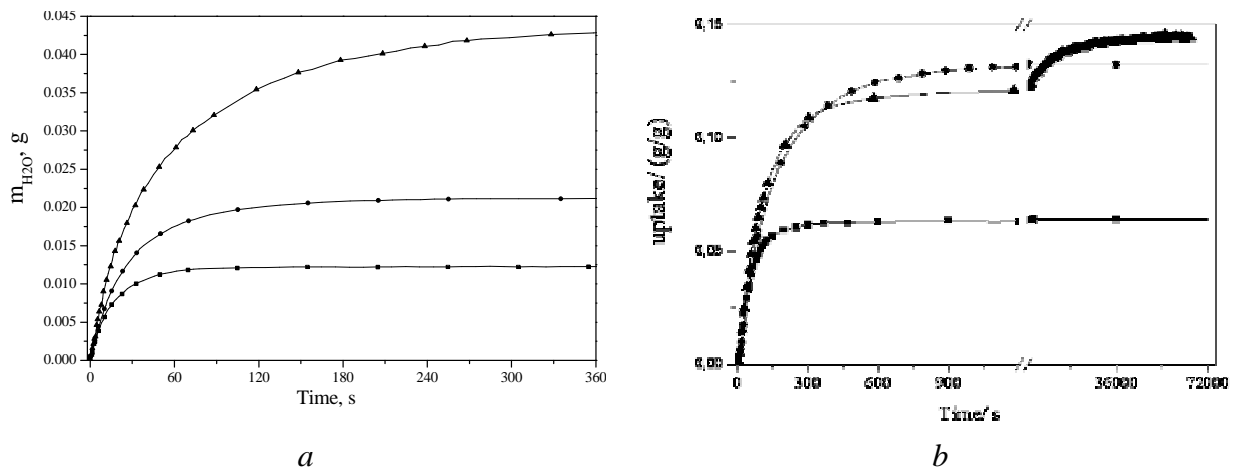


Fig. 5. Uptake curves of water adsorption on: *a* – Fuji silica grains,  $\nabla$  – one layer,  $--$  – two layers and  $8$  – four layers; run 50  $\geq 30$  °C, grain size – 0.4-0.5 mm; *b* – SWS-1L ( $\bullet$ ), Fuji type RD ( $\blacksquare$ ) and FAM-Z02 ( $\blacktriangle$ ) [25]; run 60  $\geq 35$  °C, grain size – 0.8–0.9 mm. Solid lines – exponential approximation

At  $n > 1$ , both adsorption and desorption runs are adsorbent-specific at any grain size  $R_g$  (Fig. 6). At  $n = 2$ , the characteristic ad- and desorption time increases, however, the slope  $p$  of the dependence  $\ln(\tau) = a + p \ln(2R_g)$  for larger grains remains almost equal to that at  $n = 1$ ,  $p \approx 2$ . Hence, the two-layers configuration can be described by eq. (2) with the same heat transfer coefficient  $\alpha \sim 1/R_g$ . The main reason for process slowing down is the reduction of the heat transfer area  $S$ .

At  $n = 4$ , a further depression of the ad- and desorption rate is observed (Fig. 6). The slope  $p$  certainly decreases to 1.4–1.5 that is likely to indicate contribution of the thermal resistance in the adsorbent layer.

For a thick layer ( $n \gg 1$ ), this resistance can be evaluated as  $U_1 = d/\lambda$ , where  $\lambda$  is the layer thermal conductivity,  $d$  is the layer thickness ( $d \sim n R_g$ ). The reduction of the slope  $p$  is likely to indicate that the efficient thermal conductivity of the four silica layers is larger for smaller grains.

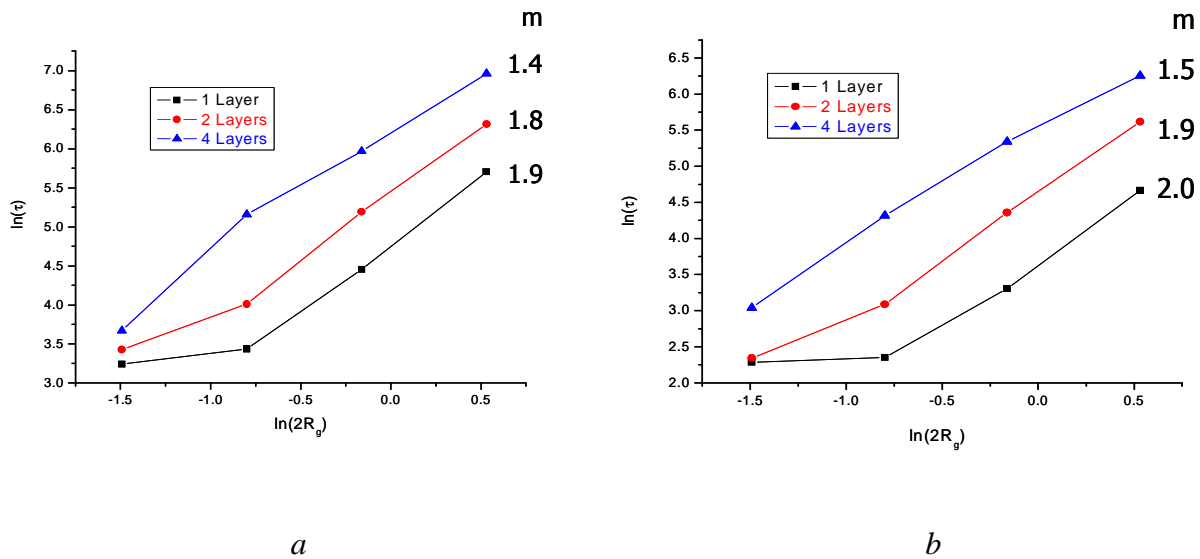


Fig. 6. Dependence of  $\ln(\tau)$  on  $\ln(2R_g)$  for one, two and four layers of Fuji silica grains: *a* – adsorption run  $50 \geq 30^\circ\text{C}$ , *b* – desorption run  $58 \geq 80^\circ\text{C}$

**Driving force for ad-/desorption process.** The metal plate is a source (sink) of heat of desorption (adsorption), and the maximal specific power  $W_{\max}$  is linked with the appropriate heat flux between the plate and the grains as  $W_{\max} = \alpha S \Delta T_{\max} / m$ . The value of  $W_{\max}$  calculated from the initial slope of uptake (release) curves is found to be proportional to  $\Delta T_{\max}$ :  $W_{\max} = K \cdot \Delta T_{\max}$  (Fig. 7) for all studied adsorbents, adsorbates and boundary conditions (more than 15 tests). The heat transfer coefficient is  $\alpha = (W_{\max} m) / (S \Delta T_{\max}) = Km/S$ , that gives

- a – for *water*,  $\alpha = 100\text{--}250 \text{ W}/(\text{m}^2 \cdot \text{K})$ , for desorption being app. twice larger than for adsorption (Fig. 7 a);
- b – for *methanol*,  $\alpha = (75 \pm 10) \text{ W}/(\text{m}^2 \cdot \text{K})$  for adsorption on grains of 0.4–0.5 mm (Fig. 7 b);
- c – for *ammonia*,  $\alpha = 115 \text{ W}/(\text{m}^2 \cdot \text{K})$  for the grains of 0.5–1 mm, and  $90 \text{ W}/(\text{m}^2 \cdot \text{K})$  for 1–2 mm grains [28].

Thus, the  $\alpha$  – value for adsorption runs is close to  $(100 \pm 20) \text{ W}/(\text{m}^2 \cdot \text{K})$  for any adsorbent and adsorbate. This value is larger than those commonly used in modeling of AHT dynamics ( $40\text{--}60 \text{ W}/(\text{m}^2 \cdot \text{K})$ ) [34,35].

Composites "salt in porous matrix" sorb water (methanol, ammonia) due to chemical reaction of adsorbate with the confined salt. In this case, the sorption rate depends on the two driving forces, namely, the driving force for chemical reaction, which is the difference  $\Delta(\Delta F)$  of the chemical potential [27], and the common driving force for heat transfer DTD. Due to this, the line  $W_{\max}(\Delta T_{\max})$  for the LiCl/silica composite intersects the X-axis at  $\Delta T_{\max} \approx 8^\circ\text{C} > 0$  (Fig. 7 b) which corresponds to the  $\Delta F$ -driving difference necessary for the gas-solid reaction  $\text{LiCl} + 3\text{H}_2\text{O} = \text{LiCl} \cdot 3\text{H}_2\text{O}$  [27].

We have compared the dynamics of ammonia adsorption by  $\text{BaCl}_2$ /vermiculite composite of 1–2 mm grains size in the laboratory LTJ unit [28] and in a prototype of air-cooling adsorptive chiller with app. the same ration  $S/m$  built in the University of Warwick. It was found that the dependence of initial heat power  $W_0$  on  $\Delta T_{\max}$  for the prototype is described by the same straight line (Fig. 7 d) as for our LTG unit (Fig. 7 c) with similar heat transfer coefficient  $\alpha = (90 \pm 15) \text{ W}/(\text{m}^2 \cdot \text{K})$ . Evidently, dynamic data obtained by the LTJM can be used for scaling-up of Ad-HEX units and optimization of real working cycles of AHT.

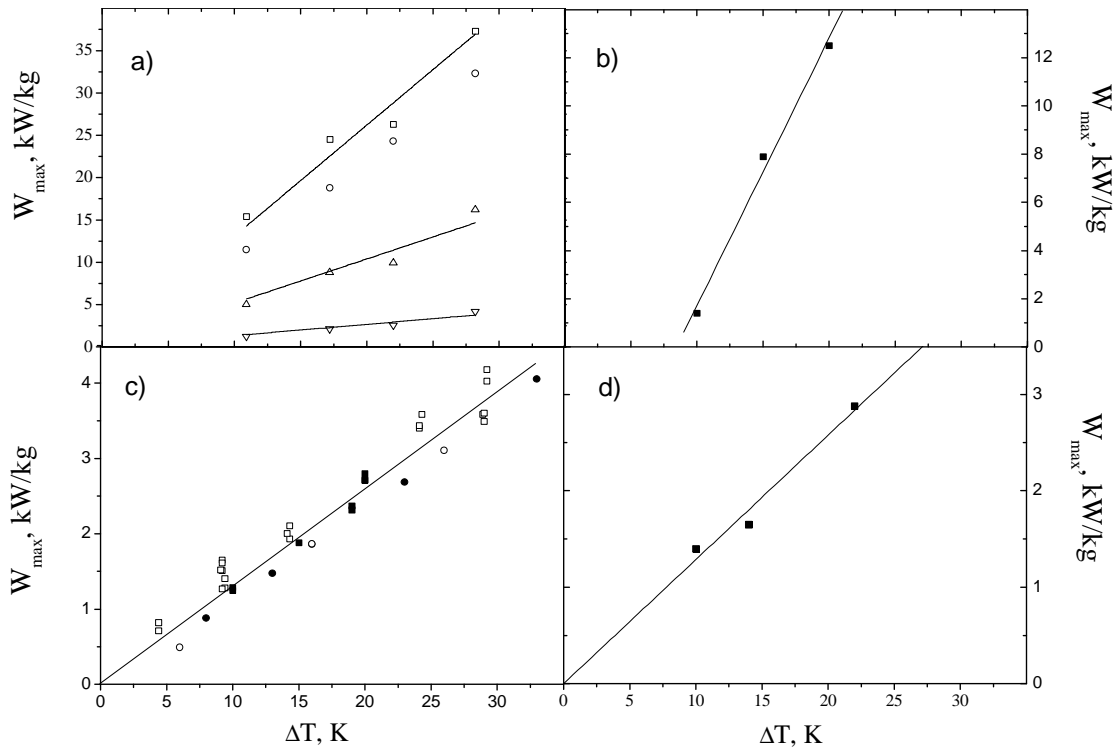


Fig. 7. The specific power  $W_{\max}$  vs. the driving temperature difference: *a* – the *water* desorption from the Fuji silica with the rain size: 0.2–0.25 mm ( $\square$ ), 0.4–0.5 mm ( $\circ$ ), 0.8–0.9 mm ( $\triangle$ ), 1.6–1.8 mm ( $\nabla$ ) [26]; *b* – the *methanol* adsorption on LiCl/silica with the grain size 0.4–0.5 mm [27]; *c* – the *ammonia* adsorption on BaCl<sub>2</sub>/vermiculite at different ammonia pressures:  $\blacksquare$  – 5.8 bar,  $\square$  – 6.9 bar,  $\bullet$  – 12.2 bar,  $\circ$  – 15.8 bar;  $\boxtimes$  – 5.8 bar [28]; *d* – the *ammonia* adsorption on BaCl<sub>2</sub>/vermiculite in the prototype of air conditioning device [24]

## MATHEMATICAL MODELING OF ADSORPTION DYNAMICS

The Fickian diffusion model of combined heat and mass transfer in a single adsorbent grain which is in thermal contact with a metal plate subjected to a fast temperature jump/drop was developed and described elsewhere [20]. It includes the system of differential equations for the heat and mass balance with the relevant initial and boundary conditions. This system is numerically solved in order to obtain the radial and temporal distributions of temperature  $T(r, t)$ , concentration  $C(r, t)$  and pressure  $P(r, t)$  in the vapour phase as well as water concentration  $q(r, t)$  in the adsorbed phase. This model is used to answer the questions "Which isobar shape is optimal for AHT?" and "How the driving forces for heat and mass transfer are being developed after the initial jump/drop of plate temperature?" The analysis has been performed for a relatively small temperature jump/drop ( $60^\circ\text{C} \leftrightarrow 70^\circ\text{C}$ ) and a set of model isobars (stepwise, linear and exponential, Fig. 8 *a*). The step positions are chosen at  $T_{\text{st}} = 60.5, 62, 65, 38$  and  $69.5^\circ\text{C}$  [33]. Adsorbent grain size  $2R_g$  is fixed at 1.5 mm.

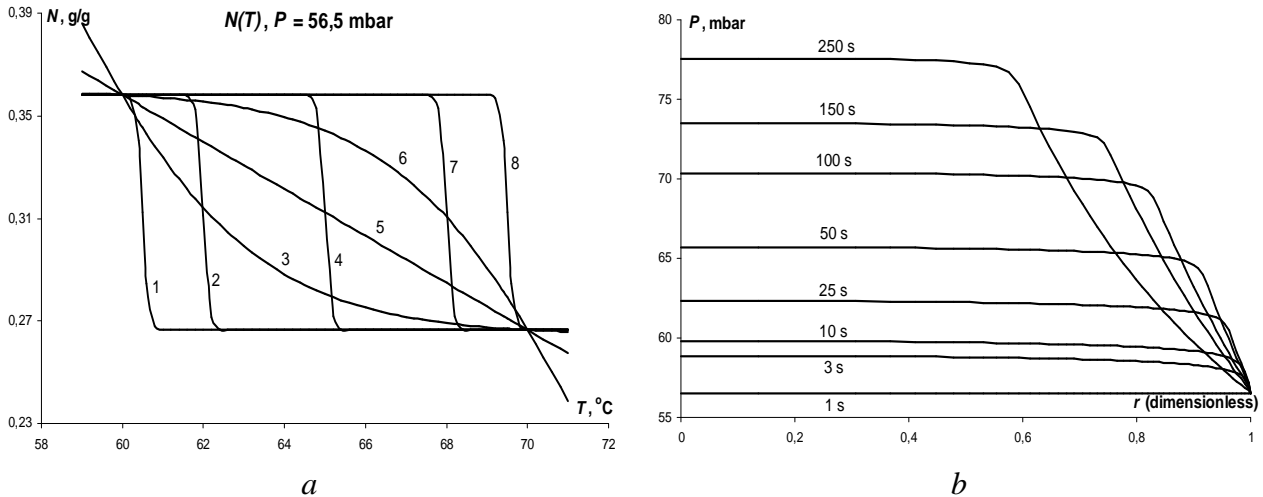


Fig. 8. *a* – Model isobars of water sorption: 1 – step at 60.5 °C, 2 – step at 62 °C, 3 – exp (concave), 4 – step at 65 °C, 5 – linear, 6 – exp (convex), 7 – step at 68 °C, 8 – step at 69.5 °C; *b* – radial distribution of the pressure inside the grain during water desorption.  $T_{st} = 62$  °C.  $r = 0$  – the grain center,  $r = 1$  – the grain surface [33]

**Driving force for heat and mass transfer.** During both adsorption and desorption steps the temperature is practically constant along the grain radius and is essentially non-steady state in time. For step-like isobars, the temporal evolution of the average grain temperature  $T_{av}$  can be divided into two parts (not presented, see [33]):

- a) a very fast drop from the initial temperature  $T_{in} = 70$  °C to  $T_{st}$  for adsorption, and very fast rise from the initial temperature  $T_{in} = 60$  °C to  $T_{st}$  for desorption. This fast process takes just 3–20 s, and is associated with the heating/cooling of the grain without appreciable contribution of the ad- and desorption process itself;
- b) a gradual change of  $T_{av}$  that reaches its final temperature  $T_f$  after 500–2000 s. The second part is much slower than the first one as the heat is consumed mostly for water desorption rather than for grain heating.

Variation of  $T_{av}$  immediately affects the pressure evolution  $P(r, t)$  inside the grain. Contrast to the temperature, the pressure is not-uniform along the grain radius during both ad- and desorption (Fig. 8 *b*) that is due to slow intragrain vapour transfer. Let us consider desorption run  $60$  °C  $\rightarrow$   $70$  °C and  $T_{st} = 62$  °C:

– driving force for heat transfer is maximal at  $t = 0$  ( $\Delta T_{dr} = T_f - T_{in} = 10$  °C). This initiates the mentioned fast heating of the grain up to app. 62 °C, means, to the step temperature  $T_{st}$  that quickly reduces the driving force for the heat transfer  $\Delta T_{dr} \approx T_f - T_{st}$  down to 8 °C. After this transient period, the heat transfer driving force  $\Delta T_{dr} = (T_f - T_{av})$  is gradually decreasing as the grain is approaching its final temperature  $T_f$ ;

– at  $t = 0$ , when the driving force for heat transfer is maximal, the driving force for mass transfer equals zero. Jumping the grain temperature to 62 °C stimulates desorption of water, first of all, to the pore voids. As desorption is fast, the diffusional flux of vapor out of the grain is not sufficient to compensate the pressure increase, thus, the gradient of pressure appears inside the grain (Fig. 8 *b*). Thereby, the temperature gradient generates the pressure gradient which is the driving force for mass transfer. The latter is proportional to the derivative  $dP(r)/dr$  near the grain external surface (at  $r = 1$ , Fig. 8 *b*). After a short *transient* period (app. 10 s) which corresponds to the fast grain heating, this slope gradually decreases with time (Fig. 8 *b*). Under this *steady-state* mode, the driving forces for heat and mass transfer are interactively reducing while the water desorption proceeds. Thus, the heat and mass transfer processes are coupled and strongly affect each other.

**Effect of the shape of water sorption dynamics.** In the majority of cases, the calculated dependences of the average water uptake/release on time are satisfactorily described by an exponential

function up to the dimensionless conversions of 0.7–0.8. The characteristic time  $\tau$  is found to be strongly dependent on the isobar shape [33]. Fastest adsorption processes is observed for the isobar step at 69.5 °C ( $\tau = 150$  s). As the process driving force is the temperature difference  $\Delta T_{dr}(t) = T_{av}(t) - 60$  °C, the adsorption rate is expected to be maximal at  $T_{st} = 69.5$  °C because the adsorption heat is removed at the maximal temperature difference. Accordingly, the fastest desorption corresponds to  $T_{st} = 60.5$  °C ( $\tau = 133$  s).

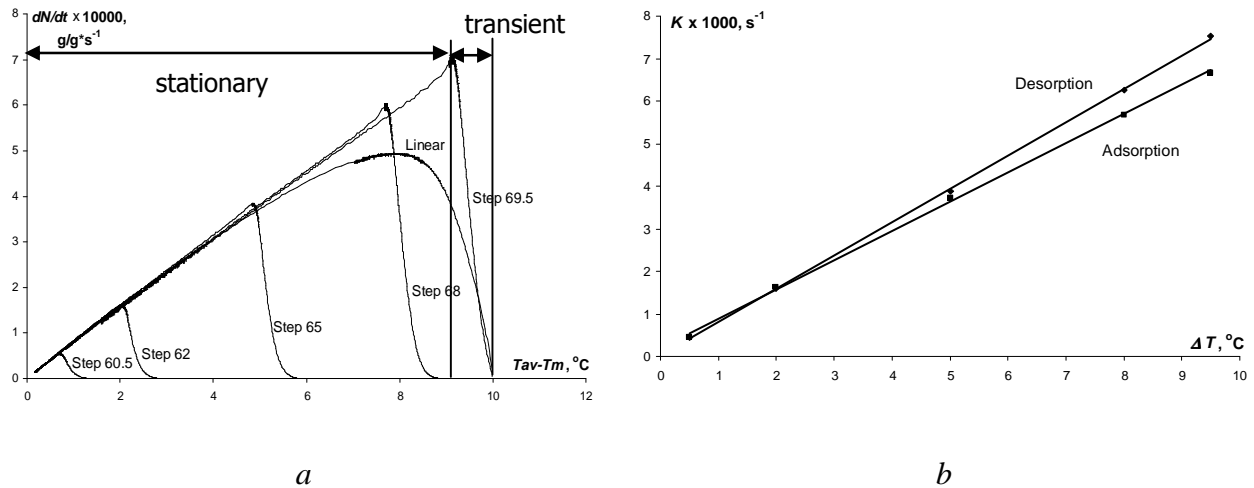


Fig. 9. *a* – Desorption rate as a function of the instant driving temperature ( $T_{av} - T_f$ ) for the isobar shapes indicated on the graph. The transient and stationary regions are shown for  $T_{st} = 69.5$  °C; *b* – ad- and desorption rate constants at various absolute values of the temperature difference  $\Delta T = |T_f - T_{st}|$ .

The simulations have shown that the instant desorption rate  $W(t)$  is a linear function of  $\Delta T_{dr}$  except for a short transient period (Fig. 9 *a*) which needs to establish a coupling between the heat and mass transfer. For this period, the grain temperature approximately reaches the temperature  $T_{st}$  at which the desorption starts. That initiates an increase in the vapour pressure inside the grain which creates the driving force for the mass transport. After that the driving forces for the heat and mass transfer change in a strict correlation with each other, so that the instant process rate is proportional to the current difference  $\Delta T_{dr} = (T_{av} - T_f)$  or  $(T_f - T_{av})$ . All the adsorption and desorption experiments fall on the same straight line, thus, indicating a universal character of the function  $W = \gamma \Delta T_{dr}$  with the constant coefficient  $\gamma$  regardless the  $T_{st}$ -value [33].

For near-exponential processes, the rate constant can be defined as  $k = 1/\tau$ . This value appeared to be a linear function of the absolute temperature difference  $\Delta T = |T_f - T_{st}|$  and the slope for the ad- and desorption stages are almost equal (Fig. 9 *b*). Thus, the maximum process rate corresponds to the maximal temperature difference between the final plate temperature which is maintained all over the sorption process and the temperature at which the ad- and desorption process starts.

**Recommendation 3.** The most profitable is a step-like sorption isobar as it was conjectured in [31]. The step should be positioned at temperature as much different from the temperature of the HE fins (the external heat source/sink) as possible to maximize the driving force for heat transfer. Interestingly, that step-like sorption isobars are the most profitable from thermodynamic point of view as well [4], however, in this case the uptake step has to be as close to the temperature of the HE fins as possible to minimize the entropy generation due to the thermal coupling. Thus, in actual practice a compromise between the two tendencies has to be reached. It can be made by optimizing the Ad-HEx system: first of all, the ration  $(\frac{m}{\alpha S})$  (see (3)).

For well-designed Ad-HEx units the driving temperature difference should be of 1–2 °C.

## DYNAMIC OPTIMIZATION OF ADSORPTIVE HEAT TRANSFORMATION CYCLES

Results obtained by LTJM have taught us that the duration of desorption phase of AHT cycle should be shorter than that of the adsorption one (recommendation 2). Hence, the equal duration of adsorption and

desorption phases is hardly to be an optimal case, and appropriate reallocation is necessary to give more time for adsorption at the expense of desorption shortening. This has been realized and tested in the single bed adsorption chiller built in CNR-ITAE in terms of cooling COP and SCP [22]. All experiments are carried out by fixing the same inlet temperatures of the external heating/cooling fluids ( $T_{des} = 95\text{ }^{\circ}\text{C}$ ,  $T_{ev} = 10\text{ }^{\circ}\text{C}$ ,  $T_{con} = 30\text{ }^{\circ}\text{C}$ ).

The prototype tests confirmed that the optimal desorption duration should indeed be 2–3 times shorter than the adsorption one, and for the optimal ratio  $t_{des}/t_{ads}$  both the COP (not presented) and SCP (Fig. 10 *a*) may increase almost twice as compared with the common case  $t_{des} = t_{ads}$ . The sharp dependence  $\text{COP}(t_{des})$  is due to the fact that at too short desorption time ( $t_{des} < 80\text{--}90\text{ s}$ ) the optimal desorption degree (app. 80%) can not be reached that reduces both the COP and SCP. If this time is longer than the optimal one, the duration of the adsorption phase is reduced accordingly, and there is not enough time for the water uptake to recover. For the tested adsorber, the optimal adsorption time can be estimated as 250–280 s. For the shorter cycle, both the COP and SCP are more sensitive to the choice of durations of the adsorption and desorption stages than for the longer cycle (Fig. 10 *a*) [22], and a proper choice of desorption time  $t_{des}$  is especially important.

The reallocation of adsorption/desorption durations proposed causes a subsequent change in cooling cycle organization, because each adsorber now is connected with an evaporator longer than the half-cycle time. Let, for instance, the time  $t_{des}$  be twice as short than  $t_{ads}$ . In this case, the following cycle rearrangements can be done:

– for a two bed configuration, the two modes are possible (Fig. 10 *b*):

- one bed is connected with the evaporator where cold is produced. At the same time, another bed is under regeneration and is connected with the condenser where heat is rejected;
- both beds are linked with the evaporator and generate a double chilling effect.

Thus, cold is continuously generated so that each bed is linked with the evaporator two thirds of the cycle time  $t_{cycle}$  and with the condenser only one third. In this case, to smooth the cooling effect produced, the chiller could be equipped with an intermediate cold storage unit. To allow the use of a continuous driving heat input an intermediate heat store or a buffer may also need. The three-beds configuration is considered in [22].

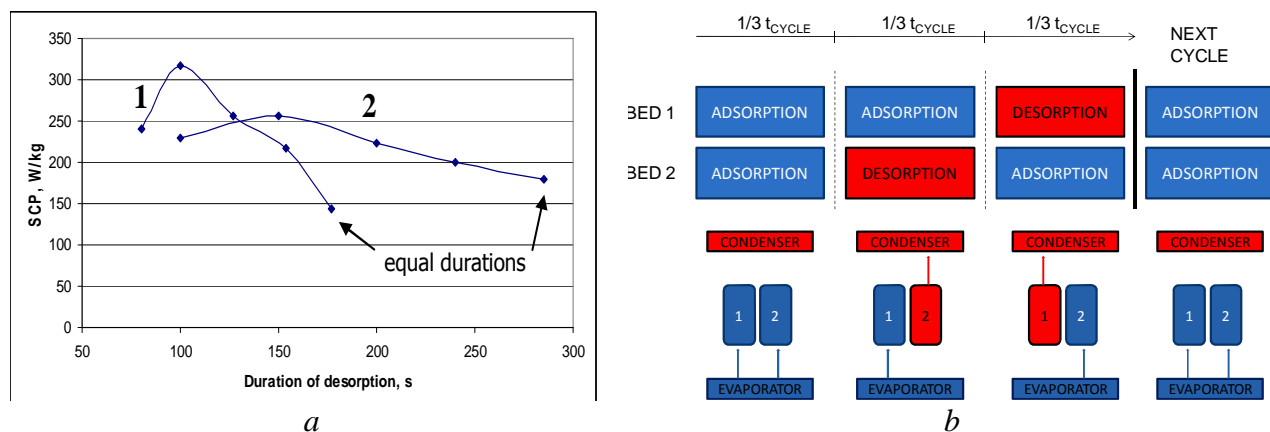


Fig. 10. *a* – SCP as a function of the desorption stage duration. Total cycle time – 385 (1) and 600 s (2); *b* – management of a 2-beds cooling unit with reallocated duration of adsorption and desorption stages [22].

## CONCLUSIONS

An “adsorbent-heat exchanger” (Ad-HEX) unit is a core of any adsorptive heat transformer (AHT), and its efficient performance is of prime importance. In this lecture, we present recent advances in understanding and trends in studying the adsorption dynamics. Dynamic experiments have been performed in laboratory Ad-HEX units which closely imitate the conditions of isobaric stages of AHT when desorption (adsorption)

is initiated by a fast jump (drop) of the temperature of a heat exchanger wall which is in thermal contact with the adsorbent layer (Large Temperature Jump Method, LTJM). All results concern configuration of Ad-HEX with one, two or four layers of loose adsorbent grains. Water, methanol and ammonia are used as adsorbates. Mathematical model of coupled heat and mass transfer during isobaric adsorption process developed in the Moscow State University (for monolayer configuration) has been used for detailed dynamical analysis and extracting the heat and mass transfer coefficients. Finally, several recommendations followed from the LTJM study have been checked with a prototype of adsorptive chiller in ITAE-CNR. These tests clearly demonstrated that dynamic performance of AHT can be significantly improved by a proper management of AHT cycle (reallocation of relative durations of isobaric adsorption and desorption phases, optimization of the cycle time and the conversion degree, etc.). The most important findings and general regularities that have been revealed as result of the LTJM application for systematic studying the adsorption dynamics of water, methanol and ammonia in AHT systems are summarized, illustrated and discussed in the paper.

### Acknowledgments

The author thanks his colleagues Drs. I.S. Glaznev, L.G. Gordeeva, M.M. Tokarev and J.V. Veselovskaya for their experimental contribution, Drs. B.N. Okunev and A.P. Gromov for mathematical modeling, the Russian Foundation for Basic Researches (project 10-08-91156) and the Siberian Branch of the Russian Academy of Sciences (Integration project N 22) for partial financial support of this activity.

### References

1. *Advances in Adsorption Technologies* / Eds. B. Saha and K. S. Ng; Nova Science Publishers, ISBN: 978-1-60876-833-2, 2010.
2. Critoph R. E., Zhong Y. Review of trends in solid sorption refrigeration and heat pumping technology // *J. Process Mech. Eng.* 2005. Vol. E 219. Pp. 285–300.
3. Wang R. Z., Oliveira R. G. Adsorption refrigeration – An efficient way to make good use of waste heat and solar energy // *Progress in Energy and Combustion Science.* 2006. Vol. 32. Pp. 424–458.
4. Aristov Yu. I. Novel materials for adsorptive heat pumping and storage: screening and nanotailoring of sorption properties (review) // *J. Chem. Engn. Japan.* 2007. Vol. 40. Pp. 1241–1251.
5. Wang L. W., Wang R. Z., Oliveira R. G. A review on adsorption working pairs for refrigeration // *Re-newable and Sustainable Energy Reviews.* 2009. Vol. 13. Pp. 518–534.
6. Kim D. S., Infante Ferreira C. A. Solar refrigeration options – a state-of-the-art review // *Int. J. Refrig.* 2008. Vol. 31. Pp. 3–15.
7. Choudhury B., Chatterjee P. K., Sarkar J. P. Review paper on solar-powered air-conditioning through adsorption route // *Renewable and Sustainable Energy Reviews.* 2010. Vol. 14. Pp. 2189–2195.
8. Aristov Yu. I., Vasiliev L. L., Nakoryakov V. E. Chemical and sorption heat engines: State of the art and development prospects in the Russian Federation and the Republic of Belarus // *J. Engineering and Thermophysics.* 2008. Vol. 80. Pp. 19–48.
9. Aristov Yu. I. Optimal adsorbent for adsorptive heat transformers: Dynamic considerations // *Int. J. Refrig.* 2009. Vol. 32. Pp. 675–686.
10. Glaznev I. S., Aristov Yu. I. Dynamic Aspects of Adsorptive Heat Transformation, In book: "Advances in Adsorption Technologies", 2010 / Eds. B. Saha and K.S. Ng; Nova Science Publishers. ISBN: 978-1-60876-833-2. Pp. 107–163.
11. Lang R., Roth M., Stricker M. Development of a modular zeolite-water heat pump // *Proc. Int. Sorption Heat Pump Conf., Munich, Germany.* 1999. Pp. 611–618.
12. Bauer J., Herrmann R., Mittelbach W., Schwieger W. Zeolite/aluminum composite adsorbents for application in adsorption refrigeration // *Int. J. Energy Research.* 2009. Vol. 33. Pp. 1233–1249.
13. Aristov Yu. I., Dawoud B., Glaznev I. S., Elyas A. A new methodology of studying the dynamics of water sorption/desorption under real operating conditions of adsorption heat pumps: Experiment // *Int. J. Heat Mass Transfer.* 2008. Vol. 51. Pp. 4966–4972.
14. Raymond A., Garimella S. Intraparticle Mass Transfer in Adsorption Heat Pumps: Limitations of the Linear Driving Force Approximation // *J. Heat Transfer.* 2011. Vol. 133. Pp. 42001–42013.

15. Saha B. B., Akisawa A., Kashiwagi T. Solar/waste heat driven two-stage adsorption chiller: the prototype // *Renew Energy*. 2001. Vol. 23. Pp. 93–101.
16. Freni A., Sapienza A., Glaznev I. S., Aristov Yu. I., Restuccia G. Testing of a compact adsorbent bed based on the selective water sorbent “silica modified by calcium nitrate” // *Int. J. Refrigeration*. 2011. Vol. 34. ([doi: 10.1016/j.ijrefrig.2010.05.015](https://doi.org/10.1016/j.ijrefrig.2010.05.015)).
17. Tamainot-Telto Z., Metcalf S. J., Critoph R. E. Novel compact sorption generators for car air conditioning // *Int. J. Refrigeration*. 2009. Vol. 32. Pp. 727–733.
18. Matsushita M. Adsorption chiller using low-temperature heat sources // *Energy Conservation*. 1987. Vol. 39. Pp. 96–106.
19. Wang D. C., Wu J. Y., Xia Z. Z., Zhai H., Wang R. Z., Dou W. D. Study of a novel silica gel-water adsorption chiller. Part II. Experimental study // *Int. J. Refrig*. 2005. Vol. 28. Pp. 1084–1091.
20. Okunev B. N., Gromov A. P., Heifets L. I., Aristov Yu. I. A new methodology of studying the dynamics of water sorption/desorption under real operating conditions of adsorption heat pumps: Modeling of coupled heat and mass transfer // *Int. J. Heat and Mass Transfer*. 2008. Vol. 51. Pp. 246–252.
21. Freni A., Aristov Yu. I., Maggio G., Glaznev I. S., Cipiti F. Simulation of water sorption dynamics in adsorption chillers: one, two and four layers of loose silica grains // *Appl. Therm. Engn*. 2011. (to be submitted).
22. Aristov Yu. I., Sapienza A., Freni A., Ovoshnikov D. S., Restuccia G. Reallocation of adsorption and desorption times for optimizing the cooling cycle parameters // *Int. J. Refrig*. Vol. 34. 2011. ([doi:10.1016/j.ijrefrig.2010.07.019](https://doi.org/10.1016/j.ijrefrig.2010.07.019)).
23. Sapienza A., Glaznev I. S., Santamaria S., Freni A., Aristov Yu. I. Adsorption chiller driven by low temperature heat: new adsorbent and cycle optimization // *Appl. Therm. Engn*. 2011. (submitted).
24. Veselovskaya J. V., Critoph R. E., Thorpe R. N., Metcalf S., Tokarev M. M., Aristov Yu. I. Novel ammonia sorbents “porous matrix modified by active salt” for adsorptive heat transformation: 3. Testing of “BaCl<sub>2</sub>/vermiculite” composite in the lab-scale adsorption chiller // *Appl. Therm. Engn*. 2010. Vol. 30. Pp. 1188–1192.
25. Glaznev I. S., Ovoshnikov D. S., Aristov Yu. I. Effect of Residual Gas on Water Adsorption Dynamics under Typical Conditions of an Adsorptive Chiller // *Heat Transfer Engineering J*. 2010. Vol. 31. Pp. 924–930.
26. Glaznev I. S., Aristov Yu. I. The effect of cycle boundary conditions and adsorbent grain size on dynamics of adsorption chillers // *Int. J. Heat & Mass Transfer*. 2010. Vol. 53. Pp. 1893–1898.
27. Gordeeva L. G., Aristov Yu. I. Composite sorbent of methanol “LiCl in mesoporous silica gel” for adsorption cooling: dynamic optimization // *Energy*. 2011. Vol. 36. Pp. 1273–1279.
28. Veselovskaya J. V., Tokarev M. M. Novel ammonia sorbents “porous matrix modified by active salt” for adsorptive heat transformation: 4. Dynamics of quasi-isobaric ammonia sorption and desorption on BaCl<sub>2</sub>/vermiculite // *Appl. Therm. Eng*. 2011. Vol. 31. Pp. 566–572.
29. Glaznev I. S., Aristov Yu. I. Kinetics of water adsorption on loose grains of SWS-1L under isobaric stages of adsorption heat pumps: the effect of residual air // *Int. J. Heat & Mass Transfer*. 2008. Vol. 51. Pp. 5823–5827.
30. Okunev B. N., Gromov A. P., Zelenko V. L., Glaznev I. S., Ovoshnikov D. S., Heifets L. I., Aristov Yu. I. Effect of residual gas on the dynamics of water adsorption under isobaric stages of adsorption heat pumps: mathematical modelling // *Int. J. Heat Mass Transfer*. 2010. Vol. 53, Pp. 1283–1289.
31. Glaznev I. S., Ovoshnikov D. S., Aristov Yu. I., Kinetics of water adsorption/desorption under isobaric stages of adsorption heat transformers: the effect of isobar shape // *Int. J. Heat & Mass Transfer*. 2009. Vol. 52. Pp. 1774–1777.
32. Glaznev I. S., Gimir I. S., Aristov Yu. I. Water sorption dynamics in adsorption chillers: a few layers of loose Fuji silica grains, Proc. VIII Minsk Intern. Seminar “Heat Pipes, Heat Pumps, Refrigerators, Power Sources”, Minsk, Belarus, September 12–15, 2011.
33. Okunev B. N., Gromov A. P., Glaznev I. S., Aristov Yu. I. Modeling of water sorption dynamics in heat transformers: An optimal shape of the sorption isobar // Proc. VIII Minsk Intern. Seminar “Heat Pipes, Heat Pumps, Refrigerators, Power Sources”, Minsk, Belarus, September 12–15, 2011.
34. Zhang L. Z., Wang, L. Momentum and heat transfer in the adsorbent of a waste-heat adsorption cooling system // *Energy*. 1999. Vol. 24. Pp. 605–624.
35. Yong L., Sumathy K. Review of mathematical investigation on the closed adsorption heat pump and cooling systems // *Renewable and Sustainable Energy Reviews*. 2002. Vol. 6. Pp. 305–337.

## EXPERIMENTAL AND NUMERICAL INVESTIGATIONS OF CRYOGENIC PULSE TUBE REFRIGERATORS

**Bakhtier Farouk and Dion Antao**

Department of Mechanical Engineering and Mechanics  
Drexel University  
3141 Chestnut Street, Randell 115, Philadelphia, PA, 19104, USA  
215-895-2287; [bfarouk@coe.drexel.edu](mailto:bfarouk@coe.drexel.edu)

### Abstract

In this paper an orifice type pulse tube refrigerator (OPTR) is studied both experimentally and computationally to provide cryogenic cooling. The OTPR is a travelling wave thermoacoustic refrigerator that operates on a modified reverse Stirling cycle. We consider a helium filled system that is comprised of a pressure wave generator (a linear motor), an aftercooler heat-exchanger, a regenerator (comprising of a porous structure for energy separation), a pulse tube (in lieu of a displacer piston as found in Stirling refrigerators) with a cold and a hot heat-exchanger at its two ends, a needle-type orifice valve, an inertance tube and a buffer volume. The experimental characterization is done at various values of mean pressure of helium (~ 0.35 MPa to 2.2 MPa), amplitude of pressure oscillations, and frequency of operation and size of orifice opening. The experimental results are then compared to a detailed time-dependent axisymmetric computational fluid dynamics (CFD) model of the OTPR. In the CFD model, the continuity, momentum and energy equations are solved for both the refrigerant gas (helium) and the porous media regions (the regenerator and the three heat-exchangers) in the OTPR. An accurate representation of heat transfer in the porous media is achieved by employing a thermal non-equilibrium model to couple the gas and solid (porous media) energy equations. The model predictions are compared with temperature measurements at selected locations. The validated model can be used for system improvement and optimization.

### KEYWORDS

Thermoacoustic-Refrigeration Cryogenics Pulse-Tube Acoustic-Streaming

### INTRODUCTION AND BACKGROUND

The pulse tube refrigerator or pulse tube cryocooler is a developing technology that emerged largely in the early 1980's with a series of other innovations in the broader field of thermoacoustics. In contrast with other cryocoolers (e.g. Stirling cryocooler and Gifford-McMahon cooler) this cryocooler can be made without moving parts in the low temperature part of the device, making the cooler suitable for a wide variety of applications. Pulse tube cryocoolers have been used in industrial applications such as semiconductor fabrication and in military applications such as for the cooling of infrared sensors [1]. Pulse tubes are also being developed for cooling of astronomical detectors where liquid cryogenics are typically used. Pulse tubes will be particularly useful in space-based telescopes where it is not possible to replenish the cryogenics as they are depleted. It has also been suggested that pulse tubes could be used to liquefy oxygen on Mars [2].

The pulse tube refrigerator is an interesting thermoacoustic device and was first discovered and reported by Gifford and Longworth in 1964 [3, 4]. They named the device 'pulse tube refrigerator' as the displacer (found in Stirling and Gifford-McMahon type refrigerators) was replaced by a hollow tube. This initial pulse tube refrigerator design is now called a Basic Pulse Tube Refrigerator (BPTR) [5]. Initial experiments using Helium as the working gas resulted in cold temperatures of around 169 K for a single stage and 123 K for a double-stage cryocooler [6]. A major breakthrough was achieved in 1984, when Mikulin [7] demonstrated that the phase and amplitude relation between velocity and temperature can be manipulated by controlling the boundary conditions at the end of the pulse tube. This was done by placing an orifice and a reservoir (compliance/surge) volume at the end of the BPTR thus allowing a finite gas flow. The presence of the orifice changes the phase angle between the velocity (mass flow rate) and temperature at the cold end and increases enthalpy flow at the hot end. Mikulin's initial experiments attained 105 K with air as the working gas. This was the first OTPR. The OTPR was shown to result in lower temperatures, increased cooling and higher efficiencies than the BPTR.

1-D computational models have been widely used for modeling thermoacoustic devices. Swift *et al.* [9-11] developed a 1-D code for the entire PTR system (and other thermoacoustic engines and refrigerators) based on Rott's [12] linear acoustic equations. While, the 1-D codes provide relatively good estimations of various operating parameters of the PTR (dimensions, operating frequencies, etc.) and provide fairly quick/instant results; they use idealistic assumptions and do not reflect the multi-dimensional nature of the flow and transport inside the PTR systems.

Lee [13, 14] developed a set of 2-D differential equations for use in describing the steady secondary flows generated by the periodic compression and expansion of an ideal gas in pulse tubes. The equations were used to obtain an insight into the physics of the pulse tube in a basic pulse tube (BPTR) and an orifice pulse tube refrigerator (OPTR) for what is known as the thermally strong case. More recently, Flake and Razani [15] carried out an axisymmetric analysis of a BPTR and a PTR and showed cycle-averaged flow fields in the pulse tube. Cha *et al.* [16] studied two IPTR systems based on the geometry of the pulse tube (for two values of L/D ratio). They showed the formation of instantaneous vortical structures in the pulse tube for the small L/D case which had a negative effect on the cooling performance of the IPTR due to the mixing of flow in the pulse tube. Ashwin *et al.* [17] used a thermal non-equilibrium model in the porous media (heat exchangers and regenerator) and considered a finite wall thickness for the various components of the IPTR. The effect of a finite wall thickness was found to increase the steady state temperature at the cold end of the pulse tube due to the heat conduction along the walls of the pulse tube from the hot end to the cold end. More recently, we studied the effect of operating frequency on the performance of an OPTR and showed for the *first* time the presence of streaming in the pulse tube of the OPTR [18]. In the same study, the effects of the operating frequency on the shapes of the streaming profiles was studied too. We also studied the possibility of acoustic streaming suppression in the pulse tube region by tapering the pulse tube by a small angle [19].

In this paper, we report an experimental characterization of an OPTR and time-dependent axisymmetric CFD simulations where the transient as well as the cycle-averaged operation of an OPTR is studied for the processes occurring in an in-line orifice type pulse tube refrigerator. The experimental characterization is done at various values of mean pressure of helium ( $\sim 0.35$  MPa to 2.2 MPa), amplitude of pressure oscillations, and frequency of operation and size of orifice opening. The compressible form of the Navier-Stokes equations is considered for the flow simulations. For the porous media regions (i.e. the regenerator and the heat exchangers), we employ the thermal non-equilibrium porous media model [17-20]. In the non-equilibrium model, the gas and the solid temperatures are different in the porous media. The effect of heat transfer between the gas and the solid phases are considered in the energy equations of the gas and solid phase regions.

## EXPERIMENTAL CHARACTERIZATION OF AN OPTR

In this section, the design, fabrication and testing of an OPTR is reported. The OPTR is characterised at various values of mean pressure, pressure amplitude, frequency of operation and the needle valve orifice flow coefficient.

### Geometry, Fabrication and Experimental Conditions

The OPTR is designed using a software DeltaEC [11]. DeltaEC is a 1-D model that allows the user to design the dimensions of a thermoacoustic cryocooler based on the constraints of the experimental setup (pressure, frequency and heat-exchanger and regenerator matrix material parameters). The pressure wave generator used in the experiments is a QDrive twin-STAR liner motor type pressure generator. The pressure wave generator has a swept volume of 15.55 cubic centimeters (maximum operating pressure of 2.5 MPa). DeltaEC derives its solution by solving a 1-D wave equation based on a shooting method. Hence, the initial dimensions and input parameters provided to the code have to be carefully chosen. We used empirical correlations from a review by Radebaugh [5] to generate these initial values. Based on the swept volume of the pressure wave generator, the mean operating pressure, the frequency of operation and the regenerator and heat exchanger characteristics, DeltaEC provided the lengths of the various components. Fig. 1 shows the general schematic of an OPTR system. The dimensions of the OPTR obtained from DeltaEC and the materials used in the fabrications are summarized in Table 1 below. The heat-exchangers and the regenerator are made from stacked woven square-mesh screen. Table 2 summarizes the materials and the mesh parameters for the various heat-exchanger components.

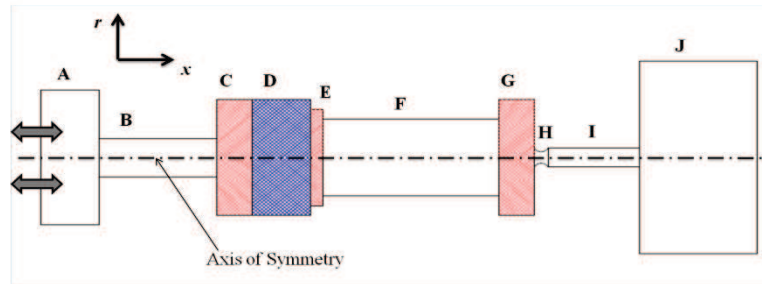


**Figure 1:** General schematic for an OPTR and geometry for numerical simulations of an OPTR

**Table 1:** Dimensions and Materials used in experimental OPTR system

Component*	Radius (cm)	Length (cm)	Wall thickness (cm)	Material	Boundary condition along the outer wall
Transfer Tube (B)	0.85	4.0	0.8	Stainless Steel	Open to ambient
Aftercooler (C)	0.85	3.0	0.107	Copper	$T_w \sim 300 K$
Regenerator (D)	0.85	6.0	0.107	Stainless Steel	Adiabatic
Cold Heat-Exchanger (E)	0.47	5.0	0.165	Copper	Adiabatic
Pulse Tube (F)	0.47	23.0	0.165	Stainless Steel	Adiabatic
Hot Heat-Exchanger (G)	0.47	3.0	0.165	Copper	$T_w \sim 300 K$
Inertance Tube (I)	0.193	150.0	0.125	Copper	Open to ambient
Compliance Volume (J)	2.6	14.9	0.5	Cast Iron	Open to ambient

\* The alphabets in parentheses correspond to the location of the components in figure 1

**Table 2:** Heat-exchanger and Regenerator material properties

Component	Material	Mesh Size/Count*	Wire Diameter (cm)	Porosity 'ε'	Permeability 'κ' (m <sup>2</sup> )	Drag Factor 'C <sub>F</sub> '
Heat-Exchangers	Copper	20 × 20	0.04064	0.774	$4.08 \times 10^{-8}$	0.2
Regenerator	Stainless Steel	325 × 325	0.003556	0.72	$9.70 \times 10^{-11}$	0.3

\* Number of woven square-mesh per inch

The pressure wave generator is connected to a signal generator (BK Precision 4011A) and an amplifier (Crown CE1000). The signal generator is capable of providing  $\pm 5.0$  V sine, square and saw-tooth/triangle waves at frequencies from 0.5 Hz up to 5.0 MHz. For the OPTR system in the study, the pressure wave generator has an upper limit for the frequency at 100 Hz and only sinusoidal waves are used to run the OPTR. Between the amplifier and the pressure wave generator, there are two multi-meters used to measure the voltage (in parallel) and the current (in series) going into the pressure wave generator. These measurements are used to calculate the Apparent Input Power to the pressure wave generator.

Due to the large temperature gradients over small lengths of the system, it is important to keep in mind the thermal properties of the materials used to fabricate the various components. The heat exchangers are made from copper. Due to the compact nature of the system, the high temperature gradients and the high gas pressures used, the other components of the OPTR are made of 316-type stainless steel tubing/piping (stainless steel exhibit relatively low thermal conductivity and high strength in the temperature range of 350 – 100 K). The orifice used in the system is a NOSHOK brass needle valve (101-MMB) capable of a maximum flow coefficient of 0.42.

The various components were connected by flange couplings. Indium wire o-rings were found to provide the best seal for the system operating with high pressure Helium and large temperature gradients.

The OPTR was instrumented with an Omega pressure transducer (PX-309-500G5V) at the exit of the pressure wave generator and an Omega K-type thermocouple (1/16" probe type). The thermocouple was used to measure the gas temperature in the cold heat-exchanger using a compression fitting to prevent leaks from the high pressure system. The thermocouple has an accuracy of around  $\pm 1$  K below 273 K.

The two heat-exchangers (i.e., the aftercooler and the hot heat-exchanger) are enclosed in copper water-jackets. Tap water at  $\sim 22$  °C is run through the water-jackets at  $\sim 1$  liter/min. The regenerator, cold heat-exchanger and part of the pulse tube are enclosed in a vacuum chamber. The vacuum chamber is used to reduce convective heat transfer losses observed for the OPTR operating in ambient conditions. The vacuum chamber is capable of reaching  $\sim 10 - 20$  Torr. High and ultra-high vacuum ( $< 10^{-6}$  Torr) can further decrease the heat transfer losses; however those levels of vacuum are beyond the capabilities of the current vacuum pump and vacuum chamber. The presence of humidity/water vapour results in the formation of frost/ice on the cold regions of the OPTR. To purge the vacuum chamber of any water vapour,  $N_2$  gas is passed through the vacuum chamber prior to running an experiment. To counter the increase of radiation heat transfer in vacuum, the components of the OPTR in the vacuum chamber are wrapped in a reflective foil. The reflective foil used in this current study is Aluminised Mylar. The advantages of using Aluminised Mylar are its high reflectivity and low thermal conductivity.

Before an experiment is run, the OPTR is purged of any residual gases. Then the system is charged with Helium to the required operating pressure.  $N_2$  gas is passed through the vacuum chamber at a pressure of 5 – 10 psig.  $N_2$  is run through the system for  $\sim 15$  minutes. Next the vacuum pump is turned on and  $N_2$  is allowed to flow through the vacuum chamber for an additional 15 minutes with the vacuum pump running. For the final step of purging the vacuum chamber, the vacuum pump is run for a further 15 minutes after closing the  $N_2$  supply before an experiment is started. The vacuum pump is run also for the entire experiment ( $\sim 60 - 70$  minutes). This procedure is followed before each experiment and is performed to ensure the highest vacuum and the lowest amount of water vapour with the given equipment.

In the following sections, the results from the various experiments performed on the OPTR are plotted and discussed. The following experiments provide a thorough characterization of the OPTR and the factors that affect its performance. The temperature results reported here are steady-state values at 60 minutes of operation. After 60 minutes, the gradient in the temporal variation of the gas temperature is fairly small. Table 3 summarizes the parameters used to experimentally characterize the OPTR.

### Optimum Frequency of Operation

Cases 1 – 6 study the frequency dependence of the system. The OPTR was operated at a constant mean pressure of 1.81 MPa, a constant value of the apparent input power 150 (Volt-Amperes) and a constant flow coefficient of the orifice valve  $C_v = 0.42$ . The OPTR was run at six different values of operating frequency, 55, 60, 62, 65, 70 and 72 Hz (cases 1 – 6 respectively). For the given system, values of operating frequency below 55 Hz and above 72 Hz resulted in current values above 8 A which is beyond the capacity of the linear motor pressure wave generator.

The most important input characteristic of an OPTR is the operating frequency. Each OPTR has an optimum/resonant frequency at which it operates the best. At the optimum frequency, all the phase relationships between the pressure and mass flow rate are at the optimum. This frequency varies for system to system and is dependent on the pressure wave generator, the regenerator and heat-exchanger matrices and the length of the various components in the system.

During the characterization of the response of the OPTR to the operating frequency, the mean operating pressure is maintained at 1.8 MPa and the apparent input power to the system is maintained at  $\sim 150$  W. The flow coefficient of the orifice valve is maintained at 0.42 and only the input frequency to the system is varied. Fig. 2 shows the temporal variation of gas temperature in the cold heat-exchanger (between the regenerator and the pulse tube) region. The exact values of the power for a particular frequency are shown in parentheses. The lowest gas temperature attained after 60 minutes of operating the OPTR was 125.74 K. This temperature was obtained for an operating frequency of 65 Hz. Fig. 3 shows the performance chart for the OPTR at the various frequencies studied. At the optimum frequency, the OPTR not only reaches its lowest temperature, but the cool-down time is the fastest.

### Effect of Mean Operating Pressure

Cases 7 – 11 study the performance of the system at various values of mean operating pressure. The OPTR was operated at a constant frequency of 65 Hz (the optimum frequency of the system, section 2.2), a

constant value of the apparent input power 121 (Volt-Amperes) and a constant flow coefficient of the orifice valve  $C_v = 0.42$ . The experiments were conducted at 0.74, 1.05, 1.41, 1.74 and 2.19 MPa (cases 7 – 11 respectively).

**Table 3:** List of cases studied in the experimental characterization of the OPTR

Case No.	Frequency (Hz)	Voltage (V)	Current (A)	Apparent Power (Volt-Amperes)	Mean Pressure (MPa)	Pressure Amplitude (MPa)	Flow Coefficient of Orifice ' $C_v$ '
1	55	28.9	5.18	149.702	1.81	0.314	0.42
2	60	35.1	4.26	149.526	1.81	0.324	0.42
3	62	37.7	4	150.8	1.81	0.394	0.42
4	65	34.9	4.3	150.07	1.81	0.476	0.42
5	70	25.7	5.86	150.602	1.81	0.332	0.42
6	72	21.8	6.89	150.202	1.81	0.376	0.42
7	65	19.2	6.31	121.152	0.74	0.181	0.42
8	65	23.7	5.13	121.581	1.05	0.236	0.42
9	65	28.2	4.27	120.414	1.41	0.337	0.42
10	65	32	3.74	119.68	1.74	0.372	0.42
11	65	32.2	3.77	121.394	2.19	0.407	0.42
12	65	16	2.02	32.32	2.2	0.237	0.42
13	65	24.8	3	74.4	2.2	0.357	0.42
14	65	34.2	4	136.8	2.2	0.399	0.42
15	65	41.2	5.04	207.648	2.2	0.465	0.42
16	65	41	5.01	205.41	2.23	0.455	0.42
17	65	41.1	5.01	205.911	2.23	0.484	0.35
18	65	41	5.02	205.82	2.23	0.477	0.2

To study the effect of the mean operating pressure on the performance of the OPTR, the frequency (65 Hz) and the input power ( $\sim 121$  W) were kept constant. The OPTR was operated at five values of mean operating pressure, from 0.7 MPa ( $\sim 100$  psig) to 2.2 MPa ( $\sim 320$  psig).

An increase in the mean operating pressure, can increase the density and the thermal conductivity of the gas. This will enhance the heat transfer in the OPTR system and lead to improved cooling. When the operating pressure is increased and input power to the system is maintained constant, the pressure amplitude in the system is increased. Fig. 4 shows this increasing trend of pressure amplitude as the mean operating pressure is increased. Due to this increase in the pressure amplitude, the acoustic power density is increased (for a constant frequency of operation). The experimentally obtained temperature at the cold heat-exchanger (Fig. 4) reflect these results. It is apparent that the cold temperature in the OPTR decreases as the mean pressure in the system increases.

However, it is interesting to note that the temperature appears to asymptotically reach a plateau (between 1.7 MPa and 2.2 MPa the difference in the steady-state temperature is  $\sim 2$  K). Helium is the most widely used refrigerant for two main reasons. First, it has the highest thermal conductivity for an inert gas and second, it has the highest ratio of specific heats ( $\gamma = 1.6$ ). A high value of  $\gamma$  implies that adiabatic expansion of the gas provides maximum cooling and adiabatic compression of the gas provides maximum heating.

Very high mean operating pressures lead to high pressure amplitudes (for a system operating at constant input power). Due to this high ratio of specific heats for Helium, an increase in pressure and pressure amplitude will lead to very high temperatures at the inlet of the regenerator. This will lead to a degradation of performance of the system at very high mean operating pressures and pressure amplitudes. Better aftercooler heat-exchangers will be required to further improve the performance of the system.

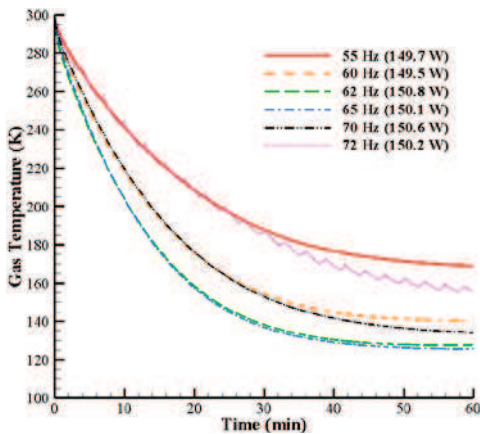


**Figure 2:** Temporal variation of gas temperature in the cold heat-exchanger at various values of operating frequency (cases 1 – 6 in Table 3)

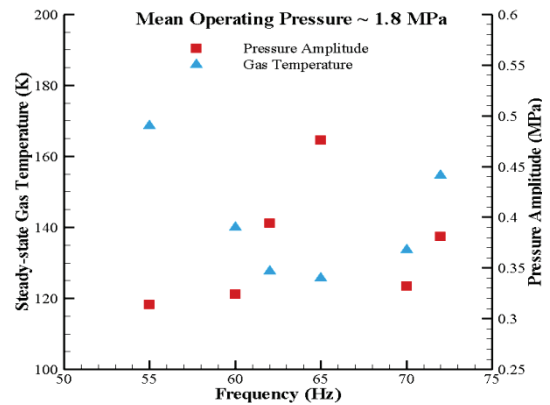


**Figure 3:** Performance chart and pressure amplitude (in the transfer tube) for the OPTR at various values of operating frequency for a constant input power of ~ 150 W

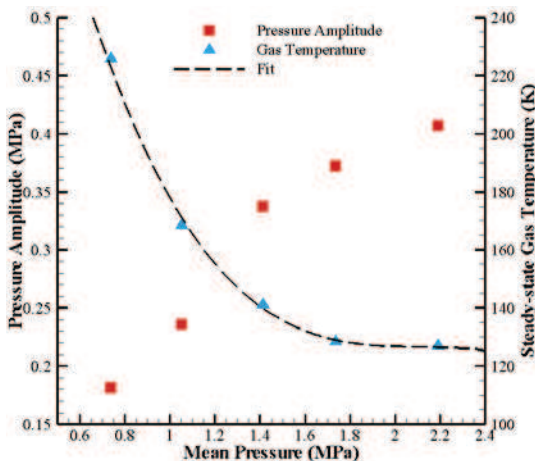


**Figure 4:** Performance map and pressure amplitude (in the transfer tube) for an OPTR operating at a constant frequency of 65 Hz (cases 7 – 11 in Table 3)

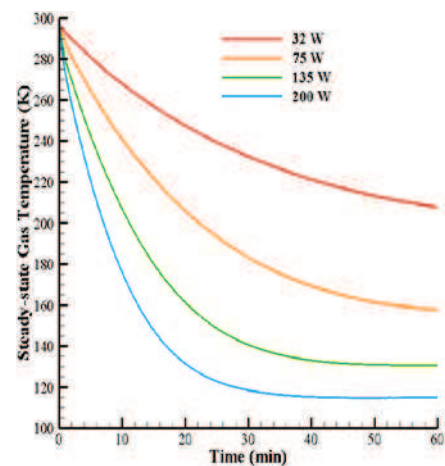


**Figure 5:** Temporal variation of the gas temperature in the cold heat-exchanger at various values of input power to the linear motor pressure wave generator (cases 12 – 15 in Table 3)

### Effect of Input Power

Cases 12 – 15 study the effect of operating pressure amplitude on the performance of the OPTR. The OPTR was operated at a constant frequency of 65 Hz, constant value of mean operating pressure 2.2 MPa and a constant flow coefficient of the orifice valve  $C_v = 0.42$ . To control the operating pressure amplitude, the input power to the linear motor pressure wave generator is varied. The experiments were conducted at 0.237, 0.357, 0.399 and 0.465 MPa (cases 12 – 15 respectively).

The effect of the applied input power on the performance of the OPTR, the mean operating pressure and the operating frequency were kept constant at 2.2 MPa and 65 Hz respectively. Fig. 5 shows the temporal variation of the gas temperature in the cold heat-exchanger at the various values of input power studied. As expected, the an increase in the applied input power results in an improvement of the performance of the OPTR. The temporal plots for gas temperature also show the cool-down time decreases with an increase in the applied input power. As the applied input power is increased, the pressure amplitude is increased (Fig. 6). This increase in the pressure amplitude leads to an increase in the mass flow rate through the regenerator and hence lower steady-state temperatures. Additionally in the pluse tube, higher pressure amplitudes increase the cooling achieved through adiabatic expansion of the gas in the cold region of the pulse tube (see step 3 of the processes occuring in the pulse tube).

### Effect of Flow Coefficient of the Orifice Valve

Cases 16 – 18 study the effect of the opening size of the orifice valve on the performance of the OPTR. The OPTR was operated at a constant frequency of 65 Hz, constant value of mean operating pressure 2.23 MPa and a constant input power to the linear motor of 205 Volt-Ampere. For a needle-type orifice valve the opening of the valve is characterized by a flow coefficient  $C_v$  (larger opening sizes correspond to larger values of  $C_v$ ). The values of flow coefficient studied were 0.20, 0.35 and 0.42 (cases 16 – 18 respectively).

After the introduction of the inertance tube, it has become the more preferred component to maintain the proper phase relationships in the system. However, it has been shown that using both the orifice and inertance tube can improve the performance for the OPTR. In the current experiment, a needle type orifice valve is used. The use of a needle valve enables the variation of the orifice flow coefficient so as to find the optimum value "sweet spot".

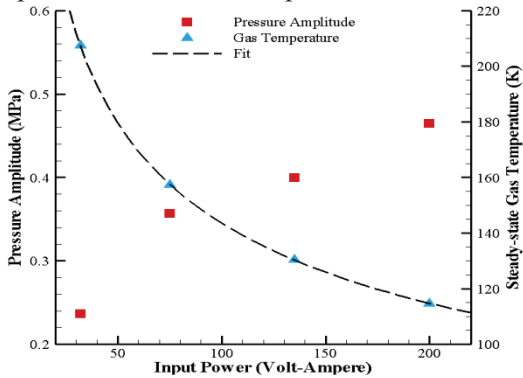


**Figure 6:** Performance map and pressure amplitude (in the transfer tube) in the OPTR for different values of applied input power

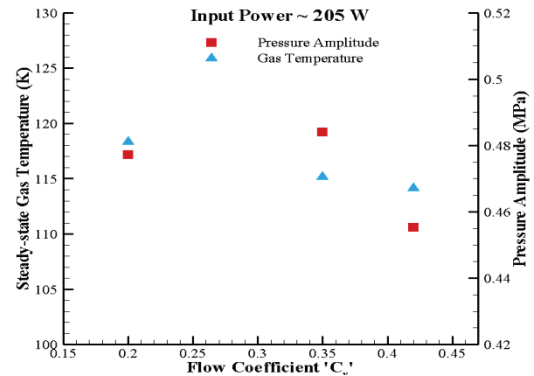


**Figure 7:** Performance map and pressure amplitude (in the transfer tube) for the OPTR at three values of orifice flow coefficient (cases 16 – 18 in Table 3)

Fig. 7 shows the performance of the OPTR as a function of the orifice flow coefficient. The plot also shows the pressure amplitude at the exit of the linear motor pressure wave generator as a function of the orifice flow coefficient. During the experiment, the applied input power is maintained constant at 205 W and the mean operating pressure in the system is 2.2 MPa. The best performance is observed when the flow coefficient is at its maximum ( $C_v = 0.42$ ) and the orifice is fully open. As the orifice is closed, the performance of the system deteriorates. Below a flow coefficient of 0.15 (for this particular needle valve), the decrease in performance is very large. This can be explained by two possible reasons. First, a decrease in the flow coefficient (closing the valve) leads to a decrease in the mass flow through the orifice and hence decrease in the cooling. Second, the constriction of the orifice opening leads to an increase in velocity and hence possible jetting can occur in the pulse tube which causes mixing of flow in the pulse tube that leads to a deterioration in the performance. Closing the orifice valve also leads to an increase in the pressure amplitude in the system. This is observed in the cool-down times for the OPTR to reach cryogenic temperature (120 K). They are 36, 26 and 28 minutes for flow coefficient values of 0.2, 0.35 and 0.42 respectively. Even though the value of  $C_v = 0.42$  has the best performance, due to the increase in pressure amplitude for  $C_v = 0.35$ , the cool-down time to 120 K is smaller for  $C_v = 0.35$  compared to  $C_v = 0.42$ .

### NUMERICAL SIMULATION OF AN OPTR

In this section, numerical simulations of an OPTR are reported. The problem geometry, equations solved and the boundary conditions applied are reported below. Some important results from the simulations are discussed and the steady-state temperature values are compared to the values obtained from the experiments.

#### Problem Geometry

Fig. 1 depicts the geometry studied (i.e. an inline OPTR system). Only half the geometry shown in figure 1 is simulated (the axisymmetric assumption) due to the cylindrical nature of an actual system and to save on computation time. The OPTR has the same components as the experimental system. These include

a compression chamber with a moving piston (which models the motion of the piston in the linear motor pressure wave generator), a transfer tube, an aftercooler (the first red hatched region), a regenerator (blue cross-hatched region), a pulse tube with two heat exchangers at its ends (the other two red hatched regions), an orifice (a simple obstruction to the flow), an inertance tube and the compliance volume.

Table 4 summarizes the various dimensions of the problem geometry and the time-invariant boundary conditions in the simulations. The dimensions are maintained the same as the experimental system in order to compare the results from the computational and experimental investigations. The mathematical boundary conditions at the various components' surfaces will be explained in detail in a following section.

**Table 4:** Dimensions of the components of the OPTR simulated and the applied boundary conditions

No.	Component	Radius (mm)	Length (mm)	Material	Boundary condition along the outer wall
A	Compression Chamber	3.0	1.1		Adiabatic
B	Transfer Tube	0.85	4.0		$h_c = 20 \text{ W/m-K}$
C	Aftercooler	0.85	3.0	Copper	$T_w = 300 \text{ K}$
D	Regenerator	0.85	6.0	Stainless Steel	Adiabatic
E	Cold Heat-Exchanger	0.47	5.0	Copper	Adiabatic
F	Pulse Tube	0.47	23.0		Adiabatic
G	Hot Heat-Exchanger	0.47	3.0	Copper	$T_w = 300 \text{ K}$
H	Orifice Valve	0.425	0.4		Adiabatic
I	Inertance Tube	0.85	150.0		Adiabatic
J	Compliance Volume	2.6	14.9		Adiabatic

### Mathematical Model

The flow and heat transfer simulation model incorporates the fluid dynamic equations of conservation of mass (continuity equation), momentum (Navier-Stokes equations) and energy in the fluid domain. The various heat exchangers and the regenerator are modeled as porous media with the relevant solid properties of the regenerator and the heat exchanger materials. The mass, momentum and energy conservation equations [21-23] for the porous media regions are solved simultaneously with the gas phase equations for the OPTR as shown in Fig. 1.

**Governing Equations:** The conservation equations for the gas phase (helium) within the system undergoing periodic compression and expansion are given as follows:

$$\frac{\partial \rho}{\partial t} + \nabla \cdot (\rho \vec{u}) = 0 \quad (1)$$

$$\frac{\partial (\rho \vec{u})}{\partial t} + \nabla \cdot (\rho \vec{u} \vec{u}) = -\nabla p + \nabla \cdot \tau_{ij} \quad (2)$$

$$\frac{\partial (\varepsilon \rho h_0)}{\partial t} + \nabla \cdot (\varepsilon \rho \vec{u} h_0) = \nabla \cdot (k_f \nabla T_f) + \nabla \cdot (\varepsilon \vec{u} \tau_{ij}) + \varepsilon \frac{\partial p}{\partial t} + S_G \quad (3)$$

where  $\rho$  is the density,  $\vec{u}$  is the (r-z) velocity vector and the total energy  $h_0$  is given by

$$h_0 = i + \frac{p}{\rho} + \frac{1}{2} (\vec{u})^2 \quad (4)$$

and the gas-phase temperature is

$$T_f = \frac{1}{c} \left[ h_0 - \frac{p}{\rho} - \frac{1}{2} (\bar{u})^2 \right] \quad (5)$$

The last term in the gas-phase energy equation is only applicable for the porous media zones (where the porosity  $\varepsilon$  is  $< 1.0$ ):

$$S_G = \frac{h_p A (T_s - T_f)}{\varepsilon} \quad (6)$$

In the gas regions, the value of  $\varepsilon$  is 1.0. For the porous media regions, refer to Table 2 for the value of  $\varepsilon$ . The value of the convective heat transfer coefficient  $h_p$  for the gas-solid interfaces is calculated from a heat transfer correlation for oscillating flow in regenerators developed by Tanaka *et al.* [20]. The equation is given by:

$$h_p = 0.33 \frac{k_f}{4r_h} \left( \frac{8\rho_f r_h V_p \rho_r}{\mu A_{sp} \varepsilon} \right)^{0.67} \quad (7)$$

where,  $r_h$  is the hydraulic diameter of the porous media material (in the case of wire mesh, it is the diameter of the wire),  $V_p$  is the volume of the solid material in the porous media,  $A_{sp}$  is the total surface area of the porous media,  $\mu$  is the viscosity of the fluid and  $\rho_r$  is the ratio of the density of the fluid to the average density of the fluid in the porous media.

The gas used in OPTR for the simulations is Helium. Helium is assumed to be an ideal gas and its viscosity and thermal conductivity are considered to be temperature-dependent. The temperature dependent properties were obtained from the NIST database [24]. The specific heat was kept constant since it does not vary considerably in the temperature range anticipated (i.e. 370 K – 90 K).

The mass and momentum equations for the porous media zones (Darcy-Forchheimer model) [17, 23] are given as follows:

$$\frac{\partial(\varepsilon\rho)}{\partial t} + \nabla \cdot (\varepsilon\rho\bar{u}) = 0 \quad (8)$$

$$\frac{\partial(\varepsilon\rho\bar{u})}{\partial t} + \nabla \cdot (\varepsilon\rho\bar{u}\bar{u}) = -\varepsilon\nabla p + \nabla \cdot (\varepsilon\tau_{ij}) - \frac{\varepsilon^2\mu}{\kappa}\bar{u} - \frac{\varepsilon^3 C_F \rho}{\sqrt{\kappa}} |\bar{u}| \bar{u} \quad (9)$$

For values of the permeability  $\kappa$  and the quadratic drag factor  $C_F$ , refer to Table 2. These values were calculated based on correlations for square-mesh screens where the weaving causes no inclination of the wires [25, 26].

For the solid matrix, the energy equation is given by:

$$\frac{\partial(T_s)}{\partial t} = \nabla \cdot (\Gamma\nabla T_s) + S_p \quad (10)$$

$$S_p = \frac{h_p A (T_f - T_s)}{1 - \varepsilon} \quad (11)$$

where  $\Gamma$  is the diffusivity of the solid porous media and  $A$  is the heat transfer area per unit volume. The value of  $\Gamma$  for copper (in the heat exchangers) is  $1.17 \times 10^{-4} \text{ m}^2/\text{s}$  and that for stainless steel (in the regenerator) is  $1.18 \times 10^{-5} \text{ m}^2/\text{s}$ .

In the heat exchangers (see figure 1) the solid phase material considered was copper. The density and specific heat of copper were assumed to be  $8950 \text{ kg/m}^3$  and  $380 \text{ J/kg-K}$  respectively and temperature dependent thermal conductivity values were considered. Similarly for the regenerator (considered as porous media), stainless steel was considered as the solid phase material and the density and specific heat were assumed to be  $7810 \text{ kg/m}^3$  and  $460 \text{ J/kg-K}$  respectively and the temperature dependent thermal conductivity values were considered.

**Initial Conditions:** At the start of the simulation, the temperature in the system is assumed to be 300 K everywhere. Table 5 lists the mean operating pressure (specified as an initial condition) for each of the cases studied.

**Table 5:** List of cases simulated

Case No.	Mean Pressure (MPa)	Piston displacement $A_0$ (cm)	Pressure Amplitude (MPa)
1	2.2	0.28	0.4
2	1.74	0.32	0.38
3	1.41	0.345	0.34

**Boundary Conditions:** Table 1 (given earlier) specifies the flow and heat transfer boundary conditions used at the surface boundaries of the various components. The piston is modeled as a reciprocating wall having an oscillatory velocity. The velocity of the piston is defined by the function,  $u = A_0\omega\cos(\omega t)$ , where  $A_0$  is the maximum displacement of the piston and  $\omega$  is the angular frequency ( $\omega = 2\pi f$ ) and  $f$  is the frequency of operation. Table 5 has the values of the maximum displacement of the piston  $A_0$  for the cases studied.

**Numerical Scheme:** The numerical scheme for solving the governing equations is based on the finite volume approach. The continuity, momentum and energy equations are solved for the fluid as well as the porous media using a 2<sup>nd</sup> order upwind scheme. The motion of the piston is captured by a moving grid scheme near the piston wall in the compression space (component A in Fig. 1). The re-meshing scheme used in the simulations is the Transfinite Interpolation scheme [23]. The various cases studied are tabulated in Table 4 above. A 2<sup>nd</sup> order Crank-Nicholson scheme (with a blending factor of 0.7) is used for the time derivatives in the continuity, momentum and energy equations. The time-step size was determined by allowing 80 time-steps/cycle, which is sufficient to accurately simulate the problem ( $\Delta t = 1.923077 \times 10^{-4}$ ). An overall convergence criterion is set for all the variables at  $10^{-4}$  in the iterative implicit numerical solver.

Due to the symmetry of the problem geometry, only one-half of the domain (figure 1) was considered for the simulations. Grid convergence studies were performed [18] at locations where high gradients (in velocity and temperature) were observed. These studies lead to the use of a hybrid (structured-unstructured) grid system in the simulations. Structured grid (non-uniform orthogonal mesh) was used in all components except the cold heat exchanger at the beginning of the pulse tube and the orifice valve. Higher density unstructured triangular mesh is used in the Cold Heat-Exchanger (CHX) and the Orifice sections to accommodate the junction geometries and the high temperature and velocity gradients. A total of 3719 grid points were used in the simulations. The governing equations and the boundary conditions were solved using CFD-ACE+ [23].

## Results and Discussion of Computational Studies

**Transient Processes in the System:** The cool-down behaviour of the OPTR is very important to its operation. Fig. 8 shows this temporal evolution of the gas temperature at the exit of the cold heat exchanger and inlet to the pulse tube section (i.e.  $x = 19.1$  cm,  $r = 0.4699$  cm) for the three cases studied.

The banded profiles are cyclic variation of the gas temperature in the system. It can be clearly seen that the values of gas temperature in cases 2 and 3 are comparatively higher than that in case 1. This emphasizes the importance of high values of mean operating pressure in an OPTR system. The higher values of mean operating pressures also lead to faster cool-down times and lower temperatures. Similar trends were observed in the experimental system (see performance chart in Fig. 4).

The insert in Fig. 8 shows the gas temperature profiles at the entrance of the pulse tube near the end of the simulation or all three cases studied. The cyclic nature of the temperature is visible here. However this gas temperature profile is not sinusoidal in nature and has a distorted structure. As can be seen, the simulations have reached close to a quasi-steady state (i.e. the temperature variation from cycle to cycle is fairly small).

It is interesting to note that the solid temperature oscillates also. However, the amplitude of this oscillation is very small due to the high density and thermal inertia of the solid. Fig. 9 compares the gas and solid temperatures at a later point in the simulations ( $\sim 15$  sec of simulation time). The difference in the solid and gas temperatures are clearly visible. Another important point of note is that the solid temperature lags the gas temperature by a certain phase angle.

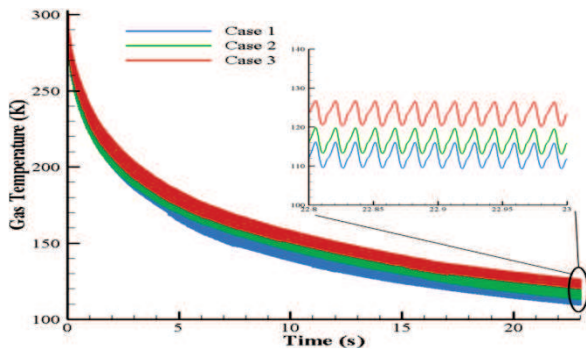


**Figure 8:** Temporal variation of the gas temperature at the entrance to the pulse tube (insert shows the cyclic nature of the temperature)

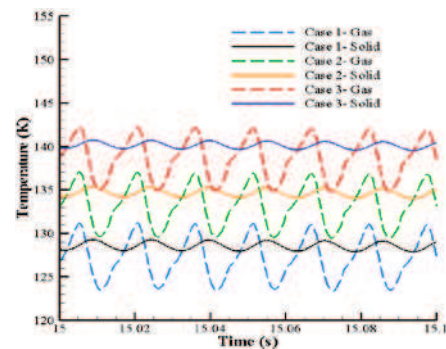


**Figure 9:** Comparison of gas and solid at temperature profiles near steady-periodic conditions

**Spatial Temperature and Velocity Profiles:** In Fig. 10, we show the axial distribution of the temperature in the system along the axis of symmetry (i.e. at  $r = 0.0$  in the simulations) for case 1. The four plots in the figure indicate the temperature profiles at four points in the cycle (1460<sup>th</sup>) i.e.  $\pi/2$ ,  $\pi$ ,  $3\pi/2$  and  $2\pi$ . The temperature is shown from the transfer tube region up to the compliance volume. Beyond the hot heat exchanger, the gas temperature barely oscillates with values around 310 – 320 K (hence these sections are not shown in the figure). The temperature profile along the regenerator and the heat exchangers (porous media) barely oscillate. This indicates that the system is in a steady cyclic mode. The comparison between experiments and numerical simulations is shown in Fig. 11. The temporal variation of the gas temperature for both the experiments and the computations are plotted as a function of the normalized time. The comparison shows fairly similar trends in the temperature variation.

## CONCLUSIONS

The performance of a cryogenic OPTR was characterized under various experimental conditions. The current OPTR was found to have an optimum operating frequency of 65 Hz. The mean operating pressure and the operating pressure amplitude are important for attaining low temperatures and fast cool-down times. The orifice valve is shown to have an effect on cooling attained. An axisymmetric time-dependent computational fluid dynamics model was used to simulate the flow and temperature fields in an OPTR at various mean operating pressures. The computational results show trends similar to the experimentally observed performance of the OPTR where higher mean pressures resulted in lower temperatures and faster cool-down times. A thermal non-equilibrium model was used to predict the differences in the gas and solid temperatures in the porous media zones. The low amplitude of gas temperature oscillation in the pulse tube region indicates the possibility that the volume of the pulse tube is too large for the system (including the linear motor). The excess volume leads to a decrease in the acoustic power density of the system and a reduction in the cooling observed in the pulse tube.

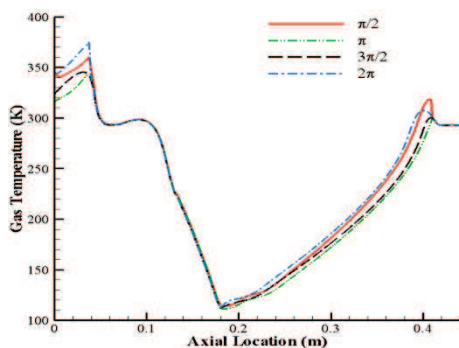


**Figure 10:** Axial distribution of the temperature ( $r = 0.0$ ) in the components D, E, F and G (figure 1 and table 3) different times in cycle 1460 (case 1)

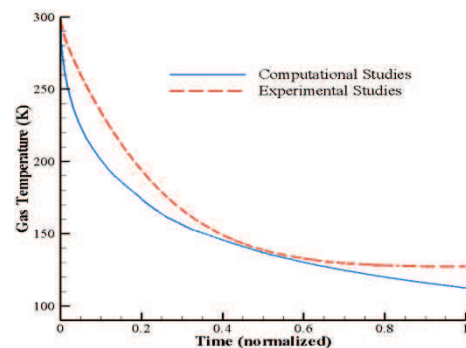


**Figure 11:** Comparison of normalized temporal variation in the gas temperature B, C, experiments (case 11) and numerical at four simulations (case 1)

## ACKNOWLEDGEMENT

Support from the National Science Foundation (USA) under grant CBET-0853959 is gratefully acknowledged.

## References

- [1] R. Radebaugh Pulse tube cryocoolers for cooling infrared sensors // *San Diego, CA, USA*, 2000. Pp. 363-379.
- [2] E. D. Marquardt and R. Radebaugh Pulse Tube Oxygen Liquefier // *Adv. Cryo. Eng.* 2000. Vol. 45. Pp. 457-464.
- [3] W. E. Gifford and R. C. Longworth Pulse-tube refrigeration // *American Society of Mechanical Engineers -- Transactions -- Journal of Engineering for Industry Series B.* 1964. Vol. 86. Pp. 264-268.
- [4] W. E. Gifford and R. C. Longworth *Pulse tube refrigeration progress* / Eds. Plenum Press, 1965. Pp. 69-79
- [5] R. Radebaugh *Review of pulse tube refrigeration* / Eds. Plenum Pub. Corp., Los Angeles, CA, United states, 1990. Pp. 1191-1205
- [6] R. C. Longworth *An Experimental Investigation of Pulse Tube Refrigeration Heat Pumping Rates* / Eds. Klaus D. Timmerhaus, Plenum Press, New York, 1967. Pp. 608-618
- [7] E. I. Mikulin, A. A. Tarasov and M. P. Shkrebyonock Low-Temperature Expansion Pulse Tubes // *Colorado Springs, CO, USA*, 1984. Pp. 629-637.
- [8] R. Radebaugh, James Zimmerman, David R. Smith and Beverly Louie A Comparison of three types of Pulse Tube Refrigerators: New methods for reaching 60 K // *Cambridge, MA, Engl*, 1986. Pp. 779-789.
- [9] G. W. Swift Thermoacoustic Engines // *J. Acoust. Soc. America.* 1988. Vol. 84. Pp. 1145 - 1180.
- [10] G. W. Swift *Thermoacoustics: A unifying perspective for some engines and refrigerators*, ed., Acoustical Society of America, Melville, NY, 2002. Pp.
- [11] User Manual: Design Environment for Low-Amplitude Thermoacoustic Energy Conversion, v. 6.2, 2008, Los Alamos National Laboratory
- [12] N. . Rott *Thermoacoustics* / Eds. Chia-Shun Yih, Academic Press, New York, 1980. Pp. 135-175
- [13] J. M. Lee, P. Kittel, Klaus D. Timmerhaus and R. Radebaugh Steady Secondary Momentum and Enthalpy Streaming in the Pulse Tube Refrigerator // *International Cryocoolers Conference 8*, 1995. Pp. 359-369.
- [14] Jeffrey M. Lee Steady Secondary Flows Generated by Periodic Compression and Expansion of an Ideal Gas in a Pulse Tube // Ph.D. thesis, University of Colorado, Boulder, 1997.
- [15] B. Flake and A. Razani Modeling pulse tube cryocoolers with CFD // *USA*, 2004. Pp. 1493-9.
- [16] J. S. Cha, S. M. Ghiaasiaan, P. V. Desai, J. P. Harvey and C. S. Kirkconnell Multi-dimensional flow effects in pulse tube refrigerators // *Cryogenics.* 2006. Vol. 46. Pp. 658-665.
- [17] T. R. Ashwin, G. S. V. L. Narasimham and Subhash Jacob CFD analysis of high frequency miniature pulse tube refrigerators for space applications with thermal non-equilibrium model // *Applied Thermal Engineering.* 2010. Vol. 30. Pp. 152-166.
- [18] D. Antao and B. Farouk Computational Fluid Dynamics Simulations of an Orifice type Pulse Tube Refrigerator: Effects of Operating Frequency // *Cryogenics.* 2011. Vol. 51. Pp. 192-201.
- [19] D. Antao and B. Farouk Numerical Simulations of Transport Processes in a Pulse Tube Cryocooler: Effects of Taper Angle // *International Journal of Heat and Mass Transfer.* 2011. Vol. *In Press.*
- [20] Makoto Tanaka, Iwao Yamashita and Fumitake Chisaka Flow and heat transfer characteristics of Stirling engine regenerator in oscillating flow // *Nippon Kikai Gakkai Ronbunshu, B Hen/Transactions of the Japan Society of Mechanical Engineers, Part B.* 1989. Vol. 55. Pp. 2478-2484.
- [21] C. Y. Wang, W. B. Gu and B. Y. Liaw Micro-macroscopic coupled modeling of batteries and fuel cells. I. Model development // *Journal of the Electrochemical Society.* 1998. Vol. 145. Pp. 3407-3417.
- [22] C. Y. Wang and P. Cheng *Multiphase Flow and Heat Transfer in Porous Media* / Eds. Thomas F. Irvine Jr Young I. Cho James P. Hartnett and A. Greene George, Elsevier, 1997. Pp. 93-182, 182a, 183-196
- [23] ESI-CFD-Inc. *CFD-ACE+ v2009.4 User Manual*, ed., ESI Group, Hunstville, AL, 2009. Pp.
- [24] NIST Standard Reference Database 12, v. 5.0, National Institute of Standards and Technology
- [25] Kwanwoo Nam and Sangkwon Jeong Investigation of oscillating flow friction factor for cryocooler regenerator considering cryogenic temperature effect // *Cryogenics.* 2005. Vol. 45. Pp. 733-738.
- [26] X. B. Zhang, L. M. Qiu, Z. H. Gan and Y. L. He CFD study of a simple orifice pulse tube cooler // *Cryogenics.* 2007. Vol. 47. Pp. 315-321.

## **NEXT GENERATION THERMALLY POWERED ADSORPTION REFRIGERATION CYCLES**

**Bidyut Baran Saha**

Mechanical Engineering Department, Faculty of Engineering, and  
The World Premier International Research Center  
Kyushu University  
744 Motoooka, Nishi-ku  
Fukuoka 819-0395, Japan  
Tel: +81-92-802-3101, Fax: +81-92-802-3125  
E-mail: saha@mech.kyushu-u.ac.jp

**Ibrahim I. El-Sharkawy**

Mechanical Power Engineering Department, Faculty of Engineering  
Mansoura University, El-Mansoura 35516, Egypt  
E-mail: ielsharkawy@mans.edu.eg

### **Abstract**

The severities of energy crisis and environmental problems have been calling for rapid developments in Freon-free air conditioning and heat pump technologies. From this viewpoint, interest in thermally activated adsorption systems using natural and/or alternative to HFC based refrigerants has been increased. In the first part of this article, several thermally activated advanced adsorption cooling cycles are overviewed. These systems have the advantages of firstly, exploiting renewable energy or waste heat of temperature below 100 °C, and secondly, very low electricity uses for the circulation of heat transfer fluids (hot, cooling and chilled water. Finally, a three-bed dual evaporator type advanced adsorption cooling cum desalination (AADC) cycle has been introduced. The evaporators work at two different pressure levels and produce cooling effects and simultaneously generates potable water from saline or brackish water.

### **KEYWORDS**

Adsorption, desalination, refrigeration, thermally powered.

### **INTRODUCTION**

The quest to accomplish a safe and comfortable environment has always been one of the main preoccupations of the sustainability of human life. Accordingly, during the last few decades research aimed at the development of thermally powered adsorption cooling technologies has been intensified. They offer double benefits of reductions in energy consumption, peak electrical demand in tandem with adoption of environmentally benign adsorbent-refrigerant pairs without compromising the desired level of comfort conditions. Alternative adsorption cooling technologies are being developed which can be applied to buildings [1–4]. These systems are relatively simple to construct, as they have no major moving parts. In addition, there is only marginal electricity usage which might be needed for the pumping of heat transfer fluids. The heat source temperature can be as low as 50 °C if multi-stage regeneration scheme is implemented [5, 6]. However, since the system is driven by low-temperature waste heat, the coefficient of performance (COP) of thermally activated adsorption systems is normally poor [7]. A recent study shows that the cooling capacity of the two-stage silica gel-water refrigeration cycle can be improved significantly when a re-heat scheme is employed [8]. In the first part of this study, several advanced thermally activated adsorption cooling cycles are overviewed. Finally, a three-bed dual evaporator type advanced adsorption cooling cum desalination (AADC) cycle has been introduced in which the evaporators work at two different pressure levels and produce cooling effects and simultaneously generates potable water from saline or brackish water. The performance of the AADC cycle has been determined based on a mathematical model.

## THERMALLY POWERED ADVANCED ADSORPTION COOLING CYCLES

Advanced adsorption cooling cycles are designed either to enhance the performance of the basic systems or to use low temperature grade heat source as low as 40 °C in combination with a coolant at 30 °C. Regenerative systems aim to achieve the former target and multi-stage systems are designed to achieve the latter. However, as this field has become so large and there is a huge number of studies that cannot be concluded entirely in one article. Selected examples of adsorption cooling systems will be presented herein. Saha et al. [5, 9–11] proposed two and three-stage adsorption cycles to use, respectively, waste heat of temperatures between 50 and 70°C, and 40 and 60°C with a coolant at 30 °C. Figs. 1 and 2 show the schematic and the pressure-temperature-concentration diagrams of two-stage adsorption cooling cycle. In this cycle, the evaporation temperature lifts ( $T_{cond} - T_{evap}$ ) is divided into two smaller lifts. The refrigerant pressure is therefore raised into two progressive steps, from the evaporator to an intermediate pressure and from the intermediate pressure to the condenser pressure. This makes it possible to use a low temperature heat source such as solar energy or waste heat (see Fig. 2).

In another endeavor, the same authors [12] have investigated a regenerative multi-bed dual-mode adsorption system as shown in Fig. 3. These cycles have a couple of objectives, the first one is to decrease the peak temperature of both of the condenser and the evaporator outlets the second objective is to improve the recovery efficiency of waste heat to the cooling load. The authors have reported that the dual-mode cycle is capable to utilize effectively low grade waste heat of temperatures between 40 and 95 °C as the driving heat sources along with a coolant at 30 °C. The chiller in the three-stage mode is operational with a heat source and heat sink temperature difference as small as 10 K.

In order to improve the performance of adsorption system, Miles and Shelton [13] introduced a two bed thermal wave system employing activated carbon-ammonia as an adsorbent-refrigerant pair. In the thermal process, only a single heat transfer fluid loop exists. Figure 4 shows a schematic diagram of the proposed cycle. A reversible pump is placed in the closed heat transfer fluid loop to invert the circulation of fluid flow. It is reported that the proposed system achieves a cooling COP as high as 1.9. Similar cycles have been investigated theoretically by Sward et al. [14].

A related concept, convective thermal wave, has been launched by Critoph [15] and Critoph and Thorpe [16]. In this cycle refrigerant works as the heat transfer medium. Activated carbon-ammonia is used as an adsorbent-refrigerant pair and the cycle seems to be suitable for automobile cooling application.

The concept of direct contact condensation and evaporation has been used by Yanagi et al. [17] to develop an innovative silica gel adsorption refrigeration system. As reported by Saha et al. [18], the concept of direct contact during evaporation and condensation (because of the elimination of metallic frames) decrease the temperature difference between hot and cold fluids which increases the heat and mass transfer. In this cycle, the main components are a pair of sorption elements neighboring on a pair of spray nozzles working either as a condenser or an evaporator housing in the same vacuum chamber. As can be seen from Fig. 5, the water vapor evaporating directly from the surface of the sprayed water jet is adsorbed by HX1 in adsorption mode while the desorbed water vapor from the HX2 is condensed on the surface of the sprayed water in the desorption mode. The rated cooling capacity of the Mayekawa pilot plant is 11.5 kW. The chiller has a COP value of 0.58 for hot, cooling and chilled water inlet temperatures are 70, 29 and 14 °C, respectively. The delivered chilled water temperature was reported at 9 °C for a 10 minute duration of adsorption/desorption cycle.

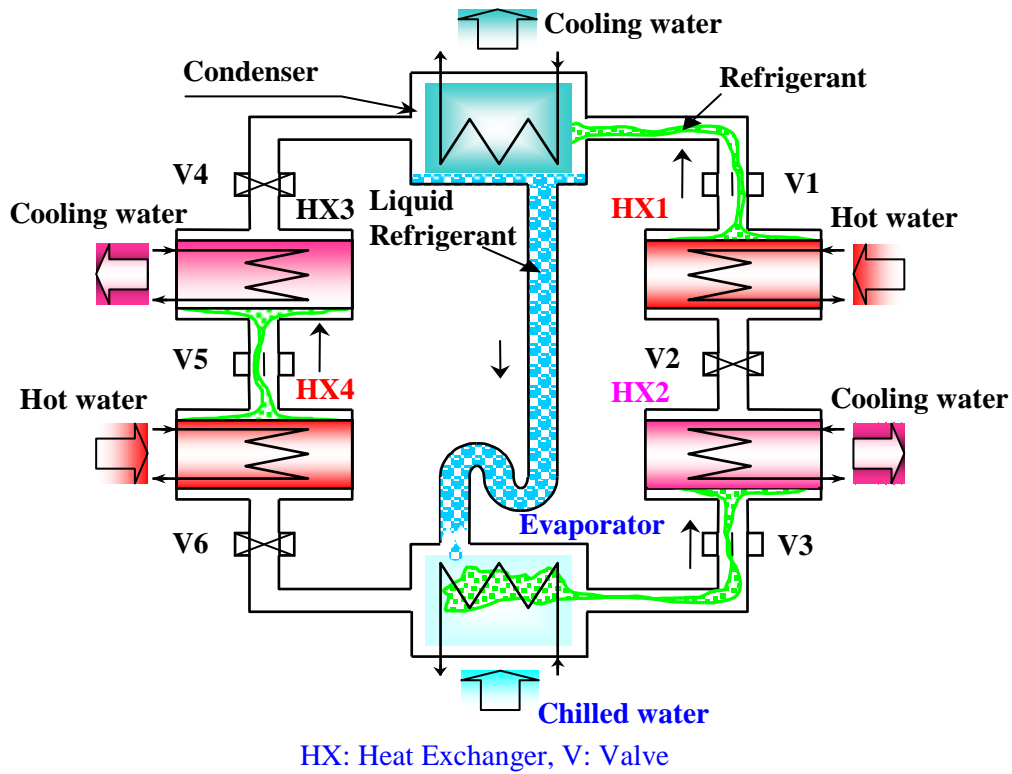


Fig. 1. Schematic diagram of two-stage silica gel/water adsorption chiller [10]

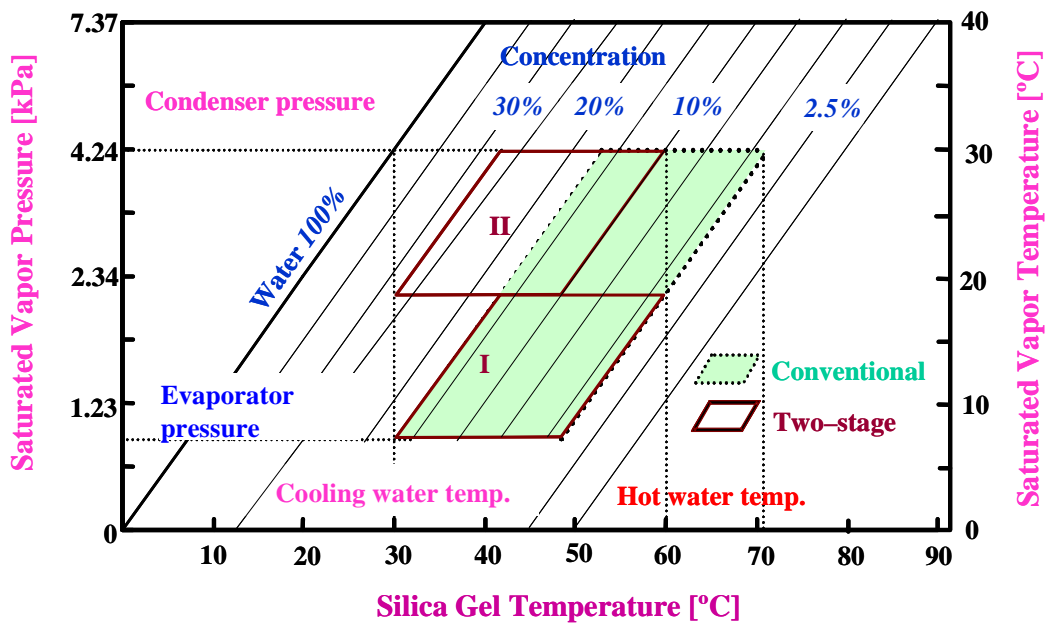


Fig. 2. Conceptual pressure-temperature-concentration diagram for the single and two stage silica gel/water adsorption cycles [10]

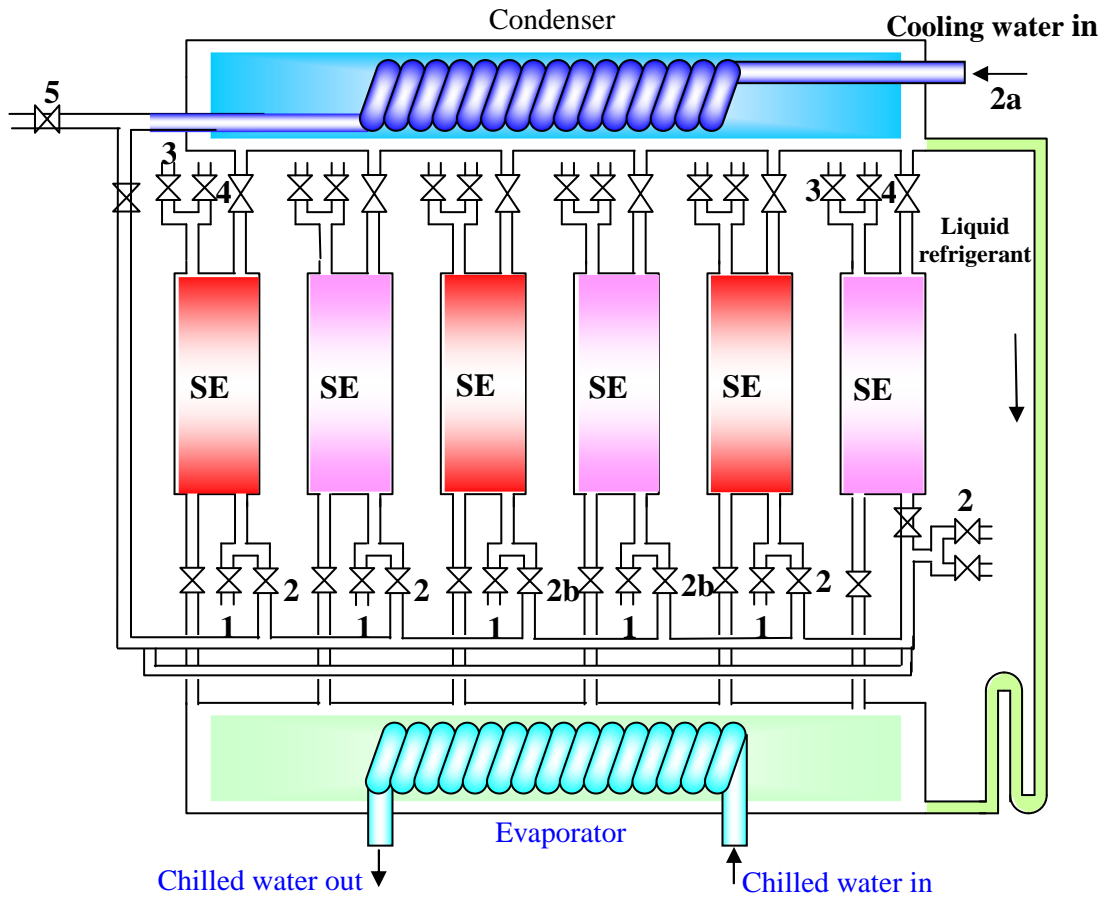


Fig. 3. Schematic diagram of the multi-bed adsorption chiller [12]

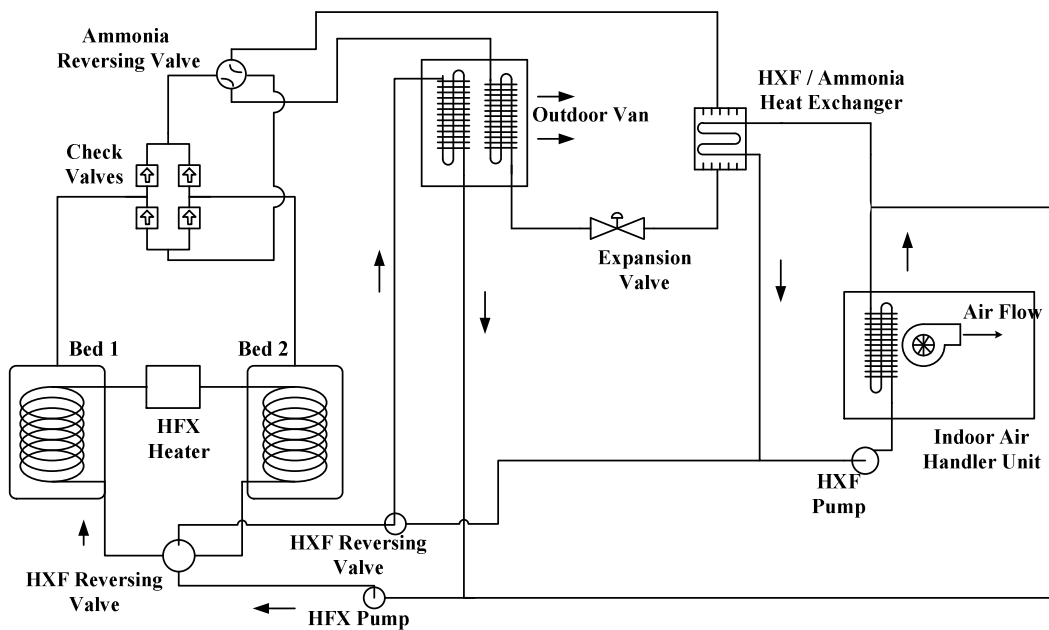
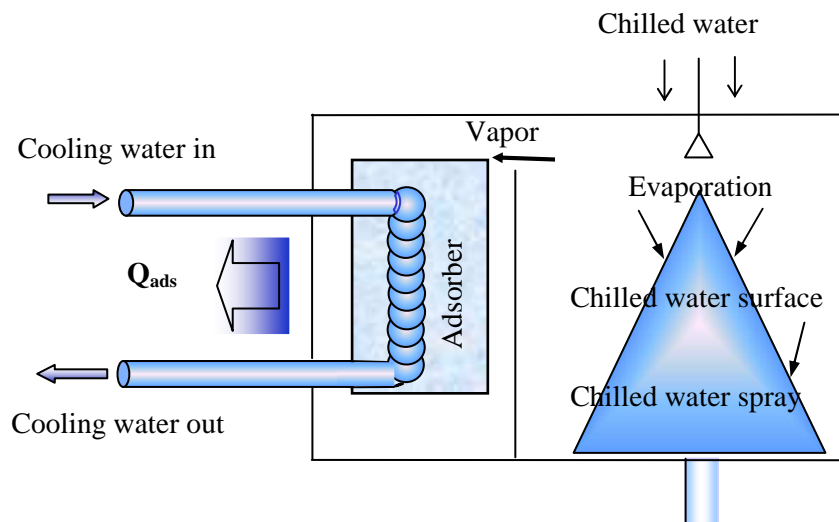
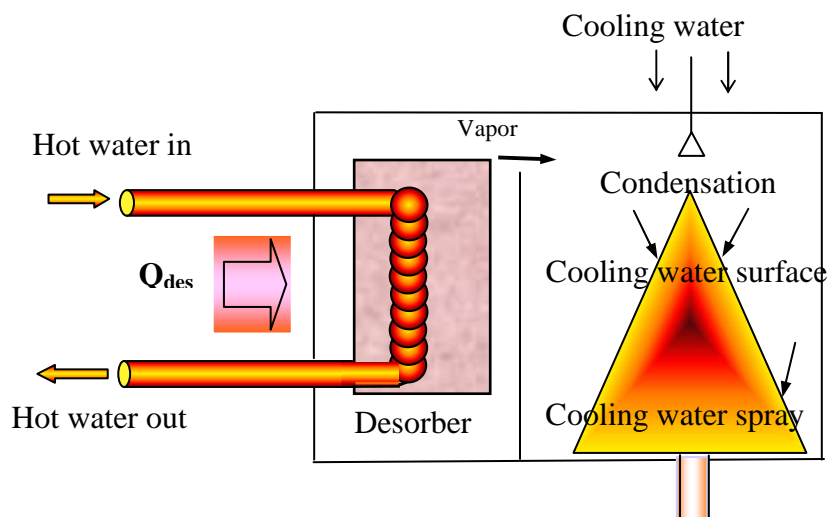


Fig. 4. Thermal wave solid sorption heat pump in cooling mode [13]



a) Adsorption cycle



b) Desorption cycle

Fig. 5. Schematic of the direct contact adsorption cycle [17]

## WORKING PRINCIPLE OF AACD CYCLE

The adsorption cycle utilizes the physisorption process between the adsorbent and adsorbate to produce cooling power from the evaporation of the saline water in the evaporator, and potable water at the condenser. These useful effects are achieved by the amalgamation of “adsorption-triggered-evaporation” and “desorption-resulted-condensation” processes driven by a low temperature hot water that can be extracted from industrial waste heat or solar energy [19].

The schematic of the innovative two-evaporator and three-reactor advanced adsorption cooling cum desalination (AACD) cycle is illustrated in Figure 6 [20]. The AACD cycle comprising three adsorbent beds, one condenser and two evaporators in which the evaporators are assembled to operate as a single adsorption device where two-temperature levels of cooling (both sensible and latent) is generated at the evaporators whilst concomitantly, fresh or potable water is produced at the condenser. The unique arrangements of the

high and low-pressure evaporators are in thermal and mass communication with the beds, operating in tandem and yet in a pre-determined manner with an externally supplied heat source.

The inventive step lies in the unique arrangement of three-bed and two-evaporator design and when operated with an optimal cycle time, the production yields of desalted water and cooling effects are almost tripled as compared to the conventional (single-evaporator type) 2-bed or 4-bed adsorption cycles. It is therefore an object of the present system to show the three-bed-assisted advanced adsorption cycle which produces optimal cooling and desalination, with only low temperature heat input varying from 60 to 80 °C.

How the proposed cycle works? During vapor communication or uptake between a bed (containing unsaturated adsorbent) with either the low or the high pressure evaporator; the said high pressure evaporator produces a cooling stream at temperatures near to the ambient temperatures, typically from 18 to 30 °C, which can be used directly for sensible or process cooling. The said low pressure evaporator, on the other hand, generates a stream of coolant at 4 to 10 °C that is useful for air conditioning or dehumidification application. Owing to these external thermal loads, two different vapor pressures in the evaporators are maintained. A desorption process refers to the removal of adsorbed water vapor from the adsorbent by the application of heat, supplied from a coolant heat source or any other means. The desorbed vapor is condensed in the condenser and the liquefied condensate which is of distilled water qualities collected in the collection tank.

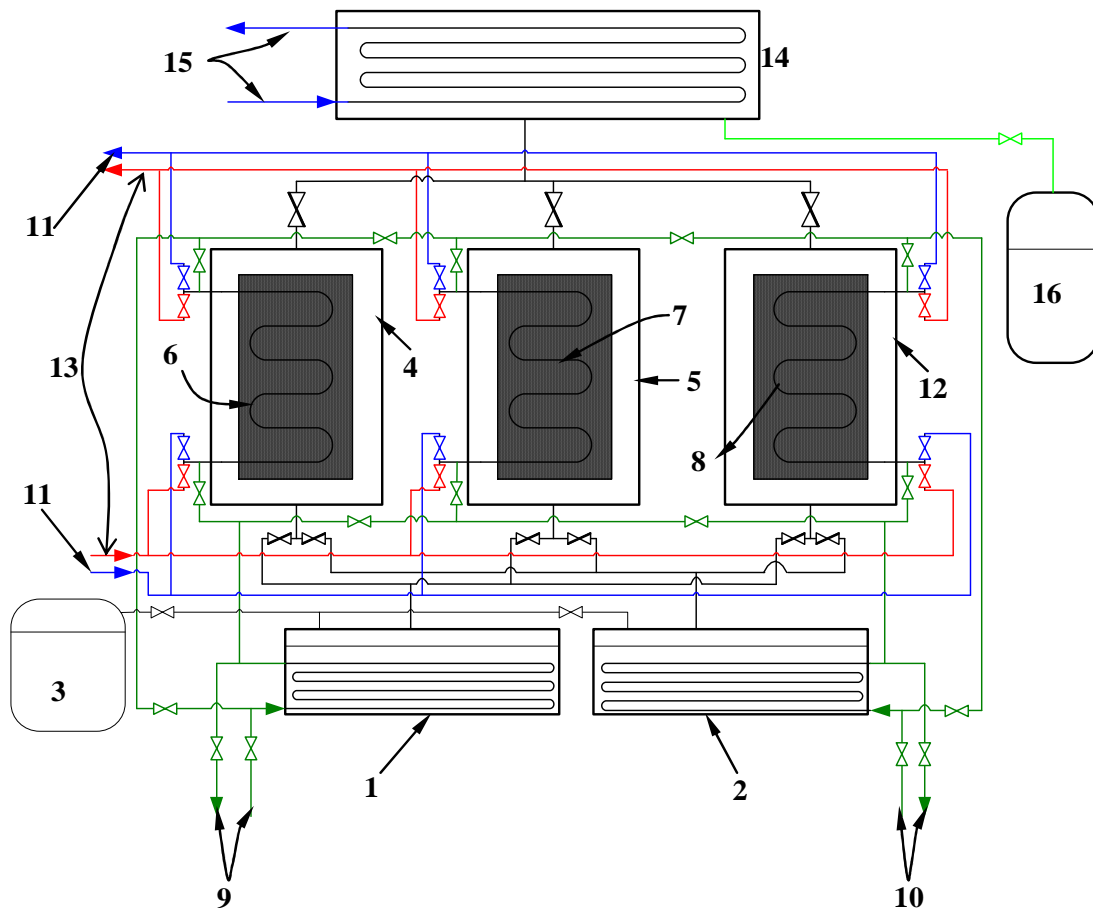


Fig. 6. Schematic diagram of the advanced adsorption cooling cum desalination system [20]:  
1 – high pressure evaporator; 2 – low – pressure evaporator; 3 – saline water reservoir; 4, 5 –  
adsorbent beds; 6–8 – tubes in adsorbers; 9, 10 – chilled water circuit; 11, 15 – coolant circuit;  
12 – enclosure; 13 – hot water circuit; 14 – condenser; 16 – potable water collection tank

## MATHEMATICAL MODELING OF THE AADC CYCLE

Mathematical modeling of a 3-bed two-evaporator adsorption cycle for cooling and desalination is developed based on adsorption isotherms, kinetics, mass and energy balances between the sorption elements, the evaporator and the condenser. Type-RD silica gel is employed as the adsorbent. Dubinin–Astakhov (D-A) equation is used to calculate the uptake of the water vapor by the silica gel at specific temperature and pressure and is given as,

$$q^* = q_0 \exp \left[ - \left( \frac{RT}{E} \ln \left( \frac{P}{P_0} \right) \right)^n \right], \quad (1)$$

where  $q_0$  is the maximum adsorbed amount,  $E$  is the characteristic energy and  $n$  is the D-A constant. The transient uptake by the silica gel can be obtained using linear driving force equation as,

$$\frac{dq}{dt} = \frac{15D_{so} \exp \left( \frac{-E_a}{RT} \right)}{R_p^2} (q^* - q), \quad (2)$$

where  $D_{so}$  is the kinetic constant for the silica gel water system,  $E_a$  is the activation energy,  $R_p$  is the particle radius and  $q$  denotes the instantaneous uptake.

The overall mass balance of the cycle is given by,

$$\frac{dM_{s,evap}}{dt} = \dot{m}_{s,in} - \dot{m}_{d,cond} - \dot{m}_{brine}. \quad (3)$$

Here,  $M_{s,evap}$  is the sea water revenue in the evaporator and  $\dot{m}_{s,in}$  is the rate of feed sea water,  $\dot{m}_{d,cond}$  is the mass of potable water extracted from the condenser and  $\dot{m}_{brine}$  is the mass of concentrated brine rejected from the evaporator. It should be noted here that the concentrated brine is discharged periodically depending on the concentration level in the evaporator. The energy balance of the evaporator in communication with the adsorber (master or slave) is written as:

$$\left[ c_{p,s}(T_{evap})M_{s,evap} + c_{p,HX}M_{HX,evap} \right] \frac{dT_{evap}}{dt} = h_f(T_{Feed})\dot{m}_{s,in} - h_{fg}(T_{evap})M_{sg} \left( \frac{dq_{Mads}}{dt} + \delta \frac{dq_{Sads}}{dt} \right) + U_{evap} A_{evap} (T_{chilled,in} - T_{chilled,out}) - h_f(T_{evap})\dot{m}_{brine}. \quad (4)$$

The value of  $\delta$  in this equation is either 1 or 0 depending on the communication of the slave adsorber with the evaporator. During the switching period, the value of  $\delta$  is 0 since only the master adsorber is connected with the evaporator.

Similarly, the energy balance of the condenser is given by:

$$\left[ c_p(T_{cond})M_{cond} + c_{p,HX}M_{HX,cond} \right] \frac{dT_{cond}}{dt} = -h_f(T_{cond})\dot{m}_{d,cond} + h_{fg}(T_{cond})M_{sg} \left( \frac{dq_{Mdes}}{dt} + \varepsilon \frac{dq_{Sdes}}{dt} \right) + U_{cond} A_{cond} (T_{cond,in} - T_{cond,out}). \quad (5)$$

The value of  $\varepsilon$  is 1 when the slave desorber bed is connected with the condenser or otherwise its value is 0.

The energy balance of the master adsorber/desorber is given by:

$$\begin{aligned} & (M_{sg} c_{p,sg} + M_{HX} c_{p,HX} + M_{abe} c_{p,a}) \frac{dT_{Mads/Mdes}}{dt} = \pm Q_{st} (T_{Mads/Mdes}, P_{evap/cond}), \\ & M_{sg} \frac{dq_{Mads/Mdes}}{dt} \pm \dot{m}_{cw/hw} c_{p,cw/hw} (T_{Mads/Mdes}) (T_{cw/hw,in} - T_{cw/hw,out}). \end{aligned} \quad (6)$$

The energy balance for the slave adsorber/desorber bed is written as,

$$\begin{aligned} & (M_{sg} c_{p,sg} + M_{HX} c_{p,HX} + M_{abe} c_{p,a}) \frac{dT_{Sads/Sdes}}{dt} = \pm Q_{st} (T_{Sads/Sdes}, P_{evap/cond}), \\ & M_{sg} \frac{dq_{Sads/Sdes}}{dt} \pm \dot{m}_{cw/hw} c_{p,cw/hw} (T_{Sads/Sdes}) (T_{cw/hw,in}'' - T_{cw/hw,out}). \end{aligned} \quad (7)$$

The third terms in the left hand side of Eqs. 6 and 7 represent the thermal mass contribution by the adsorbed phase and  $T_{cw/hw,in}''$  is the temperature of the cooling or hot water that comes out from the master adsorber/desorber bed. The isosteric heat of adsorption,  $Q_{st}$ , it is calculated [21] as follows,

$$Q_{st} = h_{fg} + E \left\{ -\ln \left( \frac{x}{x_m} \right) \right\}^{1/n} + T v_g \left( \frac{\partial P}{\partial T} \right)_g, \quad (8)$$

where  $v_g$  is the volume of the gaseous phase and  $h_{fg}$  is the latent heat.

The outlet temperature of the water from each heat exchanger is estimated using log mean temperature difference method and it is given by,

$$T_{out} = T_0 + (T_{in} - T_0) \exp \left( \frac{-UA}{\dot{m} c_p (T_0)} \right). \quad (9)$$

Here  $T_0$  is the temperature of the heat exchanger. The energy required to remove water vapors from the silica gels, here master and slave desorption, ( $Q_{Mdes/Sdes}$ ), can be calculated by using the inlet and outlet temperatures of the heat source supplied to the reactors, and this is given by,

$$Q_{Mdes/Sdes} = \dot{m}_{hw} c_{p,hw} (T_{hw,in} - T_{hw,out}), \quad (10)$$

where  $\dot{m}_{hw}$  and  $c_{p,hw}$  indicate the mass flow rate and the specific heat capacity of heating fluid.

Here the heat of evaporation ( $Q_{evap}$ ), and the condensation energy ( $Q_{cond}$ ) are given by,

$$Q_{evap} = \dot{m}_{chilled} c_{p,chilled} (T_{chilled,in} - T_{chilled,out}), \quad (11)$$

$$Q_{cond} = \dot{m}_{cond} c_{p,cw} (T_{cond,out} - T_{cond,in}). \quad (12)$$

It is noted that the roles of the reactors are switched for adsorption or desorption process in a quarter-cycle time for 4-bed AD cycle. The evaporator and condenser units communicate with at least one adsorber or desorber in every cycle operation and thus providing continuous cooling energy and the potable water.

Finally, the performance of the advanced adsorption cooling cum desalination cycle is assessed in terms of specific cooling power (SCP) and specific daily water production (SDWP). The SDWP and SCP of the cycle is defined as,

$$SCP = \int_0^{t_{cycle}} \frac{Q_{evap} \tau}{M_{sg}} dt, \quad (13)$$

$$SDWP = \int_0^{t_{cycle}} \frac{Q_{cond} \tau}{h_{fg} (T_{cond}) M_{sg}} dt. \quad (14)$$

The mathematical modeling equations of the AACD cycle are solved using the Gear's BDF method from the IMSL library linked by the simulation code written in FORTRAN Power Station, and the solver employs

a double precision with tolerance value of  $1 \times 10^{-8}$ . With the proposed system, the performances of the adsorption cycle are presented in terms of two key parameters, namely the SCP and SDWP.

## RESULTS AND DISCUSSION

Figure 7 shows the simulated temperature-time histories of the adsorber and desorber beds 4, 5, 12 of the ACD system, which is shown schematically in Figure 6. The simulation of the innovative adsorption cycle is done by using FORTAN IMSL library function. A set of modeling differential equations are solved by using Gear's BDF method. From the simulation, it is found that desorption is occurred at the temperatures ranging from 60 to 80 °C. The low and high pressure bed temperatures vary from 33 to 40 °C.

Figure 8 shows the temperature-time histories of the condenser, the low pressure and the high pressure evaporators (1 and 2) of the embodiment of the AACD cycle. It is observed from the present simulation that the temperature of the low pressure evaporator 1 ranges from 5 to 7 °C, which is very prominent for air conditioning applications. The temperature of the high pressure evaporator varies from 20 to 22 °C, which is good for sensible cooling. The feature of the present system is that it decreases the peak evaporation temperature as opposed to the conventional one evaporator type adsorption chillers.

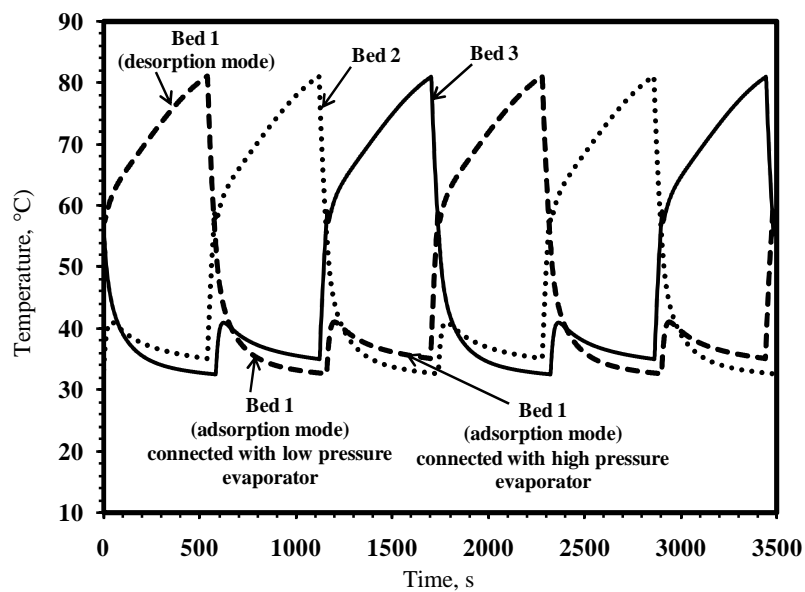


Fig. 7. Temperature profiles of the adsorber and desorber beds of the AACD system

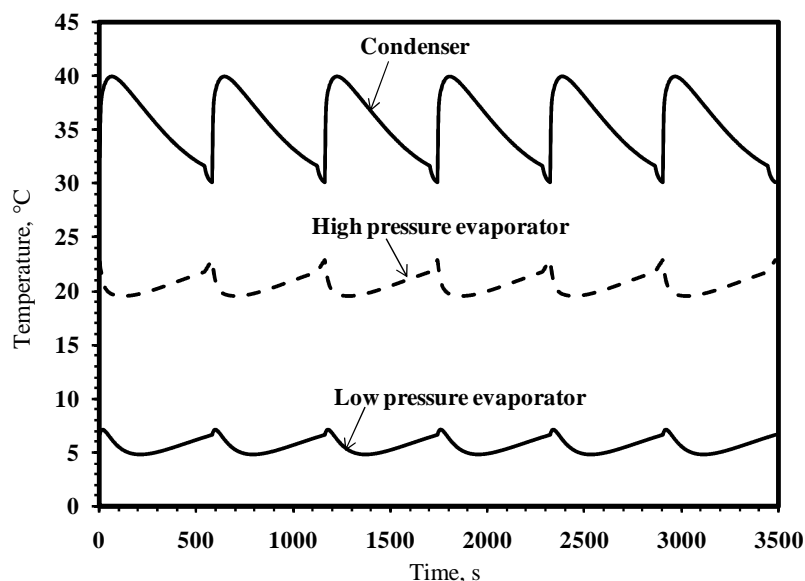


Fig. 8. Temperature profiles of the condenser, the low pressure and the high pressure evaporators of the AACD system

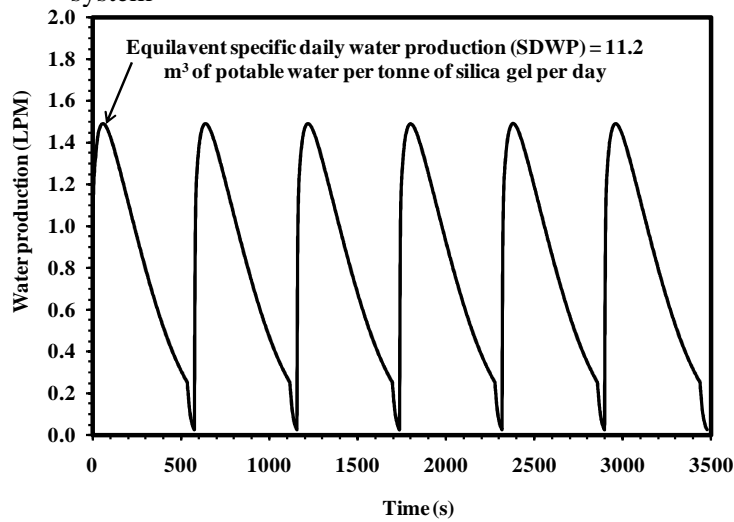


Fig. 9. Fresh water production rate of the present AACD system

Figure 9 is the predicted production rate of fresh water of the AACD system. The amount of fresh water production rate in terms of specific daily water production (SDWP) is shown in Figure 9 and the predicted SDWP is  $12.2 \text{ m}^3$  of fresh water per tonne of silica gel per day.

Finally, Figure 10 shows the effective and sensible cooling capacities as a function of operating time according to one embodiment of the present invention. The cycle average sensible cooling capacity is 6 Rton and effective cooling capacity is 3.5 Rton.

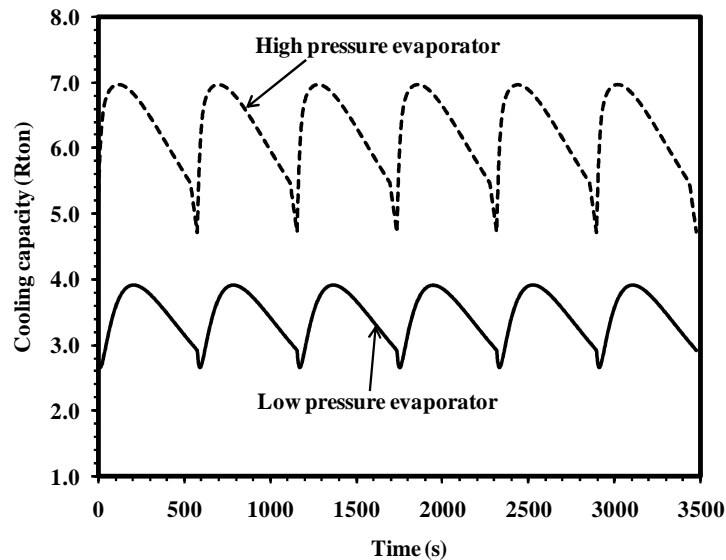


Fig. 10. The effective and sensible cooling capacities of the AACD system

## CONCLUDING REMARKS

The salient points of the present study are summarized as follows:

Silica gel-water based two-stage adsorption cycle which is powered by waste heat of temperatures between 50 and 70 °C with a coolant at 30 °C can produce cooling energy.

Silica gel-water based multi-bed, dual-mode cycle can utilize effectively low grade waste heat of temperatures between 40 and 95 °C along with a coolant at 30 °C.

The cooling COP of the activated carbon-ammonia based thermal wave cycle is as high as 1.9.

Silica gel-water based direct contact condensation and evaporation cycle can significantly improve heat and mass transfer.

The proposed AACD system describes the use of two evaporators and three adsorption beds or reactors in a thermally-driven adsorption cycle, in which both evaporators are connected with the reactors at two different pressure levels. The AACD cycle is capable of producing (i) the chilled water at 4 to 10 °C with varying cooling capacity range of 3 to 4 Rton per tonne of silica gel, and (ii) the cooling water at 20 to 25 °C with cooling capacity ranging from 5 to 7 Rton per tonne of silica gel. The former is suitable for space cooling and the latter is suitable for process cooling. Simultaneously, the proposed AACD cycle produces a specific daily water production of 12.3 m<sup>3</sup> per tonne of silica gel per day at rated operating conditions.

The primary energy consumption of the proposed three-bed, two-evaporator type adsorption cycle is as low as 1.38 kWh/m<sup>3</sup> utilizing waste heat or solar thermal energy. The authors had patented their invention and a business license has been issued to Vegalo Ltd. from the Republic of Cyprus.

### Acknowledgements

The authors express their gratitude towards Prof. K.C. Ng and Dr. K. Thu of National University of Singapore and Dr. A. Chakraborty of Nanyang Technological University for their help and enlightening advice.

### References

1. Saha B. B., Boelman E., Kashiwagi T. Computer simulation of a silica gel water adsorption refrigeration cycle - the influence of operating conditions on cooling output and COP // *ASHRAE Transactions*. 1995. Vol. 101, No. 2. Pp. 348–357.
2. Boelman E., Saha B. B., Kashiwagi T. Experimental investigation of a silica gel water adsorption refrigeration cycle - the influence of operating conditions on cooling output and COP // *ASHRAE Transactions*. 1995. Vol. 101, No. 2. Pp. 358–366.
3. Zhai X. Q., Wang R. Z. Experimental investigation and theoretical analysis of the solar adsorption cooling system in a green building // *Applied Thermal Engineering*. 2009. Vol. 20, No. 1. Pp. 17–27.
4. Grisel R. J. H., Smeding S. F., de Boer R. Waste heat driven silica gel/water adsorption cooling in trigeneration // *Applied Thermal Engineering*. 2010. Vol. 30, Nos. 8-9. Pp. 1039–1046.
5. Saha B. B., Kashiwagi T. Experimental investigation of an advanced adsorption refrigeration cycle // *ASHRAE Trans. Res.* 1997. Vol. 103. Pp. 50–58.
6. Saha B. B., Chakraborty A., Koyama S., Srinivasan K., Ng K.C., Kashiwagi T., Dutta P. Thermodynamic formalism of minimum heat source temperature for driving advanced adsorption cooling device // *Applied Physics Letters*. 2007. Vol. 91, 111902.
7. Ng K. C. Recent developments in heat-driven silica gel-water adsorption chillers // *Heat Transfer Engineering*. 2003. Vol. 24, No. 3. Pp. 1–3.
8. Alam K. C. A., Khan M. Z. I., Uyun A. S., Hamamoto Y., Akisawa A., Kashiwagi T. Experimental study of a low temperature heat driven re-heat two-stage adsorption chiller // *Applied Thermal Engineering*. 2007. Vol. 27, No. 10. Pp. 1686–1692.
9. Saha B. B., Alam K. C. A., Akisawa A., Kashiwagi T. Two-stage non-regenerative silica gel water adsorption refrigeration cycle // *Proceedings of 2000 ASME Advanced Energy System Division, Orlando, FL*. Vol. 40, 2000. Pp. 65–69.
10. Saha B. B., Akisawa A., Kashiwagi T. Solar/waste heat driven two-stage adsorption chiller: the prototype // *Renewable Energy*. 2001. Vol. 23, No. 1. Pp. 93–101.
11. Saha, B.B., Akisawa, A., Kashiwagi, T. Silica gel water advanced adsorption refrigeration cycle // *Energy*. 1997. Vol. 22, No. 4. Pp. 437–447.

12. Saha B. B., Koyama, S., Kashiwagi, T., Akisawa, A., Ng, K. C., Chua, H. T. Waste heat driven dual-mode, multi-stage, multi-bed regenerative adsorption system // *International Journal of Refrigeration*. 2003. Vol. 26, No. 7. Pp. 749–757.
13. Miles D. J., Shelton S. V. Design and testing of a solid-sorption heat-pump system // *Applied Thermal Engineering*. 1996. Vol. 16, No. 5. Pp. 389–394.
14. Sward B. K., Douglas L. M., Meunier F. Adsorption heat pump modeling: the thermal wave process with local equilibrium // *Applied Thermal Engineering*. 2000. Vol. 20, No.8, Pp. 759–780.
15. Critoph R. E. Forced convection adsorption cycles // *Applied Thermal Engineering*. 1998. Vol. 18, No. 9-10. Pp. 799–807.
16. Critoph R. E., Thorpe R. Thermal compressive device // 1996. *PCT publication no. WO96/09504*.
17. Yanagi H., Asano T., Iwase K. Komatsu F. Development of adsorption refrigerator using a direct contact condensation and evaporation on sprayed water // *Proc. of the Intl. Sorption Heat Pump Conference*, Munich, Germany, 1999. Pp. 671–676.
18. Saha B. B., Alam K. C. A., Hamamoto Y., Akisawa A., Kashiwagi T. Sorption refrigeration / heat pump cycles // *Transactions of the JSRAE*. 2001. Vol. 18, No. 1. Pp. 1–14.
19. Thu K., Ng K. C., Saha B. B., Chakraborty A., Koyama S. Operational strategy of adsorption desalination systems // *International Journal of Heat and Mass Transfer*. 2009. Vol. 52, No. (7–8). Pp. 1811–1816.
20. Saha B. B., Ng K. C., Chakraborty A., Thu. K. Desalination system and method. 2011. *PCT/IB2010/001757*.
21. Chakraborty A., Saha B. B., Koyama S., Ng, K. C. On the thermodynamic modeling of isosteric heat of absorption and comparison with experiments // *Applied Physics Letters*. 2006. Vol. 89. 171901.

## **DROPWISE CONDENSATION ON HORIZONTAL SUBSTRATES WITH AND WITHOUT A WETTABILITY GRADIENT**

**Basant Singh Sikarwar, Sameer Khandekar\*, K. Muralidhar**

Department of Mechanical Engineering

Indian Institute of Technology Kanpur

Kanpur (UP) 208016 India

\*Tel: +91-512-259-7038, Fax: +91-512-259-7408, E-mail: samkhan@iitk.ac.in

### **Abstract**

Detailed numerical modeling of dropwise condensation process on a horizontal substrate, with and without a wettability gradient is reported in this work. The model assumes nucleation occurring only on specific sites, which are randomly distributed on a substrate; drops essentially form only on these randomly specified sites and later grow by direct condensation and coalescence. Accordingly, the diffusional resistance of the liquid contained in these drops forms the primary thermal resistance of the entire process. Enhancement of heat transfer necessitates that these drops be swept away from the substrate as soon as possible so as to reduce this most prominent thermal resistance in the passage of heat, from the vapor to the substrate. Thus, possible enhancement may be achieved either by (i) inclining the substrate, or alternatively, (ii) by creating an additional force imbalance at the three-phase contact line, which induces droplet motion. The latter strategy is applicable for both, horizontal, as well as inclined substrates. Contemporary manufacturing/coating techniques can provide such a wettability gradient by physico-chemical action, leading to the additional surface forces required for inducing droplet motion. These two scenarios mentioned above are compared by formulating an exhaustive computer simulation which involves the entire dropwise condensation process, from nucleation to coalescence and eventual fall-off or slide-off of critically sized droplets from the surface, thereby exposing new nucleation sites. The wettability gradient is considered unidirectional and linear in nature. The paper first describes the mathematical model employed for the two cases respectively, and then discusses the nuances of these two situations, in terms of the achieved spatio-temporal distribution of drops, rate of condensing vapor, average area of droplet coverage, nucleation sites densities, heat transfer through drops, time cycle of growth from the minimum drop size to slide-off /fall-off and average heat transfer coefficient of dropwise condensation. Qualitative comparison of the two situations is also discussed. The results clearly indicate that wettability gradients can effectively control the condensation process by diminishing the cycle times of nucleation, growth and removal. Hence, lyophobic horizontal condensing substrates having graded wettability prove to be more efficient than their simple or traditional counterpart. Such a strategy is also attractive for achieving enhanced dropwise condensation in low-g environments.

### **KEYWORDS**

Dropwise condensation, hydrophobic substrates, modeling, simulation, wettability gradient, heat transfer.

### **INTRODUCTION**

Heat transfer coefficient for dropwise condensation can be up to an order of magnitude larger than filmwise condensation [1]. The transient process of droplet formation, growth and subsequent drainage of the condensate forms the characteristic cycle of dropwise condensation process, as shown in Figure 1. Any method of enhancing heat transfer coefficient is naturally desirable for improving system efficiency and hence, dropwise condensation is an attractive process for heat transfer enhancement in a variety of engineering applications. Success of dropwise mode of condensation depends not only in maintaining lyophobicity of the substrate but also on the efficient droplet drainage mechanism. Achieving engineering control of such liquid surface interactions necessitates the fundamental understanding of the transport mechanisms and formation of droplets.

The large body of literature available on dropwise condensation suggests three different models for mechanism of dropwise condensation [2, 3]:

1. The vapor condenses primarily between the droplets, i.e. the droplet-free area. Then, this condensate layer gets transported to the droplets in their vicinity by surface diffusion. According to this model, this thin film region between the droplets and the free surface of the droplets themselves, both contribute to the overall heat transfer.
2. According to this model, while vapor condensation begins in a filmwise mode (filmwise condensation), as the film reaches a minimum critical thickness, it ruptures due to an instability forming droplets due

the dominance of surface tension forces. It is postulated that the major part of the heat transfer takes place at the very thin condensate film, while the droplets mainly act as liquid collectors.

3. Droplets are only formed at individual nucleation sites, while the area between the droplets is regarded to be inactive with respect to condensation. In this model heat transfer occurs only through the droplets and is primarily limited by their heat conduction resistance.

Majority of studies support the last mechanism, in which the condensate is in the form of discrete drops located at the nucleation sites on or underneath a lyophobic substrate. Drops grow first by direct condensation and later by coalescence with their respective neighbors. At a later stage of growth, conduction resistance increases thereby diminishing the rate of condensation on their free surface [4–6]. This limits the heat transfer, provided a suitable means of removing the drops exists that re-exposes fresh nucleation sites. This cyclic sweeping process and generation of small droplets underneath an inclined condensing substrate is highlighted in Figure 1. Many researchers suggest that this cyclic process of wiping and re-formation of new droplets having low diffusional resistance is the primary reason for the large heat transfer coefficient observed for dropwise condensation [4, 5, 7–10]. The cyclic frequency on one hand, and the smallest drop size at which its mobility is enabled on the other, determines the overall device efficiency.

A simple approach for mobilization of drops is to incline the substrate with respect to horizontal; then gravity, surface tension and pressure are in competition. Force imbalance is generated because of drop deformation and hysteresis, making the apparent advancing and receding angles unequal. Other methods to spontaneously mobilize drops on or underneath horizontal surfaces include [11–13]: (i) apply a large temperature gradient on the substrate so that Marangoni motion is initiated and, (ii) create wettability (surface energy) gradients on the substrate by suitable physico-chemical treatment. The second approach is quite possible now by depositing organic long chain monolayers over the surfaces [14–15]. Hence, if the substrate orientation is limited in some application of dropwise condensation, it is still possible to achieve drop sliding and subsequent wiping action by creating a wettability (or surface energy) gradient on the horizontal substrate. Thus, the timescale of drop instability can be controlled by altering surface characteristics. Daniel et al. [16] reported that a small drop (1 to 2 $\mu$ l) could slide with high velocity (0.15 to 1.5 m/s) on a horizontal substrate with a wettability gradient. Moumen et al. [17] recorded video images of drop motion on a graded substrate and analyzed the relationship between drop size and velocity as functions of local wettability. Against this background, we report a detailed simulation of dropwise condensation underneath hydrophobic horizontal substrates, with and without a wettability gradient surface. The simulation is based on the nucleation mechanism model and the wettability gradient is achieved through a variation of effective apparent static contact angle. A static apparent contact angle of 108° is assumed on the horizontal hydrophobic surface having no wettability gradient. For the surface with a wettability gradient, the contact angle varies unidirectionally in a linear fashion. The mathematical model for the process includes nucleation, growth by condensation, coalescence, and drop instability arising from force imbalances due to local wettability variations.

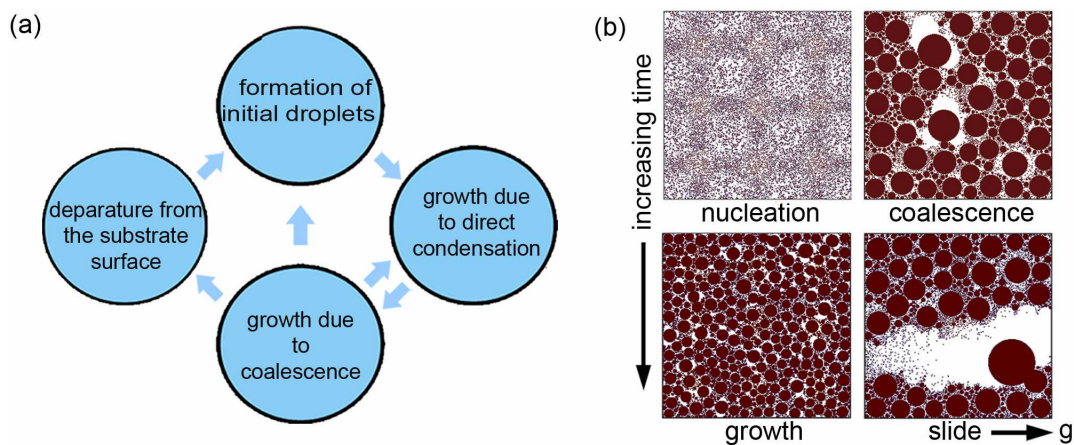


Figure 1: (a) Cycle of individual sub-processes which constitute dropwise condensation. (b) Qualitative depiction of the footprints of the droplets during the cyclic growth process (mildly inclined substrate with no wettability gradient; fluid employed is water, sub-cooling  $\Delta T_{sat} = 5^\circ\text{C}$ , contact angle = 98°, nucleation site density =  $10^9 \text{ m}^{-2}$  [5].

Simulation data have been compared with condensation patterns for a flat surface with zero-gradient and a non-zero gradient. The changes in overall cycle-times during the condensation process due to wettability-gradients of the surface are reported. Temporal-spatial distribution of drops underneath a condensing substrate, rate of condensing of vapor, heat transfer through drops, time cycle of growth from the minimum drop size to slide-off /fall-off of are reported for both cases. For comparison, a mildly inclined (5°) substrate with no wettability gradient is also considered. The paper is arranged in the following manner: section two and three describe the mathematical formulation of the dropwise condensation process underneath a horizontal hydrophobic substrate without wettability gradient substrate and its graded counterpart, respectively. Results and discussion are presented in section four and finally, conclusions are reported in the last section.

## MODEL DEVELOPMENT

Atomistic modeling of drop formation in heterogeneous dropwise condensation has been carried out by Sikarwar et al. [18]. The authors reported that the minimum drop radius does not provide controllability of macroscale dropwise condensation at large timescales when dynamic steady-state is achieved. Therefore, drops formed at the initial nucleation site are assigned a minimum possible stable radius from thermodynamic considerations, in both the cases (with and without wettability gradient). The basic methodology includes random assignment of initial nucleation sites on which droplets of radius =  $r_{\min}$  start growing following the derived growth rate model. Subsequently, a coalescence model is incorporated which continuously checks for conditions of droplet mergers. Criticality of size is checked with respect to slide-off or fall-off, as per the case. This re-exposes fresh nucleation sites where a new generation of droplets again start growing from their initial radius =  $r_{\min}$ . Depending on the surface wettability condition and inclination of the substrate, the growth model, coalescence model and criticality model needs to be chosen and activated.

### a) Horizontal lyophobic substrate without a wettability gradient

A pendant drop underneath a flat horizontal substrate is shown in Figure 2a. The drop is considered as a portion of a sphere of radius  $r$  making a contact angle  $\theta$ . From the geometry, the drop volume  $V$ , area of liquid-vapor interface  $A_{lv}$ , and area of solid-liquid interface  $A_{sl}$ , are given by:

$$V = \left( \frac{\pi r^3}{3} \right) \cdot (2 - 3 \cos \theta + \cos^3 \theta), \quad (1)$$

$$A_{lv} = 2\pi r^2 (1 - \cos \theta), \quad (2)$$

$$A_{sl} = 2\pi r^2 (1 - \cos^2 \theta). \quad (3)$$

For a specified wall sub-cooling ( $T_s - T_w$ ), the smallest stable droplet size possible can be found from thermodynamic considerations as [2]:

$$r_{\min} = \frac{2\sigma \cdot \nu_l \cdot T_w}{h_{lv} [T_{sat} - T_w]}. \quad (4)$$

Although the arguments leading to this equation do not include the substrate surface energy, Leach et al. [19] have shown that such effects are of higher order and can be neglected for engineering calculations on the micro-scale. As droplets grow in size, the meso/macro scale droplet dynamics cannot neglect the bulk contact angle ensuing from the surface energy of the substrate. The maximum drop diameter is calculated from balancing the surface tension with the weight of the drop and is derived as:

$$r_{\max} = \sqrt{\left( \frac{6 \sin^2 \theta}{2 - 3 \cos \theta + \cos^3 \theta} \right) \cdot \left( \frac{\sigma}{g \cdot (\rho_l - \rho_v)} \right)}. \quad (5)^1$$

<sup>1</sup> Eq. 5 can be interpreted as modified Bond number criterion, applicable for a pendant droplet which takes into account the effect of contact angle in the force balance. In case of a horizontal substrate, there is no contact angle hysteresis. The usual definition of Bond number is given by,

$$Bo = (2 \cdot r) \left( \sqrt{(g(\rho_l - \rho_v)) / \sigma} \right)$$

The drop in temperature, due to various resistances to heat transfer, is calculated as follows:

- (i) Conduction resistance: The drop in temperature due to conduction heat transfer is determined as:

$$\Delta T_{cond} = (q \cdot \theta) / (4\pi \cdot r \cdot k_c) \quad (6)$$

- (ii) Temperature drop due to interfacial heat transfer is:

$$\Delta T_{int} = \frac{q}{2\pi \cdot r^2 \cdot h_i (1 - \cos \theta)}. \quad (7)$$

- (iii) Curvature resistance: This resistance includes the loss of driving temperature potential due to the droplet interface curvature and is given by [18]:

$$\Delta T_{curv} = \frac{2\nu_l \cdot \sigma \cdot T_w}{h_{lv} \cdot r} = \frac{(T_{sat} - T_w) r_{min}}{r}. \quad (8)$$

The interfacial heat transfer coefficient is given by:

$$h_i = \left( \frac{2\hat{\sigma}}{2 - \hat{\sigma}} \right) \cdot \left( \frac{h_{lv}^2}{T_s \nu_{lv}} \right) \cdot \left( \frac{\bar{M}}{2\pi R T_{sat}} \right)^{1/2}. \quad (9)$$

Here,  $h_i$  is the interfacial heat transfer coefficient and  $k_c$  is the condensate thermal conductivity.

- (iv) Coating Resistance: The temperature drop due to the resistance of the coating material on the contact surface is given by:

$$\Delta T_{coat} = \frac{q}{k_{coat} \cdot \pi r^2 \cdot (1 - \cos^2 \theta)}. \quad (10)$$

- (v) Constriction Resistance: The constriction resistance measures the effect of surface thermal resistance on dropwise condensation. This is caused due to non-uniform heat flux distribution over the condensing surface. Although, there is continuing controversy about whether or not the thermal conductivity of the condensing surface has a significant role on the rate of droplet growth, we include it, as suggested by Mikic [20]<sup>2</sup>.

$$R_{const} = \frac{2}{3\pi K_w} \sum_{r_{min}}^{r_{max}} \frac{n_r r^3}{[1 - f(r)]^2}, \quad (11)$$

where,  $n_d$  is nucleation sites per unit area of radius  $r$  drops and  $f(r)$  is the fraction of the surface area covered by droplets having a radius  $r$ .

$$\Delta T_{const} = q / R_{const}. \quad (12)$$

The net temperature drop will balance the total available sub-cooling and so,

$$\Delta T_t = \Delta T_{cond} + \Delta T_{int} + \Delta T_{curv} + \Delta T_{coat} + \Delta T_{const} = \Delta T_{sat}. \quad (13)$$

The heat flux through a single droplet is derived as:

$$q = (\pi r^2 \rho_l h_{lv}) \cdot (2 - 3 \cos \theta + \cos^3 \theta) \cdot (dr / dt). \quad (14)$$

From the above set of equations, the rate of growth of individual droplets follows:

$$\frac{dr}{dt} = \left( \frac{2\Delta T}{\rho h_{lv}} \right) \times \left[ \frac{\left( 1 - \frac{r}{r_{min}} \right)}{\left( \frac{1}{h_i} + \frac{r\theta}{k_c \sin \theta} + \frac{\delta}{k_{coat} (1 - \cos^2 \theta)} + R_{const} \right)} \right] \times \frac{(1 - \cos \theta)}{(2 - 3 \cos \theta + \cos^3 \theta)}. \quad (15)$$

Equation 15 has been integrated to determine the growth of the droplet due to direct condensation. Along with the direct condensation growth-loop in the simulator, a parallel coalescence-loop is also monitored at each time step. The time for coalescence is taken to be much smaller than the other timescales of the condensation process. Hence, as soon as two droplets contact each other (or three droplets, or, very rarely,

<sup>2</sup> Although incorporated in the code, the present results do not include the effect of constriction resistance.



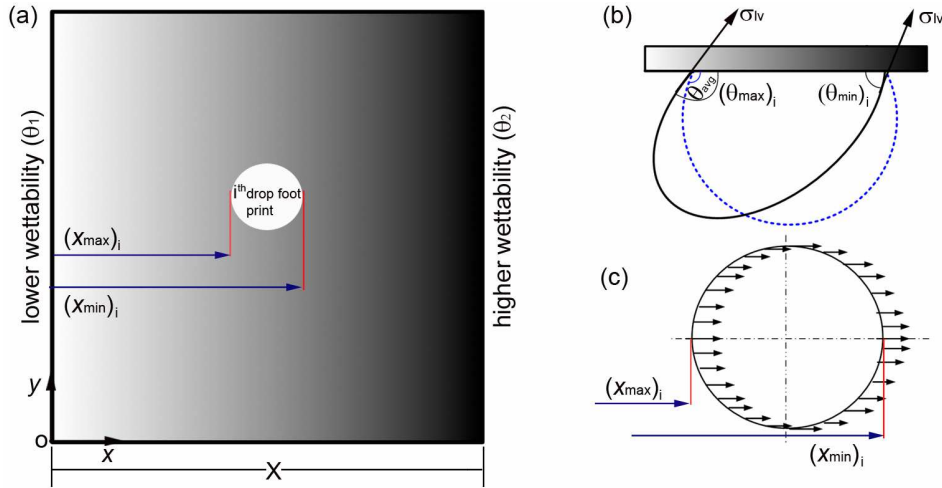


Fig. 3. (a) A substrate with wettability gradient. The footprint of  $i^{\text{th}}$  drop is assumed circular. (b) Side view of  $i^{\text{th}}$  drop and its approximate hemispherical shape (c) direction of force acting at the three phase contact line on this substrate

For a substrate with a wettability gradient, drop motion can be expected even before their shapes are altered by gravity or flow related pressure non-uniformity. Hence, the drops are fitted by a spherical cap, which is the shape assumed by a small static drops in the absence of a gravitational effect, Figure 3(b). From the drop geometry, the drop volume  $V$ , area of liquid-vapor interface  $A_{lv}$ , and area of solid-liquid interface  $A_{sl}$  are expressed on based of average contact angle as:

$$\theta_{avg} = \theta = (\theta_{\max} + \theta_{\min}) / 2. \quad (17)$$

The base radius of the drop and the contact angle difference between the trailing and leading edges is calculated at each time step (Figure 3(b)).

When two drops touch each other, they are replaced by a drop of equal volume, placed at their resultant center of mass. The distance between two nucleation sites on the substrate,  $i$  and  $j$ , was calculated by following equation:

$$d_{ij} = \sqrt{(x_i - x_j)^2 + (y_i - y_j)^2 + (z_i - z_j)^2}. \quad (18)$$

Therefore, the coalescence criterion for the present study is stated as:

$$d_{ij} - (r_i + r_j) < 10^{-3}. \quad (19)$$

The drops are allowed to grow by direct condensation as well as coalescence.

Next, we estimate the force exerted by the substrate on the drop at the contact line due to differences in contact angle (namely, contact angle hysteresis,  $\Delta\theta$ ). For this step, the top view of the footprint of the drop, assumed to be a circle is used. From Figure 3(c), it can be seen that the net contact line force that acts on the drop in the  $x$  direction can be calculated as follows:

1. Calculate the base radius of the drop. This is equal to the radius calculated at the previous step plus the effect of the growth rate of the drop (direct condensation plus coalescence).
2. Calculate the  $x_{\min}$  and  $x_{\max}$  for the  $i^{\text{th}}$  drop. After knowing these values, the value of  $(\theta_{\max})_i$  and  $(\theta_{\min})_i$  are calculated from Equation 16.
3. The contact angle at any position  $x$  is given by:

$$(\theta_x)_i = (\theta_{\max})_i + \frac{\pi - \{(\theta_{\min})_i + (\theta_{\max})_i\}}{(x_{\min} - x_{\max})} x. \quad (20)$$

4. The net force acting in the  $x$  direction on the  $i^{\text{th}}$  drop is:

$$(F_x)_i = 2\pi \cdot \sigma_{lv} \cdot (r_b)_i \cdot \left[ \int_{x_{\max}}^{x_{\min}} \cos(\theta_x)_i \cdot dx \right] = 2\pi \cdot \sigma_{lv} \cdot (r_b)_i \cdot [I], \quad (21)$$

where

$$[J] = \left[ \sin \left( (\theta_{max})_i + \frac{\pi - \{(\theta_{min})_i + (\theta_{max})_i\}}{(x_{min} - x_{max})_i} \cdot (x_{max})_i \right) - \sin \left( (\theta_{max})_i + \frac{\pi - \{(\theta_{min})_i + (\theta_{max})_i\}}{(x_{min} - x_{max})_i} \cdot (x_{min})_i \right) \right]. \quad (22)$$

The hydrodynamic force which acts to oppose the motion of the  $i^{\text{th}}$  drop is:

$$(F_{hyd})_i = C_f \cdot (0.5 \cdot \rho \cdot U_i^2). \quad (23)$$

The skin coefficient of friction  $C_f$  for a droplet is taken as [21]:

$$C_f = 58 \cdot \text{Re}^{-0.97} \cdot (\theta_{avg})_i^{-1.58}. \quad (24)$$

By setting the net force exerted by the solid on the fluid in the horizontal direction  $F_{x,i} + F_{hyd} = 0$ , a result can be obtained for the terminal speed of each drop in the form:

$$U_i = 0.0812 \cdot (F_x)_i \cdot \rho^{-0.03} \cdot (r_b / \mu)^{0.94} \cdot \theta_{avg}^{1.53}. \quad (25)$$

Similarly, velocity of each drop at its individual stage of growth is determined. Each drop moves towards the higher wettability side while the velocity of sliding depends on the base radius of the drop and the average local contact angle. As the drops slide over the substrate, hidden sites underneath the original drop become active and the process is repeated. As the drop grows, its sliding velocity increases. If the weight of the drop is higher than the net retention force normal to the plane due to surface tension, the drop will fall-off. The following falling criterion is obtained from the maximum pendant drop size that is gravitationally stable:

$$(r_{max})_i = \xi \cdot \left[ \cos \left( (\theta_{max})_i + \frac{\pi - \{(\theta_{min})_i + (\theta_{max})_i\}}{(x_{min} - x_{max})_i} \cdot (x_{max})_i \right) - \cos \left( (\theta_{max})_i + \frac{\pi - \{(\theta_{min})_i + (\theta_{max})_i\}}{(x_{min} - x_{max})_i} \cdot (x_{min})_i \right) \right], \quad (26a)$$

where

$$\xi = (6\sigma_{lv}(r_b)\sin^3\theta) / (\rho \cdot g(2 - 3\cos\theta_{avg} + \cos^3\theta_{avg})). \quad (26b)$$

### Numerical algorithm

The important steps of the numerical algorithm are listed here: (i) Initialize all variables and input material properties; (ii) randomly distribute the nucleation sites (i.e.,  $10^9/\text{cm}^2$ ) on the substrate and place drops of minimum radius at all nucleation sites; (iii) calculate the coordinates of the nucleation site and assign contact angles at each of them; (iv) solve Equation 15 by a 4<sup>th</sup> order Runge-Kutta method and find the new drop radius; (v) calculate the base radius of drop and assigned contact angle according to the wettability gradient; (vi) calculate force imbalance and shift the drop towards the region of higher wettability; (vii) calculate the intermediate distance between the nucleation sites; (viii) check for drop coalescence; (ix) identify the sites already covered by drops and make them hidden; (x) search for exposed sites and provide a drop of minimum radius on such sites; (xi) check for the critical radius of slide-off and/or fall-off (xii) find the sliding velocity, as applicable; (xii) repeat (iii)-(xii) till a dynamic quasi steady-state is reached.

## **RESULTS AND DISCUSSION**

Numerical computations are conducted for nucleation site density of  $10^9$  sites/cm<sup>2</sup> on: (i) a substrate with a wettability gradient, (ii) a horizontal substrate and, (iii) an inclined surface (5°); the latter two substrates having no wettability gradients. Condensation of water occurs on the underside of the substrate of size 25 mm × 25 mm; drops are in the pendant mode at all times. Degree of subcooling is  $(\Delta T_{\text{sat}}) = 5^\circ\text{C}$  with saturation temperature of 30°C. Detailed simulation results for modeling of dropwise condensation process on inclined surfaces are available in other related works of authors [5, 18, 22].

Simulations show that the model presented above captures the inherent mechanism of dropwise condensation over a surface with a wettability gradient. The features of the condensation cycle are similar to those of an inclined surface shown in Figure 1. The points of difference are: (i) drops shift towards the lower wettability side, (ii) for a graded surface, drops of all sizes are in motion, and (iii) larger drops acquire greater velocity.

Spatial distribution of drops at an instant just before the first drop leaves the surface on a graded substrate, first slide-off from an inclined substrate and the first fall-off from a horizontal substrate, respectively, are compared in Figure 4. Because of the fact that the wettability gradient induces motion to drops of every size, there always exists an exposed virgin area behind every droplet on the graded substrate,

as seen in Figure 4a. Hence, the active (virgin/exposed) area for a graded surface always tends to be greater than the other two configurations, respectively. This result is summarized in Table 1. The time cycle from initial nucleation to the instant when the drop leaves the surface is also given in Table 1. It is a minimum for the substrate having a wettability gradient. For such graded surfaces it is observed that smaller drops move with small velocity and larger drops with larger velocity. For an inclined substrate, only the drop that reaches the critical size is set in motion. For the horizontal surface, there is no sliding motion possible; the drop falls off when they achieve a critical size. For the surface with wettability gradient, both slide off and fall-off are possible. The latter happens during sliding also, when the accumulated weight of the sliding drop exceeds the retention surface force. This factor has been included in the simulation.

Table 1. Simulation statistics

Case study	Time of first drop slide/fall-off	Critical drop size	Active area
Wettability gradient	18 minutes	2.53 mm (slide-off)	38%
Inclined substrate	42 minutes	3.47 mm (slide-off)	23%
Horizontal	55 minutes	5.67 mm (fall-off)	18%

Figure 5(a) shows the droplet frequency as a function of drop radius on the three substrates respectively, at an instant just before the slide/fall-off criticality is attained. Looking at this distribution, it is clear that a graded substrate has larger number of smaller sized drops as compared to the other two cases. Largest size drops remain on a horizontal substrate before they fall-off. This eventually leads to a slower condensation rate on the horizontal substrate; in this regard the wettability graded substrate shows a clear promise. Figure 5 (b) shows the area of coverage created by the foot-prints of the drops on the substrate, with respect to time. As soon as the vapor flux is exposed to the virgin substrate, direct condensation starts and the coverage increase rapidly. Later, coalescence commences, leading to criticality; the coverage then tends to stabilize. On a horizontal substrate, only a fall-off criticality is possible while on a graded substrate, a slide-off criticality will be achieved first; later, the droplet may also fall-off while in transit due to increase in its weight. A quasi-steady-state is eventually reached, after which the area coverage oscillates around a mean value. It is seen that this mean quasi-steady state value of the coverage is smaller for the graded surface, making the exposed virgin area larger than the other two surfaces considered. It is also observed that incipience of droplet slide-off event is relatively earlier on the graded surface. As a direct consequence of these attributes, the heat transfer coefficient is expected to be higher for a surface with variable wettability. In fact, the calculated heat flux with graded and non-graded surface comes out to be 470 KW/m<sup>2</sup> and 386 KW/m<sup>2</sup>, respectively, for an applied degree of sub-cooling = 5°, at condensation temperature of 30°C.

Figure 6(a) shows the temporal variation of average drop size. Data is generated in such a way that accumulated growth due to direct condensation (no coalescence) and the respective drop sizes which are growing by direct condensation are tracked separately in the code. It is clear that, as time progresses the contribution of direct growth mechanism is larger in smaller sized drops only; growth of larger drops is mainly attributed to coalescence. Figure 6(b) depicts the instantaneous spatial distribution of drops underneath a horizontal substrate, two hours after commencement of the condensation process. Figure 6(c) is the pictorial depiction at this instance of time. The instantaneous distribution follows a power law, with the negative slope increasing with the substrate wettability gradient, reflecting the fact that the frequency of new nucleation sites being exposed is higher in case of the graded surface. This leads to repeated appearance of small drops at freshly exposed nucleation sites. Comparison of this instantaneous picture with Figure 5(a) reveals that the exponent of the power law varies with time, even when a quasi-stead-state is reached due to sudden disappearance of drops by sliding and/or fall-off and subsequent re-nucleation phenomenon. Further studies are needed to establish the variation band of this exponent, as a function of the absolute wettability and its imposed gradient. On a graded surface, the tendency of droplet motion towards the lyophilic side may result in a situation where larger sized drops are seen at the lyophilic end. At this end, the fall-off radius is also larger. Thus, on a graded surface there is no unique fall-off radius. At each location, localized force balance has to be done to determine the droplet dynamics.

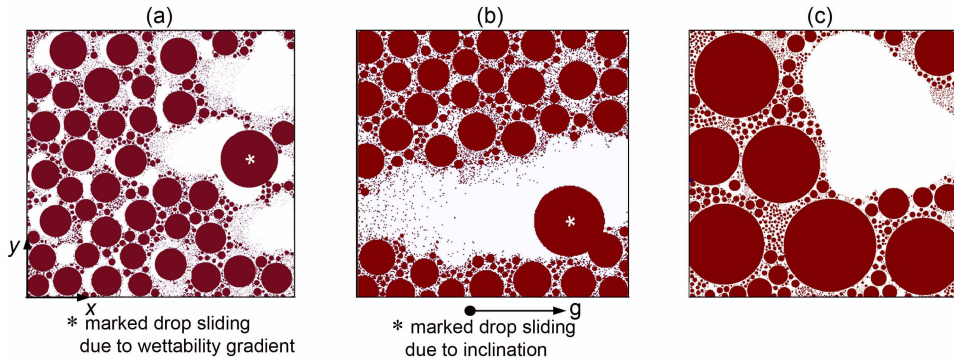


Fig. 4. Droplet motion underneath a chemically textured substrate with (a) wettability gradient imposed on a horizontal substrate, (b) inclined substrate ( $5^\circ$ ) with no wettability gradient and, (c) a drop falling-off underneath a horizontal substrate with no wettability gradient

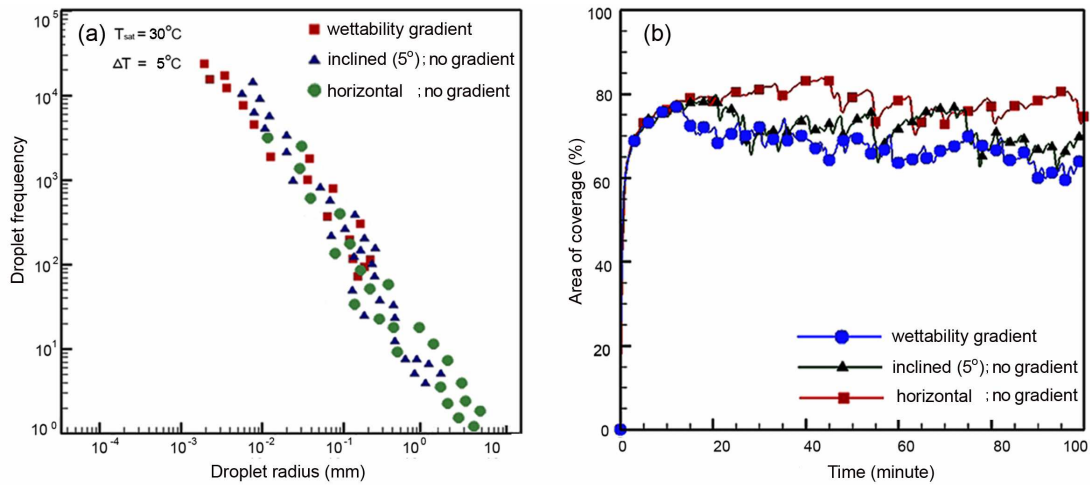


Fig. 5. (a) Droplet frequency (number of drops) as a function of the drop radius, just before the first drop leaves the surface. (b) Effect of the choice of the substrate on the percentage area of coverage

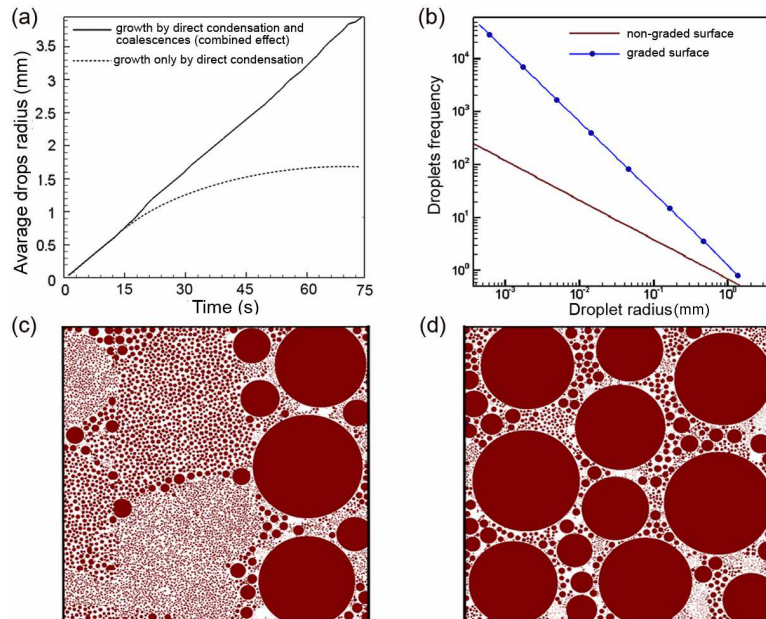


Fig. 6. (a) Temporal variation of average drop radius of condensing water. (b) Variation of droplets frequency with respect to the droplet radius, two hours after commencement of dropwise condensation (c-d) Spatial-drops distribution of droplets after two hours of commencement of dropwise condensation. (c) With wettability gradient (d) without wettability gradient.

## SUMMARY AND CONCLUSIONS

The heat transfer coefficient during dropwise condensation is two to three orders of magnitude higher than in filmwise condensation and is a preferred mode in many processes. Further enhancement can be brought about by effectively sweeping the droplets away from the surface, thereby exposing fresh nucleation sites. A passive technique to achieve such implicitly imposed and enhanced droplet mobility, especially for horizontal substrates, is by surface texturing of the substrates that result in a graded change of their surface energy characteristics. The primary macroscopic effect of such a coating is to achieve a graded change in the wettability characteristics of the substrate. Thus, a droplet experiences a net surface force due to this wettability gradient on the three-phase contact line that aids its removal from the substrate. A detailed model was presented in this study to discern the effect of imposing a wettability gradient on dropwise condensation patterns and resulting heat transfer on a horizontal surface. The results were compared with a non-graded hydrophobic surface. The following main conclusions can be drawn from the study:

1. The mathematical model presented herein is sufficiently comprehensive to capture all the major components of the quasi-cyclic dropwise condensation process on large scale engineering surfaces.
2. Essentially, in the cases under scrutiny, two distinct phases of droplet growth are observed: (a) growth due to direct condensation and, (b) growth primarily due to coalescence. Direct condensation growth occurs in the early part of growth, immediately after nucleation. Later, as radii of neighboring droplet increases due to direct condensation, they start interacting with each other resulting in growth due to coalescence. Moving further, eventually results in some form of criticality, wherein either a fall-off or a slide-off occurs.
3. Droplets either fall-off or slide off once they achieve criticality. On horizontal substrates having no wettability gradient, a droplet fall-off results when the body force due to gravity exceeds the surface retention force due to surface tension. On horizontal surfaces having wettability gradient, a critical slide-off radius is observed, which is much smaller than the fall-off radius on the non-graded horizontal surface. These critical radii, of either fall-off or slide-off, depend on the thermophysical properties of the condensate, the absolute level of lyophobicity and its gradient which has been achieved on the substrate, as the case may be.
4. It is seen that droplets move from a region of lower wettability towards one having higher wettability. Such a movement achieved passively by the surface tension gradient on the three-phase contact line, exposes fresh nucleation sites. On horizontal substrates with no wettability gradient, such an additional mobility is not possible and hence there is no droplet sweeping action. This thwarts the heat transfer coefficient.
5. It is observed that under quasi-steady state operation, the number density of small sized droplets is higher in the case of the graded surface as compared to the surface having no wettability gradient. This results in an enhanced average heat transfer scenario for the graded surface as the thermal resistance of small droplets per unit area is lower for smaller drops than their larger counterparts.
6. On the graded surface, the instantaneous sliding velocity of drops is a function of its base radius. Larger drops move with higher velocity; this, in turn, is a function of the droplet position.
7. The instantaneous active virgin area available for nucleation in the case of a graded surface is greater than what is realized for the non-graded substrate.
8. It is believed that with improving manufacturing techniques realization of such graded substrates for large scale engineering applications will be possible. Although not specifically addressed in this report, graded surfaces are also of interest to enhance and control dropwise condensation in micro-g environments, wherein wiping of the liquid layer is an issue due to the absence or influence of external body forces.

## Acknowledgments

The authors are grateful to the Board of Research in Nuclear Sciences (BRNS), Department of Atomic Energy, Government of India, for providing the financial assistance to carry out this research work.

## NOMENCLATURE

$A$	Area of cross-section ( $\text{m}^2$ )
$C_f$	Skin friction coefficient
$D$	Distance (m)
$F$	Force (N)
$H$	Latent heat of vaporization (kJ/kg)
$h$	Heat transfer coefficient ( $\text{W}/(\text{m}^2 \cdot \text{K})$ )
$k$	Thermal conductivity ( $\text{W}/(\text{m} \cdot \text{K})$ )
$L$	Length (m)
$r$	Radius (m)
$\bar{R}$	Universal gas constant ( $\text{J}/(\text{kg} \cdot \text{K})$ )
$T$	Temperature (K)
$\Delta T$	Temperature drop ( $T_w - T_{\text{sat}}$ ) (K)
$dt$	Time step (s)
$U$	Velocity of the moving drop (m/s)
$V$	Volume of the drop ( $\text{m}^3$ )
$P$	Pressure ( $\text{N}/\text{m}^2$ )
$x, y, z$	Cartesian coordinates
$X$	Maximum length of substrate in $x$ direction (m)

### Greek symbols

$\alpha$	Inclination angle (deg)
$\mu$	Dynamic viscosity (Pa·s)
$\nu$	Specific volume ( $\text{m}^3/\text{kg}$ )
$\rho$	Density ( $\text{kg}/\text{m}^3$ )
$\sigma$	Surface tension of liquid (N/m)
$\hat{\sigma}$	Accommodation coefficient (-)
$\theta$	Contact angle (radian or deg)

### Subscripts

$avg$	Average
$b$	Base
$c$	Condensate
$crit$	Critical
$d$	Drop
$g$	Gravity
$hyd$	hydrodynamic
$i$	Interfacial heat and mass transfer
$l$	Liquid
$lv$	Liquid vapor interface
$max$	Maximum
$min$	Minimum
$sat$	Saturation
$sl$	Solid-liquid interface
$v$	Vapor
$w$	Condensing wall
$x, y, z$	Cartesian coordinates

### References

1. Rose J. W. Dropwise condensation: theory and experiments: A review // *Proc. Institution of Mechanical Engineers*. 216. 2002. Pp. 115–118.
2. Carey V. P., *Liquid-vapor Phase-change Phenomena*, 2<sup>nd</sup> ed., Hemisphere Publishing Corporation, USA. 1992. Pp. 413–472.
3. Leipertz A. Dropwise condensation: *VDI Heat Atlas VDI-GVC (ed. 2)* / Eds. P. Stephan, Springer-Verlag, Germany, 2010. Pp. 933–937.
4. Burnside B. M., Hadi H. A., Digital computer simulation of dropwise condensation from equilibrium droplet to detectable size // *Intern. J. of Heat and Mass Transfer*. 1999. Vol. 42 (suppl. 11). Pp. 3137–3146.
5. Sikarwar B. S., Battoo N. K., Khandekar S., Muralidhar K. Dropwise condensation underneath chemically textured surfaces: Simulation and experiments // *ASME Journal of Heat Transfer*. 2011. Vol. 133 (suppl. 2). Pp. 021501 (1–15).
6. Rose J., Utaka Y., Tanasawa I. Dropwise condensation: in *Handbook of Phase Change: Boling and Condensation* / Eds. S. G. Kandlikar Taylor and Francis, USA, 1999. Pp. 581–594.
7. Vemuri S., Kim K. J. An experimental and theoretical study on the concept of drop wise condensation // *International Journal of Heat and Mass Transfer*. 2006. Vol. 49. Pp. 649–657.
8. Tanasawa I., Advance in Condensation Heat Transfer: in *Advances in Heat Transfer* / Eds. J. P. Hartnett, T. F. Irvine, Cho I. Y. 1991. Vol. 21. Pp. 57–59.
9. Battoo N. K., Sikarwar B. S., Khandekar S. Muralidhar K. Mathematical simulation of dropwise condensation exposed to vapor flux // *Proc. 20th National and 9th "International ISHMT-ASME Heat and Mass Transfer Conference"* Mumbai, India, 2010. Pp. 1330–1336.
10. Bansal G. D., Khandekar S., Muralidhar K. Measurement of heat transfer during dropwise condensation of water on polyethylene // *Nanoscale Microscale Thermophysical Engineering* 2009. Vol. 13, Pp. 184–201.
11. Qiang L., Hong W., Xun Z., Mingwei Z., Droplet movement on horizontal surfaces with gradient surface energy // *Science in China, Series E: Technological Sciences* 2006. Vol. 49. Pp. 733–744.
12. Lan Z., Ma X. Z., Zhang Y., Zhou X. D., Theoretical study of dropwise condensation heat transfer: Effect of the liquid-solid surface free energy difference // *Journal of Enhanced Heat Transfer* 2009. Vol. 16. Pp. 61–71.
13. Pratap V., Moumen N., Subramanian R. Thermocapillary motion of a liquid drop on a horizontal solid surface // *Langmuir* 2008. Vol. 24. Pp. 2185–5193.
14. Subramanian R., Moumen N., McLaughlin J. B. The motion of a drop on a solid surface due to a wettability gradient // *Langmuir*. 2005. Vol. 21. Pp. 11844–11849.
15. Berthier J. *Microdrops and Digital Microfluidics*, 2<sup>nd</sup> ed., Hemisphere Publishing Corporation, USA, 2008. Pp. 75–179.
16. Daniel S., Chaudhury M. K., Chen J. C. Fast drop movements resulting from the phase-change on a gradient surface // *Science*. 2001. Vol. 291 Pp. 633–636.
17. Moumen N., Subramanian R. S., McLaughlin J. B., Experiments on the motion of drops on a horizontal solid surface due to wettability gradient // *Langmuir*. 2006. Vol. 22. Pp. 2682–2690.
18. Sikarwar B. S., Khandekar S., Agrawal S., Kumar S., and Muralidhar K. Dropwise condensation studies on multiple scales // *Heat Transfer Engineering* 2012. Vol. 33 (3/4) (in press).
19. Leach R. N., Stevens F., Langford S. C., Dickinson J. T., Dropwise condensation: Experiments and simulations of nucleation and growth of water drops in a cooling system // *Langmuir*. 2006. Vol. 22. Pp. 8864–8872.
20. Mikic B. B. On the mechanism of dropwise condensation // *International Journal of Heat and Mass Transfer*. 1969. Vol. 12. Pp. 1311–1669.
21. Sikarwar B. S., Khandekar S., Muralidhar K. Simulation of flow and heat transfer inside a liquid drop sliding underneath a lyophobic surface, manuscript under preparation.
22. Sikarwar B. S., Khandekar S. Muralidhar K. Dropwise condensation of liquid metal vapor underneath a flat inclined substrate // *Proc. 7th Intern. Conf. "Computational Heat and Mass Transfer"* Istanbul, Turkey, 2003 (Paper #135).

## MODELING AND EXPERIMENTATION OF PULSATING HEAT PIPES

**H. F. Smirnov**

“The food technologies processes and apparatuses and energy management”

Odessa National Academy of Food Technology.

Kanatnaya Street 112, Odessa 65088.

phones: (work) 038–048–7124175; (home) 038–0482–402344; E – mail: g.smirnov@e-mail.ua

**I. O. Kuznyetsov**

“The heat and mass transfer and fuel oil processes”

Odessa State Academy of Refrigeration.

Dvoryanskaya Street 1/3. Odessa 65000.

phones: (work) 038–048–7209149; (home) 038–0482–340405;

E – mail: ikuznyetsov@ukr.net

### Abstract

There is presented in the paper the pulsating heat pipes (PHP) authors modeling and experimentation which were performed during a lot of previous years (beginning from 1995 up to 2005). The first author had his own experience in the first step in the topic considerable earlier (first former Soviet Union invention certificate with title “Pulsating Heat Pipe” was obtained in 1972 year), but, unfortunately, it couldn't be developed then. So, its investigation was restored again in pointed time, thanking for the company “Thermacore” key person Mr. Don Ernst serious moral and financial support. Using now their own experimentation authors obtained representative experimental data for different PHP parameters and conditions, including PHP position in the gravity field, changing charge and so on. The authors also discovered in their experiments, that the device stable work couldn't be realizing in some cases especially for looped PHP. Using their and other author experimentation results it was suggested and developed the original physical imaginations about physical nature of PHP real mechanism. There were conducted some comparison of the calculations based on the mentioned imaginations with their own experimental results and with some experimental results other authors for which were known whole necessary information about experiments conditions. Besides it, there is given also briefly analysis of key last papers top investigations in the field too.

### KEYWORDS

Pulsating heat pipe, pulsating thermo - siphon, heat exchanger, boiling, condensation, liquid and vapor slug.

### INTRODUCTION

The first sample of PHP creation and testing was done and testing in Odessa in 1971, see [7]. Before it and independently there were studied some samples of the liquid thermal control system without pump [5,6]. Unfortunately, then these works had no development. Lately, there were appeared some Japanese experts PHP, most of them were patented [1, 2]. Then there were appearing a lot investigations directed on these devices performance testing and their characteristics study [3, 4, 10] and many other. May be the first attempt for determination of the PHP place in the whole list of the two – phase heat transfer devices was done in [8]. It was suggested to consider, that the PHP principal difference in the comparison with many other devices with the same goal is connected with their moving forces physical nature. There are inertial forces, which are appearing in the liquid as the result of the vapor phase appearance during evaporation.

Lately, the paper authors began to develop some their own investigation in the field. Their experimentation results and analysis, including their approach to the PHP action theoretical modeling were presented in the publications [9, 13 – 16]. The last key publications in the field were presented in [11, 12]. The authors are trying with the last publication to introduce their own view on the problem, including comments to the nearest future activity.

## THE EXPERIMENTAL SET-UP AND RESEARCH METHODS

The experimental set-up schematic is shown in Fig. 1. The PHP experimental sample has been consisted from the coil 1 with eight branches. Every branch was stainless steel capillary tube with inner diameter 0.96 mm and outer diameter 1.9 mm. PHP have been contained three zones: «heating» I; «transport» II and «cooling» III. The branch zone lengths are heating -140 mm, transport 150 mm and cooling - 140 mm. The heat input was fulfilling from electric wire heater uniformly. The heater was located under cooper plate 3 with thickness  $\delta = 1,5$  mm.

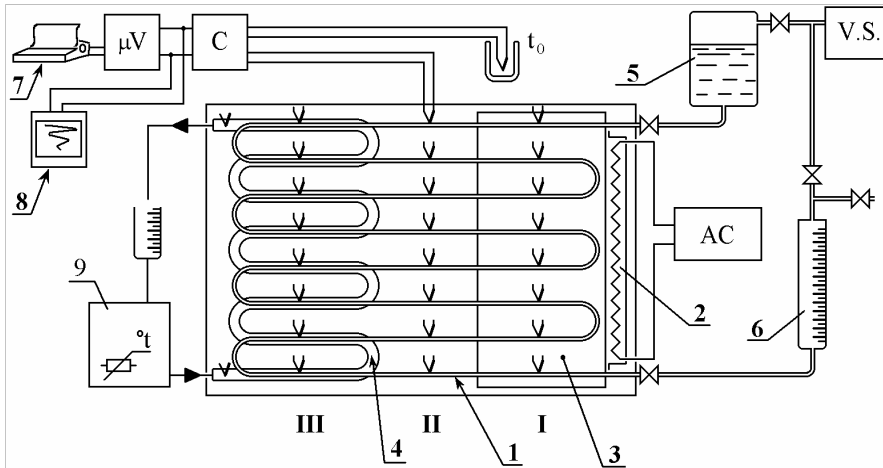


Fig. 1. The experimental set up scheme. I - heating zone; II - transport zone; III - cooling zone. 1 - PHP coil, 2 - AC heater, 3 - heater plate, 4 - cooling coil, 5 - filling volume, 6 - burette, 7 - printer, 8 - millivoltmeter curve-writer, 9 - thermostatic bath, C - programmed commutator, VS - vacuuming system

The PHP branches were soldered to the copper plate in the heating zone. The electric loading was creating from stabilized source. The PHP branches were soldered to the copper tube 4 with diameter  $\varnothing 6 \times 8$  mm in the cooling zone. The water from thermostat was supplied over tube 4. The 24 copper-constantan thermocouples were installed on the PHP capillary tube surface in the every branch every zone in the middle. These thermocouples were used for PHP temperature field determination. The transferred heat flux was

determined with cooling water flow rate, inlet and outlet water temperatures measurements help. The heat input to the heater was also registered. The heat carrier mass filling in PHP was created from filling vessel after PHP vacuum realization. The heat carrier was degassed before filling. The determined filling ratio liquid was ensured over liquid excess removing from PHP loop. The stationary regime was determined with respect thermocouples average measurements value for all branches and all zones.

The separate branches and the whole PHP working state was determined on the cooling zone average temperatures determination base. These temperatures were near the cooling liquid temperature value when the corresponding branches didn't work (didn't the heat transfer).

## THE EXPERIMENTATION RESULTS DISCUSSION

### The typical temperature regimes.

The experimental set-up was used for PHP zones average temperatures behavior study and PHP heat transfer characteristics determination. The PHP work beginning was determined, when the cooling zone average temperature began to increase. The heating and transfer zones average temperatures stable oscillations were fixed in the steady thermal regimes as it is seen from Fig. 2. The corresponding temperature behavior in discussed experiments coincided qualitative with [3,4] results.

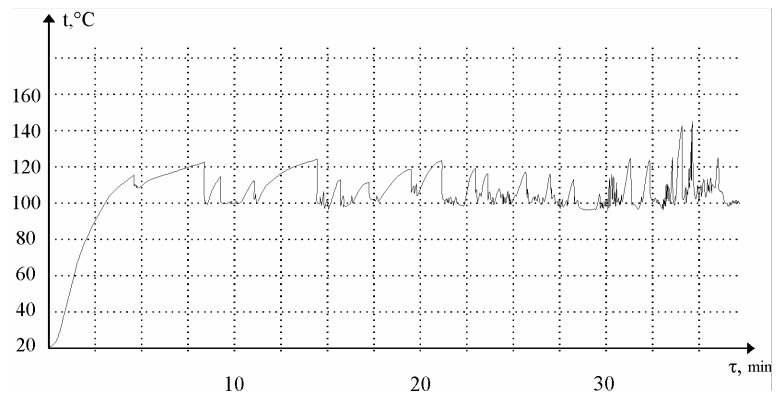


Fig. 2. Typical temperature pulsations in the transport zone of PHP

More detail observations for two neighboring branch average temperatures in the heating and transport zones were presented in [9].

The corresponding temperature behavior in discussed experiments coincided qualitative with [3,4] results. More detail observations for two neighboring branch average temperatures in the heating and transport zones were fulfilled with the automatic measuring complex help. As it is seen (Fig. 3) the heating zones temperatures oscillations form some «pulsating groups» there are the approximately «constant temperature» intervals with the duration about some seconds. The graphs in Fig. 3 are rather typical for experiments different conditions. In the same time the frequencies and temperature pulsation amplitudes dependencies from different factors (total power, the inclination angle, the filling value an etc.) didn't succeed to determine. Probably the observed temperature pulsations forms multiplicity is the statistical nature of the PHP internal processes consequence. The mean temperatures for typical thermal regimes were found for any time interval.

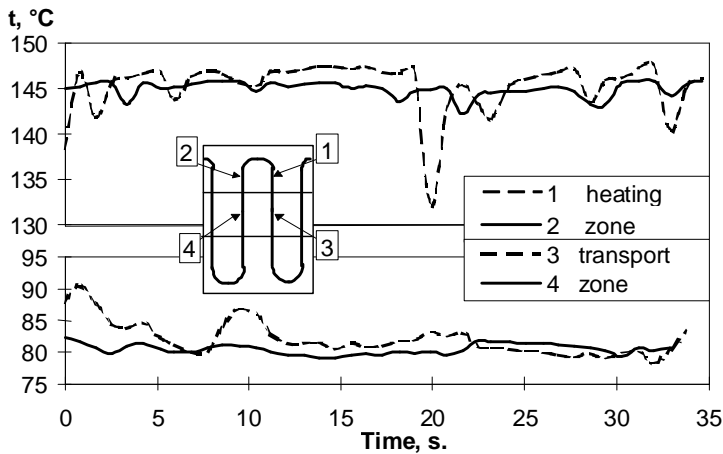


Fig. 3. Temperature pulsations in the heating and transport zones of two neighbor branches. 1,2 – heating zone temperature, 3,4 – transport zone temperature

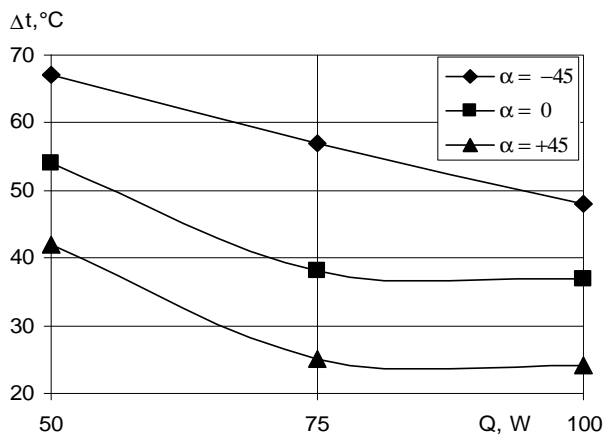


Fig. 4. The dependency of the PHP whole temperature drop on the it position in the gravity field and Power Q. 1 – heating zone under the cooling zone; 2 – horizontal position; 3 – heating zone above cooling zone

The total power increasing from 70 W to 250 W had the positive influence on the PHP work stability.

The thermal regimes with stable heat transfer in some branches and heat transfer absence in other branches were observed many times when the heat carrier removal from noncondensable gas or internal PHP volume hermetic was insufficient. The working and non-working branches distribution was different and some regularities for this parameter to define was impossible.

The thermal regimes with the working and non-working branches distribution some changing were observed. The above - pointed experimental facts gave the foundation to consider, that in PHP:

The first important results were connected with the experimental determination of the influence of PHP position and power on it whole temperature drop. Most typical experimental results of this factors influence on it whole temperature drop are presented lower in the Fig. 4.

Not lower PHP temperature field three measurements were fulfilled after PHP the steady regime to begin. The obtained results were satisfactory reproduced. The horizontal positions experimental results are presented in Fig. 5 when filling ratio with water was 50%. The total thermal resistance was defined as the heating and cooling zones mean temperatures difference ratio to the PHP total power.

### The main factors influence on the PHP work

The PHP research shown, that for some cases it was impossible to ensure this PHP construction stable work. The main factors, which had the determined influence on the work PHP stability and duration, were the how condensable gas concentration and the filling value. The PHP could not work in the horizontal position when the filling was big (more than 70%) or small (lower than 30%).

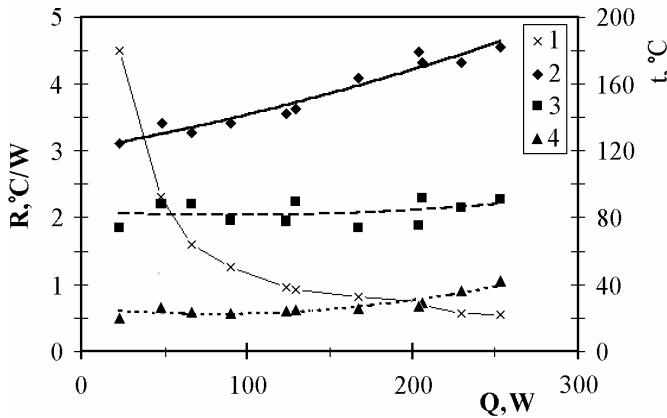


Fig. 5. Thermal resistance  $R(^{\circ}\text{C}/\text{W})$  and temperature level in the zones PHP dependence from total power 1 - thermal resistance in the horizontal position, 2 - temperature of heating zone; 3 - temperature of transport zone; 4 - temperature of cooling zone

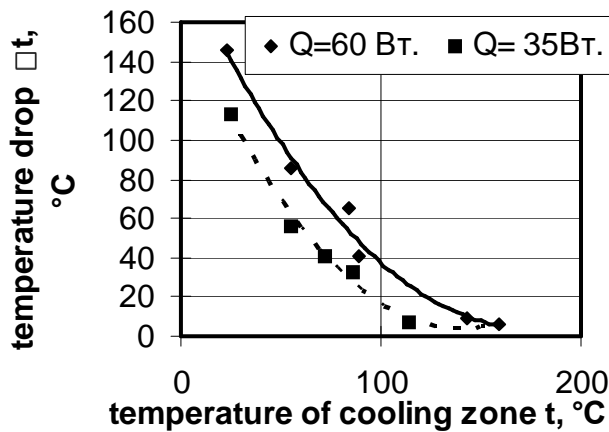


Fig. 6. The temperature drop dependency of temperature level in the cooling zone

### THE PHP ACTION APPROXIMATED MODEL

It was suggested the different branches are acting independently. This situation was observed in experiments and it consisted the physical imaginations and model foundation. It was taken as «elementary cell» two neighboring branches «i» and «i+1», which have the common «cooling zone», when every branch have «heating», «transport» and its own cooling zone. The two-phase mixture movement in elementary cell is connected with vapor mass flow generation in heating zones and their condensation in every branch cooling zones.

The vapor volume increasing in «i» branch in «vaporization» stage, when heat flux and saturation pressure are constant during the time interval  $\Delta\tau$  will be:

$$\left[ q \Pi_E L_E \varphi_E - k_2 (t_s - t_2) \Pi_C L_C \varphi_C \right] \frac{\Delta\tau}{r\rho''} = \Delta V \quad (1)$$

If the vapor generation in the neighboring branches takes place simultaneously with approximate identical intensity then instead vapor volume increasing the saturation pressure will be correspondingly increased.

The pressure drop  $\Delta P$  what corresponds the vapor volume  $\Delta V$ , when the vapor is generated simultaneously in both neighboring branches «i» and «i+1» and heat carrier movement is absent will be defined by equation:

The «individual» and «combined» heat and mass transfer mechanism have been existing in PHP.

The most probable is the «individual» mechanism, when the branches are working independently each from other.

The considerable PHP drawback is connected with the fact, when this device stable work is observed previously when there is a large temperature drop between heating and cooling zones (more than 40 °C). That is why the experiments were fulfilled with the goal to determine is it possible to decrease minimum temperature drop of the PHP stable work beginning (lower 10 °C)? It was discovered, that the most strong means for minimum temperature drop decreasing is the transient on the more high the saturation pressure level.

So, when the experiments were fulfilled with water as heat carrier application, it was discovered, that the heating zone average temperature practically didn't change with the cooling zone average temperature growth from 20 °C to 90 °C. It meant that total PHP temperature drop decreased in such way as temperature saturation (action temperature level) was increased. The minimum temperature drop in those experiments was about 40 °C. When the average saturation temperature level was reached to 140 - 160 °C the temperature drop was becoming near some grades (see Fig. 6) .

$$\left[ q \Pi_E L_E \varphi_E - k_2 (t_s - t_2) \Pi_C L_C \right] \frac{\Delta \tau_0}{r S_0 L_0 \varphi_0} = \frac{\partial \rho''}{\partial p} \Delta p \quad (2)$$

As soon as in the neighboring «i» and «i+1» branches the saturation pressure drop  $\Delta P$  balance begins to destroy for example for account «i» - heating zone wall drying, when some liquid microlayer in «i+1» heating zone will remain, then the effective head  $\Delta P_0$  is appearing. This effective head the liquid slug movement ensures. There are two effective head appearance possible reason:

The liquid microlayer whole evaporation in one of two heating zones («i» and «i+1») of the elementary cell. The cooling zone flooding with liquid completely and heat removal intensive mechanism blocking.

It was suggested, the first mechanism is main. It was taken, the PHP work have the «cyclic» character and every cycle consist from four stages. The stage 1 - the «i» branch heating zone flooded by heat carrier liquid mass (Fig. 7 a). This stage begins, when in «i» branch the liquid microlayer is evaporated completely, but in «i+1» heating the microlayer evaporation and the saturation pressure growth are continued.

The appeared effective head is leading to the liquid slug movement from «i+1» branch to «i» branch. The «i+1» cooling zone is opening when liquid slug is moving and it is accompanied with the effective head decreasing. Then, after some time interval  $\tau_2$ , what is necessary for «i» branch liquid slug overheating, the reverse vapor flow is appearing. This reverse flow decreases the effective head additionally.

That is why, the effective head for the elementary cell  $\Delta P_0(\tau)$  can be determined with above-mentioned considerations respect and, taking into the mind the hydrostatic head influence for inclined and vertical elementary cell position:  $|\beta| \neq 0$ :

$$\begin{aligned} \Delta p_0(\tau) = & \left[ q \left( \Pi_E L_E \varphi_E \right)_{i+1} - k_{20} (t_s - t_2)_{0i+1} \Pi_C W \Delta \tau'_0 \right] \left( \frac{\partial \rho''}{\partial p} \right)^{-1} \frac{\Delta \tau_0}{r (S_0 L_0 \varphi_0)_{i+1}} - \\ & - q \Pi_E W (\Delta \tau'_0 - \tau_2) \left( \frac{\partial \rho''}{\partial p} \right)^{-1} \frac{\Delta \tau_0}{r (S_0 L_0 \varphi_0)_i} + \rho' g (1 - \varphi) L_0 \sin \beta, \end{aligned} \quad (3)$$

here  $\Delta \tau_0$  - the small time interval during thus the  $\varphi$ ,  $k_{20}$ ,  $t_s$  values can be considered constants;  $\Delta \tau'_0$  - the time interval from the movement beginning. The second item in eq. (3) expression is equal 0 when  $\Delta \tau'_0 \leq \tau_2$ . The effective head is compensated the hydraulics resistance and the moved liquid slug inertia, during the slug movement.

$$\Delta p_\mu = \frac{32 \mu' L_0 W}{d^2 (1 - \varphi)^2} + L_0 \rho' (1 - \varphi) \frac{dW}{d\tau} \quad (4)$$

The assumptions were taken in the expressions :  $W \Delta \tau'_0 = L_0 K_L$ ;  $W = L_0 / \Delta \tau_0$ ;  $\frac{dW}{d\tau} = \frac{L_0}{(\Delta \tau_0)^2}$ ;

with it respect, we obtain

$$A_q \Delta \tau_0^3 + (A_g + A_\tau) \Delta \tau_0^2 - A_\mu \Delta \tau_0 - A_L = 0 \quad (5)$$

$$\text{where: } \left\{ q \Pi_E L_E \varphi_E - [k_2 (t_s - t_2) \Pi_C L_0 + q \Pi_{Ei} L_0] K_L \right\} \left( \frac{\partial \rho''}{\partial p} \right)^{-1} \frac{\Delta \tau_0}{r (S_0 L_0 \varphi_0)} = A_q, \quad (6)$$

$$L_0^2 \rho' (1 - \varphi_0) = A_L \quad (7)$$

$$q \Pi_i L_0 \tau_2 \left( \frac{\partial \rho''}{\partial p} \right)^{-1} \frac{1}{r (S_0 L_0 \varphi_0)_i} = A_\tau \quad (8)$$

$$\rho' g (1 - \varphi_0) L_0 \sin \beta = A_g \quad (9)$$

$$\frac{32 \mu' L_0^2}{d^2 (1 - \varphi)^2} = A_\mu \quad (10)$$

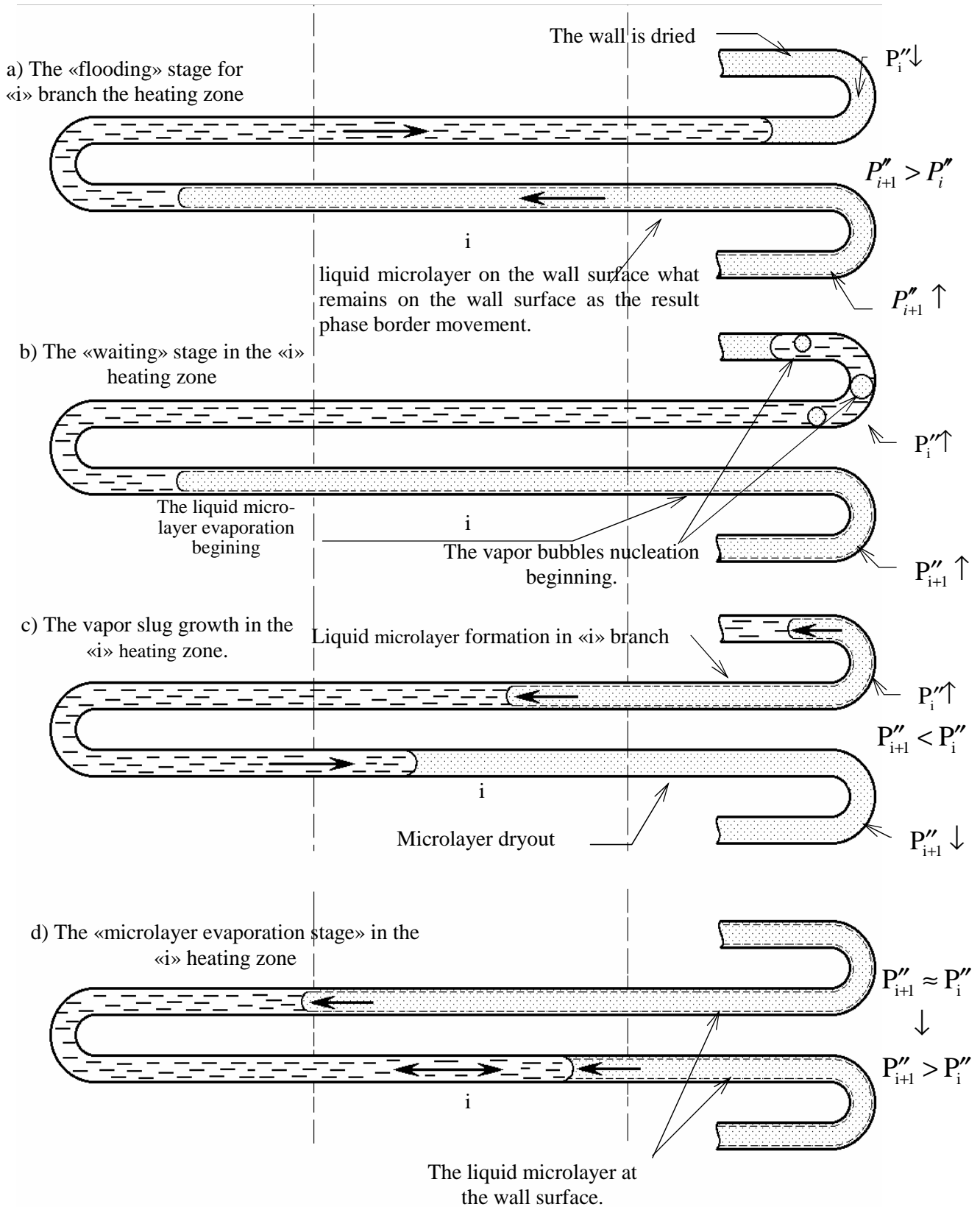


Fig. 7. The pictures illustrated the hydrodynamic and thermal phenomenon which take place in the elementary cell in the correspondence with authors physical imaginations

For authors experiments conditions, the  $A_L$  parameter is small and eq. (5) is transformed to quadratic algebraic equation.

$$A_q \Delta \tau_0^2 + (A_g + A_\tau) \Delta \tau_0 - A_\mu = 0 \quad (11)$$

This equation solution can be written in such way  $\Delta \tau_0 = \frac{A_g + A_\tau}{2A_q} \left[ \sqrt{1 + \frac{4A_\mu A_q}{(A_g + A_\tau)^2}} - 1 \right]$  (12)

The equation is right when  $\beta > 0$ . If  $\beta < 0$ , the solution is determined in the next view:

$$\Delta \tau_0 = \frac{|A_g| - A_\tau}{2A_q} \left[ \sqrt{1 + \frac{4A_\mu A_q}{(|A_g| - A_\tau)^2}} + 1 \right] \quad (13).$$

here when  $\tau_2 > \Delta \tau_0 A_\tau = 0$ .

The «waiting» stage follows after the «flooding» stage Fig. 6b. The time interval  $\tau_2$ , which corresponds the waiting stage period, is necessary for capillary wall and liquid slug overheating before the vapor bubble appearance. It is possible to use for estimation the next expression:

$$\tau_2 = (K_A \rho' c' \vartheta_* d / 4 + \rho_w c_w \delta_w \vartheta_w) / q \quad (14)$$

here, the  $\vartheta_*$  value is taken as mean temperature difference for heating and cooling zones,  $\vartheta_w$  is nucleation temperature drop,  $K_A$  is accounting the liquid overheating irregularity coefficient ( $K_A \leq 1$ ).

The «vapor generation» («vapor growth») stage begins after the «waiting» stage in the heating zone (Fig. 6c). The «vapor growth» law the «energy» model is determined and can be written in the next view:

$$q \varphi_E \Pi_E d \tau = S_E \rho'' r d \varphi \quad (15) \text{ and } \varphi_E = \frac{2d}{3L_E} \exp\left(\frac{4q\tau}{r\rho''d_E}\right) \quad (16)$$

The «growth» stage duration  $\tau_g$  can be determined from eq. (16), if  $\varphi_E = \varphi_{\max} = 1 - \frac{4\pi d \delta_0}{\pi d^2} = 1 - 4\delta_0 / d$ , then

$$\tau_p = \frac{r\rho''d_E}{4q} \ln \left[ \frac{3L_E}{d} \left( 1 - \frac{4\delta_0}{d} \right) \right] \quad (17)$$

Usually, the «grout» stage time is the small value in comparison with the total cycle duration and it can be neglected. The stage IV the liquid microlayer «drying» in the heating zone (Fig. 6d) is following after the

«growth» stage. The drying stage duration is determined with the equation help.  $\tau_\delta = \frac{r\rho'\delta_0}{q}$  (18)

The working cycle is repeated after the drying stage to be completed.

The liquid microlayer thickness is determined in the first approximation as the channel diameter proportional value:  $\delta_0 = K_d \cdot d$ .

The parameters  $K_L$ ,  $\varphi_L$ ,  $K_2$  are very complex for the determination. That is why in the first approximation frames it as suggested, that complex  $\{q\Pi_E L_E \varphi_E - [k_2(t_s - t_2)\Pi_C L_0 + q\Pi_{Ei} L_0] K_L\}$  is proportional  $q\Pi_E L_E$ . Then it is possible to mark:

$$A_q = \frac{qK_q \Pi_E L_E}{rS_0 L_0 \varphi_0} \left( \frac{\partial \rho''}{\partial p} \right)^{-1} \quad (19)$$

The coefficient  $K_d$ ,  $K_q$  were determined on the experimentation results analysis base.

It was suggested, when in «i» branch there was the «flooding» stage, the (i+1) heating zone wall began to be dried. It was supposed also, the drying wall existence mean time was equal an one half of the «flooding» stage duration  $(\Delta\tau_0) \bar{\tau}_0 = \Delta\tau_0/2$ . The evaporation zone thermal resistance in that period can be determined as  $R_{1E} = \xi_1 \bar{\tau}_0 / [\delta_w \rho_w c_w F]_E$ , here  $\xi_1$  is the «flooding» stage existence time ratio to the total time of the heat transfer one cycle in the elementary cell.

The heat transfer «contact» mechanism was considered in the next «waiting» stage (the duration  $\tau_2$ ). The corresponding thermal resistance was determined as  $R_{2E} = const \xi_2 \sqrt{a' \tau_2} / [\lambda' (F_E + F_{TR})]$ , here  $\xi_2$  is the same value for this stage as  $\xi_1$  is for the previous stage «waiting».

The heat transfer in the heating zone was determined by the liquid microlayer evaporation in the «growth» stage:  $R_{3E} = \delta_0 \xi_3 / (\lambda' F_E)$ ;  $\xi_3$  corresponds  $\xi_1$ , but for the «waiting» stage.

The heat transfer intensity in the cooling during the «flooding» stage can be estimated as for stationary laminar flow in the long microchannels.  $Nu = Nu_{min} \approx 4.0$ ,  $\alpha_{..} = Nu_{min} \lambda' / d$ .

The cooling zone thermal resistance during the microlayer evaporation (the «growth» stage and «waiting» stage) was determined by contact mechanism. Corresponding it can be written:

$$R_{1C} = \frac{1}{\alpha_{..}} \cdot \frac{\xi_1}{F_C}; R_{2..} = \frac{K_{\tau} \sqrt{a'(\tau_2 + \tau_{\delta})}}{\lambda' F_{..}} (\xi_2 + \xi_3).$$

The parts  $\xi_i$  which determined every thermal resistance  $R_i$  input in the total thermal resistance  $R_0$ ; they were taken the corresponding stage duration times  $\tau_i$  ratio:  $\xi_1 : \xi_2 : \xi_3 = \bar{\tau}_0 : \tau_2 : \tau_{\delta}$ .

The total thermal resistance was defined the next way:

$$R_0 = \left[ \frac{1}{\alpha_{..} F_{..}} + \frac{\bar{\tau}_0}{\delta_w \rho_w c_w F_E} \right] \xi_1 + \frac{K_{\tau} \xi_2}{\lambda'} \left[ \frac{\sqrt{a' \tau_2}}{F_E + F_{TR}} + \frac{\sqrt{a'(\tau_2 + \tau_{\delta})}}{F_C} \left( 1 + \frac{\xi_3}{\xi_2} \right) \right] + \frac{\delta_0 \xi_3}{\lambda' F_E} \quad (20)$$

## THE PHP ACTION DYNAMIC APPROXIMATELY MODEL (IT WAS DEVELOPED BY DR VASILY BUZ)

Let's consider one PHP element, which scheme is submitted in the Fig. 8. Internal volume PHP contains three sites - two vapor volumes 1 and 2 on evaporator and pulsating liquid lock. The mathematical model contains the movement quantity conservation equation of a liquid lock eq. (21), till two equations of vapor mass conservation eq. (22), liquid mass conservation eq. (23), one equation of the evaporator wall heat balance eq. (24), and equations, which approximate dependence of working fluid properties from

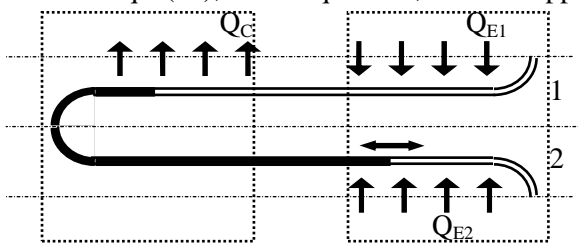


Fig. 8. The scheme of PHP element

temperature –  $p_s = f(t)$ ,  $\rho_s' = f(t)$ .

$$\rho' l' \frac{d^2 z}{d\tau^2} = p_1 - p_2 - \zeta \frac{l' \rho' \left( \frac{dz}{d\tau} \right)^2}{2d}, \quad (21)$$

$$\frac{dm''}{d\tau} = \frac{Q_E - \alpha \pi d l'' (t - t_0)}{r}, \quad (22)$$

$$\frac{dm'}{d\tau} = \frac{Q_E}{r}, \quad (23)$$

$$m_w c_w \frac{dt_w}{d\tau} = Q_{\Sigma} - Q_{E1} - Q_{E2}, \quad (24)$$

The condition of evaporator drying is formulated by next:  $\delta > 0$  then if  $Q_E = \frac{\lambda' \pi d l'_E (t_{WE} - t)}{\delta}$  else  $Q_E = 0$ .

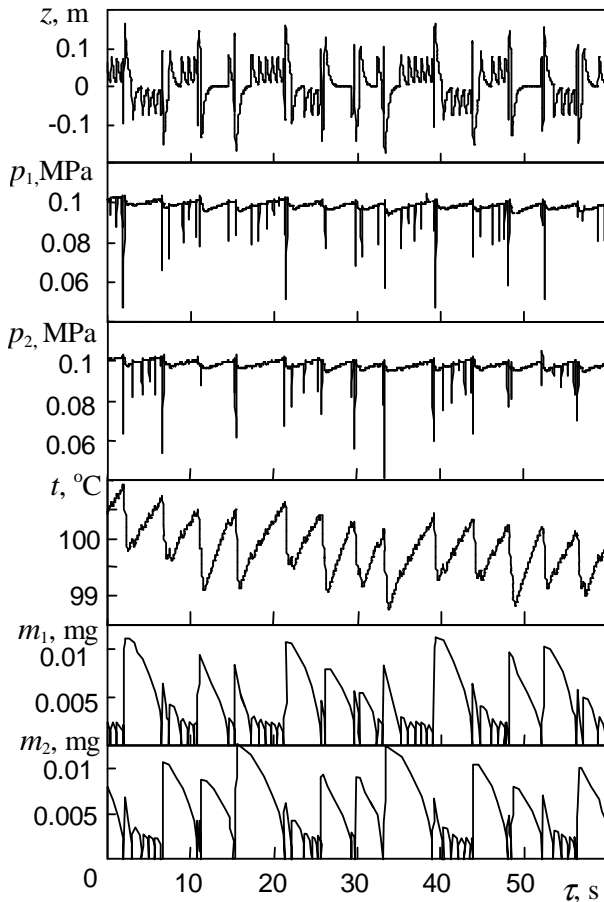


Fig. 9. Dependency from time the liquid lock coordinate  $z$ , vapor pressure  $p$ , evaporator wall temperature  $t$ , liquid microfilm mass  $m'$  in two PHP branches (1 and 2)

period of order 4 seconds. In some cases is observed the work cessation of device. At  $\delta_0 = 1.10 \cdot 10^{-5}$  m were received protracted steady pulsation with period of order 2 second.

### CALCULATION AND EXPERIMENTATION RESULTS COMPARISON.

The author experimental data (with heat carrier water) [9] and Japanese specialists experiments results (with refrigerant R142b as heat carrier) [1] were used for comparison with theoretical calculations. It was taken for the experimentation conditions [1] the next initial parameters: the branches number - 40; the channel diameter  $d = 1$  mm; the wall thickness  $\delta = 0.5$  mm; the heating, transport and cooling zones lengths every on 200 mm. The identical empirical coefficients  $K_q = 10^{-5}$ ;  $K_d = 0.01$  and  $K_r = 1$  were taken in the calculations.

The calculation algorithm was organized in such way, that the power input and the wall temperature in the cooling zones were taken as initial data, the thermophysical properties were determined by using the mean value between the cooling and heating zones average temperatures. The total PHP thermal resistance value was determined with the iteration method.

The theoretical calculations and experimental data comparison is given in Fig. 10 and Fig. 11. The experimental data agreement with calculations results can be considered satisfactory.

As to dynamic approximated model results comparison with experiments, it was discovered some qualitative agreement between theoretical and experimental temperature pulsations frequencies values.

It is accepted, that at achievement by a liquid lock of the evaporator  $z_E$  the internal surface evaporator becomes covered by a film of a liquid, thickness  $\delta_0$ , and the film surface area is proportional  $z_{\max} - z_E$

The calculation results for  $Q_{\Sigma} = 5$  W,  $d = 1$  mm,  $m_w c_w = 1$  J/K,  $l_{\Sigma} = 0,6$  m,  $l_E = 0,14$  m,  $l_C = 0,14$  m,  $t_0 = 30^\circ\text{C}$ , working fluid - water, are submitted on Fig. 9. Both schedules testify about sharp fall of pressure at liquid film dry up in one of the evaporators. The pressure at first drops in vapor volume of dry evaporator, and after it and in other evaporator. After it the sharp increase of pressure inside of device approximately to initial one is observed. In difference from pressure the sharp change of coordinate liquid lock happens only on dry up moment in one of evaporators. The return moving happens enough slowly to next dry up. The slow moving is connected that the liquid film exists in both evaporators, but area occupied by it and effective thickness  $\delta$  are different, that defines the unequal flow rate of evaporating liquid and slow moving of main liquid volume.

Among sizes, significance of which is necessary to be set as initial data, is presented  $\delta_0$  -the effective thickness of liquid film, remaining on evaporators wall after replacement of liquid. The significance of this size is not known and can change in enough wide limits. As show the calculations, significance  $\delta_0$  influence on the results even qualitatively. At  $\delta_0 = 2.10 \cdot 10^{-5}$  m (Fig. 9) are observed the poorly ordered pulsation with average

period of order 4 seconds. In some cases is observed the work cessation of device. At  $\delta_0 = 1.10 \cdot 10^{-5}$  m were received protracted steady pulsation with period of order 2 second.

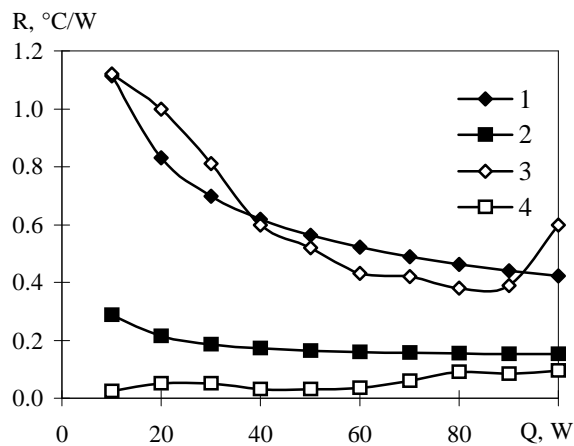


Fig. 10 Experimental data [1] and calculation results comparison. 1, 2 - Experimental data in the horizontal and bottom positions, liquid fill rate: 50%. 3, 4 - Calculation in the horizontal and bottom positions; heat carrier R142b, branches quantity - 40,  $d_{in}=1$  mm,  $\delta_w=0,5$  mm,  $t_{cool}=20^\circ\text{C}$ ,  $L_E=200$  mm,  $L_C=200$  mm,  $L_{tr}=200$  mm.

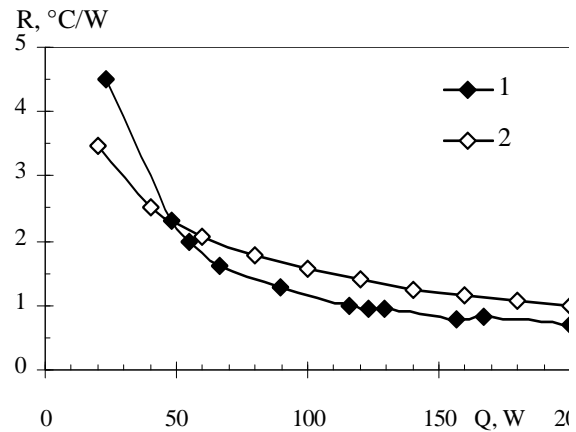


Fig. 11. The authors experimental data [9] and calculations result comparison. 1 - Experimental data. Horizontal position, filling ratio 50%. 2 - Calculation result: water as heat carrier, branches quantity - 8,  $d_{in}=1$  mm,  $\delta_w=0,3$  mm,  $t_{coll}=20^\circ\text{C}$ ,  $L_E=140$  mm,  $L_C=140$  mm,  $L_{tr}=150$  mm

## CONCLUSION

1. The PHP simplest type workability was confirmed experimentally as for horizontal both for vertical positions, including the position when evaporator is located above cooling zone in the gravity field. The thermal regimes with approximately constant mean parameters and accompanied the some heat power value, what is transferred with PHP help were characterized with large scale hydrodynamic and temperatures pulsation.

2. It was stated some thermal regimes in the experiments, when separate branches didn't work (didn't heat transfer. It was discovered for the branches with cold cooling zones). Together with it the stage heat transfer thermal regime saved in the neighboring branches. The facts testified about «individual heat transfer mechanism in PHP» determined meaning.

3. The heat and mass transfer «individual» mechanism model for PHP is based on the imagination that the moving force is formed as the «evaporation» stages completed times difference for two neighboring «i» and «i+1» branches, what is appearing occasionally. This difference is connected with the «drying» stage more earlier completion in one branch in comparison with neighboring other.

4. The approximated quasi-stationary thermo hydrodynamic model, which is worked out on these simplest physical imaginations base, allows the all known PHP work regularities to explain without contradictions. This model gives possibility to build the semi empirical theory for PHP thermal resistance calculations. The calculation results agree satisfactory with experimental data.

The physical imaginations and mathematical modeling development the next objects, determined PHP work and its practical applications, have to be:

- a) the PHP «common» action model;
- b) the PHP two-phase hydrodynamic process exists in the small diameter channels phase separation mechanism doesn't work;
- c) the «individual» and «common» mechanisms thermal and hydrodynamics stability and these mechanisms interaction problem;
- d) the crisis phenomena and PHP critical heat fluxes determination;
- e) the minimum heat fluxes (minimum temperature drops), when the PHP stable work mechanism is saved yet.

5. The dynamic PHP action model allows obtaining non-stationary PHP temperature characteristics.

6. It is necessary to consider the suggested physical imaginations, based on them thermo hydrodynamic model and calculation method, as PHP theory development only the first step, it isn't final theory version.

## NOMENCLATURE

- $C_p$  – specific heat capacity, J/(kg·K);  
 $d$  – diameter, m;  
 $G$  – heat carrier mass flow rate, kg/s;  
 $l$  – length, m;  
 $m$  – mass, kg;  
 $Q$  – heat flux, W;  
 $q$  – heat flux density, W/m<sup>2</sup>  
 $F$  – heat exchange surface area, m<sup>2</sup>;  
 $K$  – empirical dimensionless coefficient;  
 $P$  – pressure, Pa;  
 $R$  – specific thermal resistance, m<sup>2</sup>·K/W;  
 $r$  – latent heat, J/kg;  
 $t$  – temperature, °C;  
 $w$  – velocity, m/s;  
 $\Delta P$  – motor pressure, pressure losses, pressure difference, Pa;  
 $\alpha$  – heat transfer coefficient, W/(m<sup>2</sup>·K);  
 $\zeta$  – hydraulic resistance coefficient;  
 $\rho$  – density, kg/m<sup>3</sup>;  
 $\omega$  – cross section area, m<sup>2</sup>;  
 $\Delta\tau$  – time interval, sec;  
 $\delta$  – liquid film thickness; wall thickness, m;  
 $\lambda$  – heat conduction coefficient, W/(m·K);  
 $\xi$  – time portion of  $i^{\text{th}}$  heat exchange mechanism "action" in total duration of one cycle of pulsing;  
 $\tau$  – time, s

## Indexes

- $C$  – condensing section;  
 $d$  – diameter;  
 $E$  – evaporation section;  
 $tr$  – transport section;  
 $cool$  – cooling zone;  
 $i, i+1$  – branch number;  
 $S$  – saturation;  
 $W$  – heating wall parameter;  
 $0$  – initial state;  
 $'$  – liquid;  
 $''$  – vapor;

## Acknowledgments

The authors are very thankful for extremely great support from company "Thermacore", key person it vice – president Mr. Don Ernst and besides it for the same Dr. Konstantin Goncharov too for support and very high attention to this work experimentation and theoretical investigation state and development.

## References

1. Akachi H. Structure of a Heat Pipe. Patent USA No.4,921,041,1990
2. Akachi H. Structure of Micro-Heat Pipe. Patent USA No.5,219,020,1993.
3. Maezawa S., Arai K.Gi. and T. Experimental study on Capillary looped thermosyphon // *Journal of J.A.H..P.*, 1994. Vol. 3. No.1. Pp. 19–23.
4. Akachi H. Looped Mending Capillaries Heat Pipe // The 71st J.S.M.E Spring Annual Meeting, No-940-10,Mar.30th, 1994. Pp. 606–611.
5. Gorobetz V.S., Kapitanchuk I.I. Evaporating pulsation thermal control system working out and it's investigation for pump-less conditions. - Electronic system cooling problems. Ser. TRTO., iss.3, 1971, Pp. 61–65.(in Russ.)
6. Gorobetz V.S., Timofeev V.N. Liquid cooling small pump-less system. - Electronic system cooling problems. Ser. TRTO., iss.2, 1975, pp. 3-9.(in Russ.)
7. Smirnov H.F., Savchenkov G.A. Pulsating Heat Pipe.- USSR invention. certificate. №504065 class. F28D 15/00. With priority from 30.IV.1971year.(in Russ.)
8. Smirnov H.F., The closed heat transfer evaporative systems fundamentals theory // Thesis of doctor dissertation. Leningrad Food and Refrigeration Techn. Inst 1979year. (in Russ.)
9. Kuznyetsov I.O.,Smirnov H.F.,Garda A.N. Experimentation of Pulsating Heat Pipes with segregated channels characteristics investigations // Proceedings of Russian National Heat Transfer Conference 1998 year Vol. 4 pp. 364 – 368. (in Russ.)
10. Maezawa S., Gi K., Minamisawa A.and Akachi H. Thermal Performance of Capillary Tube Thermosyphon // Proceedings of 7th Int.Heat Pipe Conference. 1997. Stuttgart.
11. Yang H., Khandekar S., Groll M. Performance characteristics of pulsating heat pipes in integral thermal spreaders // *International Journal of Thermal Sciences*, 48 (2009) pp.815 – 824.
12. Yuwen Zhang, Amir Faghri. Advances and Unsolved Issues in Pulsating Heat Pipes // *Heat Transfer Engineering*. 2008. 29 (1). Pp. 20–44.
13. Kuznyetsov I.O.,Smirnov H.F.,Garda A.N. «Experimentation of Pulsating Heat Pipes with segregated channels characteristics investigations // Proceedings of Russian National Heat Transfer Conference 2002 year Vol. 4 pp. 37 – 50. (in Russ.)
14. Smirnov H.F., Kuznyetsov I.O., Buz V.N. and Borisov V.V. The approximated pulsating heat pipes theory and experimentation // Preprint of the 12th IHPC Tokyo. September. 1999.
15. Kuznyetsov I.O.,Smirnov H.F.,Garda A.N. "Experimentation of Pulsating Heat Pipes with segregated channels characteristics investigations, results and analysis", "Industrial Thermal Engineering", Kiev, 1999, N6. pp. 12 – 16.
16. Smirnov H. F., Kuznyetsov I.O., Borisov V.V. The approximated pulsating heat pipes theory and experimentation // Proc. of Int. Workshop. "Non – Compression Refrigeration and Cooling". Pp. 121–125. 1999.

## ON MULTISCALE AND MULTIPHYSICS TRANSPORT PHENOMENA IN FUEL CELLS

**Bengt Sundén, Jinliang Yuan**

Department of Energy Sciences, Lund University, Box 118, Lund 22100, Sweden

E-mail: [Bengt.sunden@energy.lth.se](mailto:Bengt.sunden@energy.lth.se), [Jinliang.yuan@energy.lth.se](mailto:Jinliang.yuan@energy.lth.se)

### Abstract

Various reacting transport phenomena appear at different scales in fuel cells. These are multi-component/-phase reactants and products flow in cells and manifolds, transfer of charges (ions and electrons), heat and mass in various functional components and sites. These physical processes are strongly affected by chemical/electrochemical reactions in nano-/micro-structured electrodes and electrolytes. For example, the electrochemical reactions generate or consume chemical species together with electric current production, and take place at the active sites (so-called three-phase boundaries, or TPBs) in all kinds of fuel cells. Potential water phase change in proton exchange membrane fuel cells (PEMFCs) and internal reforming reactions of hydrocarbon fuels in solid oxide fuel cells (SOFCs) are strongly coupled with the electrochemical reactions and other transport processes. To understand and analyse these phenomena at the unit-cell and component level, typically computational fluid dynamics (CFD)-based approaches are employed, while microscopic modeling methods, like molecular dynamics (MD) and Monte Carlo (MC), are required to analyse the various processes in catalyst layers and active surfaces, but methods like lumped parameter analysis and overall heat/mass balances are more suitable for stack and system studies. In this paper, different kinds of the analysis approaches are outlined and discussed for multi-physics reacting transport processes at various scales in fuel cells, together with typical results predicted by various models.

### KEYWORDS

Fuel cell, transport phenomena, catalytic reaction, modeling, water phase change, multi-phase flow.

### INTRODUCTION

High performance, low cost and high reliability have been considered as the major aspects and concerns for fuel cells to compete with other well-developed power generation devices, such as internal combustion engines. However, most research interests have focused on fuel cell new material development, processing and manufacturing techniques for specific systems, and various industries now focus on fuel cell design and optimization for better performance, improved durability, cost reduction and better cold-start characteristics, and system studies including hybrid or integrated fuel cell systems. In these cases more attention is placed on detailed analysis and modeling of transport processes and reactions in fuel cell functional materials, components and unit cells, even at micro- and nano-scale levels, due to the fact that the majority of the physical and chemical processes take place in such small regions that are inaccessible to experimental investigations. Furthermore, water-phase change/multi-phase flow and internal reforming reactions of hydrocarbon fuels are strongly coupled with the electrochemical reactions and other transport processes in the catalyst layers to make the physical phenomena extremely complicated. On the other hand, extensive research work is also needed for fuel cell stacks in order to achieve proper water/thermal management for an integrated power plant including various units.

Well-developed multi-scale models have been extremely important tools for many industrial applications. The microscopic approaches, e.g., Density Functional Theory (DFT) and Molecular Dynamics (MD), and the meso-scale ones, e.g., Monte Carlo (MC) and Lattice-Boltzmann methods (LBM), take into account the effects of the multi-functional materials microscopic structures on the charge-transfer (electrochemical) reactions at active sites, the surface chemistry and the gas-phase chemistry based on elementary reaction kinetics (individual chemical reaction steps between intermediates) in the porous electrodes. On the other hand, there are well-developed computational fluid dynamics (CFD) codes, which are widely applied to optimize design or investigate the structures of a flow at a macroscopic level. Similarly commercial codes are available for simulating integrated power systems including several units. It is possible to use such simulation tools to make improvements of the product design where physical design and testing are too expensive or not even possible. It is worthwhile to note that this work is limited to solid oxide fuel cell (SOFC) and proton exchange membrane fuel cell (PEMFC) systems, the most promising and well developed ones during the last decades.

## MULTI-PHYSICS TRANSPORT PROCESSES AND REACTIONS IN FUEL CELLS

Fuel cells can be examined from different points of view: as an electrochemical generator in a viewpoint of electrochemical reactions at continuum level, as a heat and mass exchanger in a perspective of fluid dynamics and transport phenomena, or as a chemical reactor in viewpoints of chemical reactions depending on fuel composition and heat effects associated with the electrochemical conversion [1]. The major processes relevant to the fuel cell characteristics consist of the gas-phase species (reactants and products) transport, electrochemical reactions, electronic and ionic transport, and heat transfer and temperature distribution. A unit-cell structure of fuel cells includes various components, such as fuel and oxidant ducts, electrolyte (polymer electrolyte membrane for PEMFCs), anode and cathode diffusion layers, catalyst layers in between them, as well as current inter-connectors/-connectors, as shown in Fig. 1.

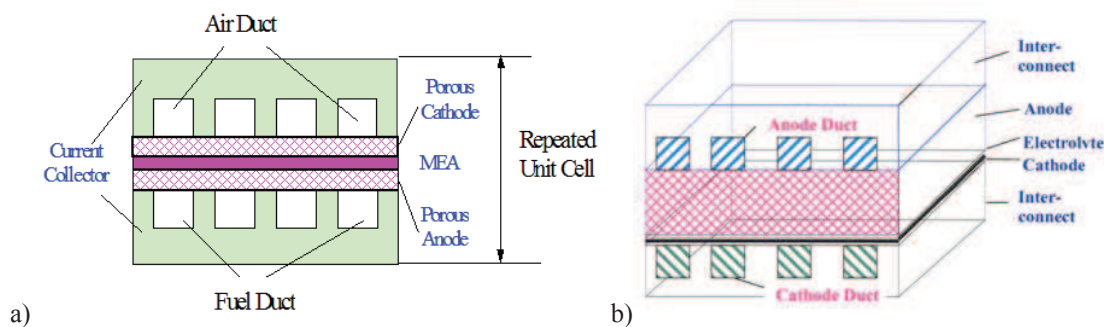


Figure 1. A schematic sketch of a unit cell for: a) PEMFC, and b) SOFC.

Unit cells are further organized together into stacks to supply the required electricity. In a fuel cell stack, the gas transport processes consist of the fuel and oxidant gas flows which are separated through the gas manifolds. The fuel and oxidant gases flow along cell ducts. In the porous layers (electrodes), transport of the reactant gases occur towards triple-phase boundary (TPB, where electrode, electrolyte and gas meet) close to the interface between the electrolyte and the electrodes, and the exhaust gases are rejected to the cell ducts through the open pores (voids). The exhaust gases from each individual cell are discharged through the gas output manifolds.

The electrolyte is a non-porous material, for instance,  $Y_2O_3$  stabilized  $ZrO_2$  (YSZ) in SOFCs. At an operating temperature (between 600-1000 °C for SOFCs and around 80 °C for PEMFCs), the electrolyte becomes non-conductive for electrons, but conductive to oxygen ions (in SOFCs) and hydrogen protons (in PEMFCs). The SOFC cathodes are mostly made from electronically conducting oxides or mixed electronically conducting and ion-conduction ceramics, while the anode material is normally nickel/yttria stabilized zirconia (Ni/YSZ) cermet. SOFCs can be designed with planar, tubular or monolithic structures. The planar design is normally more compact, compared to the tubular design, i.e., a higher specific volume power can be obtained. Tubular and planar SOFCs can be either electrolyte-, anode-, cathode- or metal-supported. An electrolyte-supported cell has thin anode and cathode ( $\sim 50 \mu\text{m}$ ), and the thickness of the electrolyte is more than  $100 \mu\text{m}$ . This design works preferably at temperatures around 1000 °C for SOFCs. In an electrode-supported SOFC either the anode (anode-supported) or the cathode (cathode-supported) is thick enough to serve as the supporting substrate for cell fabrication, normally between 0.3 and 1.5 mm. The electrolyte is in this configuration very thin, and the operating temperature can be reduced to an intermediate range.

For PEMFCs a polymer membrane is used in between anode and cathode. The membrane is made by substituting fluorine for hydrogen in long chain polymers and the process is called perfluorination. After this, a side chain is added, ending with sulfonic acid. The perfluorination of the polymer gives it the chemical resistance and mechanical strength while the addition of sulfonic acid gives it the property to carry the positive ions (hydrogen ions in this case). Therefore, the electrolyte in PEMFCs is sometimes also called proton exchange membranes. It is a fact that the performance of the membranes, in terms of proton conductivity, strongly depends on the water content.

Factors influencing the water content in the electrolyte are generally two transport processes, i.e., water drag through the electrolyte (a shell of  $H_2O$  is transported via the electrolyte for every proton transported), and back diffusion of generated water from the cathode into the anode through the electrolyte. The first one is often referred to as electro-osmotic transport in the literature, and the latter one is due to the gradient of water content [2-4]. On the other hand, water is generated by the electrochemical reactions at TPBs (between the phases of the carbon/Pt catalyst (for electrons), Nafion (for ions) and pores (for chemical species)) in the catalyst layers of 10-50  $\mu\text{m}$ , as revealed in Fig. 2a. As shown in Fig. 2b, the composite porous structure facilitates the simultaneous transport of electrons, protons, and reactants/products, as well as the oxygen reduction reaction (ORR) [5]. Oxygen in the pores must dissolve in the Nafion and then diffuse to the TPBs. It is understood that the diffusivity of oxygen through Nafion, around  $10^{-12} \text{ m}^2/\text{s}$ ,

is much smaller than ion conductivities, hence the chemical species transport may be considered as the rate-limiting factor for ORR [5].

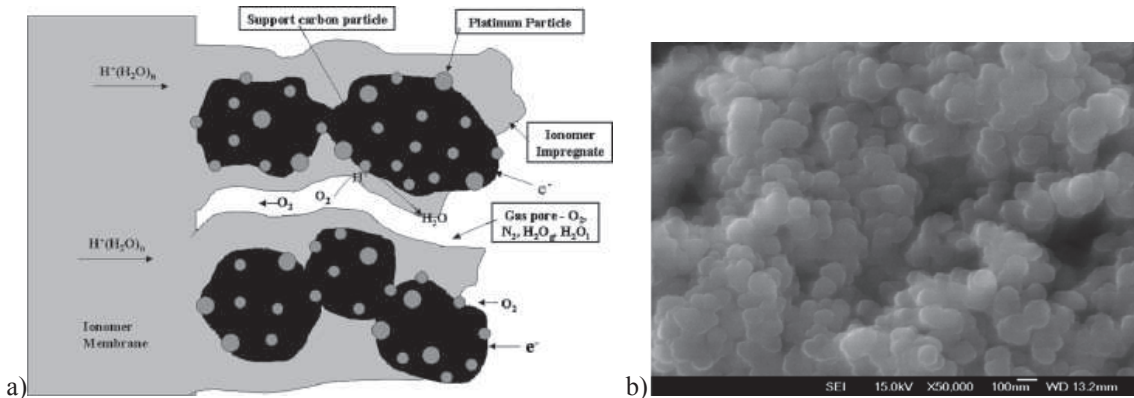
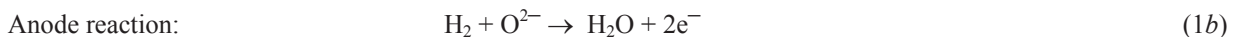
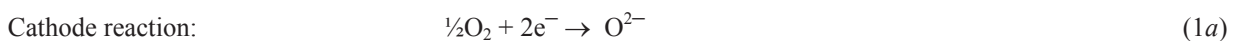


**Figure 2. a) A schematic description of composite processes in PEMFC microstructured pores and agglomerates [4], and b) SEM image of a typical catalyst layer [3].**

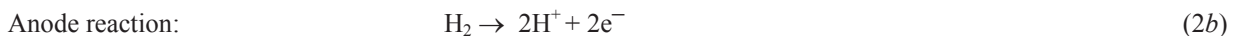
In the anode duct, the fuel (e.g.,  $H_2$ ) is supplied and air ( $O_2 + N_2$ ) is introduced in the cathode duct. The reactants are transported by diffusion and/or convection to the TPBs, where electrochemical reactions take place. Fuel cell ducts and manifolds should be designed/configured to have appropriate gas flow rates and flow uniformity to the reactive surface. An important requirement is the net pressure loss, which should be as low as possible to reduce parasitic power needed to operate pumps or compressors. Consequently, a laminar flow regime occurs in most of the fuel cells by employing a small velocity and cross-sections in the manifolds and ducts [6]. The appropriate mass flow rate of reactants (fuels and oxidants) is determined by the electrochemical reactions, proper thermal and water management, and internal fuel reforming reactions (in SOFCs), etc.

The electrochemical reactions take place close to the TPBs. However there is some controversy regarding the actual pathway and nature of the elementary steps. More discussion can be found in, e.g., [7]. It is believed that an electrochemical oxidation reaction at the anode produces electrons that flow through the intercollector (bipolar plate, for PEMFC) or -connector (for SOFC) to the external circuit, while the oxide ions (in SOFCs) or protons (in PEMFCs) pass through the electrolyte to the opposing electrode. The electrons return from the external circuit to participate in the electrochemical reaction at the cathode. In the electrochemical reaction, part of the oxygen is consumed in the cathode, while the hydrogen is consumed in the anode. Heat and water ( $H_2O$ ) are the only by-products during the process. The water generated is injected into the anode further along the duct in SOFCs, while in PEMFCs, it enters into the cathode duct.

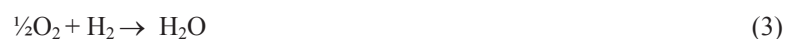
The electrochemical reactions in SOFCs can be written as:



and for PEMFCs:



The overall reaction is as follows:



The overall performance are usually expressed by:

$$I = i_0 \left[ \exp\left(\frac{\alpha_a F}{RT} \eta\right) - \exp\left(\frac{\alpha_c F}{RT} \eta\right) \right] \quad (4)$$

in which,  $i_0$  is the exchange current density, while  $\alpha_a$  and  $\alpha_c$  are the anodic and cathodic transfer coefficients, respectively. Equation (4), usually known as the Butler-Volmer equation and describing a large variety of electrode reactions, is further reduced to linear or Tafel expressions under certain conditions, e.g., facile and sluggish kinetics [8]. It should be mentioned that the exchange current density  $i_0$  for a reaction depends on the species composition and temperature at TPBs.

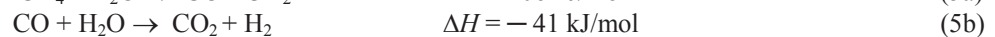
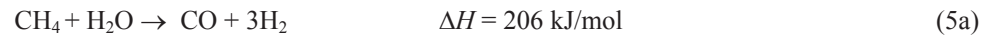
There are three potential drops in a fuel cell that cause the actual output potential to be lower than the ideal value of the electrochemical reaction. The **activation losses** are caused by the slowness of the reaction taking place on the catalyst surfaces of the electrodes. A part of the voltage generated is lost in driving the chemical reaction that transfers the electrons to or from the electrode. The **ohmic losses** are due to the straightforward resistance to the flow of electrons through the material of the electrodes and various inter-connections, as well as the resistance to the flow of ions through the electrolyte, while the **mass transport losses** result from the change in concentration of the reactants at TPBs as the fuel is used, i.e., because of a failure to transport sufficient reactants to the electrode active surfaces [9].

The impact of the electrochemical reactions on the gas mass balance is represented by the absorption of reactants and generation of products at the TPBs, in terms of mass flux rates  $J$  (kg/m<sup>2</sup>s). The mass flux rate is related to local current density  $I$  (A/m<sup>2</sup>), and more detailed discussion can be found in, e.g., [10]. Due to the flow resistance in the fuel cells, the pressure drop ( $\Delta P$ ) along the ducts and in the manifolds can cause non-uniform flow distribution. Furthermore, as an effect the output of electrical energy will differ in terms of voltage potential and in some cases even gas recirculation occurs. At some severe conditions, the lack of gas in some ducts can cause the irreversible damage to the fuel cell components. The pressure drop depends on the duct and manifold structures, flow streams, etc. [11].

The temperature is always non-uniform even when the mass flow rate is kept uniform in the ducts. This is caused by the heat transfer, phase change (in PEMFCs), and internal reforming reactions (in SOFCs), which in turn cause fluctuation in the available  $\Delta T$ . Heat transfer occurs between the cell components and the flowing air and fuel streams; between the fuel and air streams across the interconnect layer in terms of the overall heat transfer coefficient including convection and conduction; in solid structures in terms of heat conduction with different thermal conductivities in the electrolyte, electrodes and inter-conductors. It is a fact that the convective heat transfer coefficients for simple cases without the chemical reactions can be found in heat transfer textbooks, in terms of the Nusselt number  $Nu$ . As discussed later in this paper, the convective heat transfer coefficients are significantly affected by the fuel cell chemical reaction related mass transfer (consumption/generation), the boundary conditions on the duct walls and the porous electrode characteristics (configuration, material/transport properties, etc.). For the purpose to improve fuel cell modeling and analysis, it is essential to predict the local heat transfer coefficients for the anode/cathode ducts by considering the fuel cell design and configuration.

Water management in the electrolyte is one of the major issues in PEMFCs, due to the fact that during PEMFC operation anode gases can be dried out if the electro-osmosis transport rate is higher than that of back diffusion, which consequently causes the electrolyte membrane to become dehydrated and too resistive to conduct current. On the other hand, water is generated at the cathode active surface and transported to the cathode duct. Cathode flooding may occur when the water removal rate fails to reach its threshold transport/generation rate. Both dry-out and water flooding should be avoided, and various water management schemes have been proposed. It should also be noted that condensation can occur in the cathode when local vapor saturation condition occurs. This case mainly happens at high current densities and low operating temperatures in PEMFCs.

On the other hand, the high operating temperature SOFC can also reform hydrocarbon compounds into reactant fuels. For instance, methane can be converted to H<sub>2</sub> and CO in a steam reforming process within the anode of SOFCs. This reforming process takes place at the catalyst (Ni) surfaces and in a very thin layer of the anode porous cermet [12]. It is often referred to as internal reforming reactions in the literature, as written below:



Equation (5a) is usually referred to as the steam reforming reaction, while Eq. (5b) is the water-gas shift reaction. The overall reforming reaction is:



It should be mentioned that the above processes in Eq. (5) are net endothermic and the overall balance of the reaction requires external heat input. This heat can be supplied by the exothermic electrochemical reaction, as given in Eqs. (1) and (2). Due to the fast reforming reaction compared to the electrochemical reaction, the endothermic steam reforming process (Eq. (5a)) may lead to local sub-cooling, and/or mechanical failure due to induced thermal stresses [12].

More recently, with the rapid development of nano science and technology, the incorporation of nano-structured catalysts into the catalyst layers (CLs) has been proven highly successful in increasing the lengths of the active TPBs and catalyst activity, thus leading to significant improvements in performance and the utilization of precious-metal (Pt) catalysts in PEMFCs. As shown in Fig. 3a, Pt particles with sizes of around 2-4 nm are dispersed on high surface area carbon supports, as well as the impregnation with Nafion ionomer. In this way, the catalyst loading can be reduced significantly. However, it must be recognized that the reduction of the particle/pore sizes would significantly affect the chemical species and product water transport processes to and from the reaction sites (TPBs), even though the kinetic activity and utilization of the catalysts would be improved. Moreover, liquid water, due to water transport and generation by the reaction, blocks the porous pathways in the CL, hence causing hindered oxygen transport to the reaction sites (TPBs), then increasing surface overpotential (potential loss) [2-5]. This so-called water management has attracted tremendous research, for the objectives to improve the overall performance and the transport phenomena in different details.

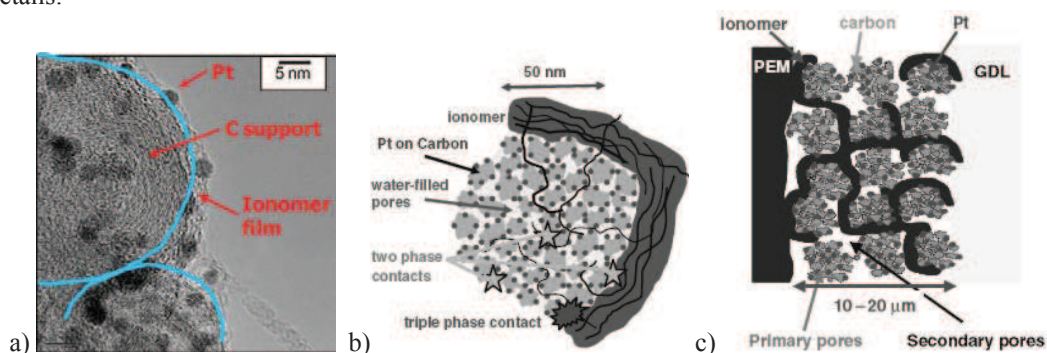


**Figure 3. a) High resolution transmission electron microscope (TEM) image of nano particles, and CL microscopic models for: b) an agglomerate and c) complete catalyst layer [5].**

Understanding how structure, composition and even operating conditions control the multi-phase transport and the effects of the reactions is the basic task of cell analysis. The modeling approach needs to capture the structure and composition to relate transport processes and reactions, which depends on how precisely and reproducibly the relevant structures can be fabricated and characterized by diagnostics [5]. As shown in Fig. 3b, carbon particles (10-20 nm) aggregate and form agglomerates, and there are primary pores (<10 nm) existing inside agglomerates, while the secondary pores with the sizes between 10-50 nm build the open spaces between agglomerates (Fig. 2c). It is believed that the competition between ionomer (for proton transfer) and void spaces (for chemical species and product water diffusion) mainly unfolds in the secondary pores [5, 13-14].

Fuel cell science and technology cut across multiple disciplines, including materials science, interfacial science, transport phenomena, electrochemistry and catalysis. It is often found that the endothermic and exothermic chemical reactions of the hydrocarbon fuels in SOFCs are strongly coupled by the electrochemical reactions on the active sites. There are various challenges in understanding and analysis of the multi-phase transport processes involving the catalytic chemical reactions and on their modeling at various scales.

## FUEL CELL MODELING AND APPROACHES OF ANALYSIS

Modeling at different levels has already played an important role in fuel cell development because it facilitates a better understanding of parameters affecting the physical processes and the performance of fuel cell components and stacks. Such models are advantageous because experimental studies are costly and time consuming. Furthermore, experimentation is limited to designs, which already exist, thus does not facilitate innovative design. It is often impossible to measure critical parameters, such as temperature, pressure, potential gradients, and gas- and surface-phase species concentration, due to the fuel cell reactive environment. However, there is no complete model for fuel cell stacks including all the phenomena together. Available models have generally been obtained for very restricted and idealized situations, and do not take into account other phenomena than the ones investigated.

In general, a model should be developed by considering the following features, such as testing, design and optimization. Given a predetermined configuration and operating conditions, the model should be able to provide a detailed description of the gas concentration, the charge transfer and the temperature distribution in the cells. This information should be useful for calculating the overall power density, the efficiency and fuel utilization. The approach should be possible to extend to different cell configuration/geometry (i.e., planar, tubular and monolithic vs. electrolyte- and electrode-supported cell) and manifold arrays (co-, counter- and cross-flow). A set of optimal operating conditions should be possible to determine based on different trade-offs, such as operating voltage vs. current density, fuel utilization vs. maximum cell temperature, etc.

The macroscopic fuel cell models developed during the last decades can be categorized as analytical, semi-empirical or mechanistic (often referred to as theoretical). Usually many simplifying assumptions are applied in an analytical approach concerning variable profiles within the cell, which is useful if quick calculations are required for fuel cell systems and does not give an accurate picture of transport processes occurring within the fuel cell components/cells. On the other hand, based on experimental data specific to the applications and operating conditions, semi-empirical fuel cell models combine theoretically derived differential or algebraic equations with empirically determined relationships/correlations, when the physical phenomena are difficult to model, or when the theory governing the phenomena is not well understood. Based on detailed electrochemical, fluid dynamics, species/charge transport and heat transfer relationships, a theoretical fuel cell modeling approach usually employs the basic equations (differential and algebraic ones), to be solved using some sort of computational methods for the tightly coupled electrochemical and transport processes. For proper water and thermal management, this approach includes not only the electrochemical reactions but also thermal- and fluid-dynamic equations. The output of the modeling can provide details of the processes, such as fuel cell species distribution/flow pattern, current density/temperature distribution, voltage and pressure drop, etc. The theoretical models can be further divided into multi- or single-domain ones, based on the regions being treated (unified vs. multi) and the equations being solved (separately vs. simultaneously) [15].

On the other hand, the microscopic approaches (e.g., DFT and MD) and the mesoscale ones (e.g., LBM) are more related to theoretical knowledge compared to the global models. The detailed chemistry and surface reaction models are able to take into account the effects of the multi-functional materials microscopic structures on the charge-transfer reactions taking place at active sites, the surface chemistry and the gas-phase chemistry based on elementary reaction kinetics (individual chemical reaction steps between intermediates). Such reaction schemes usually consist of more than 10 surface-phase species and around 40 irreversible reactions. Implementation of such large reaction mechanisms in fuel cell design or conduction of parameter studies using CFD approaches is a CPU demanding task. More discussion on the microscopic fuel cell modeling development and multi-scale integration technique can be found in recent review works, e.g., [1, 16].

It is clear that the theoretical modeling approach is flexible to applications and operating conditions, and may be appreciated when detailed studies are desired. However, development and implementation of this approach takes a longer time, and it is difficult to validate due to lack of detailed data in the open literature. Although the semi-empirical and analytical approaches are already validated to some extent, they do not provide sufficient details. It should also be noted that the semi-empirical models must be modified for each new application or operating conditions, and may not be suitable in all cases.

## TYPICAL SIMULATION RESULTS AND DISCUSSION

### Friction Factors and Heat Transfer Coefficients in Fuel Cell Ducts

For example, various CFD codes have been developed and applied for fuel cells particularly during the last few years, as outlined and discussed in recent review papers [1, 16]. The governing equations to be solved are conservation of mass, momentum, charge, thermal energy and reacting species. These transport equations are coupled with electrochemical processes and other ones (such as chemical reactions of hydrocarbon fuels in SOFCs and water phase change in PEMFCs) through source/sink terms to describe the relevant processes in fuel cells, as presented in [10]. In the unified approach, all the governing differential equations can be arranged into a standard form (convection-diffusion-source), which can be discretized using the principles of CFD or solved using a commercial CFD software package.

In fuel cells, the gaseous reactants flows in both the cathode and anode are subject to fluid injection and suction along the porous interface to the electrolyte. Of vital interest is the effect that the duct/porous layer geometry and material parameters have on cell performance. For example, dimensionless pressure differences and convective heat transfer coefficients, represented by friction factors and Nusselt numbers, respectively, are calculated to account for the electrochemical reactions related mass transfer effects in fuel cell ducts [17].

To characterize the overall pressure difference between the inlet and outlet, either a pressure coefficient  $C_p$  or an apparent friction factor  $f_{app}$  of the gas flow in a duct can be employed as

$$C_p = \frac{(P_{in} - P)}{(\rho U_{bulk}^2 / 2)} \quad (6a)$$

$$4f_{app} = \frac{D_h}{(\rho U_{bulk}^2 / 2)} \frac{dP}{dx} \quad (6b)$$

where  $U_{bulk}$  is the mean velocity of the main flow,  $D_h$  the hydraulic diameter defined in the conventional manner,  $dP/dx$  the pressure gradient along the main flow direction. The bulk velocity is calculated as:

$$U_{\text{bulk}} = \frac{\int U dA}{\int dA} \quad (7)$$

and the hydraulic diameter is defined as:

$$D_h = \frac{4A}{P^*} \quad (8)$$

$A$  is the cross-sectional area and  $P^*$  the wetted perimeter. The apparent friction factor  $f_{\text{app}}$  is employed to incorporate the combined effect of wall shear and the change in momentum flow rate due to the effects of mass generation and consumption by the electrochemical reactions. The Nusselt number  $Nu_w$  can be defined as:

$$Nu = \frac{hD_h}{k} = \frac{q_w D_h}{k(T_w - T_{\text{bulk}})} \quad (9)$$

where  $Nu$  is the spanwise variable Nusselt number of the heated wall at location  $x$ ,  $q_w$  the wall heat flux,  $T_w$  spanwise variable temperature of the heated wall.

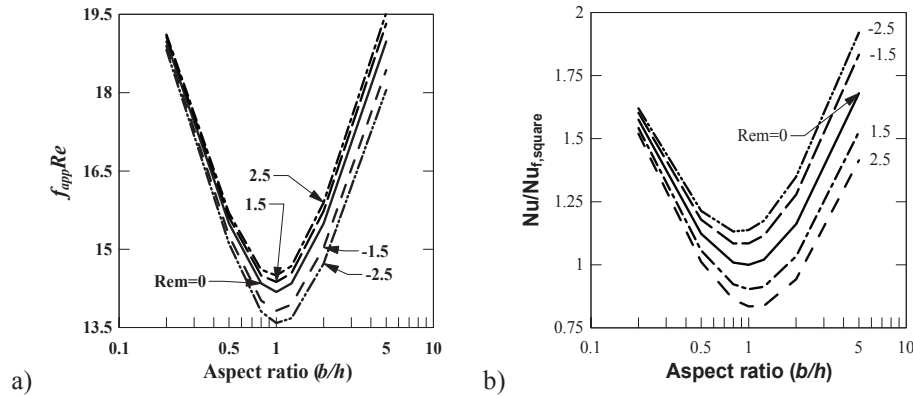


**Figure 4. Mass transfer ( $Re_m$ ) effects on the gas flow: a) the apparent friction factor; and b) Nusselt number in a rectangular fuel cell duct [10].**

### Mass Transfer in Fuel Cell Ducts

Mass transfer effects on the friction factor and Nusselt number are shown in Figure 4 for a rectangular duct in fuel cells. For the case of mass injection (mass generation by the electrochemical reactions) from the porous wall, additional mass is induced to the duct and thus the axial velocity increases. As clarified in [17], the  $f_{\text{app}} Re$  is related to the pressure gradient as well as changes in the momentum flux in the main flow direction. As can be seen from Fig. 4a,  $f_{\text{app}} Re$  always increases for mass injection ( $Re_m > 0$ ), while it decreases for mass suction (mass consumption,  $Re_m < 0$ ). On the other hand for heat transfer, the temperature of the fluid will increase due to the heat induced by mass injection, while a decrease appears for the case of mass suction. The  $Nu / Nu_f$  is thus reduced by mass injection, which can be seen in Figure 4b. A large aspect ratio of fuel cell ducts has a significant effect on both  $f_{\text{app}} Re$  and  $Nu / Nu_f$ , while a small aspect ratio gives less effect. Both  $f_{\text{app}} Re$  and  $Nu / Nu_f$  approach the values for the case without mass transfer ( $Re_m = 0$ ), if the aspect ratio becomes about 0.1. The figures show also that the  $f_{\text{app}} Re$  and  $Nu / Nu_f$  has a minimum when the aspect ratio is unity, i.e., a square duct [10].

The performance of the intermediate temperature anode-supported SOFC is also analyzed using the vertical component of the total hydrogen mass flux vector at the active site (bottom surface), which is proportional to the local current density produced. It is given by

$$(J_{H_2,y})_b = \left( \rho_{\text{eff}} Y_{H_2} V - \rho_{\text{eff}} D_{H_2,\text{eff}} \frac{\partial Y_{H_2}}{\partial y} \right)_b \quad (10)$$

The first part on the right hand side of Eq. (10) represents the mass convection, while the second part is the contribution by the mass diffusion. Figure 9 shows a comparison of the hydrogen mass fluxes by convection, diffusion and the total value. It can be seen that the convection mass flux has a large negative value (i.e., fuel gas species transport to the reaction sites) at the inlet region. Due to the decreasing pressure difference along the duct, this convection becomes weaker. On the other hand, water generation caused by the electrochemical reaction at the active sites, together with back permeation clarified in [17], contributes to species flowing back to the flow duct. This is confirmed by a small positive value of the convection flux. It is also clear that the hydrogen diffusion flux maintains an almost constant value. By comparing the absolute values of the mass convection and the mass diffusion fluxes, it is

found that the convection is stronger in the entrance region. However, the diffusion dominates the species transport further downstream. The position, where this change occurs, is about 1/6 of the length from the inlet for this specific case. Consequently the total flux from Eq. (10) is controlled by the convection in the entrance region, and dominated by the diffusion for the rest of the duct, see Figure 5.

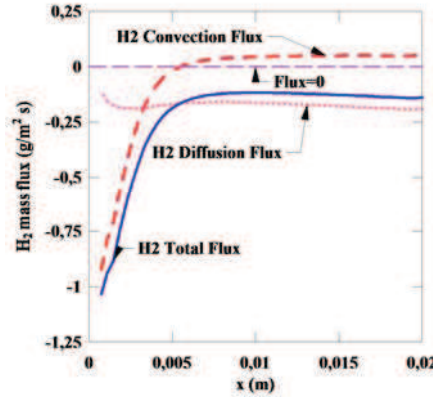


Figure 5. Various contributions to hydrogen flux at the bottom wall of ITSOFC anodes [17].

### Chemical Reaction Rates and Effects

Based on extensive reviews in [1, 10], it is found that the reforming reaction rate data presented in the literature varies greatly due to the use of different material structures and different amount of catalyst. In this work, the following global reaction rates were employed to express the kinetic rates of absorption or production of the fuel gas species, based on partial pressure, temperature and species compositions:

$$R_r = k_r^+ P_{\text{CH}_4} P_{\text{H}_2\text{O}} - k_r^- P_{\text{CO}} (P_{\text{H}_2})^3 \quad (11)$$

$$R_s = k_s^+ P_{\text{CO}} P_{\text{H}_2\text{O}} - k_s^- P_{\text{CO}_2} P_{\text{H}_2} \quad (12)$$

in which,  $k^+$  and  $k^-$  are velocity constants of the forward and backward reactions,  $P$  partial pressure. The corresponding source terms to be implemented in the mass governing equations read [1]:

$$\begin{aligned} S_{s,\text{H}_2} &= (3R_r + R_s)M_{\text{H}_2}; S_{s,\text{CH}_4} = -R_r M_{\text{CH}_4}; \\ S_{s,\text{H}_2\text{O}} &= (-R_r - R_s)M_{\text{H}_2\text{O}}; S_{s,\text{CO}} = (R_r - R_s)M_{\text{CO}} \end{aligned} \quad (13)$$

As for the kinetics of the methane reforming reactions on the cermet SOFC anodes, an extensive review can be found in [1]. It is common to employ the forward kinetic reforming reactions in the following form:

$$k^+ = k_0 F(P_i) \exp\left(-\frac{E_a}{\Re T}\right) \quad (14)$$

where  $\Re$  is the universal gas constant with unit  $J/(\text{mol K})$ ,  $F$  the function of the species partial pressure, while  $E_a$  stands for the activation energy and  $k_0$  is the pre-exponential constant. It is revealed that the first order kinetic expression is considered typical of direct internal reforming reaction in SOFC performance [1]. The following expressions employed in [17] may be adopted in this work:

$$k_r^+ = 2395 \exp(-231266 / \Re T) \quad (15)$$

$$k_s^+ = 0.0171 \exp(-103191 / RT) \quad (16)$$

The backward kinetics  $k_r^-$  and  $k_s^-$  can be determined based on the following equilibrium constants  $K_e$  for the two reactions,

$$K_{er} = \frac{k_r^+}{k_r^-}; K_{es} = \frac{k_s^+}{k_s^-} \quad (17)$$

which are functions of temperature given by the following empirical equations [10]:

$$K_{er} = 1.0267 \times 10^{10} \times \exp(-0.2513Z^4 + 0.3665Z^3 + 0.5810Z^2 - 27.134Z + 3.27770) \quad (18)$$

$$K_{es} = \exp(-0.2935Z^3 + 0.6351Z^2 + 4.1788Z + 0.3169) \quad (19)$$

$$Z = \frac{1000}{T} - 1 \quad (20)$$

Both the predicted steam reforming and the water-gas shift reaction rates are shown in Figs. 6a and b, respectively. It is found that both reactions are strong at the interface and the entrance regions within the porous layer close to the fuel flow duct (with a large reaction rate value). No reactions can be observed in the rest of the porous anode, particularly after a certain distance downstream the inlet. The distance for this specific case is about half the duct length.

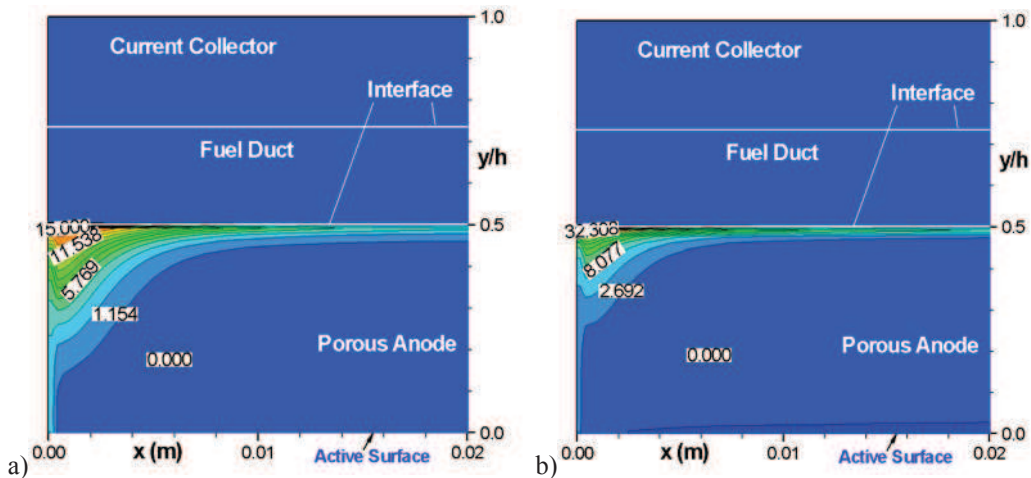


Figure 6. Distribution of: a) steam reforming reaction rate  $R_r$ ; and b) water-gas shift reaction rate  $R_s$  along main flow direction in an ITSOFC [17].

### Charge Transfer in SOFCs

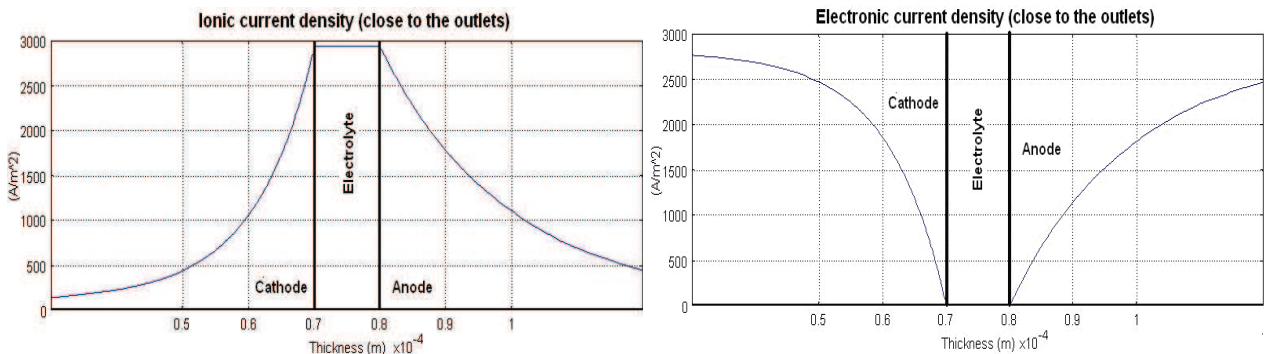


Figure 7. Cross-sectional distribution of: a) ionic and b) electronic current density ( $A/m^2$ ) close to electrolyte/electrode interfaces at the exit of the cell [18].

The distributions of ionic and electronic current densities in YSZ and Ni, respectively, are shown in Fig. 7. It can be seen that the current density gradients (the ionic one as well as the electronic one) are steeper on the cathode side, compared to the anode side, and around 60 % of the electrochemical reactions occur within 10  $\mu m$  from the electrolyte interface on the cathode side compared with around 60 % within 20  $\mu m$  on the anode side. As expected the current density distribution in the flow direction shows small changes (not shown here). The cross-section distribution of the potential difference is shown in Fig. 8 for the positions close to the inlet as well as to the outlet positions. It is a fact that the reversible open-circuit voltage decreases along the flow direction, mainly due to the temperature increase. It can be

concluded that around 60 % of the polarization losses occur in the anode, 10 % in the electrolyte and 30 % in the cathode, i.e., efforts to improve the fuel cell performance should be focused on decreasing the activation polarization on the anode side, or with other words to improve the volumetric current density on the anode side.

When water condensation occurs the transport process becomes two-phase, which besides flooding the PEMFC cathode porous layer can considerably complicate the modeling procedure as few experimental results are available. Instead, much attention has been paid on numerical investigations to reveal the relationships between the water saturation, proton conductivity (ohmic loss), the level of catalyst flooding (activation loss), and the effective diffusivity of the porous layer (concentration loss), see [16].

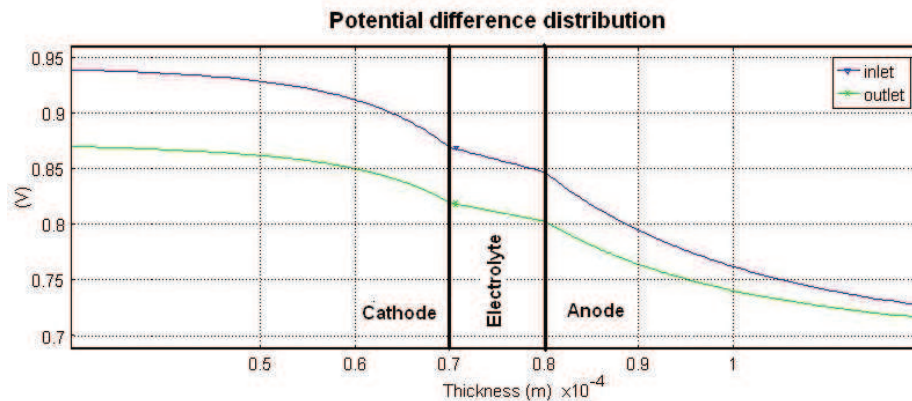


Figure 8. Distribution of potential difference (V) at inlet and outlet cross-sections [18].

#### Water-phase Change and Two-phase Flow in PEMFCs

Based on the methodologies to account for the liquid water motion and surface tension (capillary diffusion) effects, there are several types of models to treat liquid water formation/transport phenomena in PEMFCs, particularly in the porous electrodes. The **porosity correction model** simplifies the two-phase problem by neglecting the transport of liquid water. In this case, the local saturation level and temperature are calculated iteratively with the internal energy and density of the water. The volume fraction open to the gas phase is written [10]:

$$\varepsilon_g = \varepsilon(1 - s) \quad (21)$$

where  $\varepsilon$  is the porosity,  $s$  the saturation level. This approach is particularly efficient when saturation levels are low, and no additional transport equations are solved in this model. However, this model does not account for liquid water motion at all.

The second approach, namely the **moisture diffusion model**, treats the liquid water motion by surface tension, and the liquid water phase is considered as a scalar species with no convection terms when it is incorporated into a CFD code. This approach is rather simple because only an additional equation is required compared to the single-phase model. It should be mentioned that this approach cannot model inter-phase transfer of heat and species, and its application is limited to surface tension (the dominant force on the liquid), and/or the case of low capillary numbers (small pores and low permeability). The **mixture** model has been extensively developed to include the effects of liquid water convection during last few years. In the mixture approach, the gas and liquid water transport is considered to share the same velocity field, and the interfacial tension effect is completely ignored. The true **two-phase** (or **multi-fluid**) model is a more rigorous one in which the two phases have different velocities, and the interfacial tension effect is accounted for. Depending on the local properties, the phase change between the water vapor and liquid water can be either evaporation or condensation. Generally, this approach solves the highest number of variables, but it also needs a lot of computational resources.

It should be noted that, to complete the two-phase model, two methods are available to deal with the water phase change rate between the water vapor and liquid water. The first one is the kinetic theory, based on maximum amount of water vapor that can be accommodated at the vapor/liquid interface. The maximum rate of evaporation for liquid water can then be determined based on the approximation of the evaporation/condensation coefficient. While for the second method, the liquid water is assumed to exist in the form of a spherical droplet, and the mass transfer is determined from the diffusion rate between the bulk water vapor and the surface of the droplet by employing a mass transfer Nusselt number as a measure of the droplet's ability to exchange mass.

To properly model liquid water generation/transport/removal and analyze effects on PEMFC performance, several issues should be considered and implemented into the future modeling. One of these is the catalytic surface coverage by

the liquid water; while another one is liquid water transport through hydrophobic porous layer, because teflonation of the carbon fiber paper is essential for water removal in PEMFC cathode, and it significantly complicates the prediction of capillary pressure, as revealed in [16].

### Nano/Micro Structure Reconstruction by Large Scale Molecular Dynamics for PEMFC Catalyst Layer

As expected, the size and shape of catalyst particles, their distribution within the porous materials, and their interactions with the supporting materials are key aspects determining the catalyst activity in the catalyst layer of the fuel cells. Impressive development of electron microscopy and other high-resolution imaging techniques in the last years enabled the researchers to focus on the detailed modeling and reconstruction of catalytic layer morphology and its influence on the cell performance. A large group of the detailed models is based on digital, computer-aided reconstruction of porous medium that can provide realistic description of its morphology and consequent simulation of various reaction and physical processes inside the reconstructed system.

Digital reconstruction of porous structure may employ simplified approaches or methods to (in the best way) reflect the processes occurring during real catalyst and support materials preparation, for example, utilization of random packing of defined particles followed by partial sintering. The constructed porous medium may be represented by a discrete phase function in the form of 3D matrix containing the information about the phase in each volume discretization. The parameters of the reconstruction model (e.g., shapes and sizes of the particles and their agglomerates, level of sintering) are chosen on the basis of the information obtained from SEM and TEM images of the real catalysts. To this end, the pore size and distribution can then be evaluated and further used for model validation [14].

The molecular dynamics (MD) model was employed to predict the time evolution of a system involving interacting particles and provide insights into structural correlations and transport processes of the catalyst layers, particularly in TPBs. Furthermore, it provides the information about atomic positions, velocities and forces. In classical MD simulations, the system is treated as a set of  $N$  interacting particles. The atoms are presented by spherical nuclei that attract and repel each other. After assigning point charges to each particle, the forces acting on the particles are derived from a combination of bonding, non-bonding, and electrostatic potentials. The motions of the atoms are calculated using the laws of classical mechanics. The result of a MD simulation is a trajectory in term of positions and velocities of all  $N$  particles in the system. The thermodynamic properties, spatial and temporal correlation functions, and transport properties can be exactly calculated, when simulating with an appropriate time step and a sufficient time duration [14].

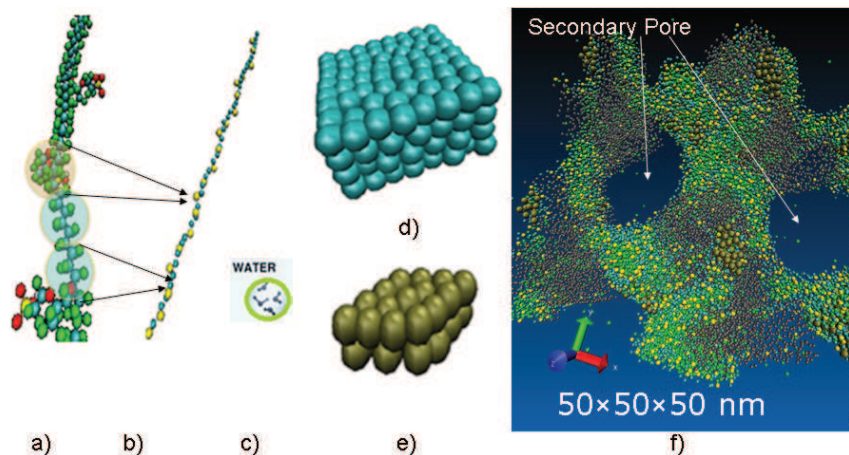


**Figure 9. a) Atomistic molecular structure of a Nafion copolymer by classical MD, b) its large-scale molecular structure (30 nm length) by coarse grinning (CG) method, which further applied for c) water; d) carbon slab; and e) fcc-Pt(111) cluster, and f) (primary and secondary) pores and solid phases shown in a final reconstruction by processing based large-scale MD method [14].**

Based on the MD simulation, the coarse-grinning (CG) method can be further applied to reconstruct the microscopic structures of the functional materials, as shown in Fig. 9. Density functional theory (DFT) has also become a choice for large systems, especially for solid-state surfaces, based on the Hohenberg-Kohn theorems. The electron density determines the ground-state wave function and all other electronic properties of the system. The correct density is the case that has the minimum energy. Because the electron density is a function of the positions, the DFT model could significantly reduce computational demand. Firstly, a fictitious reference system of non-interacting particles was

introduced to obtain the electron density. Its state can be calculated by solving a set of one-electron Schrödinger equations.

The microscopic modeling approaches at the secondary pores levels, having capabilities to bridge molecular dynamics and continuum theory, are able to describe the morphology of heterogeneous materials and rationalize their effective properties beyond length- and time-scale limitations of atomistic simulations. Monte Carlo (MC) methods, Dissipative Particle Dynamics (DPD) and Lattice Boltzmann method (LBM) are some examples from this category. For example, a polymer system is usually treated with a field description or microscopic particles that incorporate molecular details implicitly. Therefore, they are able to simulate the phenomena on the length and time scales currently inaccessible by the classical CFD methods [1, 14].

## CONCLUSIONS

Due to the complexity of fuel cells, fundamental understanding of multi-component transport phenomena at different scales and details is essential for the cell performance, particularly when two-phase flow/water management in PEMFCs and internal reforming reactions/thermal management in SOFCs are included. Due to the fact that in situ measurements are often difficult to get detailed experimental data such as local temperature fields or surface-phase species distribution, the development of very detailed models to predict global/local quantities such as current density, voltage, and temperature have been appeared. As discussed in the paper, the CFD approach is able to involve various interacting physicochemical submodels and can be applied for the fuel cell components, the unit cells, and stacks. On the other hand, the microscopic approaches (e.g., Molecular Dynamics (MD)) are more related to theoretical/fundamental knowledge compared to the global models. The detailed chemistry and surface reaction models are able to take into account the effects of local nano-/micro structures in the multi-functional materials on the charge-transfer reactions taking place at the active sites and the catalyst layers, the surface chemistry and the gas-phase chemistry based on elementary reaction kinetics.

## ACKNOWLEDGMENTS

The financial support from the Swedish Research Council (VR-621-2010-4581) and the European Research Council (ERC-226238-MMFCs) is gratefully acknowledged.

## References

1. Andersson M., Yuan, J., Sundén B. Review on Modeling Development for Multi-scale Chemical-reactions-coupled transport phenomena in SOFCs // *Applied Energy*. 2010. 87 (5). Pp.1461–1476.
2. Wang Y., Chen K. S., Mishler J., Cho S. C., Adroher, X. C. A Review of Polymer Electrolyte Membrane Fuel Cells: Technology, Applications, and Needs on Fundamental Research // *Applied Energy*. 2011. 88. Pp. 981–1007.
3. Mukherjee P. P., Kang Q., Wang C. Y. Pore-scale Modeling of Two-phase Transport in Polymer Electrolyte Fuel Cells—Progress and Perspective // *Energy & Environmental Science*. 2011. 4 (2). Pp. 346-369.
4. Yan Q., Wu J., Modeling of Single Catalyst Particle in Cathode of PEM Fuel Cells // *Energy Conversion and Management*. 2008. 49. Pp. 2425-2433.
5. Andreaus B., Eikerling, M. Catalyst Layer Operation in PEM Fuel Cells: From Structural Pictures to Tractable Models, book chapter in *Device and Materials Modeling in PEM Fuel Cells* / Eds. S.J. Paddison, K.S. Promislow, 2009, Springer Science.
6. Kee, R.J., Korada, P., Walters, K., Pavol, M. A Generalized Model of the Flow Distribution in Channel Networks of Planar Fuel Cells // *J. Power Sources*. 2002. 109. Pp. 148-159.
7. Vogler, M., Bieberle-Hütter, A., Gauckler, L, Warnatz, J. and Bessler, W.J. Modelling Study of Surface Reactions, Diffusion, and Spillover at a Ni/YSZ Patterned Anode // *J. Electrochem. Soc.* 2009. 156, Pp. B663-B672.
8. Wang, C.Y. Fundamental Models for Fuel Cell Engineering // *Chem. Rev.* 2004. 104. Pp. 4727-4766.
9. Larminie, J. and Dicks, A. *Fuel Cell Systems Expained*, 2<sup>nd</sup> Ed. 2003. John Will & Sons Ltd., England.
10. Sundén B., Yuan J. On Modeling of Heat and Mass Transfer and other Transport Phenomena in Fuel Cells // *Frontiers in Heat and Mass Transfer*. 2010. Pp. 1- 013008.
11. Wang J., Yuan J., Sundén B., Yan J. On Flow Maldistribution in PEMFC Stacks // *Int. J. Green Energy*. 2011 (in press).
12. Lehnert W., Meusinger J., Thom F. Modelling of Gas Transport Phenomena in SOFC Anodes // *J. Power Sources*. 2000. 87. Pp. 57–63.
13. Moore K. L., Reeves K. S. Microstructural Characterization of PEM Fuel Cell MEAs, // *Proceedings of DOE Hydrogen Program Annual Merit Review*, Arlington, VA, USA, May 23–26, 2005.
14. Xiao Y., Yuan J., Sundén B. Review on the Properties of Nano-/micro- Structures in the Catalyst Layer of

PEMFC // *ASME J. Fuel Cell Sci., Technol.* 2011. 8. Pp. 1-13.

15. Cheddle D., Munroe N. Review and Comparison of Approaches to Proton Exchange Membrane Fuel Cell Modeling // *J. Power Sources*. 2005, 147, Pp. 72-84.
16. Khan M., Sundén B., Yuan J. Analysis of Multi-phase Transport Phenomena with Catalyst Reactions in PEMFC- A Review // *J. Power Sources*. 2011 (in press).
17. Yuan, J., Sundén, B. Analysis of Intermediate Temperature Solid Oxide Fuel Cell Transport Processes and Performance // *ASME J. Heat Transfer*. 2005. 27. Pp. 1380-1390.
18. Andersson, M., Yuan, J., Sundén, B. SOFC Modeling Considering Electrochemical Reactions at the TPBs / in proceedings: *2011 Int. Conf. Power Energy Eng. (CPEE2011)*, Oct. 28-30, 2011, Shanghai.

## DEVELOPMENT OF A SILICON-BASED PASSIVE GAS-LIQUID SEPARATION SYSTEM FOR MICROSACLE DIRECT METHANOL FUEL CELLS

C.C. Hsieh<sup>1</sup>, Yousef Alyousef<sup>2</sup>, S.C. Yao<sup>1</sup>

<sup>1</sup>Department of Mechanical Engineering  
Carnegie Mellon University  
Pittsburgh, PA 15213, USA

<sup>2</sup>Energy Research Institute  
King Abdulaziz City for Science and Technology  
Riyadh, Saudi Arabia

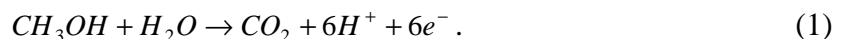
### Abstract

The design, fabrication, and performance characterization of a passive gas-liquid separation system is presented in this paper. The gas-liquid separation system is silicon-based and its fabrication is compatible with the existing CMU design of the microscale direct methanol fuel cell (DMFC). Both gas and liquid separators consist of staggered arrays of etched-through holes fabricated by deep reactive ion etching (DRIE). The gas separator is coated with a thin layer of hydrophobic polymer to substantiate the gas-liquid separation. To visually characterize the system performance, the gas-liquid separation system is made on a single wafer with a glass plate bonded on the top to form a separation chamber with a narrow gap in between. Benzocyclobutene (BCB) is applied for the low-temperature bonding. The maximum pressure for the liquid leakage of the gas separators is experimentally determined and compared with the values predicted theoretically. Several successful gas-liquid separations are observed at liquid pressures between 14.2 and 22.7 cm H<sub>2</sub>O, liquid flow rates between 0.705 and 1.786 cc/min, and CO<sub>2</sub> flow rates between 0.15160 to 0.20435 cc/min.

### INTRODUCTION

Microscale direct methanol fuel cell (DMFC) is a promising substitution of conventional batteries as the primary power source for low-power portable consumer electronics. Research on microscale DMFC has been extensively conducted in both industrial and academic institutes [1–5] in the past few years.

As a portable power source, the DMFC holds many advantages over other types of fuel cell systems. One of them is the direct electrochemical oxidation. In a DMFC, methanol reacts with water on the anode of the fuel stack. The reaction is



The electrons are drawn to the external circuit to generate electricity, and the protons migrate through the electrolyte and react with oxygen to produce water on the cathode. Carbon dioxide is evolved in the anode stream in the form of gas bubbles due to its limited solubility in the methanol/water solution. The CO<sub>2</sub> bubbles could be swept by the liquid flow as small, discrete bubbles (0.1 to 0.5 mm in diameter), which may either cling to the surface and grow into large bubbles until they are eventually absorbed by a larger slug in the free stream, or coalesce in the flow directly to form a slug [6]. The existence of CO<sub>2</sub> bubbles without escaping from the system could be destructive to the DMFC. Therefore, removing CO<sub>2</sub> bubbles from the flow stream is essential in maintaining the cell performance.

There are many well-established approaches, such as buoyancy-driven, centrifugal and chemical absorption, for effective gas-liquid separation in macroscale applications. Nevertheless, those concepts are difficult to be duplicated in microscale degassing applications. In developing a 20-kW proton exchange membrane fuel cell (PEMFC) for powering spacecrafts, Hoffman et al. [7] adopted a gas-liquid separator utilizing hydrophobic and hydrophilic membranes to remove the product water from the oxygen gas stream. The concepts of the modification of the surface's wettability for gas-liquid separation has been introduced to the development of a distributed gas breather for micro DMFC [8]. The gas breathing holes (50 μm in

diameter) on a hydrophilic liquid passage were coated with a hydrophobic layer of Teflon to capture the CO<sub>2</sub> bubbles. The liquid passage is 1.5 mm height and the bubbles are collected utilizing buoyancy. Although their results are successful, the gravity-dependent separation scheme makes their system difficult for portable applications, which may experience different system orientations.

In the proposed gas-liquid separation system the channel width is only 320 micron that bubbles are coalesced and squeezed to get in touch with the separation holes. The ejection of the gas mainly relies upon the pressure difference between the bulk liquid and the ambient. Hence, the proposed system is gravity-independent. The separation holes are designed to sustain a system pressure as high as 3.45 kPa (0.5 psi) without liquid leakage. In addition, the separation system is silicon-based so that it is compatible with the microscale DMFC currently under development at CMU [9].

## GAS-LIQUID SEPARATION SYSTEM

### Principle of Operation

The proposed gas-liquid separation system as shown in Figure 1 consists of two parallel silicon wafers with an array of etched-through holes. The gas separator is coated with a thin layer of hydrophobic (non-wetting) polymer to create an effective passage for gas bubble to discharge and to prevent the liquid from getting into these holes. On the other hand, the liquid separator is hydrophilic (wetting) to facilitate the liquid removal from the gas-liquid mixture. The two wafers are then bonded together to form a chamber with a narrow gap in between. The two-phase flow is directed to the narrow chamber and the gas-liquid separation takes place passively.

The gas-liquid separation mechanisms are also shown in Figure 1. The system is slightly pressurized ( $P_s$ ) and the outside of the gas separator is at the ambient pressure of  $P_0$ . Figure 1(a) shows that the surface of the gas separator is exposed to the liquid. Since the gas separator is hydrophobic, the liquid forms a meniscus at the inner mouth of the opening and cannot flow into the hole. The pressure difference across the phase boundary is balanced by the capillary pressure over the meniscus. This capillary pressure comes from the surface tension at the interface. Assuming a hemispherical liquid cap, one can easily relate the pressure difference to the surface tension by the well-known Young-Laplace equation. The pressure difference can then be expressed as

$$P_s - P_0 = \frac{2\gamma}{D/2 \cos(180^\circ - \theta)} = \frac{4\gamma \cos(180^\circ - \theta)}{D}. \quad (2)$$

On the other hand, since the separation chamber is narrow, the gas bubbles will be squeezed in a pancake-like shape as they enter the chamber. The mechanisms responsible for this gas escape are complicated with two possible processes. First, because the system is slightly pressurized, the edge of the gas bubbles will deform so that it conforms to the contour of the opening as shown in Figure 1 (b). Since the opening has a sharp edge, there exists a curvature variation along the gas-liquid interface, inducing a pressure gradient in the liquid adjacent to the interface. This local pressure gradient tends to draw the liquid from the neck (the narrowest region between the bubble and the opening) where the pressure is  $P_c$  to the bulk fluid where the pressure is  $P_s$ , and resulting the thinning of the liquid film until the interface touches the opening. The thin liquid film will eventually break up and thus, create a passage for gas discharge. Moreover, if some of the edge is not sharp, this asymmetry will cause a pressure variation inside the thin liquid film. This pressure imbalance will drive the flow from the sharper edge to the smoother edge and results in a faster thinning process of the liquid film.

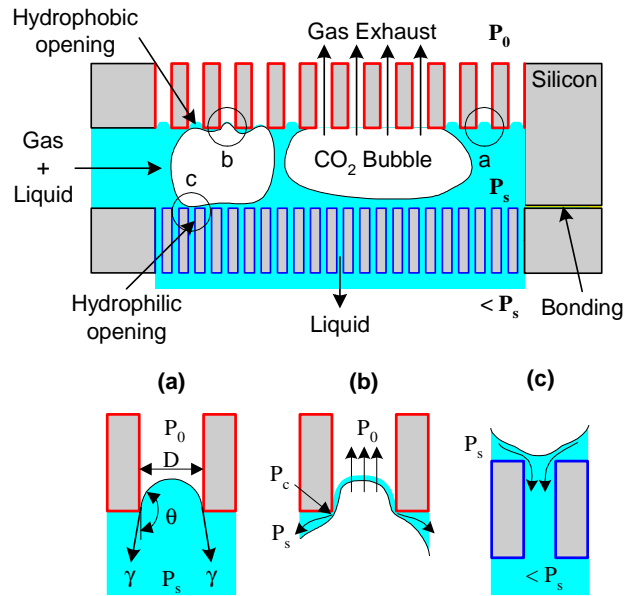


Fig. 1. Gas-liquid separation system with hydrophobic and hydrophilic polymer coating on gas separator and liquid separator

There could be another relevant mechanism. Since the pancake bubbles are pressurized due to its curvature at the rim, the thin liquid film between the pancake-like gas bubble and the chamber wall will be gradually expelled. Since the entire surface of the gas separator is hydrophobic, it is likely that eventually dry out spots would occur when the liquid film becomes very thin. A dry out spot once appears, it tends to expand and the liquid front is withdrawing. When the liquid front passes over an opening, it also draws the liquid from the liquid cap held at the mouth of the opening to the bulk liquid. Eventually, the holes are exposed and the gas passage is formed.

The liquid separation occurs at the hydrophilic surface of the chamber. As shown in Figure 1(c), the liquid can flow through the hole easily because no gas-liquid interface has to be created. On the other hand, for a gas bubble larger than the hole it requires a large pressure difference to deform the large bubble and squeeze through the hole. Hence, the gas bubble encounters a greater resistance in penetrating the liquid separator due to the surface tension.

### Design Considerations

It is essential to the gas separator that the pressure difference between the system and the ambient does not exceed the maximum capillary pressure the hydrophobic opening can stand for. Thus, Equation (2) can serve as a primary design guideline for the gas separator. Given an applied system pressure  $P_s$ , the maximum sustainable opening diameter ( $D_{max}$ ) without letting the liquid flow into the gas separation hole can be derived from Equation (2) as

$$D_{max} = \frac{4\gamma \cos(180^\circ - \theta)}{P_s - P_0}. \quad (3)$$

For example, using 1 M (1 mole solute in 1 L water) methanol solution ( $\gamma = 66.1$  mN/m) as the working fluid, the  $D_{max}$  for a gas separator coated with octafluorocyclobutane ( $C_4F_8$ ,  $\theta = 110^\circ$  [10]) is estimated to be  $26.1 \mu\text{m}$  at a system pressure of 3.45 kPa (0.5 psi) and  $25^\circ\text{C}$ .

Two gas separators denoted as gas separator I and II are considered in this study to characterize the gas-liquid separation performance. Figure 2 shows the design of the characterization system. Both separators consist of an array of circular etched-through openings and cover an area of 4 mm in width and 25 mm in length. The holes are arranged in a staggered array to effectively utilize the surface area. The diameter of the

opening in gas separator I and II are 20.0  $\mu\text{m}$  and 30.0  $\mu\text{m}$ , respectively. Both types have the same pitch (center-to-center distance) of 40  $\mu\text{m}$ . Thus, the porosity (opening-to-separator area ratio) of the gas separator I and II are calculated to be 22.7 % and 51.0 %. The geometric parameters are summarized in Table I in parenthesis.

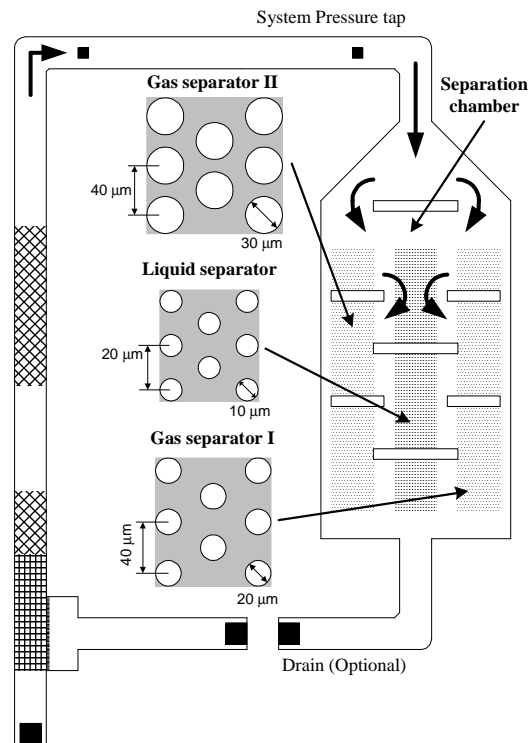


Fig. 2. Schematic of gas-liquid separation characterization system

Since the liquid separator is designed to have greater resistance for gas bubbles flowing through, the liquid separator has smaller openings (10  $\mu\text{m}$ ) than the gas separators. The liquid separator also has an effective area of 4 mm x 25 mm, and is made of a staggered array of square etched-through openings. The geometric parameters of the liquid separator are also listed in Table I in parenthesis.

In order to visually observe the gas-liquid separation, the gas and liquid separator are fabricated on a single wafer. The separation chamber with the gap of 250  $\mu\text{m}$  is sealed by bonding a glass wafer on the top of the separator plate. The incoming flow network is made of a 3 mm wide, 250  $\mu\text{m}$  deep microchannel. Openings are also made for the liquid and gas inlet, pressure measurement tap and system drain.

### Fabrication

The fabrication process of the gas-liquid separation system is depicted schematically in Figure 3. The process began with a 4-inch diameter, 540- $\mu\text{m}$ -thick, double-side-polished silicon wafer. The double-side alignment keys were marked on both sides of the wafer before the process. A two-step DRIE process was performed to pattern the gas-liquid separation system in an STS (Surface Technology Systems) ICP (Inductively Coupled Plasma) system. The first step of DRIE is to define all the openings including the gas and liquid separation holes, the bubble generation holes, the water inlet, the drains, and the pressure taps on the wafer as shown in Figure 3(a). Provided a known etch rate, the etched depth is simply time-controlled. A 260-min etch was performed to achieve about 220- $\mu\text{m}$ -deep liquid separation holes. As shown in Figure 3(b), the second DRIE process was applied to define the microchannel and the separation chamber on the backside of the patterned wafer. This etching process persisted until all the openings were exposed. The depth of the microchannel and the separation chamber was measured to be about 280  $\mu\text{m}$  and 320  $\mu\text{m}$ , respectively, under an optical microscope. The opening size of the gas separators and the liquid separator was also measured and documented in Table 1.

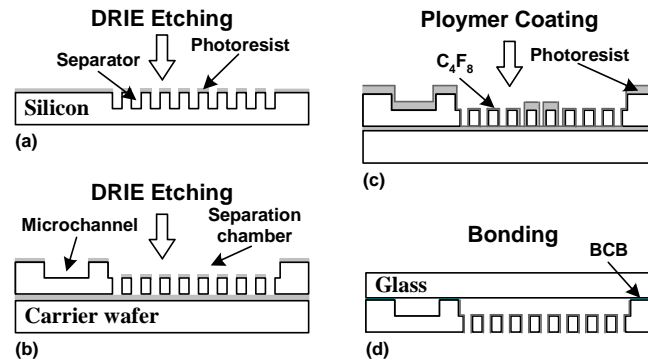


Fig. 3. Schematic of process flow to fabricate the gas-liquid separation characterization system

Table 1. Measured geometric parameters of the gas-liquid separation characterization system\*

Type	Opening Shape	Opening diameter ( $\mu\text{m}$ )	Opening pitch ( $\mu\text{m}$ )	Porosity (%)
Gas separator I	Circular	16.2·(20.0)	40.0	14.9·(22.7)
Gas separator II	Circular	32.0·(30.0)	40.0	58.0·51.0)
Liquid separator	Square	8.4·(10.0)**	20.0	20.4·(28.9)

\*All values in parenthesis are the design values

\*\*Length

A hydrophobic thin film was then deposited on the gas separators by placing the wafer in the same system for DRIE for 5 min., while suppressing the etch cycle, as shown in Figure 3(c). The deposited material is  $C_4F_8$ , which is similar to Teflon and has a contact angle of  $110^\circ$  with water [10]. The  $C_4F_8$  film has a very good resistance to methanol. Since the deposition rate is fixed at about  $0.1 \mu\text{m}/\text{min}$ , the thickness of the deposited thin film was estimated to be  $0.5 \mu\text{m}$ . The photograph of the open gas-liquid separation system is given in Figure 4. As shown in Figure 3(d), a piece of  $700\text{-}\mu\text{m}$ -thick Borofloat glass (similar to Pyrex glass) was bonded to the fabricated wafer to form a closed system using benzocyclobutene (BCB) as the adhesive. The cure of the BCB film is carried at a pressure of 2.4 bar and a temperature of  $185^\circ\text{C}$  to keep the deposited polymer film intact. The cured BCB film also has a very good resistance to methanol. Finally, the bonded wafer was put on a Plexiglass test bed, which provides the interconnections between the wafer and the external piping system, as shown in Figure 5.

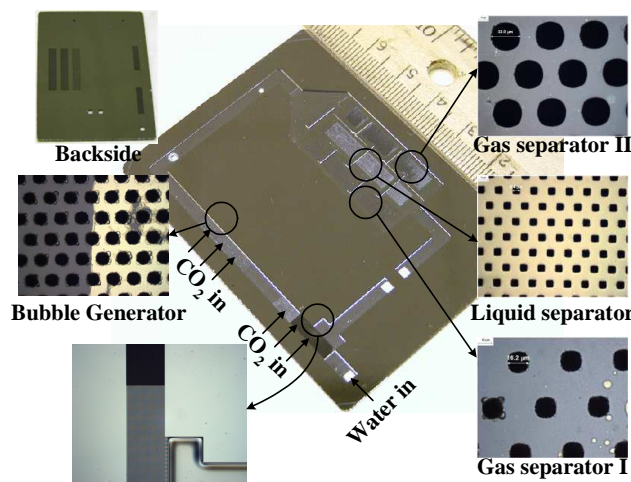


Fig. 4. Fabricated gas-liquid separation characterization system

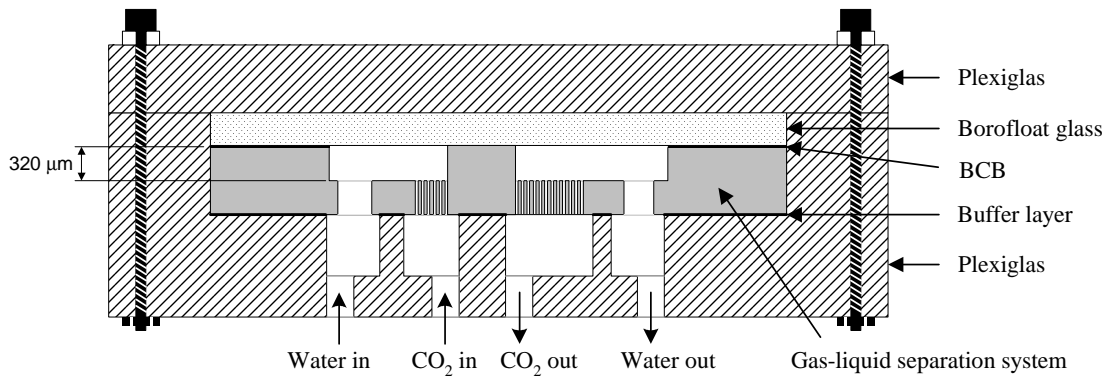


Fig. 5. Schematic of test bed

## EXPERIMENTAL SETUP AND PROCEDURES

The experiments were carried out using de-ionized (DI) water and CO<sub>2</sub> as the working fluids. The substitution of methanol solution with DI water is reasonably acceptable, because the surface tension of DI water is only 10% higher than that of 1M methanol solution, which is a rather common concentration in a regular DMFC.

Figure 6 shows the schematic of the experimental setup. The water flow was driven by a water reservoir mounted on a precision slide. The height of the water column, i.e. the applied pressure, can be fine tuned using the slide. The slide has a resolution of 5 μm. The water flow rate was measured using a micro rotameter (FL-110, Omega). In addition, a micro control valve was used to control the water flow rate. On the other hand, the gas flow was driven by a compressed CO<sub>2</sub> cylinder. The pressure and the flow rate of the supplied gas were controlled by a pressure regulator and a micro control valve. The flow rate was then measured in a micro rotameter (FL-320, Omega). A U-shape tube filled with water was connected to the pressure tap right before the inlet of the separation chamber to measure the system pressure.

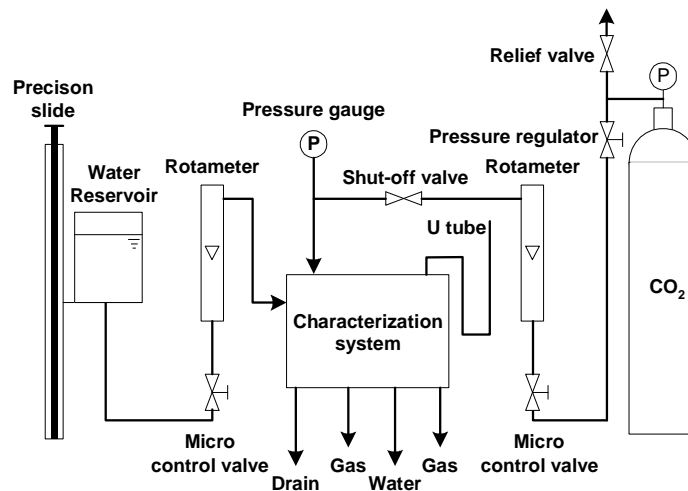


Fig. 6. Experimental setup

Between each run, the characterization system was heated to 45 °C and blown with N<sub>2</sub> for at least 2 h to dry up the gas separators. The water feeding line was then connected to the water inlet. The gas pressure was set to system pressure, and then the valve was opened to feed the CO<sub>2</sub> gas into the system. The system pressure, the water flow rate and the gas flow rate were independently adjusted to reach the working condition. A good working condition is achieved after the gas-liquid separation lasts at least 3–5 min.

## RESULTS AND DISCUSSION

It can be seen from Table I that the fabricated opening for all the components deviates from their design value. The deviation results from the non-ideal fabrication during the anisotropic etching. The reason that the fabricated opening of the gas separator II is bigger than the design value, but the gas separator I and the liquid separator are smaller than their designs, can be explained as follows. After the first DRIE process, the opening profile of each component was observed. As shown in Figure 7, while the gas separator II has a barrel-like profile, the gas separator I and the liquid separator have a positively tapered profile. Because the hole is opened up from the backside of the wafer, the measured opening size of the component having a positively tapered profile will be smaller than the design value. On the other hand, because the gas separator II has a higher etch rate, the resulting etched depth is higher than the gas separator I and the liquid separator. When the separation hole was opened up from the backside of the wafer, it was over-etched. Therefore, the fabricated opening of separator II is bigger than the design value.

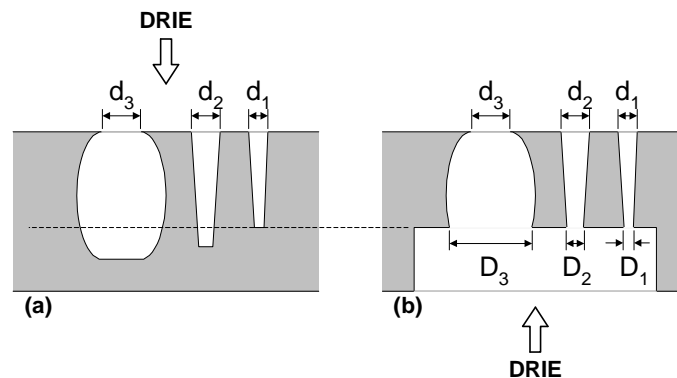


Fig. 7. Deviation in opening size due to the RIE lag effect and the non-ideal trench profile

The passive gas-liquid separation mainly relies on the hydrophobic coating on the gas separator. The coating coverage on the top surface of the gas separators can be examined under an optical microscope because the  $C_4F_8$  film shows a different color from the plain silicon surface. The bubble generator insert in Figure 4 clearly reveals this contrast. On the other hand, it is very difficult to directly evaluate the coating effectiveness on the surface inside of the holes. However, by carefully inspecting the surface of the carrier wafer, it was found that the area covered by the gas separators was also coated with a thin layer of  $C_4F_8$ . Because the polymer passivation is an isotropic process, it is believed that the surface inside the holes and even the bottom part of the surface of the gas separation holes was well-coated.

The maximum working pressure ( $P_{max}$ ) of the proposed gas-liquid separation system is set by Equation (2). The system should not be operated at a pressure higher than  $P_{max}$ . If the system pressure exceeds this limit, the surface tension is not able to hold the meniscus at the mouth of the opening, and liquid leakage through the gas separation holes occurs. Using DI water as the working fluid, the theoretical  $P_{max}$  for gas separator I ( $D = 16.2 \mu\text{m}$ ) and II ( $D = 32.0 \mu\text{m}$ ) are 62.0 cmH<sub>2</sub>O (6.08 kPa) and 31.4 cmH<sub>2</sub>O (3.07 kPa), respectively. The experimental  $P_{max}$  was obtained by feeding the water to the system and gradually raising the water reservoir height until the water flowed through the gas separator. The experimental  $P_{max}$  for gas separator I and II was measured to be 31.3 cmH<sub>2</sub>O and 27.2 cmH<sub>2</sub>O, respectively.

Although the experimental  $P_{max}$  of the gas separator II has a reasonable agreement with the theoretical prediction, the experimental  $P_{max}$  of the gas separator I is about 50 % lower than the theoretical prediction. Two possible reasons could attribute to the discrepancy: improper etching and imperfect coating. The improper etching results in a deviation in the opening curvature of the mouth of the hole from a sharp angle, while the imperfect coating alters the surface properties, such as contact angle and surface wettability. They are both tends to decrease the  $P_{max}$ . Exact reasons of this discrepancy are not well known at this moment.

Several successful gas-liquid separation tests were recorded with the liquid pressures ranged from 14.2 to 22.7 cmH<sub>2</sub>O. The results are shown in Figure 8. During the experiments, the CO<sub>2</sub> slug bubble entered the

separation chamber and escaped through the gas separator, while the water was drained from the liquid separator. No liquid was found in the gas outlet. The gas pressures were always set closely to the corresponding liquid pressures. The corresponding flow rate ranges are 0.705 to 1.786 cc/min for the water and 0.15160 to 0.20435 cc/min for the CO<sub>2</sub>, and the time-averaged void fractions are from 10.3% to 21.3%. The system pressure was measured at the pressure tap (as shown in Figure 2), which is close to the separation chamber, without the supply of CO<sub>2</sub> gas and right after the experiment was done. Since the CO<sub>2</sub> flow rates are much lower than the water flow rates, the introduction of CO<sub>2</sub> into the water stream does not significantly affect the system pressure.

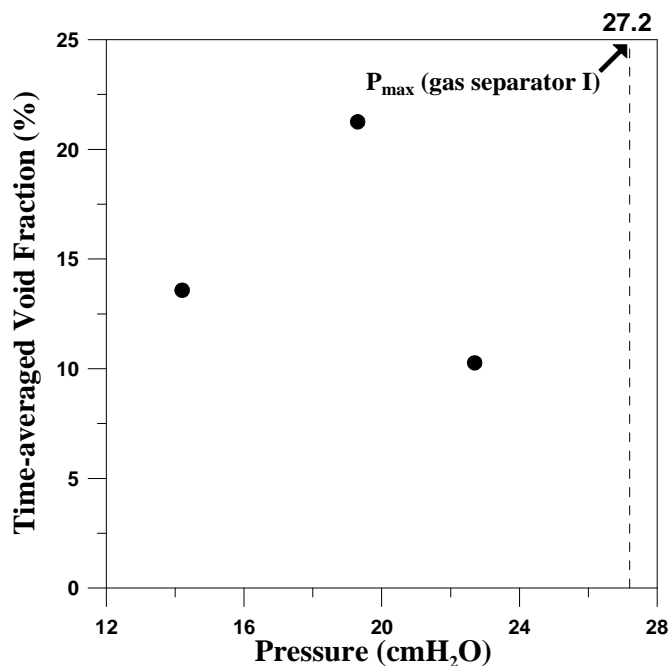


Fig. 8. Corresponding data points of successful gas-liquid separation

This microscale passive gas-liquid separation system has demonstrated its ability to effectively remove gas bubbles from a two-phase flow stream within a certain pressure range. This separation system performs well as long as the limiting pressure does not exceed.

## CONCLUSIONS

A passive microscale gas-liquid separation system, which is fabricated on a single silicon wafer with a glass cover bonded on the top for visual characterization, is presented in this paper. The liquid separator is simply made of an array of holes on a hydrophilic silicon wafer. The gas separator, which is also made of an array of holes, is coated with a thin hydrophobic layer of C<sub>4</sub>F<sub>8</sub> to remove the gas bubble from the two-phase mixture. The opening size could deviate from the design values slightly due to the non-ideal anisotropic etching. The maximum tolerable pressure of gas separator is compatible with the prediction for the separator of 32- $\mu$ m holes but not so consistent for that of 16- $\mu$ m holes due to the non-ideal fabrication of small holes. This passive gas-liquid separation system performs well over a range of experimental conditions.

## Nomenclature

$D$  – opening diameter, m;  $P$  – pressure, Pa;  $\gamma$  – surface tension, N/m;  $\theta$  – contact angle, degree.

### Subscripts

0 – ambient, max – maximum, s – system.

### Acknowledgments

The authors wish to express their sincere appreciation on the supports of DARPA Micro Power Generation program and the Pennsylvania Infrastructure Technology Alliance (PITA) through this study.

### REFERENCES

1. Nanayanan S. R., Clara F., Valdez T. I. Development of a miniature direct methanol fuel cell system for cellular phone applications // Presented at *199th Electrochemical Society Proceedings*, 2001.
2. Kelly S. C., Deluga G. A., Smyrl W. H. Miniature fuel cells fabricated on silicon substrate // *AIChE Journal*. 2002. Vol. 48. Pp. 1071–1082.
3. Bruijn F. A. d., Papageorgopoulos D. C., Sitters E. F., M. Janssen G. J. The Influence of carbon dioxide on pem fuel cell anodes // *Journal of Power Sources*. 2002. Vol. 110. Pp. 117–124.
4. Mench M. M., Wang Z. H., Bhatia K., Wang C. Y. Design of a micro direct methanol fuel cell ( $\mu$ DMFC) // Presented at *IMECE 2001*.
5. Thomas S. C., Ren X., Gottesfeld S., Zelenay P. Direct methanol fuel cells: progress in cell performance and cathode research // *Electrochimica Acta*. 2002. Vol. 47. Pp. 3741–3748.
6. Mench M. M., Boslet S., Thynell S., Scott J., Wang C. Y. Experimental study of a direct methanol fuel cell // Presented at the *Symposium on Direct Methanol Fuel Cell, Princeton, NJ*, 2001.
7. Hoffman W. C., Vasquez A., Lazaroff S. M., Downey M. G. Development of a space-rated proton exchange membrane fuel cell powerplant // *Proceedings of the ASME Advanced Energy Systems Division*, 1999.
8. Meng D.-S., Kim J., Kim C.-J. A distributed gas breather for micro direct methanol fuel cell ( $\mu$ -DMFC) // Presented at *IEEE The 16<sup>th</sup> International Conference on Micro Electro Mechanical Systems*, 2003.
9. Yao S. C., Fedder G. K., Amon C. H., Hsieh C. C., Tang X., Alyousef Y. Design of direct methanol micro fuel cell fluidic systems // Presented at *2002 ASME IMECE*, 2002.
10. Andersson H., Wijngaart W. v. d., Griss P., Niklaus F., Stemme G. Hydrophobic valves of plasma deposited octafluorocyclobutane in DRIE channels // *Sensors and Actuators B*. 2001. Vol. 75. Pp. 136–141.

## HEAT AND MASS TRANSFER IN CAPILLARY STRUCTURES. APPLICATION TO LOOP HEAT PIPES

M. Prat<sup>1,2</sup>

<sup>1</sup>Université de Toulouse; INPT, UPS; IMFT  
Avenue Camille Soula – F 31400, France

Tel: 0033 5 61 28 58 83 (fax: 0033 5 61 25 58 99), E-mail: prat@imft.fr

<sup>2</sup>CNRS; IMFT – F 31400

### Abstract

This paper presents an overview of results obtained using pore network models developed for the study of vaporization phenomena in the porous wick of loop heat pipes (LHP). These models are based on a representation of the pore-space in terms of a system of sites (pores) connected by throats (constrictions). First developed for studying steady-state regimes, pore network models are now used for the study of transient regimes in relation with the start-up phase of LHP and changes in the applied heat load during normal operation. Combined with experiments in model porous media, pore network models can help explaining for instance the premature percolation of the vapour through the wick due to the formation of vapour fingers. Also, it is shown that pore-network models can explain hysteretic effects associated with variations in the applied heat load. Some open problems are discussed.

### KEYWORDS

Loop heat pipes, capillary evaporators, porous wick, pore-network.

### INTRODUCTION

Fluid flow with phase change heat transfer in porous media occurs in many engineering applications such as in drying processes, e.g. [1], heat pipes [2, 3], enhanced boiling heat transfer [4], flows in geothermal systems [5] and severe nuclear reactor accident scenarios [6], to name only a few.

As other transport processes in porous media, the modelling of these situations is usually performed within the traditional framework of the continuum approach to porous media, e.g. [7]. Although useful as effective models, the weakness of such models is that they often lack an understanding of the phenomena at the pore or pore-network scale. Also, these models are implicitly based on the existence of a separation of scale between the pore size and the porous domain size, a condition that is not well satisfied in some systems, such as for example the porous coatings often used for heat transfer enhancement [4]. Also, under certain circumstances, the distribution of the fluids in the pore space resulting from the two-phase flow is fractal and therefore not compatible with a condition of length scale separation. The continuum approach is also unable to reproduce the transient flow pattern, in relatively small porous media, when small-scale instabilities induced by capillarity lead to the formation of elongated fingers of length comparable to or exceeding the length of the medium, e.g. [8]. Owing to the limitations of the traditional approaches, many recent works have used instead pore network models (PNM).

As sketched in Fig. 1, a pore network model is based on the representation of pore space in terms of a network of pores (or sites) connected by throats (or bonds). The "pores" roughly correspond to the larger voids whereas the throats connecting the pores correspond to the constrictions of the pore space. This approach to understanding flow and transport in porous media is distinct from other methods. No macroscopic constitutive relationship is assumed *a priori* and it can be used even in the absence of length scale separation. However, the relevant transport equations are not solved directly in the pore space and this permits considering systems containing a relatively large number of pores, a distinguishing advantage compared to the direct simulations based on lattice Boltzmann methods or Navier-Stokes equations.

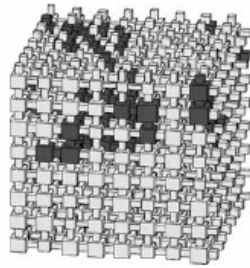


Fig. 1. Modelling of pore space by a regular cubic network of pores (sites) and throats (bonds)

Initially mostly developed in relation with oil recovery related problems, e.g. [9], pore scale models have been successfully applied to many other domains. To mention just two examples, they have been very helpful to significantly improve our understanding of drying phenomena, e.g. [1, 10] and references therein, and of water invasion in the porous layers of PEM fuel cells [11, 12].

Owing the interest of PNM, situations of heat transfer driven vaporisation in capillary structures were also studied [13–16]. The study presented in [13] focuses on the growth of a single vapour bubble in a porous medium. The works reported in [14–16] were developed in relation with the study of vaporization processes in the thin porous wick of loop heat pipe evaporators and focus on the study of the vaporization front inside the wick.

In complement to the review paper [16] we present here an overview of some additional results that are of interest for the study of heat and mass transfers with vaporization in the porous wick of loop heat pipes. In close relation with the development of pore network models, experiments with two-dimensional capillary networks are often very useful to gain insights into the studied situations and/or to validate the pore network models, e.g. [11]. This system can be machined using drilling machines or made using the techniques now well developed in relation with microfluidic studies, e.g. [17]. This will be illustrated in what follows.

The paper is organized as follows. After a recall of the typical computational domain considered in pore network studies on LHP evaporators and a brief summary of previous results, we first discuss a recent experimental study based on a model porous medium. Then we present the main results of a pore network study showing a temperature hysteretic effect resulting from variations in the applied heat load.

## EVAPORATOR UNIT CELL

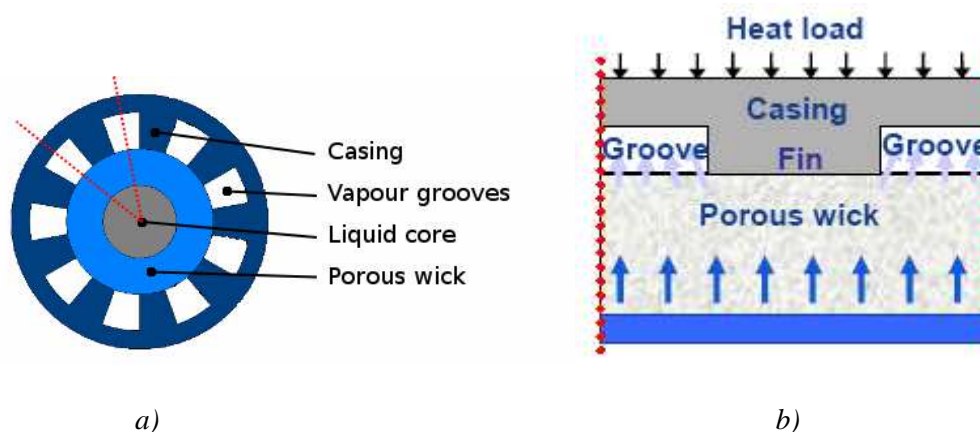


Fig. 2. a) Sketch of cylindrical evaporator cross section; b) Unit cell of capillary evaporator internal structure

Fig. 2a shows a sketch of the cross-section of a cylindrical evaporator. Although real systems are often more complicated and may include for example a secondary wick structure and a bayonet, e.g. [18], only the simpler situation depicted in Fig. 2a has been studied so far using PNM. Owing to the spatial periodicity of the evaporator structure, computations are restricted to a unit cell of the structure, such as the one shown in Figure 2b.

## OVERVIEW OF SOME PREVIOUS RESULTS

An overview of previous results obtained using pore network models and two-dimensional physical model porous media in relation with the study of CPLs and LHPs is presented in [16]. We very briefly summarize here the main results. The first studies, e.g. [14, 15, 19], focused on the development and the exploitation of pore network models under steady-state conditions. An important outcome was the prediction that a vapour pocket (see Fig.5a and the section on the hysteresis effect below) should exist under the fin when the imposed heat load is sufficiently high. As exemplified in [15], pore network models are well-adapted to explore the impact of the wick transport properties on evaporator performance. The detailed study presented in [19] suggests that a two-layer wick should improve performance. The layer in contact with the casing should be of relatively high thermal conductivity so as to limit the casing overheat whereas the layer in contact with the liquid artery should be of lower thermal conductivity (so as to limit the parasitic heat losses) and with smaller pores (so as to avoid the vapour breakthrough across the wick). Also, the simulations presented in [19] are in good agreement with experiments with a model porous medium made from a random distribution of metallic beads. As discussed in [16], it is possible also to use a pore-network model as an element in a nodal network of a LHP in order to improve the modeling of transfers in the evaporator.

The next step, [20], was to study transient phenomena (start-up, variation in the applied heat load). It was shown that the process of vapour pocket pressurization (when the vapour pocket grows right under the fin (Fig. 5a)) /depressurization (when the growing vapour pocket reaches the vapour grooves) can lead to quasi-periodic vapour growth (during the pressurization step) and liquid re-invasion under the fin (right after the vapour pocket depressurization). This type of phenomenon may explain in part the temperature oscillations that can occur during start-up or normal operation of a LHP.

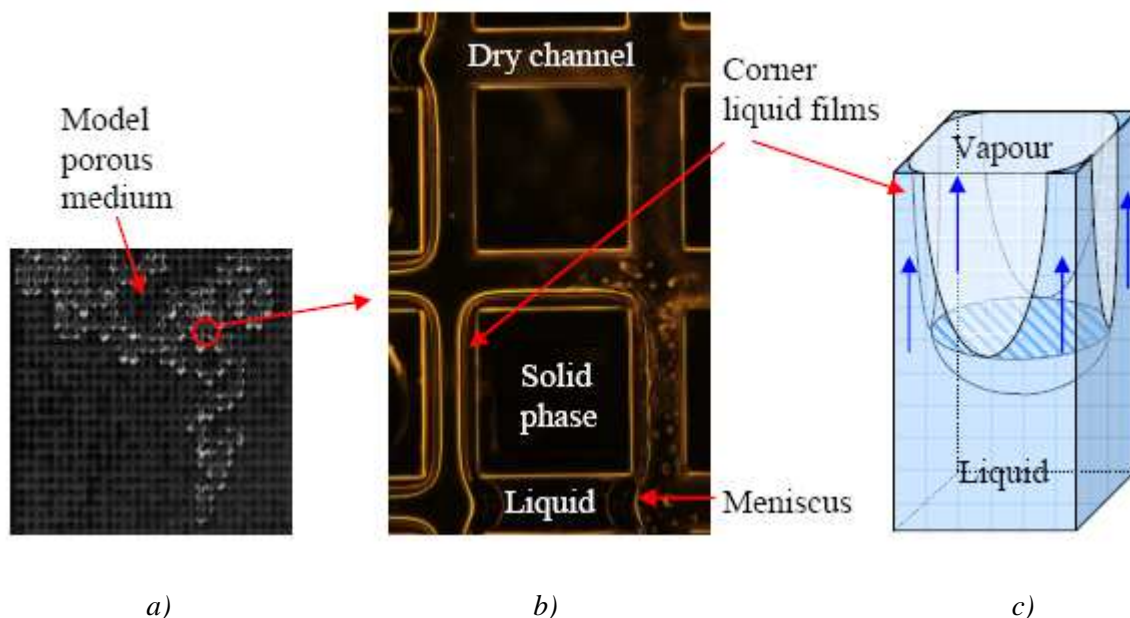


Fig. 3. a) Two dimensional model porous medium; b) Enlarged view of pore space and liquid films, c) Corner films in a channel of square cross section

As also briefly evoked in [16], the experiments presented in [20], reveal the existence of capillary liquid films in the corners of the pores invaded in the bulk by the vapour. This is illustrated in Fig. 3.

As pointed out in [16], liquid film effects have been neglected in all the pore network simulations performed so far in relation with LHPs or CPLs. The liquid films forming in the corners or others geometrical singularities of the pore space are referred to as capillary liquid films. They can be distinguished from the very thin films driven by the disjoining pressure that form on a flat surface. Contrary to capillary films, the thin films are not expected to extend over large regions of the system during a vaporization process. It is well known that capillary films played a major role in several cooling devices, such as heat pipes or thermal spreaders. It has been shown that capillary films play also a major role in the related field of mass transfer driven evaporation (drying) in porous media, e.g. [21, 22] and references therein. These studies show that the evaporation rate can be strongly underestimated when the liquid transport by the capillary films is neglected. Pore network models of drying taking into account the effect of capillary films have been developed and successfully compared to experimental results, [21]. A similar work has not yet been performed for the vaporization process driven by heat transfer corresponding to the situation expected in the porous wicks of LHP evaporators. Owing to the crucial importance of capillary liquid films in grooved heat pipes for example on the one hand and in the drying of porous media on the other hand, the effect of capillary films on the performance of capillary evaporators would deserve to be studied. It is expected that the models ignoring the films overestimate the casing overheat for example.

Two other results obtained in [20] are now briefly presented and discussed .

### HEAT PIPE EFFECT WITHIN A POROUS WICK

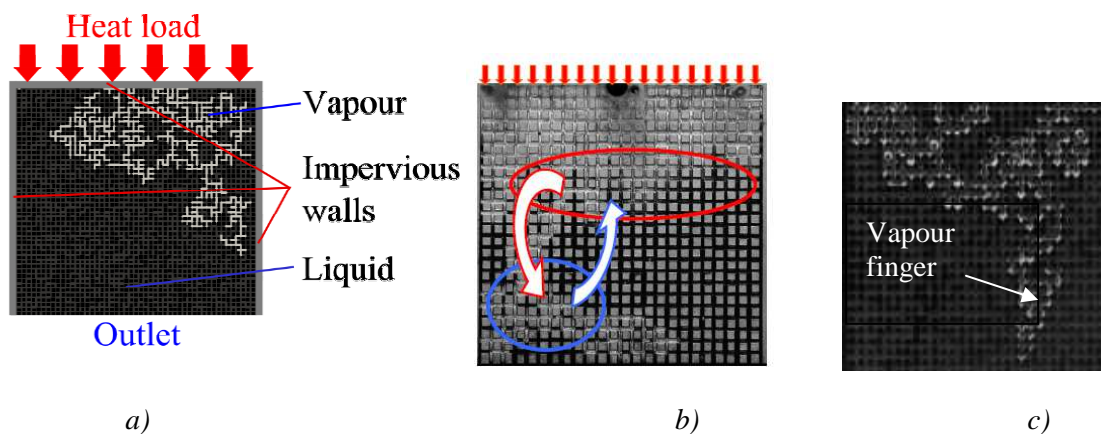


Fig. 4. a) Schematic representation of the situation studied, b) Detailed view of phase distribution at breakthrough in the experiment: as can be seen, there are no liquid in the upper part of network (liquid is in black). The arrows in Fig. 4b illustrate the evaporation-condensation effect discussed in the text (heat pipe effect). The red arrow represents the vapour flux whereas the blue arrow represents the transport in liquid phase between the condensation zone (blue ellipse) and the evaporation zone (red ellipse) (adapted from [23]); c) as discussed in the text, this situation can lead to the formation of vapour fingers leading to a premature percolation of vapour through the wick

In order to gain insights into the phenomena occurring in the porous wick for configurations close to the ones expected in the porous wick of a LHP evaporator, the simple experiment sketched in Fig. 4a was developed, [20],[23]. The system shown in Fig. 4 is supposed to be representative of what could happen right under the casing fin in Fig. 2 before the vapour pocket reaches the vapour grooves. In this experiment, the pore network is saturated with ethanol initially. The device is placed horizontally and is connected to a pressure transducer and thermocouples. Electric power is applied at a cartridge heater placed on the top side

of the network. This generates a heat load of 10W applied directly at the cartridge heater of 10 cm<sup>2</sup> external surface, which therefore leads to an imposed heat flux (red arrows in Fig. 4b) of 1 W/cm<sup>2</sup> along the top side of network. Images of the phase distribution are taken every 20 seconds so as to analyse the displacement of the liquid by the vapour generated as a result of the imposed heat load. More details can be found in [23]. Fig. 4b shows a detailed view of the phase distribution at breakthrough (i.e. when the vapour reaches the outlet).

First, it should be noticed that the vapour density of ethanol at the atmospheric pressure and close to the saturation temperature is about 1.5 kg/m<sup>3</sup> whereas the liquid ethanol density is about 650 kg/m<sup>3</sup>. Thus, to form a given volume  $V$  of vapour, only a liquid volume  $V_l = V \times 1.5/650$ , hence about 400 times smaller, needs to be vaporized. This indicates that the volume of liquid needed for producing the volume of vapour observed in the network at breakthrough is on the order of a few throat volumes only. The conclusion is that the volume of liquid displaced and leaving the porous medium through the outlet is about 400 times greater than the volume vaporized during the vapour cluster growth. Thus this growth process is characterized by a significant liquid flow. The main direction of the liquid flow is obviously away from the heated side. This is in contrast with the steady-state solutions studied in [14] where the flow is directed toward the liquid-vapour interface, that is toward the heated side. As discussed in more details in [23], the situation illustrated in Fig. 4, that is when the liquid flow is directed toward the outlet, can be analyzed as an invasion process in a destabilizing gradient, see for instance [24] for more details. The interesting practical result is that this situation can lead to the formation of thin vapour fingers (as illustrated in Fig. 4c) leading to a premature percolation of the vapour through the wick. This phenomenon can contribute to the start-up problems often encountered in the operation of LHPs. This phenomenon can be simulated using pore-network model, e.g. [23], but not with the traditional continuum models.

Another interesting observation is that the top region of the network in Fig. 4b is completely dry at breakthrough. As discussed in some detail in [23], this is somewhat intriguing and needs an explanation. The remarkable phenomenon is that the liquid disappears in the upper region even before vapour breakthrough. Since the mass of liquid needed to produce the volume of vapour occupying the network at breakthrough is quite small (on the order of one pore/throat volume), it can be concluded that the liquid disappearance do not lead to a significant net production of vapour. As sketched in Fig. 4b, the explanation is as follows. Vapour forms in the hot upper region of the system as a result of liquid vaporization and vapour condenses in colder region. Thus the present study indicates an evaporation – condensation effect (a heat pipe effect) within the capillary structure during the vapour bubble growth. This also indicates the existence of vapour pressure gradients in the vapour cluster since the vapour is transported from the hotter region to the colder regions. This suggests that it could be important to consider evaporation – condensation effects in the analysis of transfers in porous wicks. Note however, as discussed in [23], that this effect becomes negligible when the temperature difference across the wick is small, which should be the case in a LHP porous wick operating under stationary conditions. Hence this effect is likely to be more significant at start –up for example.

## HYSTERESIS EFFECT

In this section, we consider the domain sketched in Fig. 2b and we are interested in steady-state solutions for different applied heat loads, especially when a vapour pocket is present in the wick (Fig. 5a). As depicted in Fig. 5b, a succession of heat fluxes is considered. The heat flux is first increased in constant steps of 1000 W/m<sup>2</sup> up to a maximum value denoted by  $\Phi_{\max}$ . This first phase is referred to as the increasing ramp. Then, in a second step, the heat flux is decreased in constant steps of again 1000 W/m<sup>2</sup>, starting from  $\Phi_{\max}$ . This second phase is referred to as the decreasing ramp.

Examples of the vapour pocket in the porous wick computed thanks to pore network simulations, [20], are presented in Fig. 6a. As can be seen, the interface between the vapour region and the liquid region is different depending on whether the considered heat flux is reached through a succession of increasing heat fluxes (increasing ramp) or a succession of decreasing fluxes (decreasing ramp). For the same applied heat flux, the interface is more ramified and the vapour pocket smaller when obtained in the increasing ramp whereas the vapour pocket is larger and the interface smoother when the solution is obtained in the

decreasing ramp. This can be explained as follows.

In this problem, vapour is a non-wetting fluid and the liquid is a wetting fluid. In the increasing ramp, the size of the vapour pocket grows when the heat flux is increased. The growth of the vapour pocket induces the displacement of the liquid. The immiscible displacement of a wetting fluid (the liquid here) by a non-wetting one (the vapour) is referred to as a drainage process in the porous medium literature, e.g. [25]. In the decreasing ramp, the liquid re-invades regions previously occupied by the vapour when a lower heat flux is applied. In this case, the invasion process is similar to the displacement of a non-wetting fluid by a wetting fluid, a process referred to as an imbibition process in the porous medium literature, e.g. [25]. It is well known in the context of continuum models, e.g. [25], that the capillary pressure curve is different in imbibition (increasing wetting fluid saturation) and in drainage (decreasing wetting fluid saturation). A somewhat similar phenomenon is observed here.

The advantage of the pore network approach is that it can be relatively easily explained and computed. The fundamental difference between imbibition and drainage in a pore network lies in the local rules controlling the invasion. This is explained in some details in [10], [26]. In drainage, the invasion is controlled essentially by the constrictions of the pore space and the pores (seen as the large voids between constrictions) do not influence the invasion. By contrast, the pores play an important role in imbibition. In particular, the invasion criterion of a pore depends on the number of adjacent constrictions already occupied by the wetting fluid. The greater the number of adjacent constrictions occupied by the wetting fluid, the easier the invasion of the pore by the wetting fluid. The fact that the invasion of a pore depends on the fluid occupancy of neighbour constrictions and not only on the pore geometrical properties (as in drainage) is referred to as a cooperative phenomenon. These cooperative phenomena between adjacent menisci are responsible for the smoothing of the interface obtained in imbibition (decreasing ramp) compared to the ramified interface obtained in drainage (increasing ramp in Fig. 6a).

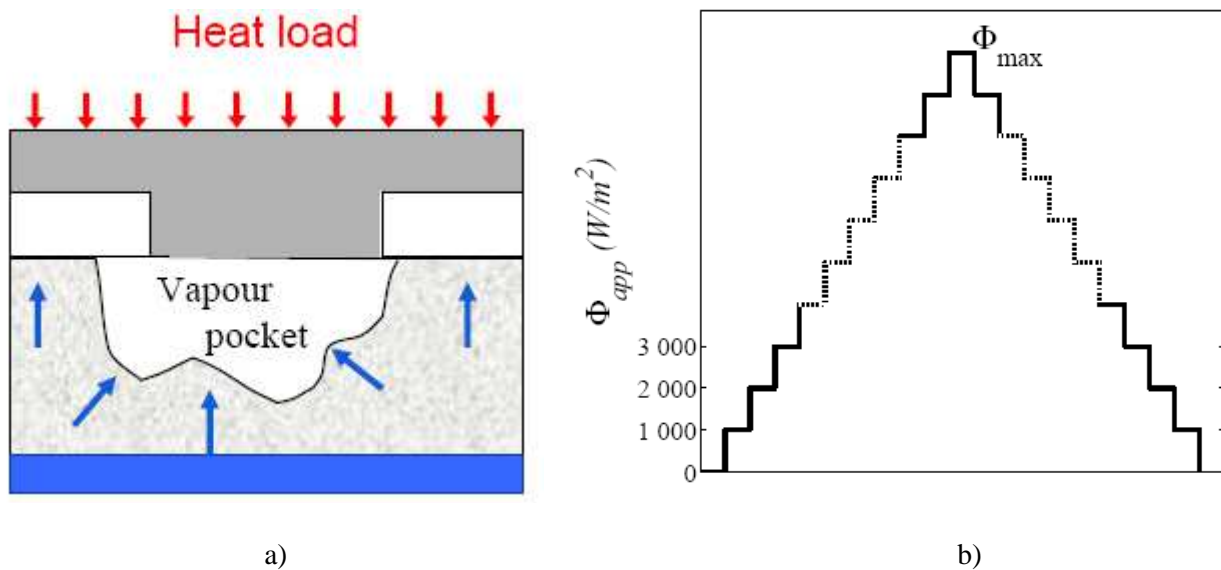
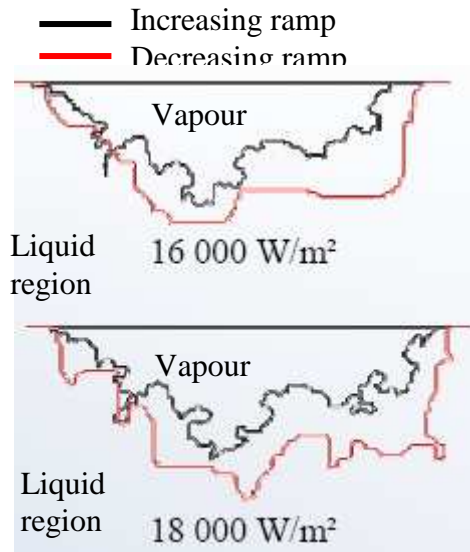


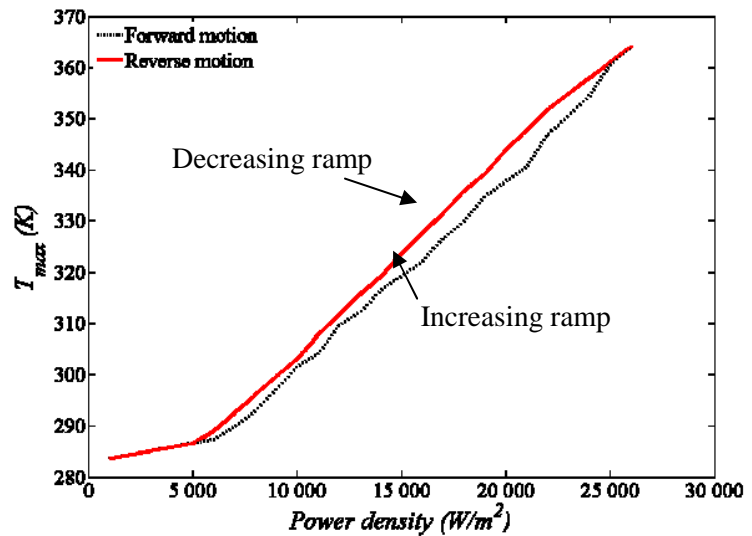
Fig. 5. a) Sketch of vapour pocket in the wick of evaporator unit cell,  
b) increasing and decreasing heat flux ramps

As illustrated in Fig. 6b, this has an impact on macroscopic quantities. Fig. 6b shows the evolution of the maximum temperature  $T_{max}$  of the casing as a function of the imposed heat flux. As can be seen  $T_{max}$  is greater when the imposed heat flux is reached in the decreasing ramp. This is of course fully consistent with the extensions of the vapour pocket depicted in Fig. 6a. The size of the vapour pocket is greater in the decreasing ramp. This induces a greater thermal resistance in the wick and as a result a greater casing

temperature.



a)



b)

Fig. 6. a) boundary of the vapour pocket computed using a pore network model for two values of imposed heat flux (interface obtained in the increasing ramp in black, interface obtained in the decreasing ramp in red); b) evolution of casing maximum temperature as the function of imposed heat flux

This illustrates that the temperature of the casing as well as other macroscopic quantities, [20], depends on the history of the heat flux variations. This can contribute to explain in part the hysteretic phenomena sometimes observed at the scale of a LHP.

More details on this work will be presented in a forthcoming paper.

## OPEN ISSUES AND FUTURE WORK

As pointed out in [16], there is still a lot to learn from pore-network simulations (PNS), especially for the transient regimes (start-up, change in the heat load). All the PNS presented or mentioned in this article were performed with two-dimensional networks. Although much insight can be gained from 2D simulations, there are also some drawbacks. In particular, the organisation of fluid phases can be significantly different in 3D (possibility of percolation for both phases). An obvious and interesting option yet to come is to perform the simulations in 3D.

Also, only regular pore networks have been considered so far. According to the most advanced developments, see for example [27] and references therein, the pore network could be constructed from direct imaging of the real wick microstructure, by micro-x-ray computerized tomography typically. An alternative would be to use synthetic 3D structure generated numerically, such as for instance a random packing of overlapping spheres for representing the metallic sintered materials often encountered in evaporator wicks. This leads to “morphological” pore networks since the pore network is constructed directly from the “real” microstructure. The method is for example illustrated in [11] with a two-dimensional network constructed from a model fibrous medium. Although simulations based on simple regular pore networks are very instructive, using morphological pore networks is certainly an attractive approach for future developments.

It is well known that the detail of the vaporisation process along a meniscus in a pore, e.g. [28], can be significantly more complicated than considered in the PNM developed so far. For example, the effect of the

microregion, e.g. [29], is ignored. This is not necessarily a problem, however, when one is primarily interested in sensitivity studies and in a better understanding of the macroscopic phenomena taking place within the wick. Owing to the pore shape and pore wall roughness, there is first a need for further detailed studies of the vaporisation process at a meniscus since the details of the contact line region in the pores of a sintered material are probably far from the flat, smooth surface considered so far in the microregion models. A simple first option, however, would be to introduce in the PN approach the concept of apparent contact angle, e.g. [30] and references therein.

Also, it will be interesting to compare continuum model simulations and pore network simulations. The pore network simulations could serve as references and this would permit to assess the validity domain and the relevance of continuum models. Pore network simulations, especially in 3D, are computer time consuming. For this reason, the simulation of a complete evaporator using pore network models is out of reach. It can therefore become desirable at some point to rely on continuum models, which can be significantly more efficient in terms of computational times. This outlines an up-scaling strategy, using successively pore network models (evaporator unit cell), continuum models (3D section of an evaporator) and finally a nodal network (evaporator scale, LHP scale) to develop numerical studies at the system scale based on a thorough understanding of the phenomena at the lower scales.

## CONCLUSION

The results outlined in this paper show that pore network models are useful tools for a better understanding of vaporization processes in capillary structures. Coupled with percolation theories and experiments with model systems, they represent an interesting alternative for studying problems that cannot be handled adequately by classical phenomenological models. Although not described in this paper, they also offer a possibility for predicting the effective parameters of phenomenological models. There are still many issues in the operation of LHP that need to be clarified and there is also a need for optimizing these systems, notably the evaporator wick. New advances in these areas can be expected from pore network simulations.

## Acknowledgements

Financial supports from CNES and Région Midi-Pyrénées are gratefully acknowledged. This work has benefited from numerous discussions within CNRS-GDR 'SYREDI' (Systèmes de Refroidissement Diphasiques).

## REFERENCES

1. Prat M. Recent advances in pore-scale models for drying of porous media // *Chem. Eng. J.* 2002. Vol. 86. Pp. 153–164.
2. Peterson G.P. *An Introduction to Heat Pipes, Modeling, Testing and Applications*, Wiley Interscience, New York, 1994.
3. Faghri A. *Heat Pipe Science and Technology*, Taylor & Francis, Washington, 1995.
4. Min D.H., Hwang G.S., Usta Y., Cora O.N., Koc M., Kaviany M. 2-D and 3-D Modulated Porous Coatings for Enhanced Pool Boiling // *Int. J. Heat and Mass Transfer*. 2009. Vol. 52. Pp. 2607–2613.
5. Woods A.W. Liquid and vapor flow in superheated rock // *Ann. Rev. Fluid Mech.* 1999. Vol. 31. Pp. 171–199.
6. Lipinski R.J. A coolability model for post-accident nuclear reactor debris // *Nucl. Technol.* 1984. Vol. 65. Pp. 53–66.
7. Kaviany M. *Principles of Heat Transfer in Porous Media*, Second Edition (Second Printing), Springer-Verlag, New York, 1999.
8. Aker E., Maloy K. J., Hansen A. Simulating temporal evolution of pressure in two-phase flow in porous media // *Phys. Rev. E*. 1998. Vol. 58. Pp. 2217–2226.

9. Blunt M.J., Jackson M.D., Piri M., Valvatne P.H. Detailed physics, predictive capabilities and macroscopic consequences for pore-network models of multiphase flow // *Adv. Water Resour.* 2002. Vol. 25. Pp. 1069–1089.
10. Chapuis O., Prat M. Influence of wettability conditions on slow evaporation in two-dimensional porous media // *Phys. Rev. E.* 2007. Vol. 75. 046311.
11. Chapuis O., Prat M., Quintard M., Chane-Kane E, Guillot., O., Mayer N. Two-phase flow and evaporation in model fibrous media. Application to the gas diffusion layer of PEM fuel cells // *J. of Power Sources.* 2008 . Vol.178. Pp. 258–268.
12. Rebai M., Prat M. Scale effect and two-phase flow in a thin hydrophobic porous layer. Application to water transport in gas diffusion layers of PEM fuel cells // *J. of Power Sources.* 2009. Vol.192. Pp. 534–543.
13. Satik C., Yortsos Y. A pore-network study of bubble growth in porous media driven by heat transfer // *ASME J. of Heat Transfer.* 1996. Vol. 118. Pp. 455–462.
14. Figus C., Le Bray Y., Bories S., Prat M. Heat and mass transfer with phase change in a porous structure partially heated. Continuum model and pore network simulations // *Int. J. of Heat and Mass Transfer.* 1999. Vol. 42. Pp. 2257–2569.
15. Coquard T., Prat M., Larue de Tournemine A., Figus C. Pore-network models as a tool for the analysis of heat and mass transfer with phase change in the capillary structure of loop heat pipe // *Proc. 14<sup>th</sup> International Heat Pipe Conference (14<sup>th</sup> IHPC)*, Florianópolis, Brazil, 2007.
16. Prat M. Application of pore network models for the analysis of heat and mass transfer with phase change in the porous wick of loop heat pipes // *Heat Pipe Science and Technology.* 2010. Vol. 1 (2). Pp.129–149.
17. Squires T.M., Quakes S.R. Microfluidics: fluid physics at the nanoliter scale // *Rev. of Mod. Physics.* 2005. Vol. 77. Pp. 977–993.
18. Launay S., Sartre V., Bonjour J. Parametric analysis of loop heat pipes operation: a literature review // *Int. J. of Thermal Sciences.* 2007. Vol. 46. Pp. 621–636.
19. Coquard T. // Ph.D Thesis, Université de Toulouse, 2006.
20. Louriou C. // Ph.D Thesis, Université de Toulouse, 2010.
21. Prat M. On the influence of pore shape, contact angle and film flows on drying of capillary porous media // *Int. J. of Heat and Mass Transfer.* 2007. Vol. 50. Pp. 1455–1468.
22. Chauvet F., Duru P., Geoffroy S., Prat M. Three periods of drying of a single square capillary tube // *Phys. Rev. Lett.* 2009. Vol.103. 124502.
23. Louriou C., Prat M. Experimental and numerical pore network study of bubble growth by vaporisation in a porous medium heated laterally // submitted to *Int. J. of Therm. Sciences.*
24. Prat M., Bouleux F, Drying of capillary porous media with stabilized front in two-dimensions // *Phys. Rev. E.* 1999. Vol. 60. Pp. 5647–5656.
25. Dullien F. *Porous Media: fluid transport and pore structure.* New York. Academic Press, 1991.
26. Chraïbi H., Prat M., Chapuis O. Influence of contact angle on slow evaporation in two dimensional porous media // *Phys. Rev. E.* 2009. Vol. 79. 026313.
27. Dong H., Blunt M.J. Pore-network extraction from micro-computerized-tomography images // *Phys. Rev. E.* 2009. Vol.80. 036307.
28. Khrustalev D., Faghri A. Heat transfer in the inverted meniscus type evaporator at high heat fluxes // *Int. J. of Heat and Mass Transfer.* 1995. Vol. 38 (16). Pp. 3091–3101.
29. Stephan P.C., Busse C.A.. Analysis of the heat transfer coefficient of grooved heat pipes evaporator walls // *Int. J. of Heat and Mass Transfer.* 1992. Vol.35 (2). Pp.383–391.
30. Bertossi R., Lataoui Z Ayel V., Romestant C., Bertin Y. Modeling of thin liquid film in grooved heat pipes // *Num. Heat Transfer, Part A: Applications.* 2009. Vol. 55. Pp. 1075–1095.

## PROGRESS ON HEAT AND MOISTURE RECOVERY FROM VENTILATION AIR: FROM FUNDAMENTALS TO ENGINEERING APPLICATIONS

Li-Zhi Zhang

Key Laboratory of Enhanced Heat Transfer and Energy Conservation of Education Ministry  
School of Chemistry and Chemical Engineering, South China University of Technology  
Guangzhou 510640, China

Tel/Fax: 86-20-87114268; E-mail: Lzzhang@scut.edu.cn

### Abstract

Membrane based heat and moisture recovery from ventilation air has become a hot topic for building energy conservation in these years. Over the past 10 years, much work has been conducted in South China University of Technology for the research on this topic, from fundamentals to engineering applications. This paper gives some new developments: the new concepts for membrane heat and mass transfer analysis, the developments of high vapor permeable membranes with finger-like macrovoids, the studies of convective heat and mass transfer in plate-fin ducts, and the application of air dehumidification with membrane based total heat exchangers. The results are that a sensible effectiveness of 0.8 and a latent effectiveness of 0.7 are obtained for a total heat exchanger with novel materials and new constructions. When the total heat exchanger is combined with a fresh air refrigeration dehumidification unit, the system COP is improved to 5.8.

### KEYWORDS

Heat and moisture recovery; Membrane; Air conditioning; Heat and mass transfer.

### INTRODUCTION

Membrane-based total heat exchanger has become a key equipment for heat and moisture recovery. The concept is shown in Fig.1. The device is like a parallel-plates air-to-air heat exchanger. However, in place of common metal foils, membranes that are permeable to water vapor, but impermeable to other unwanted gases like CO<sub>2</sub>, are used as the plates. Therefore both the sensible heat and the latent heat (moisture) can be exchanged between the incoming fresh air and the rejected exhaust air. Due to the sensible heat and moisture exchange, heat and humidity would be recovered from the exhaust stream in winter (especially in cold climates like in Beijing) and excess heat and moisture would be transferred to the exhaust in order to cool and dehumidify the incoming fresh air in summer. With total heat exchangers, 70-90% of the energy for conditioning fresh air could be saved [1].

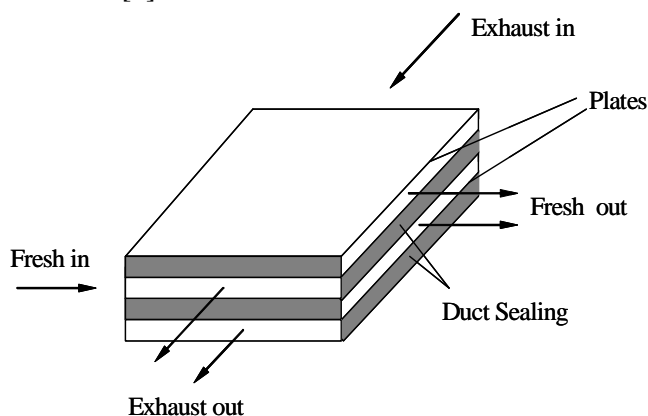


Fig. 1. Schematic of a parallel-plates total heat exchanger

Over the past 10 years, accommodating the local weather conditions, and to satisfy the social and market demands, the center of energy saving technologies for built environment of South China University of Technology has conducted many researches on this topic, from fundamentals to engineering applications. This paper gives some new developments in this topic.

## NOVEL CONCEPTS-FRACTAL MODEL

This work is to build the relations between membrane performance and its micro structures. Porous membranes have been used as the support layer for heat and moisture recovery. Gas diffusivity in porous membranes is a key parameter for system design and membrane optimization [2]. The micro structures of the porous membranes are usually disordered and extremely complicated. This makes it very difficult to analytically find the permeability. In order to get a better understanding of the mechanisms for permeability, a new perspective is considered in the analysis of membrane permeability: fractal models [3].

Figure 2 shows the SEM (Scanning Electron Micrograph) picture for a typical porous Cellulose Acetate membrane. The disordered nature of pore structures in these porous membranes suggests the existence of a fractal structure formed by the macro and micro pores in membranes. These pores and their distributions are analogous in the microstructure to pores in sandstone, to islands or lakes on earth. Therefore, it is possible to obtain the permeability of porous membranes through a fractal analysis on pore microstructures.

Fractal theory is a new theory to analyze natural phenomenon, which allows the characterization of objects in terms of their self-similar (scale invariant) properties (i.e., parts of the object are similar to the whole after rescaling). Fractal techniques have been used in diverse engineering applications that involve physical phenomena in disordered structures and over multiple scales. In all these applications, the fractal dimensions have been very effective in rendering complex structures tractable for analysis, and it is this capability which is explored for describing the membrane structures in the present context.

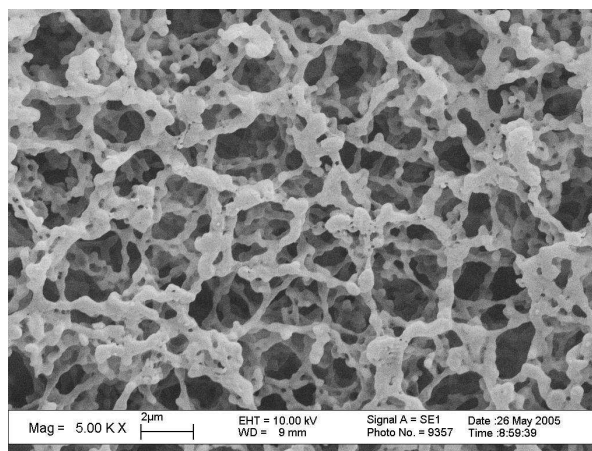


Fig. 2. The micro structure of the surface of a Cellulose Acetate membrane.

Porous membrane has numerous pores with various sizes in the through-plane direction, and can be considered as a bundle of tortuous capillary tubes with variable radius for the two-dimensional case. Let the diameter of a capillary tube be  $\lambda_p$ , and its tortuous length along the flow direction be  $L(\lambda)$ . The relationship between them exhibits the fractal scaling law [3]:

$$\frac{L(\lambda_p)}{L_0} = \left( \frac{L_0}{\lambda_p} \right)^{D_i - 1}, \quad (1)$$

where  $L_0$  is the representative length of a straight capillary, which is equal to membrane thickness.  $D_t$  is the tortuosity dimension, with  $1 \leq D_t \leq 2$ . Large value of  $D_t$  within this range corresponds to a highly tortuous capillary, while  $D_t=1$  denotes a straight capillary pathway,  $D_t=2$ , corresponds to a highly tortuous line that fills a plane.

The relationship between the number of pores and the pore size  $\lambda_p$  is another important property of fractals. The pores in a porous medium are analogous to the islands or lakes on the earth. The cumulative size distribution of them follows the power law relation [3]:

$$N(L \geq \lambda_p) = \left( \frac{\lambda_{p,\max}}{\lambda_p} \right)^{D_f}, \quad (2)$$

where  $N(L \geq \lambda_p)$  represents the total number of pores with diameter greater than  $\lambda_p$  on unit cell  $A_0 (=L_0^2)$ .  $\lambda_{p,\max}$  is the maximum pore diameter,  $D_f$  is area dimension.

It proves that  $\lambda_{p,\min} \ll \lambda_{p,\max}$  must be satisfied for fractal analysis of a porous membrane. If not, the porous membrane is a non-fractal medium. For those membranes that have relative uniform pore sizes, the fractal theory is not appropriate to use. Fortunately, most porous membranes have wide pore size distributions.

The permeability ( $m^2$ ) through the membrane can be deduced to [3]

$$Pe = \frac{\pi D_f L_0^{-1-D_t} \lambda_{p,\max}^{D_f}}{128(3+D_t-D_f)} \left( \lambda_{p,\max}^{3-D_t+D_t} - \lambda_{p,K}^{3-D_t+D_t} \right) + \frac{\pi \mu L_0^{-1-D_t} D_f \lambda_{p,\max}^{D_f}}{12 p_m (2+D_t-D_f)} \sqrt{\frac{8RT}{\pi M_A}} \left( \lambda_{p,P}^{2-D_t+D_t} \right) \quad (3)$$

where  $\lambda_{p,K}$  refers to the pore diameter where gas diffusion changes from Knudsen diffusion to ordinary diffusion,  $\lambda_{p,P}$  refers to the pore diameter where viscous Poiseuille flow begins to dominates,  $p_m$  is the mean partial pressure of vapor (Pa) in pores,  $R$  is ideal gas constant (8.314J/(mol·K)),  $M_A$  is vapor molecule weight (kg/kmol),  $\mu$  is the viscosity of vapor (Pas).

The area dimension  $D_f$  can be determined by the box-counting method. This method is based on the image analysis of a unit cell or a sufficiently large cross section of a sample on the membrane. According to this method, the cross section under consideration is discretized using square boxes of size  $L$ . Then the number,  $N(L \geq \lambda_p)$ , of boxes required to completely cover the pore areas is counted. The pore area fractal dimension,  $D_f$ , can be determined by the value of the slope of a linear fit through data on a logarithmic plot of the cumulative number of pores  $N(L \geq \lambda_p)$  versus the square box size  $L$ .

The tortuosity dimension  $D_t$  represents the extent of convolution of the capillary pathways for gas flowing through the membrane. Since the tortuosity of the flow pathways results from the convolution of the boundaries of the porous regions in membrane cross section, the tortuosity dimension may therefore be evaluated as the fractal dimension of the perimeter of the porous regions on cross section, which may also be obtained by the box-counting method mentioned above.

The above procedures provide the basic data for fractal models. With Eq. (3), the relations between the membrane structure and membrane permeability can be set up. Membrane porosity, mean pore diameter, tortuosity, thickness are the determining factors influencing membrane moisture diffusion. The model provides a new tool for membrane structure optimization. Figure 3 is the prediction with the established model. As seen, the new fractal model predicts permeability well.

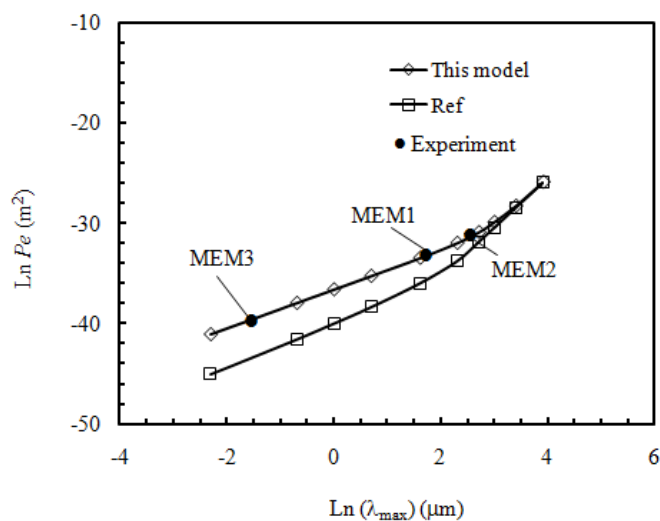


Fig. 3. Prediction of permeability for three membranes with the fractal model [3]

### NOVEL MEMBRANE-MEMBRANE WITH FINGER-LIKE MACROVOIDS

Phase-inversion method has been the widely used technology for membrane preparation since it was successfully used by Loeb and Sourirajan to develop cellulose acetate membranes for seawater desalination in 1960s. According to this method, the formation of membrane structure is controlled by both the thermodynamics of the casting solution and the kinetics of transport process. Usually, depending on the rate of phase separation, two different structures, namely a symmetric sponge-like (from delayed phase demixing) or an asymmetric finger-like structure (from instantaneous phase demixing) can be expected. Figure 4 shows a typical asymmetric finger-like structure [4]. It is composed of three parts from bottom to top: a sponge-like porous support, a porous media with finger-like and nearly parallel macrovoids, and finally a very thin skin layer with rather small pores. Due to the existence of large finger-like macrovoids, it is qualitatively believed that the asymmetric membranes have less resistance than symmetric membranes, and thus are beneficial for permeation performance.

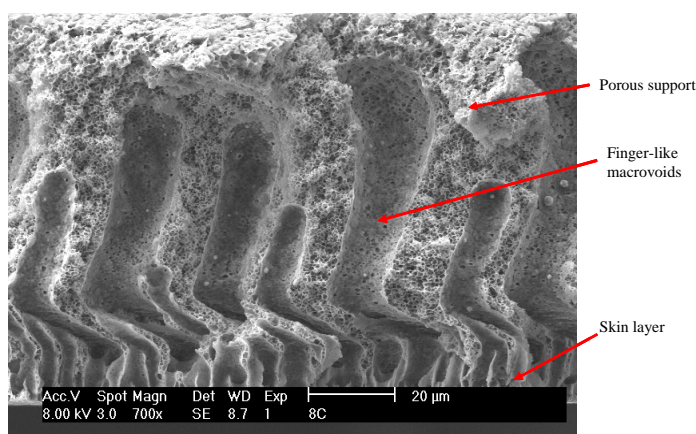


Fig. 4. SEM graph of the cross section of an asymmetric porous membrane

The membrane structure is schematically depicted in Fig.5 [4]. It is composed of three layers: a sponge-like porous layer, a sponge layer with finger-like macrovoids, and a skin layer. Their dimensions are plotted in the figure. Though the macrovoids may have differences, more or less, in length and dimension, in the model, they are approximated as identical cylinders, to ease the mathematical analysis. To account for their zigzag nature, a tortuosity is used to compensate this feature.

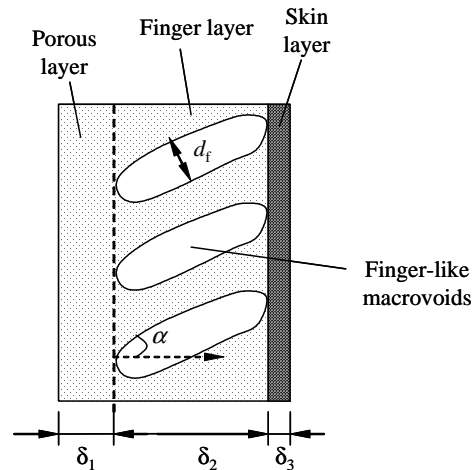


Fig. 5. Simplified structure of a finger-like macrovoids asymmetric membrane

Resistance in the membrane is analyzed [4]. It is found that the second layer has the highest gas diffusivity through a single pore or finger. This is because that the larger the pore (finger) diameter, the higher the gas diffusivity. Nevertheless, the diffusivity through a finger is in the same order with the diffusivity through a small pore. Due to the existence of straight finger voids, the total porosity in the second layer is greatly improved, and consequently the effective gas diffusivity through this layer is one order higher than that through the sponge support layer. In one word, due to the increased porosity by straight finger voids, effective diffusivity can be greatly improved.

## PLATE-FIN DUCTS

Plate-fin ducts are the common structure for compact heat exchanger design. The structure is shown in Fig.6. It is mechanically strong, compact, and high efficient. Ducts of well-conductive materials and with regular cross sections have been studied in classical textbooks. Recently, our laboratory has extended the studies with boundary fitted coordinates to plate fin ducts of non-metal materials which have lower fin heat and mass conductance parameters [5–8].

At any location along the fin, there is a balance between the net conduction along the fin and the heat transfer from the surface of the fin to the fluid. The heat flux at the lower surface and the upper surface are skew symmetric. The one dimensional heat and mass transfer equations in ducts are solved in combination with the solution of heat and mass transfer equations in fins.

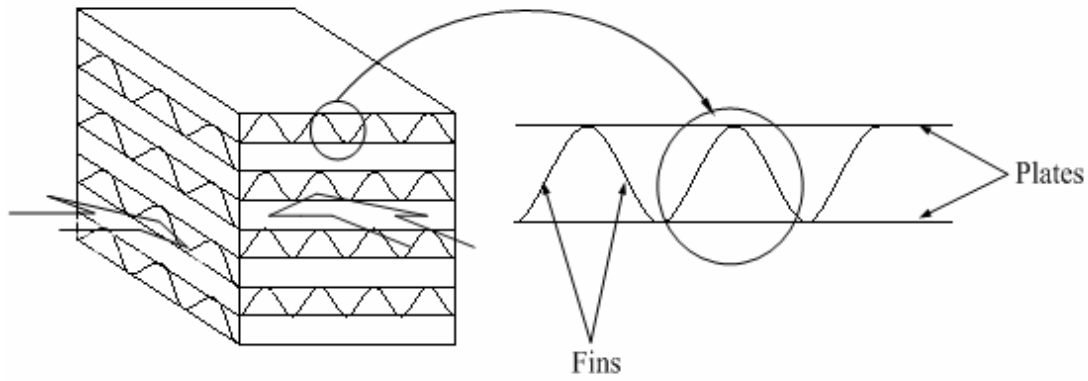


Fig. 6. Schematic of a plate-fin structure

Fin heat conductance parameter is defined by

$$\Omega_{\text{sen}} = \frac{\lambda_{\text{fin}} \delta}{\lambda_a (2a)}. \quad (4)$$

Fin mass conductance parameter is defined as

$$\Omega_{\text{Lat}} = \frac{\delta \rho_{\text{fin}} D_{\text{w,fin}} k_p}{\rho_a D_{\text{va}} (2a)}, \quad (5)$$

where  $a$  is half the channel pitch (or half fin height).

Fin efficiency for heat transfer is defined as the ratio of  $Nu$  at a finite fin heat conductance to that at  $\Omega_{\text{sen}}=\infty$ , or

$$\eta_{\text{fin}} = \frac{Nu_{\Omega_{\text{sen}}}}{Nu_{\Omega_{\text{sen}}=\infty}}. \quad (6)$$

Fin efficiency for mass transfer is defined as the ratio of  $Sh$  at a finite fin mass conductance to that at  $\Omega_{\text{Lat}}=\infty$ , or

$$\eta_{\text{fin}} = \frac{Sh_{\Omega_{\text{Lat}}}}{Sh_{\Omega_{\text{Lat}}=\infty}}. \quad (7)$$

As the mass transfer equations are in the same forms as the heat transfer equations, fin efficiency for mass transfer will equal to that for heat transfer, if the fin mass conductance parameter is equal to the fin heat conductance parameter.

Table 1 lists the obtained  $Nu$  and/or  $Sh$  and fin efficiencies for various aspect ratios and fin conductance parameters. They are the basic data that can be used for compact heat exchanger or total heat exchanger design. The fin heat conductance parameters are determined by duct geometry and heat conductivity of fin materials. Table 2 lists the values of fin heat conductance parameters for some frequently encountered materials, including metal and non-metals, for a sinusoidal duct of height 2 mm, aspect ratio 0.5, and fin thickness 0.1 mm.

Table 1. Fully developed Nusselt or Sherwood numbers and fin efficiencies for plate-fin sinusoidal ducts.

$\tau_1$	$\Omega$	$Nu$ or $Sh$	$\eta_{fin}$	$\tau_1$	$\Omega$	$Nu$ or $Sh$	$\eta_{fin}$
0.2	$\infty$	1.551	1.0	0.5	$\infty$	2.181	1.0
	25	1.523	0.982		25	2.133	0.978
	10	1.201	0.774		10	2.107	0.966
	5	1.033	0.666		5	1.908	0.875
	2	0.863	0.556		2	1.524	0.699
	1	0.791	0.510		1	1.260	0.578
	0.5	0.739	0.476		0.5	1.055	0.484
	0.1	0.694	0.447		0.1	0.824	0.378
	0	0.641	0.413		0	0.737	0.338
1.0	$\infty$	2.521	1.0	2.0	$\infty$	2.888	1.0
	25	2.492	0.988		25	2.714	0.940
	10	2.369	0.940		10	2.651	0.918
	5	2.167	0.860		5	1.922	0.666
	2	1.721	0.683		2	1.511	0.523
	1	1.379	0.547		1	1.194	0.413
	0.5	1.081	0.429		0.5	0.926	0.321
	0.1	0.751	0.298		0.1	0.631	0.218
	0	0.576	0.228		0	0.358	0.124
5.0	$\infty$	2.586	1.0	5.0	1	1.015	0.392
	25	2.390	0.924		0.5	0.833	0.322
	10	2.170	0.839		0.1	0.661	0.256
	5	1.654	0.640		0	0.173	0.067
	2	1.274	0.493				

Notes:  $\tau_1$ , duct aspect ratio

Table 2. Values of fin heat conductance parameter for some fin materials with duct height, 2 mm; aspect ratio 0.5, fin thickness, 0.1 mm; fluid, air

Fin materials	$\lambda_{fin}$ ( $Wm^{-1}K^{-1}$ )	$\Omega_{sen}$
Pure copper	401	751.00
Bronze	52	97.40
Iron	80.2	150.20
Steel	60.5	113.30
Aluminium	237	443.90
Carbon	1.6	3.00
Plywood	0.12	0.22
Wood	0.16	0.30
Clay	1.3	2.43
Glass	1.4	2.66
Paper	0.18	0.34
Teflon	0.35	0.66
Polymer Membrane	0.13	0.24

Notes:  $\lambda_{fin}$  fin heat conductivity;  $\Omega_{sen}$  fin heat conductance parameter.

As seen, for almost all the metals, the fin heat conductance parameters are larger than 100, and the resulting fin heat efficiencies can be as high as 0.90–0.98. For such traditional metal compact heat exchangers, the influences of finite fin heat conductance on heat transfer are negligible. Direct utilization of heat transfer properties for a common duct is acceptable. For the investigated compact total heat exchangers which use non-metals to simultaneously transfer heat and moisture, the fin heat conductance parameters are usually less than 1.0, and the resulting fin efficiencies for heat transfer can be as low as 0.40. Though it's true that the fins still participate in the heat transfer enhancement, at least partially, at this stage, the effects of finite fin heat conductance on heat transfer will be substantial.

The values of fin mass conductance parameters are in the order of  $10^{-3}$ . With such low mass conductance parameters, the fin efficiencies for mass transfer will be below 0.1 to 0.2. Under such circumstances, nearly all the mass transfer between the two air streams will be accomplished by the plate, rather than by the fins. The fins seem to behave only like supporting materials, if excluding their role in partial participation in heat transfer. In engineering, sometimes supporting materials or spacers are necessary to separate the two streams because the plates are thin and soft.

## APPLICATIONS

### Fresh air dehumidification with total heat recovery

Previous studies reveal that desiccant cooling combined with total heat recovery are promising for humidity control and energy saving in hot and humid regions [9–12]. However they are bulky and additional outside heat sources are required, which is not easy for densely populated urban areas like Guangzhou.

To address the problem, recently, a fresh air refrigeration dehumidification system with membrane total heat exchanger is investigated and built in our laboratory [13–15]. The system comprises of all the necessary parts for real application. A detailed mathematic model based on cell-by-cell approach has been developed to optimize the system [16]. Experiments are conducted to validate the model. Then the effects of operating conditions on the dehumidification capacity and the coefficient of performance are investigated. The results help to optimize the demonstrative unit.

The theory is that in this system, a membrane based total heat exchanger is used before the fresh air is pumped to a heat pump for air dehumidification. The total heat exchanger has a membrane core where the incoming fresh air exchanges moisture and temperature simultaneously with the exhaust air. In this manner, the total heat or enthalpy from the exhaust is recovered. The schematic for this system is shown in Fig. 7.

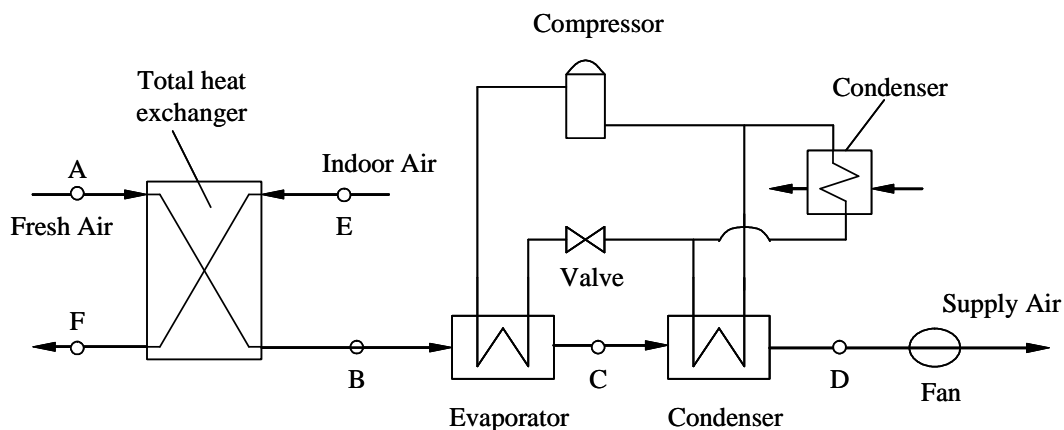


Fig. 7. Schematic of mechanical fresh air dehumidification with membrane-based total heat exchanger

Energy savings effects on a one-year basis are modeled with the weather conditions in Guangzhou [15]. In hot and humid regions like Guangzhou, air dehumidification is required most of the year. The outside temperatures usually exceed 35 °C and humidity exceed 80%RH. The COP of a traditional common

refrigerator is usually below 2.8. The new system is modeled. The variations of the yearly COP of the system are shown in Fig.8 [16]. As seen, the COP is greatly improved, in comparison with a traditional system. In most days, it is from 4.0 to 6.8. In addition, energy analysis found that in January and February [16], when it is the dry season, energy requirements are the least energy. In August, it is the most humid season, required energy is the largest. Five months from May to September account for 60.5% of the yearly energy load. Other 7 months account for the rest 39.5%. South China has a long hot and humid summer. The energy for air dehumidification is substantially large. To save energy while ensuring a healthy built environment with enough fresh air ventilation, an independent air dehumidification system with energy recovery is necessary.

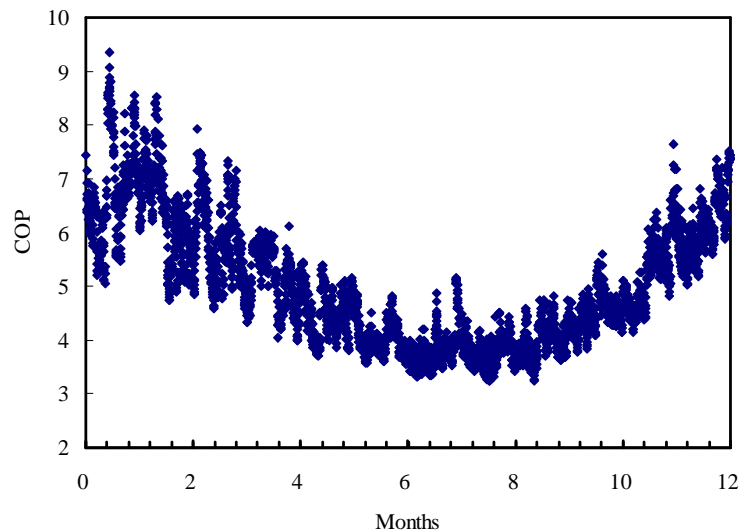


Fig. 8. Distribution of *COP* of the air dehumidification system in a year, by hourly simulations

To extend the system in real engineering applications, a demonstrative machine has been built in our laboratory. The demonstrative unit has been used in real buildings and is experimented. The results are:

- (1) The total heat exchanger has a sensible effectiveness of 0.8 and a latent effectiveness of 0.7. The Number of transfer units is 4.2, with 8m<sup>2</sup> composite membranes.
- (2) The fresh air dehumidification system has a high air dehumidification rates with a high *COP*. The air dehumidification rates and *COP* are 3.57 kg h<sup>-1</sup> and 5.8, respectively. The test conditions are: fresh air temperature 35 °C, fresh air humidity 70%, room temperature 27°C, room humidity 53%, and supply air temperature 20 °C. The prototype has a fresh air flow rate of 200m<sup>3</sup>/h. Comparing with a conventional mechanical dehumidification system, the air dehumidification rate of the proposed system is 3.5 times higher, and the *COP* is 2.2 times higher. This implicates that the membrane-based total heat exchanger improves the performances greatly. The new system is a promising and efficient air dehumidification system in hot and humid environment.

## CONCLUSIONS

Conditioning of ventilation fresh air accounts for 20-40% of the total energy cost in air-conditioning industry. Stringent ventilation regulations make the problem more serious. Total heat recovery from ventilation air has become one of the most important fraction of HVAC energy conservation. The energy savings potential is great. However there are full of challenges. The difficulties come from the small temperature and humidity differences between the fresh air and the exhaust air. Novel membranes as well as novel structures should be searched. In heat and mass transfer modeling, novel concepts should be used.

Under these backgrounds, much work in this direction has been conducted in South University of Technology in these years. There has been great progress made in these areas: new material fabrication, new system design, novel heat and mass transfer modeling and system engineering applications. With the newly designed composite membranes, and novel exchanger structures, a total heat exchanger developed has a sensible effectiveness above 0.8 and latent effectiveness above 0.7. When the developed exchanger is combined to a refrigeration fresh air dehumidification unit, the *COP* is above 5.8, and dehumidification rates are 3.57 kg/h. The unit has been successfully used in a 200m<sup>2</sup> room. About 70-80% of the energy for conditioning fresh air is saved. They provide a solution for sustainable air conditioning systems in hot and humid regions. In future, developing more cost-effective membranes is the direction for commercial applications.

## Acknowledgments

The researches on heat and moisture recovery in South China University of Technology has been supported by the following grants: (1) Natural Science Foundation of China, 50306005; 50676034; (2) The National High Technology Research and Development Program of China (863), 2008AA05Z206; (3) The Fundamental Research Funds for the Central Universities, 2009ZZ0060; (4) Natural Science Foundation of Guangdong Province, 05006557; 8151064101000041; (5) Tsinghua-Daikin Research Center from Daikin Industrial Co. Ltd. (6) and grants from other sources.

## NOMENCLATURE

$A$	half channel pitch or half fin height (m)
$COP$	coefficient of performance
$D$	diffusivity (m <sup>2</sup> /s)
$D_f$	area dimension
$D_t$	tortuosity dimension
$H$	convective heat transfer coefficient (kWm <sup>-2</sup> K <sup>-1</sup> )
$k$	convective mass transfer coefficient (m/s)
$k_p$	partition coefficient
$L$	length (m)
$N$	number
$Nu$	Nusselt number
$P$	pressure (Pa)
$P_a$	atmospheric pressure (101325 Pa)
$p_m$	mean partial pressure of vapor in pores (Pa)
$Pe$	permeability (m <sup>2</sup> )
$Sh$	Sherwood number

### Greek letters

$\tau$	tortuosity
$\tau_1$	duct aspect ratio
$\rho$	density (kg/m <sup>3</sup> )
$\lambda$	heat conductivity (Wm <sup>-1</sup> K <sup>-1</sup> )
$\lambda_p$	pore diameter (m)
$\delta$	membrane thickness (m)
$\eta_{fin}$	fin efficiency
$\Omega$	fin conductance parameter

### Subscripts

$a$	air
$fin$	fin

Lat moisture, latent  
sen sensible  
v vapor  
w water

## REFERENCES

1. Zhang L. Z. *Total Heat Recovery: Heat and Moisture Recovery from Ventilation Air*, Nova Science Publishing Co., New York, 2009. Chapter 1, Pp. 14.
2. Zhang L. Z., Mass diffusion in a hydrophobic membrane humidification/dehumidification process: the effects of membrane characteristics // *Separation Science and Technology*. 2006. Vol. 41. Pp. 1565–1582.
3. Zhang L. Z. A fractal model for gas permeation through porous membranes // *International Journal of Heat Mass Transfer*. 2008. Vol. 51. Pp. 5288–5295.
4. Zhang L. Z. Coupled heat and mass transfer through asymmetric porous membranes with finger-like macrovoids structure // *International Journal of Heat Mass Transfer*. 2009. Vol. 52. Pp. 751–759.
5. Zhang L. Z. Heat and mass transfer in plate-fin enthalpy exchangers with different plate and fin materials // *International Journal of Heat Mass Transfer*. 2009. Vol. 52. Pp. 2704–2713.
6. Zhang L. Z. Heat and mass transfer in plate-fin sinusoidal passages with vapor-permeable wall materials // *International Journal of Heat Mass Transfer*. 2008. Vol. 51. Pp. 618–629.
7. Zhang L. Z. Thermally developing forced convection and heat transfer in rectangular plate-fin passages under uniform plate temperature // *Numerical Heat Transfer, Part A-Applications*. 2007. Vol. 52. Pp. 549–564.
8. Zhang L. Z. Laminar flow and heat transfer in plate-fin triangular ducts in thermally developing entry region // *International Journal of Heat Mass Transfer*. Vol. 50. Pp. 1637–1640.
9. Zhang L. Z., Niu J. L. Indoor humidity behaviors associated with decoupled cooling in hot and humid climates // *Building and Environment*. 2003. Vol. 38. Pp. 99–107.
10. Zhang L. Z., Niu J. L. Performance comparisons of desiccant wheels for air dehumidification and enthalpy recovery // *Applied Thermal Engineering*. 2002. Vol. 22. Pp. 1347–1367.
11. Niu J.L., Zhang L.Z. Effects of wall thickness on the heat and moisture transfers in desiccant wheels for air dehumidification and enthalpy recovery // *International Communications in Heat and Mass Transfer*. 2002. Vol. 29. Pp. 255–268.
12. Niu J.L., Zhang L.Z., Zuo H.G. Energy savings potential of chilled-ceiling combined with desiccant cooling in hot and humid climates // *Energy and Buildings*. 2002. Vol. 34. Pp. 487–495.
13. Zhang L. Z., Niu J. L. A pre-cooling Munters Environmental Control cooling cycle in combination with chilled-ceiling panels // *Energy*. 2003. Vol. 28. Pp. 275–292.
14. Zhang L.Z., Zhu D.S., Deng X.H., Hua B. Thermodynamic modeling of a novel air dehumidification system // *Energy and Buildings*. 2005. Vol. 37. Pp. 279–286.
15. Zhang L.Z. Energy performance of independent air dehumidification systems with energy recovery measures // *Energy*. 2006. Vol. 31. Pp. 1228–1242.
16. Liang C.H., Zhang L.Z., Pei L.X. Independent air dehumidification with membrane-based total heat recovery: modeling and experimental validation // *International Journal of Refrigeration*. 2010. Vol. 33. Pp. 398–408.

## HEAT TRANSFER INTENSIFICATION IN MINI CHANNELS WITH POROUS COATING ON HEAT-LOADED WALL

Leonard Vasiliev, Alexander Zhuravlyov, Leonid Grakovich  
Porous Media Laboratory

A.V. Luikov Heat & Mass Transfer Institute of the National Academy of Sciences of Belarus  
15 p. Brovka str., 220072, Minsk, Belarus  
Tel/Fax: +375 17 284 2133, E-mail: Leonard\_Vasiliev@rambler.ru

### Abstract

In the paper the authors present the results of investigation of mini/micro scale heat transfer of two-phase fluids (propane) at heat flux ranges  $10^2$ – $10^5$  W/m<sup>2</sup>. The data obtained in the liquid pool and in confined space (from 0.1 to 2.5 mm) on a flooded or partially flooded horizontal tube with porous coating testify the phenomena of micro heat pipe inside a porous structure. The cylindrical heat loaded tube with porous coating was disposed inside the transparent coaxial glass tube. Such combination of plates, or tubes is the reason of the evaporation and two-phase convection heat transfer enhancement. The availability of annular mini channel significantly promotes to intense heat transfer (up to 2.5–3 times as high) at heat fluxes  $< 50$  kW/m<sup>2</sup>, as compared with process in the liquid pool.

### KEYWORDS

Heat transfer, evaporation, two-phase flow, porous body, confined space, flow in a gap channel.

### INTRODUCTION

Following the literature many investigations have been performed to provide a better understanding of two-phase heat transfer at microscale, which is very important in electronics and optoelectronic components cooling, micro heat exchangers. However, these studies haven't yet led to a general conclusion. The investigation of processes involving microchannels flow less than 3 mm has attracted great interest from both academia and industry. The potential application of this technology into diverse fields, providing extremely favorable results, makes it a prominent issue in the area of transport phenomena. In recent years, the advances in microscale heat transfer and fluid flow were remarkable and applications using microscale phenomena have become popular. Especially, innovations in electronic technology and biotechnology are striking. A large number of experiments and numerical analyses are being carried out in many laboratories all over the world. Evaporative and boiling cooling is widely applied for electronic apparatus based on two-phase thermal control and heat pipe application [1]. In the fuel cells applications the heat transfer system also need to provide reduced weight, be compact and have the least possible number of components. The subcooled boiling flow heat transfer from plain and enhanced surfaces in automotive applications was investigated and the results of experiments were published in [2]. The reduction of the size of mobile computing devices and phones will create problems for designers related to thermal control [3]. The modern requirements for high heat transfer rates in compact, efficient cooling systems used in the miniature refrigerators can be met by special heated wall treatment. It has been shown in many experimental studies that porous coatings on the heated surfaces can intensify the boiling process markedly [4]. In several of these investigations hydrocarbons were used as boiling fluids and some results were presented for propane. Experimental studies of flow boiling of propane and other hydrocarbons in channels were published in [5]. These data are important in considering hydrocarbons application in air-conditioning, refrigeration and heat pump systems. Most of the available in the literature experimental data are related to conventional channels ( $D_{in} \geq 3$  mm). A few number of experiments were published for hydrocarbons flow in small and mini channels ( $D_{in} < 3$  mm). The results of experiment presented in this paper were compared to the heat transfer in mini channels with plane surface. It was found, that the mode of hydrodynamic and heat transfer in mini channel with micro/nano porous coating on the wall is basically different to compare with two-phase flow heat transfer and hydrodynamic in the mini channel with plain polished walls, or in the pool. If the boiling

heat transfer on the polished surface is related with four stage transient phenomena: 1) superheating of the liquid on the wall, 2) nuclear arrival on micro roughness of the wall, 3) vapor bubble expanding and departure, 4) saturated liquid penetration to the place of the bubble departure. On the contrary the two-phase heat transfer on the porous coating is one stage heat transfer with constant points of vapor generation in fixed macropores. The general goal of this investigation is to increase the heat transfer efficiency of the electronic components cooling and transport mini-channel heat exchangers applying the micro-heat pipe phenomena inside the thin layer of porous material. This paper discusses the development of an advanced hybrid technology that incorporates elements from both passive and active loop technologies. The result is a high performance cooling technology development that can be used to remove high heat fluxes from large heat input areas. This technology we consider to represent substantial improvement over state of the art of multi-channel evaporators, heat pipes, loop heat pipes and spray cooling devices.

## 1. EXPERIMENT

The heat releasing component is cooled with liquid evaporation inside the porous structure and by pulsating forced convective two-phase heat transfer in the annular mini channel, Fig. 1. The experimental facility, consists of a closed loop with forced convection two-phase flow driven by bubbles generation on the heated surface of mini channel (Fig. 1 *a*). The same fluid circulation can be realized with the help of miniature mechanical pump (Fig. 1 *b*). The experimental investigation of evaporation heat transfer on the single horizontal tube (smooth and with porous coating) was performed for the reasons of analysis of its cooling capacity.

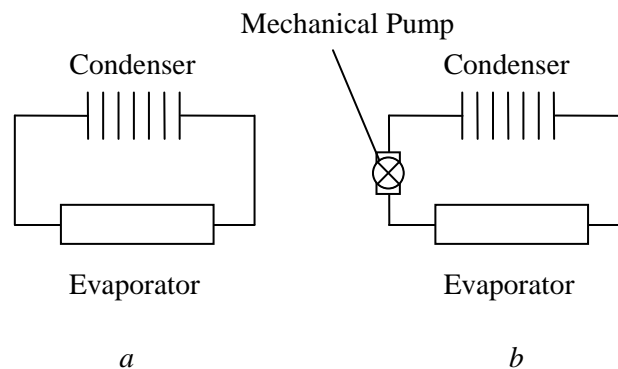


Fig. 1. Two-phase loop with annular mini-channel (evaporator) consisted of copper tube and glass tube: *a*) thermosyphon loop; *b*) loop with mechanical pump

This experimental investigation was devoted to analysis of saturated propane two-phase flow hydrodynamic and heat transfer in transparent horizontal annular mini channel. Experiments were carried out on the experimental set-up, Fig. 2, the main parts of which consisted on the test vessel, insulated chamber with temperature controlled liquid circuit, cooling machine, thermostats, condenser liquid loop, temperature control system, vacuum pump, liquid feed system. A cylindrical test sample – copper tube ( $D = 20$  mm,  $L = 100$  mm) with copper sintered porous coating (porosity  $\sim 50\%$ , particle diameter  $63\text{--}100$   $\mu\text{m}$ , mean particle diameter  $82$   $\mu\text{m}$ , mean pore hydraulic diameter  $24.5$   $\mu\text{m}$ , thickness  $300$   $\mu\text{m}$ ) was placed horizontally in the liquid pool of the test vessel. A heat flow to the tube was supplied by the cartridge heater. The condenser was disposed above the liquid pool and ensured the saturation temperature  $T_s$  inside the vessel. To prevent the heat losses between the test vessel and ambient medium the temperature inside a thermally-controlled chamber was maintained equal to  $T_s$ . All experimental results were obtained for the steady state working conditions. In order to verify the reliability of the experimental data, a series of experiments with boiling on plain stainless steel and copper tubes were carried out in the past [6]. The subject of interest was the heat transfer coefficient as the function of the heat flux  $q$  at constant pressure.

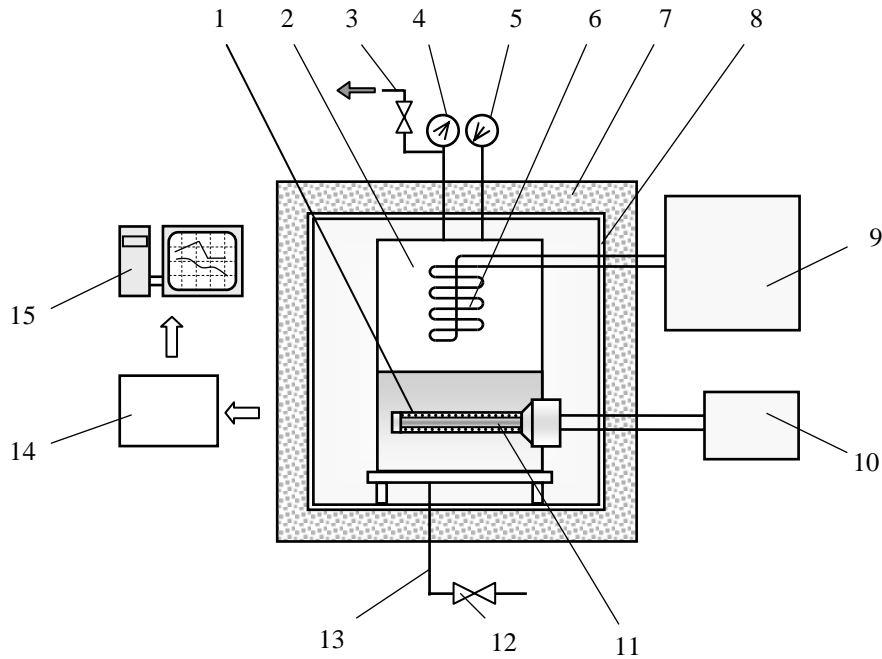


Fig. 2. Experimental set-up: 1 – annular mini-channel, 2 – vessel with the pool, 3 – exhaust system for non condensable gases, 4 – manometer, 5 – vacuum meter, 6 – condenser, 7 – thermal controlled box, 8 – liquid loop for temperature regulation of the guard thermal screen, 9 – cooling machine, 10 – power supply, 11 – cartridge heater, 12 – valve, 13 – liquid feeding system, 14 – data acquisition system, 15 – computer

The experimental setup was designed and made to investigate the thermal performance of different kinds of evaporators. A data acquisition system with a set of thermocouples and basement support with an optical system of sample space orientation was installed to transfer the information to a computer. To perform the tests at low temperatures, the thermal bath was supplied with an additional heat exchanger connected to two cooling machines. To cool down the isothermal guard screens (liquid loop) a Joulabo F12 recirculation thermal bath with temperature regulated accuracy of  $\pm 0.5$  °C was used.

The constant pressure inside the chamber was hold within narrow limits of error using temperature controlled condenser. The subject of analysis was the influence of fluid properties, boundary conditions at the liquid-gas interface, heating rate of the flow, nano-, micro- and mini-structure of the porous coating and its thermal conductivity on contact line-dominated flow dynamics and transport processes. The experimental techniques included the temperature field measurements of the sample, the measurement of porous layer thickness distribution along the channel and two-phase flow visualization. Experiments were performed at the heat flux range of  $10^2$ – $10^5$  W/m<sup>2</sup> on the heat loaded wall. The temperature of the guard screens was maintained constant with a maximum temperature deviation within 1.5 °C. The test vessel had three windows and a sleeve for thermocouples for visual observation and control of the process. All the temperature measurements were performed in a steady-state regime. The tube surface temperature was measured by copper-constantan thermocouples placed into narrow channels and covered by copper brackets. The temperature difference  $T_w - T_s$  between the sample  $T_w$  and the saturated temperature of the pool  $T_s$  was measured directly by four thermocouples, one junction of which was on the tube wall, the other was placed in the liquid. The saturation conditions were maintained by regulation of temperature and fluid flow through the condenser. The heat transfer coefficient was calculated as

$$h = q/\Delta T = q/(T_w - T_l). \quad (1)$$

### 1.1. Measurement Uncertainty

An Agilent 34970A data acquisition system was used to record all temperature measurements. This device has a resolution of 0.02 °C. The data acquisition unit and T-type thermocouples were compared to a precision digital resistance temperature device with a rated accuracy of 0.03 °C. The system accuracy is found to be within 0.2 °C over the range of interest. In the steady state, the readings of the thermocouples fluctuate within 0.2 °C. The uncertainty of the electrical power through the power analyzer is 0.5% of reading.

### 1.2. Working Fluid

Propane (R290) was chosen as a beneficial fluid for small heat pumps and heat pipes due to its good thermodynamic properties, low cost, availability, compatibility with constructional materials, and environmental friendliness [7]. The latest circumstance is very important because of the ozone depletion by chlorofluorocarbons (CFC) and hydrochlorofluorocarbons (HCFC). Some physical properties of propane at  $T_s = 20$  °C are given in Table 1 [7, 8].

Table 1. Propane Properties at  $T_s = 20$  °C

$\rho_l$ (kg/m <sup>3</sup> )	$\rho_g$ (kg/m <sup>3</sup> )	$\sigma \cdot 10^3$ (N/m <sup>2</sup> )	$p_s$ (bar)	$p_r = p_s/p_{cr}$
502	18.2	7.35	8.4	0.197

### 1.3. Porous Media as the Copper Tube Coating

A copper sintered powder wick was chosen as a system with open micro and macro pores (Figs. 3, 4). The capillary-porous coating was made by sintering the loose copper powder in argon with the specific equipment application. The parameters of the wick are presented in the Table 2.

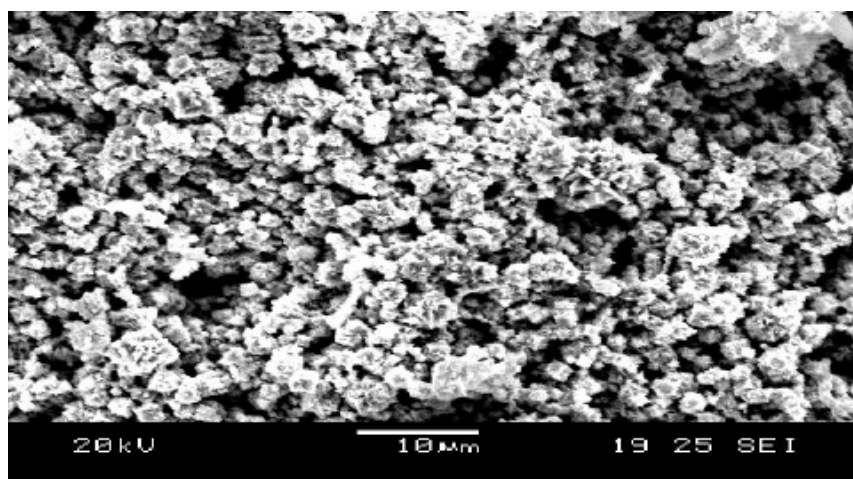


Fig. 3. Copper sintered powder coating on copper tube

Table 2. Characteristics of Sintered Copper Powder Porous Coatings

Porosity (%)	Particle Diameter ( $\mu\text{m}$ )	Mean Particle Size ( $\mu\text{m}$ )	Mean Pore Hydraulic Diameter ( $\mu\text{m}$ )	Coating Thickness (mm)
50–55	63–100	81.5	24.5	0.3

This wick is typical for copper heat pipes used for the electronic component cooling. The micro pores of the heat pipe evaporator are used as capillary channels for liquid transport to zones of evaporation (meniscus). The macro pores are used for radial vapor transport to mini-channel. The vapor is generated on the surfaces of menisci in the orifices of micro pores. The wick with open pores can be considered as a porous media in which a great number of micro heat pipes with zones of evaporation and condensation are active (Fig. 4).

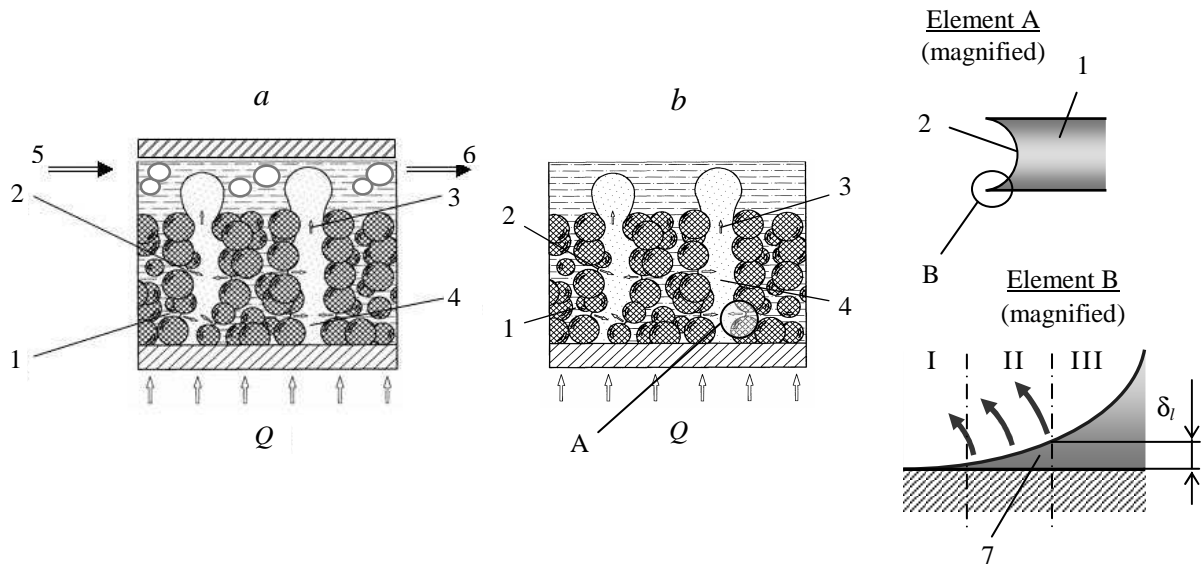


Fig. 4. The cross of the porous coating on the heat releasing wall: *a*) annular mini channel; *b*) liquid pool; 1 – micro pore, 2 – interface meniscus of evaporation, 3 – bubble, 4 – vapor stream, 5 – two-phase flow input in mini channel, 6 – two-phase flow output, 7 – three zones of evaporation on micro pore and macro pore interface: I – zone with adsorbed liquid film, II – zone of high intensity evaporation, III – zone with high resistance of liquid film

It means that a rise of the heat flux may occur following only a slight increasing of the wall temperature due to the super high effective thermal conductivity of the wick. In such a wick the bubble formation is realized in a very short time. A vapor bubble arrives immediately after the previous bubble detachment from the wick. The diameter of the bubble is restricted by the macro pore diameter. The distribution of pores is such that the pores are disposed close to each other. This pore distribution stimulates the heat transfer from the wall to the liquid, and the heat is consumed mostly by vapor generation, Fig. 4. Inside the wick high intensity of vapor generation (evaporation) occurs in zone II of meniscus 2 (transition zone). The liquid film thickness in zone I is close to the size of a molecular sorption film (adsorbed film), and there are no favorable conditions for evaporation. In zone III (intrinsic meniscus zone), a liquid film is too thick to be influenced by the liquid-solid interactions, its thermal resistance is many times higher than in zone II. There are a great number of such menisci over the volume of a porous medium, so the total surface of evaporation is very high. There are two limitations for the heat transfer intensity in such a porous body: the hydrodynamic ability of micro pores to transport liquid and a finite number of evaporation zones (curvilinear menisci in the orifices of micro pores). It is known that the heat transfer intensity depends on the curvature  $K$  of menisci. Since the curvature  $K$  does not exceed some value  $K_{max}$ , the capillary suction of liquid is good. When the curvature of a meniscus rises to  $K > K_{max}$ , the drainage of the heated surface begins. After a certain value of the heat flux  $q_{max}$  is reached, the menisci of evaporation moves inside the micro pores, the meniscus curvature  $K$  increases and exceeds  $K_{max}$ . Consequently, “dry spots” appear and spread over the entire surface. The liquid interface becomes lower; the heat transfer coefficient is decreasing.

## 2. THE MODELING OF THE HEAT TRANSFER IN THE POROUS COATING

It is known that porous wick enhances the boiling process by providing many more nucleation sites than in plane boiling. Unlike the heat transfer with boiling on the smooth surface the liquid boiling/evaporation on the porous deposit (like copper sintered powder, or aluminum oxide nanoparticles coating) is characterized by the constant sources of nucleation. It is due to the limited number of evaporation menisci inside the porous wick. In porous coatings the liquid/vapor interface consists of menisci situated inside the macropores and numerous menisci between macro and micropores. The menisci of the evaporation disposed on macropore interface liquid/vapor are typical for low value of heat flux, when the wick is completely saturated with liquid. For low heat fluxes the heat transfer is realized by conduction through the wick. The menisci of the evaporation in micropores are typical for the case, when the menisci in macropores recede and are open for the vapor flow. For such a case many nucleation sites (micro menisci exist on the interface between macro and micropores), are becoming the centers of vapor generation inside the macropore, Fig. 4. There are two possibilities for heat transfer:

1. If the liquid is subcooled, the vapor condenses on the interface vapor/liquid in macropores (micro heat pipe phenomena). The vapor sphere on the macropore output is stable, disposed above the wick surface as is serving as the heat pipe condenser (vapor spheres on the wick surface, Fig. 4 *b*). The liquid is sucked through micropores to the heat loaded zone of the wick. The heat transfer is a steady state.

2. If the liquid is saturated the vapor streams (jets) are escaping from macropores and interacting with the liquid film (micro heat pipe open type). Vapor jets initiate the additional turbulence of the two-phase flow and enhance the heat transfer in the channel.

3. If the liquid film is thin, the vapor can escape the wick and vapor jet push the liquid toward the mini channel exit serving as micro compressor.

$$q = \frac{T_w - T_v}{\frac{\delta_w}{k_{ef}} + \frac{1}{h_e}}, \quad (2)$$

where  $T_w - T_v = \Delta T_t$  and is determined as

$$\Delta T_t = T_w - T_v = \frac{2\sigma T_v}{h_v \rho} \left( \frac{1}{r_v} - \frac{1}{r} \right). \quad (3)$$

The heat flux due to the liquid phase change in the wick pores can be calculated as [9]

$$q = \frac{\frac{2\sigma \cos \Theta_{\min}}{R_p} - \rho_l g L \sin \varphi}{\left( \frac{\mu_l}{\rho_l K A_w} + \frac{1}{N_{\max}} \frac{8\mu_v \delta_w}{\rho_v r_v^4 L} \right) \frac{L A_e}{r^*}}. \quad (4)$$

The effective thermal conductivity of porous systems is the subject of interest since last two centuries. By now numerous experimental materials has been accumulated and a lot of formulae have been proposed to calculate the effective thermal conductivity of porous systems [10].

The elementary cell of the wick and a diagram of its thermal resistances are shown in Fig. 5.

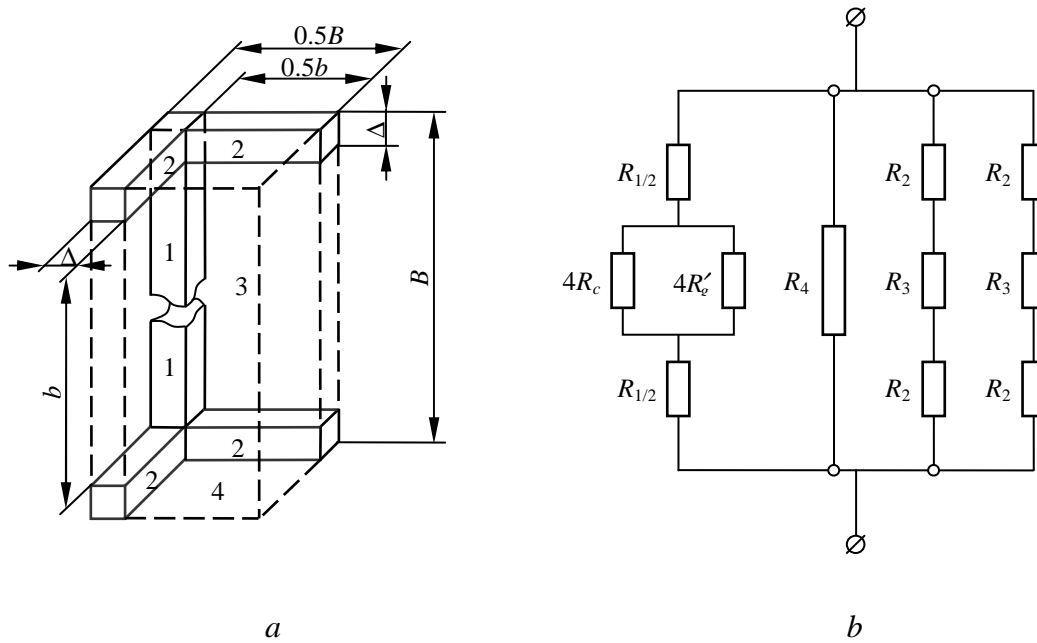


Fig. 5. One quarter of the porous coating elementary cell (a) and a diagram of its thermal resistances (b)

The effective thermal conductivity of the wick (copper sintered powder) is calculated as

$$\frac{k_{ef}}{k_s} = \frac{1}{\frac{1}{(h/B)^2 + A}} + v_g (1-B)^2 + \frac{2}{1 + s/b + \frac{1}{v_g (s/b)}}, \quad (5)$$

where

$$A = \frac{1}{\frac{k_c}{k_s} + \frac{v'_g}{4k_k k_m} \left(\frac{s}{B}\right)^2 \cdot 10^3}, \quad B = b + s, \quad s = 2\Delta.$$

The equations (2)–(5) were used to calculate the porous coating thermal resistance, when the pores were completely filled with liquid (low values of heat flux –  $q = 500\text{--}1500 \text{ W/m}^2$ ) and to compare the calculated data with experimental one. The obtained results were close to each other ( $R_{cal} = 3.2 \cdot 10^{-3} \text{ m}^2 \text{ K/W}$ ;  $R_{exp} = 4 \cdot 10^{-3} \text{ m}^2 \text{ K/W}$ ). When the front of the evaporation was penetrated inside the porous structure due to the heat flux increasing up to  $3500\text{--}70000 \text{ W/m}^2$ , the sharp decreasing of the porous structure thermal resistance  $R_{exp}$  was found ( $R_{exp} = 1.4 \cdot 10^{-4} \text{ m}^2 \text{ K/W}$ ).

### 3. EXPERIMENTAL RESULTS

Within the frame of the program two sets of experiments were done. The first one was performed to compare the hydrodynamics and heat transfer for tested sample (heat loaded tube) disposed inside the liquid pool (macro scale heat transfer), Figs. 6 and 7 a. The second set of experiments was done with annular mini-channel, Figs. 6 c and 7 b, c. To visualize the hydrodynamics of the process transparent glass tube was fixed over the copper tube.

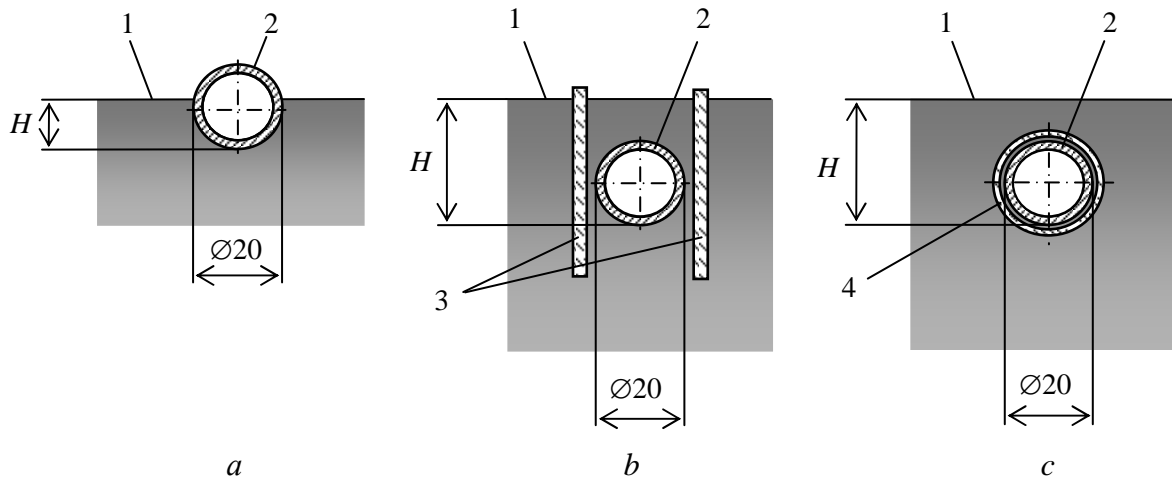


Fig. 6. The cross section of the copper tube: 1 – liquid interface of the pool, 2 – tested tube, 3 – vertical plates, 4 – glass tube. Different height  $H$  of the pool: a) copper tube in the pool, b) copper tube in the pool between two transparent vertical plates, c) copper tube inside the glass tube

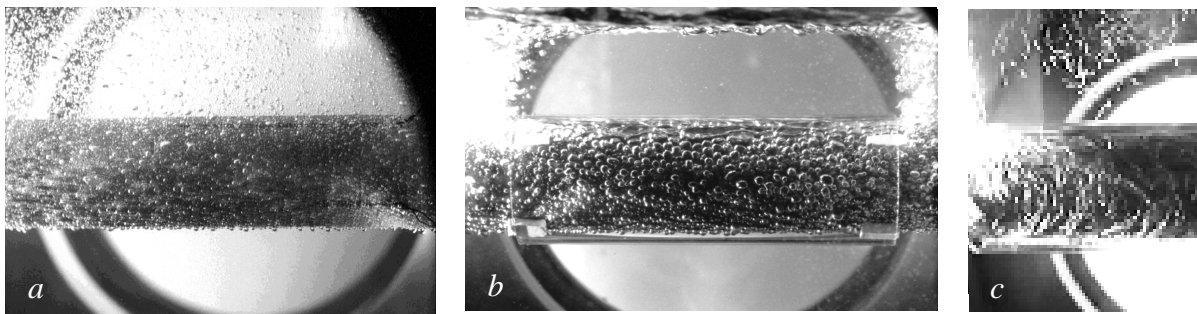


Fig. 7. The generation of vapor bubbles: a) nucleation sites on the copper tube with copper sintered powder coating, placed in the pool; b) nucleation sites on the same copper tube, placed inside the glass tube (annular mini-channel); c) the traces of the vapor streams from macro pores of the tube in the annular mini-channel

The distance between glass tube and copper tube was 1.8 mm. This thickness of the annular mini channel (widths) is close to the capillary constant  $\kappa$ :

$$\kappa = [2\sigma/(\rho_l - \rho_v)g]^{1/2}. \quad (6)$$

For propane the capillary constant is equal 1.8 mm and the influence of capillary forces on the process is substantial. The propane saturation temperature is  $T_s = 20\text{ }^\circ\text{C}$  ( $p_s = 8.4\text{ bar}$ ). The heat transfer intensity of the porous tube placed in a liquid pool or inside the annular mini channel at different heights of the liquid interface  $H$  is shown on Figs. 8, 9. The heat flux versus the temperature drop  $\Delta T = T_w - T_s$  is shown on Fig. 10. The heat transfer between the tube and liquid was investigated at different heights of  $H$ . This liquid height  $H$  was varied from 75 to 5 mm above the tube lower generatrix.

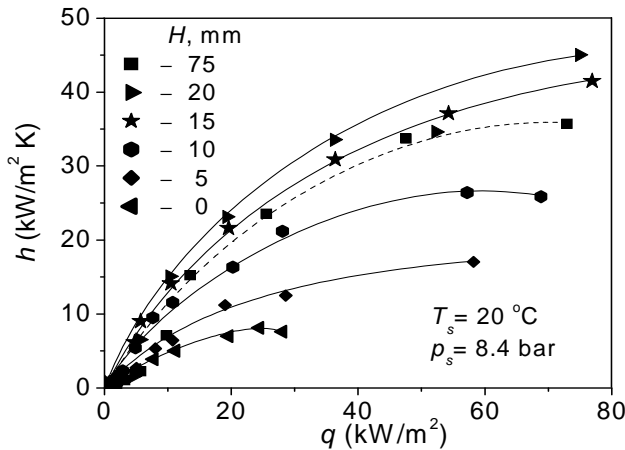


Fig. 8. Heat transfer coefficient versus heat flux for different heights of the liquid interface  $H$  (copper tube in the pool)

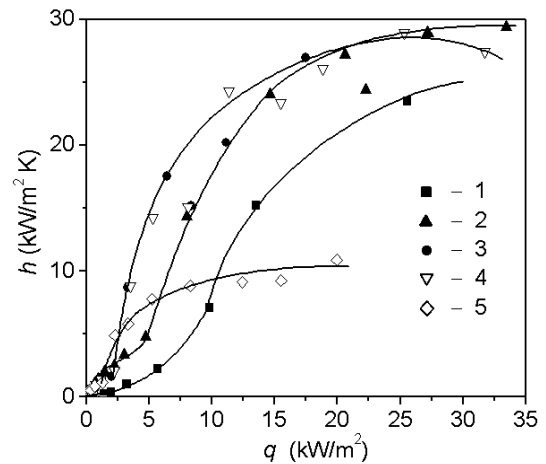


Fig. 9. Heat transfer of porous tube placed in a liquid pool and inside the annular mini channel at different liquid interface  $H$ : 1) liquid pool,  $H = 75 \text{ mm}$ ; 2–5) annular mini channel,  $H = 75, 20, 15, \text{ and } 10 \text{ mm}$

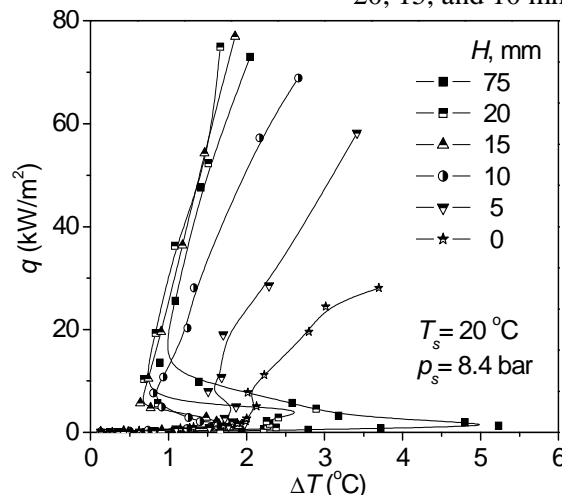


Fig. 10. Heat flux versus the temperature drop  $\Delta T$  between the surface of the tube  $T_w$  and the temperature of saturated liquid  $T_s$  in the vessel for different  $H$

### 3.1. Heat Transfer in a Liquid Pool

When the tests of the porous tube were performed in the pool, Fig. 7 *a*, the tested sample (copper tube with porous deposit) was completely immersed in the liquid. To analyze the specific features of heat transfer of the copper tube in the pool experiments were carried out at various positions of  $H$ , Figs. 6, 7. The results of measurements are shown in Fig. 8. Following the definition of the efficient boiling surface [11], to keep the temperature difference ( $\Delta T = T_w - T_{loc}$ ) constant all the cavities (macro pores) of the porous coating must have the same radii; it means we have a mono-cavity pattern.

The thermodynamic superheat of the wall corresponding to this cavity pattern is the same for the whole surface. All macro pores in the porous coating of the tube are expected to become activated simultaneously at the same superheat, Fig. 7 *a, b*. As the vapor generation mainly occurs at the three-phase line (TPL, liquid, solid, vapor), the wall superheat remains unchanged, whereas the heat flux increases, Fig. 10.

Analyzing the behavior of the  $q$  versus  $\Delta T$  we can conclude, that the heat flux increasing is possible with only slight increasing of  $\Delta T$ . It means that the number of vapor generating sites (vapor jets) inside the porous media (active macropores of the same diameter) is proportional to the heat flux value. The heat flux is increasing the new sites of vapor generation are activated. In such a case the main contribution to the heat transfer intensity of the tube is related with the liquid evaporation inside the wick. The efficiency of heat

transfer during liquid evaporation in the sintered powder wick with open pores is up to 6–8 times higher than the boiling heat transfer efficiency on a smooth tube. The heat flux value is up to  $q = 100 \text{ kW/m}^2$  [12].

### 3.2. Heat Transfer of a Partially Flooded Tube in a Liquid Pool

When the tested sample is partially immersed in the liquid pool (partially flooded), Fig. 6 *a*, the heat transfer coefficient consist of two parts – heat transfer with evaporation from the upper part of the sample (the vapor part of the vessel) and heat transfer with vapor microjets generation inside macropores into the pool from the lower part of the sample. These microjets are intensely interacting with the liquid pool. An additional increase of heat transfer coefficient in a certain range of heat flux was found for a partially flooded tube, Fig. 8 to compare with a tube completely immersed in the liquid pool. The experimental data obtained on flooded ( $H = 75 \text{ mm}$ ) or partially flooded ( $H = 20, 15, 10, 5 \text{ mm}$ ) samples show the sufficient difference. For low heat fluxes the influence of the height  $H$  of the liquid interface above a porous coating is important at  $H$  less than 2 mm. A decrease in  $H$  by a quarter of the tube diameter promotes significant increase of the mean heat transfer coefficient at low and moderate heat fluxes  $q < 100 \text{ kW/m}^2$ . The data of temperature heads  $\Delta T$  between the heat releasing surface and liquid pool temperatures  $\Delta T = T_w - T_l$  in various zones of porous tube shows that it occurs due to the  $\Delta T$  decrease on the unflooded part of the tube. More efficient heat transfer in this part of the sample is obvious. It can be explained in the following way. It is not boiling, but rather evaporative heat transfer mechanism which occurs in open pores structure with capillary transport of liquid through micro pores from the liquid pool to the heated zone and vapor output through the macropores. The hydrodynamic conditions for vapor release through the macro pores of a sample are better for the flood-free part of the porous tube as compared to a completely flooded tube. Direct heat transfer can occur by evaporation at the existing vapor – liquid interface that interacts with the heating surface (TPL). This phenomenon is operative and dominant for open type porous media when the micro pores are contacting with macro pores (vapor channels) inside the porous structure, Fig. 4.

### 3.3. Evaporation Heat Transfer in an Annular Mini Channel

An approximate physical criterion for the macro-to-micro scale threshold diameter [13] is based on the confinement effects on the bubble geometry within a channel. According to them, for hydraulic diameters smaller than the threshold value  $D_{th}$ , the macroscopic laws fail to predict either the heat transfer coefficient or flow pattern transitions, where  $D_{th}$  is given by

$$D_{th} = [4\sigma/g(\rho_l - \rho_v)]^{1/2}. \quad (7)$$

Usually this hydraulic diameter is smaller than 3 mm for mini channels and 200  $\mu\text{m}$  for microchannels [14]. In our experiments, a sample was placed inside a transparent glass tube organizing an annular mini channel with its thickness 1.8 mm (Fig. 6). Visual observation of the process showed that the motion of vapor bubbles in an annular mini channel has a complicated behavior. At low and moderate heat fluxes ( $< 100 \text{ kW/m}^2$ ) the micro heat pipe effect is observed in the pores accompanied by two-phase forced convection in the annular mini channel, including the Marangoni convection, Fig. 7. Vapor jets move not only perpendicularly to the surface of the sample but also form a swing two-phase flow along a tube axis from the inlet (bottom) of the glass tube toward its outlet (the upper part) before the jets reach the liquid pool (Fig. 7). This 2D mode of heat transfer (internal and external) increases the value of the total heat transfer coefficient nearly 10 times against boiling heat transfer on a plain tube in a liquid pool. The convective two-phase heat transfer in the annular channel is summed up with the heat transfer inside the porous media. The flow boiling in a conventional channel or small-diameter tubes was considered by Mikielewicz et al. [15] as:

$$h_{tot} = Sh_b + Fh_c, \quad (9)$$

where  $S$  and  $F$  reflect the influence of the vapor flow rate on forced convection and vapor quality on heat transfer.

So the total heat transfer intensity on the same sample at moderate heat flows was higher in mini channel than in the liquid pool. But in our case, forced convection was not caused by mechanical pumping.

The bubbles generated inside the porous media as micro compressors push two-phase flow along the channel. At high heat fluxes the problems with the vapor friction in the annular mini channel limit the hydrodynamic efficiency and heat transfer intensity.

### 3.4. Heat Transfer in Partly Flooded Annular Mini Channel

For partly flooded mini channel the heat transfer coefficient was found to be dependent on the position of the liquid/vapor interface inside the glass tube. It was the highest, when the interface position ( $H = 15\text{--}20$  mm) was accompanied by partial flooding of the tube. The mean heat transfer rate in the annular channel was highest in comparison with the heat transfer rate in the pool, or confined space between two vertical plates (flat channel), Fig. 6. However, it is important to note that the positive effect in the annular mini channel was achieved without active regulation and control of the flow in a system (no mechanical pumping).

The lowering of the liquid interface  $H$  in the annular mini channel, Fig. 9, to a quarter of the sample diameter contributed to further increase in the heat transfer coefficient. The decrease in the superheating and increase of the local heat transfer coefficient was noted on the part of tube disposed above the liquid interface of the pool, Figs. 9, 10. With further lowering of the liquid interface  $H$ , the system of capillaries stop to provide a sufficient amount of liquid to the upper part of the porous coating, Fig. 11 *c*, and a sharp decrease in the heat transfer intensity is inevitable due to the vapor blanket arrival inside the porous coating.

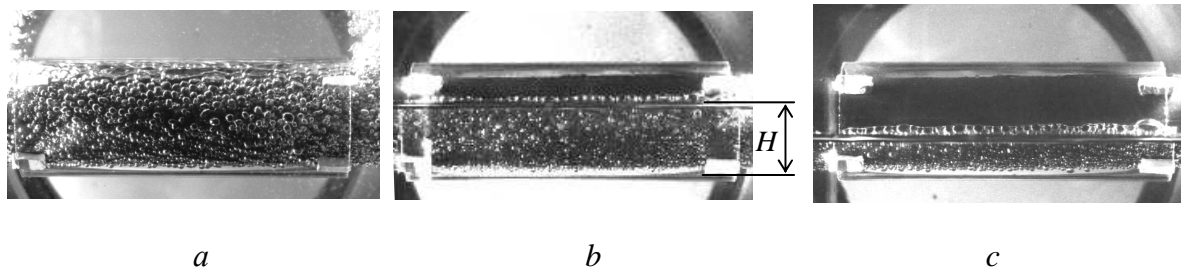


Fig. 11. Annular mini channel with partially flooded copper tube with porous deposit on its surface:  $H = 75$  mm (*a*), 15 (*b*), 5 (*c*)

So, step-by-step the investigation of heat transfer on a porous heat-loaded wall was useful in determining the optimal conditions for intense heat transfer. The data of the heat transfer intensity obtained on flooded and partially flooded horizontal copper tube with porous deposit inside annular mini channel testify the micro heat pipe phenomena in the porous coating, which ensures the temperature field uniformity inside the porous media and along the mini channel. A micro scale effect took place inside a porous body, and a mini scale effect is available in the flat and annular mini channels. Visual analysis and experimental validation show that mini/micro porous coating on the heat-loaded wall is useful to enhance heat transfer (2.5–3 times) to compare with the heat transfer of the same tube with plain walls inside the flat and annular mini channels and completely modify the hydrodynamics of a two-phase flow.

Fig. 12 summaries of the heat transfer coefficient versus the heat flow for various positions of the porous tube at fixed height of the liquid interface ( $H = 75$  mm) for three cases: 1) the tube is in the liquid pool, 2) the tube is between vertical plates (flat mini gap), 3) the tube is in annular mini channel. The data of the heat transfer coefficient versus the heat flow for the plain copper from the one side, and the steel tube with the gas-plasma sprayed stainless steel coating on the other side disposed inside the pool with liquid propane are also available. For the reasons of comparison there are also the data of a propane pool boiling heat transfer on the integral-fin tube with modified Gewa-T-x type fins to form re-entrant grooves [16] and of R12 heat transfer with boiling in a mini channel [17]. The results presented in the Fig. 12 show that the heat transfer coefficient in mini channel with porous coating is nearly 8-10 times higher than pool boiling heat transfer on a smooth horizontal tube and up to 2 times higher than the heat transfer on the tubes with Gewa-T-x type surface.

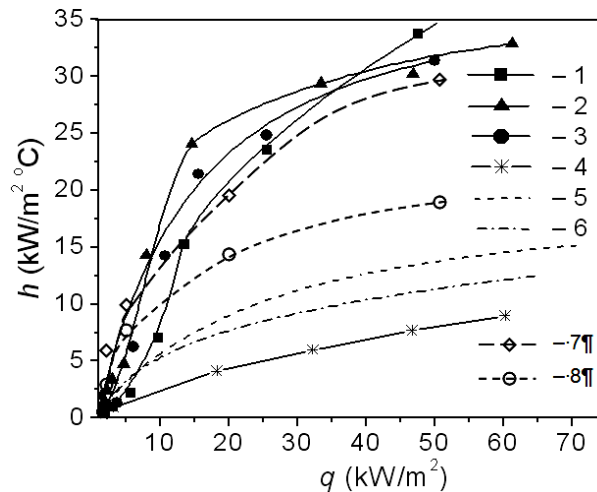


Fig. 12. Heat transfer data: horizontal copper tube with porous deposit on its surface, 1 – liquid pool, 2 – annular mini-channel, 3 – flat mini gaps; 4 – horizontal plain tube disposed in the pool, 5 – tube with a gas-plasma sprayed stainless steel coating, 6 – boiling flow of R12 in a mini channel [17], 7 – and 8 – propane pool boiling on the tube with modified Gewa-T-x type fins surface at  $T_s = 49,9$  and  $9.3$  °C correspondingly [16]

### 3.5. Grooved Mini-Channels with Porous Coating

The main aim of the experiments with ammonia is to improve the cooling capability of the grooved heat pipes (GHP) with  $\Omega$  shape grooves, applying thin (nano particles) deposit (25–100  $\mu\text{m}$ ) on the surface of the mini fins inside the heat pipe evaporator, Fig. 13. In the present study two similar GHPs with  $\Omega$  shape grooves, were tested simultaneously. One GHP has grooves with smooth surface. Another GHP has porous layer on the grooves surface. The experimental part was devoted to validate by experimentally the role of porous layer in the improvement of evaporation efficiency within grooves. Therefore the present experimental plan was related with the determination of  $\Delta T_{e/v}(Q)$ ,  $R_{e/v}(Q)$ ,  $R_{v/c}(Q)$  at the fixed temperatures in adiabatic zones for both GHPs. Here  $\Delta T_{e/v}$  is the temperature difference between mean temperature of evaporator and the vapor temperature in the middle of the adiabatic zone, while  $R_{e/v} = \Delta T_{e/v}/Q$  and  $R_{v/c} = \Delta T_{v/c}/Q$ . Seven different adiabatic temperature levels  $T_v$  were chosen namely  $-30$ ,  $-10$ ,  $0$ ,  $10$ ,  $40$ ,  $50$ ,  $80$  °C for the comparable tests. Both heat pipes were tested at the same time on the same experimental set-up in Luikov Heat and Mass Transfer Institute, Minsk. GHPs with porous layer and classical one were tested in the vapor temperatures diapason between  $-30$  and  $+70$  °C. It was found, that for all vapor temperatures the evaporator thermal resistances ( $R_{e/v}$ ) of GHP with porous layer is low to compare with  $R_{e/v}$  for classical GHP, Fig. 14. The difference in thermal resistances is between 1.3 and 1.8 times (or 0.015–0.02 K/W for GHP with porous layer and 0.025–0.035 K/W for classical one). The practical application of GHP with porous layer in the evaporator and classical condenser is alternative to conventional grooved heat pipes and heat exchangers.

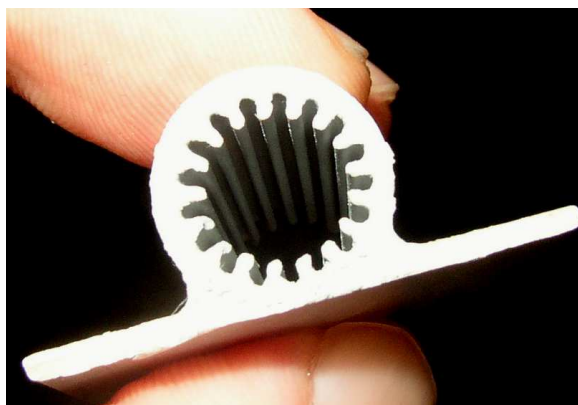


Fig. 13. Cross section of the grooved heat pipe with nano porous deposit on mini grooves

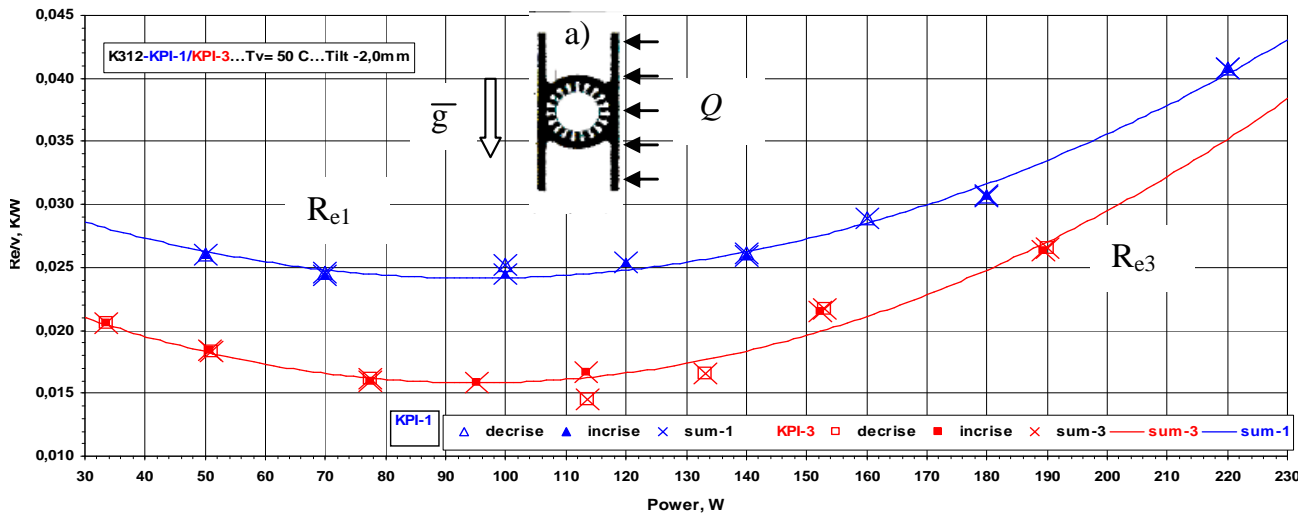


Fig. 14. Thermal resistance  $R_{e/v} = (T_e - T_v)/Q$  of evaporators.  $R_{e1}$  – thermal resistance of classical GHP evaporator,  $R_{e3}$  – thermal resistance of GHP evaporator with porous layer 50  $\mu\text{m}$ . Vapour temperature is 50  $^{\circ}\text{C}$ ,  $L_e = 0.2$  m,  $L_{HP} = 1$  m; a – GHP cross section

#### 4. CONCLUSIONS

1. The mini heat exchanger with thin copper sintered powder structure has completely different hydrodynamic and heat transfer behavior to compare with gas-plasma sprayed stainless steel coating with pores closed type, or tube with mini fines disposed in the pool, or in mini channels.

2. A thin copper sintered powder structure with micro and macro pores open type ensures the micro heat pipe phenomena in the wick and stimulates the evaporative heat transfer in mini channels. The heat transfer coefficient in mini channel with such porous coating is nearly 8–10 times higher than pool boiling heat transfer on a smooth horizontal tube, and up to 2 times higher than on the integral-fin tubes with modified fins to form re-entrant grooves (propane).

3. By reducing the size of the cooling system we increase its efficiency, improve the system performance by adding a micro scale function (micro heat pipe effect) to macro scale engineering application.

4. With stable propane bubble generation on a thin (0.3 mm) porous surface of the heat releasing tube stimulates the Marangoni convection and enhances heat transfer 2–3 times as compared to the same tube heat transfer in a liquid pool without additional power supply (no mechanical pumping).

5. The practical application of GHP with porous layer in the evaporator and classical condenser is alternative to conventional GHPs. Proposed method of evaporator heat transfer enhancing is perspective for mini grooves heat exchangers.

#### Nomenclature

$A$  – complex;  $B$  – characteristic size of an elementary cell (particle diameter),  $\mu\text{m}$ ;  $b$  – characteristic size of a pore,  $\mu\text{m}$ ;  $D$  – diameter, mm;  $F$  – coefficient, non-dimensional;  $g$  – gravitational constant,  $\text{m/s}^2$ ;  $H$  – height, mm;  $h$  – heat transfer coefficient,  $\text{W}/(\text{m}^2\cdot\text{K})$ ;  $h_{lv}$  – heat of evaporation,  $\text{kJ/kg}$ ;  $K$  – curvature,  $\text{mm}^{-1}$ ;  $k$  – thermal conductivity,  $\text{W}/(\text{m}\cdot\text{K})$ ;  $L$  – length, mm;  $n$  – coefficient ( $n = 1$  for a spherical pore);  $p$  – pressure, bar;  $q$  – heat flux,  $\text{W}/\text{m}^2$ ;  $R$  – thermal resistance,  $\text{K/W}$ ;  $S$  – coefficient, non-dimensional;  $T$  – temperature,  $^{\circ}\text{C}$ ;  $v$  – mass flow coefficient;  $\delta$  – thickness, mm;  $\kappa$  – capillary constant, mm;  $\mu$  – dynamic viscosity,  $\text{N}\cdot\text{s}/\text{m}^2$ ;  $\lambda$  – thermal conductivity,  $\text{W}/(\text{m}\cdot\text{K})$ ;  $\Theta$  – contact angle, degree;  $\rho$  – mass density,  $\text{kg}/\text{m}^3$ ;  $\sigma$  – surface tension coefficient,  $\text{N/m}$ ;  $\varphi$  – angle of inclination, degree;  $\Delta T$  – temperature difference,  $^{\circ}\text{C}$ .  
Subscripts:  $b$  – boiling,  $c$  – convection,  $cal$  – calculated,  $cr$  – critical,  $e$  – evaporation,  $ef$  – effective,  $exp$  – experimental,  $g$  – gas,  $in$  – inner,  $l$  – liquid,  $r$  – reduced,  $s$  – saturation,  $th$  – threshold,  $tot$  – total,  $v$  – vapour,  $w$  – wall.

### References

1. Ohadi M., Qi J. Thermal management of harsh-environment electronics: *Microscale Heat Transfer, Fundamentals and Applications, NATO Science Series. II. Mathematics, Physics and Chemistry*. Vol. 193 / Eds. S. Kakaç, L. Vasiliev, Y. Bayazitoglu, Y. Yener, Springer, Dordrecht, The Netherlands, 2005. Pp. 479–498.
2. Ramstorfer F., Steiner H., Brenn G., Korrmann C., Rammer, F. Subcooled boiling flow heat transfer from plain and enhanced surfaces in automotive applications // *J. Heat Transfer*. 2008. Vol. 130. Pp. 1–10.
3. North M., Rosenfeld J.H., Shaubach R.M. Liquid film evaporation from bidispersed capillary wicks in heat pipe evaporators // *Proc. of IX Intern. Heat Pipe Conf., Albuquerque, New Mexico, USA*. 1995. Vol. 1. Pp. 143–147.
4. Kotthoff S., Gorenflo D. Pool boiling heat transfer to hydrocarbons and ammonia: a state-of-the-art review // *Int. J. Refrigeration*. 2008. Vol. 32. Pp. 573–602.
5. Thome J. R., Cheng L., Ribatski G., Vales L.F. Flow boiling of ammonia and hydrocarbons: a state-of-the-art review // *Int. J. Refrigeration*. 2008. Vol. 32. Pp. 603–620.
6. Vasiliev L., Zhuravlyov A., Shapovalov A., Litvinenko V. Vaporization heat transfer in porous wicks of evaporators // *Arch. Thermodynamics*. 2004. Vol. 25, No. 3. Pp. 47–59.
7. Palm B. Hydrocarbons as refrigerants in small heat pump and refrigeration systems – a review // *Int. J. Refrigeration*. 2008. Vol. 32. Pp. 552–563.
8. *Heat Exchanger Design Handbook*. Vol. 2, Part 5, Hemisphere Publishing Corporation, New York – Washington D. C. 1983.
9. Reay D., Kew P. *Heat Pipes: Theory, Design and Applications*, Batterworth, Heinmann, 2006.
10. Luikov A. V., Shashkov A. G., Vasiliev L. L., Fraiman Yu. E. Thermal Conductivity of Porous Systems // *Int. J. Heat Mass Transfer*. 1968. Vol. 11. Pp. 117–140.
11. Mitrovič, J. How to create an efficient surface for nucleate boiling? // *Int. J. Thermal Sci*. 2006. Vol. 45. Pp. 1–15.
12. Vasiliev L., Zhuravlyov A., Novikov M., Vasiliev L., Jr. Heat transfer with propane evaporation from a porous wick of heat pipe // *J. Porous Media*. 2001. Vol. 4, No. 2. Pp. 103–111.
13. Kew P. A., Cornwell K. Correlations for the prediction of boiling heat transfer in small-diameter channels // *Appl. Thermal Eng.* 1997. Vol. 17. Pp. 705–715.
14. Thome J. R., Ribatski G. State-of-the-art of two-phase flow and flow boiling heat transfer and pressure drop of CO<sub>2</sub> in macro- and micro-channels // *Refrigeration*. 2005. Vol. 28. Pp. 1149–1168.
15. Mikielwicz D., Mikielwicz J., Białas-Tasmar J., Klugmann M. A semi-empirical method for calculation of flow boiling heat transfer coefficients for conventional channels and small diameter tubes // *HTRSE-2006. Proc. of XI Intern. Symp. "Heat Transfer and Renewable Sources of Energy", Szczecin – Międzyzdroje, Poland*. 2006. Pp. 591–598.
16. Gorenflo D., Blein P., Rott W., Schömann H., Sokol P. Pool boiling heat transfer from a Gewa-T-x finned tube to propane and propylene // *Proc. Inernt. Seminar EURO THERM No. 8 "Advances in Pool Boiling Heat Transfer," Paderborn, FRG*, 1989. Pp. 116–126.
17. Kuznetsov V. V., Shamirzaev A. S., Ershov I. N. Flow boiling heat transfer and regimes of upward flow in minichannels // *Proc. of 3rd Intern. Symp. on Two-Phase Flow Modelling and Experimentation, Pisa, Italy*, 2004. Vol. I. Pp. 305–312.

## TWO-PHASE LOOP THERMOSYPHONS

Yury F. Maydanik, Valery I. Dmitrin, Vladimir G. Pastukhov

Institute of Thermal Physics, Ural Branch of RAS,  
620016, Ekaterinburg, Amundsen St., 106  
Tel: +7 (343) 267-87-91 Fax: +7 (343) 267-87-99  
e-mail: maikanik@etel.ru

### Abstract

The paper presents the results of development and investigation of two-phase loop thermosyphons with different working fluids operating in the temperature range from 40 to 150 °C at heat loads from 10 to 3000 W and also various heat-transfer devices created on their basis.

### KEYWORDS

Loop thermosyphon, heat transfer, cooling system, heating system, evaporation, condensation.

### INTRODUCTION

Among two-phase heat-transfer devices, such as heat pipes [1], loop heat pipes [2], oscillating heat pipes [3] and thermosyphons [4], the last ones are the simplest both in design and manufacture and for the description of thermophysical and hydrodynamic processes observed in them. At the same time two-phase thermosyphons (TS) are efficient enough heat-transfer devices, which may be used both for heat transfer in heating and heat-supply systems and for cooling various devices, including electronics. These devices may be separated into two main types: conventional thermosyphons and loop thermosyphons (LTS) [5–14].

The schematic diagram of these devices is presented in Fig. 1.

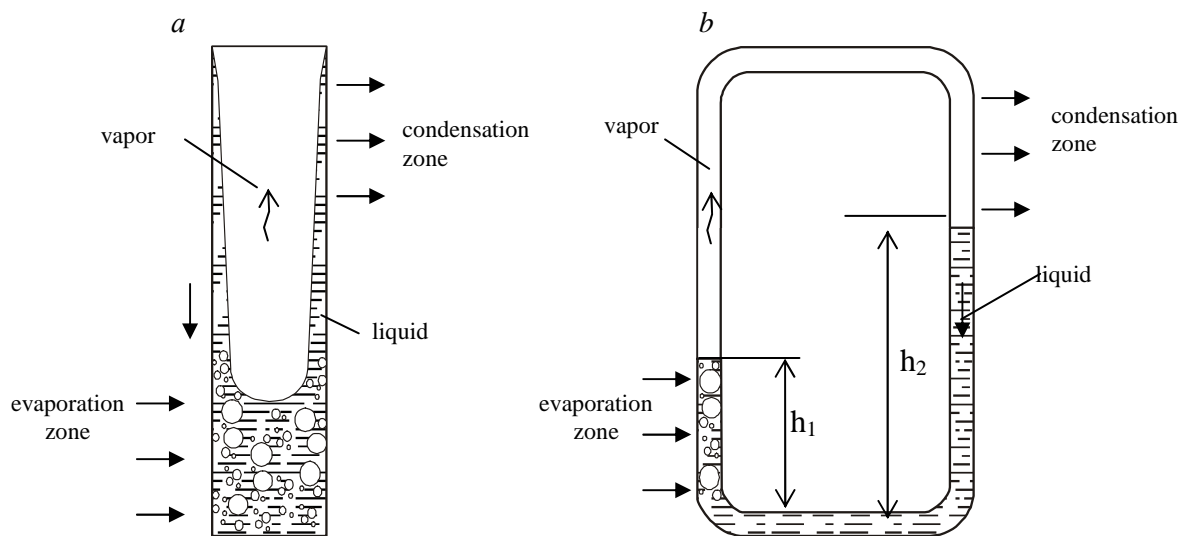


Fig. 1. Schematic diagram of two-phase thermosyphons:  
*a* – conventional thermosyphon, *b* – loop thermosyphon

A conventional thermosyphon consists of a vacuum-sealed pipe, which is partially filled with a working fluid in the vapor and liquid phase. The volume fraction of the liquid phase of the working fluid in a TS is usually 30–50%. When heat is supplied to the evaporation zone, the liquid begins to boil. The beginning of boiling is, as a rule, preceded by a certain superheating, whose magnitude is determined by the thermal properties of the working fluid. The vapor generated in this case rushes into the condensation zone, where it

condenses and passes the heat through the condenser wall to an external heat sink. The motions of the liquid and the vapor phase of the working fluid are countercurrent to each other. The upward current of vapor moves along the pipe axis from the evaporation zone, where the pressure is higher, into the condensation zone, where the pressure is lower. The downward current of the condensate in the form of a film flowing down over the inner surface of the pipe returns into the evaporation zone under the action of gravity forces. This circumstance leads to a limitation on the TS heat-transfer capacity owing to an additional hydrodynamic resistance resulting from the viscous interaction between the counter flows of vapor and liquid, which increases with an increase in the heat load, and also a decrease in the diameter and an increase in the device length.

The problem mentioned may be solved by using the loop scheme presented in Fig. 1, *b*. The first information about realization of this scheme in this device under the name of "evaporation-condensational apparatus", designed for electronics cooling, related to 1967 [5]. The fundamental difference of such a scheme consists in the fact that the motion of vapor and liquid flows here proceeds in different pipelines separated spatially. This makes it possible to avoid a negative hydrodynamic and thermal interaction between the opposite flows of the vapor and liquid phases of the working fluid.

When heat is supplied to the evaporation zone, the vapor speeds into the condensation zone, where it condenses and gives up heat to an external heat sink. The condensate returns into the evaporation zone through the liquid line under the action of the hydrostatic pressure  $\Delta P_g$  arising from the difference of the liquid levels in the evaporation and condensation zones:

$$\Delta P_g = (\rho_l - \rho_v) \cdot g(h_2 - h_1), \quad (1)$$

where  $\rho_l$  and  $\rho_v$  are the liquid and vapor densities, respectively;  $h_1$  and  $h_2$  are the heights of the liquid levels;  $g$  is the free fall acceleration.

Thus the return of the condensate into the evaporator in both a conventional and a loop thermosyphon is realized under the action of gravity forces. Hence follows the obligatory condition of serviceability of these devices which requires that the "vapor-liquid" interface in the condenser be higher than such an interface in the evaporation by  $\Delta h = h_2 - h_1$ .

In this case it is necessary to fulfill the condition:

$$\Delta P_g = \Delta P_v + \Delta P_l, \quad (2)$$

where  $\Delta P_v$  is the pressure losses for the motion of vapor;  $\Delta P_l$  is the pressure losses for the liquid motion. The LTS serviceability in this case may be retained in a sufficiently wide range of slopes towards a horizontal plane, as pressure losses in this adiabatic zone are considerably lower.

Among additional advantages of LTS is the possibility to use flexible pipelines connecting evaporation and condensation zones, which may have relatively small diameters. This allows simplifying considerably their tracing during the location of LTS in various objects. Besides, there appears a possibility of different embodiments of evaporation and condensation zones, which may be made in the form of separate elements - evaporator and condenser - specially adapted to the conditions of heat load supply and removal (Fig. 2).

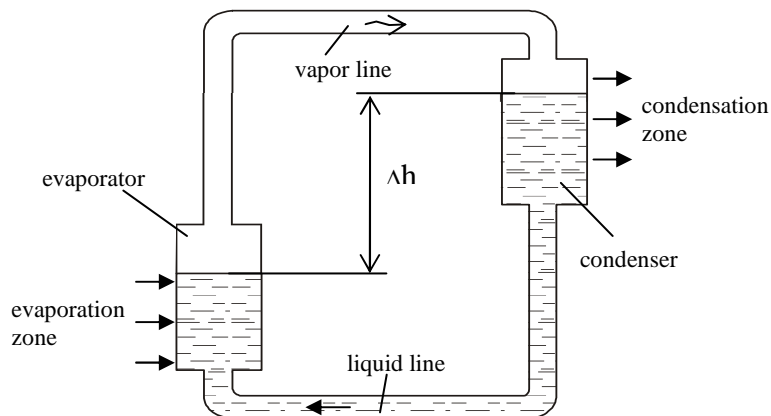


Fig. 2. Scheme of a loop thermosyphon with an evaporator and condenser

The paper generalizes and presents the results of development and investigation of two-phase loop thermosyphons, and also various heat-transfer devices created on their basis. This work has been performed at the Institute of Thermal Physics of UB RAS and aimed at the solution of problems connected with both heating and cooling of different objects.

### INVESTIGATION OF LTS THERMAL CHARACTERISTICS

Among the main thermal characteristics of two-phase heat-transfer devices are the maximum capacity, the heat flux in the evaporation zone and thermal resistance. For analysis use is also often made of the dependence of the characteristic operating temperature on the heat load supplied to the evaporation zone. For the characteristic temperature one can use the temperature of the evaporator wall or the vapor, whose heat-load dependence have qualitatively similar forms. To determine the thermal resistance of a device, which is usually written as:

$$R = \frac{T_e - T_c}{Q}, \quad (3)$$

where  $T_e$  and  $T_c$  are the average wall temperatures of the evaporator and the condenser, respectively, and  $Q$  is the heat flow transferred, it is also necessary to know the temperature of the condenser wall.

Several experimental devices made of stainless steel with water as a working fluid have been developed for investigating the thermal characteristics and peculiarities of LTS. The scheme of one of them is presented in Fig. 3.

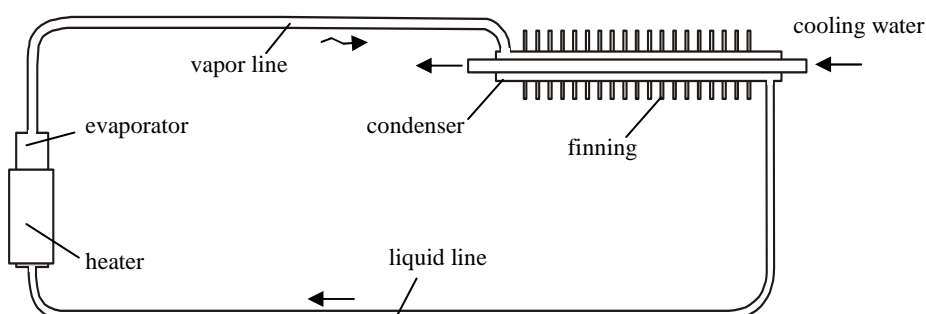


Fig. 3. Scheme of an LTS with air-liquid cooling of the condenser

The main structural characteristics of an LTS are given in Table 1.

Table 1. The main structural characteristics of an LTS

Evaporator active zone length / diameter, mm	140 / 24
Condenser length / diameter, mm	400 / 18
Vapor line length / diameter, mm	750 / 6
Liquid line length / diameter, mm	1300 / 4

The volume of filling with a working fluid was 60% of the total internal volume of the device.

The LTS was tested at different slopes towards a horizontal plane in the range from 0 to  $-90^\circ$ . The zero slope corresponded to the device position shown in Fig. 3, where the height difference between the upper end of the evaporator and the lower generator of the condenser was equal to 45 mm. At an LTS orientation with a slope of  $-90^\circ$  the condenser was situated vertically, and the evaporator occupied the lower horizontal position. To cool a condenser made in the form of a pipe-in-pipe heat exchanger, use was made of running water with a temperature of  $7.5 \pm 0.5^\circ\text{C}$ , and also forced air convection. The latter was created by three compact fans connected in parallel, which blew over the aluminum annular radiator enveloping the outer surface of the condenser. An electrical heater was used for heating the evaporator. Its active length

corresponded to the length of the evaporation zone. The heat load magnitude varied stepwise with a step of 50 W to a maximum value of 900 W and was limited by the heater capacity. Measurements were also made of the wall temperatures of the evaporator and the condenser, and also of the temperatures of the vapor and condensate lines. Standard copper-constantan thermocouples with data acquisition unit were used for the measurements.

Figs. 4 and 5 present experimental results in the form of heat load dependences of the evaporator wall temperature at various slopes for different means of condenser cooling.

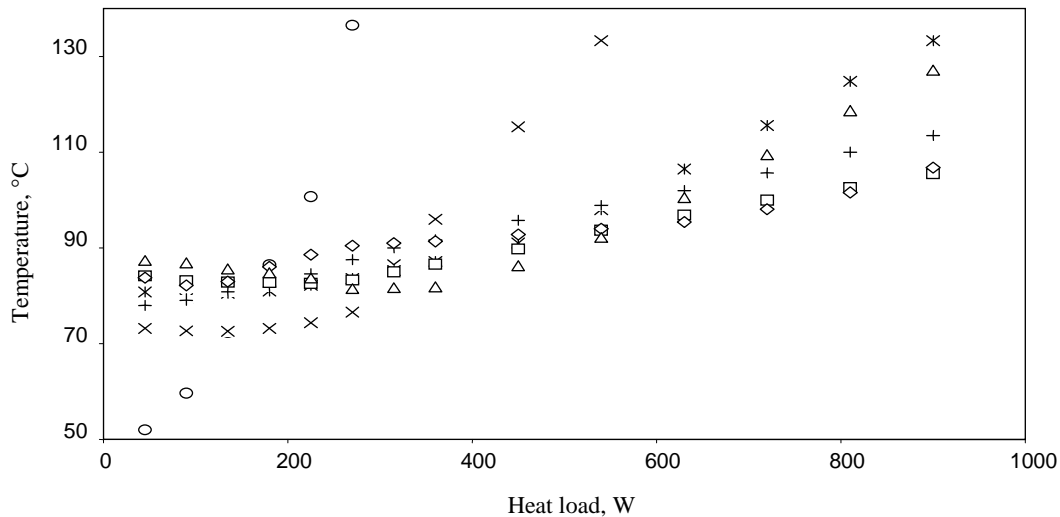


Fig. 4. Heat-load dependence of the evaporator temperature under liquid cooling of the condenser. Slope: o - 0°, x - 15°, ж - 30°, + - 45°, ◇ - 60°, □ - 75°, Δ - 90°

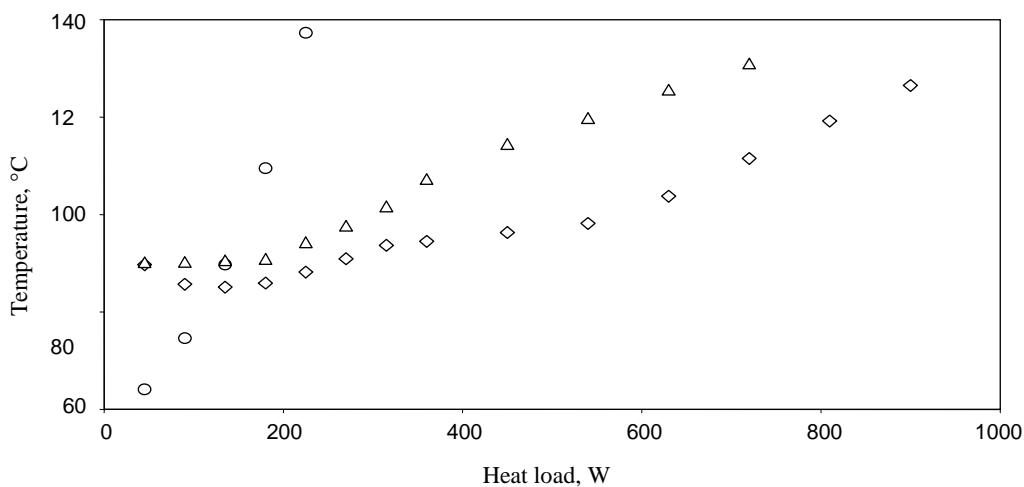


Fig. 5. Heat-load dependence of the evaporator temperature under air cooling of the condenser. Slope: o - 0°, ◇ - 60°, Δ - 90°

The test results have shown that an LTS is capable of operating at all slopes both with liquid and with air cooling of the condenser. In both cases the highest efficiency was achieved at slopes close to -60°, when the thermal resistance of the device had a minimum value equal to 0.05 °C/W for liquid cooling and to 0.03 °C/W for air cooling at a heat load of 900 W. At the same time minimum values of the operating temperature were attained at a zero slope, when the evaporator orientation was the most favorable for the beginning of boiling. However, the maximum capacity of the device operating in such a position did not exceed 300 W. It should also be mentioned that one can trace well the range from 50 to 400 W, where the operating temperature varies rather slightly with increasing heat load at slopes from -15 to -90°. Such a behavior is not observed during the operation of conventional thermosyphons, but it is quite typical of loop

heat pipes operating in variable-conductance behaviour. This peculiarity manifests itself as a result of a progressive displacement of the liquid from the condenser with an increase in the heat load up to a certain value. Also specific is the process of LTS operation accompanied by pulsations of the operating temperature and sound effects typical of the operation of oscillating heat pipes [16]. The amplitude and the frequency of these pulsations changing with increasing heat load and also depending on the slope. A characteristic temperature diagram for an LTS operating at a slope of  $-45^\circ$  is given in Fig. 6.

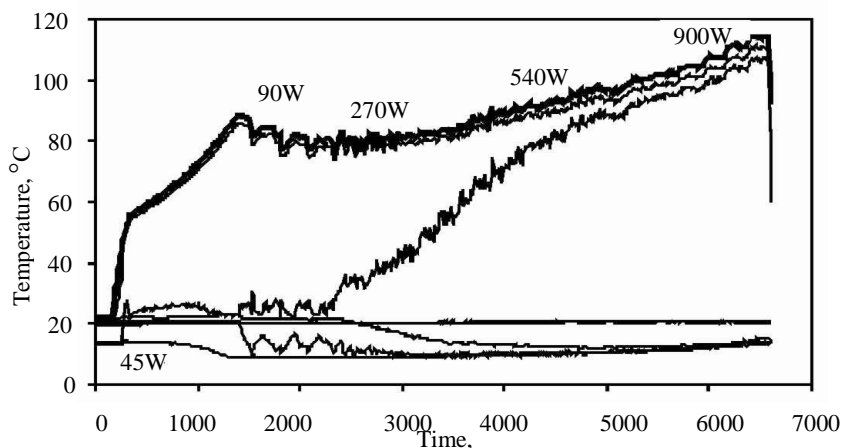


Fig. 6. Operating temperature diagram of an LTS at slope  $-45^\circ$

It should be mentioned that at slopes exceeding  $-15^\circ$  no heat-transfer crisis has been attained in the LTS evaporation zone. A further increase in the heat load was limited only by the capacity of the heater. According to calculations made for different vapor temperatures, whose results are presented in Fig. 7, the value of the limiting capacity for the LTS under discussion, on the basis of hydrodynamic restrictions, may be considerably higher than that obtained in experiments.

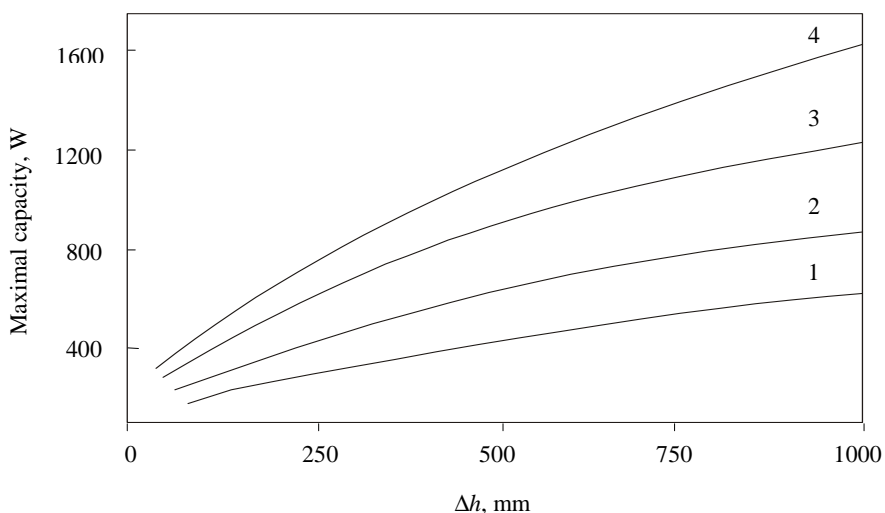


Fig. 7. Calculated dependence of LTS limiting capacity on  $\Delta h$  at different vapor temperatures.  
Vapor temperature: 1 – 80 °C, 2 – 100 °C, 3 – 120 °C, 4 – 140 °C

## HEATING DEVICE

The high heat-transfer capacity of loop thermosyphons, which is determined by the product of the magnitude of the heat flow transferred by the heat-transfer distance, makes it possible to use them, in

particular, for heating or thermostating objects far removed from the heat source. A number of experimental devices on the basis of LTS with water as a working fluid have been created for these purposes. The scheme of one of them is presented in Fig. 8.

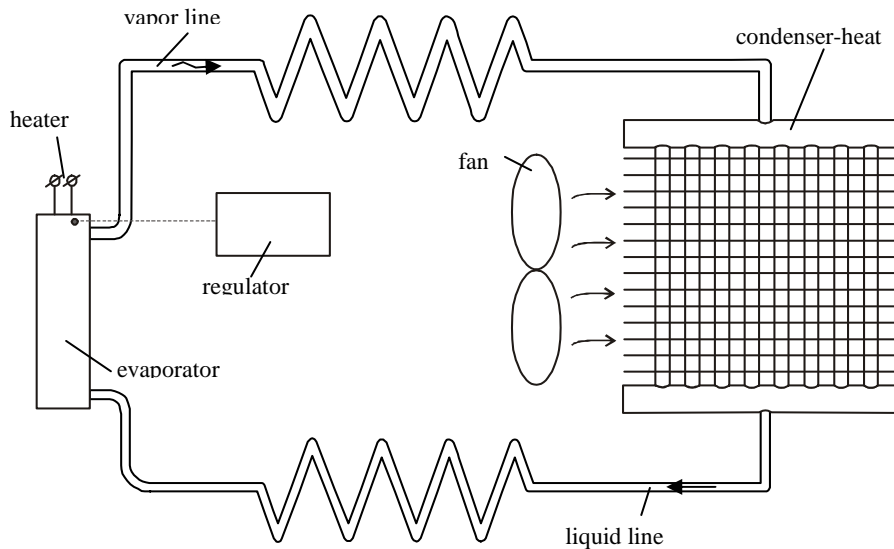


Fig. 8. Scheme of a heating device

The device was equipped with a cylindrical evaporator 48 mm in diameter and 330 mm in length, inside of which there was a heater with a maximum capacity of 3 kW. The condenser-heat exchanger made in the form of a bundle of tubes connecting the liquid and vapor collectors had a finning formed by parallel plates with a total area of about 1 m<sup>2</sup> and was located in a casing together with a fan. The evaporator and the condenser were joined by a flexible vapor and liquid lines with an internal diameter of 6 mm and a length of 120 mm. The evaporator heater was connected with an electronic controller, which made it possible to maintain the vapor temperature in the device at a prescribed level. Fig. 9 shows the characteristic dynamics of temperature variation during the operation of a device with a heating controller.

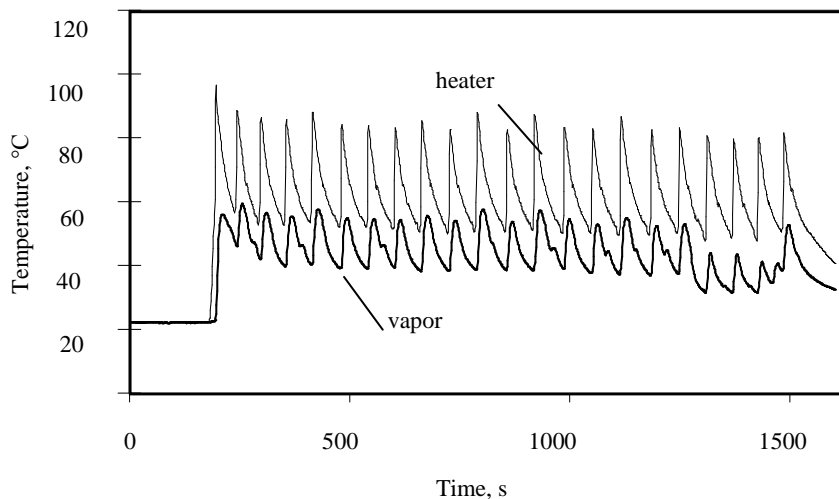


Fig. 9. Dynamics of temperature variation during the operation of heating device at a heat load of 3000 W

### COOLING SYSTEM "LTS-TEM"

The use of an LTS in combination with a thermoelectric module (TEM) operating on the basis of the Peltier effect allows creating an efficient system for cooling compact objects, in particular, optical sensors

operating at temperatures lower than the outside ambient. It is known that for maintaining a low temperature on the "cold" side during the operation of a TEM it is necessary to remove heat from its "hot" side. Special radiators are usually used for this purpose. If such radiators operate under natural air convection, they have a large heat-transfer surface and a sufficiently massive base for providing acceptable isothermality as the area of their thermal contact with the TEM is relatively small. Such a system has an extra mass and an increased thermal resistance. Besides, the radiator has always to be in direct thermal contact with the TEM, which is far from being acceptable in all cases.

Fig. 10 presents one of experimental versions of a cooling system based on a loop thermosyphon and a thermoelectric module of MDI-127 -1,4/1,6 type. Such a system was used to cool an electric simulator of a heat source.

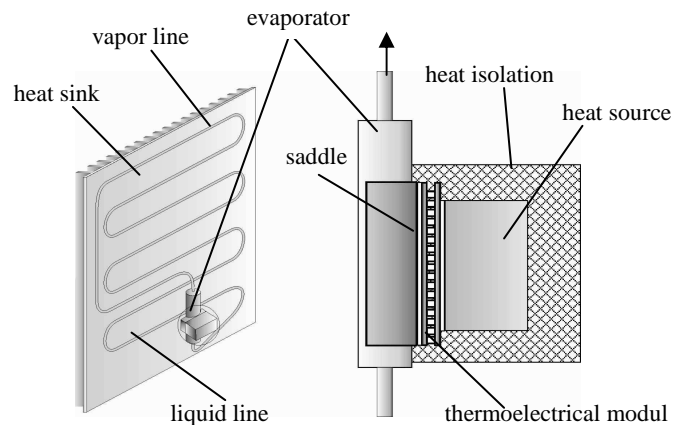


Fig. 10. Scheme of a cooling system "LTS – TEM"

In this system use was made of an LTS with ammonia as a working fluid, which had a compact cylindrical evaporator 70 mm in length and 9 mm in diameter. Evaporator was equipped with a copper thermal interface with dimensions of the thermocontact surface  $40 \times 40 \text{ mm}^2$  corresponding to the dimensions of the TEM. The condenser was made in the form of a flat coupled with a light aluminum radiator with corrugated finning, which measured  $400 \times 400 \times 10 \text{ mm}^3$ . The diameter of the tubes of the vapor line, the liquid line and the condenser was equal to 4 mm. The TEM ensured a maximum refrigerating capacity of 55 W at an inherent power consumption of 37 W.

Fig. 11 presents the heat-load dependence of the temperature of the object being cooled in cooling the radiator by means of natural air convection at an ambient temperature of 25 °C.

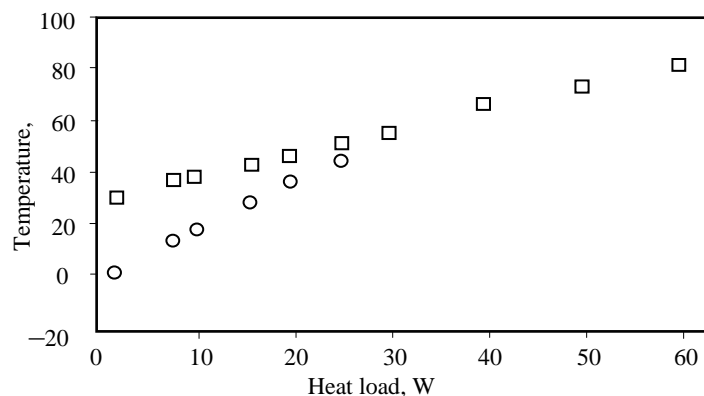


Fig. 11. Heat- load dependence of the temperature of the object being cooled: □ – LTS, o – LTS-TEM

The results obtained show that the cooling system "LTS-TEM" allows maintaining the temperature of the object being cooled below that of outside ambient at heat loads up to 15 W. This exceeds considerably the maximum heat flow dissipated by optical sensors or quantum-electronic modules, for cooling of which this system may be used.

## TRANSFORMER COOLING

One of the first experimental developments aimed at the industrial application of LTS was a cooling system for windings of electric transformers with capacities of 100 and 160 kVA [18].

The scheme of the device is given in Fig. 12.

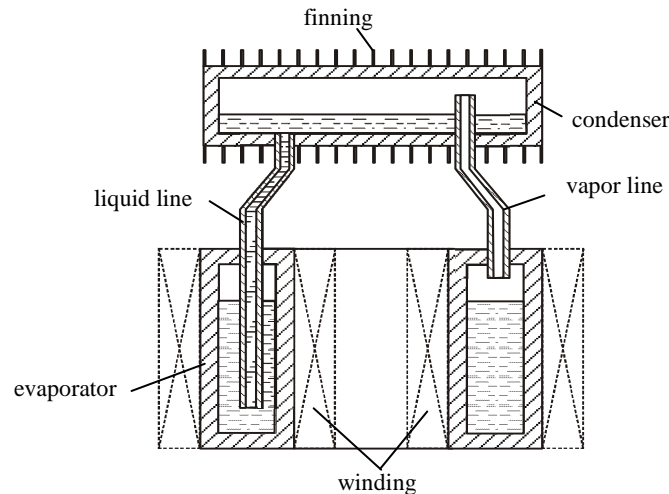


Fig. 12. Scheme of transformer cooling

The distinctive feature of this cooling system consisted in the fact that the LTS had a coaxial cylindrical evaporator located vertically in the gap between the transformer windings. The cylindrical condenser was situated horizontally right above the evaporator. The entrance of the liquid line and the exit of the vapor line which had diameters of 6 and 8 mm, respectively, were located in the upper butt-end part of the evaporator. The finning the condenser was equipped with was intended for operation with cooling by means of natural convection.

## COOLING OF PERSONAL COMPUTERS

The most heat-tensioned components of personal computers (PC) are central (CPU) and graphic (GPU) processors, which can dissipate heat flows up to 130W and more. In this case the admissible temperature at the surface of their shell may not, as a rule, exceed 70–80 °C. Since the temperature inside the body of a PC may reach 50 °C, the thermal resistance between the shell and the surrounding air, which is to be provided by a cooler, must be about 0.23 °C/W. Modern coolers with appropriate thermal characteristics, which have in their composition from 4 to 6 conventional copper-water heat pipes from 6 to 8 mm in diameter and a radiator with a finning area of about 1 m<sup>2</sup>, are equipped, as a rule, with a fan 120 mm in diameter with a number of rotation per minute from 1800 to 2200. Besides, all of them must be located right on the object being cooled, which limits the possibilities for optimum arrangement of the system block. In this case the finned heat sink has to operate at a higher temperature of the surrounding air as it is situated inside the PC case.

The use of LTS for cooling computers has a number of advantages which allow locating the heat sink at a certain distance from the object being cooled in the coldest place, for instance, right on the wall of the case of the PC. This enables one to use forced-ventilation fans, which direct to the radiator colder air with a temperature close to room temperature. In its turn, this makes it possible to decrease the finning area and, as a result, to reduce the mass and the dimensions of the cooler.

Fig. 13 presents the scheme of a cooler developed on the basis of a copper-water loop thermosyphon for a PC graphic processor.

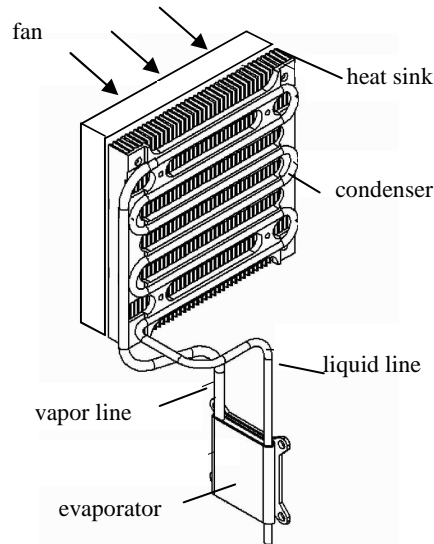


Fig. 13. Scheme of a cooler for a PC graphic processor

The LTS had a flat-oval evaporator 7 mm thick with an evaporation zone measuring  $40 \times 40 \text{ mm}^2$ . The condenser in the form of a flat coil was located between two aluminum radiator plates with appropriate hollows and through holes for the passing of an air flow directed by a forced-ventilation fan 120 mm in diameter. The total finning area was  $0.48 \text{ m}^2$ . The diameters of the tubes of the liquid line and the vapor line were respectively equal to 4 and 5 mm.

The results of testing a cooler with a thermal simulator of a graphic processor are presented in Fig. 14.

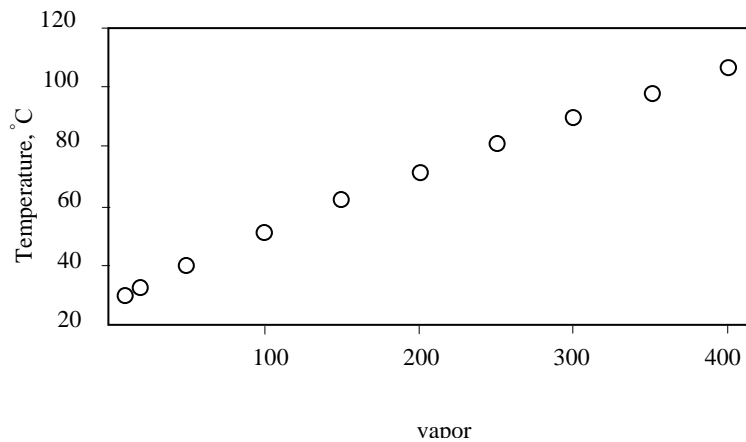


Fig. 14. Heat-load dependence of the temperature of a GPU thermal simulator

Tests were conducted at an ambient temperature of  $22 \text{ }^\circ\text{C}$  with the heat sink blown by an air flow at a rate of  $2 \text{ m/s}$ . The heat load varied in the range from 20 to 400 W. Judging from the operating characteristic, no crisis phenomena were observed in this case. At a nominal heat load of 130 W the thermal resistance of the cooler was  $0.23 \text{ }^\circ\text{C/W}$ , the temperature of the thermal simulator not exceeding  $55 \text{ }^\circ\text{C}$ .

## PASSIVE COOLING SYSTEMS OF ELECTRONICS

Among passive systems there are such ones which do not require for operation any means consuming additional energy, in particular, fans or pumps of different types. The main advantages of passive cooling systems are their economical operation, high reliability and long service life, and also the absence of noise and mechanical vibrations. One of the drawbacks is the necessity to use sufficiently large heat – transfer surfaces connected with the condenser, which make it possible to dissipate the heat flow being removed by means of natural convection and radiation.

Loop thermosyphons as passive and at the same time simple and highly efficient devices, which adapt well to different conditions of location and operation, in many cases are an ideal variant for using in such systems as a heat-transfer link between the heat source and the heat sink.

Presented in Ref. [19] are the results of development and tests of different versions of a passive cooling system on the basis of LTS for electronic components used in automotive industry. The maximum power dissipated by such components is 30W, and the temperature may not exceed 155 °C. The main problem which arose in solving this issue consisted in the choice of a working fluid as, by the specifications, the cooling system is to operate in the range of ambient air temperatures from –40 to +105 °C. As a result, the choice was made of heptane, which does not freeze at low temperatures and has acceptable thermal properties in the whole range of operating temperatures. The scheme of one of the experimental versions of a passive cooler on the basis of LTS is given in Fig. 15.

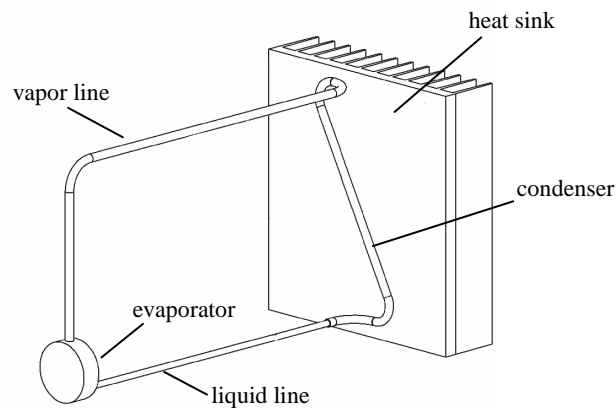


Fig. 15. Scheme of a passive cooler for electronic components

The LTS was equipped with a copper disk-shaped evaporator 30 mm in diameter and 10 mm in thickness with a flat thermocontact surface, on which the object being cooled was situated. The condenser was joined with an aluminum heat sink measuring 120×120×30 mm<sup>3</sup>. The distance from the evaporator to the radiator was 200 mm. The diameter of the vapor line and the condenser was equal to 4 mm, and that of the liquid line to 3 mm.

The device was tested at an ambient air temperature of (22±2) °C in condition of natural convection. The results of the tests are presented in Fig. 16 in the form of a temperature - time dependence of the heat source on the heat load, which varied in the range from 10 to 40 W. It can be seen here that at a heat load of 30 W the temperature of the object being cooled is at a level of 73 °C. On conversion to the given maximum ambient air temperature of 105 °C the equivalent temperature of the heat source must be equal to 156 °C, which does not practically differ from the value prescribed.

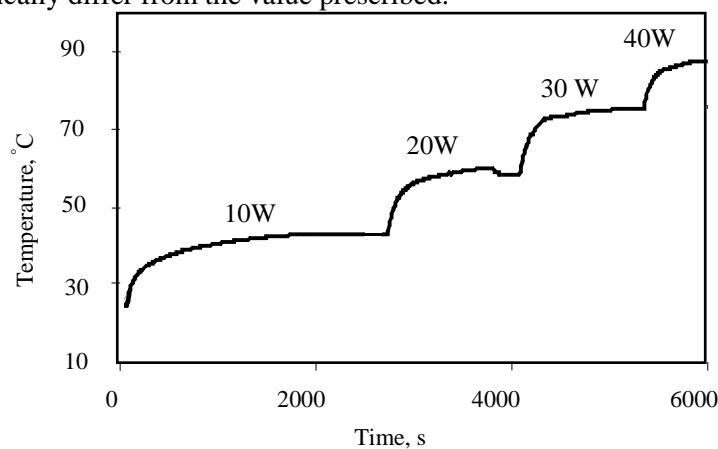


Fig. 16. Temperature - time dependence of a heat source on the heat load

## CONCLUSION

Two-phase loop thermosyphons are rather simple and at the same time quite efficient heat-transfer devices capable of operating in a wide range of variation of mode parameters and slopes. The possibility of using these devices in various fields of technology both for heating and for cooling objects remote from heat sources and sinks has been demonstrated.

## References

1. Dan P.D., Reay D.A. *Heat Pipes*, Moscow: Energy, 1979. Pp. 272 (in Russian).
2. Maydanik Yu. F. Review: Loop heat pipes // *Appl. Thermal Eng.* 2005. Vol. 5. Pp. 635–657.
3. Acachi H., Polasek F., Stuls P. Pulsating heat pipes // *Proc. of the 5<sup>th</sup> Int. Heat Pipe Symp., Melbourne, Australia*, 1996. Pp. 208–217.
4. Pioro L.S., Pioro I.L. *Two-Phase Thermosyphons and Their Application in the Industry*, Kiev^ Naykova Dumka, 1988. Pp. 134 (in Russian).
5. Kapitanchuk I.I. Development of evaporating cooling systems // *Voprosy Radioelektroniki, Ser. TRTO*. 1967. No. 2. Pp. 69–74 (in Russian).
6. Kolenko E.A., Verdiev M.G. Application of thermosyphons for heat-transfer from elements of REA to Radiators // *Voprosy Radioelektroniki, Ser. TRTO*. 1972. No. 2. Pp. 108–112 (in Russian).
7. Fayzilberg S.N., Kolosova N. Yu., Semena M.G. Generalization of experimental data on investigation of limiting heat flows in two-phase thermosyphons // *Izvestia Vuzov. Energy*. 1978. No. 6. Pp. 86–88 (in Russian).
8. Imura H., Takeshita K., Doi K., Noda K. The effect of the flow and heat transfer characteristics in a two-phase loop thermosyphon // *Proc. of the 4<sup>th</sup> Intern. Heat Pipe Sym., Tsukuba, Japan*, 1994. Pp. 95–106.
9. Pioro I. Small scale two-phase loop thermosyphons for cooling telecommunication MCM // *Proc. 10<sup>th</sup> Int. Heat Pipe Conf., Stuttgart, Germany*, 1997, Paper N A2-1.
10. Rossi L., Polasek F. Thermal control of electronic equipment by heat pipes and two-phase thermosyphons // *Proc. of 10<sup>th</sup> Intern. Heat Pipe Conf., Stuttgart, Germany*, 1997. Pp. 50–74.
11. Lee Y. et al. Use two-phase loop thermosyphons for heat extraction of enclosed spaces: Experiment and analysis // *Proc. of the 11<sup>th</sup> Intern. Heat Pipe Conf., Tokyo, Japan*, 1999. Pp. 299–304.
12. Khrustalev D. Loop thermosyphons for cooling of electronics // *Proc. of the 18<sup>th</sup> SEMI-THERM Symp., San Diego, California, USA*, 2002. Pp. 145–150.
13. Nisgoski A.R., da Silva A.K., Mantelly M.B.H. Theoretical and experimental study of two-phase vertical and loop thermosyphons // *Proc. of the 12<sup>th</sup> Int. Heat Conf. Moscow, Russia*, 2002. Pp. 279–284.
14. *Pat. 2194935*. Heat-transfer device / Yu.F. Maydanik, V.I. Dmitrin; 2002.
15. Milanez F.H., Mantelly M.B.H. Heat transfer limit due to pressure drop of a loop thermosyphon // *Prep. of the 15<sup>th</sup> International Heat Pipe Conf., Clemson, USA*, 2010.
16. Maydanik Yu.F., Dmitrin V.I. Compact cooler for electronics on the base of a pulsating heat pipe // *Appl. Thermal Eng.* 2009. Vol. 29. Pp. 3140–3143.
17. *Certificate No. 15386*. Heating device / Yu.F. Maydanik, V.I. Dmitrin; 2000.
18. *Inventor certificate No. 1690003*. Induction device / A.L. Amromin, A.A. Levin, B.A. Vyhodtsev, Yu.F. Maydanik, S.V. Rudyuk; 1991.
19. Pastukhov V.G., Maydanik Yu.F., Dmitrin V.I. Development and investigation of a cooler for electronics on the basis of two-phase loop thermosyphons // *Heat Pipe Science and Technology*. 2010. Vol. 1, No. 1. Pp. 47–57.

## FOOD NANOTECHNOLOGIES. SPECIFICITY AND DEVELOPMENT DIRECTIONS

**O. G. Burdo, V. N. Bandura, I. I. Yarovoy, N. V. Ruzhitskaya**

Food Technology Processes, Apparatuses and Energy Management Department  
Odessa National Academy of Food Technologies  
Kanatnaya street 112, 65090, Odessa, Ukraine  
Tel.: 038-048-712-41-75; E-mail: terma@onaft.edu.ua

### Abstract

The specificity of food nanotechnologies is discussed. It has been shown that the organization of transport processes subject to food raw nanoscale objects (spores, microorganisms, cell walls etc.) features will allow to decrease energy consumption, increase the product quality, and even get in essence new products. Mechanism of barodiffusion processes during drying and extraction has been studied. Confirmations of proposed hypotheses about the effectiveness of combined processes of nano- and macrotransport have been given. The results of use of barodiffusion nanotechnologies in drying equipment, coffee and cognac production extractors have been presented.

### KEYWORDS

Food nanotechnologies, barodiffusion, drying, extraction, drying equipment, extractors.

### INTRODUCTION

It is expected that this decade wide range of goods got by using nanotechnologies will appear in(at) a market. The preconditions for this are the energetic dynamics of increase, considerable financing volumes and wide interest of different establishments in nanotechnologies [1]. The nanotechnologies success is often determined on with the depth connection of interdisciplinary sciences raw and existing technologies. Such "convergence of technologies" [2] is leading to the appearance of new products, materials and methods.

The nanotechnologies in food industry using will allow to decrease the level of thermal influence on food materials state, to increase the energy use efficiency and to create basically new products which have no analogs in modern cooking [3].

### The Food Nanotechnologies Specificity

The nanotechnologies (NT) classification in the industry different fields given by authors [4] has shown that classical nanotechnologies are aimed at making man-made nanostructures, getting new nanostructures of separate atoms or molecules by the "upwards" principle.

Food NT have a specificity which is connected with as the problems of food raw material treatment processes both raw material features. Food NT can be developed in two directions. The first one is the nanoscale elements manipulation with goal to "create" artificial products (milk, meat etc.). The direction is rather difficult and problematic. The second one is the control of transport processes at a food raw material nanoscale level. It is a new, prospective and revolutionary scientific direction.

The future of food nanotechnologies is the fundamental bases of physics, chemistry and biotechnology deep coordination. The approach is corresponded the "nanotechnology" definition. The researches subjects here are (Fig. 1) microorganisms (of 7 nm), vegetable raw material nanopores and nanocapillars (from 5 nm), cell walls (7...30 nm), protein (10...100 nm), polysaccharides (1...10 nm) and water molecules ( $\approx 0,1$  nm). These are the objects which the main steps of food technologies are aimed at. That's why biotechnology, sterilization, extraction, drying, juice output processes etc. can be organized at nanoscale level.

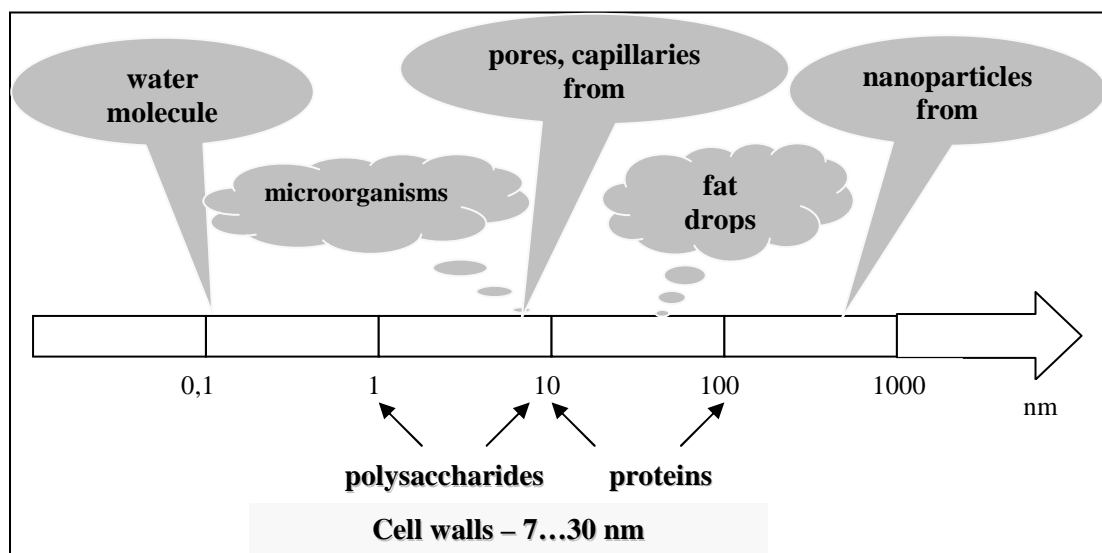


Fig. 1. Nanoscale food raw elements

### The Nano-Processes Thermodynamic Prescription Schematic

Main food production processes are combined with energy input into a product. The modeling is based on phenomenological approach and comes to the uninterrupted system analysis if the product is a liquid. The modeling schematic is based on using the mass, energy and momentum conservation laws. Phenomenological laws include well-known irreversible processes linear relations: Newton position, Fourier equation, Fick equation and etc. The modeling results are material and energy balances, space - time parameters distribution.

Such approach was caused to be acceptable for many analysis of chemical-engineering processes with parameters slow changing. Liquid food systems (suspensions, aerosols etc.) are specific. The cellular-fibrous structure presence is not considered in the stated above approach. As cellular content is the technology main purpose, the model have to be a mirror of the transport through the boundary "cell-environment", inside a pore or a capillary, kinetics. The regularities understanding is the base for the processes intensification, the food production basically new technologies realization. Especially interesting result can be expected from the parameters jump in the volume, impulse input of energy, combined process behavior. It's envisaged that the approach to the combined processes in food systems modeling have to provide for combined methods with using system analysis.

Let's imagine the food disperse medium as homogeneous uninterrupted system in which the parameters distribution is a boundary condition for the working cell (cell, solid porous or fibrous phase). The working cell is formed as a heterogeneous system. A phase 2 surface (capsule) can be solid phase fibers, elastic walls cell or microorganism. As a rule, the phase 2 surface is permeable and has hydraulical connection channels with environment. In the cases different known and unexpected effects are possible in the combined influence on the system processes [5].

The discordance between heat leakage to the phase 2 and heat sink from the phase can be the temperature drop  $\Delta T$  growth in phase 2 reason. The liquid phase part can turn into vapor as the result. It is leading to the pressure drop ( $\Delta P$ ) increasing. The process evolution can be developed in two forms:

- a mass flow  $M$  from phase 2 into phase 1 is appearing;
- a phase 2 capsule rupture will be caused.

It is also possible reaching  $P+\Delta P$  in phase 2 for account of sharp pressure decrease in uninterrupted system 1. An uninterrupted phase 1 will react immediately and switch on the process to the boundary surface capsule as the abrupt pressure decreasing for account of incompressibility result. It is possible to reach  $P+\Delta P$  technically, with respect of connection between the large volume system (by excess pressure) with atmosphere, in phase 2 and sometimes in phase 1 the volume increasing must be caused. The process development may be the following: liquid boiling will take place in phase 1; the crush of phase 2 will take place; the phase 2 capsule rupture will occur.

The process thermodynamically phenomenological description before the phase 2 catastrophic change (crushing, capsule rupture) moment using some defined simplifications can be leading to the next substance M mass flux and heat flux Q over any valve (pore, membrane) expression (1):

$$M = a_{11}V\Delta P + a_{12} \frac{\Delta T}{T} ; \quad Q = a_{21}V\Delta P + a_{22} \frac{\Delta T}{T} \quad (1)$$

Therefore the problem can be coming to the hydraulic and thermal processes imagination using.

So, from author point of view, it is possible to describe known processes and forecast new technologies: drying in microwave field, extraction in electromagnetic field; dispersion and homogenization in processes of discrete-impulsive energy input; low-temperature pasteurization under discrete-impulsive energy input; activation of material; juice output increasing using the positions. The authors assume also that, it is possible to organize the processes with the baro - diffusion technologies (BDT) help.

The key problem in the mentioned action success is the phenomenological coefficients  $a_{ij}$  determination. Let's to consider some barothermic influence processes in uninterrupted-heterogeneous systems in details.

### Heat-mechanic models of cellular structure.

The following mechanism of barothermic activation including three steps can be proposed. The first step is pressure  $P$  and temperature  $T$  growth during the period of time  $\tau_0$  to  $\tau_1$ , the second step is exposure the raw material mass under pressure  $P_r$  and at temperature  $T_r$  during time  $\tau_e$  and the third one is sharp pressure dump from  $P_r$  to  $P_0$  during time  $\tau_2$  and sharp decrease of temperature from  $T_r$  to  $T_0$  during time  $\tau_2$ .

It is necessary to be considered as the initial parameters all values what have influence on the baro - thermo treatment process:  $V_c$  - cell volume;  $F_c$  - cell surface area; cell pores diameter -  $d_p$ ;  $\delta$  - cell walls thickness;  $\varepsilon$  - cell wall porosity;  $T_c$  - cell temperature;  $P_c$  - intracellular pressure;  $\tau$  - process time;  $Q$  - quantity of heat. Optimized pressure in the reactor ( $P_{opt}$ ), raw material exposure time ( $\tau_e$ ) at the temperature ( $T_r$ ) can be presented as output parameters. The optimization criterion in the case can be mass adhesion after reaction, what is expressed over the breakout force ( $F$ , N/m<sup>2</sup>):  $F=f(P_r, T_r, \tau_e)$ .

Let us to consider the model of associated processes of hydrodynamic, thermal and mass transfer processes interaction between single cell and dispersion media. Cell volume  $V_c$ , temperature  $T_c$ , pressure  $P_c$  and soluble components concentration  $C_c$  change can be imagined by the following way eq. (2):

$$\tau_0 < \tau < \tau_1; \quad P_0 < P \leq P_1; \quad T_0 < T \leq T_1 \quad (2)$$

$$\frac{dV_c}{d\tau} = \beta \cdot \varepsilon \cdot F \frac{\rho_r}{\rho_c} [C_r(\tau) - C_c(\tau)] + F_c \cdot \varepsilon \frac{P(\tau) - P_c(\tau)}{\delta} + \frac{1 - \varepsilon}{r \cdot \rho^u} \cdot \int q_v \cdot dF \quad (3)$$

The first item in expression (3) takes into account on the mass carry, the second item takes into account on the volume change infiltration caused, the third one takes into account on the heat-transfer process caused volume change. Heat flow imparting to the cell is spent for the "dry" part heating, heating and partial evaporating of liquid, eq.(4):

$$Q_c = \int_0^{\tau} \int_0^{\tau} c_{pd} \{ [1 - C_c(\tau)] V_c(\tau) \} \rho_c dV d\tau + \int_0^{\tau} \int_0^{\tau} c_{pw} \cdot C_c(\tau) \cdot V_c(\tau) dV d\tau + \int_0^{\tau} \int_0^{\tau} q_v dV d\tau \quad (4)$$

The cell wall elasticity is leading to the cell "swelling" by  $V_c$  growth and corresponding porosity change  $\varepsilon$ , that is:  $F_c = f(V_c); \varepsilon = f(T_c; T; P_c; P)$

Pressure and temperature in the apparatus and inside the cell are changing time-dependently:

$$P = f(\tau); P_c = f(\tau); T = f(\tau); T_c = f(\tau).$$

### Barodiffusion Transport Processes Mechanism

The combined moisture from fibrous structure into the flow nano- and macro - transport mechanism can be explained from author point of view on the scheme (fig. 2 a) and the electro - diffusion model (Fig 2 b) base. The diffusion resistances consistent chain consists from the sum:  $\Sigma R = R_{NC} + R_{MC} + R_{MT}$  items. The convective mass transfer process from the product surface to the flow has the lowest diffusion resistance ( $R_{MT}$ ). The water moves inside product micro-capillaries to the product external surface overcoming the diffusion resistance ( $R_{MC}$ ). The process is the convective diffusion in tightened conditions ( $j_1$ ). The nano-capillaries diffusion resistance is designated as ( $R_{NC}$ ). It is the highest diffusion resistance because the diffusion processes tightness is maximal.

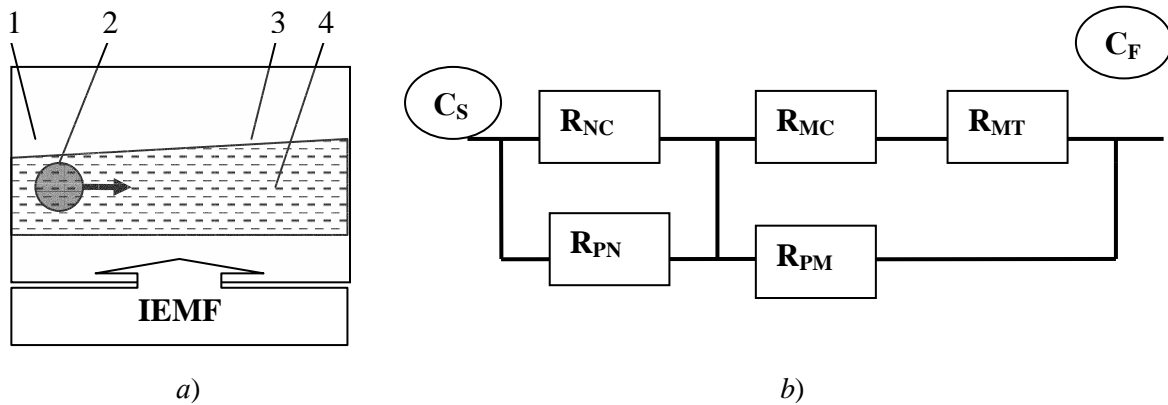


Fig. 2. The Barodiffusion process: a) –scheme, b) –electro-diffusion model  
1 –solid body, 2 –vapor bubble, 3 –capillary wall, 4 – liquid

The moisture flow from the capillaries ( $j_2$ ) is realized under an impulse electromagnetic field (IEMF) action. Really, it is a barodiffusion, its action is determined by pressure rising in capillaries  $P_c$  (Fig. 2). Some capillaries, in which the vapor phase generating conditions are formed, begin the liquid to throw out capillaries to the external media periodically. Moisture from nano - capillaries is thrown out into micro - capillaries and gets by overcoming a diffusion resistance ( $R_{PN}$ ). These blowouts frequency and the acting capillaries number is increasing with the radiation power ( $N$ ) growth.

The analogy of evaporation centers is proposed [5, 6] by the problem statement. Cumulative flow ( $j$ ) can be determined using as the traditional mass transfer coefficient ( $K$ ) both the baro-diffusion flow mass-transfer coefficient ( $\beta_p$ ), eq. (4):

$$j_1 = j_2 + j_3 = K (C_S - C_F) + \beta_p (P_C - P_F) \quad (5)$$

The flow is realizing the boundary layer turbulization as well. So, the flow hydrodynamic situation is determined on the equivalent diameter ( $d$ ), the diffusion media motion ( $w$ ) relative velocity. The transport process is complicated by the vortex motion diffusion from the solid phase canals, IEMF impulse unsteady forms, whole these factors determine the mass transfer places number and their productivity.

The type problems were solved using the experimentation. The equation structure in non-dimensional variables is assigned as the "dimensional analysis" method. The energy criterion effect is suggested in the next view:  $Bu = N (r w d^2 \rho)^{-1}$  it is taken into account the IEMF action influence. The  $Bu$  criterion physical meaning is the next: the ratio between the radiation energy density scale and the energy density scale, what it is necessary for the whole mass moisture evaporating in the product to be realized. The value  $r$  is latent heat and  $\rho$  is water density in the expression .

The closer the  $Bu$  criterion to 1, the more vapor phase is generated, the more the pressure gradient is, the more intensive blowouts of wet saturated vapor take place. The boundary layer turbulization is growing commonly with it the solid phase energy consumption is increasing.  $Bu$  criterion describes micro- and nano-kinetics of baro-diffusion mass transfer intensity [5, 6]. The baro-diffusion intensity is determined on the

pressure growth in a capillary. The blowouts frequency and the capillaries acting number is increasing proportionally to the electro - physical influence.

### The Dehydration Process by Baro-Diffusion Technology Effectiveness

The mechanical removal of moisture from the product surface while delivering it by barodiffusion mechanism which is realizing with help of the impulse electromagnetic field (IEMF) is expected to be possible. It is necessary, firstly, to release the air from the heat carrier function and to leave for it only the moisture "receiver" leaving task, secondly, to organize the product drying with minimal moisture evaporating from it, thirdly, to use mechanical removing of moisture from the product surface by blowing it with air from the environment media, fourthly, to organize barodiffusion from the product volume with the help of IEMF, in view of the aforesaid.

The considered mechanism is demonstrated by the schematic (fig. 3). It is natural, that water being heated gives the thermal energy some part to the product dry part, but this part has to be considerably less than at convectional drying, that is to mean the less energy is spent. It is the prerequisite of the IEMF method drying energy efficiency [3, 6].

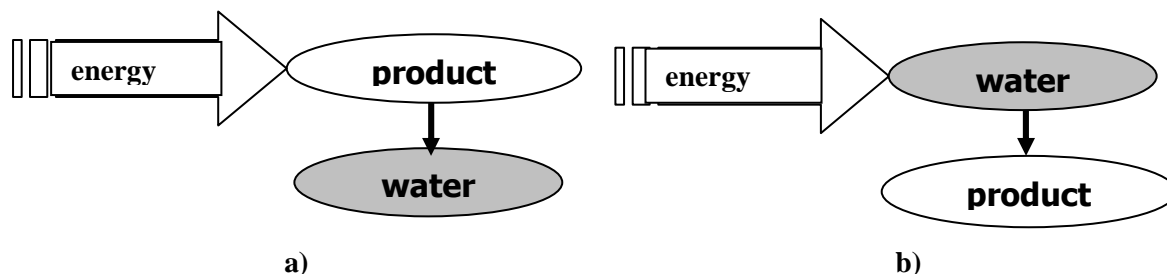


Fig. 3. Schemes of energy supply: a) – traditional convection drying; b) IEMF-drying

The experimentation results analysis showed that energy specific consumption was connected with the temperature change range, especially at the product blowing mode (filtration drying). The correlation has been found out and it was allowing to do a conclusion that the energy consumption achieved level is lower than the water latent heat. This way was by authors suggested to be the key hypothesis about the principal possibility of water removal in the IEMF conditions, without necessity on whole water transform in vapor, it has been confirmed [6].

### The extraction process based on the baro - diffusion technology using effectiveness

The instant coffee and cognac production prospective on the BDT base was investigated. The coffee bean extraction modern technologies are characterized by many contradictions. On the one hand there is a problem the valuable components from beans maximal value extraction to reach. The such problem effective method of solving is the process temperature and pressure inside the apparatus and stepped extraction increasing. The problem of separating the extract and sludge is solved by simple gravitational draining of solution and sludge mechanical removal. On the other hand, the separating extract and sludge methods, high pressure in the apparatus complicates the use of flow-through schemes and use of stirring rod in the construction. The extraction from coffee beans modern technology is characterized by bulkiness, laboriousness, energy intensity, there were obtained a lot results [3, 7]. The extraction from coffee beans traditional methods possibility were practically exhausted.

The extractor sample, based on BDT method using, has been created. The combined electro - physical action on the extraction process is allowing to intensify mass transfer processes in many times and it is also realizing intensive and soft modes of extraction [3, 7]. The extraction degree of components from beans shows a 15% growth. The pressure inside apparatuses was supported not higher than corresponding by 100°C. Energy consumption is decreased by 50%.

The researches and perspectives of their development results are given it table 1.

Table 1. Energy effect of food nanotechnologies

Technological process	Mechanism	Effect
Low temperature pasteurization	Selective action upon the microorganism	Increase of energy efficiency $10^3$ times
Energy efficient drying	Three-dimensional energy supply, barodiffusion initiation	Decrease of energy consumption 40...50 times
Electromagnetic intensifier assisted extraction	Three-dimensional energy supply, barodiffusion initiation	Mass carry intensification $5 \dots 10^3$ times

It's envisaged that barodiffusion mechanisms are able to intensify extraction, to depress microorganisms activation and inactivation processes substantially.

### The hypothesis achieved applied result and practical confirmation

There are facts which can be explained only on nano - science positions using at present time. The facts, received by ONAFT Processes and Apparatuses Department Chair are: changings and transformations of product flavouring and aromatic complexes structure, products sterilization at low temperatures and so on. The reason of these facts is the common – BDT effect. The researches results information and perspectives of their development are given below.

Testing of the extractor with the electromagnetic intensifier took place in cognac production environment. It was discovered the mass transfer intensity increased in tens and thousands times by different performance conditions. The testing results confirmed the proposed mechanism of combined extraction process and the technology perspectives. Some invited degustators discovered the great special mention of product positive structural changing and foremost the aromatic constituents changing. The possibility of building the alcohol flavor at nanoscale level appears.

Generating the conditions for selective forming of ice slab with ice crystals close packing in the low-temperature reactor allowed to get clean water with salt content less than 4 mg/kg.

The complex of realized researches and manufacturing tests confirmed the key suggestion relating mechanisms and hypothesis formulated in the presentation. It is obvious that combined processes open new abilities in product structure changing operation, energy intensity decreasing and basically new food nanotechnologies creation.

### References

1. Azoev G.L. et. al. *Nano Market: from Nanotechnologies to Nanoproducts*. Moscow: BINOM, 2011. Pp. 289 (in Russian).
2. Zaycev S.J. *Supramolecular Nanosize Systems at Phase Boundary Surface: Concepts and Prospects for Bionanotechnologies*. Moscow: LENAND, 2010. – 208 p. (in Russian).
3. Burdo O.G. *The food industry energy monitoring*, Poligraf Publishing House, Odessa, 2008. – 244 pp. (in Russian).
4. Burdo O.G. Nanotechnologies. Leading, prospective and fundamental projects in agro-industrial complex // *Scientific works of Odessa National Academy of Food Technologies*, 2006. Vol. 2. Iss. 28. Pp. 242–251 (in Russian).
5. Burdo O.G. Nanoscale effects in food technologies // *Ingenerno-Fizichesky Zhurnal*. 2005. Vol. 78, No. 1. Pp. 88–93. (in Russian).
6. Burdo O.G. *The Dryers Manufacturing Evolution*, Poligraf Publishing House, Odessa, 2010. – 368 p. (in Russian).
7. Burdo O. G., Ryashko G. M. *Extraction in “Coffe-Water” System*, Odessa, 2001. – 176 p. (in Russian).

## WATER SORPTION DYNAMICS IN ADSORPTION CHILLERS: A FEW LAYERS OF LOOSE FUJI SILICA GRAINS

Ivan S. Glaznev, Yuriy I. Aristov

Boreskov Institute of Catalysis

Pr. Lavrentieva 5, 630090, Novosibirsk, Russia

Te/Fax: +7 383 330 95 73; E-mail: glaznev@catalysis.ru

Ilya S. Girnuk

Novosibirsk State University

Pirogova st, 2, 630090, Novosibirsk, Russia

Tel: +7 383 363 43 33; Fax: +7 383 363 43 33 16

### Abstract

Investigation of dynamic performance of adsorption chillers (ACs) which utilize adsorbent beds of loose grains is addressed in this paper. We have measured a temporal evolution of quasi-isobaric adsorption uptake/release curves for simple, but practical configuration of the adsorbent bed, namely,  $n$ -layers of loose Fuji silica grains located on a metal plate ( $n = 1, 2$  and  $4$ ). The plate is subjected to fast temperature drop ( $50\text{ °C} \rightarrow 30\text{ °C}$ ) or jump ( $58\text{ °C} \rightarrow 80\text{ °C}$ ) that are typical for AC cycles driven by low temperature heat. The measurements have been performed by a Large Temperature Jump method which closely simulates conditions of AC cycle. The size of the Fuji silica RD grains is varied from  $0.2$  to  $1.8$  mm to investigate its effect on the water sorption dynamics.

For this boundary set and any grain size, the experimental kinetic curves can be satisfactorily described by an exponential function up to  $50$ – $90\%$  of the equilibrium conversion, so that the dynamics of water ad-/desorption can be described by a *single* characteristic time  $\tau$ . This permits stupendous simplification of the analysis and easy quantitative characterization of AC dynamics. The tail of the experimental kinetic curves can be slower than the exponential one and the deviation tends to increase for smaller grains and thicker layer.

For all experimental runs, a gradual slowing down of the ad-/desorption process with increasing the number of layers  $n$  is observed. In the first approximation, the characteristic time of water ad-/desorption linearly grows with the number of layers,  $\tau = Kn$ , and the slope  $K$  significantly increases for larger grains that is due to enhanced intraparticle diffusional resistance. For the desorption runs, the slope  $K$  is app. 2 times smaller, thus, the desorption runs are always faster than appropriate adsorption runs. For any grain size, a ratio of the characteristic times  $\tau_{0.9}/\tau_{0.8}$  is  $1.4$ – $1.8$  that prompts to restrict the duration of AC isobaric stages by the time  $\tau_{0.8}$  or less. This would allow avoiding a dramatic drop of the specific cooling power at longer times with just little reduction of the cycle COP.

The grain size appears to be a powerful tool to manage the dynamics of isobaric stages of AC cycle. The configurations containing one layer of  $0.4$ – $0.5$  and  $0.8$ – $0.9$  mm grains, two and four layers of  $0.2$ – $0.25$  mm grains or two layers of  $0.4$ – $0.5$  mm grains ensure the average cycle power larger than  $1$  kW/kg that could be attractive for practical use. Application of silica grains larger than  $1$  mm is not recommended due to significant reduction of the cooling power.

### KEYWORDS

Heat and Mass Transfer, Adsorption kinetics, Adsorbent, Transport Processes, Adsorption Chillers, Large Temperature Jump Method.

### INTRODUCTION

Adsorption dynamics depends on heat and mass transfer in an "adsorbent bed – heat exchanger" (Ad-HEX) unit and determines the specific power of adsorption chillers. Two basic configurations of the Ad-HEX were suggested in literature [1–5]: a) loose adsorbent grains that contact the HEX surface, and b) the HEX surface coated with a consolidated adsorbent layer. Here we analyze the former configuration because it is very simple in realization and ensures a good vapour transport in the adsorbent bed [6]. On the other hand, it is considered to suffer from a poor heat transfer due to the high thermal resistance in the adsorbent layer as

well as between the adsorbent grains and the HEx surface. Because of this, the layer should not be too thick and its optimization is strictly necessary. So far, the loose grain configuration has been successfully realized in several prototypes [7–10] as well as commercial units [11, 12] of adsorption chillers and heat pumps.

Very simple *monolayer* configuration of loose adsorbent grains results in a quite fast sorption dynamics and large specific cooling power  $W$  [13]. The measurements were performed by a Large Temperature Jump (LTJ) method which was specifically developed to study the adsorption dynamics under typical conditions of isobaric stages of AC cycle [14]. The study was performed under four various boundary conditions of an adsorptive heat transformation cycle typical for air-conditioning application driven by low temperature heat [13]. For each boundary set and grain size the experimental kinetic curve were described by an exponential function up to 80–90% of the equilibrium conversion. Desorption runs are found to be faster than appropriate adsorption runs by a factor of 2.2–3.5. The size  $R$  of the adsorbent grains was found to be a powerful tool to manage the dynamics of isobaric water ad-/desorption. For large grains, the characteristic time was strongly dependent on the grain size and proportional to  $R^2$ . Much less important appeared to be an impact of the boundary conditions which variation just weakly affected the dimensionless kinetic curves for the four tested cycles. The maximal specific cooling/heating power exceeded 10 kW/kg, that is very attractive for designing compact AC units. Thus, very simple monolayer configuration of loose adsorbent grains results in quite fast sorption dynamics and large specific power.

However, one can expect that the COP is not optimal because the mass of adsorbent housed in the monolayer is small as compared with the inert masses of AC unit. Because of this, more realistic are configurations with the number of loose grains layers more than one. Thus, investigation of adsorption dynamics in a thin bed containing a *low number*  $n$  of loose grain layers ( $1 < n < 10$ ) is of high practical interest. Mathematical models of non-isothermal adsorption dynamics found in literature are mainly focused on two extreme cases: *a single adsorbent grain* ( $n = 1$ ) and *a porous adsorbent bed* composed of a *high number* of loose grain layers ( $n > 20$ ). New mathematical model based on a COMSOL Multiphysics simulation environment, which allows a simulation of the adsorption dynamics in the adsorbent beds consisting of a low number of adsorbent grains ( $1 \leq n < 10$ ) are being under development [15], however more mathematical and physical validations are still required.

The aim of this study was to make LTJ measurements and analyze the dynamics of water adsorption for multilayer configuration "*n*-layers of loose grains of a silica Fuji RD" with  $n = 2$  and 4 to see the effect of the number of layers. This configuration reflects a quite realistic situation of compact heat exchanger of a finned flat-tube type in which 2–4 adsorbent grains are housed in a 1–2 mm gap between the fins [9]. We have selected for the measurements only one boundary set typical for AC cycles driven by low temperature heat. The size of the Fuji silica grains was varied from 0.2 to 1.8 mm to investigate its effect on water sorption dynamics.

## EXPERIMENTAL PROCEDURE

The detailed diagram of LTJ procedure and an experimental test rig were described elsewhere [13, 16]. The LTJ method allows measuring the uptake curves for adsorbent layer located on a metal holder (fin) subjected to a fast temperature jump/drop. The jump was from the minimal desorption temperature  $T_2 = 58$  °C to the maximal desorption temperature  $T_{HS} = 80$  °C (run  $58$  °C  $\rightarrow$   $80$  °C) at the almost constant vapour pressure  $P \approx 56.6$  mbar. The latter corresponds to the condenser temperature  $T_c = 35$  °C. The drop was from the maximal adsorption temperature  $T_4 = 50$  °C down to the minimal adsorption temperature  $T_c = 30$  °C (run  $50$  °C  $\rightarrow$   $30$  °C) at the almost constant vapour pressure  $P \approx 8.8$  mbar ( $T_e = 5$  °C). The adsorption (desorption) process initiates a slight variation of the vapor pressure  $P(t) = P_0 \pm \Delta P(t)$ . The weight of dry sample was  $(0.314 \pm 0.004)$  g. The relative variation of total pressure  $\Delta P/P_0$  less than 10%, and water sorption process can be considered as a quasi-isobaric in a close analogy of isobaric AC stages. The temperatures  $T_2$  and  $T_4$  were taken directly from the working cycle diagram plotted in [13]. The specific uptake change  $\Delta w$  was 0.066 g/g.

Data of the pressure evolution  $P(t)$  required for calculating the water uptake  $q(t)$  were recorded each 1 s by a data acquisition system. The dimensionless *uptake* was calculated as

$$\chi = \frac{q_t}{\Delta q} = \frac{q(t) - q(t=0)}{q(t \rightarrow \infty) - q(t=0)} = \frac{P(t) - P(t=0)}{P(t \rightarrow \infty) - P(t=0)}. \quad (1)$$

The accumulated error in the absolute water loading showed a maximum *value* of  $\pm 10^{-3}$  kg/kg that leads to the accuracy of the differential water loading  $q(t)$  equal to  $\pm 3\%$ .

The grains of Fuji silica type RD of four sizes were tested as fractions 0.2–0.25, 0.4–0.5, 0.8–0.9, and 1.6–1.8 mm. The dry sample weight was maintained constant, so that the diameter  $D$  of the circle covered by the layer and the heat transfer surface  $S = \pi D^2/4$  were reduced accordingly (Fig. 1 and Table 1).

Table 1. Diameter  $D$  (mm) of the area covered by one, two and four layers of silica Fuji RD grains

Grain size $d$ , mm	Number of layers $n$		
	1	2	4
0.2–0.25	57.8	41.0	29.1
0.4–0.5	41.3	29.3	20.9
0.8–0.9	29.3	20.8	14.7
1.6–1.8	20.9	14.8	10.4

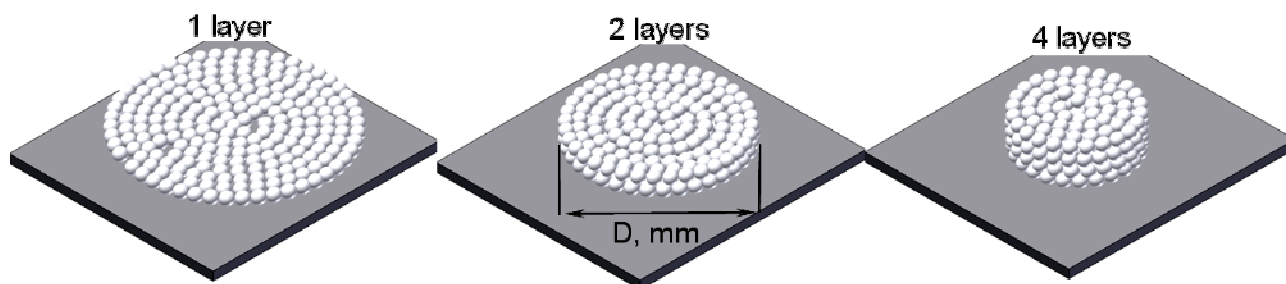


Fig. 1. Schematics of the loose grains configurations with  $n = 1, 2$  and  $4$

## RESULTS AND DISCUSSION

We have studied effects of the number of layers  $n$  and the adsorbent grain size  $d$  on the water sorption dynamics under conditions close to isobaric stages of AC cycle. The data obtained are used to estimate the cooling power per unit adsorbent mass and unit HEX surface area.

**Effect of the number of layers.** The near-exponential shape of ad- and desorption kinetic curves  $\chi(t) = 1 \pm \Delta\chi \exp(-t/\tau)$  has been revealed for all experimental runs (Fig. 2). Surprisingly, the complex coupled heat and mass transfer in the adsorbent later results in the very simple kinetic law, so that the dynamics of water ad-/desorption can be described by a *single* characteristic time  $\tau$  (Table 2). This kinetic law, probably, reflects the universal regularity of the nature that the rate of relaxation to equilibrium is proportional to the deviation from the equilibrium. For our particular case, it means that a Linear Driving Force (LDF) model can be satisfactorily applied to analyze the major part of isobaric ad-/desorption processes under conditions specified. However, on contrary to common application of the LDF model [17], the formally derivable rate constant  $K = 1/\tau$  has to be independent on temperature [18]. This universal kinetic law permits stupendous simplification of the analysis and easy quantitative characterization of AC dynamics. The tail of the experimental kinetic curves can be slower than the exponential one and the deviation tends to increase for smaller grains and thicker layers. This long tail can be caused by a poor accordance between the driving force for heat transfer and the derivative  $dq/dT$  which defines the heat demand for desorption or heat release during adsorption as discussed in [18, 19].

For all experimental runs, a gradual slowing down of the ad-/desorption process with increasing the number of layers  $n$  is observed as seen from Fig. 2. The kinetics curves for the smallest grains (0.2–0.25 mm) reveal the least sensitivity to the layers thickness. It is especially representative for the desorption run: the kinetics at  $n = 1$  and 2 virtually coincide (Fig. 2 b). This is because the water sorption itself on so small grains is very fast and controlled by the heating scenario of the system "metal plate and adsorbent". As the main time is taken for heating the metal plate (app. 10 s [13]), the desorption dynamics is almost similar for  $n = 1$  and 2. For the thicker layer ( $n = 4$ ), the desorption becomes slower and the characteristic times increases by a factor of 2.0 (Fig. 2 b). Table 2 summarizes the characteristic times  $\tau$  and  $\tau_{0.5}$ ,  $\tau_{0.8}$ ,  $\tau_{0.9}$  that correspond to reaching 50, 80 and 90% of the equilibrium uptake. The data for the monolayer configuration are taken from [13].

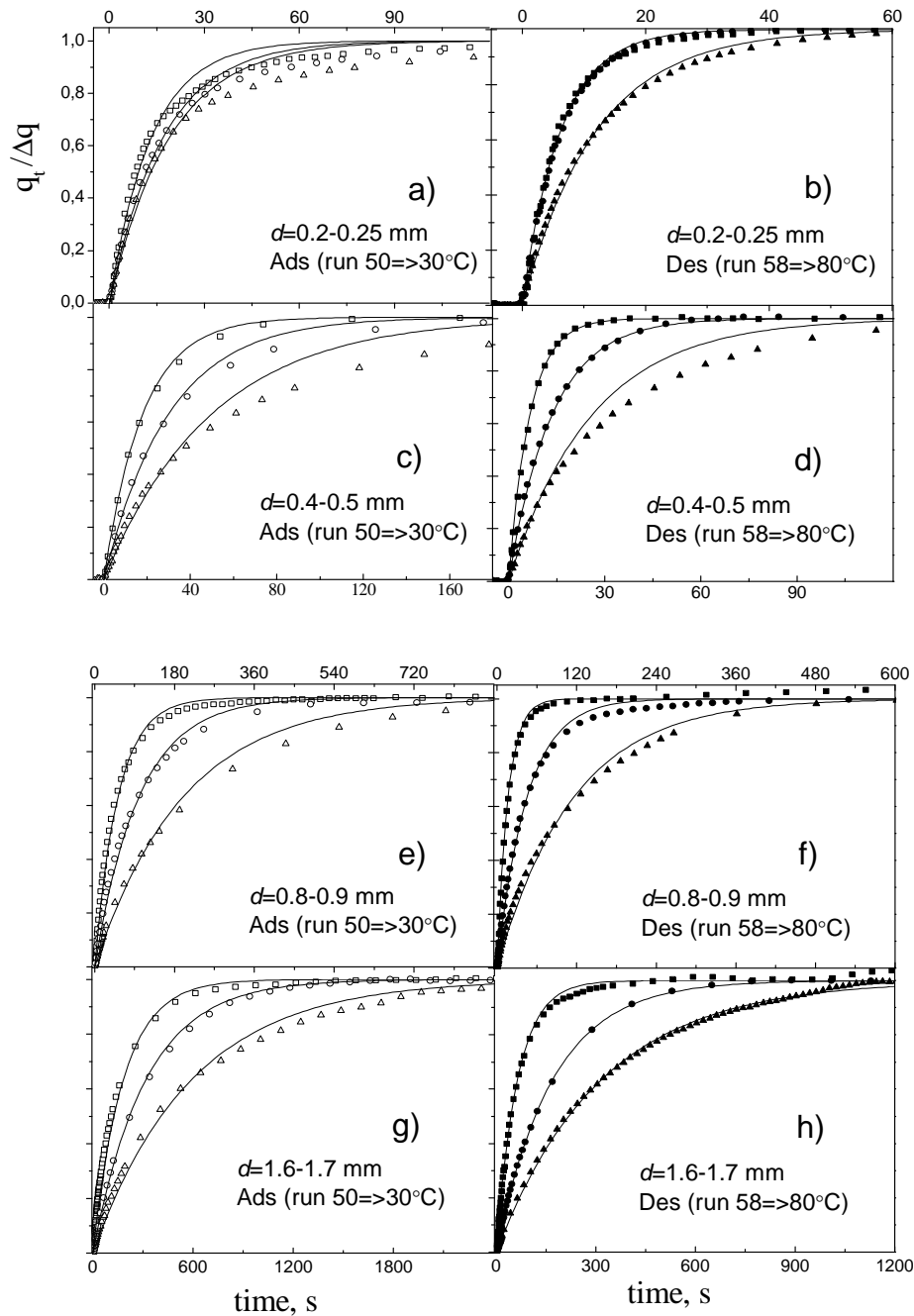


Fig. 2. Dimensionless uptake/release curves of water ad-/desorption for one (□, ■), two (○, ●) and four (Δ, ▲) layers configurations. Solid lines – exponential approximation

In the first approximation, the characteristic time  $\tau_{0.8}$  linearly grows with the number of layers,  $\tau_{0.8} = Kn$ , and the slope  $K$  significantly increases for larger grains (Fig. 3). Hence, both adsorption and desorption are slower for these grains, first of all, due to enhanced intraparticle diffusional resistance. For desorption runs, the slope  $K$  is app. 2 times smaller. It indicates that under the tested conditions, the desorption is always faster than appropriate adsorption. In our opinion, this could be due to higher average temperature and vapor pressure during the desorption stage. A concave shape of the water sorption isobar of Fuji silica RD is profitable for desorption process as well [19]. The precise ratio <adsorption time/desorption time> is found to have a tendency to reduce with the increasing number of layers (Fig. 4). The marked difference in durations of these stages allows optimization of the overall cycle COP and the specific cooling power by appropriate prolongation of adsorption phase at the expense of shortening of desorption phase as suggested in [9].

Table 2. The characteristic sorption times  $\tau$ ,  $\tau_{0.5}$ ,  $\tau_{0.8}$ ,  $\tau_{0.9}$  and the specific powers  $W_{\max}$  and  $W_{0.8}$  for the two boundary conditions and various  $n$

Grain size, mm	Run, °C	$N$ of layers	$\tau$ , s	$\tau_{0.5}$ , s	$\tau_{0.8}$ , s	$\tau_{0.9}$ , s	$W_{\max}$ , kW/kg	$W_{0.8}$ , kW/kg	$\overline{W}_{0.8}$ , kW/kg	$W_{0.8}^{sur}$ , kW/m <sup>2</sup>
0.2–0.25	50.0=>30	1	13.3	8.0	25.6	42.0	11.9	5.11	3.70	0.61
		2	17	11	30.9	57.3	9.0	4.23	3.16	1.00
		4	19	12.2	39.3	78.6	8.6	3.32	2.17	1.57
	58.0=>80	1	6.2	4.2	9.8	15.2	–	–	–	–
		2	6.2	4.4	10.4	15.2	–	–	–	–
		4	12	8.3	20.9	31.4	–	–	–	–
0.4–0.5	50.0=>30	1	18	11.8	31.1	46.2	8.4	4.2	3.14	0.98
		2	30	20.1	55.3	88.6	5.1	2.36	1.69	1.10
		4	50	36.2	115.3	188	3.6	1.13	0.76	1.03
	58.0=>80	1	6.7	4.7	10.5	14.9	–	–	–	–
		2	13.5	9.1	21.9	31.7	–	–	–	–
		4	26	21	56.7	84	–	–	–	–
0.8–0.9	50.0=>30	1	47.3	31.2	86.2	135	3.9	1.51	1.15	0.70
		2	100	65.1	180	284.5	1.85	0.72	0.50	0.67
		4	200	145	391	580	1.05	0.33	0.22	0.61
	58.0=>80	1	16.5	11.1	27.2	41	–	–	–	–
		2	45	30.3	78.2	125	–	–	–	–
		4	115	79	209	300	–	–	–	–
1.6–1.8	50.0=>30	1	182	112	300.4	470	1.16	0.43	0.32	0.39
		2	316	225	553	795	0.59	0.23	0.15	0.42
		4	588	380	1053	1570	0.31	0.12	0.08	0.44
	58.0=>80	1	64	42.8	106	160	–	–	–	–
		2	169	116	275	390	–	–	–	–
		4	315	216	520	740	–	–	–	–

**Estimation of the specific power.** Knowledge of experimental curve  $q(t)$  readily allows the calculation of the instant and average specific cooling power  $W$  released in the evaporator during the adsorption stage (Table 2). The maximal specific power releases at the beginning of adsorption stage. It can be calculated from the initial slope  $dq/dt$  of uptake curve as  $W_{\max} = h_{fg} dq/dt$ , where  $h_{fg}$  is the latent heat of water

vaporization (2478 kJ/kg). For any grain size, a ratio of the characteristic times  $\tau_{0.9}/\tau_{0.8}$  is as much as 1.4–1.8 that prompts to restrict the duration of AC isobaric stages by the time  $\tau_{0.8}$  or less. This would allow avoiding a dramatic drop of the specific cooling power at longer times with just little reduction of the cycle COP.

For practice, the most valuable are the specific cooling power  $W_{0.8} = h_{fg} 0.8\Delta q / \tau_{0.8}^{ads}$  and its cycle average value  $\overline{W}_{0.8}$ . Neglecting durations of the isosteric stages, the latter can be estimated as (Table 2)

$$\overline{W}_{0.8} = \frac{0.8\Delta q h_{fg}}{\tau_{0.8}^{ads} + \tau_{0.8}^{des}}. \quad (2)$$

The grain size appears to be a powerful tool to manage the dynamics of isobaric stages of AC cycle. To increase the value of  $\overline{W}_{0.8}$  it is profitable to reduce the size of adsorbent grains. The maximal average cycle power is obtained for monolayer of the smallest grains (0.2–0.25 mm),  $\overline{W}_{0.8} = 3.8$  kW/kg (Table 2). On the other hand, the adsorbent mass per unit surface area  $m/S = 0.12$  kg/m<sup>2</sup> is quite low in this case. It seems to be unpractical in terms of low COP-value because of too small mass of adsorbent with respect to the mass of metal fins and other inert masses. More realistic are multi-layer configurations containing, e. g., 2 and 4 layers of 0.2–0.25 mm grains or 2 layers of 0.4–0.5 mm grains. A monolayer configuration of 0.4–0.5 and 0.8–0.9 mm grains also can result in the average cycle power larger than 1 kW/kg (Table 2) that is very attractive for practical use. The value of  $\overline{W}_{0.8}$  rapidly decreases with rising the grain size, and application of silica grains larger than 1 mm is not recommended. This conclusion is confirmed by Fig. 5 which clearly demonstrates that the cooling power calculated per 1 m<sup>2</sup> of the metal support (heat exchanging surface) strongly reduced for the large silica grains. One again, the grains smaller than 1 mm should be used.

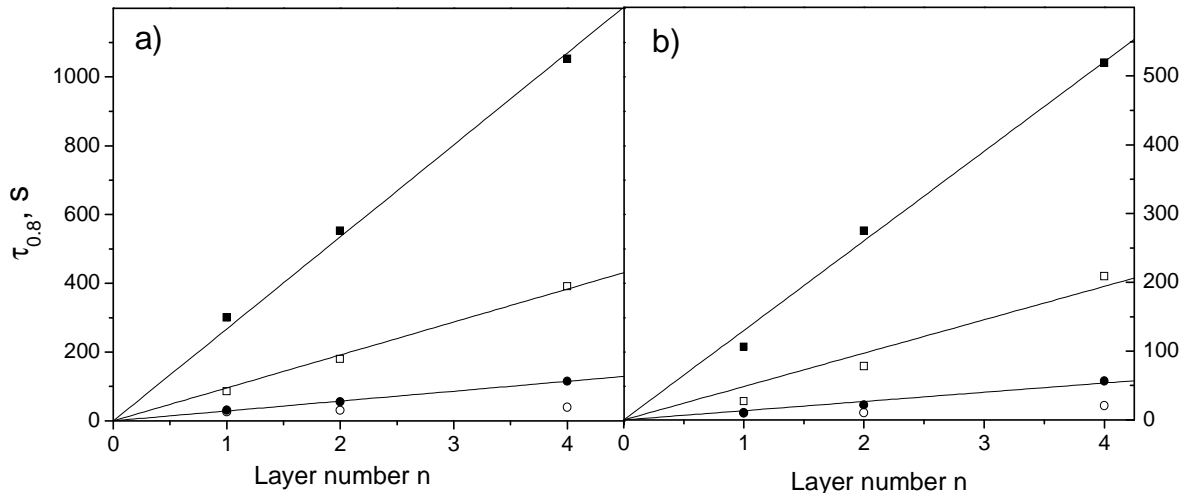


Fig. 3. Characteristic time  $\tau_{0.8}$  vs. the number of layers for adsorption (a) and desorption runs (b), ○ – 0.2–0.25, ● – 0.4–0.5, □ – 0.8–0.9 and ■ – 1.6–1.8 mm

Interestingly that the cooling power generated by the unit surface area of the heat exchanger does not depend on the number of layer, but only on the adsorbent grain size (Fig. 5). Hence, for sufficiently large grains even a monolayer configuration is capable to ensure the surface power  $W_{0.8}^{sur}$  that is maximal possible at a fixed grain size. For small grains, this maximal power can be realized only for multilayer configuration. Thus, the total cooling power of AC unit can be easily estimated by knowing  $W_{0.8}^{sur}$  and the contact area  $S$ .

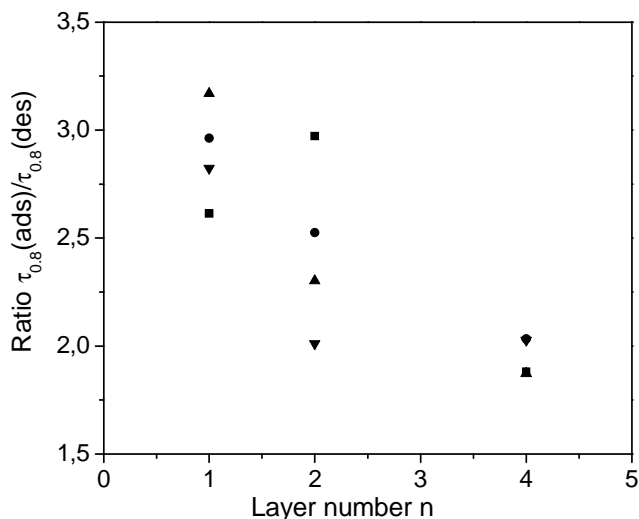


Fig. 4. Time ratio of 80% equilibrium uptake reaching for adsorption and desorption. ■ – 0.2–0.25, ● – 0.4–0.5, ▲ – 0.8–0.9 and ▼ – 1.6–1.8 mm

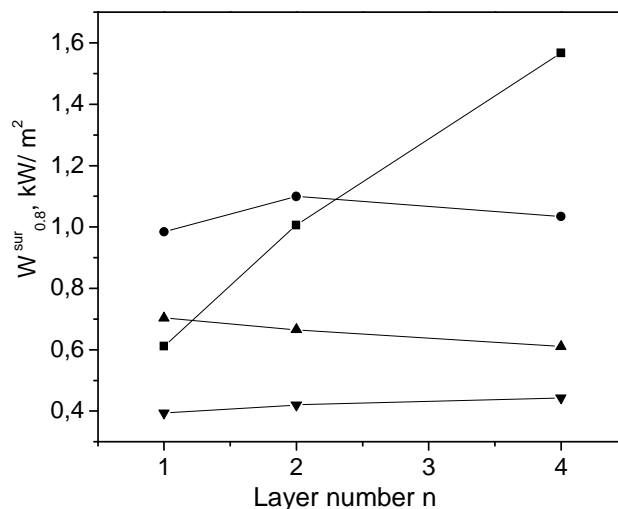


Fig. 5. Specific cooling power for adsorption stage related to the surface area covered by adsorbent. ■ – 0.2–0.25, ● – 0.4–0.5, ▲ – 0.8–0.9 and ▼ – 1.6–1.8 mm

## CONCLUSIONS

The aim of this paper is to analyze the water sorption dynamics for a simple configuration of the “adsorbent – heat exchanger” unit, namely,  $n$ -layers of loose adsorbent grains located on a metal plate ( $n = 1, 2$  and  $4$ ). The plate is subjected to fast temperature drop ( $50\text{ °C} \rightarrow 30\text{ °C}$ ) or jump ( $58\text{ °C} \rightarrow 80\text{ °C}$ ) that are typical for AC cycles driven by low temperature heat. The study is performed by a Large Temperature Jump method which closely simulates conditions of ACs. The size of the Fuji silica RD grains is varied from 0.2 to 1.8 mm to investigate its effect on the water sorption dynamics. The loose grain configuration is often used in laboratory prototypes and real units of adsorption chillers, and is an alternative to the consolidated layer configuration as mentioned in the Introduction.

This study shows that for any grain size the experimental kinetic curves are nearly exponential up to the equilibrium conversion of 50–90%, so that the dynamics of water ad-/desorption can be approximated by a *single* characteristic time  $\tau$ . This permits stupendous simplification of the analysis and easy quantitative characterization of AC dynamics. The tail of the kinetic curves can be slower than the exponential one and the deviation tends to increase for smaller grains and thicker layers.

For all experimental runs a gradual slowing of the ad-/desorption process with increasing number of layers  $n$  is observed. In the first approximation, the characteristic times of ad-/desorption linearly grow with the number of layers,  $\tau = Kn$ , and the slope  $K$  significantly increases for larger grains that is due to an enhanced intraparticle diffusional resistance. For the desorption runs, the slope  $K$  is app. 2 times smaller, thus, the desorption is always faster than appropriate adsorption. For any grain size, a ratio of the characteristic times  $\tau_{0.9}/\tau_{0.8}$  is 1.4–1.8 that prompts one to restrict the duration of AC isobaric stages by the time  $\tau_{0.8}$  or less. This would allow avoiding a dramatic drop of the specific cooling power at longer times with just little reduction of the cycle COP. Some other recommendations on improving the cycle dynamics are also made.

### Acknowledgments

The authors thank the Russian Foundation for Basic Researches (grants 10-08-91156a) as well as the Siberian Branch of the Russian Academy of Science (project N 022) for partial financial support and Dr. M. Ito (Fuji Silysia Chemical Ltd.) for providing us with the Fuji silica type RD.

### References

1. Guilleminot J. J., Choisier A., Chalfen J. B. Heat transfer intensification in fixed bed adsorbers // *Heat Recovery Systems & CHP*. 1993. Vol. 14. Pp. 297–300.
2. Strauss R., Schallenberg K., Knocke K. F. Measurement of the kinetics of water vapor adsorption into solid zeolite layers // *Proc. Int. Symp. Solid Sorption Refrigeration, Paris*. 1992. Pp. 227–231.
3. Lang R., Roth M., Stricker M. Development of a modular zeolite-water heat pump // *Proc. Int. Sorption Heat Pump Conf., Munich, Germany*. 1999. Pp. 611–618.
4. Bauer J., Herrmann R., Mittelbach W., Schwieger W. Zeolite/aluminum composite adsorbents for application in adsorption refrigeration // *Int. J. Energy Research*. 2009. Vol. 33. Pp. 1233–1249.
5. Bonaccorsi L., Proverbio E. Synthesis of thick zeolite 4A coatings on stainless steel // *Microporous Mesoporous Materials*. 2004. Vol. 74. Pp. 221–229.
6. Raymond A., Garimella S. Intraparticle Mass Transfer in Adsorption Heat Pumps: Limitations of the Linear Driving Force Approximation // *J. Heat Transfer*. 2011. Vol. 133. Pp. 42001–42013.
7. Saha B. B., Akisawa A., Kashiwagi T. Solar/waste heat driven two-stage adsorption chiller: the prototype // *Renew Energy*. 2001. Vol. 23. Pp. 93–101.
8. Freni A., Sapienza A., Glaznev I. S., Aristov Yu. I., Restuccia G. Testing of a compact adsorbent bed based on the selective water sorbent "silica modified by calcium nitrate" // *Int. J. Refrigeration*. 2011. Vol. 34. ([doi: 10.1016/j.ijrefrig.2010.05.015](https://doi.org/10.1016/j.ijrefrig.2010.05.015))
9. Aristov Yu. I., Sapienza A., Freni A., Ovoshnikov D. S., Restuccia G. Reallocation of adsorption and desorption times for optimizing the cooling cycle parameters // *Int. J. Refrigeration*. 2011. Vol. 34. ([doi:10.1016/j.ijrefrig.2010.07.019](https://doi.org/10.1016/j.ijrefrig.2010.07.019)).
10. Tamainot-Telto Z., Metcalf S.J., Critoph R.E. Novel compact sorption generators for car air conditioning // *Int. J. Refrigeration*. 2009. Vol. 32. Pp. 727–733.
11. Matsushita M. Adsorption chiller using low-temperature heat sources // *Energy Conservation*. 1987. Vol. 39. Pp. 96–106.
12. Wang D. C., Wu J. Y., Xia Z. Z., Zhai H., Wang R. Z., Dou W. D. Study of a novel silica gel-water adsorption chiller. Part II. Experimental study // *Int. J. Refrigeration*. 2005. Vol. 28. Pp. 1084–1091.
13. Glaznev I. S., Aristov Yu. I. The effect of cycle boundary conditions and adsorbent grain size on dynamics of adsorption chillers // *Int. J. Heat & Mass Transfer*. 2010. Vol. 53. Pp. 1893–1898.
14. Aristov Yu. I., Dawoud B., Glaznev I. S., Elyas A. A new methodology of studying the dynamics of water sorption/desorption under real operating conditions of adsorption heat pumps: Experiment // *Int. J. Heat and Mass Transfer*. 2008. Vol. 51. Pp. 4966–4972.
15. Freni A., Aristov Yu. I., Maggio G., Glaznev I. S., Cipiti F. Simulation of water sorption dynamics in adsorption chillers: one, two and four layers of loose silica grains // *Appl. Therm. Engn.* 2011 (submitted).
16. Glaznev I. S., Aristov Yu. I. Kinetics of water adsorption on loose grains of SWS-1L under isobaric stages of adsorption heat pumps: The effect of residual air // *Int. J. Heat and Mass Transfer*. 2008. Vol. Pp. 5823–5827.
17. Sakoda A., Suzuki M. Fundamental study on solar powered adsorption cooling system // *J. Chem. Engn. Japan*. 1984. Vol. 17. Pp. 52–57.
18. Aristov Yu. I. Optimal adsorbent for adsorptive heat transformers: Dynamic considerations // *Int. J. Refrigeration*. 2009. Vol. 32. Pp. 675–686.
19. Okunev B. N., Gromov A. P., Heifets L. I., Aristov Yu. I. A new methodology of studying the dynamics of water sorption/desorption under real operating conditions of adsorption heat pumps: Modeling of coupled heat and mass transfer // *Int. J. Heat and Mass Transfer*. 2008. Vol. 51. Pp. 246–252.

## THERMAL MANAGEMENT OF THE ADSORPTION-BASED VESSEL FOR HYDROGENOUS GAS STORAGE

Leonard L. Vasiliev, Larisa E. Kanonchik, Valery A. Babenko  
Luikov Heat & Mass Transfer Institute, National Academy of Sciences  
P. Brovka, 15, 220072, Minsk, Belarus  
Phone/Fax: (375-17) 284-21-33; E-mail: kanon@hmti.ac.by

### Abstract

Heat management is the design bottleneck in creation of rational gas storage sorption systems. Inefficient heat transfer in sorption bed is connected with relatively low thermal conductivity (0.1–0.5 W/(m·K)) and appreciable sorption heat of activated gas storage materials. This work is devoted to development and research of the thermally regulated onboard system of hydrogenous gas (methane, and hydrogen) storage applying the novel carbon sorbents. We suggested the hydrogenous gas storage based on combined gas adsorption and compression at moderate pressures (3–6 MPa) and low temperatures (from the temperature of liquid nitrogen about 77 K to 273 K).

### KEYWORDS

Vessel, sorbent, hydrogen, heat pipe, sorption storage.

### INTRODUCTION

Success in development of new hydrogen technologies, such as fuel cells, transport systems on hydrogen and methane, sorption heat pumps has shown that the use of hydrogenous gas results in qualitatively new solutions of ecological and power problems. The advantage of hydrogen and natural gas use is associated with ecological cleanliness. Adsorbed hydrogenous gas is a promising alternative to both existing technologies for gas storage since the same amount of gas can be stored at much lower pressure (2–6 MPa) in thinner walled tank and the method does not require expensive and cumbersome compression or liquefaction equipment. Key points of adsorption gas technology are high sorbent property and the vessels thermal management. The problem is that according to the thermodynamic laws, during the process of adsorption, the sorbent and gas temperature is increased, and hydrogen (methane) uptake by the sorbent diminishes as function of filling time. Correspondingly, lowering the temperature during adsorption provides for reduction of the vessel filling time and increase of hydrogenous gas uptake. At the high intensive gas output the degree of the stored gas can decrease up to 50–60 %. This is in contrast to hydrogen and methane storage by cryogenic liquefaction and by compression at very high pressure, where the stored gas is easily accessible for use.

Hydrogen can potentially be stored at high density and low pressure by absorption in metallic hydrides. Currently metal hydrides have been commercialized and hydride tanks are commercially available. Daimler Benz, Honda and Mazda are among the several car companies to have tested metal hydrides for vehicular propulsion. Daimler Benz has demonstrated a combination of low temperature (FeTi) and high temperature hydride (Mg<sub>2</sub>Ni) tanks to store hydrogen [1]. The uptake capacity of hydrogen in the case of hydrides is dependent on temperature, pressure and alloy composition. It is expected that the hydride tanks will be charged at ambient conditions. While most metal hydrides are too heavy, too expensive or bond too strongly to hydrogen, recent research has identified sodium alanate (NaAlH<sub>4</sub>) as a potentially practical hydride for vehicular applications. However, multiple issues remain. Hydrides release considerable thermal energy as they adsorb hydrogen and require significant thermal energy (10–20% of the H<sub>2</sub> lower heating value) input to release hydrogen. Therefore, hydride beds typically need to be built with heating and cooling passages to allow fast refuelling and desorption, reducing the system volumetric and gravimetric energy storage density. Many metals and alloys can also reversibly adsorb large amounts of hydrogen, but the adsorption energy is in the region of 50–100 kJ/mol [2]. Problems of technical design of metal hydride hydrogen accumulators are next: 1) necessity of introduction of gas filters or elaboration of metal hydride composites giving no dusting wear; 2) possible appearance of substantial stresses in the container walls at too high density of the

powdered bed (maximum allowed powder density of a of metal hydride material in the container should be no more than 60% of its true density).

Hydrogen and methane physisorption is considered as one of the most promising storage technology for meeting the DOE goals. In contrast to the chemisorptions in metal hydrides, the phenomenon of physical adsorption of the undissociated hydrogen molecules on a surface of microporous carbon fibres or particles is a good direction to improve the situation. The sorption energy of different carbon materials is only 2–10 kJ/mol [2]. Reducing the storage pressure while maintaining a high gravimetric and volumetric density represents a goal to reduce costs and enhance safety. As it was demonstrated in [3] the stored methane capacity is much more sensitive to level temperatures and heat transfer than to mass transfer limitations. It is possible to counteract to negative effects by the sorbent heating during gas output with help of a special thermal control system. Same thermal control system can be used for sorbent cooling during hydrogenous gas refuelling [4]. In the patent [5] the overlapping of channels for an air flow (temperature control) and sorbent sections natural gas storage) for vehicle tank is described. Another perspective direction is sorbent bed thermal conductivity increasing by briquetting with high thermal conductivity inert material (graphite) or without [6].

In an ordinary adsorptive storage cylinder the gas flows axially through the carbon bed, which means that radial heat transfer takes place mainly by conduction. This is not particularly effective because granular beds are known to exhibit poor heat transfer characteristics. Chang and Talu [7] proposed changing the flow direction during discharge from axial to radial by a perforated tube inserted at the centre of the cylinder. Thin perforated tube helps to organize radial motion of gas inside the sorbent bed. The powdery activated carbon with rather high methane sorption capacity was used as the sorbent. For example, capacity was 0.134 m<sup>3</sup>/kg at ambient temperature 293 K and pressure 2 MPa. During the gas output from the tank temperature drops up 37 K inside the sorbent and total amount of desorbed natural gas was in 25 % less in comparison with isothermal conditions.

With the reduction of storage pressure through the use of the AHG technology, it is possible to use other vessels geometries which endure the high pressures created by the GNG technology. This imparts the design greater versatility. Another advantage of storage pressure reduction allows us to use lighter materials in the making of AHG vessels, as for example, aluminium because the stresses obtained would be smaller. The purpose of this approach is to reduce vessel weight, which today is around 70 kg. The DOE targets for operating temperature range are 233 to 323 K. Cryogenic temperatures are not expected to be acceptable for economic reasons. Nevertheless, it has been shown [8], that the hydrogen DOE target for 2005 (4.5 wt% H<sub>2</sub>) could be met with an isolated aluminium container (Fig. 1 a) and a commercially available activated carbon material (300 g/m<sup>2</sup>) at a temperature of 77 K and a pressure of 5–10 MPa.

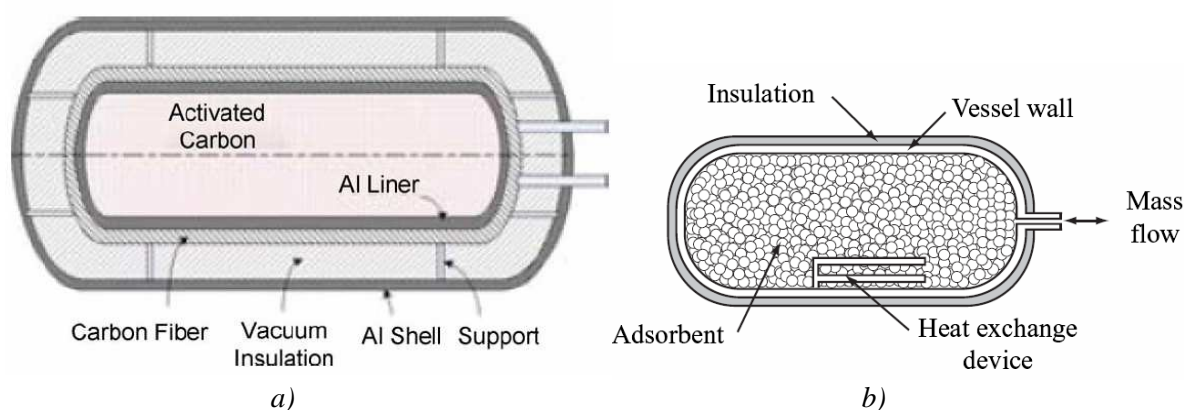
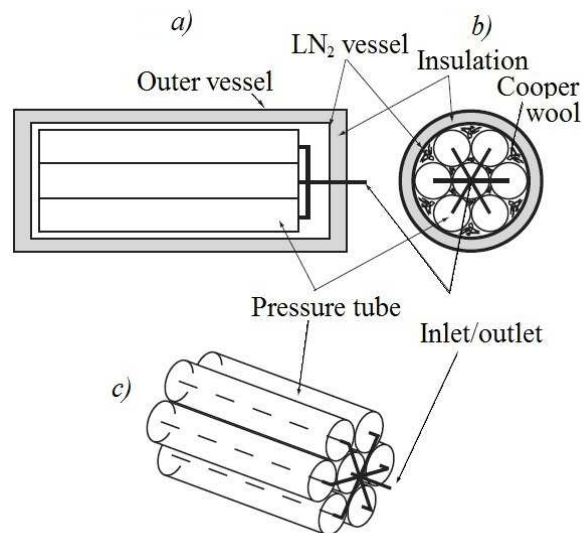


Fig. 1. Typical (a) low temperature carbon hydrogen storage system [8] and a scheme (b) for a cryogenic adsorption-based vessel [9]

The work [9] considers an adsorption hydrogen vessel with multilayer vacuum super insulation and 3.5 MPa maximum operating pressure. The purpose of the heat exchange device is to cool or heat the system (Fig. 1 b). The vessel was designed to store 5 kg of hydrogen at the temperature 80 K (internal volume

158 L, mass of activated carbon in the vessel 110 kg). The used adsorbent, superactivated carbon AX-21<sup>TM</sup>, was pellets with a bulk density of 700 kg/m<sup>3</sup>. At 3.5 MPa, the cooled vessel stores three times more mass than the adiabatic vessel.

The paper [10] presents cryo-adsorption vessel for hydrogen storage (Fig. 2). It has seven pressure tubes



which are filled with powdered activated carbon for hydrogen storage. The tubes are one meter long with internal diameter of 80 mm and made of austenitic steel. The pressure tubes are located inside a vessel that can be filled with liquid nitrogen (LN<sub>2</sub>) to cool down the vessel. The LN<sub>2</sub> vessel is as well filled up with cooper wool in order to achieve a better thermal distribution along the tubes, smooth boiling effects and physically connect the pressure tubes and the LN<sub>2</sub> vessel wall, on the outer surface of which a heating mat is located for heating. The adsorbent (superactivated carbon AX-21<sup>TM</sup> made by Future Carbon GmbH from

Fig. 2. The experimental adsorption vessel with the different parts and components: (a) view along the axis; (b) axial cross-section view; (c) pressure tubes arrangement inside the N<sub>2</sub> vessel [10]

coconut shells, a specific surface area of 1800 m<sup>2</sup>/g) was slightly compressed into the pressure tubes so that a bed density of 340 kg/m<sup>3</sup> could be achieved. With this parameterization, each pressure tube contains 2 kg of adsorbent and can store about 144 g of hydrogen, so that 35 pressure tubes are necessary in order to achieve a storage capacity of 5 kg at the pressure 3 MPa. The removal of 9.54 MJ of energy is required for filling the pre-cooled vessel from the evacuated state to 3 MPa at 77 K, which corresponds to the evaporation heat of about 60 litres of liquid nitrogen.

It should be mentioned, that the heat or cold must be delivered as evenly as possible to all sorbent portions, placed into vessel. The currently employed methods of heating using electrical heaters, water coils, hot exhaust gas tubes, etc. do not provide required heat uniformity in the vessel and have very low efficiency. To complicate the matters, only direct blowing of the vessel or using of expensive and complex water heat exchangers or special refrigerators can deliver the cool. The heat pipes that are proposed as a basic element of the thermal management system for storage vessels are known in principle in the art. In general, a heat pipe is a hollow thin-walled metal cylinder or component of any other configuration. The inner surface of the heat-pipe wall is coated with a capillary-porous material impregnated with evaporating liquid. The inside channel of the heat pipe is filled with vapour of the above liquid. There are several Japanese applications (05-092369, 60042867) and patents (JP59003001, JP622204099), also single US patent (4,599867) concerning to employing of heat pipes for hydrogen storage tanks.

A new method of hydrogenous gas storage and transportation by L. L. Vasiliev et al. published in the works [11, 12] discloses a multicell gas storage tank including heat pipes located in the tank internal crosspieces (Fig. 3). The design pressure of the tank is 3.5–6 MPa. Every separate section has the case made from an aluminium (or reinforced plastics) and filled with briquette sorbent material where hydrogenous gas is situated in adsorbed and compressed states. Heat pipes can easily be implemented inside the sorption storage vessel due to its flexibility, high heat transfer efficiency, cost-effectiveness, reliability, long operating life, and simple manufacturing technology. The metal fins on the heat pipe surface serve for intensification of heat transfer in the sorbent bed. The efficient system to perform the thermal control of sorbent bed during its sorption/desorption is heat pipe heat exchanger. A flat rectangular, rather than cylindrical form is convenient for gas vessel location in the automobile. The collector channels for gas supply and release were manufactured by extrusion inside of aluminium case. Longitudinal grooves in the case can be replaced with cylindrical channels in a sorbent body at the centre of each section in parallel to

the axis of heat pipe. Suggested design (sorbent "Busofit-M8") provides a hydrogen-supply of  $330 \text{ nm}^3/\text{m}^3$  at average pressure 6 MPa and the liquid nitrogen temperature (Fig. 4).

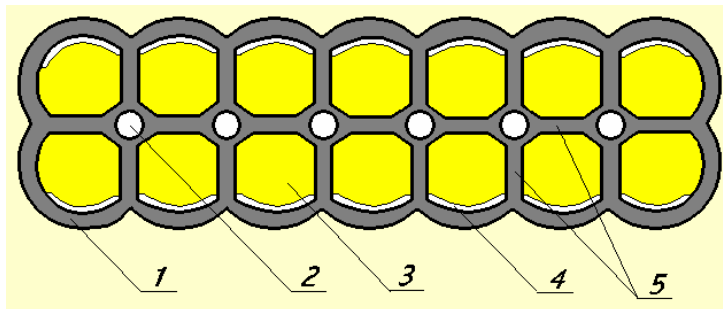


Fig. 3. The flat sectional vessel for natural gas (or hydrogen) sorption storage: 1 – vessel case, 2 – heat pipe, 3 – sorbent, 4 – channel for gas removal, 5 – longitudinal fins/partitions [12]

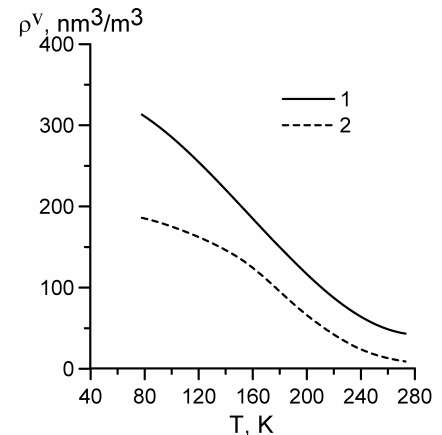


Fig. 4. Volume storage density of hydrogen (1 – the adsorbed and compressed gases; 2 – the adsorbed gas) vs. temperature

This paper presents a numerical investigation of the thermally regulated cylindrical vessel for storage of hydrogenous gas. To diminish the negative influence of latent heat of adsorption on the process of gas refuelling/extraction of the vessel a heating element (HE) is placed near the cylinder axis. This heating element can be finned heat pipe, thermosyphon or two-phase heat exchanger. There is a small annular gap between sorbent bed and cylinder wall. The annular channel acts like a gas collector for input or output of the gas. Cartridge type of gas storage system, assembled of the separate cylindrical vessels, is proposed to diminish thickness of sorbent bed. The separate cylindrical vessel is located inside a flat casing that can be filled with a heat-transfer agent. They are arranged in parallel, completely separated from each other and share the same vessel inlet/outlet opening through a manifold. A micro-porous solid sorbent (carbon fibre "Busofit-M") is packed in the cylinder to increase the storage density and to reduce operating pressure (3.5–6 MPa). The sorbent had the following characteristics: the specific heat capacity  $840 \text{ J}/(\text{m}^2 \cdot \text{K})$ , the sorbent bed density  $500 \text{ kg}/\text{m}^3$ , the effective heat conductivity  $0.24 \text{ W}/(\text{m} \cdot \text{K})$ , the total porosity 0.78, advanced surface area  $S_{\text{BET}} = 1939 \text{ m}^2/\text{g}$  and the big number of micropores  $V_{\text{DR}} > 1 \text{ ml}/\text{g}$ .

## NUMERICAL STUDY

A peculiarity of the designed storage vessel is the combination of heat transfer processes and accumulation of hydrogenous gas in one volume. The rate of hydrogen charging (time of filling) is determined by the reaction rate of gas adsorption and heat transfer processes in a sorbent bed. In vessel during charging non-steady variation of temperature and pressure takes place. The pressure in vessel increases, and the temperature can, both to increase, and to decrease depending on the size of thermal source due to sorption reaction and heat exchange conditions on sorbent borders. The equilibrium adsorption  $a_{eq}(P, T)$  depends on the two thermodynamic variables. It increases with the growth of pressure and the reduction of temperature. To charge a cylinder fully, it is necessary that the pressure and temperature in sorbent reach their nominal values, and these parameters should be sustained during a certain time necessary for sorption reaction. Sorption reaction is exothermal and slow enough, and for full transiting of reaction one should take away the heat generated in sorbent in the course of charging. The nonequilibrium adsorption tends to its equilibrium value but with a considerable delay determined by sorption kinetics. This delay is of the order of tens seconds, and it should be considered at design of optimum modes of charging. It is technically possible to realize sharp build-up of pressure in vessel at the moment of its connection to the high-pressure tank. As to variation of temperature, it has slower character in view of essential heat capacity of structural materials. Therefore, it is hardly probably to realize sharp decreasing of sorbent temperature.

Even if such drop of temperature would manage to be realized, it would cause a raise of reaction rate and by virtue of it an increase of temperature, i.e. the negative feed-back is implemented. Sharp pressure raise in vessel (pressure jump) is inexpedient for a variety of reasons. First, it can cause tiredness and destruction of construction parts especially dangerous combined with the low temperature of charging. Second, such a process is nearly adiabatic, heat removal from sorbent has no time to decrease its temperature, and reaction nearly suspended in view of releasing heat. For a short time the reaction can even change its sign, and instead of sorption the desorption will be realized. The problem of the adsorption-based vessel modelling came thus to the consideration of different charge/discharge scenarios and to choice of the best one. It is assumed that at the initial stage of charging the mode is realized with a constant inlet mass flow rate until the working pressure is reached inside the vessel. After that, the redactor is switched off and further the charging is continued in a mode of a constant high pressure at the inlet. It is described mathematically by the change of boundary condition at the moment when nominal pressure is reached at the inlet.

**Mathematical model** of cylindrical system for storage of hydrogenous gas in adsorbed state represents the system of 2D partial differential equations of non-steady balance: for energy, mass and momentum in porous homogeneous medium, supplemented by the equations of equilibrium sorption and sorption kinetics. For free gas in voids of vessel also equations of mass and energy balance were solved together with Navier – Stokes equations. For construction elements made of metal, non-steady heat conduction equation was solved. All the equations were formulated in cylindrical coordinates. The system of equations was solved with finite element method.

The model of heat transfer and gas sorption processes in the vessel is based on the following assumptions: 1) the hydrogenous gas is assumed to obey the perfect gas law (this assumption is valid below 20 MPa); 2) the porous medium is assumed homogenous and isotropic; 3) the temperature of the solid phase is equal to the temperature of the gas phase at each point, because of the high coefficient of the volumetric heat transfer between them; 4) heating and cooling of the sorbent material is carried out by heat pipe (HP) with inner heat transfer coefficient  $\alpha_{HP} = 10^3 - 10^4$  W/(m<sup>2</sup>·K), this coefficient is uniform along the surface and high in comparison with the thermal resistance of interface HP-sorbent bed.

In essence, the porous media model is nothing more than an added momentum sink in the governing momentum equations. The time-dependent mass conservation equation for the hydrogen flow in a sorbent bed may be written as:

$$\frac{\partial \rho_g}{\partial \tau} + \nabla \cdot (\rho_g \mathbf{v}) = -\rho_s \frac{(1-\varepsilon)}{\varepsilon} \frac{\partial a}{\partial \tau}, \quad (1)$$

Neglecting the momentum loss due to adsorption phenomena, the time-dependent momentum transport equation is similar to the one used for classical homogenous porous media:

$$\frac{\partial}{\partial \tau} (\rho_g \mathbf{v}) + \nabla \cdot (\rho_g \mathbf{v} \mathbf{v}) = -\nabla P + \nabla \cdot (\overline{\tau}_{st}) + \mathbf{F}, \quad (2)$$

where  $\rho_g$  is the gas density,  $P$  – the static pressure,  $\mathbf{v}$  – the velocity vector,  $\overline{\tau}_{st}$  – is the stress tensor;  $\mathbf{F}$  represents an additional friction term due to the porous medium. The friction source term accounts for the interactions between the flowing gas and the solid porous medium. These interactions include a local viscous dissipation at the pore scale and an inertial force due to the strong geometrical variation of the flow lines at the pore scale. These are accounted for with the expression the case of simple homogeneous porous media:

$$\mathbf{F} = -\left( \frac{\mu}{K} \mathbf{v} + C_2 |\mathbf{v}| \mathbf{v} \right), \quad (3)$$

where  $\mu$  is the viscosity,  $K$  – the permeability and  $C_2$  – the inertial resistance factor.

The energy balance equation is similar to those classically used to describe flow in porous media. It includes however a source term, that accounts for the energy release during adsorption process:

$$\frac{\partial}{\partial \tau} (\varepsilon \rho_g E_g + (1 - \varepsilon) \rho_s E_s) + \nabla \left( \frac{r}{v} (\rho_g E_g + P) \right) = \nabla (\lambda_{ef} \nabla T) + q_{st} \rho \frac{\partial a}{\partial \tau}. \quad (4)$$

Here, total gas energy can be expressed as  $E_g = C_g T - P / \rho_g$  and total solid sorbent energy as  $E_s = C_s T$ . The isosteric heat is calculated from the relation  $q_{st} = R_\mu T \left[ \partial \ln P / \partial \ln T \right]_{a=\text{const}}$ . Under conditions, existing in sorbent bed, viscous dissipation term in the above equation is neglected.

The time-derivative of a current adsorption  $a$  represents the overall mass transfer between the solid and gas phase. Its expression may be derived from the Linear Driving Force model (the equation of sorption kinetic):

$$\frac{\partial a}{\partial \tau} = (a_{eq} - a) \cdot K_{s0} \exp \left( -\frac{E}{R_\mu T} \right), \quad (5)$$

where  $K_{s0} = 15 D_{s0} / R_p^2$ ,  $D_{s0}$  – phenomenological constant,  $R_p$  – the average radius of particle. The estimation of the source term requires determining the equilibrium gas adsorption over all the pressure and temperature domains experienced in the vessel during the charging/discharging process. It may be presented through the Dubinin – Radushkevich equation of the state of gas

$$a_{eq} = \frac{W_0}{v_a} \exp \left\{ - \left[ \frac{R_\mu T}{E} \ln \left( \frac{P_{cr}}{P} \cdot \left( \frac{T}{T_{cr}} \right)^2 \right) \right]^2 \right\}. \quad (6)$$

The two-dimensional model enables the prediction of the time-variations of the flow velocity, temperature, pressure and adsorption fields in an axisymmetrical storage vessel during the gas charging/discharging.

## RESULTS AND DISCUSSION

On the ground of 2D computer modelling of a 12-liter cylindrical vessel the effect of finning parameters to the sorbent active volume disposed inside the vessel was analyzed. In a total, the vessel contains 4.5 kg of the sorbent. High-heat conducting metal insertions can be attached to the interior of housing or to built-in system of heat flux input/output. Round continuous aluminium fins 0.8 mm wide were uniformly distributed on the heat pipe (HP) envelope length. Their thermal contact to sorbent and heat pipe envelope was considered ideal. Such optimistic situation exists fairly from being always. Thermal resistance of contact depends on a mode of fin attaching and can be essential enough. The fin spacing varied from 16 up to 1600 mm. The maximum value of spacing matched to the length of sorbent bed of 1600 mm. The fin spacing determines the amount of fins and the effective thermal resistance of the sorbent bed. The amount of fins relevant to the selected scope of spacing varied from 2 to 101. Figure 5 shows an example of calculated area with indication of different zones, which are the vessel case and heat pipe envelope made from stainless steel, aluminium fins, sorbent, and the free gaps filled with hydrogenous gas.

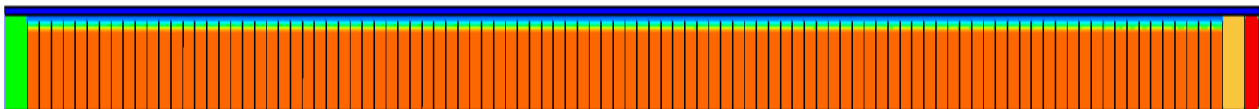
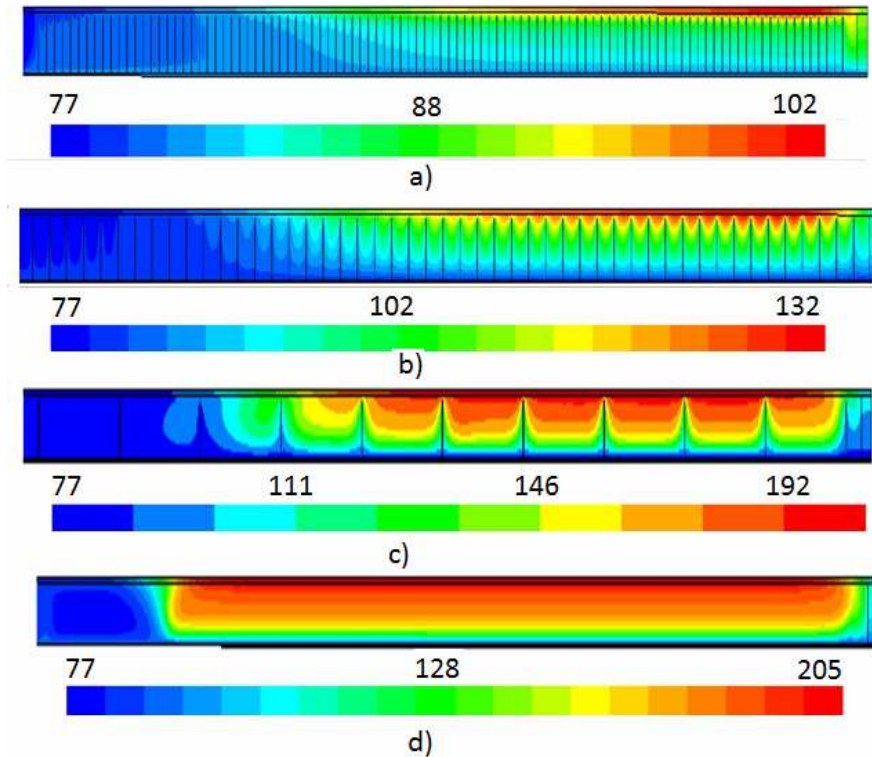


Fig. 5. Scheme of calculation domain of the adsorption based vessel with finned HP, where top-down: vessel case (outer diameter 0.102 m), annular gas channel formed by the sorbent bed and the vessel case, sorbent, envelope of HP (outer diameter 0,02 m); left-to-right: gas volume before the sorbent bed, sorbent, HP fins, gas volume behind sorbent bed, vessel flange

The calculation results corresponding to the time distribution of volume averaged characteristics at various charging processes of identical duration of 1500 s, are generalized on the two-dimensional color diagrams and graphs (Figs. 6–10). We analyzed the variant of vessel cooling from within a HP with constant operating temperature 77 K, when the case is thermally isolated and influence of finning parameters affects more strongly.



Color diagrams (Figs. 6, 8) show the calculated fields of temperature and adsorption at the end of the 1500 s charging of the vessel with various fin spacing of HP. Note, the advantage of the gilled pipe is more uniform and fast cooling of sorbent accompanied by intensive hydrogen absorption over all its volume. The reduction of fin spacing, on the one hand, promotes the best cooling of

Fig. 6. 2-D surfaces of temperature (K) in the adsorbed vessel at the end of gas charging for various fin configurations of HP: (a)  $S=16$  mm, (b)  $S=32$  mm, (c)  $S=160$  mm, (d)  $S=1600$  mm

sorbent and augmentation of stored mass, both in adsorbed and compressed state. On the other hand, more closely spaced fins of the HP reduces useful volume, mass of sorbent and mass of stored gas, this effect being more essential for thick fins. Figure 7 presents the dynamics of pressure variation in a sorbent bed and the mass rate of hydrogen flow entering through the vessel inlet/outlet. Seen, that the time of achievement of rating value of pressure 6 MPa

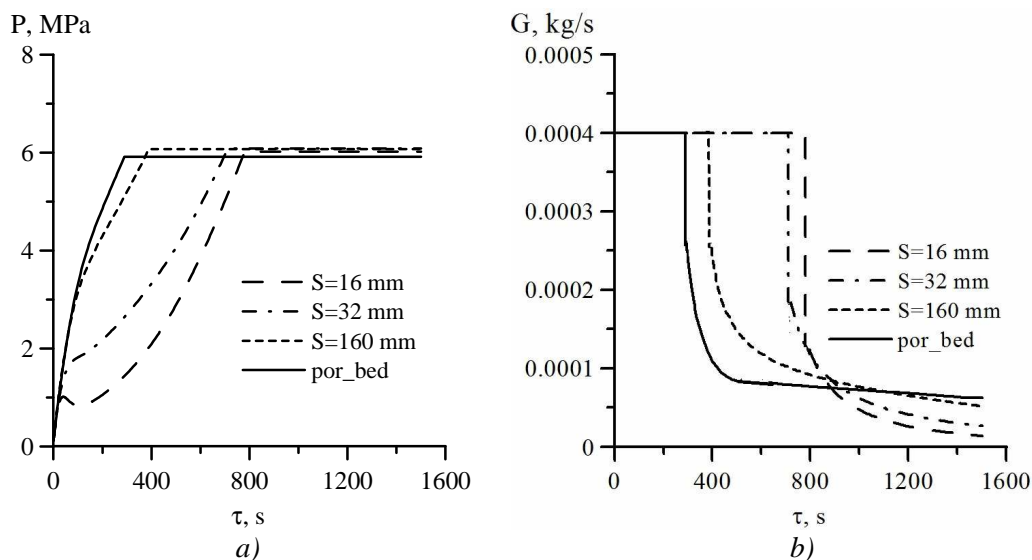
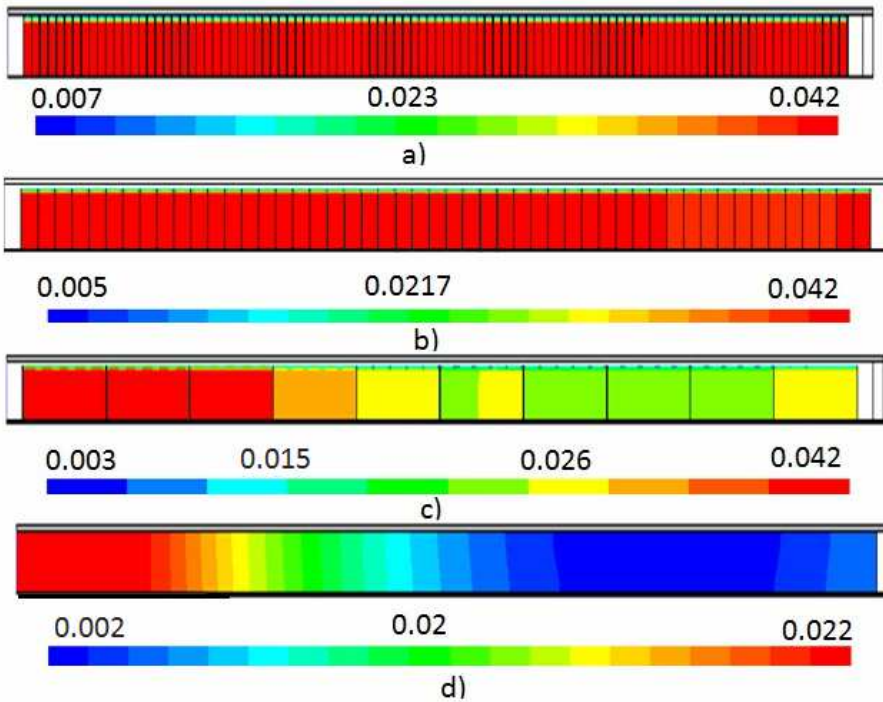


Fig. 7. The mean sorbent pressure (a) and mass rate of hydrogen flow (b) during gas charging of the cylindrical vessel cooled by HP for various fin spacing

was increased almost three times with increasing the number of metal inserts from 2 to 101. For variants of rare finning the pressure raised quickly with the input of hydrogen. In view of low effective thermal conductivity the sorbent cooled slowly and adsorbed a few amount of gas molecules. The stored amount increases steeply at low-pressures because the isotherms at low-temperatures and pressures are very steep.



At higher pressures, adsorption isotherms are saturated and the stored amount increases less steeply with pressure, the increase being mainly due to gas density increase in the bulk gas volume. The variation of hydrogen mass flow at vessel inlet determined the character of pressure change.

Fig. 8. 2-D fields of adsorption value (kg/kg) in the cylindrical vessel at the end gas charging for various fin configurations of HP: (a)  $S=16$  mm, (b)  $S=32$  mm, (c)  $S=160$  mm, (d)  $S=1600$  mm

In starting time interval of charging, corresponding to pressure increase in sorbent to rating value of 6 MPa, the mass flow equal of 0.0004 kg/s was sustained. Further the change to the condition of the fixed delivery pressure, the hydrogen mass flow tending asymptotically to zero.

From the resulted graphs at Fig. 9 one can see that the reduction of fin spacing to hundred times down to 16 mm has provided the temperature drop of sorbent from 186 to 81.5 K. At the same time on the contrary,

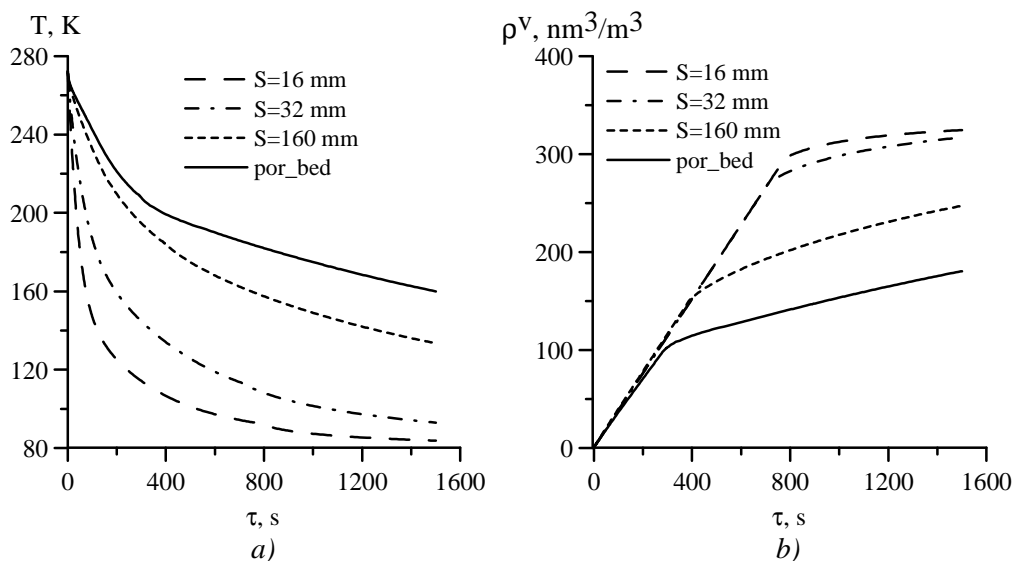


Fig. 9. Mean sorbent temperature (a) and volumetric storage density of hydrogen (b) during gas charging up to pressure 6 MPa of the cylindrical vessel cooled by HP for various fin spacing

the volumetric storage density of gas in vessel has increased from 210 to 392  $\text{nm}^3/\text{m}^3$ . Despite the distinctions in the temperature and pressure variations, the charging characteristics for the vessel with HP fin spacing of 16 and 32 mm are close each other. For rare finning of HP, volumetric storage density of hydrogen in the thermally regulated vessel is limited by non-uniform temperature field of the sorbent bed in consequence of the low effective thermal conductivity of sorbent.

The axial profiles of temperature at the border sorbent-gas (Fig. 10 *a*) at the end of charging process testify to cooling basically the regions adjoining to zone of gas inlet. So, for the fin spacing 1600 mm all sorbent at the border had the temperature 199 K, and for  $S=160$  mm the temperature – 186 K. The close location of metal inserts/fins (16 mm) has provided the sorbent cooling from 273 to 83 K in the course of 1500 s charging. Figure 10 *b* shows some general characteristics of the vessel filled with hydrogen, such as mean volumetric sorbent temperature, volumetric density of storage and the mass of stored hydrogen, as the functions of fin spacing. Fins were round aluminum disks with the thickness 0.8 mm. The amount of the stored hydrogen is determined by the quantity of adsorbed gas in sorbent and the free pressured gas in macropores and voids of system. The sorption value as the inertial characteristic varies extremely slowly, following the pressure and sorbent temperature variations with a definite time gap. As a result, the stored mass of hydrogen at the end of charging to 6 MPa and steady temperature for the considered variants of fin spacing (16, 32, 160, 1600 mm) has reached the values of 0.342, 0.334, 0.26 and 0.19 kg that corresponds to volumetric density of hydrogen storage 392, 375, 286 and 210  $\text{nm}^3/\text{m}^3$ . The exothermal character of sorption reaction and poor heat transfer the rare finning of HP has not provided heat removal during charging (1500 s) and was so the reason of hydrogen store reduction nearly twice.

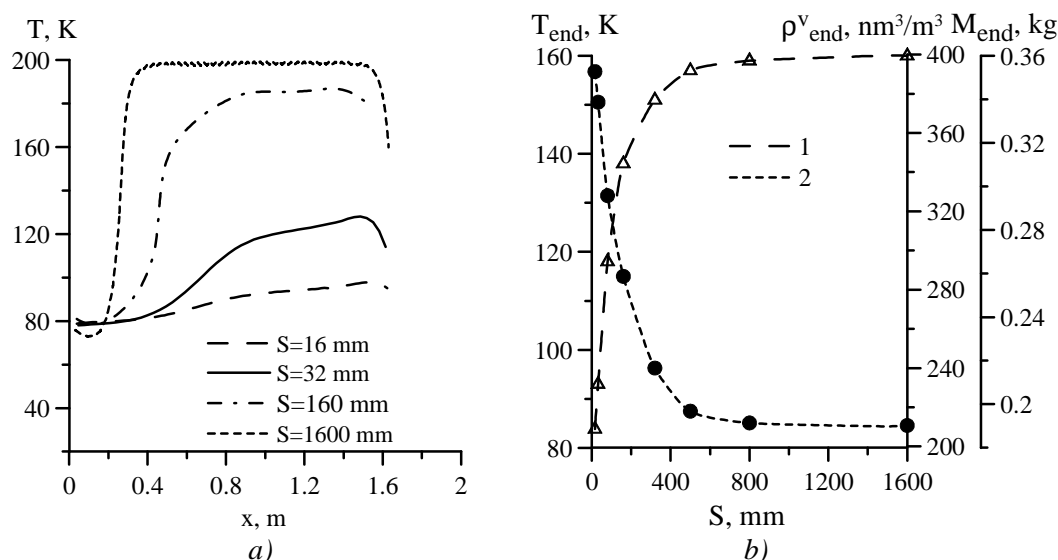


Fig. 10. Influence of the HP fin spacing on the characteristics of the adsorption-based vessel with hydrogen: ( $G=0.4$  g/c): (a) axial profile of the temperature at the border sorbent-circular gas channel; (b) the mean sorbent temperature (1) and volumetric storage density of hydrogen (2)

## CONCLUSION

Successful development of a getter system of hydrogenous gas storage presumes a presence of an active thermal regulation and special properties of materials capable to store up hydrogen efficiently. The design of a sorption vessel for rational storage of hydrogenous gas must include the following components:

- a microporous solid sorbent, packed in the vessel envelope (to increase the storage density and to reduce operating pressure (3.5–6 MPa));
- several sections (cartridge type of a vessel to diminish thickness of sorbent bed);
- a heat-exchange element (HE), placed near the cylinder axis (to diminish the negative influence of latent heat of adsorption). This element can be two-phase heat exchanger, finned heat pipe or thermosyphon.

- The HE fins and perforated tube effectively change the flow direction from axial to radial, which promotes energy transfer by convection from the cold or hot wall to the central region. Furthermore, the high conductivity of the fins increases the overall conductive radial heat transfer.

The developed vessel with the finned heat pipe and microporous carbon-base sorbent is perspective for the power engineering and for the gas domestic and small business industry.

## Nomenclature

$a$  – adsorption, kg/kg;  $a_{eq}$  – equilibrium adsorption, kg/kg;  $C_g$  – specific heat capacity of free gas, J/(kg·K);  $C_a$  – specific heat capacity of adsorbed gas, J/(kg·K);  $E$  – activation energy, J/kg;  $G$  – gas output from the cylinder, kg/s, g/s;  $K$  – permeability, m<sup>2</sup>;  $M$  – mass of the gas in the cylinder, kg;  $P$  – pressure, Pa;  $q_{st}$  – latent isosteric heat of sorption, J/kg;  $R_\mu$  – gas constant, J/kg/0K;  $T$  – temperature, K;  $\nu_a$  – specific volume of adsorbed medium, m<sup>3</sup>/kg;  $V_a$  – partial molar adsorption volume;  $V_g$  – molar gas-phase volume;  $W_0$  – maximum microporous specific volume, m<sup>3</sup>/kg.

*Greek Letters:*  $\varepsilon$  – total porosity;  $\lambda_{ef}$  – effective thermal conductivity of the sorbent bed, W/(m·K);  $\mu$  – dynamic viscosity, kg/(m s);  $\rho$  – bulk density of the sorbent, kg/m<sup>3</sup>;  $\rho_g$  – density of free gas, kg/m<sup>3</sup>;  $\rho'$  – volumetric storage density of gas, nm<sup>3</sup>/m<sup>3</sup> (where nm<sup>3</sup>/m<sup>3</sup>=m<sup>3</sup>(STP)/m<sup>3</sup>);  $\tau$  – time, s.

*Subscript:* a – adsorbate; ch – charge; cr – critical state; end – finite value; eq – equilibrium conditions; HP – heat pipe; 0 – initial value.

*Abbreviations:* AHG – Adsorbed hydrogenous gas; HP – heat pipe, STP – standard of temperature (273 K) and pressure (0.1 MPa).

## References

1. Buchner H, Povel R. The Daimler-Benz hydride vehicle project // *Int. J. Hydrogen Energy* 1982. Vol. 7, No. 3. Pp. 259–266.
2. Strobel R., Garche J., Moseley P. T., Jorissen L., Wolf G. Hydrogen storage by carbon materials // *J. Power Sources*. 2006. Vol. 159. Pp. 781–801.
3. Biloe S., Goetz V. and Guillot A. Optimal design of activated carbon for an adsorbed natural gas storage system // *Carbon*. 2002. Vol. 40. Pp. 1295–1308.
4. *Pat. BY, Int.Cl. F02M 21/4*. The request on The method and device for sorption of hydrocarbons / Vasiliev L. L., Mishkenis D. A.; № a 19991158, Appl. 27.12. 1999.
5. Inomata K. Kanazava K. Urabe Y., Hosono H., Araki T. Natural gas storage in activated carbon pellets without a binder // *Carbon*. 2002. Vol. 40. Pp. 87–93.
6. *Patent 5323752 US*, 1994. Utilization system for gaseous fuel powered vehicles.
7. Chang K. J. and Talu O. Behavior and Performance of Adsorptive Natural Gas Storage Cylinders During Discharge // *J. Applied Thermal Engineering*. 1996. Vol. 16, No. 5. Pp. 359–374.
8. Dillon A. C., Parilla P. A., Zhao Y., Kim Y.-H., Gennett T., Curtis C., Blackburn J. L., Gilbert K. E. H., Alleman J. L., Jones K. M., Zhang S. B., Heben M. J. // *Proc. of U.S. DOE, Hydrogen Program Review*, 2005.
9. Paggiaro R, Michl F., Benard P., Polifke W. Cryo-adsorptive hydrogen storage on activated carbon. II: Investigation of the thermal effects during filling at cryogenic temperatures // *Int. J. of Hydrogen Energy*. 2010. Vol. 35. Pp. 648–659.
10. Paggiaro R., Benard P., Polifke W. Cryo-adsorptive hydrogen storage on activated carbon. I: Thermodynamic analysis of adsorption vessels and comparison with liquid and compressed gas hydrogen storage // *Int. J. of Hydrogen Energy*. 2010. Vol. 35. Pp. 638–647.
11. Vasiliev L. L., Kanonchik L. E., Mishkinis D. A., Rabetsky M. I. A new method of Methane Storage and Transportation // *Int. J. Environmentally Conscious Design & Manufacturing*. 2000. Vol. 9. Pp. 35–62.
12. Vasiliev L. L., Kanonchik L. E., Alyousef Yousef M. Advanced Sorbents for Thermally Regulated Hydrogen Vessel // *Int. J. Applied Thermal Engineering*. 2010. Vol. 30. Pp. 908–916.

## **PROGRAM TOOLKIT FOR MODELING AND OPTIMIZATION OF ADSORPTION AND CHEMICAL HEAT PUMPS AND REFRIGERATORS**

**Vasiliev L.L., Lyah M.Yu., Rabinovich O.S.**

A.V. Luikov Heat and Mass Transfer Institute, NAS of Belarus  
15 P.Brovka St., Minsk, 220072, Belarus  
Tel/fax: 375 (17) 2842133; E-mail: lvasil@hmti.ac.by

### **Abstract**

A set of programs for numerical modeling and optimization of adsorption and chemical heat pumps and refrigerators has been developed. The modeling is based on one-dimensional (in the radial direction) consideration of dynamic adsorption or chemical reversible reactions in a cylindrical reactor filled with adsorbent. The program toolkit allows investigation of various heat-conversion devices designed as a combination of one or several reactors with condensers and evaporators. The programs have options for varying reactor parameters, thermal reservoir temperatures, resistance of control valves connecting the reactors and time of their opening and closing. The graphical representation of time history for mean temperature and sorbate content in the reactors is shown in the program screen as well as the effective Clausius-Clapeyron-diagram dynamics of working medium. As a result of modeling, the programs calculate main characteristics of thermal energy conversion such as COP, SHP (SCP), and the maximal temperature difference between the heat carrier and adsorbent during the process. The program tool has also an option for optimizing characteristics of heat conversion for a chosen set of parameters. Optimizing part of the code is based on the simplex-method algorithm. The developed approach and algorithms were validated by comparison of numerical results with experimental data.

### **KEYWORDS**

Adsorption, chemical reaction, heat pump, refrigerator, modeling.

### **INTRODUCTION**

Thermal energy conversion by the use of the heat of physical or chemical adsorption has rather long history with partaking of such great names as Faraday and Einstein [1, 2]. In spite of this, the attention to this problem given by investigators and engineers does not reduce, that is caused by general energy demands as well as due to emergence of new materials and compounds for adsorption and suggesting new heat conversion schemes [3–16]. Needs for further improvements of adsorption and chemical heat pumps and refrigerators make of current importance the development of programming tools for numerical modeling of most commonly used schemes and methods of heat conversion with adsorbers having different fillings, kinetics and transport properties, dimensions. The present work is aimed at development such a toolkit with rather diverse options, working as "meccano" and helpful for engineers, designers and students specializing in the related fields of engineering science. The idea lying in the base of the work is to use a simple (one-dimensional) model of an adsorber unit and to provide means for modeling of heat conversion in an apparatus comprised of different combinations of such units with heat sources, condensers and evaporators, connected through control valves.

### **MODEL OF ADSORPTION-CHEMICAL THERMAL ENERGY CONVERTER**

#### **Description of the adsorber unit**

The sketch of the adsorber unit is shown in Fig. 1. The reactor represents a cylinder filled with a porous adsorbent of arbitrary composition (it can be a monotype matter or a complex compound of adsorbents having different nature, capacity and kinetic properties). The adsorbent has an effective porosity  $\epsilon$  and thermal conductivity  $\lambda$ . There are external jacket and central tube in the reactor. If the sorbate is supplied through the central tube, the wall of the tube has perforations and the impermeable external jacket serves for

the forced circulation of the heat carrier (with the temperature  $T_f$ ). In the opposite case, the heat carrier can be supplied through the central tube (which should be impermeable in this situation) and gas-sorbate is fed through the external jacket having perforated internal wall. In further description of the numerical model we will suppose the first of above described possibilities. The tube for gas-sorbate supply is equipped with a control valve having the hydraulic resistance  $K_v$ .

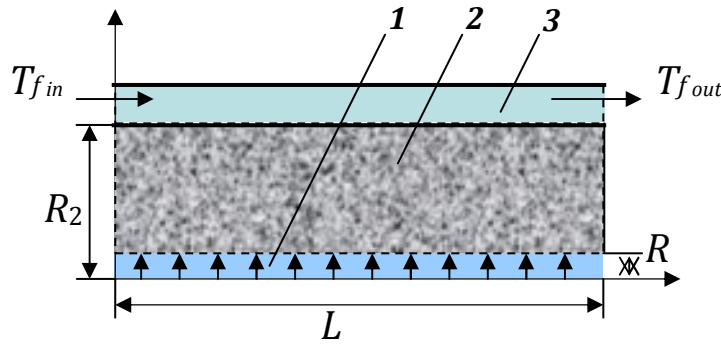


Fig. 1. The sketch of adsorber unit. 1 is the channel for sorbate supply; 2, the sorbent; 3, the heat carrier jacket

### Kinetics of physical and chemical adsorption

The program toolkit is adapted for the usage of two types of sorbent, i.e. with physical and chemical adsorption. The activated carbon fibers in the form of "Busofit" [5, 6] is used as a prototype for the adsorbent with physical adsorption, while chemical reversible adsorption is meant on metal salts like  $\text{BaCl}_2$ ,  $\text{CaCl}_2$ ,  $\text{NiCl}_2$ , etc [4]. There is also an option for the use of composite adsorbent which combines properties of both physical and chemical adsorption. In this case, the composite adsorbent is treated as simple (independent) superposition of two or more adsorbents with different properties. Studies of heat converters with composite adsorbents are also widespread [5, 6, 11, 15].

The Dubinin-Astahov equation [17] is used for description an equilibrium physical adsorption of gases :

$$a_{eq} = \frac{W_0}{b} \exp \left( -B \frac{T^2}{\beta^2} \left[ \ln \left( \left( \frac{T}{T_{cr}} \right)^2 \frac{P_{cr}}{P} \right)^2 \right] \right), \quad (1)$$

where  $a_{eq}$  is the equilibrium capacity of sorbent, and other constants are defined conventionally:  $T_{cr}$  and  $P_{cr}$  are critical temperature and pressure for sorbate,  $W_0$  is the limiting volume of adsorption space,  $B$  is the structure constant related to the size and distribution of micro pores,  $b$  is Van-der-Waals constant,  $\beta$  is affinity coefficient,  $T$  and  $P$  are the current temperature and pressure.

The equations for the kinetics of physical adsorption have the following form [18] (the adsorption rate):

$$\frac{da}{dt} = W_{ad} = K_{s0} \exp \left( -\frac{E}{RT} \right) (a_{eq} - a), \quad (2)$$

where  $E$  is the activation energy,  $K_{s0}$  is the preexponential factor,  $a$  is the current value of adsorption and  $\tau$  is the time

For the kinetics of chemical adsorption the following equation were used, correspondingly for the reactions of synthesis and decomposition [9] (the synthesis and decomposition rates):

$$W_{syn} = a_0 \frac{dx}{d\tau} = A a_0 (1-x)^b \left( 1 - \frac{P_{eq}}{P} \right); \quad W_{dec} = a_0 \frac{dx}{d\tau} = A a_0 x^b \left( 1 - \frac{P_{eq}}{P} \right), \quad (3)$$

where  $x$  is the degree of reaction completion,  $x = a/a_0$ .

The equilibrium pressure for the chemical adsorption is given by Clausius-Clapeyron equation (4):

$$R \ln P_{eq} = -\Delta H/T + \Delta S. \quad (4)$$

Generally, chemical adsorption of a gas-sorbate can proceed in different reaction paths by forming different chemical compounds of gaseous and solid reactants. The equilibrium for each type of reactions obeys to separate equation (4) with different sets of parameters. The developed program can be adapted to multi-reaction sorption as well.

### Main assumptions for the model of heat and mass transfer in the adsorber unit

To describe the transport processes in the adsorber the following simplifying assumption were used:

- the gas in the reactor is the pure sorbate, so the diffusion limitations are absent and the pressure in the reactor is distributed homogeneously;
- the temperatures of solid and gaseous phases are equal in the same point due to high interphase heat transfer coefficient;
- the gas in the reactor obeys the ideal gas law;
- the heat evolved/consumed due to compression/expansion of the gas in pores is negligible.

### Mass balance equation

Accordingly to the described assumption the local mass balance in the cylindrical adsorber is expressed by the mass conservation equation:

$$\varepsilon \frac{\partial \rho_g}{\partial \tau} + \frac{1}{r} \frac{\partial}{\partial r} (r \rho_g v) = -W_{ad} \rho_s. \quad (5)$$

Variations of the pressure in the adsorber caused by changes of temperature and gas content can be found by accounting integral mass balance:

$$\frac{dm_g}{d\tau} = w - K_v (P - P_0), \quad (6)$$

where

$$m = \int_V \varepsilon \rho_g dV \quad \text{and} \quad w = \int_V W_{ad} \rho_s dV. \quad (7)$$

The gas density is given by the ideal gas law:

$$\rho_g = \frac{P\mu}{RT}, \quad (8)$$

$\mu$  is the molar mass of sorbate.

### Energy equation

Conservation of energy into within the cylindrical reactor is expressed by Eq. 9:

$$\left( \varepsilon \rho_g c_g + \rho_s c_s + \rho_s a c_a \right) \frac{\partial T}{\partial \tau} + \left( \rho_g v c_g \right) \frac{\partial T}{\partial r} = \frac{1}{r} \frac{\partial}{\partial r} \left( r \lambda_{eff} \frac{\partial T}{\partial r} \right) + q \rho_s \frac{\partial a}{\partial \tau}. \quad (9)$$

It is worth noting the absence of axial convection in the porous sorbent.

Thus, the current state of adsorber, determined by internal pressure,  $P$ , and radial distributions of the temperature,  $T(r)$ , and sorbate content,  $a(r)$ , can be found as the solution of the system of equation (1)–(9) supplemented by initial and boundary conditions.

### Initial and boundary conditions

In the beginning of operation of any adsorber its temperature is set equal to the initial temperature,  $T_{ini}$ , and the pressure within the adsorber is given as  $P_0$ .

The conditions for heat exchange at the internal ( $R_1$ ) and external ( $R_2$ ) boundaries of sorbent are regulated by the convective heat exchange law with the coefficients  $\alpha_1$  and  $\alpha_2$ :

$$\alpha_1(T_{r=R_1} - T_0) = -\lambda_{eff} \left. \frac{\partial T}{\partial r} \right|_{r=R_1}, \quad \alpha_2(T_{r=R_2} - T_{f,in}) = -\lambda_{eff} \left. \frac{\partial T}{\partial r} \right|_{r=R_2}. \quad (10)$$

### Interaction of adsorber with others elements of heat converter

The adsorber unit described in the previous sections should be connected to others elements of a modeled heat transformer, such as another adsorber, evaporator and condensers. All these connections are performed with the use of control valves; each of them is characterized by a respective hydraulic resistance  $K_v$ . Each condenser or evaporator is maintained at a given temperature  $T_{ev/cond}$  and pressure  $P_{ev/cond}$ , which satisfy the equation of liquid/vapor phase equilibrium, similar to Eq. (4).

Also, the inlet temperature of a heat carrier,  $T_{f,in}$ , is equal always to the temperature of respective heat reservoir. The outlet temperature of a heat carrier is determined from the heat exchange balance

$$\alpha_2(T_{r=R_2} - T_{f,in}) = G_f c_{p,f} (T_{f,out} - T_{f,in}). \quad (11)$$

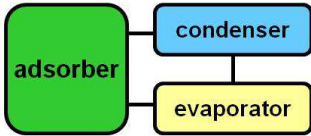
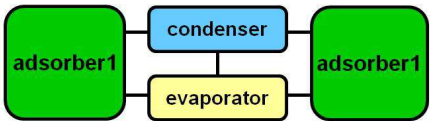
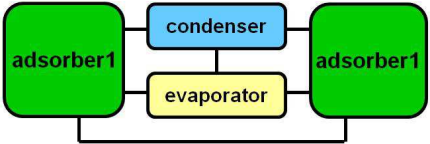
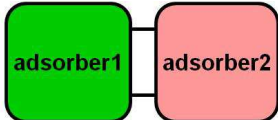
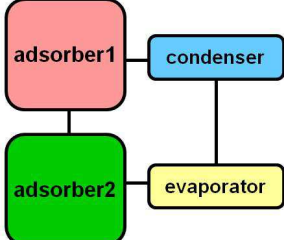
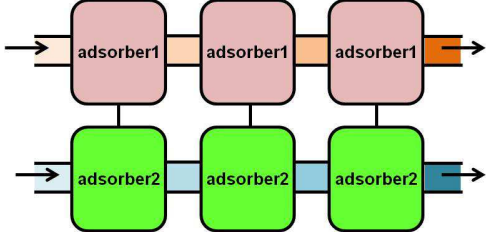
The program provides the options of choosing if the heat transfer between a heat carrier and adsorber is completed, or the outlet heat carrier and sorbent surface have different temperatures.

## CAPABILITIES AND OPTIONS OF COMPUTER PROGRAM

### Available heat converter models

The set of programs for modeling adsorption-chemical heat converters provides a choice of model from the list presented below (Table 1).

Table 1. Heat converter models

1	<p><b>One absorber with condenser and evaporator</b></p> 	2	<p><b>Two similar absorbers with condenser and evaporator</b></p> 
3	<p><b>Two similar absorbers with condenser and evaporator, and with mass recovery</b></p> 	4	<p><b>Two absorbers with different sorbents</b></p> 
5	<p><b>Two absorbers with different sorbents and with condenser and evaporator</b></p> 	6	<p><b>Thermal wave in two-channels with high-and low-temperature adsorbers</b></p> 

These models allow investigating the most of "classical" designs represented in scientific publications. For example, the model #6 relates to the study of idea of successive amplification of the heat-upgrading

thermal wave in the channel with high-temperature adsorbers. This design provides mark improvement of SHP and the temperature of heat upgrading.

A light modification of program codes is needed to adapt the tool for modeling heat conversion systems with other configurations.

### Examples of program results and output screen

The programs have options for varying reactor parameters, thermal reservoir temperatures, resistance of control valves connecting the reactors and time of their opening and closing. There is also a possibility to optimize the main characteristics of heat conversion for a chosen set of parameters. Optimizing part of the code is based on the simplex-method algorithm.

The first example of program output screen is shown in Fig. 2. Modeling was performed for the two-adsorber heat converter represented by the scheme #2 of Table 1. Chemical adsorption of ammonia on the calcium chlorate salt was considered in this modeling. This output contains the plots of reaction degree, pressure and temperature in both adsorbers vs. the time. The bottom graph represents Clausius-Clapeyron diagram. Quantitative data on ideal (Carnot) COP for refrigeration ( $COP_{ideal}$ ), heating COP ( $COP_{heat}$ ), refrigeration COP ( $COP_{ref}$ ), specific cool and heat production (SCP and SHP), and the cycle time ( $dt$ ) are presented also in the bottom part of the screen.

As a second example of numerical modeling on the base of developed codes we present here the results for heat upgrading in the two-channel chemical-adsorption system which corresponds to the model #6 in Table 1. The considered system includes high-temperature adsorbers of ammonia filled with  $MnCl_2$  and low-temperature adsorbers with  $CaCl_2$ . The heat carrier at the inlet of high-temperature channel is fed from a middle-temperature reservoir with the constant temperature  $T_M$ . The temperature of the heat carrier in the low-temperature channel is switched from low-temperature  $T_L$  at the beginning of the process to  $T_M$ , and then again to  $T_L$ . The thermal wave in the high-temperature channel is amplified while the wave passes the series of adsorber pairs. Table 2 shows that addition a new pair of adsorbers into the system leads to the increase of main heat conversion characteristics though the rate of this increase gradually drops.

### VALIDATION OF THE MODEL

The developed programs were tested in two aspects; first, with respect to sensitivity of numerical results to the choice of space and time meshes, and, second, by comparison with known experimental measurements.

#### Comparison with two-adsorber heat upgrading experiment

Results of modeled heat upgrading in the system of two different adsorbers (with  $MnCl_2$  and  $CaCl_2$  salts) were compared with the experimental data presented in [16] (Fig. 3). As can be seen from the figure, the durations of heat converter operation cycle for modeling and experiment are very close. There is a mark difference between modeling and experiment for the initial phase of the process that can be explained by discrepancy of initial conditions for compared cases. There is also discrepancy between calculated and experimental results for low-pressure stage of the process, when the temperature in the adsorber with low-temperature salt sharply drops to the temperature of heat carrier, whereas the behavior of similar temperature in the experiment much smoother. These disagreements can be related to limitations of 1D model of an adsorber, which does not take into account longitudinal thermal conductivity in the reactor. Nevertheless, the stated disagreements are not high, and one can conclude that the developed model has sufficiently acceptable level of adequacy.

#### Comparison with the experimental data for the system of two adsorbers filled with different composite sorbents

Another validation of the developed program was performed by comparison with experimental data from the paper [19], more specifically, with the cooling stage for two-adsorber system. In the experiment the adsorbers were filled by composite sorbents: "Busofit +  $MnCl_2$ " for high-temperature adsorber and "Busofit +  $BaCl_2$ " for low-temperature one. Figure 4 illustrates the results of the comparison, which again looks acceptably good.

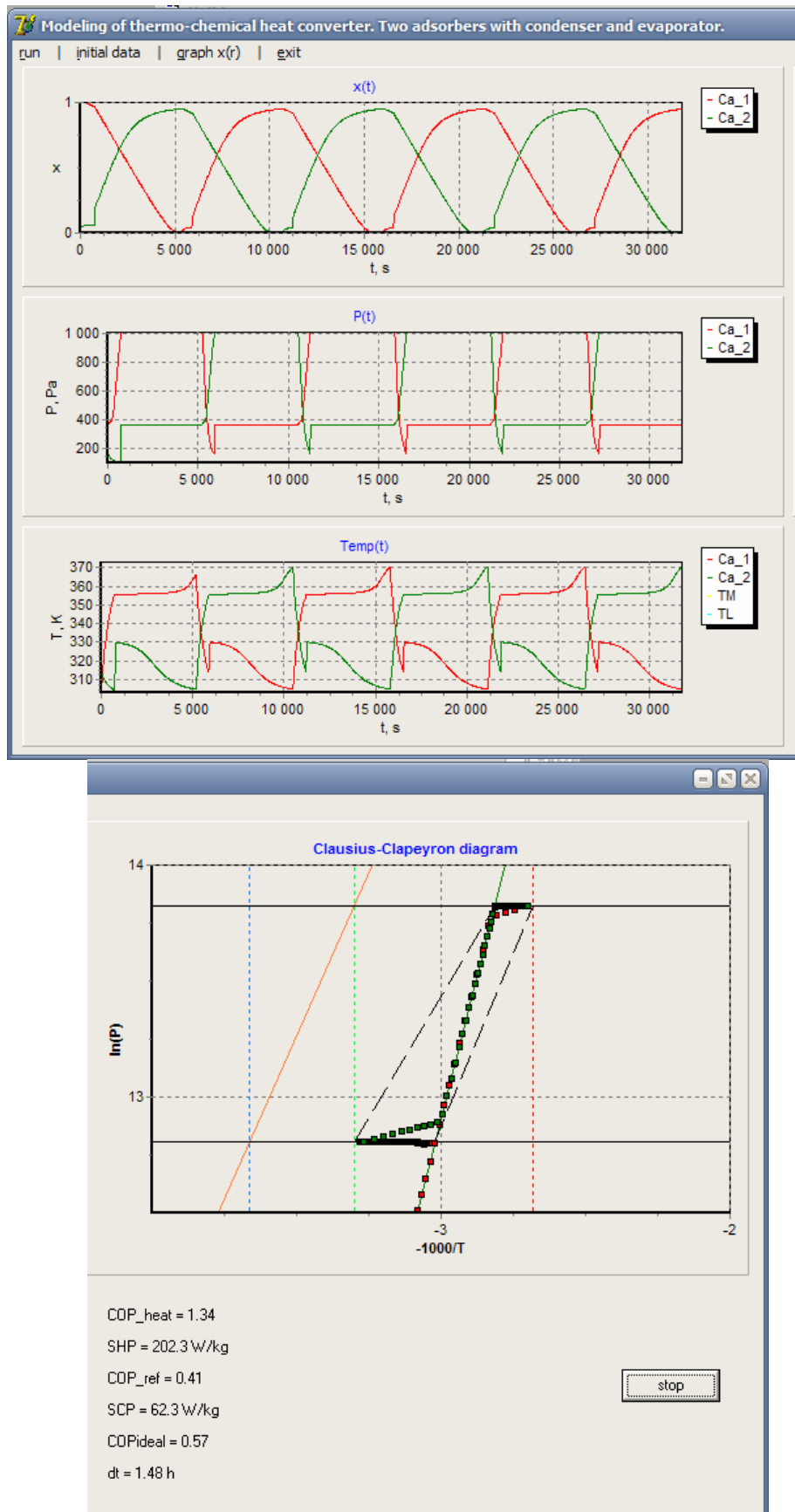


Fig. 2. Fragments of output screen for modeling chemical heat converter in the system with two similar adsorbents ( $\text{NH}_3$  chemo-sorption on  $\text{CaCl}_2$ )

Table 2. Modeling of heat upgrading with the use of thermal wave

Characteristics of heat upgrading	One pair of adsorbers	Two pairs of adsorbers	Three pairs of adsorbers
COP ideal	0.54	0.54	0.54
COP	0.35	0.42	0.44
SHP, Wt/kg	11.9	22.9	32.7
$dT_{\max}$ , K	8	13.8	18

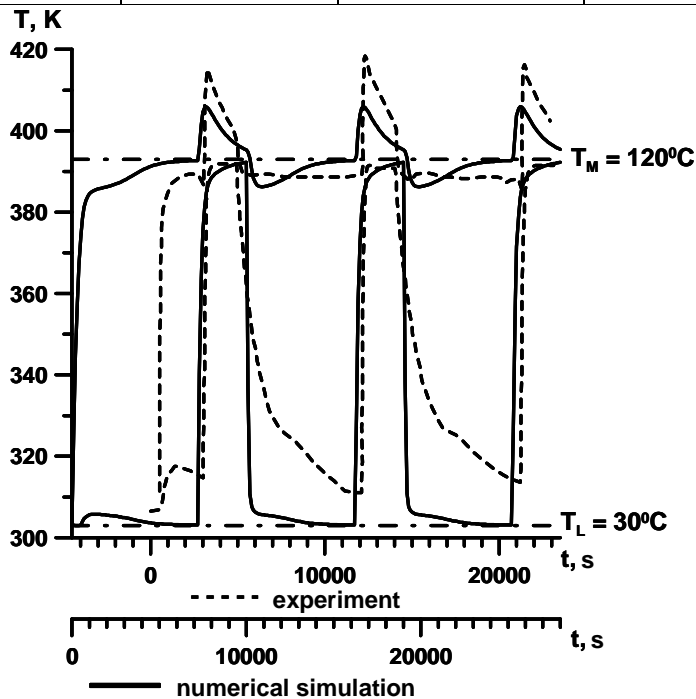


Fig. 3. Comparison of temperature vs. time evolution in the modeled two-adsorber system with the experimental results from [16]

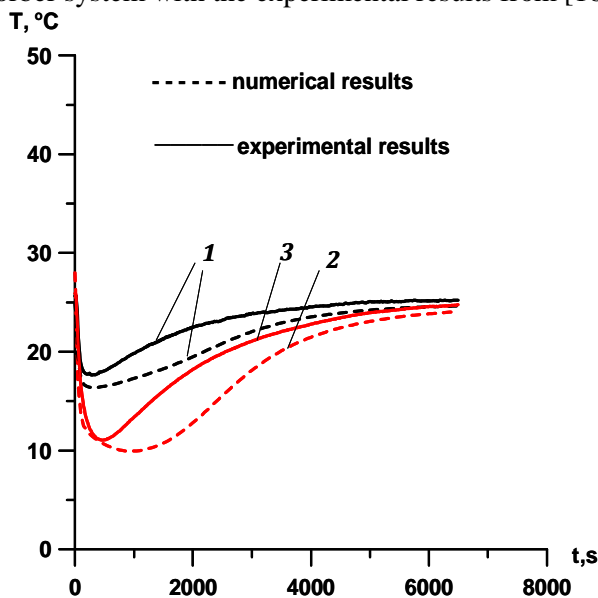


Fig. 4. Comparison of numerical results with the experiment [19] on cooling stage in the heat converter containing two adsorbers with composite sorbents. 1 is the temperature of heat carrier at the outlet of low-temperature adsorber; 2, the mean calculated temperature within the low-temperature adsorber; 3, the experimental temperature at the external surface of low-temperature adsorber

## CONCLUSION

The program toolkit for numerical modeling of adsorption-chemical heat conversion has been developed. The modeling is based on one-dimensional (in the radial direction) consideration of dynamic adsorption or chemical reversible reactions in a cylindrical reactor filled with adsorbent. The program toolkit allows investigation of various heat-conversion devices designed as a combination of one or several reactors with condensers and evaporators. The programs have options for varying reactor parameters, thermal reservoir temperatures, and resistance of control valves connecting the reactors and time of their opening and closing. The program tool has also an option for optimizing characteristics of heat conversion for a chosen set of parameters. The developed approach and algorithms were validated by comparison of numerical results with experimental data. The comparison showed some marked but not high roughness of used 1D model for the heat and mass transfer in an adsorber. Enhancement of the model by their extension for 2D and 3D cases and by more precise description of elementary processes in an adsorber can be considered as the next step of the work.

## References

1. Faraday M. On the condensation of several gases into liquids // *Philosophical transactions of the Royal Society of London*. 1823. Vol. 113. Pp. 189-198.
2. *Patent 1,781,541*. USA. Refrigeration / A. Einstein, L. Szilard. 1930.
3. Demir H., Mobedi M., Ulku S. A review on adsorption heat pump: Problems and solutions // *Renewable and Sustainable Energy Reviews*. 2008. Vol. 12. Pp. 2381-2403.
4. Wang L.W., Wang R.Z., Oliveira R.G. A review on adsorption working pairs for refrigeration // *Renewable and Sustainable Energy Reviews*. 2009. Vol. 13. P. 518-534.
5. Vasiliev L.L., Mishkinis D.A., Antukh A.A., Vasiliev L.L. Jr. Solar-Gas Solid Sorption Refrigerator // *Manufactured in The Netherlands. Adsorption*. Kluwer Academic Publishers. 2001. Vol. 7. Pp. 149–161.
6. Lu Z.S., Wang R.Z., Wang L.W., Chen C.J.. Performance analysis of an adsorption refrigerator using activated carbon in a compound adsorbent // *Carbon*. 2006. Vol. 44. Pp. 747–752.
7. Basova YV., Edie D.D., Badheka P. Y., Hari-Chandana Bellam. The effect of precursor chemistry and preparation conditions on the formation of pore structure in metal-containing carbon fibers // *Carbon*. 2005. Vol. 43. Pp. 1533–1545.
8. Tamainot-Telto Z., Metcalf S.J., Critoph R.E., Zhong Y., Thorpe R.. Carbon–ammonia pairs for adsorption refrigeration applications: ice making, air conditioning and heat pumping // *International journal of refrigeration*. 2009. Vol. 32. Pp. 1212–1229.
9. Wang C., Zhang P., Wang R.Z. Performance of solid–gas reaction heat transformer system with gas valve control // *Chemical Engineering Science*. 2010. Vol.65.,No.10. Pp. 2910-2920.
10. Аристов Ю.И., Васильев Л.Л., Накоряков В.Е. Современное состояние и перспективы развития химических и сорбционных тепловых машин в РФ и РБ // *Инженерно-физический журнал*. 2008. Том 81, №1. С. 19-48.
11. Li T.X., Wang R.Z., Wang L.W., Lu Z.S., Wu J.Y. Influence of mass recovery on the performance of a heat pipe type ammonia sorption refrigeration system using CaCl<sub>2</sub>/activated carbon as compound adsorbent // *Applied Thermal Engineering*. 2008. Vol. 28. Pp. 1638–1646.
12. Taylan O., Baker D. K., Kaftanoglu B. COP trends for ideal thermal wave adsorption cooling cycles with enhancements // *International journal of refrigeration*. 2010. Vol. 30. Pp. 1-9.
13. Li T.X., Wang R.Z., Kiplagat J.K., Wang L.W., Oliveira R.G. Thermodynamic study of a combined double-way solid–gas thermochemical sorption refrigeration cycle // *International journal of refrigeration*. 2009. Vol. 32. Pp. 1570–1578.
14. Babenko V.A., Kanonchik L.E., Vasiliev L.L. Heat and mass transfer intensification in solid sorption systems // *Enhanced Heat Transfer*. 1998. Vol. 5. Pp 111-125.
15. Han J.H., Lee K.H., Kim D.H., Han H.K. Transformation Analysis of Thermochemical Reactor Based on Thermophysical Properties of Graphite-MnCl<sub>2</sub> Complex // *Ind. Eng. Chem. Res*. 2000. Vol. 39. Pp. 4127-4139.
16. Wang C., Zhang P., Wang R. Z.. Investigation of Solid–Gas Reaction Heat Transformer System with the Consideration of Multistep Reactions // *AIChE Journal*. 2008. Vol. 54, № 9. Pp. 2464-2478.
17. Dubinin, M.M., Astakhov, V.A. Description of adsorption equilibria of vapors on zeolites over wide ranges of temperature and pressure // *Advances in Chemistry Series*. 1971. Vol. 102. Pp. 69–85.
18. Babenko V.A., Kanonchik L.E. Mathematical Modeling of a Cylinder with a Sorbent and Natural Gas // *J. Eng. Phys. and Thermophys*. 2000. Vol. 73. Pp. 516-529.
19. Antukh A.A., Tsitovich A.P., Vasiliev L.L., Alousef Y. Solid sorption cooler with composite sorbent bed and heat pipe thermal control // *Proc. of VIII Minsk International Seminar "Heat Pipes, Heat Pumps, Refrigerators, Power Sources"*, Minsk, Belarus, 2011.

## THERMODYNAMIC EFFICIENCY OF HEAT PUMP DRYERS FOR DRYING OF WOOD WITH THE FULL RECYCLING OF THE DRYING AGENT

**M.K. Bezrodny, D.S. Kutra**

The chair of theoretical and industrial heat engineering  
Heat-and-Power engineering department  
National Technical University of Ukraine  
"Kyiv Polytechnic Institute"  
03056, Kyiv-56, pr. Peremogy, 37, Ukraine  
Tel./fax: +380444068078, email: m.bezrodny@kpi.ua

### Abstract

The authors examine heat pump drying dehumidifier for drying of wood with the full recycling of used drying agent. The theoretical thermodynamic analysis shows that this type of circuit solutions including heat pump drying path leads to a significant increase in thermodynamic efficiency of the dryer (about 2-fold compared with the heat pump recirculation schemes), due to lack of fresh air supply and the need for energy consumption for its heating, re-use (circulation) of spent vapor through the cycle of cooling and dehumidification (evaporator in heat pump) and heating (in the condenser) in front of a stack of wood. Due to this, so high thermodynamic efficiency leads to saving of primary energy resources.

### KEYWORDS

Heat pump dryer, wood, full recycling, thermodynamic efficiency.

### INTRODUCTION

World trends in the market of energy resources are forcing humanity to pay attention to the opportunities and prospects for the use of various resource-saving technologies, not only for the needs of civil heating, but also for heat power engineering processes. The most energy-intensive industries include drying processes, in particular, the drying of wood, which is one of the main materials of the construction industry. Using heat pumps (HP) technology in the woodworking industry allows us not only to create a rational scheme for drying and dispose of secondary energy resources, but also leads to significant improvements in energy efficiency of the drying process, which is directly related to energy savings.

In spite of obvious energy-economic perspective of using heat pumps in drying processes, there are no published analytical expressions and techniques to objectively estimate the efficiency of heat pump technology, depending on the different circuit design of heat pump dryers (HPD), process conditions of the drying process, operating parameters of heat pump.

In [1, 2] the authors carried out a comparative analysis of thermodynamic and energy efficiency of a few of traditional heat pump and recirculation schemes of the low-temperature drying of wood for a wide range of variation of process parameters at constant parameters of the heat pump. Noted that the using of heat pump drying technology of wood can significantly increase the efficiency of the drying process by increasing the recycling rate of used drying agent as compared with the settings of the traditional type, without breaking of drying technology of wood. The need to implement the partial removal of waste damp air is connected with the presence and unacceptable accumulation of energy deposited in a drying cycle with the compressor, which is redundant as shown in [3]. However, there are alternative schemes of including heat pump unit to the drying process, which is described in [4] and do not require the implementation of the partial removal of the spent drying agent. Installations of this kind are known as heat pump dryers with *full recycling of the drying agent*.



where  $\Delta d_{dc}$  is the increment of moisture content of drying agent by passing stacks of wood, which is depending on technological change temperature of drying agent in the drying chamber.

Temperature differential of drying agent during the passage of the chamber depends on the kind of wood and is governed by the technology [5]:

- for softwoods  $\Delta t_{dc} = 2 \dots 3$  °C;
- for birch,  $\Delta t_{dc} = 1.5 \dots 2.5$  °C;
- for oak, larch  $\Delta t_{dc} = 1 \dots 1.5$  °C.

Capacity of the compressor can generally be identified by the following equation

$$L_{hp} = Q_{hp}^{ev} / (\epsilon_{hp} - 1). \quad (3)$$

Heat load of the evaporator, in this case, can be determined as follows

$$Q_{hp}^{ev} = V_2' \rho_2' (h_2' - h_{ev}), \quad (4)$$

where the values of enthalpies of the drying agent  $h_2'$  and  $h_{ev}$  in the characteristic points are determined by the well-known equations.

The coefficient of performance of heat ideal Carnot cycle, taking into account the thermal irreversibility in the condenser and evaporator of HP, can be defined as

$$\epsilon_{hp} = \frac{273 + t_{mix} + \Delta t_{cond}}{(273 + t_{mix} + \Delta t_{cond}) - (273 + t_{ev} - \Delta t_{ev})}. \quad (5)$$

As we can see from eq. (5), the value of thermal irreversibility in the condenser and evaporator of HP, which are characterized by the temperature difference  $\Delta t_{cond}$  and  $\Delta t_{ev}$  between drying agent and refrigerant, significantly effect on the magnitude of the coefficient of performance. In most modern air heat pumps the value of the temperature difference between the working flows varies over a relatively wide range, reaching  $\Delta t = 15$  °C, that significantly affects the efficiency of the unit. This problem is analyzed in [6]. In our analysis this quantity will variable.

The temperature of the drying agent  $t_{ev}$  at the outlet of the evaporator heat pump in the eq. (5) can be determined from the approximation eq. (6) or  $h-d$ -diagram as a function of technological parameters  $d_{ev} = d_{mix}(t_{mix}; \Phi_{mix})$

$$t_{ev} = 6,18 \cdot 10^{-3} d_{ev}^{0,465}. \quad (6)$$

An important problem is to determine the temperature at the outlet of an external cooler  $t_2'$ , which depends both on the technological parameters and the parameters of the heat pump. This problem is solved by the energy balance of the external cooler, and can be determined from the following equation

$$t_2' = t_2 - \frac{(c_{da} + c_s d_{mix})(t_{mix} - t_{ev})}{\epsilon_{hp} (c_{da} + c_s d_2')}. \quad (7)$$

With a glance of eq. (2)–(4), and well-known equations for determine enthalpies of air, the equation for determining the coefficient of utilization of external energy for evaporation of moisture (eq. (1)) will be follow

$$\eta_{HPD} = \frac{r(t_w) \Delta d_{dc}}{[c_{da} (t_2' - t_{ev}) + r \Delta d_{dc} + c_s (d_2' t_2' - d_{ev} t_{ev})]} (\epsilon_{hp} - 1). \quad (8)$$

## RESULTS AND DISCUSSIONS

As we can see from eq. (7), the temperature  $t'_2$  depends on the technological parameters of drying process  $t_{mix}$  and  $\varphi_{mix}$  (which determines  $d_{mix}$ ), temperature gradient of drying agent during the passage of the stack  $\Delta t_{dc} = t_{mix} - t_2$ , and the coefficient of performance of heat pump  $\varepsilon_{hp}$ , which is determined by the intensity of the heat transfer process between the drying agent and refrigerant, and can be characterized by thermal irreversibility  $\Delta t_{cond}$  and  $\Delta t_{ev}$ .

At Fig. 2 shown the dependence of  $t'_2$  from the range of these factors for various technological parameters of drying process ( $t_{mix}$  and  $\varphi_{mix}$ ).

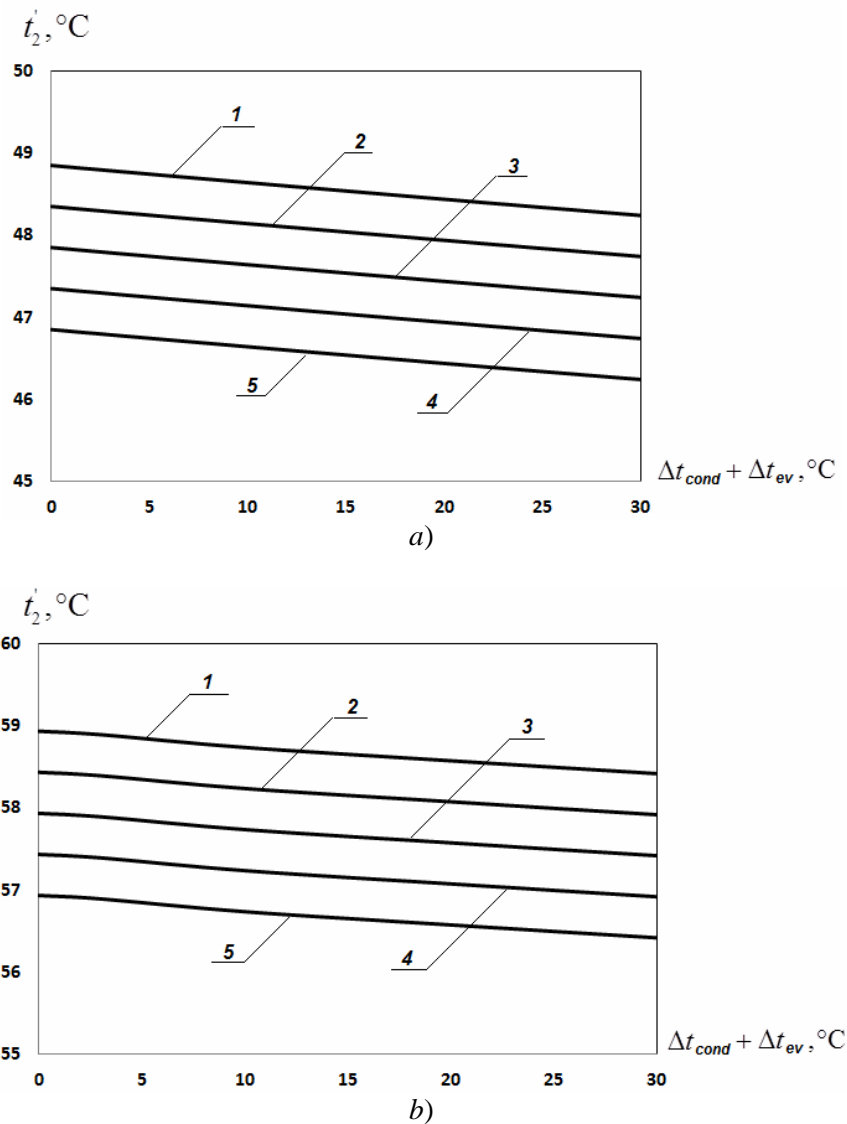


Fig. 2. Dependence of the temperature of the drying agent at the exit of the external cooling from the total thermal irreversibility: a) for  $t_{mix} = 50$  °C,  $\varphi_{mix} = 70$  % ; b) for  $t_{mix} = 60$  °C,  $\varphi_{mix} = 80$  % ; 1 –  $\Delta t_{dc} = 1$  °C; 2 – 1.5; 3 – 2; 4 – 2.5; 5 – 3

As we can see from the Fig. 2, with increasing thermal irreversibility, the exhaust drying agent is amenable to a better cooling due to the increase of the compressor capacity by reducing the rate of coefficient of performance.

Numerical analysis allows to evaluate the effectiveness of the full recycling of drying agent, which is characterized by the coefficient of utilization of external energy for evaporation of moisture, calculated according to expression eq. (1) for different values of process temperature changes  $\Delta t_{dc}$ , and technological parameters of drying, depending on the total thermal irreversibility in heat exchange between the drying agent and refrigerant in the heat pump.

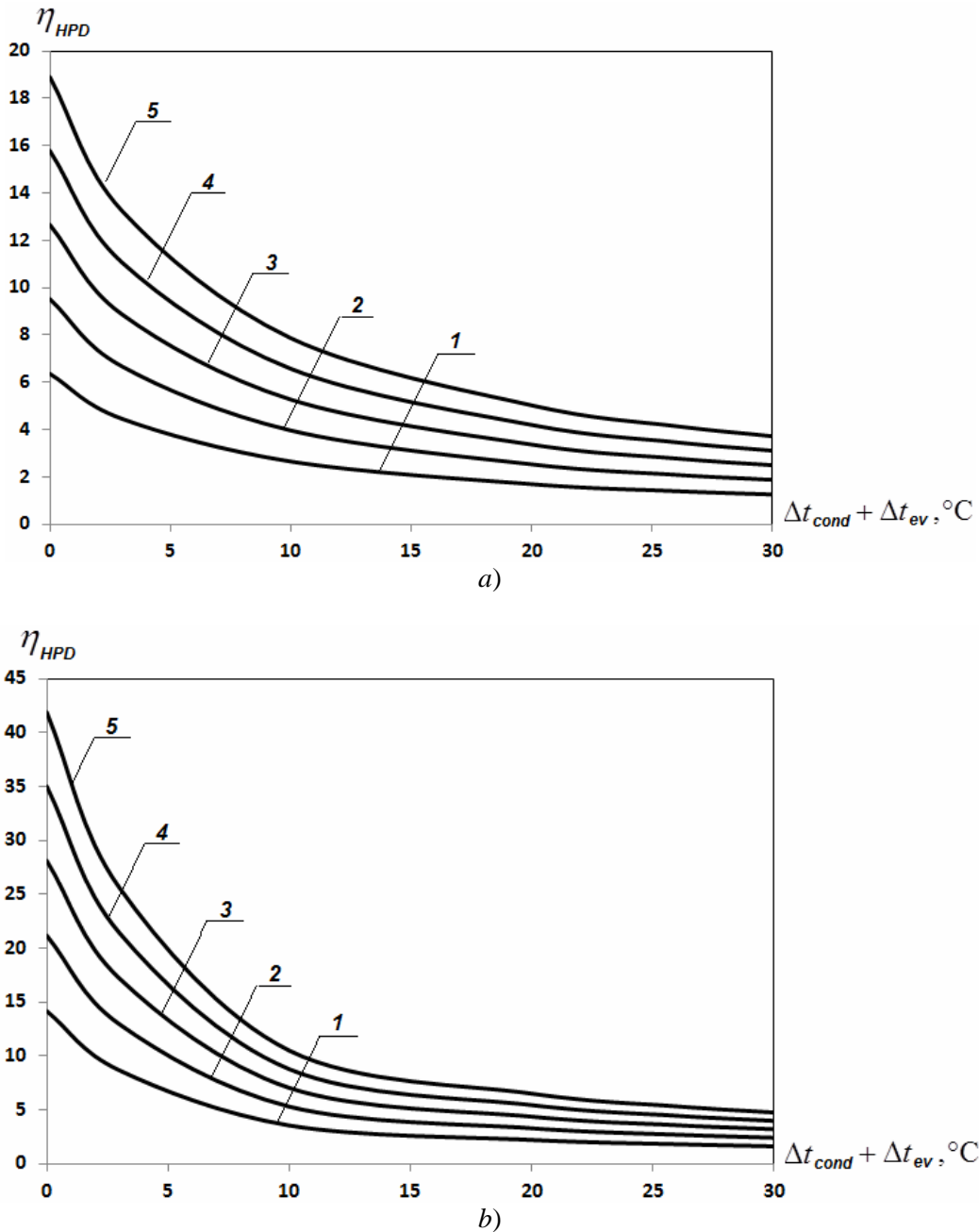


Fig. 3. Dependence of the coefficient of utilization of external energy from the total thermal irreversibility: a) for  $t_{mix} = 50 \text{ }^\circ\text{C}$ ,  $\phi_{mix} = 70 \%$  ; b) for  $t_{mix} = 60 \text{ }^\circ\text{C}$ ,  $\phi_{mix} = 80 \%$  ; 1 –  $\Delta t_{dc} = 1 \text{ }^\circ\text{C}$ ; 2 – 1.5; 3 – 2; 4 – 2.5; 5 – 3

As we can see from the Fig. 3, there are a sharp increase of  $\eta_{HPD}$  at the magnitude  $(\Delta t_{cond} + \Delta t_{ev})$  below the value  $\Delta t_{cond} + \Delta t_{ev} = 10^\circ\text{C}$ , in the range of  $\Delta t_{cond} + \Delta t_{ev} = 10...30^\circ\text{C}$  the curves of  $\eta_{HPD}$  are more gentle in nature, which qualitatively corresponds with the data, which are presented for HPD with partial recirculation of the drying agent [7].

However, for a fixed value of the total thermal irreversibility, efficiency of the HPD with full recycling is much higher than for HPD with partial recirculation of exhaust air [7], as is shown in Fig. 4.

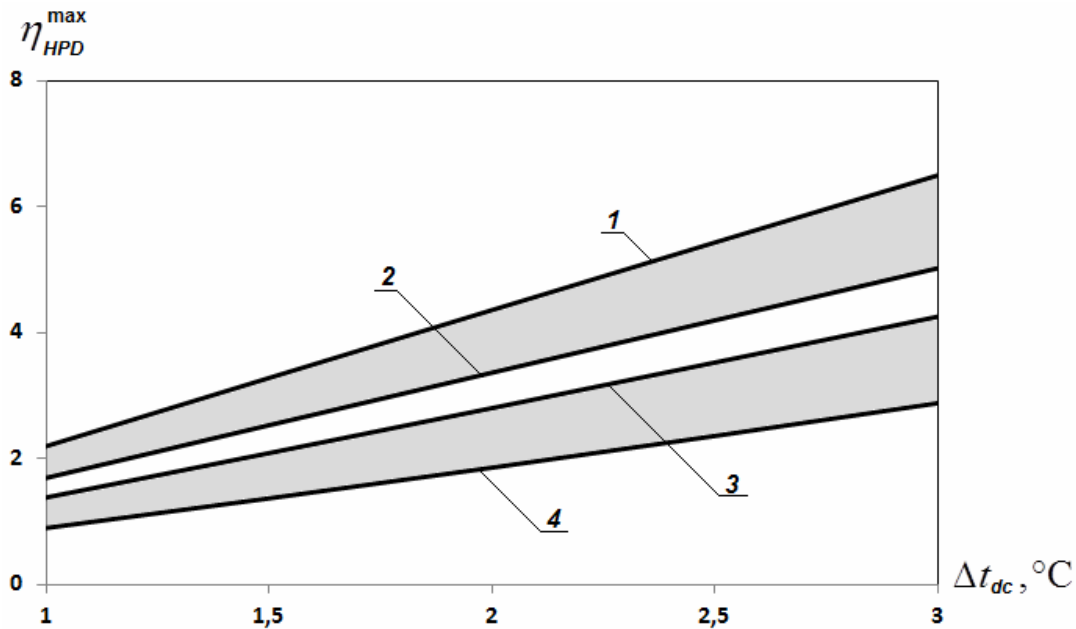


Fig. 4. Dependence of maximum of the coefficient of utilization of external energy from the technological change temperature of drying agent in the drying chamber with  $\Delta t_{cond} = 10^\circ\text{C}$ ;  $\Delta t_{ev} = 10^\circ\text{C}$ : 1, 2 – for HDP with full recycling (1 –  $t_{mix} = 60^\circ\text{C}$ ,  $\phi_{mix} = 80\%$ ; 2 –  $t_{mix} = 50^\circ\text{C}$ ,  $\phi_{mix} = 70\%$ ); 3, 4 – for HDP with partial recycling (3 –  $t_{mix} = 60^\circ\text{C}$ ,  $\phi_{mix} = 80\%$ ; 4 –  $t_{mix} = 50^\circ\text{C}$ ,  $\phi_{mix} = 70\%$ )

As we can see from the illustration, the efficiency gains in the application of technology with full recirculation of drying agent is to averages of 55 % for  $t_{mix} = 60^\circ\text{C}$ ,  $\phi_{mix} = 80\%$  that is a significant advantage in using this scheme.

The disadvantages of heat pump systems with full recycling of air include a more complex mode of installation due to the presence of external coolers and related financial costs. Therefore, the efficiency of various schemes should be based on the technical and economic indicators.

### Nomenclature

$c$  – specific heat,  $\text{kJ}/(\text{kg}\cdot^\circ\text{C})$ ;  $d$  – moisture content,  $\text{kg}_{\text{moist}}/\text{kg}_{\text{da}}$ ;  $L$  – compressor power,  $\text{kW}$ ;  $Q$  – heat transfer rate,  $\text{kW}$ ;  $r$  – evaporation heat,  $\text{kJ}/\text{kg}_{\text{moist}}$ ;  $t$  – temperature,  $^\circ\text{C}$ ;  $V$  – air flow,  $\text{m}^3/\text{s}$ ;  $\varepsilon$  – coefficient of performance (COP);  $\eta$  – coefficient of utilization of external energy;  $\rho$  – density,  $\text{kg}/\text{m}^3$ ;  $\phi$  – relative humidity. **Subscripts:** cond – condenser, da – drying agent, dc – drying chamber, ev – evaporator, gen – general, hp – heat pump, mix – mixture, moist – moisture, s – steam, w – wet.

## References

1. Bezrodny M. K., Kudelya P. P., Kutra D. S. Thermodynamic analysis of a heat pump drying unit for desiccation of wood // *Eng. Therm. Phys. and Industrial Heat Engineering* / Dnipropetrovsk. 2010. Iss. 2. Pp. 35–48 (in Ukrainian).
2. Bezrodny M. K., Kutra D. S. Energy analysis of a traditional and heat pump configurations of units for desiccation of wood // *Industrial Heat Engineering*. 2010. No. 4. Pp. 43–53 (in Ukrainian).
3. Bezrodny M. K., Kutra D. S. Influence of heat loss of drying chamber on an efficiency of operation of a heat pump drying unit for desiccation of wood: Power Engineering, Economics, Technologies, Ecology. Kyiv, 2010. No. 2. (in Ukrainian).
4. Saensabai P., Prasertsan S. Effects of component arrangement and ambient and drying condition on the performance of heat pump dryers // *Drying Technology*. 2003. Vol. 21 (1). Pp. 103–127.
5. Bogdanov E. S., Kozlov V. A., Kuntyshev V. B., Melekhov V. I. *Desiccation of Wood Handbook*, Lesnaya Promyshlennost, Moscow. 1990. 394 p. (in Russian).
6. Morozuk T. V. *Theory of Refrigerating Machines and Heat Pumps*, "Negotsiant" Studio, Odessa, 2006. 712 p. (in Russian).
7. Bezrodny M. K., Kutra D. S. On the upper boundary of a thermodynamic effectiveness of heat pump configurations of units for desiccation of wood // *Industrial Heat Engineering*. 2011. No. 4 (in Ukrainian).

## EXPERIMENTAL COMPARISON OF THE HEAT TRANSFER PERFORMANCE OF MICROCHANNEL GEOMETRIES

**Yiğit Ata Ağartan**

Mechanical Engineering Department  
Middle East Technical University  
06800 Ankara, Turkey  
+90 312 210 5275/2536; yagartan@metu.edu.tr

**Almila G. Yazicioğlu**

Mechanical Engineering Department  
Middle East Technical University  
06800 Ankara, Turkey  
+90 312 210 5263/2536; yalmila@metu.edu.tr

### Abstract

In this work, heat transfer for the two-phase refrigerant flow inside three microchannels has been experimentally investigated for use in evaporators of refrigerators. Current literature shows that the low mass flow rates and the constant wall temperature approach common to refrigerator applications is not of general interest in the investigation of flows in microtubes and microchannels. As a result of this observation, first, an experimental setup has been constructed to test the two phase flow of R134a in three different microchannels in terms of heat transfer performance. For different quality and saturation temperature conditions, the experimental two phase forced convection heat transfer coefficient of the refrigerant has been determined. Two phase flow and quality values of the saturated refrigerant have been adjusted with the use of a winding cable preheater. A gear pump has been used to adjust the uniform low mass flow rates. A secondary cycle of water-ethylene glycol mixture has been used to keep the wall temperature of the test section constant. A concentric counter flow heat exchanger has been used in the test section to maintain the heat transfer to the refrigerant. For the three microchannels, the heat transfer coefficient for the refrigerant has been determined for constant mass flux and constant average quality conditions. As a result of data analysis, it has been seen that the 7-port grooved microchannel has the best heat transfer performance.

### KEYWORDS

Microchannel, forced convection two phase heat transfer, refrigerant, R134a, constant wall temperature.

### INTRODUCTION

Nowadays the need for energy increases with developing technologies. The careful use of energy sources and efficiency issues in the transport of energy become more important issues. Heat transfer, being one of the major subjects in the area of energy, appears in our daily life and industrial applications frequently. One of the most common areas, in which heat transfer takes place is cooling; in both industrial applications and household devices, such as refrigerators and air conditioners. For example, it is estimated that energy consumption by refrigerators is approximately 13% of the total domestic energy consumption. In cooling systems and especially in refrigerators, evaporators with pipes are used. Evaporators in conventional refrigerators are produced by wrapping around a shell, which has a rectangular cross-section and formed by bending metal plates, with pipes. Heat transfer occurs with the help of natural convection.

Microtube and microchannel applications have started being used in many industries because of their compactness and the higher heat transfer coefficients they provide. Developments in manufacturing techniques cause microchannel applications to be applied in different sectors. In recent years, especially in heat exchangers used in automotive and air conditioner technology, microchannel applications appear more frequently. In automotive and air conditioner systems, mass flow rates are quite high. As a result, distributors and collectors are needed for a uniform distribution of the fluid used. In literature there are many studies on the design of distributors and collectors for microchannel applications. In refrigerators, on the other hand, mass flow rates are much less than those in industrial cooling and air conditioning systems. Therefore, to

prepare microchannel heat exchangers for refrigerators, there is no need to design a distributor or a collector; microchannels can be used in conventional and no-frost refrigerators, and evaporators with increased efficiencies can be designed.

In the last thirty years, investigation of heat transfer in micro- and minichannel has become quite widespread. In the very first work, water flow was investigated in a microchannel for cooling of the CPU in a computer. Higher heat transfer was observed in laminar flow in microchannels with respect to macrochannels [1]. When the literature on two-phase flow in microchannels is investigated, it is seen that most of the studies show that saturation pressure has a negligible effect on heat transfer [2–4]. For microchannels, two phase flows with low qualities is advantageous in terms of heat transfer. But for high qualities, an increase in quality causes either a continuous increase or an increase up to a maximum, then a decrease in the heat transfer coefficient [2, 3, 5]. Some of the researchers propose a correlation as a result of their experimental or numerical studies, which are valid for only their conditions [6–11]. Some studies stress the difficulty of obtaining high qualities [10, 12]. Additionally it is observed that with respect to liquid flows, two phase flows have higher pressure drop. Moreover heat transfer coefficient is higher in two phase flows than those in single phase for all different fluids investigated. Especially in experimental studies, mostly constant heat flux boundary condition is used [11]. Dry-out problem, vertical and horizontal configurations, and the need of high heat fluxes for high qualities are some other points faced in literature.

The main purpose of this study is to determine the most suitable microchannel for refrigerator applications among the three microchannels with different geometries, by comparing them experimentally for their two-phase flow heat transfer performance. Due to the actual conditions observed in the evaporators of refrigerators, a constant surface temperature boundary condition was applied. Also, the mass flow rates were kept low, corresponding to those in domestic refrigerators.

## EXPERIMENTAL ANALYSIS

The experimental setup, shown in Fig. 1, was designed for two phase R134a flow experiments. For the constant wall temperature approach two cycles were needed; thus a counter flow, annular heat exchanger was designed in the microchannel test section. In this heat exchanger, R134a flows through the microchannel and a mixture of water and ethylene glycol (to decrease the freezing temperature of the fluid, and called water from hereon, for simplicity) flows in the annular side in the counter direction, with a high flow rate to provide constant wall temperature on the outer surface of the microchannel. To be able to arrange the temperatures of the two fluid cycles, cooling baths are used in both cycles. To provide the circulation of the fluids in the system pumps are used. A pre-heater is used in the R134a cycle to determine the quality value at the inlet of the microchannel test section. A micro-flow meter in the R134a cycle and two rotameters in the water cycle are used to measure flow rates. RTDs and thermocouples are used to measure the temperatures in different locations of the experimental setup and pressure transducers are used to determine the system pressure. Additionally, the experimental setup has a differential pressure transducer for measuring the pressure drop of R134a in the test section along the microchannel. Calibration of the pressure transducers and temperature measurement devices were made by Arçelik Inc. which is the technical supporter of this work. Also before two phase flow experiments, to determine how much heat is transferred to the refrigerant from the pre-heater, a calibration process was conducted.

The geometrical properties of the three microchannels used in the two-phase flow experiments can be seen in Table 1. The drawings of the cross sectional areas of the microchannels are given in Fig. 2. Units of length values specified in Fig. 3 are millimeters (mm).

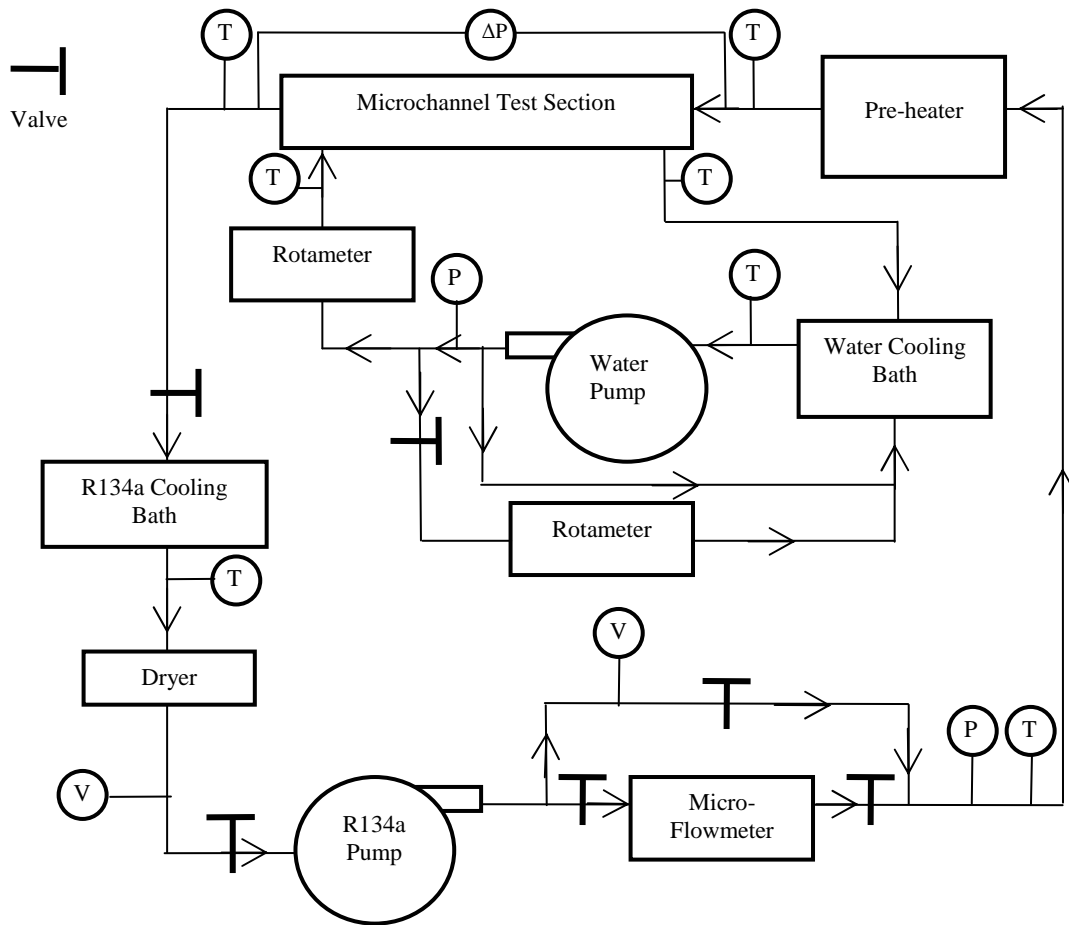


Fig. 1. The schematic view of the experimental setup

Table 1. The geometrical properties of the three microchannels

Name	Microchannel 1	Microchannel 2	Microchannel 3
Width (mm)	16	22	20
Height (mm)	2.1	5	2.1
Wall thickness (mm)	0.3	0.6	0.4
Channel height (mm)	1.5	3.8	1.3
Channel width (mm)	1.94	3.68	2.35
Number of channels (mm)	7	5	7
Channel length (mm)	465	440	525
Cross sectional area (mm <sup>2</sup> )	20.4	66.27	21.84
Wetted parameter (mm)	48.2	68.79	51.8
Hydraulic diameter* (mm)	1.69	3.85	1.69
Inner heat transfer area (mm <sup>2</sup> )	22413	30268	27195

\* The range of hydraulic diameters corresponding to "micro"channels varies in literature. Some texts would describe the current channels as micro, while some as mini. It is common practice to call all small channels microchannels in industry. This approach has been followed herein.

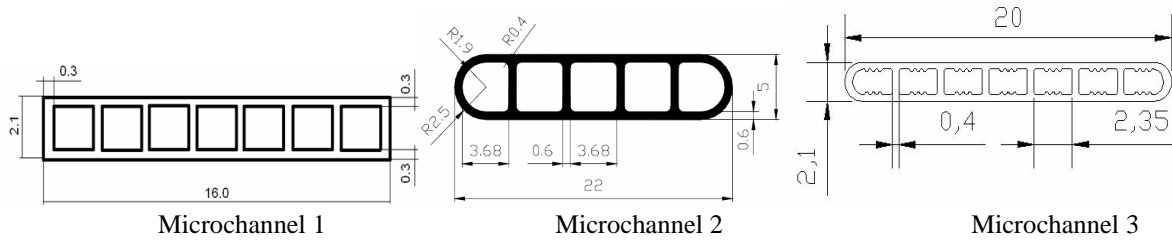


Fig. 2. The drawings of the cross sectional areas of the microchannels (all dimensions in mm)

## Two Phase Flow Experiments

### Viscous Heating

After mounting the microchannels within their shells to the experimental setup, leakage tests were conducted for each microchannel. Before two phase flow experiments, to determine the rate of heat transferred to the refrigerant side from the water side in the test section, viscous heating tests were performed. It is known that in flows having low velocities and Reynolds numbers, viscous heating is an important issue [13]. By setting the temperatures of the ambient, R134a, and water side to the same value, and by providing different flow rates in the water side, experiments were conducted to see the relation between Reynolds number and viscous heating. As a result, the correlation given below has been obtained.

$$\dot{Q}_V = 0.0623 \cdot Re_w - 1.4424 \quad (1)$$

Here,  $\dot{Q}_V$  is viscous heating, in [W] and  $Re_w$  is Reynolds number on the water side.

The viscous heating experiments conducted with the first microchannel were not repeated for the other microchannels and eq. (1) was used for the other microchannels as well. Discrepancies in viscous heating values for the other microchannels were neglected. The rate of heat transferred to the refrigerant from the water side,  $\dot{Q}_w$ , can be determined as below, knowing the temperature, pressure values, and the flow rates on both sides in the test section.

$$\dot{Q}_w = \dot{V}_w \rho_w (h_{wi} - h_{we}) + \dot{Q}_V - \dot{Q}_{w,loss} \quad (2)$$

Here,  $\dot{V}_w$  is water volumetric flow rate,  $\rho_w$  is water density, and  $h_{wi}$  and  $h_{we}$  are inlet and outlet enthalpies on the water side,  $\dot{Q}_V$  is viscous heating, and  $\dot{Q}_{w,loss}$  is heat loss from the water side to the ambient. In eq. (2), the heat loss from the water side to the ambient, shown as  $\dot{Q}_{w,loss}$ , is determined to be only 2.5% of the heat transferred to R134a side, even for the maximum temperature difference; thus it has been neglected.

### Experimental Conditions

The maximum and minimum values of the refrigerant side experiment conditions; namely mass flow rate, saturation pressure, saturation temperature, average quality, and pressure drop are shown in Table 2. Refrigerant properties were calculated by using the software REFPROP 7. As it is seen in Table 2, due to the capability of the flow meter used, the mass flow rates of the refrigerant are above 1 g/s, and not in the range of 0.2–1.0 g/s, common to household refrigerators. The maximum mass flow rates were 5.60, 6.40, and 4.88 g/s, respectively, for the three microchannels investigated.

In the experiments, higher pressures at the inlet of the microchannels than those in refrigerators were obtained due to the temperatures not being sufficiently low in the cooling bath to condense the refrigerant. On the other hand, the studies in literature show that saturation pressure has a negligible effect on heat transfer. Since the pressure drop values shown in Table 2 are low, the average values of the pressures at the inlet and outlet of the microchannels are considered as saturation pressure in the experiments. Quality values in the test section are the average of the qualities at the inlet and outlet of the test section, a common procedure followed in literature. It is taken into account that high variations in quality may cause some deviations in the trends on the graphs, depending on the quality values. For example, in the 3<sup>rd</sup> microchannel, large differences occurred in the quality values at the inlet and outlet section because of the high heat transfer rates from the water side to the refrigerant in the test section; this will be discussed later. Some data given as minimum or maximum in Table 2 weren't used for the investigation of the microchannels, because of few data values under similar conditions.

The temperature of the cooling bath and the flow rate on the water side were changed depending on the changes in the refrigerant properties during two-phase flow experiments. Due to the incompressibility of liquid water, the effect of pressure variations on water properties was neglected. The ranges of the parameters on the water side during two-phase flow experiments are given in Table 3.

Table 2. The refrigerant side parameters for the two phase flow experiments

Parameter	unit	Microchannel 1		Microchannel 2		Microchannel 3	
		min	max	min	max	min	max
Refrigerant mass flow rate	g/s	1.04	5.60	1.33	6.40	1.08	4.88
Refrigerant saturation pressure	bar	2.98	4.88	2.49	6.48	2.95	4.81
Refrigerant saturation temperature	°C	0.49	14.97	-4.36	24.12	0.22	20.02
Refrigerant average quality	-	4.41%	32.61%	5.29%	50.17%	14.48%	69.10%
Refrigerant pressure drop	bar	0.0003	0.0570	0.0025	0.0269	0.0039	0.0312

Table 3. The water side parameters for the two-phase flow experiments

Parameter	unit	Microchannel 1		Microchannel 2		Microchannel 3	
		min	max	min	max	min	max
Water volumetric flow rate	l/min	1.30	1.88	1.68	2.1	1.51	2
Water mass flow rate	g/s	23.50	34.04	30.52	37.78	27.17	36.00
Water Reynolds number	-	127.87	266.77	60.50	226.27	149.66	273.42
Water inlet temperature	°C	8.70	20.87	1.68	30.20	10.95	23.18
Water outlet temperature	°C	8.15	20.51	1.09	29.52	9.97	21.99

In the experiments with the microchannels water flow rate was controlled by the valves and flow rate values were read from the rotameter manually. To provide constant wall temperature on the microchannels, the highest flow rates which the rotameter can read (about 2.1 g/s) were provided. As it is seen in Table 3, during the experiments Reynolds number in the water side didn't exceed 273, so developing laminar flow correlations were used. Moreover the mass flow rate on the water side is kept much higher than that for the refrigerant side, to increase the validity of the constant wall temperature approach by decreasing the temperature variations along the microchannel.

In the test section, to obtain different quality values, the pre-heater in the system was used by entering different voltage values on the computer for different experiments. The ranges of the voltage values entered for the pre-heater, the rates of heat transferred from the pre-heater to the refrigerant corresponding to the voltage values entered, viscous heating on the water side in the test section, and heat transfer from the water side to the refrigerant side are shown in Table 4.

Table 4. The rates of heat transfer in the pre-heater and the test sections for two phase flow experiments

Parameter	unit	Microchannel 1		Microchannel 2		Microchannel 3	
		min	max	min	max	min	max
Pre-heater voltage value entered	V	2	6	3	7	2	7
Pre-heater power received, $\dot{Q}_{RH}$	W	20.21	78.98	34.90	136.86	20.21	136.86
Viscous heating, $\dot{Q}_V$	W	6.52	15.18	2.33	12.65	7.88	15.59
Heat transfer to refrigerant, $\dot{Q}_W$	W	31.97	125.17	28.67	109.72	105.90	216.61

#### Data Analysis and Reduction

After the experiments were completed and the data collected, the analysis of data is the next process. The refrigerant and water flow rates and the pre-heater power measurements are recorded manually. Pressure and temperature measurements are recorded on the computer through a data acquisition system. These measurements are conducted by pressure transducers, RTDs, and thermocouples. The computer program (HP

VEE) used for collecting data on the computer and controlling the pre-heater is arranged to take data every 15 seconds. The values read are shown on graphs momentarily, so the steady state conditions can be observed easily. During the experiments after the steady state condition was obtained, refrigerant pressure, temperatures at the inlet and outlet of the pre-heater test section, and the inlet and outlet temperatures of the test section were observed. By using these values and the refrigerant mass flow rate the quality at the inlet of the test section was calculated. When a quality value was obtained, that is when two phase flow was obtained at the inlet of the test section, the procedure needed for two phase flow experiments was applied, the experiment time was noted down and for different mass flow rates, saturation pressures, and qualities, the experiments were conducted. Data analysis was carried out at the end of the experiment day.

The main purpose in the calculations is to find the heat transfer coefficient of R134a in the two phase flow experiments. As a result of the experimental calculations performed using the experimental data, the heat transfer coefficients were calculated for different quality values on the refrigerant side in two phase flow. To provide two phase flow on the refrigerant side in the test section, the refrigerant is heated by the pre-heater. By using eq. (1), the rate of heat transferred to the refrigerant from the pre-heater is calculated according to the voltage value entered on the computer. During the two phase flow experiments at the inlet of the pre-heater section, pure liquid flow was supplied to be able to find the state of the refrigerant at this point by knowing only its pressure and temperature. If the enthalpy is known at the inlet of the pre-heater section, by adding the enthalpy change due to the heat transfer from the pre-heater, the enthalpy at the inlet of the test section can be calculated as shown in eq. (3).

$$\dot{Q}_{RI} = \dot{m}_R (h_{he} - h_{hi}) . \quad (3)$$

Here  $\dot{Q}_{RI}$  is the rate of heat transferred to the refrigerant from the pre-heater,  $\dot{m}_R$  is the refrigerant mass flow rate,  $h_{he}$  is the enthalpy of the refrigerant at the outlet of the pre-heater section (inlet of the test section) and  $h_{hi}$  is the enthalpy of the refrigerant at the inlet of the pre-heater section. To determine the quality at the outlet of the test section the enthalpy value there is needed. By adding the enthalpy change due to heat transfer from water side to the enthalpy at the inlet of the test section, the enthalpy at the outlet can be calculated as shown in eq. (4). Pressure drop along the microchannels are measured and by using the pressure at the outlet of the test section and by knowing the enthalpy value of this point, the outlet quality value can be determined.

$$h_{re} = \frac{\dot{Q}_W}{\dot{m}_R} + h_{ri} . \quad (4)$$

Here  $h_{re}$  is the enthalpy at the outlet of the test section and  $\dot{Q}_W$  is the rate of heat transferred to the refrigerant from the water side, given by eq. (2).

In calculations of average heat transfer coefficient, the wall temperature of the microchannels is needed. So the temperature values were measured with the help of the 7 thermocouples placed on the outer surface along the microchannel. When the maximum and minimum values of the wall temperatures measured were in the range of 0.5°C, which is the sensibility value for the thermocouples used, the condition was considered as constant wall temperature. Then, the average of these 7 measurements was taken as the constant wall temperature. Overall heat transfer coefficient was calculated by using the logarithmic mean temperature difference method and after it was calculated, the heat transfer coefficient was found.

$$\Delta T_{LM} = \frac{(T_w - T_{ri}) - (T_w - T_{re})}{\ln \left( \frac{T_w - T_{ri}}{T_w - T_{re}} \right)} . \quad (5)$$

Here  $\Delta T_{LM}$  is the log mean temperature difference,  $T_w$  is the wall temperature,  $T_{ri}$  is the refrigerant temperature at the inlet of the test section, and  $T_{re}$  is the refrigerant temperature at the outlet of the test section. Inner heat transfer area can be calculated as below.

(6)

Here  $A_i$  is the inner heat transfer area,  $P_h$  is the heated parameter, and  $L$  is the microchannel length. Overall heat transfer coefficient,  $U_i$ , is written in terms of the heat transfer area,  $A_i$ .

$$U_i = \frac{\dot{Q}_w}{A_i \Delta T_{LM}} \quad (7)$$

Overall heat transfer coefficient is a combination of the two phase forced convection heat transfer coefficient of the refrigerant and the thermal conductivity of aluminum, the microchannel material. Finally the average heat transfer coefficient,  $\bar{h}_{TP}$ , of two phase refrigerant flow is calculated.

$$\bar{h}_{TP} = \left( \frac{1}{U_i} - \frac{t}{k_{Al}} \right)^{-1} \quad (8)$$

Here,  $t$  is the wall thickness of the microchannel and  $k_{Al}$  is the thermal conductivity of aluminum.

## RESULTS AND DISCUSSION

In this section, the experimentally determined two-phase heat transfer coefficient is presented for the three microchannels and a comparison among them is carried out. The experimental data are investigated at constant quality and constant mass flux values. On the two graphs drawn for the comparison of the microchannels, the number of the channel (see Fig. 2), to which the constant values belong is shown in parentheses.

As mentioned previously, the refrigerant quality value calculated for an experiment is the average of the qualities at the inlet and outlet of the test section. Since the average channel quality is not an independent parameter in the experiments, the data having the closest average quality values within a narrow margin of error were selected as the constant quality value. For the 1<sup>st</sup> microchannel 12%, for the 2<sup>nd</sup> microchannel also 12%, and for the 3<sup>rd</sup> microchannel 28% and 35% were selected as constant quality values and Fig. 3 was prepared to show the variation of the heat transfer coefficient with mass flux.

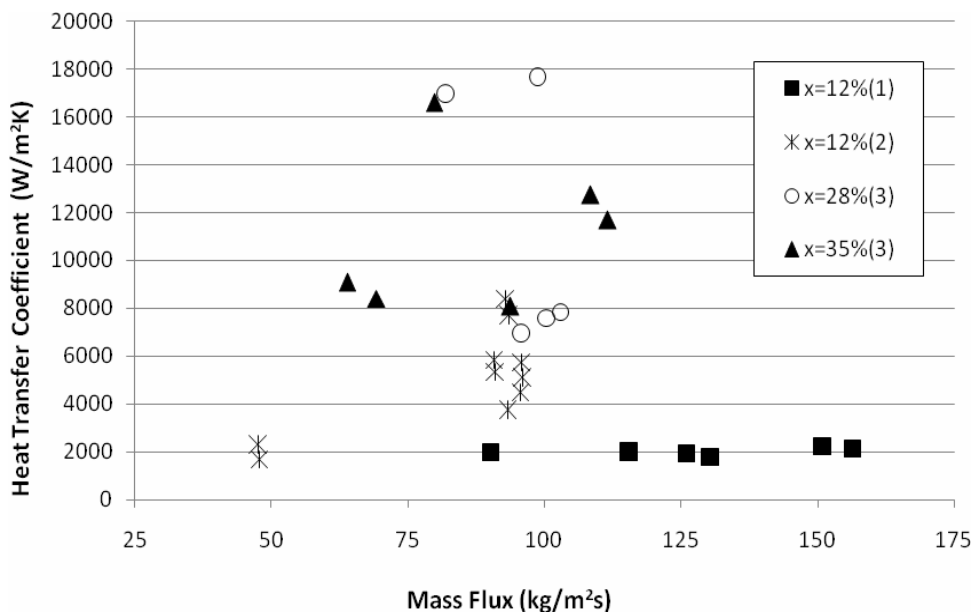


Fig. 3. Variation of heat transfer coefficient with mass flux for constant refrigerant quality values

With the 3<sup>rd</sup> microchannel, the smallest average quality value obtained was 28%, while with the other two microchannels average quality values were not as high. The difficulty of obtaining high quality values, even with the constant wall heat flux boundary condition, is stressed in literature [10]. When the 2<sup>nd</sup> and 3<sup>rd</sup> microchannels are compared, it is seen that all the heat transfer coefficient values obtained with the 3<sup>rd</sup> microchannel are higher than those in the 2<sup>nd</sup> microchannel. However, it should be mentioned that this comparison is made at lower mass flux values for the 2<sup>nd</sup> microchannel. When the 1<sup>st</sup> and 2<sup>nd</sup> microchannels are investigated at 12% quality value, at about 92 kg/(m<sup>2</sup>s) mass flux the 2<sup>nd</sup> microchannel has higher heat transfer coefficient. Additionally at this quality value, in the 2<sup>nd</sup> microchannel, the heat transfer coefficient has a much sharper increase. This tendency may show that for mass fluxes greater than about 50 kg/m<sup>2</sup>s, higher heat transfer coefficients can be obtained in the 2<sup>nd</sup> microchannel than those in the 1<sup>st</sup> microchannel.

If the data of these three microchannels are investigated together, heat transfer coefficients in the 3<sup>rd</sup> microchannel, especially in the range of 64-112 kg/(m<sup>2</sup>s) mass fluxes, are clearly higher than those in the others. While the reason may be the presence of inner grooves in the 3<sup>rd</sup> microchannel, it should be noted that the quality values of the 3<sup>rd</sup> microchannel are higher than the ones in the other microchannels.

Comparison of the three microchannels at constant mass flux was made with 67 and 94 kg/(m<sup>2</sup>s) for the 1<sup>st</sup> microchannel, 60 and 94 kg/(m<sup>2</sup>s) for the 2<sup>nd</sup> microchannel, and 65 and 95 kg/(m<sup>2</sup>s) for the 3<sup>rd</sup> microchannel. The variation of heat transfer coefficient with quality at constant mass flux values is presented in Fig. 4.

When 67 kg/(m<sup>2</sup>s) mass flux for the 1<sup>st</sup> microchannel, 60 kg/m<sup>2</sup>s mass flux for the 2<sup>nd</sup> microchannel, and 65 kg/(m<sup>2</sup>s) for the 3<sup>rd</sup> microchannel are investigated together, it is seen that the qualities less than 33% were obtained in the 1<sup>st</sup> and 2<sup>nd</sup> microchannel, but the quality values obtained for the 3<sup>rd</sup> microchannel are higher than 34%. There are two main reasons for this: First, the heat transfer area for the 3<sup>rd</sup> microchannel is higher than those for the other two; as a result, the rate of heat transfer is higher. Secondly, due to this high heat transfer, the variation of quality along the channel was also higher; as a result, average quality values were not low. The power limit of the preheater did not allow obtaining higher inlet quality values for the 1<sup>st</sup> and 2<sup>nd</sup> microchannels. In addition, in the experiments of the 2<sup>nd</sup> microchannel, due to its higher hydraulic diameter, higher flow rates were used to achieve similar levels of mass fluxes with the other microchannels. These high flow rates resulted in low quality changes along the 2<sup>nd</sup> microchannel.

During the experiments, when a constant mass flow rate was desired, the same flow rate could not always be provided because of different saturation temperature and pressure conditions of the experiments. Although the variation of heat transfer coefficient with quality at constant mass flux is given in Fig. 4, this variation doesn't show the variation of heat transfer coefficient with increasing quality along the flow in the microchannel. Flow visualization is needed for determination of this type of variation.

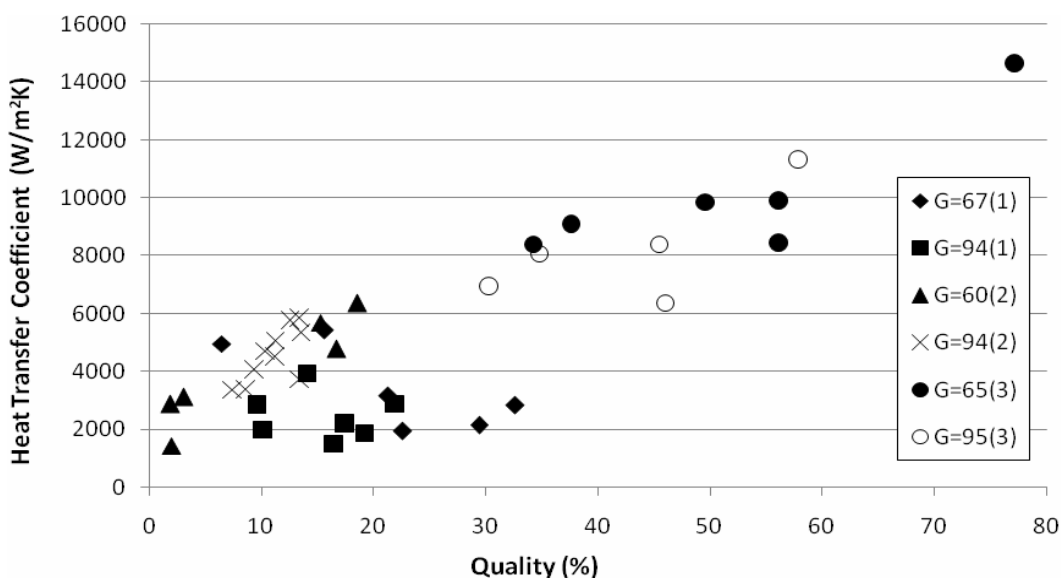


Fig. 4. Variation of heat transfer coefficient with quality for constant mass flux values

By looking at the data in Fig. 4 it is possible to make a good comparison of the microchannels at 94-95 kg/(m<sup>2</sup>s) mass fluxes. At these mass fluxes, between 7 and 22% quality values, higher heat transfer coefficients were obtained with the 2<sup>nd</sup> microchannel than the 1<sup>st</sup> microchannel. For the 3<sup>rd</sup> microchannel at 95 kg/(m<sup>2</sup>s) mass flux, again the data are in the higher quality range than the others, and higher heat transfer coefficients are obtained. However when all data in Fig. 4 are investigated together, it is seen that the 3<sup>rd</sup> microchannel cannot be compared appropriately with the 1<sup>st</sup> and 2<sup>nd</sup> ones in terms of the change in the average quality values. Nevertheless it is thought that in refrigerator applications full evaporation is desired and in the 3<sup>rd</sup> microchannel high outlet and average qualities can be obtained. As a result, the 3<sup>rd</sup> microchannel can be considered as the most suitable choice among the three microchannels in terms of heat transfer performance.

As it is well known, the local quality value affects the local heat transfer coefficient in two phase flow. Especially at low qualities, commonly at the entrance of the channels, the bubbles forming at the wall oscillate and may cause instabilities. As a result there may be sudden increase and decrease in the local heat transfer coefficient. For microchannels, bubble dynamics is increasingly important because the bubble sizes may be comparable to channel diameters. This may explain the wide variation in the heat transfer coefficient values for each microchannel, seen in Figs. 3 and 4 for the same mass flux and quality values, respectively. Due to these reasons, flow visualization is vital in the analysis of two-phase flow in microchannels, as previously mentioned.

## CONCLUSIONS

In this work, by investigating the heat transfer performances of three multiport microchannels having different geometries, a comparison has been made based on their heat transfer coefficients. For this purpose, firstly an experimental setup has been prepared. Then by performing two-phase flow and heat transfer experiments with the three multiport microchannels, their performances were investigated. As a result of the two phase flow experiments conducted, the conclusions can be summarized as follows.

1. Evaluations made for heat transfer coefficient show that higher heat transfer coefficients are obtained in the 3<sup>rd</sup> microchannel than in the other two microchannels.
2. For the quality of 12% for constant mass flux higher heat transfer coefficients are obtained in the 2<sup>nd</sup> microchannel compared to the values obtained in the 1<sup>st</sup> one.
3. Comparison of the 1<sup>st</sup> and 2<sup>nd</sup> microchannels shows that in the quality values between 7-22% for 94 kg/m<sup>2</sup>s mass flux, higher heat transfer coefficients are obtained in the 2<sup>nd</sup> microchannel.
4. The 3<sup>rd</sup> microchannel is the most appropriate microchannel for refrigerator applications in terms of heat transfer performance among the three microchannels investigated, under the given experimental conditions.

## Acknowledgments

The authors would like to thank TÜBİTAK (The Scientific and Technological Research Council of Turkey) Project No 107M504 for financial support, Arçelik Inc. for technical support, and METU Mechanical Engineering Department, especially technician Mustafa Yalçın, for the construction of the experimental set-up.

## NOMENCLATURE

$A_i$	Inner heat transfer area of the microchannel, m <sup>2</sup>
$G$	Mass flux, kg/(m <sup>2</sup> s)
$\bar{h}$	Average convection heat transfer coefficient of R134a, W/(m <sup>2</sup> K)
$h$	Enthalpy, kJ/kg
$k_{Al}$	Thermal conductivity of Aluminum, W/(mK)
$L$	Length of the test section, m
$\dot{m}$	Mass flow rate, kg/s
$\dot{Q}$	Heat transfer rate, W
$P_h$	Heated perimeter of the inner side of the microchannel, perpendicular to the flow, m
$Re$	Reynolds Number

T	Temperature, K
	Wall thickness, m
$U_i$	Overall heat transfer coefficient based on the inner surface area of the microchannel, W/(m <sup>2</sup> K)
$\dot{V}$	Volumetric flow rate, m <sup>3</sup> /s
x	Quality of the refrigerant

#### Greek letters

$\Delta$	Difference; $\rho$	density
----------	--------------------	---------

#### Subscripts

he	Pre-heater exit
hi	Pre-heater inlet
LM	Logarithmic mean
R	Refrigerant
RI	Input to the refrigerant from the pre-heater
re	Refrigerant test exit
ri	Refrigerant test inlet
TP	Two-phase
V	Viscous heating
w	Water
w, loss	Water side loss to the surroundings
we	Water test exit
wi	Water test inlet

#### References

1. Tuckerman D. B., Pease R. F. Optimized convective cooling using micromachined structure // *J. of the Electrochem. Soc.* 1982. Vol. 129(3). P. 98.
2. Bertsch S. S., Groll E. A., Garimella S. V. Effects of heat flux, mass flux, vapor quality, and saturation temperature on boiling heat transfer in microchannels // *Int. J. Multiphase Flow.* 2008/11. Vol. 35. Pp. 142–54.
3. Bertsch S. S., Groll E. A., Garimella S. V. Refrigerant flow boiling heat transfer in parallel microchannels as a function of local vapor quality // *Int. J. Heat and Mass Transfer.* 2008/04. Vol. 51. Pp. 4775–4787.
4. Revellin R., Thome J. R. Experimental investigation of R-134a and R-245fa two-phase flow in microchannels for different flow conditions // *Int. Journal of Heat and Fluid Flow.* 2007. Vol. 28. Pp. 63–71.
5. De Rossi F., Mauro A. W., Rosato A. Local heat transfer coefficients and pressure gradients for R-134a during flow boiling at temperatures between -9°C and +20°C // *Energy Conversion and Management.* 2008/04. Vol. 50. Pp. 1714–1721.
6. Yan Y. Y., Lin T. F. Evaporation heat transfer and pressure drop of refrigerant R-134a in a small-pipe // *Int. J. Heat and Mass Transfer.* 1998. Vol. 41. Pp. 4183–4194.
7. Yarin L. P., Ekelchik L. A., Hetsroni G. Two-phase laminar flow in a heated microchannels // *Int. J. Multiphase Flow.* 2002. Vol. 28. Pp. 1589–1616.
8. Jung J. Y., Kwak H. Y., Hetsroni G. Fluid flow and heat transfer in microchannels with rectangular cross section // *Heat Mass Transfer.* 2007. Vol. 44. Pp. 1041–1049.
9. Park H. S., Punch J. Friction factor and heat transfer in multiple microchannels with uniform flow distribution // *Int. J. Heat and Mass Transfer.* 2008. Vol. 51. Pp. 4535–4543.
10. Liu D., Garimella S. V. Flow Boiling Heat Transfer in Microchannels // *ASME Journal of Heat Transfer.* 2008. Vol. 129. Pp. 1321–1332.
11. Choi K. I., Pamitran A. S., Oh J. T. Boiling heat transfer of R-22, R-134a, and CO<sub>2</sub> in horizontal smooth minichannels // *Int. J. Refrigeration.* 2007. Vol. 30. Pp. 1336–1346.
12. Agostini B., Bontemps A. Vertical flow boiling of refrigerant R134a in small channels // *Int. J. Heat and Fluid Flow.* 2005. Vol. 26. Pp. 296–306.
13. Morini G. L. Viscous heating in liquid flows in micro-channels // *Int. J. Heat and Mass Transfer.* 2005. Vol. 48. Pp. 3637–3647.

## MODELING OF WATER SORPTION DYNAMICS IN HEAT TRANSFORMERS: AN OPTIMAL SHAPE OF THE SORPTION ISOBAR

**Boris N. Okunev, Anton P. Gromov**

Moscow State University

Vorobiev Gori, 119992, Moscow, Russia

Tel: +7 495 939 46 49; Fax: +7 495 939 33 16; E-mail: okunev@tech.chem.msu.ru

**Ivan S. Glaznev, Yuriy I. Aristov**

Boreskov Institute of Catalysis

Pr. Lavrentieva 5, 630090, Novosibirsk, Russia

Te/Fax: +7 383 330 95 73; E-mail: aristov@catalysis.ru

### Abstract

Optimization of sorption dynamics at the isobaric stages of an adsorption heat transformer is addressed in this paper. We have used a mathematical model of coupled heat and mass transfer in a spherical adsorbent grain that is in thermal contact with a metal plate subjected to a fast temperature jump/drop (from 60 to 70°C and back). Model isobars of the water sorption (step-like, linear and exponential) are tested to elucidate the effect of the isobar shape. Temporal evolution of radial profiles of the temperature, pressure and adsorbed water concentration inside the grain is calculated and analyzed. In the majority of cases, the calculated dependences of the average water uptake/release on time can be satisfactorily described by an exponential function up to the dimensionless conversions of 0.7–0.8. Significant deviations are observed at larger conversions. The characteristic sorption time  $\tau$  is found to be strongly dependent on the isobar shape. The fastest adsorption and desorption processes are found for the step-like isobar with the step positioned at the initial process temperature because in this case the driving force for heat transfer is maximal. For step-like isobars, the ads-/desorption rate constants are found to be linear functions of the difference between the heat source (sink) temperature and the temperature of the isobar step.

### KEYWORDS

Mathematical modeling, adsorption heat transformers, sorption dynamics, isobar shape, optimal adsorbent.

### INTRODUCTION

To make adsorption heat transformers (AHTs) competitive with absorption and compression units it is a great big deal to improve ATH dynamic performance [1]. It is affected by many factors [2] among which are the heat-exchanger (HEX) design [3, 4], heat transfer intensification [5–7] and process control strategy [8, 9]. Adsorbent properties are of extreme importance as well. It is recommended augmentation of the adsorbent thermal conductivity [5, 10], reduction of the grain size [11, 12] and intensification of the intraparticle mass transfer [13, 14]. It was found that the sorption dynamics in AHTs is closely linked with equilibrium properties of the adsorbent, in particular, with the shape of the segment of water sorption isobar between the initial and final temperatures of the AHT isobaric stages [15]. In particular, under the same boundary conditions desorption is faster than adsorption for a concave isobar segment and vice versa for a convex one [16]. The authors conjectured that the most challenging shape of isobar is a step-like one.

In this paper we comprehensively investigate the effect of the isobar shape on the dynamics of isobaric water ad-/desorption under isobaric stages of AHT cycles. For the analysis, we used a model of the coupled heat and mass transfer in a spherical adsorbent grain which was developed elsewhere [15]. The model was validated by comparing with experimental data obtained for the composite sorbent SWS-1L [17]. This analysis is aimed in answering the question "Which isobar shape is optimal for AHT?" and in giving recommendations on selection or synthesis of adsorbent materials which ensure the best dynamic performance of a particular AHT cycle with fixed boundary temperatures.

## MATHEMATICAL MODEL

The Fickian diffusion model of combined heat and mass transfer in a single adsorbent grain which is in thermal contact with a metal plate subjected to a fast temperature jump/drop was developed and comprehensively described in [15]. This model closely simulates conditions of isobaric phases of real AHT cycles. It includes the system of differential equations for the heat and mass balance with the relevant initial and boundary conditions. We assumed the local adsorption and thermal equilibrium in each point of the grain. This system was numerically solved by methods of runs and iterations including an implicit finite difference method in order to obtain the radial and temporal distributions of temperature  $T(r, t)$ , concentration  $C(r, t)$  and pressure  $P(r, t)$  in the vapour phase as well as water concentration  $q(r, t)$  in the adsorbed phase. An iso-volumetric discretization in the radial direction was applied as it was done in [18]. The dimensionless water uptake  $\chi$  was calculated as

$$\chi = \frac{(q(t) - q(0))}{(q(\infty) - q(0))} \quad (1)$$

The adsorbent specific heat as a function of the uptake and temperature was taken from [19]. The vapour diffusivity  $D = 3.0 \cdot 10^{-6} \text{ m}^2/\text{s}$  and the coefficient of heat transfer between the grain surface and the vapour  $h_s = 60 \text{ W}/(\text{m}^2 \cdot \text{K})$  were fixed the same as in [15]. These three values are equal to those corresponding to the composite sorbent SWS-1L which is considered to be promising for AHT [20]. The grain size  $R$  was 1.5 mm. The calculations were performed at a constant vapour pressure  $P = 56.5 \text{ mbar}$  for the case of a relatively small driving force of the isobaric desorption which was a temperature jump from the initial plate temperature  $T_{in} = 60 \text{ }^\circ\text{C}$  down to the final plate temperature  $T_f = 70 \text{ }^\circ\text{C}$  ( $60 \text{ }^\circ\text{C} \rightarrow 70 \text{ }^\circ\text{C}$ ). These boundary conditions are typical for isobaric desorption in AHTs driven by external heat source at low temperature. To initiate the back adsorption process the plate was unevenly cooled from  $T_{in} = 70 \text{ }^\circ\text{C}$  up to  $T_f = 60 \text{ }^\circ\text{C}$  ( $70 \text{ }^\circ\text{C} \rightarrow 60 \text{ }^\circ\text{C}$ ). The effect of various model shapes of water sorption isobars – step-like, exponential and linear (Fig. 1) – was analyzed. The step was positioned at  $T_{st} = 60.5, 62, 65, 68$  and  $69.6 \text{ }^\circ\text{C}$  (Fig. 1). Both concave and convex exponential functions were applied.

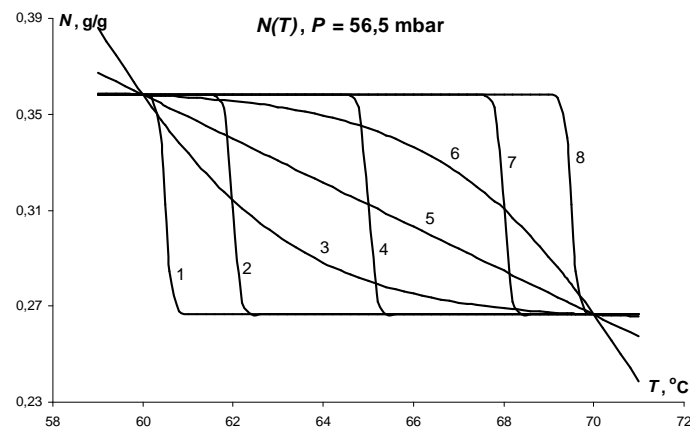


Fig. 1. Model isobars of water sorption at  $P = 56.5 \text{ mbar}$ : 1 – step at  $60.5 \text{ }^\circ\text{C}$ , 2 – step at  $62 \text{ }^\circ\text{C}$ , 3 – exp (concave), 4 – step at  $65 \text{ }^\circ\text{C}$ , 5 – linear, 6 – exp (convex), 7 – step at  $68 \text{ }^\circ\text{C}$ , 8 – step at  $69.5 \text{ }^\circ\text{C}$

## RESULTS AND DISCUSSION

*Distribution of temperature and pressure inside the adsorbent grain.* Since we deal with a spherically symmetric problem, it is worthy to obtain information about the radial and temporal distributions of temperature  $T(r, t)$ , concentration  $C(r, t)$  and pressure  $P(r, t)$  in the vapour phase as well as water concentration  $q(r, t)$  in the adsorbed phase which is not easily available via direct measurements.

Temporal evolution of the average grain temperature can be divided into two parts (Fig. 2, a):

a) a very fast drop of the temperature from the initial temperature  $T_{in} = 70\text{ }^{\circ}\text{C}$  down to app.  $62\text{ }^{\circ}\text{C}$  for adsorption, and very fast rise of the temperature from the initial temperature  $T_{in} = 60\text{ }^{\circ}\text{C}$  again to app.  $62\text{ }^{\circ}\text{C}$  for the desorption. This fast process takes just 2.0–2.5 s for desorption and 14–17 s for adsorption, and is associated with the heating/cooling of the adsorbent grain without appreciable contribution of the adsorption (or desorption) process itself. Indeed, during this period the efficient specific heat  $C = (dQ/dT)/m$  of the grain is close to the specific heat of the grain with the constant water uptake  $q = 0.274\text{ g/g}$  for adsorption and with  $q = 0.358\text{ g/g}$  for desorption (Fig. 3 a);

b) a gradual change of the grain temperature that reaches its final temperature  $T_f$  after app. 2000 s for adsorption and app. 700 s for desorption. Thus, the second part is much longer than the first one. The reason becomes clear if consider the efficient specific heat  $C$  as a function of the average grain temperature  $T_{av}$ . E.g., for the second part of the heating process, its value is much larger than for the first part (Fig. 3, a), because the heat is consumed mostly for desorption of water rather than for heating the grain. The function  $C(T)$  has a break at  $T \approx 62\text{ }^{\circ}\text{C}$  (Fig. 3 a) for both the adsorption and desorption runs  $60\text{ }^{\circ}\text{C} \leftrightarrow 70\text{ }^{\circ}\text{C}$  which is caused by the step on the isobar of water adsorption at  $T_{st} = 62\text{ }^{\circ}\text{C}$  (Fig. 1). This break correlates with a break of the functions  $T_{av}(t)$  and  $P_{av}(t)$  (Fig. 2).

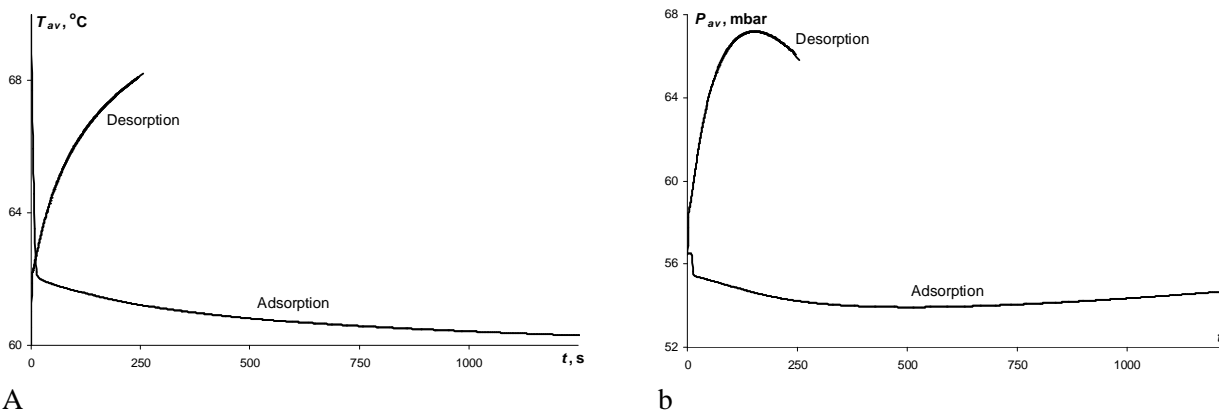


Fig. 2. Temporal evolution of the average grain temperature (a) and the average pressure (b) inside the grain during ad- and desorption processes. Step at  $62\text{ }^{\circ}\text{C}$

Thus, during both the adsorption and desorption processes the grain temperature is essentially non-steady state that indicates the governing role of the heat transfer from the plate to the grain (or back) at all times.

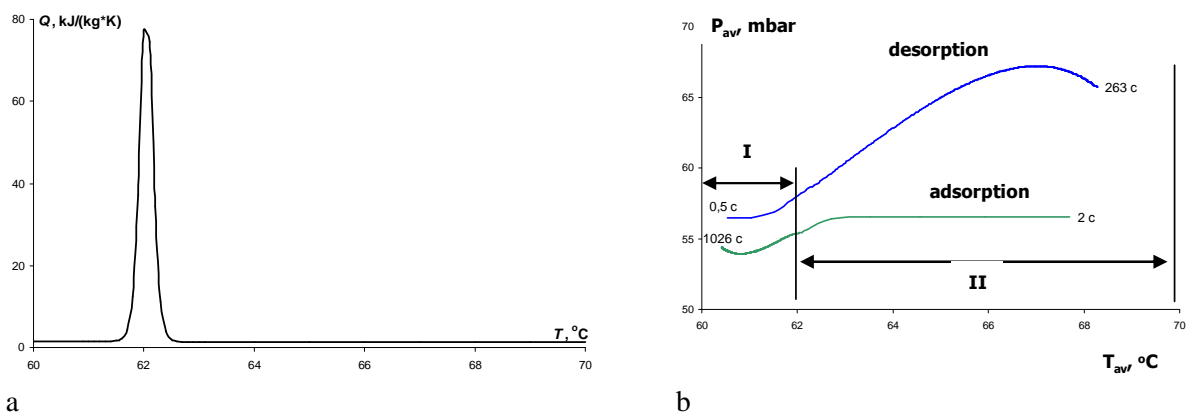


Fig. 3. a – Efficient specific heat of the grain as a function of the average grain temperature (1 – desorption, 2 – adsorption). b – The "phase diagram" that links the average pressure inside the grain and the average grain temperature: I and II are the transient periods for desorption and adsorption respectively.  $T_{st} = 62\text{ }^{\circ}\text{C}$

Variation of the grain temperature immediately affects the pressure evolution inside the grain. Contrast to the temperature, the pressure is not-uniform along the grain radius during both ad- and desorption (Fig. 4) that is due to the slow intragrain vapour transfer. The average pressure increases in time, then passes a maximum and finally decreases approaching the pressure outside the grain,  $P = 56.5$  mbar (Fig. 2 b). This is also clearly seen from the "phase diagram" which links the average pressure inside the grain and the average grain temperature (Fig. 3 b). For desorption run  $60\text{ }^{\circ}\text{C} \rightarrow 70\text{ }^{\circ}\text{C}$  at  $t = 0$  the driving force for heat transfer is maximum (and proportional to  $\Delta T_{\text{dr}} = \Delta T_{\text{max}} = T_f - T_{\text{in}} = 10\text{ }^{\circ}\text{C}$ ), while the driving force for mass transfer equals zero. This initiates the mentioned fast heating of the grain up to app.  $62\text{ }^{\circ}\text{C}$ , means, to the step temperature  $T_{\text{st}}$  that reduces the driving force for the heat transfer  $\Delta T_{\text{dr}} \approx T_f - T_{\text{st}} = 8\text{ }^{\circ}\text{C}$ . On the other hand, jumping the grain temperature stimulates desorption of water molecules first to the gas phase inside the pores. As the desorption is fast, at short times the diffusional flux of vapor out of the grain is not sufficient to compensate the pressure increase, thus, the gradient of pressure appears inside the grain (Fig. 4 a). This gradient generates the driving force for mass transport which, in the first approximation, is proportional to the slope of the  $P(r)$ -curve near the grain external surface (at the dimensionless radius approaching 1). After the short transient period of app. 10 s, this slope gradually decreases with time (Fig. 4 a). Hence, the driving forces for heat and mass transfer interactively reduce while the water desorption proceeds under the steady-state mode. The same is valid for the adsorption process (Fig. 4b). Thus, the heat and mass transfer processes in the system A-HE involved are inevitably coupled and strongly affect each other.

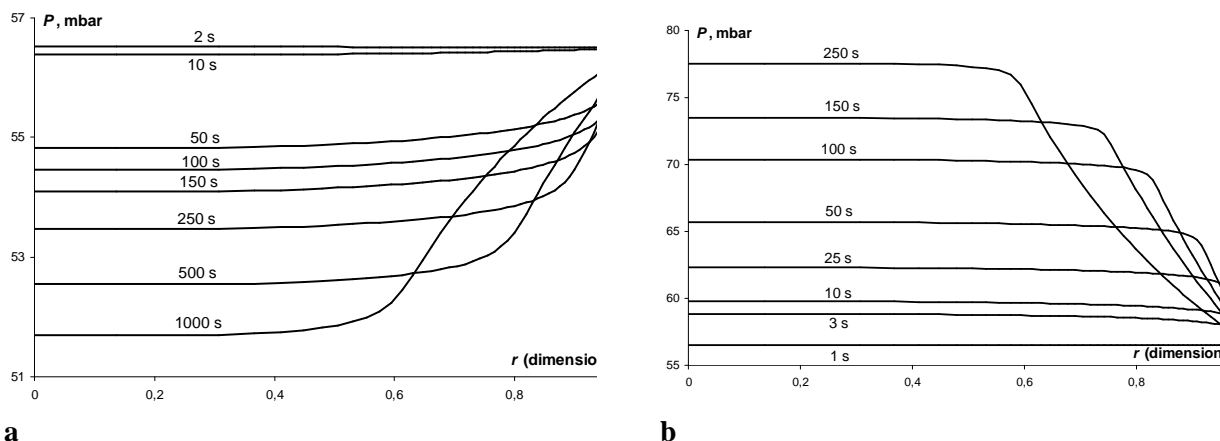


Fig. 4. Radial distribution of the pressure inside the grain during desorption (a) and adsorption (b) processes.  $T_{\text{st}} = 62\text{ }^{\circ}\text{C}$ .  $r = 0$  - the grain center,  $r = 1$  - the grain external surface.

*Temporal evolution of the uptake/release curves.* All uptake curves are presented as the dimensionless conversion degree  $\chi$  vs. the process time  $t$  (Fig. 5) that gives information about the rate of reaching equilibrium rather than about the absolute sorption rate. The calculated uptake/release curves are exponential  $\chi(t) = 1 - \exp(-t/\tau)$  until the conversion degree reaches  $\chi = 0.70\text{--}0.75$  (Fig. 5). At larger conversions, the kinetics calculated for step-like isobars are faster than the exponential one and the process is completed in a finite time (Fig. 5 a, b). For the linear isobar, the exponential approximation is quite precise until  $\chi = 0.7\text{--}0.8$  (Fig. 5 c). Meaningful deviations (up to  $\Delta\chi = 0.05$ ) are observed only for the concave exponential isobar during the adsorption process (Fig. 5 d) and for the convex exponential isobar during the desorption process (not presented).

Thus, at the relatively small temperature jump/drop ( $60\text{ }^{\circ}\text{C} \leftrightarrow 70\text{ }^{\circ}\text{C}$ ), the calculated dependences of the average water uptake/release on time, in the majority of cases, can be satisfactorily described by an exponential function up to the dimensionless conversions of  $0.7\text{--}0.8$ . It is amazing that the quite complex and strictly non-isothermal process of water ad-/desorption which is strongly affected by both heat and mass transfer to/inside the grain can be described by so simple kinetic law.

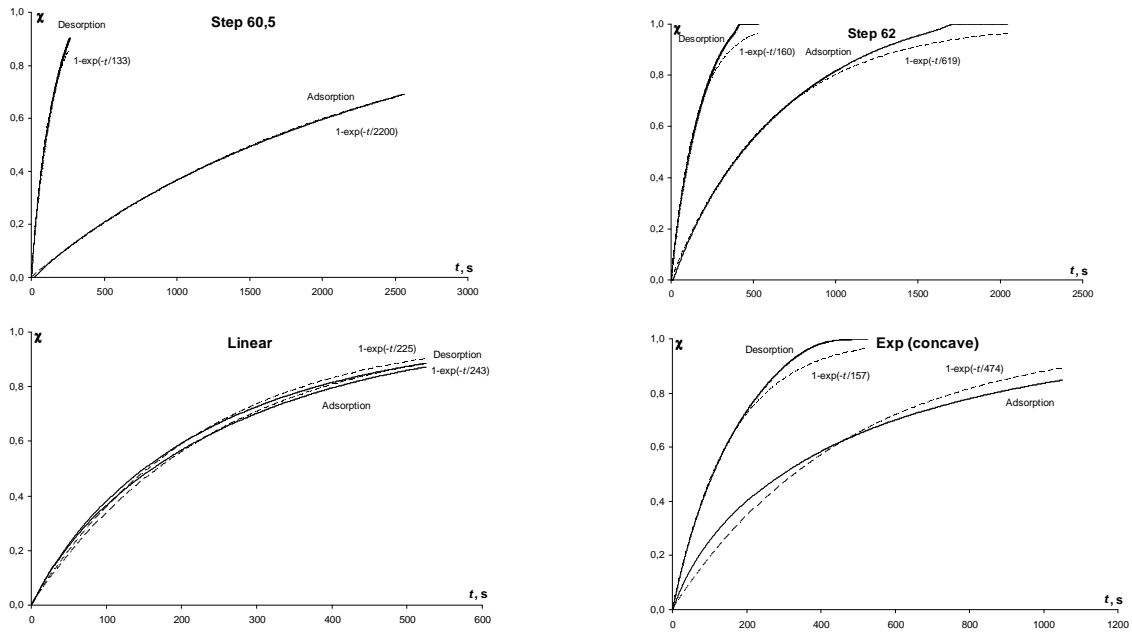


Fig. 5. Dynamics of the water adsorption and desorption for various isobar shapes and appropriate exponential approximations. Legends are on the graphs

*Effect of the shape of water sorption isobar.* Although the near-exponential character of the sorption dynamics is poorly sensitive to the shape of water sorption isobar, the characteristic time  $\tau$  does strongly depend on this shape (Table 1). The fastest adsorption processes is observed for the isobar step at  $69.5\text{ }^{\circ}\text{C}$  ( $\tau = 150\text{ s}$ ). This can be understood if assume that the process driving force is the temperature difference  $\Delta T_{dr}(t) = T_{av}(t) - T_f = T_{av}(t) - 70\text{ }^{\circ}\text{C}$  between the current temperature of the adsorbent grain  $T_{av}$  and the final temperature of the metal support  $T_f$ . In this case, the sorption rate is expected to be maximal at  $T_{st} = 69.5\text{ }^{\circ}\text{C}$  because the adsorption heat is removed at the maximal temperature difference. Accordingly, the fastest desorption corresponds to the step at  $T_{st} = 60.5\text{ }^{\circ}\text{C}$  ( $\tau = 133\text{ s}$ ) because in this case the driving force for the heat supply  $\Delta T_{dr} = T_f - T_{av} = 70\text{ }^{\circ}\text{C} - T_{av}$  is maximal. Indeed, we have found that the instant desorption rate  $W(t)$  is a linear function of  $\Delta T_{dr}$  except for a short transient period  $t_{tr}$  right after the temperature jump/drop (Fig. 6 a). The same is valid for the adsorption rate (Fig. 6 b).

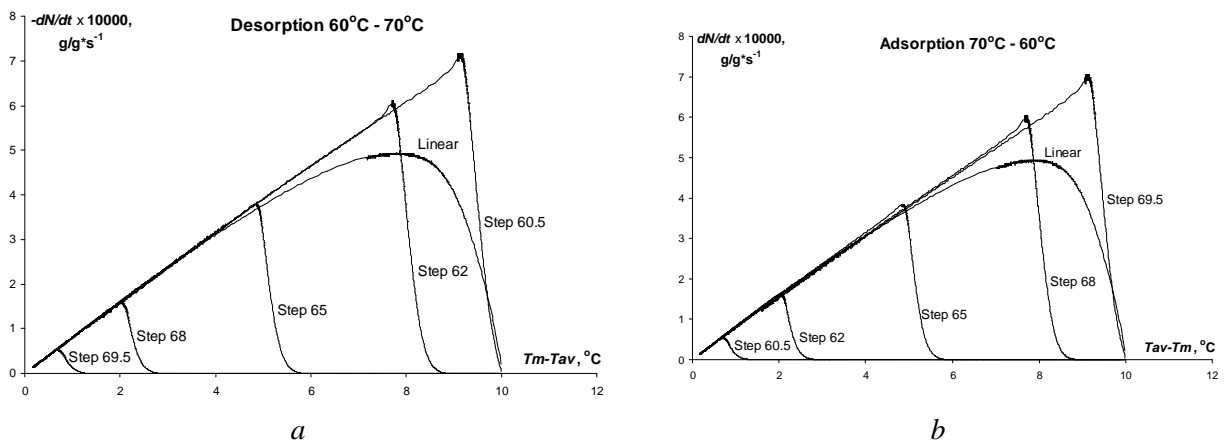


Fig. 6. Desorption (a) and adsorption (b) rates as a function of the instant driving force for the isobar shapes indicated on the graph. The transient and stationary regions are shown for  $T_{st} = 62\text{ }^{\circ}\text{C}$ .

Table 1. Characteristic time (in seconds) of water adsorption and desorption at various isobar shapes

Isobar shape	Desorption	Adsorption
Step at 60.5 °C	133	2200
62 °C	160	619
65 °C	258	269
68 °C	625	176
69.5 °C	2280	150
Exponent (concave)	157	474
Exponent (convex)	469	172
Linear	225	243

Moreover, all the ad- and desorption experiments fall on the same straight line, thus, indicating a universal character of the function  $W = \gamma \Delta T_{dr}$  with the constant coefficient  $\gamma$  regardless the  $T_{st}$ -value. The transient period is necessary for establishing a coupling between the heat and mass transfer (see also Figs. 3 and 4). For this period, the grain temperature approximately reaches the temperature  $T_{st}$  at which the desorption starts. Accordingly, this initiates an increase in the vapour pressure inside the grain which creates the driving force for the mass transport. After that the driving forces for the heat and mass transfer change in a strict correlation with each other, so that the instant process rate is proportional to the current difference  $(T_{av} - T_f)$  or  $(T_f - T_{av})$ . For the step-like isobars, the transient (induction) period rises almost linearly with the absolute difference  $|T_{in} - T_{st}|$  (Table 2).

Table 2. Absolute value of difference  $|T_{in} - T_{st}|$  and the transient period  $t_{tr}$  for various isobar shapes.

Isobar shape	Desorption		Adsorption	
	$ T_{in} - T_{st} , ^\circ\text{C}$	$t_{tr}, \text{s}$	$ T_{in} - T_{st} , ^\circ\text{C}$	$t_{tr}, \text{s}$
Step at 60.5 °C	9.5	-	0.5	-
62 °C	8.0	4.2	2.0	16.8
65 °C	5.0	9.5	5.0	9.5
68 °C	2.0	16.8	8.0	4.2
69.5 °C	0.5	-	9.5	-
Exponent (concave)	-	5.3	-	9.5
Exponent (convex)	-	10.5	-	4.2
Linear	-	6.3	-	5.3

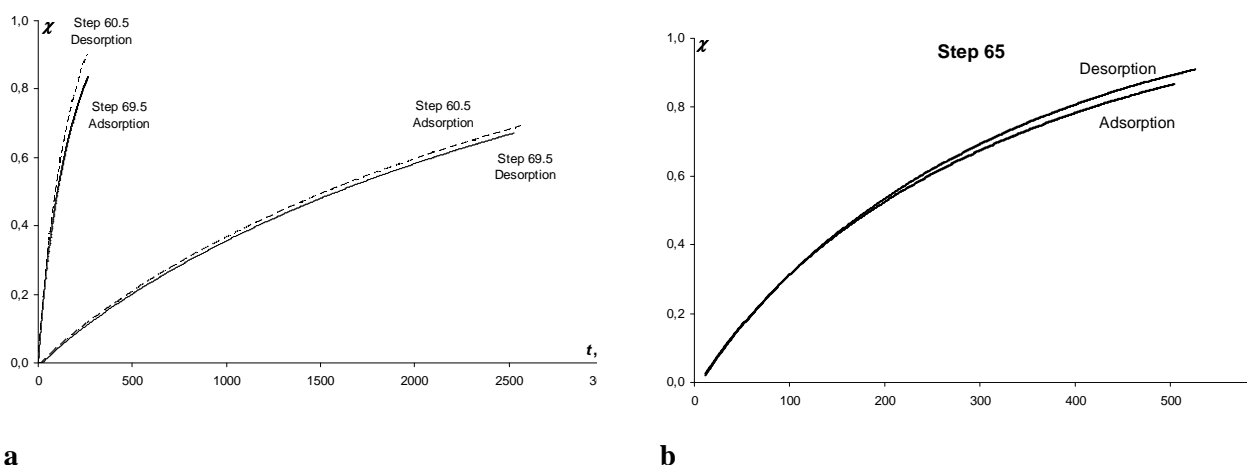


Fig. 7. Uptake and release curves plotted at various isobar shapes indicated near the curves: *a* – steps at  $T_{st} = 60.5$  °C and 69.5 °C; *b* – step at  $T_{st} = 65$  °C.

It is interesting to mention that the dimensionless kinetic curves are invariant with respect to the absolute value of the difference  $|T_{in} - T_{st}|$  (or  $|T_f - T_{st}|$ ). For instance, the water adsorption at  $T_{st} = 69.5^\circ\text{C}$  ( $|T_{in} - T_{st}| = |60^\circ\text{C} - 69.5^\circ\text{C}| = 9.5^\circ\text{C}$ ) proceeds almost identical (Fig. 7 a) as the water desorption at  $T_{st} = 60.5^\circ\text{C}$  ( $|T_{in} - T_{st}| = |70^\circ\text{C} - 60.5^\circ\text{C}| = 9.5^\circ\text{C}$ ). The same is true for the steps at  $62$  and  $68^\circ\text{C}$  (not presented) and  $65^\circ\text{C}$  (Fig. 7 b). Near-equality of the adsorption and desorption characteristic times  $\tau$  at equal  $|T_{in} - T_{st}|$ -values is also clearly seen from Table 1.

For near-exponential processes, the rate constant can be defined as  $k = 1/\tau$ . This value appeared to be a linear function of the absolute temperature difference  $\Delta T = |T_f - T_{st}|$  and the slope for the ad- and desorption stages are almost equal (Fig. 8). Thus, the maximum process rate corresponds to the maximal temperature difference between the final plate temperature which is maintained all over the sorption process and the temperature at which the ad-/desorption process starts.

Thus, from dynamical point of view the most profitable is the situation when the adsorbent has a step-like sorption isobar as it was conjectured in [16]. The step should be positioned at temperature as much different from the temperature of the HE fins (the external heat source/sink) as possible to maximize the driving force for heat transfer. Interestingly, that step-like sorption isobars are the most profitable from thermodynamic point of view as well [21], however, in this case the uptake step has to be as close to the temperature of the HE fins as possible to minimize the entropy generation due to the thermal coupling [22]. Thus, in actual practice a compromise between the two tendencies has to be reached that can be made, first of all, by optimizing A-HEX system.

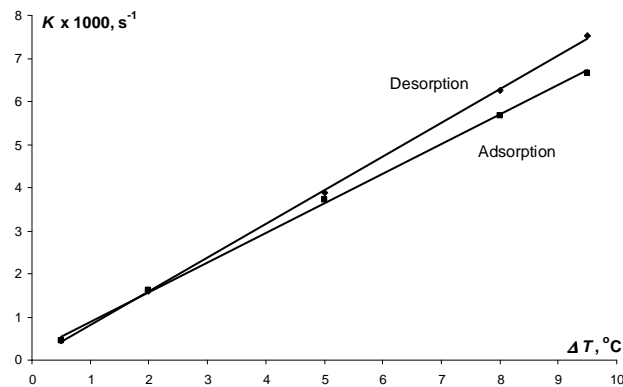


Fig. 8. Adsorption and desorption rate constants at various absolute values of the temperature difference  $\Delta T = |T_f - T_{st}|$

## CONCLUSIONS

The mathematical model of coupled heat and mass transfer in a spherical adsorbent grain that is in thermal contact with a metal plate subjected to a fast temperature jump/drop ( $60^\circ\text{C} \leftrightarrow 70^\circ\text{C}$ ) was used for analysing the effect of adsorption isobar shape on the dynamics of isobaric water ad-/desorption. Model isobars of the water sorption (stepwise, linear and exponential) were tested. Temporal evolution of radial profiles of the temperature, pressure and adsorbed water concentration inside the grain was calculated and analyzed. In the majority of cases, the calculated dependences of the average water uptake/release on time were satisfactorily described by an exponential function up to the dimensionless conversions of  $0.7$ – $0.8$ . The characteristic sorption time  $\tau$  is found to be strongly dependent on the isobar shape. From the dynamical point of view the most profitable is the situation when the adsorbent has a step-like sorption isobar with the step positioned at temperature as much different from the temperature of the HE fins as possible. For step-like isobars, the ads-/desorption rate constants are found to be linear functions of the difference between the heat source (sink) temperature and the temperature of the uptake lift. It is interesting that the dimensionless kinetic curves are invariant with respect to the absolute value of the difference  $|T_f - T_{st}|$ .

## References

1. Aristov Yu. I. Optimal adsorbent for adsorptive heat transformers: Dynamic considerations // *Int. J. Refrig.* 2009. Vol. 32. Pp. 675–686.
2. Yong L., Wang R. Z. Adsorption refrigeration: A survey of novel technologies // *Recent Patents on Engineering*. 2007. 1. Pp. 1–21.
3. Chang W. S., Wang C. C., Shieh C. C. Experimental study of a solid adsorption cooling system using flat-tube heat exchangers as adsorption bed // *Appl. Therm. Eng.* 2007. Vol. 27. Pp. 2195–2199.
4. Tamainot-Telto Z., Metcalf S. J., Critoph R. E. Novel compact sorption generators for car air conditioning // *Int. J. Refrig.* 2009. Vol. 32. Pp. 727–733.
5. Guillemintot J. J., Choisier A., Chalfen J. B. Heat transfer intensification in fixed bed adsorbers // *Heat Recovery Systems & CHP*. 1993. Vol. 14. Pp. 297–300.
6. Zhu D., Wang S. Experimental investigation of contact resistance in adsorber of solar ad-sorption refrigeration // *Solar Energy*. 2002. Vol. 73. Pp. 177–185.
7. Vasiliev L. L. Sorption machines with a heat pipe thermal control // *Proc. of the International Sorption Heat Pump Conference Shanghai, China*. 2002. Pp. 408–413.
8. Pat. 2004116812. Japanese. / C. Kan, A. Akahira, Y. Hamamoto, T. Kashiwagi, 2004.
9. Aristov Yu. I., Sapienza A., Freni A., Ovoschnikov D. S., Restuccia G. Reallocation of adsorption and desorption times for optimizing the cooling cycle parameters // *Int. J. Refrig.* 2011 (doi: 10.1016/j.ijrefrig.2010.07.019).
10. Pino L., Aristov Yu. I., Cacciola G., Restuccia G. New adsorbent composite material based on zeolite 4A for adsorption heat pumps // *Adsorption*. 1996. Vol. 3. Pp. 33–40.
11. Glaznev I. S., Aristov Yu. I. The effect of cycle boundary conditions and adsorbent grain size on dynamics of adsorption chillers // *Int. J. Heat & Mass Transfer*. 2010. Vol. 53. Pp. 1893–1898.
12. Sun L. M., Meunier F. A detailed model for non-isothermal sorption in porous adsorbents // *Chem. Eng. Sci.* 1987. Vol. 42. Pp. 1585–1593.
13. Sakoda A., Suzuki M. Fundamental study on solar powered adsorption cooling system // *J. Chem. Engrn. Jpn.* 1984, Vol. 17. Pp. 52–57.
14. Raymond A., Garimella S. Intraparticle Mass Transfer in Adsorption Heat Pumps: Limitations of the Linear Driving Force Approximation // *J. Heat Transfer*. 2011. Vol. 133. Pp. 42001–42014.
15. Okunev B. N., Gromov A. P., Heifets L. I., Aristov Yu. I. A new methodology of studying the dynamics of water sorption/desorption under real operating conditions of adsorption heat pumps: Modeling of coupled heat and mass transfer // *Int. J. Heat and Mass Transfer*. 2008. Vol. 51. Pp. 246–252.
16. Glaznev I. S., Ovoschnikov D. S., Aristov Yu. I. Kinetics of water adsorption/desorption under isobaric stages of adsorption heat transformers: the effect of isobar shape // *Int. J. Heat&Mass Transfer*. 2009. Vol. 52. Pp. 1774–1777.
17. Aristov Yu. I., Dawoud B., Glaznev I. S., Elyas A. A new methodology of studying the dynamics of water sorption/desorption under real operating conditions of adsorption heat pumps: Experiment // *Int. J. Heat and Mass Transfer*. 2008. Vol. 51. Pp. 4966–4972.
18. Sun L. M., Feng Y., Pons M. Numerical investigation of adsorptive heat pump systems with thermal wave heat regeneration under uniform-pressure conditions // *Int. J. Heat and Mass Transfer*. 1997. Vol. 40. Pp. 281–293.
19. Aristov Yu. I. Adsorptive transformation of heat: principles of construction of adsorbents database // *Applied Therm. Eng.* 2011. (doi: 10.1016/j.applthermaleng.2011.02.024).
20. Saha B. B., Chakraborty A., Koyama S., Aristov Yu. I. A new generation cooling device employing CaCl<sub>2</sub>-in-silica gel-water system // *Int. J. Heat&Mass Transfer*. 2009. Vol. 52. Pp. 516–524.
21. Sharonov V. E., Aristov Yu. I. Chemical and adsorption heat pumps: comments on the second law efficiency // *Chem. Eng. J.* 2008. Vol. 136. Pp. 419–424.
22. Meunier F., Poyelle F., LeVan M. D. Second-law analysis of adsorptive refrigeration cycles: the role of thermal coupling entropy production // *Appl. Therm. Eng.*, 1997. Vol. 17. Pp.43–55.

## **SOLID SORPTION COOLER WITH COMPOSITE SORBENT BED AND HEAT PIPE THERMAL CONTROL**

**A. A. Antukh, A. P. Tsitovich, L. L. Vasiliev, O. S. Filatova**

Luikov Heat & Mass Transfer Institute  
P. Brovka, 15, 220072, Minsk, Belarus.  
Tel./ Fax (375)-17-284-21-33  
E-mail: leonard\_vasiliev@rambler.ru

**Y. Alousef**

Energy Research Institute (KACST)  
Kingdom of Saudi Arabia

### **Abstract**

Three adsorbers solar cooler was experimentally investigated. Ammonia was chosen as a working fluid. Two adsorbers (twins) were filled with the same complex compound (activated carbon fibre with  $\text{MnCl}_2$  microcrystals on the filament surface). The third low temperature adsorber has second complex compound (activated carbon fibre with  $\text{BaCl}_2$  microcrystals on the filament surface). The cycle of physical adsorption and chemical reactions in the sorbent bed of adsorber was followed by condensation/evaporation of ammonia inside the pores. This combination of adsorption/condensation and evaporation/desorption is a novelty of cooler design, which increases the heat and cold generation in adsorber. The specific feature of third adsorber is the time of its cold generation. This time includes the liquid evaporation and desorption/regeneration time of ammonia in the sorbent bed. The cooler thermal management is based on heat pipes. The solar heating is a source of energy for cooler. The sink of the cold is the air flow.

### **KEYWORDS**

Adsorption, chemical reactions, heat recovery, heat pipes, solar heating.

### **INTRODUCTION**

Refrigeration technologies have been critical in the evolution of production and distribution systems a long period of time. Reduction in use of synthetic refrigerants and production of  $\text{CO}_2$  provide a new opportunity for solar cooling and refrigeration. The concept of solar-powered refrigeration cycles is known at least two decades and several refrigerators operating on this principle are commercially available.

There were many projects for the development or demonstration of solar refrigeration technologies and solar refrigeration continued to be an important issue, J. Bougard, G. Veronikis, 1992 [1]. Adsorbents like zeolite, silica gel, activated carbon and alumina oxide are considered as physical adsorbents having highly porous structures with surface-volume ratios in the order of several hundreds that can selectively catch and hold refrigerants. When saturated, they can be regenerated simply by being heated. If an adsorbent and a refrigerant are placed in the same vessel, the adsorbent would maintain the pressure by adsorbing the evaporating refrigerant. The process is intermittent because the adsorbent must be regenerated when it is saturated. For this reason, multiple adsorbent beds are required for continuous operation. Conventional working pairs include activated carbon and methanol, or ammonia, Pons and Guillemot, 1986 [2]; Wang et al., 1997, 2001 [3, 4], Critoph, 2002 [5] and silica gel-water, Grenier et al., 1988 [6]. Current solar adsorption technology can provide a daily ice production of 4–7 kg per unit square meters of solar collector with a solar-to-cooling COP between 0.1 and 0.15, Wang and Oliveira, 2005 [7]. Different small-capacity silica gel-water adsorption chillers have been developed for solar air conditioning, Saha et al., 2001 [8]. Its cooling capacity was reported between 3.2 and 3.6 kW; COPs ranged from 0.2 to 0.6 for the working temperature diapason from 55 to 95 °C. Unlike the more common single-staged double-bed systems, Saha et al. (2001) [8] developed a double-staged four-bed cycle machine to use at very low driving temperatures. The machine produced 3.2 kW cooling and 55 °C hot water output with COP of 0.36. However, there has been a little research made into the integration of short time cycles sorption machines of solar power with natural gas, or electrical immersion heater as a back-up, Vasiliev et al., 1999 [9].

The combined action of physical adsorption and chemical reactions for the cold production in the same space and at the same time is attractive initiative to enhance the COP of a system, Vasiliev et al., 1994 [10]. The use of heat pipes to improve the performance of carbon-ammonia adsorption refrigerator was suggested by Vasiliev et al., 1996 [11]. It was shown that heat transfer in the sorbent bed can be improved by the use of finned heat pipe as the heat exchanger. The concept aim of such research program was to extract the most enthalpy from the low-grade heat before it is purged into the surrounding. A solar-gas refrigerator based on a reversible solid sorption phenomena is competitive, if the process allow to store the energy of a high density, and if the heating, or cooling power is enough for consumers, Vasiliev et al., 2001 [12].

Recently it was shown, Atsushi Akisawa and Takahito Miyzaki, 2010 [13], that compression chillers with high energetic COP have the same efficiency as that of adsorption chillers in terms of exergy. It means that physical performance of adsorption chiller is not low, taking Carnot efficiency into account. Actually it is evident that adsorption coolers are very efficient from the view point of the second Law of thermodynamics.

It is known, that cascading cycles are options to improve the adsorption coolers efficiency because they recover heat from one cycle to another internally, N. Douss and F. Meunier, 1989 [14] and Y. Liu, K. Leonig, 2006 [15]. The cascading cycles, which couple solid gas reactions with the liquid-gas absorption process, D. Stitou, B. Spinner, P. Satzger, F. Ziegler, 2000 [16], L. L. Vasiliev, D. A. Mishkinis, L. L. Vasiliev Jr., 1996 [17] have COP more than 30% compared with conventional double effect of adsorption cycles.

Three adsorbers chiller was experimentally tested by Chua, 2001 [18], which operated similar to a single stage cycle. The next improvement to the three adsorbers cycle was incorporated by Saha, 2003, [19]. A new three adsorbers cycle was suggested by Khan, 2006 [20]. The cycle is working like a single stage (two adsorbers) and one additional third adsorber is connecting to the other two adsorbers. The main particularity of the cycle is as follows: the third adsorber runs twice as quickly as the other two adsorbers. The working fluid purged from the third reactor in mass recovery process is absorbed into the other two reactors.

## 1. THE THREE ADSORBERS COOLER DESIGN

Our intention is to design and test a chiller, which would operate consuming a chip energy (solar concentrator and autonomous, low pressure adsorbed natural gas storage vessel as the back- up system), that can be built and maintained in the country of use, be light and portable and that is low enough in cost [12]. This can be achieved if we use a solar energy as a main source, a gas flame as a second (alternative, or additional) source of energy and a set of sorbent beds which are heating and cooling alternatively. The original heat pipes (thermosyphon) are used as heat exchangers for external heat recovery and adsorbers thermal control. Activated carbon fibre (ACF) “Busofit” is used for ammonia adsorption/desorption. The micro/nano crystals of  $MnCl_2$  and  $BaCl_2$  are used as the chemical sorption material to increase the sorption capacity of the sorbent bed.

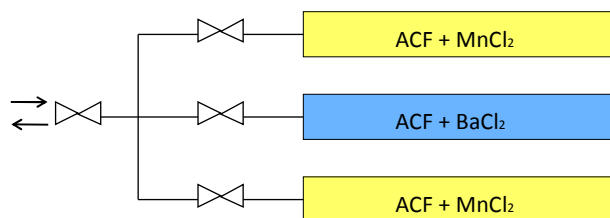


Fig. 1. The schematic of the three adsorbers cooler

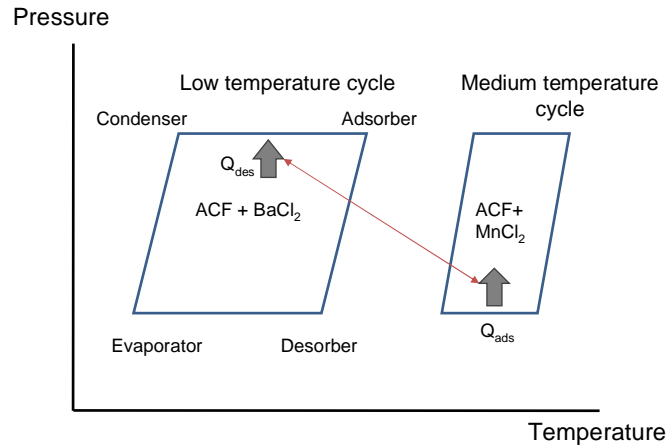


Fig. 2. Schematic of the three adsorbers cycle with complex utilization of energy of low temperature adsorber

The schematic of the three adsorbers cooler is shown on Figs. 1, 2. The experimental set-up includes two medium temperature adsorbers (ACT + MnCl<sub>2</sub>), one low temperature adsorber (ACF = BaCl<sub>2</sub>). The thermal management system consists of four unites: vapordynamic thermosyphon, two loop thermosyphons and a loop heat exchanger joint to the low temperature adsorber.

The system management consists only in actuating valves to change the direction of the fluid inside the heat exchangers.

The main characteristic of the cooler efficiency is the Coefficient of Performance (COP) for cooling:

$$COP_c = Q_e / Q_{des} \quad (1)$$

Dynamics of the cooling cycle is defined by the Specific Cooling Power (SCP):

$$SCP = Q_e / (\Delta w \cdot \tau), \quad (2)$$

where  $\Delta w$  is the adsorbate uptake exchanged during the cycle;  $\tau$  - the time of the cycle.

The quality of sorbent material affects both the COP and SCP, and its proper choice is of prime importance. The choice of sorbent material should be based on comprehensive analysis that takes into consideration both thermodynamic and dynamic aspects. Kinetic properties of the sorbent material have the strong influence on the dynamic behavior heat and mass transfer inside the sorbent bed and contribute to the specific power of the cooler.

The mass of each adsorber is equal to the sum of masses of the adsorbent, metal of adsorber and heat pipe heat transfer system.

## 2. VAPOR-DYNAMIC THERMOSYPHON

The schematic of the four evaporators, two condensers vapour-dynamic thermosyphon is shown in Figs. 3, 4. Vapor-dynamic thermosyphon [21] is made from SS steel and used for thermal coupling of solar collector and two adsorbers (Fig. 3) [22]. The working fluid is water. The evaporators of the vapour-dynamic thermosyphon are disposed inside the vacuum glass solar collectors. The thermosyphon condensers are placed inside two medium temperature adsorbers. Such vapor-dynamic thermosyphon has low thermal resistance ( $R = 0.01-0.05$  K/W), its length is one meter. The thermosyphon consists of four evaporators (gas flame heated evaporator as a back-up), the vapor and liquid minichannels and two-condensers switched on and off alternatively, Fig. 4. To heat adsorbers the constant heat flow from the thermosyphon evaporator

(solar energy) was transformed into intermittent heat flow generating in condensers by alternative closing/opening valves, Fig. 4, disposed on liquid pipes of the vapor-dynamic thermosyphon.

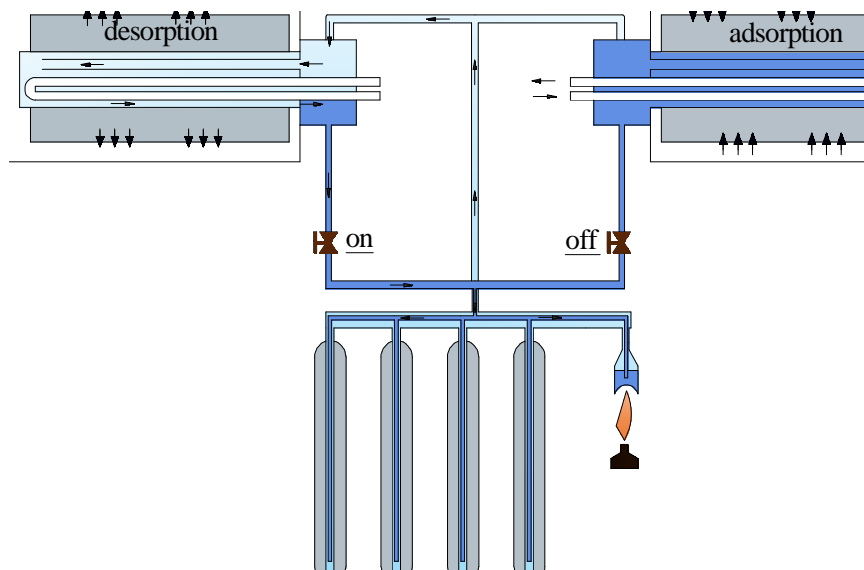


Fig. 3. Solar heater with two adsorbers, solar collectors (with flame as the back-up), vapor-dynamic thermosyphon, two loop thermosyphons and two valves

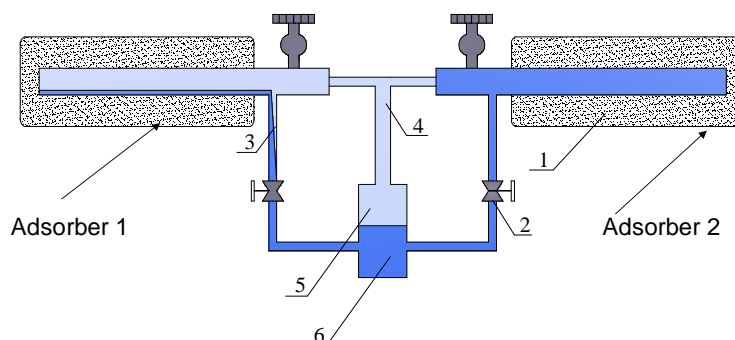


Fig. 4. Schematic diagram of the vapour-dynamic thermosyphon: 1 – condensers, 2 – valves, 3 – liquid line, 4 – vapour line, 5 – evaporator, 6 – liquid pool of the evaporator

The advantages of this vapor-dynamic thermosyphon are: 1) low thermal resistance; 2) ability to transport the heat flow over a long distance in the horizontal position, which is difficult to achieve, using conventional thermosyphons; 3) possibility to transform the constant heat load in the evaporator to intermittent heat load in condensers.

### 3. LOOP THERMOSYPHON HEAT EXCHANGER

The cooling of the sorbent bed inside the medium temperature adsorbers was performed by stainless steel loop heat exchangers, Fig. 5.

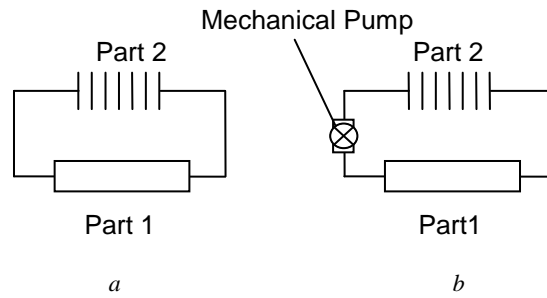


Fig. 5. Loop heat exchanger

The loop heat exchanger was made as a 2 mm tube placed inside the annular gap of the vapor-dynamic thermosyphon condenser. The working fluid is water. When the vapor-dynamic thermosyphon is closed (valve closed) the loop thermosyphon cools the sorbent bed, realizing two-phase heat transfer inside the annular gap. Thus the process of the heating/cooling of the sorbent bed in adsorbers is performed.

The time of the cycle (adsorption/desorption) was near 12 minutes, Fig. 6. During the tests the temperature of the evaporator envelope (curve 1) was constantly near 110 °C, while the temperature of adsorbers envelope (curves 2, 3) was changing from ambient temperature 20 °C (adsorption) up to 90 °C (desorption).

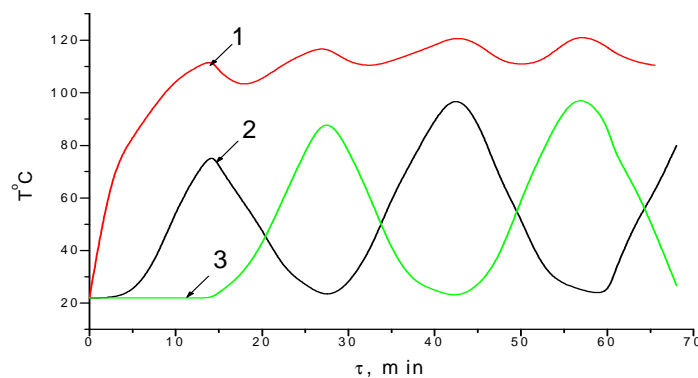


Fig. 6. The temperature evolution of the thermosyphon evaporator 1, adsorber 2 and adsorber 3 envelope during the cycles of heating/cooling

The heat transfer intensity between the thermosyphon condenser and the adsorber is limited by the thermal conductivity of the sorbent bed.

#### 4. LOW TEMPERATURE ADSORBER.

The low temperature adsorber (ACF + BaCl<sub>2</sub>) has the liquid loop system of thermal control (heat exchanger), Fig. 5 b, to transfer the cold from the adsorber to the air. The working fluid of this loop heat exchanger is propane.

The part 1 of the loop heat exchanger is placed inside the adsorber; the finned part 2 of the heat exchanger is disposed outside the adsorber and dissipates the cold/heat to the air. There is alternative to use a small pump to circulate propane in the heat exchanger, or to use the loop heat exchanger without pump, Fig. 5 a.

## 5. MEDIUM TEMPERATURE ADSORBERS.

The schematic of the experimental set-up is shown on Fig. 1. The solid sorption cooler is composed on the low temperature adsorber (ACF + BaCl<sub>2</sub> microcrystals) and two medium temperature adsorbers (ACF + MnCl<sub>2</sub> microcrystals) connecting by valves.

The mass of ammonia inside two medium temperature adsorbers is equal to the mass of the adsorbed ammonia in third low temperature adsorber plus the mass of liquid ammonia in the pores of the sorbent bed of this adsorber. Thus there is a possibility to store ammonia in the low temperature adsorber in two qualities (adsorbed gas inside the sorbent material and the liquid in its pores).

The sorption capacity potential of the mean temperature adsorbers is higher than the sorption capacity potential of the low temperature adsorber.

Such three adsorbers cooler has some advantages:

1. The liquid is disposed inside the capillary porous media and uniformly distributed along its volume (non sensitive to gravity due to the capillary forces action).

2. During the time of cold generation the intensive two-phase heat transfer occur inside the porous media. The effective thermal conductivity of the sorbent bed is at least ten times more (micro-heat pipe effect) to compare with the resorption cooler.

3. Two-phase micro-jets of ammonia during the evaporation inside the porous media impact the loop heat exchanger and the adsorber envelope ensuring the uniform cooling.

The effect of the BaCl<sub>2</sub> decomposition also enhances two-phase flow heat transfer and increase the total cooling capacity of the desorber/evaporator.

## 6. THE SOLID SORPTION COOLER FUNCTIONING

The cooler is working as follows:

1. Initially (at night) three adsorbers have the same temperature. The valves are opened.

2. At the time  $\tau_1$  (in the morning) the medium temperature adsorbers start to be heated by sun, the pressure in the adsorbers is increasing, heat and mass transfer between medium and low temperature adsorbers is initiated.

3. The heat absorbed by the medium temperature adsorbers from the source of energy (solar collectors, gas flame) due to the pressure drop is transferred to the low temperature adsorber by the ammonia flow. The low temperature adsorber during the time of ammonia adsorption dissipates this energy to the surrounding through the loop heat exchanger.

4. At the time  $\tau_2$  one of medium temperature adsorbers starts to cool down to the ambient temperature (by loop heat exchanger) and begin to suck the ammonia from the low temperature adsorber. The cold generation inside the low temperature adsorber is divided to two stages. Initially there is a volumetric evaporation of the liquid ammonia inside the porous media of the sorbent bed following the intense two-phase heat transfer. The second stage is based on desorption/regeneration of ammonia vapor in the sorbent bed. The cold from the low temperature adsorber is dissipated to the ambient with the help of the heat exchanger. The total time of cooling is equal to the time of the liquid evaporation and the time of the ammonia vapor adsorption/decomposition:

$$\Delta\tau_{\text{cooling}} = \Delta\tau_e + \Delta\tau_{d/r}, \quad (3)$$

where  $\Delta\tau_e$  – the time of liquid evaporation;  $\Delta\tau_{d/r}$  – the time of ammonia vapor desorption/regeneration from the sorbent bed.

5. At the time  $\tau_3$  the cold generation is finished. The ammonia is accumulated in the medium temperature adsorbers, the valves are switched off. The cooler is ready for the next cycle operation.

In order to study the sorption capacity of the sorbent material it is necessary to know the quantity of gas adsorbed on each point of the cycle, Fig. 2. There is a general need to have a good fit of experimental isotherms and temperature and to extrapolate some isotherms (Fig. 7). For ACF "Busofit" the approach of Dubinin is well adapted and allows linking quite simply the physical properties of "Busofit" to the capacity of adsorption of this carbon fiber.

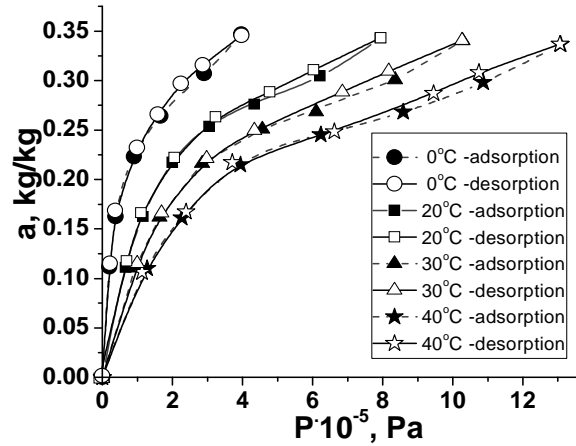


Fig. 7. Dynamic ammonia sorption capacity (adsorption/desorption) for ACF "Busofit" at different temperatures versus pressure

The theory of micro porous volume filling, suggested by Dubinin, is widely used for quantitative characteristic of adsorptive properties and basic varieties of porous structure.

The basic equation of this theory is Dubinin – Astakhov's equation, which describes the equilibrium gas adsorption by the micro porous homogeneous structure that has the following form:

$$a = \left( \frac{W_o}{V} \right) \exp \left( - \left[ \frac{A}{E_o \beta} \right]^n \right). \quad (4)$$

Dubinin – Radushkevich equation is a special case of Dubinin-Astakhov equation, (n=2):

$$a = \left( \frac{W_o}{V} \right) \exp \left( - BT^2 \left[ \lg \left( \frac{P_s}{P} \right) \right]^2 \right). \quad (5)$$

In these relationships:  $a$  – sorption capacity, g/g, mmole/g,  $A = RT \ln \left( \frac{P_s}{P} \right)$  – characteristic sorption energy, kJ/mole;  $B$  – structural constant, which characterizes the size and distribution of micro pores,  $K^{-2}$ ;  $E_o$  – characteristic energy of standard gas (usually – benzene), kJ/mole;  $P$  – pressure, Pa, kPa, MPa;  $T$  – temperature, °C, K;  $R$  – universal gas constant, kJ/(mole K);  $V$  – volume,  $m^3$ ;  $W_o$  – micro porous volume limit,  $cm^3/g$ ;  $z$  – compressibility factor;  $\beta$  – affined coefficient,  $\nu$  – adsorptive substance molar volume,  $cm^3/mmole$ .

The empirical coefficient in the equation (5) for the ammonia adsorption ACF "Busofit AYTМ-055" case is:  $W_o = 0,491$  and  $B = 8,56 \cdot 10^{-6}$ .

The affined coefficient  $\beta$  is an independent argument and is defined as a ratio of two adsorptive potentials at invariable adsorbent in the equation (5). The ammonia calculated affined coefficients to benzene (this substance is usually taken as a standard one) differ from each other in different references. The  $\beta$  ammonia coefficient to benzene for ACF like "Busofit",  $\beta_{Busofit} = 0,309$  was obtained on the basis of the experimental data.

Another important sorbent material characteristic is a peculiar porous size. It can be defined according to the empiric expression for slit-like porous model, proposed by Dubinin:  $x = k/E_o$ , where  $x$  – half-width of the micro pore, nm;  $E_o$  – the characteristic energy of benzene, 20.5 kJ/mole;  $k$  – constant of proportionality, equal 12,0. The porous peculiar size of the ACF «Busofit AYTМ-055» is 11.7 Å.

It is very important to estimate the COP of the process. The thermodynamic cycle is defined by three levels of temperatures-  $T_{evap}$ ,  $T_{amb}$ ,  $T_{ad}$  and the two levels of pressure  $P_{evap}$ ,  $P_{cond}$ .

The sorption cooler works based on the four-phase cycle:

- isosteric heating,

- desorption/condensation,
- isosteric cooling,
- adsorption/evaporation.

$COP^R = \text{cold output/high-grade heat input}$

The saturating vapor pressure is obtained from Clapeyron equation:

$$\ln(P_0) = -\Delta H/RT + \Delta S/R \text{ (for } T < T_c\text{),}$$

and by extrapolation of this equation for the temperature  $T > T_c$ .

If we have two adsorbers filled with different sorbent beds, the cycle is separated in two main phases corresponding to two pressure levels. Due to the effect of adsorption/desorption of the ACF this pressure difference is dynamically changing during the cycle (completely different comparing with chemical reactors). The carbon fibre as a fast sorbent material starts to react with ammonia in the early stage of heating/cooling time (up to 5 min) and accomplish its reaction after the chemical reaction of the salt is finished. The dynamic of the pressure change in the reactor is also fast and starts before the salts are beginning to react. During the regeneration stage carbon fibre as a host material helps to distribute microcrystals through the whole volume of a sorbent bed (ammonia capillary condensation, salts dissolution in the liquid ammonia, salt rich liquid ammonia penetration into the sorbent material due to capillary forces).

Fig. 7 shows the ammonia sorption isotherms for ACF "Busofit". The micro/nano crystals deposit on the filament surface increase the sorption capacity of the sorbent compound "Busofit+ BaCl<sub>2</sub>" 2–3 times.

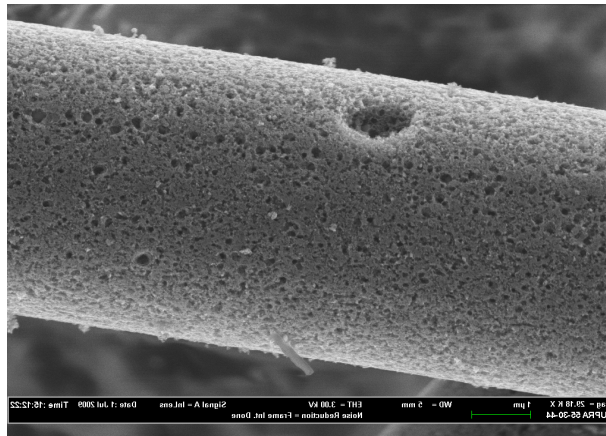


Fig. 8. Activated carbon fibre "Busofit"

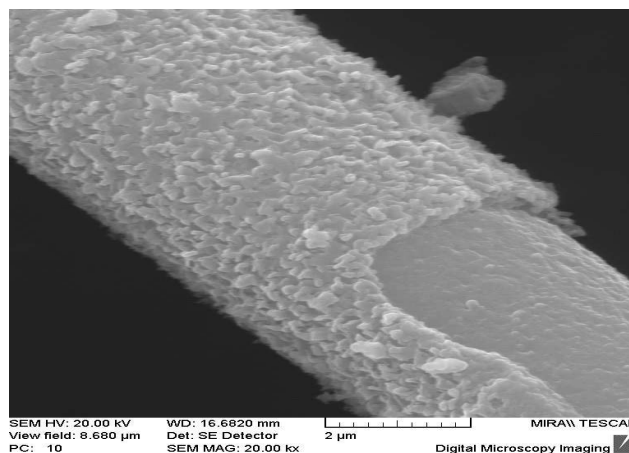


Fig. 9. Activated carbon fibre "Busofit" with micro crystals of BaCl<sub>2</sub> on the filament surface

The activated carbon filaments and micro/nano crystals enhanced the COP of the system to compare with conventional chemical heat pumps. To minimize a void space and increase the adsorbent capacity of the active carbon fibre we need to compress "Busofit" together with a binder (monolithic material). The complex compound microstructure obtained in the Luikov Heat & Mass Transfer Institute has been studied using Scanning Electro Microscope (SEM Carl Zeiss Supra™ 55), Fig.8,9.

The characterization should reveal a porous structure with a uniform micro and nano pore distribution on the filament surface and inside the filament. There is also available a uniform distribution of microcrystals on the filament surface without formation of agglomerates. Fig. 9 testifies the fact that even for maximal concentration of salt BaCl<sub>2</sub> (low temperature adsorber) on the filament surface its structure around the filament rest porous. It is convenient for heat and mass transfer enhancement.

## 7. THE RESULTS OF THE EXPERIMENTS

Three bed cycles of the adsorption cooler were experimentally investigated, Fig. 10. Two medium temperature adsorbers (twins) operate in the sorption process alternatively and there are mass recovery process, preheating process, desorption process and precooling process. When one adsorber is exhausted, the second adsorber starts to do the same procedure up to the time, when the third low temperature adsorber accomplish its adsorption and condensation process.

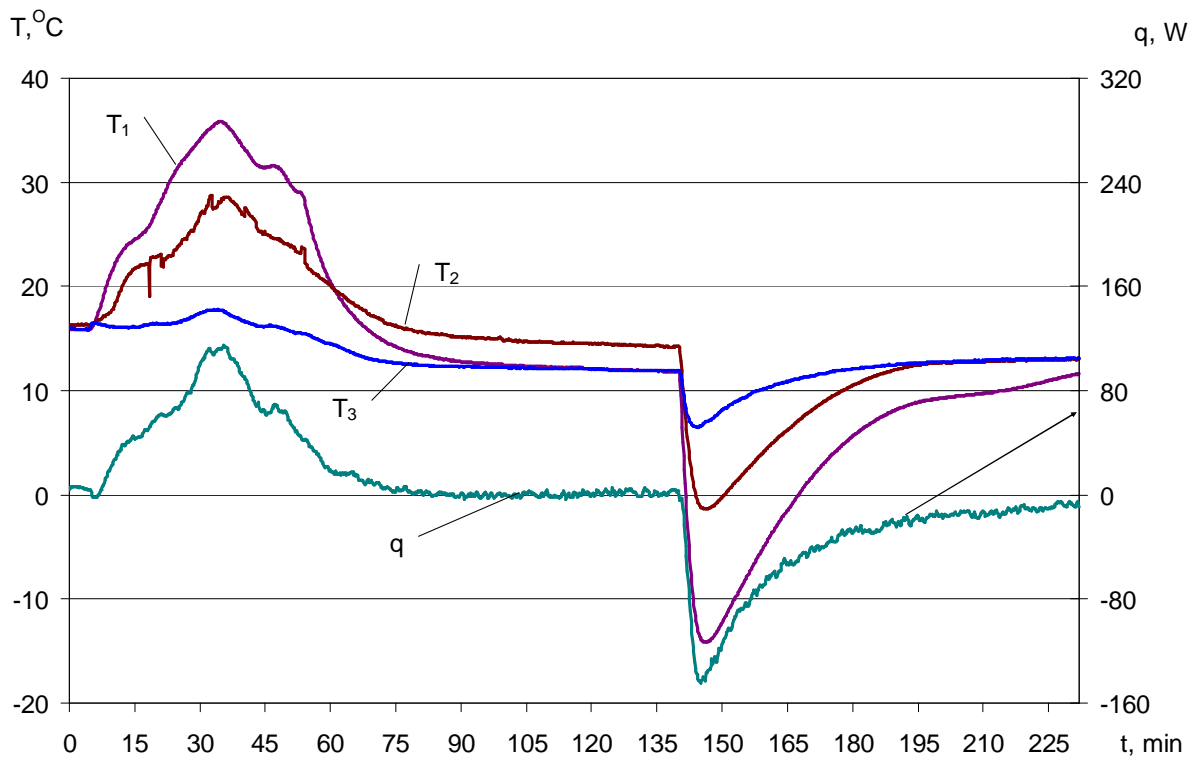


Fig. 10. Temperature field evolution on the low temperature ( $T_1$ ,  $T_2$ ) adsorber (ACF + BaCl<sub>2</sub>) as the function of cycle,  $T_3$  – mean temperature of liquid inside the loop heat exchanger,  $q$  – heat flow to/from the liquid heat exchanger to the sorbent bed inside the low temperature adsorber

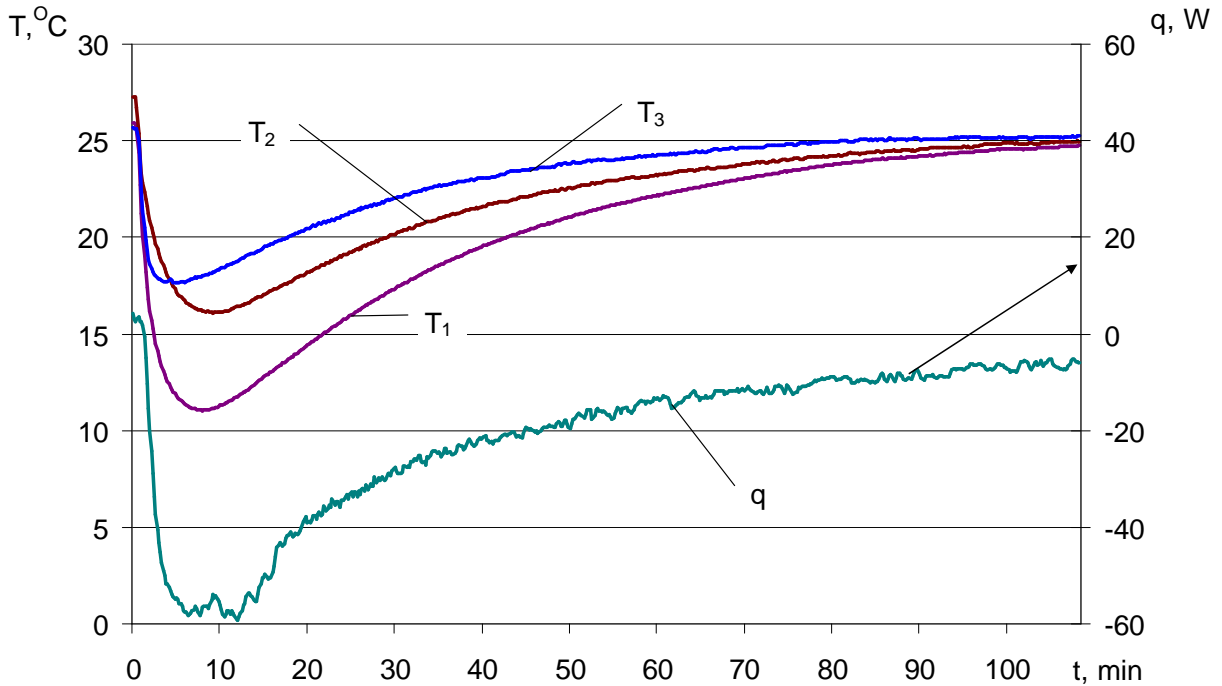


Fig. 11. Temperature profiles of the low temperature adsorber ( $T_1$  – beginning of adsorber,  $T_2$  – end of adsorber), liquid in the loop heat exchanger ( $T_3$ ), and mean heat flow  $q$  from the liquid heat exchanger to the sorbent bed inside the low temperature adsorber

It is interesting to consider two cases:

1. when in the low temperature adsorber the process of adsorption-regeneration and desorption/decomposition is realized without the process of evaporaton/condensation (Fig. 11);
2. when in the low temperature adsorber the process of adsorption-regeneration and desorption/decomposition is accompany by the process of evaporaton/condensation (Fig. 10, Fig. 12).

The first case is typical for the resorption cooler application. Temperature profiles on the surface of the low temperature adsorber ( $T_1$ ,  $T_2$ ), the mean temperature ( $T_3$ ) of the working fluid (propane) in the loop heat exchanger and the heat flow  $q = c_p G \Delta T$  to/from the loop heat exchanger to the sorbent bed are shown. The room temperature is  $28^\circ\text{C}$ , there is a heat insulation on the adsorber surface.

The second case is adsorption coolers with new effects due to the evaporation of ammonia inside the porous bed, Fig. 12. The pressure of the low temperature adsorber is boosted up to the pressure of the ammonia condensation and liquid ammonia is accumulated in the pores of the sorbent bed. The temperature evolution in two adsorbers during the cycle of heating/cooling shows the temperature decrease in the low temperature adsorber at least  $12 - 15^\circ\text{C}$  to compare with the resorption cooler.

During the time of cold generation the evaporation of the liquid in the pores of the sorbent bed is the reason of first stage cooling. The second stage cooling is due to the ammonia desorption and  $\text{BaCl}_2$  micro crystals decomposition. For such a cycle we have the cold generation at least of two times more. Such a cooling cycle is shown on Fig. 12. The mass flow meters were used for the calculation of the degree of advance of chemical reactions and physical adsorption. Instantaneous cooling and heating rate was also recorded. The cooling capacity obtained is equal  $250-300$  KJ.

The specific cooling power SCP of low temperature adsorber is  $107$  W/kg (for the sorbent bed). The time of the cooling cycle is near  $35$  min to compare with one hour for the conventional resorption cycle.

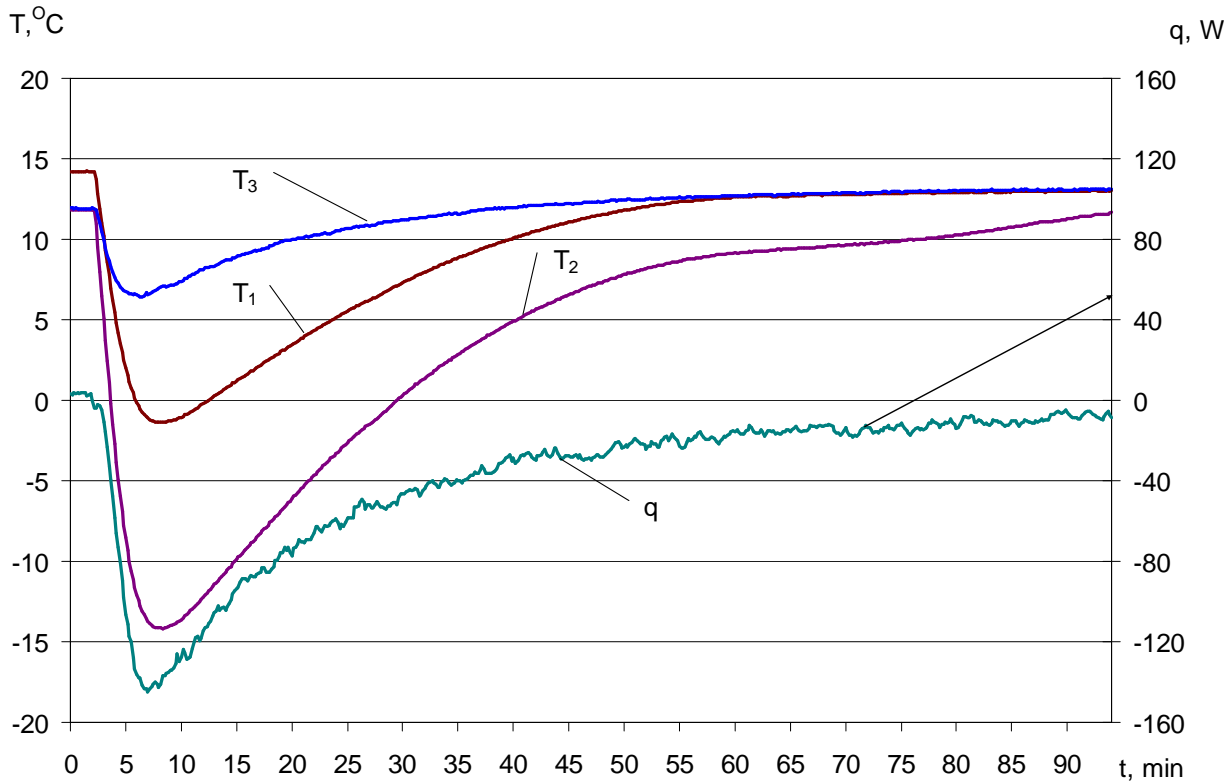


Fig. 12. Temperature profiles on the surface ( $T_1$ ,  $T_2$ ) of the low temperature adsorber, as the time of cold generation,  $T_3$  – mean temperature inside the liquid heat exchanger,  $q$  – heat flow from the liquid heat exchanger to the sorbent bed inside the low temperature adsorber

## CONCLUSIONS

1. A novel three bed cooler based on two (ACF + MnCl<sub>2</sub>) bed and a low temperature bed (ACF + BaCl<sub>2</sub>) was suggested and experimentally investigated.
2. A new stream in the solid sorption chillers application is related with complex compounds sorbent materials development (for example, as active carbon fibre and microcrystals of the salts on its surface) and heat pipe thermal management of adsorbers.
3. The above mentioned sorbent bed has the advantages of chemical coolers (high sorption capacity) and high speed of adsorption, typical for adsorption coolers. Simultaneously there is a strong interaction (intensive heat and mass transfer) between adsorptive materials and chemical materials (active carbon/microcrystals of salts) during the cycle of heating/cooling.
4. Three bed cycle has higher performance of cooling compared with double stage cycle, using four adsorbers. The mass recovery process is the key to improve cooling capability of adsorption cycle with low temperature heat sources.
5. The specific cooling power (SCP) of about 100 W/kg was achieved, which is two times more comparing with conventional coolers.
6. The heat pipe technique ensures an efficient thermal control of adsorbers and eliminates hot spots in the sorbent bed.

## Nomenclature

- $\tau$  – the time of a single cycle of the cooling/heating, s  
 $\Delta\tau_{\text{cooling}}$  – the total time of cooling, s  
 $\Delta\tau_e$  – the time of liquid evaporation, s  
 $\Delta\tau_{d/r}$  – the time of ammonia vapor desorption/regeneration from the sorbent bed, s

$a$  – sorption capacity, g/g, mmole/g  
 $A$  – characteristic sorption energy, kJ/mole  
 $P$  – pressure, Pa.  
 $B$  – structural constant, which characterizes the size and distribution of micro pores,  $K^{-2}$   
 $E_o$  – characteristic energy of standard gas (usually – benzene) kJ/mole  
 $P$  – pressure, Pa, kPa, MPa.  
 $P_s$  – pressure over the surface of the sorbent, Pa, kPa, MPa.  
 $T$  – temperature, °C, K  
 $R$  – universal gas constant, kJ/(mole K)  
 $V$  – volume,  $m^3$   
 $W_o$  – micro porous volume limit,  $cm^3/g$   
 $z$  – compressibility factor  
 $\beta$  – affinity coefficient  
 $v$  – adsorptive substance molar volume,  $cm^3/mmole$   
 $x$  – half-width of the micro pore, nm  
 $E_o$  – the characteristic energy of benzene, 20.5 kJ/mole  
 $k$  – constant of proportionality in the Dubinin equation

### References

1. Bougard J., Veronikis G., Adsorbent modulaire pour machine frigorifique solaire charbon actif-ammoniac // *Symposium "Le froid a sorption solide"*, Paris, 18–20 November 1992. Pp. 282–287.
2. Pons M., Guilleminot J.J., Design of an experimental solar powered, solid-adsorption ice maker // *J. of Solar Energy Engineering ASME*. 1986. Vol. 108. Pp. 332–337.
3. Wang R. Z., Jia J. P., Zhu Y. H., Tong Y., Wu J.Y., Cheng J., Wang, Q. B. Study on the new solid adsorption refrigeration pair: active carbon fiber – methanol // *J. of Solar Energy Engineering ASME*. 1997. Vol. 119, No. 3. Pp. 214–218.
4. Wang R. Z. Performance improvement of adsorption cooling by heat and mass transfer recovery operation // *Int. J. of Refrigeration*. 2001. Vol. 24, No. 7. Pp. 602–611.
5. Critoph R.E. The use of thermosyphon heat pipes to improve the performance of a carbon-ammonia adsorption refrigerator // *Proc. of the IV Minsk International Seminar "Heat Pipes, Heat Pumps, Refrigerators"*, Minsk, Belarus, September 4–7, 2000. Pp. 35–41.
6. Grenier Ph., Guilleminot J.J., Meunier F., Pons P. Solar powered solid adsorption ice maker // *J. of Solar Energy Engineering ASME*. 1988. Vol. 108. Pp. 332–337.
7. Wang L.W., Wang R.Z., Oliveira R.G. A review on Adsorption Working Pairs for refrigeration // *Renewable and Sustainable Energy Reviews*. 2009. 13 (3). Pp. 518–534.
8. Saha B. B., Akisawa A., Kashiwagi T. Solar/waste heat driven two-stage adsorption chiller: the prototype // *Renewable Energy*. 2001. 23,(1). Pp. 93–101.
9. Vasiliev L. L., Mishkinis D. A., Antukh A. A., Vasiliev L. L., Jr. A solar and electrical solid sorption refrigerator // *Int. J. of Thermal Sciences*. 1999. Vol. 38. Pp. 220–227.
10. Vasiliev L., Kanonchik L., Antukh A., Kulakov A., Rosin I. *Waste Heat Driven Solid Sorption Coolers*, SAE Technical Paper 941580, 1994.
11. Vasiliev L. L., Kanonchik L. E., Antukh A. A., Kulakov A. G. NAX Zeolite, carbon fiber and  $CaCl_2$  ammonia reactors for heat pumps and refrigerators // *Adsorption*. 1996. 2. Pp. 311–316.
12. Vasiliev L.L., Mishkinis D.A., Antukh A.A., Vasiliev L.L., Jr. A solar-gas solid sorption refrigerator // *Adsorption*. 2001. Vol. 7. Pp. 149–161.
13. Akisawa A., Miyzaki T. Multi-bed adsorption heat pump cycles and their optimal operation // *Advances in Adsorption Technology*, Ed. B.B. Saha and K.C. NG, pp.241-279, 2010 Nova Science Publishers, Inc.
14. Douss, N., Meunier, F., Experimental study of cascading adsorption cycles // *Chemical Engineering Science*. 1989. Vol. 44. Pp. 225–235.
15. Liu, Y.; Leonig, K., Numerical study of a novel cascading absorption cycle // *Int. J. of Refrigeration*. 2006, Vol. 29. Pp. 250–259.

16. Stitou D.; Spinner B.; Satzger P.; Ziegler F.. Development and comparison of advanced cascading cycles coupling a solid/gas thermochemical process and a liquid/gas absorption process // *Applied Thermal Engineering*, 2000, Vol. 20, Pp. 1237–1269.
17. Vasiliev L. L., Mishkinis D. A., Vasiliev L. L., Jr.: *Complex Compound/Ammonia Coolers* // SAE Technical Paper Series 961462, 26th Intern. Conference on Environmental Systems, Monterey, 1996.
18. Chua, H. T., Ng. K. C., Malek A., Kashiwagi T., Saha, B.B. Multi-bed regenerative adsorption chiller - improving the utilization of waste heat and reducing the chilled water outlet temperature fluctuation // *Int. J. of Refrigeration* 2001. Vol. 24. Pp. 124–136.
19. Saha B. B.; Koyama S., Lee J. B.; Kuwahara K.; Alam, K. C. A. Hamamoto, Y., Akisawa, A., Kashiwagi T. Performance evaluation of a low-temperature waste heat driven multi-bed adsorption chiller // *Int. J. of Multiphase Flow* 2003. Vol. 29. Pp. 1249–1263.
20. Khan, M. A.I., Saha B. B., Aram K. C. A., Miyazaki T., Akisawa A., Kashiwagi T. // *Trans. JSRAE*, 2006. Vol. 23. Pp. 399–408.
21. *Patent 455966 US*. Heat Transfer Device / L.L. Vasiliev et al.: 1985.
22. Vasiliev L. L., State-of-the-art on heat pipe technology in the Former Soviet Union // *Applied Thermal Engineering*. Vol 16. № 7 1998, Pp. 507–551.

## COMPARISON OF HIGH TEMPERATURE HEAT PUMPS ON 4-TH GENERATION REFRIGERANTS

Ildar A. Sultanguzin, Alina A. Potapova, Alexandre V. Govorin, Andrey V. Albul

Industrial Thermal Engineering Systems Department  
Moscow Power Engineering Institute (Technical University)  
Krasnokazarmennaya street, 14, Moscow, Russian Federation 111250  
+7-495-362-7217; SultanguzinIA@mpei.ru

### Abstract

The present work is devoted to the use of a two-stage heat pump with 17 MW heat capacity with the R-134a refrigerant for central heating systems. An energy and ecological efficiency comparison of new refrigerants, based on fluorinated propylene, that have less effect on the global warming, with R-134a refrigerant is made. The comparison is made on a high-temperature heat pump, that uses the heat of sewage waters.

### KEYWORDS

Fluorinated propylene, refrigerant, global warming potential, thermodynamic cycle, vapor compression heat pump, two-stage centrifugal compressor, district heating system, high temperature heat pump, sewage.

### INTRODUCTION

In the world the biggest vapor-compression heat pumps have heat capacity up to 30 MW with two-stage radial compressors [1, 2]. A heat pump station with six heat pumps with a total capacity of 180 MW is built and functioning in Stockholm (Sweden) for the city heat supply. The sea water is used as a heat source, which at winter period has a temperature of +2...+4 °C [1]. In Helsinki (Finland) and Oslo (Norway) the heat pumps operate on sewage water [2]. In the summer period they produce both the heat for hot water supply and cold for air conditioning needs of big trade and business centers.

The use of heat pumps of large capacities is most effective in large cities, where heavy heat and cold loads are demanded for a long period, where waste recycling (particularly heat waste of sewage waters) is a big problem.

In Russia, where the main source of heat are centralized heat supply systems, the use of high-temperature heat pumps with ecological 4th generation refrigerants could have great significance.

### SEWAGE WATER HEAT PUMP WITH R-134a REFRIGERANT

A two-stage heat pump with 17 MW heat capacity shall be regarded, which works on R-134a refrigerant (1,1,1,2-tetrafluoroethane  $\text{CH}_2\text{F}-\text{CF}_3$ ) with critical temperature 101.08 °C and pressure 40.603 bar, that does not affect the ozone layer, but has a global warming potential  $\text{GWP} = 1340$  compared to  $\text{CO}_2$ . The sewage waters are use as a heat source. Fig. 1 presents a heat pump setup with the temperature level in the evaporator at 3.5 and 90.1 °C in the condenser.

The results of calculation of the heat pump [3] showed that energy consumption of the compressor is  $N_e = 7075$  kW. The transformation ratio is defined by equation 1:

$$\mu = \frac{Q_{cond}}{N_e} = \frac{17000 \text{ kW}}{7075 \text{ kW}} = 2.40. \quad (1)$$

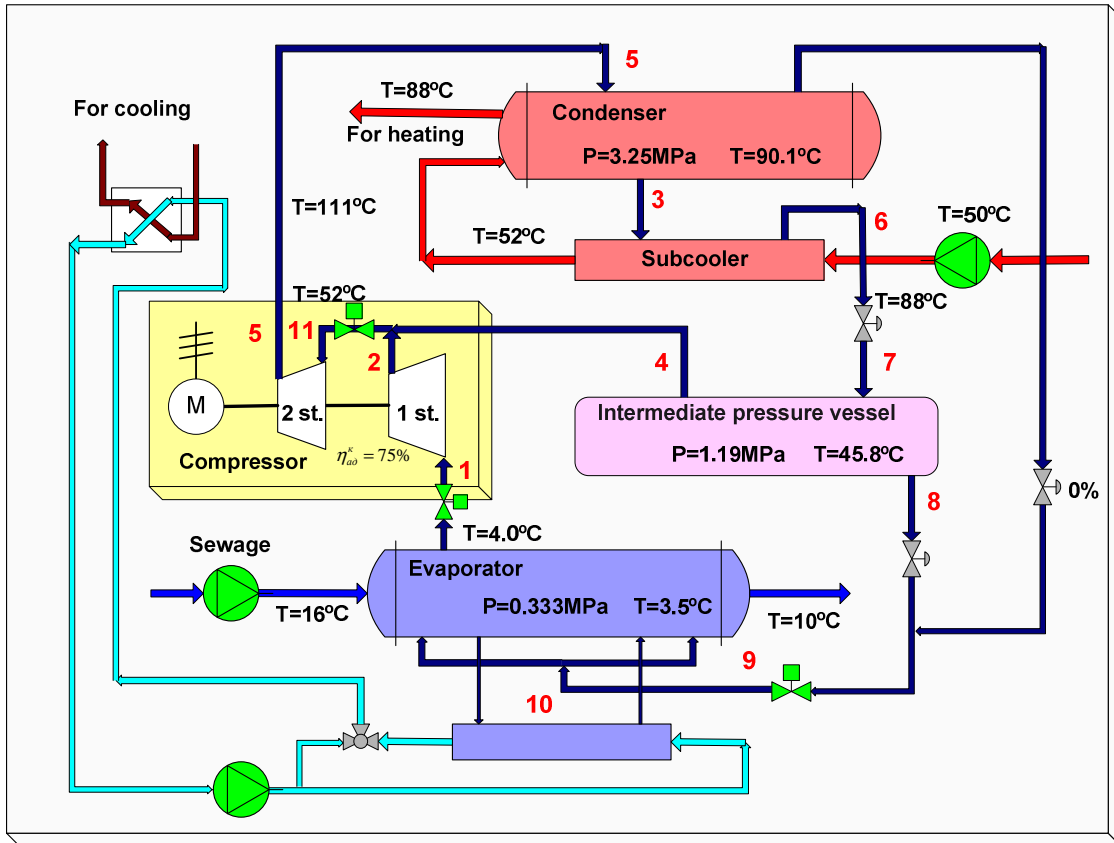


Fig. 1. Heat balance diagram of a high-temperature heat pump with sewage water as a heat source

In the summer period the cooled water is supplied to the condenser instead of sewage waters, thus the heat pump can also produce cold for air conditioning systems with cooling capacity at  $Q_{evap} = 10073 \text{ kW}$ .

Fig. 2 displays the heat processes diagram based on the calculation results (pressure  $P$  – enthalpy  $H$ ).

The diagram on fig. 2 shows that the two-stage scheme with intermediate pressure vessel allows to heat the system water most simply and with high reliability [4]. The intermediate vessel works as a phase separator at intermediate pressure after receiving vapor-fluid (flow 8 on Figs. 1 and 2) and over-heated steam (flow 2), and is the simplest way of creating a two-stage scheme (without the risk of fluid going to the second stage of the compressor with flow 3). Additional efficiency upgrading is achieved by subcooling the refrigerant in the supercooler (process 6, 7) since the transferred heat in condenser is raised (5, 6) and the flow rate of refrigerant is constant.

The transformation rate  $\mu = 2.4$  occurred not to be big enough, but it has to be considered, that the large span between the temperatures of refrigerant in the condenser and evaporator was intentionally chosen (2):

$$\Delta t = t_{cond} - t_{evap} = 90.1 - 3.5 = 86.6 \text{ } ^\circ\text{C} . \quad (2)$$

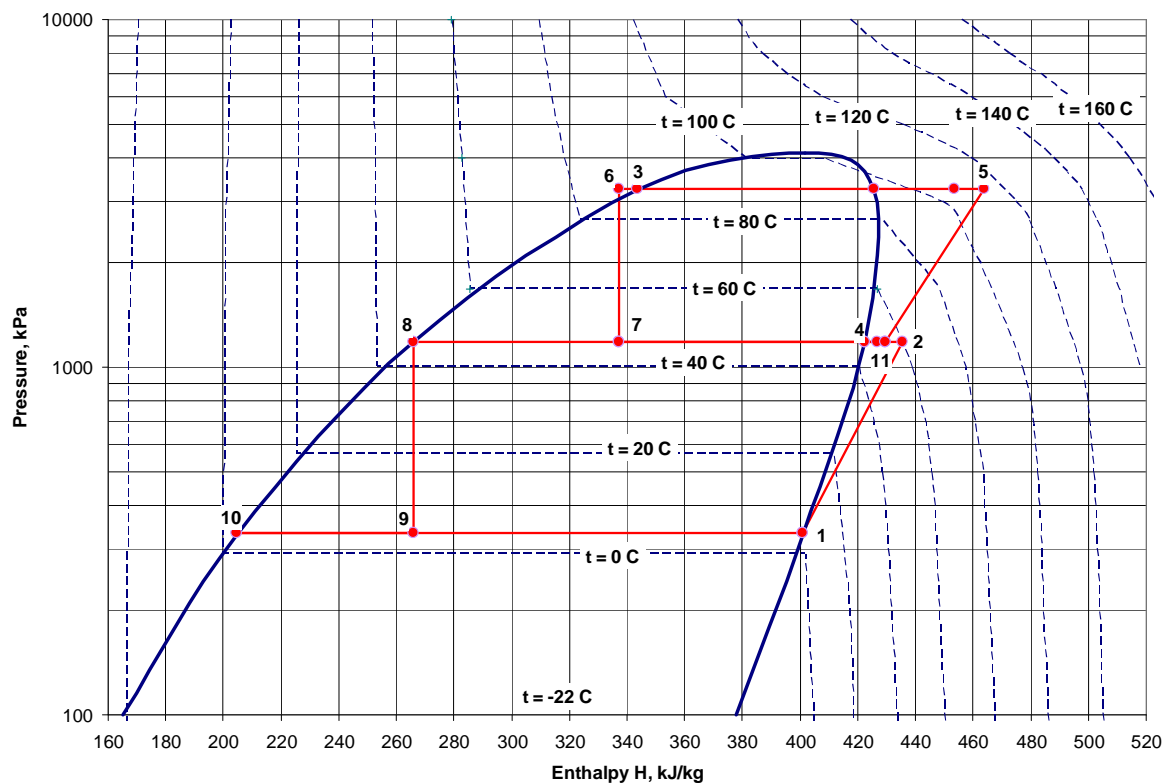


Fig. 2. P-H diagram of heat processes of two-stage heat pump with R-134a refrigerant on sewage water

### CHARACTERISTICS OF THE HIGH-TEMPERATURE HEAT PUMP WITH DIFFERENT REFRIGERANTS

The goal of this work is to compare the energy and ecological efficiency of new refrigerants based on fluorinated propylene, that have little impact on the global warming, with R-134a.

The comparison of energy efficiency of different refrigerants is a difficult multiple-factor task, in which their positive properties are compared with their negative ones. Table 1 shows the comparison of characteristics of high-temperature heat pumps with new ecological refrigerants and R-134a. Table 1 uses initial data from different sources: R-1234yf [5, 6], R-1234ze(E) [7], R-1243zf [8], R-1234ye(E) [9].

During the recalculation of stages of compressor with R-134a for another refrigerant a method displayed in [10] was used. The positive properties of new refrigerants are higher critical temperature (apart from R1234yf), bigger flow rate in both compressor stages, bigger transformation ratios, coefficient of compressibility in the 1<sup>st</sup> compressor stage closer to 1, which moves them closer to the ideal gas. But there are significant negative properties of refrigerants based on fluorinated propylene: less specific heating power in the condenser  $\Delta h_{cond}$ , less volume heat capacity (VHC) and cold capacity (VCC), less heat pump capacity  $Q_{cond}$  with same design characteristics.

Table 1. Comparison of characteristics of high-temperature heat pump with new environmentally refrigerants

Refrigerant	R-134a	R-1243zf	R-1243ze(E)	R-1243ye(E)	R-1234yf
Global Warming Potential (GWP)	1340	3	-	6	4
Molar weight $\mu$ (kg/kmol)	102.03	96.05	114.04	114.04	114.04
Acentric factor, $\omega$	0.3268	0.305	0.296	0.29	0.2780

Boiling point at atmospheric pressure $T_b$ , K	247.09	251.65	253.92	251.15	243.80
Critical temperature $T_c$ , K	374.23	376.2	382.51	379.85	367.85
Critical pressure $P_c$ , bar	40.60	38	36.32	35.34	33.75
Heat capacity $C_p$ , kJ/(kmol·K)	85.0	88.3	93.1	94.4	98.9
$\tau = T_c / T_{c \text{ R-134a}}$	1	1.005	1.022	1.015	0.983
AF = $\omega / \omega_{\text{R-134a}}$	1	0.933	0.906	0.887	0.851
CP = $C_p / C_{p \text{ R-134a}}$	1	1.039	1.095	1.111	1.164
Heat pump					
Condenser heat capacity $Q_{cond}$ , kW	17000	15260	12540	13670	10412
Evaporator heat $Q_{evap}$ , kW	9852	8605	7178	8076	4747
Power consumption $N_e$ , kW	7294	6903	5811	6069	6079
Coefficient of performance COP, $\mu$	2.331	2.211	2.158	2.252	1.713
Lower cycle flow $G_L$ , kg/s	73.08	64.1	58.0	67.9	43.2
Higher cycle flow $G_H$ , kg/s	134.06	157.6	114.8	143.0	152.6
$G_H/G_L$	1.834	2.459	1.980	2.107	3.535
Specific heat consumption in condenser $\Delta h_{cond}$ , kJ/kg	126.81	96.8	109.2	95.6	68.3
Volume heat capacity in condenser VHC, kJ/m <sup>3</sup>	2065	1344	1480	1372	1320
Specific volume $v_1$ , m <sup>3</sup> /kg	0.0614	0.0721	0.0738	0.0697	0.0517
Volume flow in stage 1 $V_1$ , m <sup>3</sup> /s	4.487	4.620	4.280	4.731	2.231
Specific heat consumption in evaporator $\Delta h_{evap}$ , kJ/kg	134.8	134.2	123.8	119.0	110.0
Volume cold capacity VCC, kJ/m <sup>3</sup>	2195	1863	1677	1707	2127
Volume flow in stage 2 $V_2$ , m <sup>3</sup> /s	2.453	3.185	2.422	2.874	2.564
1 compressor stage					
Coefficient of gas compressibility $Z$	0.906	0.919	0.927	0.922	0.901
Adiabatic $k$ -value $k$	1.180	1.104	1.094	1.089	1.091
Sonic speed $a$ , m/s	155.2	155.9	143.0	142.4	140.8
Gas speed $u_2$ , m/s	206.0	212.1	196.5	217.2	102.4
Mach number $Mu = u_2 / a$	1.327	1.360	1.374	1.525	0.727
Pressure ratio $\varepsilon_1$	3.566	3.548	3.587	3.518	3.212
Rotation rate, 1/c	139.6	140.2	128.6	128.0	149.1
Density proportion, $k_{v1} = v_1 / v_2$	1.799	1.852	1.860	1.896	2.34
2 compressor stage					
Gas speed $u_2$ , m/s	144.6	145.2	133.3	132.7	154.5
Mach number $Mu$	0.916	0.934	0.920	0.925	1.104
Pressure ratio $\varepsilon_2$	2.740	2.732	2.762	2.740	2.896
Density proportion $k_{v2} = v_{11} / v_5$	1.382	1.416	1.371	1.410	1.624

## ANALYSIS OF TABLE OF COMPARISON OF ENERGETICAL EFFICIENCY OF DIFFERENT REFRIGERANTS IN HEAT PUMPS

The main parameters that affect the properties of refrigerants are:

$\tau = T_c / T_{c_{R-134a}}$ . Relative critical temperature  $\tau$  of R-1234ze(E) is the largest, next, decreasingly, are R-1234ye(E), R-1243zf. High temperature is an advantage of refrigerants in question.

$AF = \omega / \omega_{R-134a}$ . The acentric factor of molecules of refrigerants in hand is less, than of R-134a, which «squeezes» their  $P-H$  characteristic (lessens the specific heat of evaporation) and is a disadvantage. The closest to R-134a is R-1243zf.

$CP = C_p / C_{p_{R-134a}}$ . Specific molar heat capacity  $CP$  is a characteristic of vapor-liquid compound. The raise of  $CP$  leads to a raise of decline of the top in the critical point of  $P-H$  characteristic and moves it to the right. All refrigerants in question have  $CP$  larger than R-134a, which as a disadvantage. Refrigerant R-1243zf is closest to R-134a.

The analysis cannot be narrowed only by three examined parameters. In reality the efficiency of the heat pump is affected by lost of other factors.

The more heat is transferred in the condenser  $Q_{cond}$ , the more effective is the refrigerant. This parameters is one of the main when it comes to choosing the recommended refrigerant. R-1243zf has maximum  $Q_{cond}$ . The amount of heat of R-1234ye(E) and R-1234ze(E) is significantly less.

The amount of heat of every kg of the cooled refrigerant, transferred to water in the condenser  $\Delta h_{cond} = h_5 - h_6$  (Fig. 2) of refrigerants in question is less than R-134a has. That is a disadvantage.

The volume heat capacity of the top cycle (with the second stage of the compressor) VHC of refrigerants in hand is less than R-134a has. That is their substantial disadvantage.

The decrease of volume cold capacity of the lower cycle (with the first stage of compressor) VCC compared to R-134a is a disadvantage of refrigerants in hand.

The specific volume  $v_1$  of refrigerants in question is bigger than R-134a has. That is a disadvantage. The volume flow in the first stage of the compressor is equal  $V_{1(R-1234ze(E))} = 0,0786 \text{ m}^3/\text{kg}$ , which negatively affects the work of the compressor.

The volume flow  $V_1 = G_1 / v_1$  of refrigerants in hand in the first stage of compressor is a bit more than R-134a has (except for R-1234ys). That is and advantage. The raise of the volume flow is explained by the raise of the volume proportion of refrigerants in hand compare to R-134a. This leads to a bigger mass flow ratio of the working fluid.

The volume flow  $V_{11} = G_H v_{11}$  in the second stage of compressor of refrigerant R-1243zf is bigger than the same for other refrigerants. That is and advantage.

The mass flow ratio of the lower stage of the heat pump  $G_L = G_H (h_4 - h_7) / (h_4 - h_9)$  of refrigerants in hand is less than R-134a has. That is a disadvantage, especially for R-1234yf.

The mass flow ratio in the lower stage of the heat pump of refrigerants in hand is less than R-134a has. That is a disadvantage, especially for R-1234yf.

The mass flow ratio in the upper stage of the heat pump  $G_H = (Q_{cond}) / (h_5 - h_6)$  allows to raise the flow of the working fluid in the upper cycle. For R-1243zf this parameter is significantly larger compared to other refrigerants. This is the substantial advantage when it comes to choosing a refrigerant. For R-1234yf it does not give a significant advantage due to a small value of  $\Delta h_{cond}$ .

The power consumption for both stages of compressor  $N_e$  for refrigerant R-1234ze(E) are the lowest, then (ascending) R-1234ye(E), R-134a, R-1243zf. The less the power consumption, the cheaper the heat pump is to run.

Coefficient of transformation of heat COP,  $\phi$  is maximal for R-134a, for R-1234yf it is minimal, which is a disadvantage. COP is a ratio between heating capacity and consumed power.

The coefficient of compressibility of gas  $Z$  is taken from the main parameters table. The closer the value is to 1, the closer the refrigerant is to the ideal gas by it's properties. The refrigerants in hand are closer to 1, than R-134a, which is their advantage,

The energy consumption is proportional to the adiabatic  $k$ -value. The decrease of this index of refrigerants in hand compared to R-134a is their disadvantage.

Sonic speed. R-1243zf has a maximal sonic speed, which lowers the Mach number with same gas speed in the compressor and less possibility of hit. The Mach number is defined as the ratio of the speed of body,

that moves in an environment, to the sonic speed in that environment. For home compressors the maximum Mach number is about 1.4. The raise of  $Mu$  above this level can lead to lowering the efficiency coefficient of stages of compressor.

Rotary velocity of gas on the exit of a stage of compressor  $u_2 = 3.14(\text{wheel size})(\text{number of revolutions})$ . The raise of this parameter for the most of refrigerants in hand compared to R-134a is an advantage. The limiting factor for most of new refrigerants is the Mach number in the first stage of compressor, for R-1234yf – in the second stage.

Number of revolutions per minute influences to the speed  $u_2$ , the bigger value, the bigger speed we can achieve. R-1243zf has a maximum allowable rotary velocity.

The raise of ratio of density of gas on the exit of the stage of compressor to the density of gas on the entrance  $k_\gamma$  of the gases in hand compared to R-134a brings to raise of volume flow, which is a positive factor.

The results of calculations show, that the best alternative for R-134a is R-1243zf. It has the maximum heat pump capacity  $Q_{cond}$  mainly because the maximum sonic speed, that compensates the volume heat capacity, it is widely used to produce polymers. It has some drawbacks, e.g. R-1243zf is flammable. It can be assumed, that it's influence on the global warming is low ( $GWP = 3$ ).

The second recommended refrigerant is R-1234ye(E). It can be assumed, that by influence on the global warming it will be close to R-1234yf which has  $GWP = 4$ . But his  $Q_{cond}$  is significantly less. The third by energy efficiency is the R-1234ze(E) refrigerant. The refrigerant R-1234ys cannot be recommended for use in high-temperature heat pumps because of low critical temperature.

### References

1. Bailer P., Pietrucha U. District heating and district cooling with large centrifugal chiller – heat pumps // *Proc. 10<sup>th</sup> Intern. Sympos. on District Heating and Cooling*, Hanover, Germany, 3–5 September 2006.
2. 5 Unitop 50FY heat pump/chiller units simultaneously generate 90 MW heat energy and 60 MW chilled water // <http://www.friotherm.com>
3. Sultanguzin I. A., Potapova A. A. High-temperature high power heat pumps for a heat supply // *Novosti Teplosnabzheniya (News of a Heat Supply)*. 2010. No. 10. Pp. 23–27 (in Russian).
4. Potapova A. A., Sultanguzin I. A. Use of heat pumps in the heat supply system of a factory and a city // *Metallurgist*. 2010. Vol. 54. Nos. 9–10. Pp. 635–640.
5. Leck T. J. Evaluation of HFO-1234yf as a Potential Replacement for R-134a in Refrigeration Applications // *Proc. 3<sup>rd</sup> IIR Conf. on Thermophysical Properties and Transfer Processes of Refrigerants*, Boulder, CO, 2009. Paper 155.
6. Akasaka R., Tanaka K., Higashi Y. Thermodynamic property modeling for 2,3,3,3-tetrafluoropropene (HFO-1234yf) // *Int. J. of Refrigeration*. 2010. Vol. 33. Pp. 52–60.
7. Akasaka R. An application of the extended corresponding states model to thermodynamic property calculations for trans-1,3,3,3-tetrafluoropropene (HFO-1234ze(E)) // *Int. J. of Refrigeration*. 2010. Vol. 33. Pp. 907–914.
8. Brown J. S., Zilio C., Cavallini A. Thermodynamic Properties of Eight Fluorinated Olefins // *Int. J. of Refrigeration*. 2010. Vol. 32. Pp. 235–241.
9. Zernov V. S., Kogan V. B., Lyubetsky S. G., Duntov F. I. Equilibrium liquid–vapor in an ethylene–trifluorinepropylene system // *Zhurnal Prikladnoi Himii (J. of an Applied Chemistry)*. 1971. No. 3. Pp. 683–686 (in Russian).
10. Sarevski M. N. Influence of the new refrigerant thermodynamic properties on some refrigerating turbo compressor characteristics // *Int. J. of Refrigeration*. 1996. Vol. 19. Pp. 382–389.

## INVESTIGATION OF HEAT AND MASS TRANSFER IN A FLAT EVAPORATOR OF A COPPER-WATER LOOP HEAT PIPE UNDER UNIFORM AND CONCENTRATED HEATING

**Mariya A. Chernysheva, Yury F. Maydanik**

Institute of Thermal Physics, Ural Branch of the Russian Academy of Sciences,  
Amundsena St., 106, Yekaterinburg, 620016, Russia  
Tel: (7-343) 2678-791; Fax: (7-343) 2678-799; E-mail: maidanik@etel.ru

### Abstract

An evaporator model has been developed for investigating heat and mass transfer in a flat evaporator of a copper-water loop heat pipe. It takes into account heat-transfer processes in the active zone, the barrier layer of the wick, the wall and the compensation chamber. The problem was solved by the finite difference method with the use of a nonuniform grid adapted to the configuration of a flat evaporator and its geometric peculiarities. The model examined a uniform and concentrated heat supply to the evaporator. In the first case the heat-supply area was 9 cm<sup>2</sup>, in the second 1 cm<sup>2</sup>. Numerical simulation of temperature fields of the evaporator has been performed for a heat load range from 20 to 900 W. Data have shown that a decrease in the heating area at a fixed heat load results in increasing temperature on the evaporator wall under the heater. With a concentrated heat supply the evaporation zone spreads beyond the "heating spot", and at heat loads above 400 W the drying of the part of the wick under the heater begins. No disturbance of serviceability of the heat-transfer device is observed in this case as the crisis of operating heat transfer is of a local nature. In such conditions the evaporation front shifts in the direction of peripheral areas located beyond the "heating spot". Under uniform heating the wick drying was not registered in the investigated heat load range.

### KEYWORDS

Loop heat pipe, flat evaporator, 3D-modeling, heat and mass transfer, porous structure.

### INTRODUCTION

A loop heat pipe (LHP) is a high-performance heat-transfer system with a capillary pumping of the working fluid. LHPs utilize the evaporation and condensation of a working fluid to transfer heat from a heat source to a heat sink, and the capillary forces developed in a fine pored wick to circulate the fluid inside the closed loop of the device. Various aspects of the LHP theory and its main working principles have been examined in detail by the authors of Refs. [1, 2]. In this way, the LHP physical concept proposed in Ref. [1] allowed the authors to formulate three conditions of LHP operation. One of them, connecting temperature and pressure of saturated vapor in the locations of the vapor-liquid interface, was obtained on the base of thermodynamic analysis applied to the LHP as a two-phase heat-transfer system. Depending on the working fluid distribution in an LHP regimes of variable and constant conductivity are distinguished. The first one is observed at low and medium heat loads. A characteristic feature of this regime is the partial filling of the compensation chamber (CC) by a liquid above the surface of which a saturated vapor is situated. For a working fluid circulation in this regime the condition should be satisfied which connects the driving temperature difference  $\Delta T_{q-cc} = T_q^s - T_{cc}^s$  with the pressure drop on the external, relative to the wick, transport areas:

$$\Delta P_{tot} - \Delta P_w = \frac{dP}{dT} (T_q^s - T_{cc}^s). \quad (1)$$

With increasing heat load the condenser gradually rids itself of the liquid which moves in the CC. At a maximum emptying of the condenser and a completely filled compensation chamber the LHP passes into an operation regime with a constant conductivity. In this case, instead of the relation (1), use is made of an equation which relates the thermal condition of a working fluid on the interfaces, one of which is in the active zone of the evaporator, and the another is in the condenser, with the corresponding pressure drop on the transport areas between them:

$$\Delta P_{vg} + \Delta P_{vl} + \Delta P_{cond} = \frac{dP}{dT} (T_q^s - T_{cond}^s). \quad (2)$$

Equations (1) and (2) make it possible to determine the LHP temperature depending on the heat load and at different filling rates of the CC. Methods of calculating the LHP thermal state for each regime with their own distinctive features are described in detail in Ref. [3]. It should be noted that one of the most difficult moments of a calculation procedure is to determine the temperature difference in the evaporator  $\Delta T_{q-cc} = T_q^s - T_{cc}^s$  (Eq.1). Thus, the paper [4] talks about a heat transfer model in the cylindrical evaporator of an LHP at a partially filled CC. The authors took into account the problem symmetry on the azimuthal coordinate and assuming that the liquid core of the wick was completely filled with a liquid, considered a one-dimensional problem of the radial temperature distribution in the wick. In this case there was an assumption that the heat flow was directed from the external wick surface to the internal one only along the r-axis. In the opposite direction the liquid flow was moving from the liquid core to the evaporation zone placed at the external wick surface. It was also supposed that the temperature of the working fluid in the CC was approximately equal to the temperature at the absorbing wick surface of the liquid core. As a result a relation connecting the temperature difference  $\Delta T_{q-cc}$  with the heat load was obtained:

$$T_q^s - T_{cc}^s = (T_q^s - T_{in-cc}) \left( \frac{D_{int}}{D_{ext}} \right)^{\theta_w}, \quad (3)$$

where  $\theta_w = \frac{c_p Q}{2\pi L_q h k_{eff}}$ .

According to [5] at similar simplifications an analogous relation can be obtained for disk-shaped evaporators:

$$T_{cc}^s - T_{in-cc}^s = (T_q^s - T_{in-cc}) e^{\theta_w}, \quad (4)$$

where  $\theta_w = \frac{c_p Q B_w}{S_q h k_{eff}}$ .

Flat-oval evaporators (Fig. 1) having a thickness of no more than 7–8 mm [6–8] have been actively developed in recent years. As a rule, there is no central liquid channel in these evaporators owing to their limited thickness. But at the same time the active zone can be located at one as well as at both its flat surfaces.

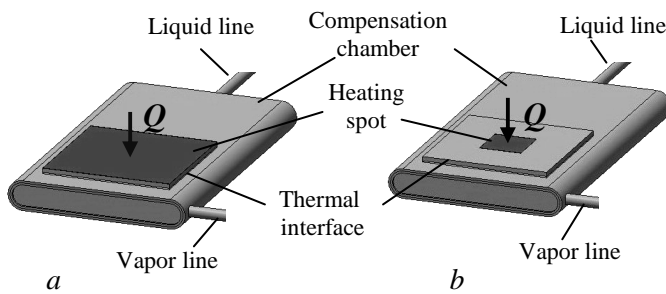


Fig. 1. View of the flat evaporator under various sizes and locations of "heating spot": a – uniform heating, b – concentrated heating

The heating spot area  $S_h$  may be less than the area of the active zone  $S_q$  ( $S_h \leq S_q$ ), as is shown in Fig. 1 b. The placement of some mini-sized heat sources with a small thermocontact surface is also possible in the active zone of the evaporator. The specific character of heat flow direction in the evaporator at one-sided heating and a random placement of heat sources, as well as the liquid filtration peculiarities, does not allow simplifying the problem of heat and mass transfer on the axial coordinate components. In this case it becomes rather problematical to obtain an analytical solution of the three-dimensional problem of heat and mass transfer and the temperature distribution in the evaporator, which is necessary to determine the motive temperature difference  $\Delta T_{q-cc}$  and to calculate the working characteristics of the device. A 3D model of a flat evaporator and the results of numerical calculations of the heat and mass transfer problem at different heat load concentrations in the active zone are proposed in this paper.

## 1. PHYSICAL MODEL

The schemes of the flat evaporator and its calculated model are presented in Fig. 2. Instead of a flat-oval cross-section, for simplicity, use is made of its rectangular analog, and the circular cross-section of vapor-removal grooves has been replaced by a square one. All the other peculiarities of the configuration and assembling of the flat evaporator have been accounted for in the model. The evaporator is examined in isolation from the other component parts of the LHP, but a thermal link with them is realized by means of two external, as related to the evaporator, temperature parameters, which are taken as input data. They are the vapor temperature at the evaporator outlet  $T_{out\_evp}$  and the liquid temperature at the inlet into the compensation chamber  $T_{in\_cc}$ . The third external parameter of the problem which affects the thermal state of the evaporator is the temperature of the outside ambient  $T_{amb}$ .

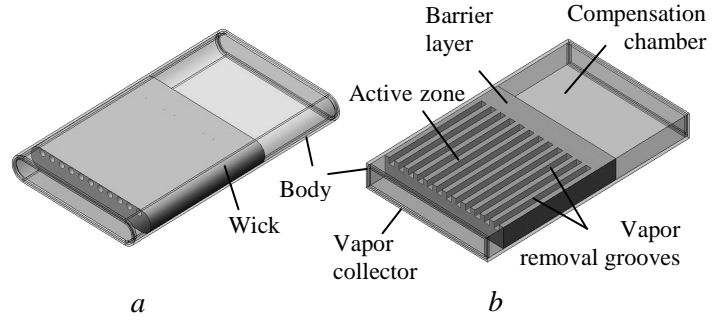


Fig. 2. Scheme of flat evaporator (a) and its model (b).

Evaporation takes place at wick surface facing the vapor removal grooves  $\Omega_{vg}$  and the vapor collector  $\Omega_{coll}$ . So the total evaporation heat flow consists of two components:

$$Q_{ev} = Q_{ev\_vg} + Q_{ev\_coll} \quad (5)$$

Owing to the nonuniformity of the temperature field of the evaporator, the intensity of heat-exchange at the evaporating surfaces must be different, depending first of all on the difference  $\Delta T_{ev}$  between the local value of the temperature  $T_{\zeta}$  at the evaporating surface and the temperature of the saturated vapor in the grooves or in the vapor collector  $\Delta T_{ev} = T_{\zeta} - T^s$ , where  $\zeta$  is a point at the evaporating surface:  $\zeta \in \Omega_{vg} \vee \zeta \in \Omega_{coll}$ . With allowance for this, the evaporation intensity will be determined as  $I_{ev} \sim T_{\zeta} - T^s$ . The difference between the temperature at the wick surface and the corresponding vapor temperature  $\Delta T_{ev}$  also determines the value of the local liquid superheating in the pores and is used as a condition describing the process of drying of the wick owing to the boiling-up of a superheated liquid. The condition of the wick drying may be formulated as follows:

$$\Delta T_{ev} \geq \Delta T_{nucl} \quad (6)$$

And the lower level of nucleation superheating  $\Delta T_{nucl}$  according to [9] is determined by the formula

$$\Delta T_{nucl} = \frac{2 \cdot \sigma \cdot T^s}{h \cdot R_p \cdot \rho_v} \quad (7)$$

If the inverse relation is observed:

$$\Delta T_{ev} < \Delta T_{nucl} \quad (8)$$

In this case the wick must continue to remain saturated with a liquid. This approach is used for revealing dried sections in the wick. The appearance of such "dry spots" at the surface of the wick in the active zone and at the butt-end surface facing the vapor collector means that there may be no liquid evaporation in these places, and these fragments of the wick surface should be excluded from the process of evaporating heat transfer.

## 2. MATHEMATICAL FORMULATION

The heat transfer equation for the evaporator body with allowance for the three-dimensionality of the mathematical model will look like:

$$\frac{\partial^2 T_b}{\partial x^2} + \frac{\partial^2 T_b}{\partial y^2} + \frac{\partial^2 T_b}{\partial z^2} = 0 \quad (9)$$

For the evaporator being investigated here the liquid velocity at the butt-end surface of the wick on the CC side at a uniform absorption according to evaluations may vary from  $3 \cdot 10^{-4}$  to  $1.4 \cdot 10^{-2}$  m/s under changes

of heat load from 20 to 900 W. It is well known that at small filtration rates of a working fluid through the capillary structure the temperatures of the wick framework and liquid get equalized to an extent that in very small elementary volume they may be considered equal. So, for describing of the thermal processes in the wick one can use the approach presented in [10, 11], in which for a stationary case of heat transfer in a wick the authors used the heat transfer equation:

$$\frac{\partial^2 T_w}{\partial x^2} + \frac{\partial^2 T_w}{\partial y^2} + \frac{\partial^2 T_w}{\partial z^2} = 0. \quad (10)$$

And the convective component of heat transfer during the liquid filtration through the wick  $Q_{cp}$  should be allowed for in the energy balance equation:

$$Q = Q_{ev} + Q_{cp} + Q_{cc} + Q_{amb}. \quad (11)$$

The value of  $Q_{cp}$  depends on the specific mass flow rate of the working fluid  $\dot{m}_\zeta$  and the liquid temperature  $T_\zeta$  at the point  $\zeta$  at the evaporating surface ( $\zeta \in \Omega_{vg} \vee \zeta \in \Omega_{coll}$ ):

$$Q_{cp} = c_p \cdot \int \dot{m}_\zeta \cdot (T_\zeta - T_{cc}) d\Omega. \quad (12)$$

And the specific mass flow rate is:

$$\dot{m}_\zeta = \frac{q_\zeta}{h}. \quad (13)$$

The heat flux  $q_\zeta$  is determined according to the condition

$$-k_{eff} \cdot \left. \frac{\partial T}{\partial n} \right|_\zeta = \alpha_{ev} \cdot (T_\zeta - T^s) \quad (14)$$

The total heat flow expended for vapor generation is determined by the expression

$$Q_{ev} = \int_{\Omega_{coll}} q_{ev} d\Omega + \int_{\Omega_{vg}} q_{ev} d\Omega. \quad (15)$$

For dried sections, which arise when the condition (6) is fulfilled, instead of (15) use is made of

$$k_{eff} \cdot \left. \frac{\partial T}{\partial n} \right|_\zeta = 0. \quad (16)$$

The rest boundary conditions can be stated as follows. At the heat-supply surface of the evaporator  $\Omega_q$ :

$$-k_b \cdot \frac{\partial T}{\partial y} = q. \quad (17)$$

The supplied heat flux is uniform:

$$q = \frac{Q}{B_h \cdot L_h}, \quad (18)$$

where  $L_h$  and  $B_h$  are the length and width of the "heating spot". At the boundary between the wet area and the dry area of the wick:

$$k_{eff} \cdot \left. \frac{\partial T_{wick}}{\partial n} \right|_{wet} = k_w \cdot \left. \frac{\partial T_{wick}}{\partial n} \right|_{dry}. \quad (19)$$

At the outer surface of the evaporator outside the "heating spot"  $\Omega_{amb}$ :

$$-k_b \cdot \left. \frac{\partial T}{\partial n} \right|_\zeta = \alpha_{amb} \cdot (T_\zeta - T_{amb}) \quad \text{and} \quad Q_{amb} = \int_{\Omega_{amb}} q_\zeta d\Omega. \quad (20)$$

At inner surfaces limiting the compensation chamber ( $\Omega_b \wedge \Omega_w$ ):

$$-k_b \cdot \left. \frac{\partial T}{\partial n} \right|_\zeta = \alpha_{in\_cc} \cdot (T_\zeta - T_{cc}) \quad , \quad -k_{eff} \cdot \left. \frac{\partial T}{\partial n} \right|_\zeta = \alpha_{in\_cc} \cdot (T_\zeta - T_{cc}). \quad (21)$$

$$\text{and } Q_{cc} = \int_{\Omega_b} q_{\zeta} d\Omega + \int_{\Omega_w} q_{\zeta} d\Omega. \quad (22)$$

The liquid flow that arrives at the CC from the liquid line ensures a sufficiently intense agitation of the working fluid making its temperature  $T_{cc}$  practically uniform through-out the whole inner space of the CC. In its turn, the value of  $T_{cc}$  depends on the temperature of the condensate at the entrance into the CC, its flow rate, and also the heat flow  $Q_{cc}$  penetrating from the active zone into the CC:

$$T_{cc} = T_{in\_cc} + \frac{Q_{cc}}{c_p \cdot G}. \quad (23)$$

At the boundary between the evaporator body and the wick with allowance for the saturation of the porous structure (wet or dry) and the specific contact thermal resistance  $R_c^*$  we have the following conditions:

$$k_b \left. \frac{\partial T}{\partial n} \right|_{\zeta_{+0}} = \frac{T_{\zeta_{+0}} - T_{\zeta_{-0}}}{R_c^*} = k_{eff} \left. \frac{\partial T}{\partial n} \right|_{\zeta_{-0}}, \quad (24)$$

$$k_b \left. \frac{\partial T}{\partial n} \right|_{\zeta_{+0}} = \frac{T_{\zeta_{+0}} - T_{\zeta_{-0}}}{R_c^*} = k_{wick} \left. \frac{\partial T}{\partial n} \right|_{\zeta_{-0}}, \quad (25)$$

The value of the specific contact thermal resistance, according to [12], may vary from  $10^{-5}$  to  $10^{-4}$   $m^2 \cdot K/W$ . In calculations use was made of its averaged value:  $R_c^* = 5.5 \cdot 10^{-5}$   $m^2 \cdot K/W$ . The wick thermal conductivity and effective thermal conductivity are determined by formulas:

$$k_w = k_{comp} \cdot (1 - \varepsilon) \cdot (1 + \varepsilon)^{-2.1} \quad \text{and} \quad k_{eff} = k_w + \varepsilon \cdot k_l. \quad (26)$$

The mathematical model was solved numerically. To construct a finite-difference analogy of the governing partial differential equations and the boundary conditions, use was made of a control volume method which ensures the conservation of a finite-difference scheme [13]. An explicit method was chosen for obtaining a difference solution. Use was made of an irregular computational grid adapted to the geometric peculiarities of the evaporator and containing 6300 nodes:  $I(x) \times J(y) \times K(z) = 28 \times 9 \times 25$ .

### 3. RESULTS AND DISCUSSION

Numerical results were obtained for a flat evaporator with the parameters presented in Table 1.

The experimental study results for a copper-water LHP with such an evaporator are presented in the Ref. [6]. The placement of heaters at a uniform  $S_h = 9 \text{ cm}^2$  and a concentrated heating  $S_h = 1 \text{ cm}^2$  is shown in Fig. 1. The solution result is a three-dimensional temperature field. As an example, Fig. 3 presents a temperature distribution at the surface of the evaporator body to which the heat load is supplied. The placement of the hot active zone and the cold CC is quite well seen, as well as the profile of "heating spots". Besides, one can see the decreasing of the "heating spot" influence on the evaporator temperature. This influence is demonstrated more clearly in Fig. 4, where the temperatures change on the evaporator wall along the symmetry line is shown. The experimental temperature values, which were registered by two thermocouples installed on the evaporator body are also presented in this figure. One thermocouple was at the centre of the "heating spot", and the other one – at the centre of the CC, as is shown on the scheme included in Fig. 4. One can see that the change of the heating area, first of all, influenced the heat condition of the active zone. In the compensation chamber these changes manifest themselves much more slightly. According to the obtained results (Fig. 5) such a

Table 1. The main parameters of the flat evaporator.

Evaporator	
Total length, mm	80
Width, mm	42
Thickness, mm	7
Case thickness, mm	0.5
CC length, mm	40
Active zone length, mm	32
Vapor removal grooves	
Number	12
Length, mm	32
Diameter, mm	1.8
Heating zone	
Length, mm	30
Width, mm	30
Wick	
Wick length, mm	40
Porosity	0.66
Breakdown radius, $\mu\text{m}$	20

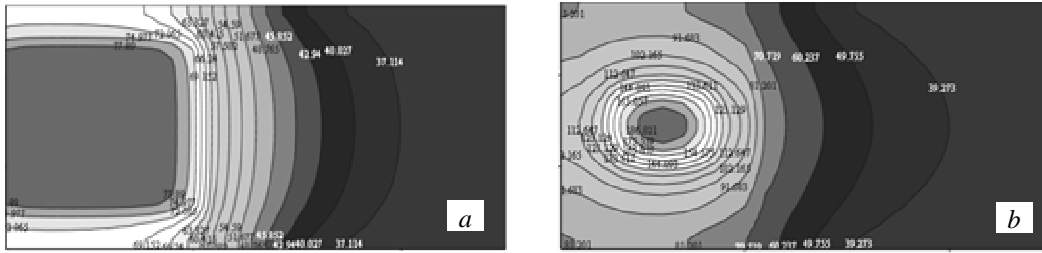


Fig. 3. Temperature field of the evaporator upper surface at a heat load of 590 W: *a* – uniform heating, *b* – concentrated heating

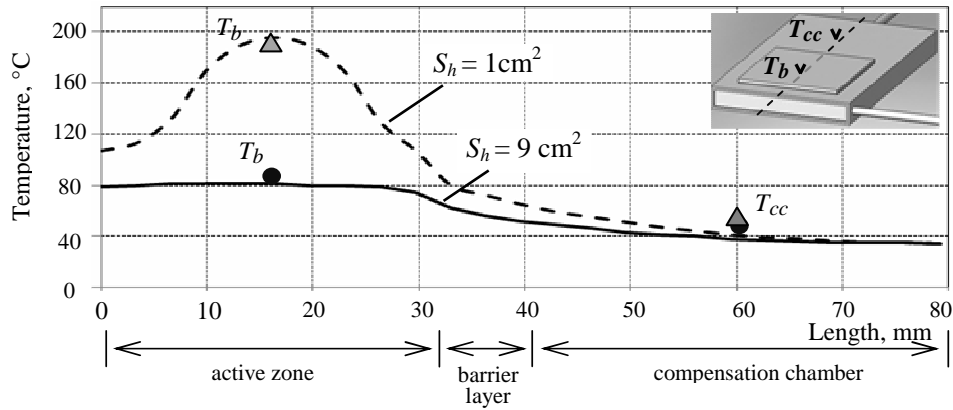


Fig. 4. Temperature profile along the evaporator symmetry line at a heat load of 590 W for concentrated and uniform heating

▲ ● experimental data, —, - - - calculated data.

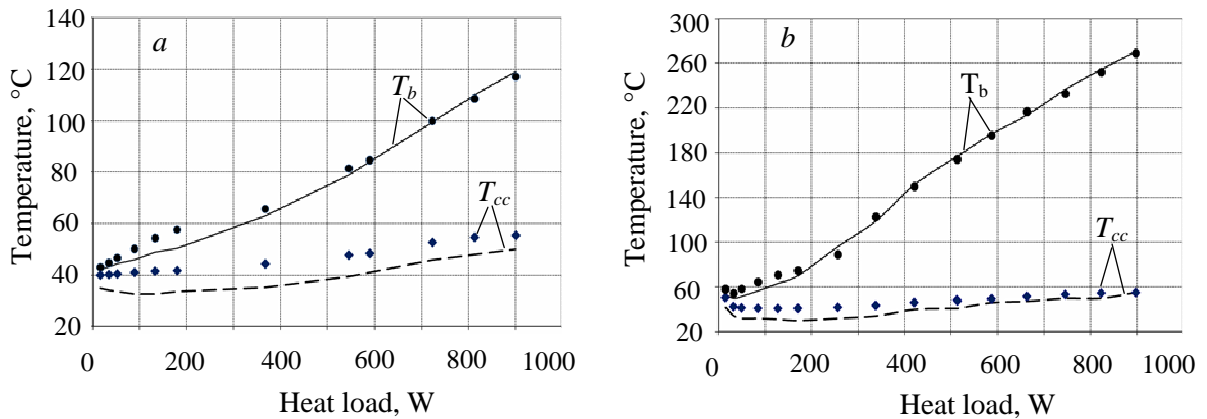


Fig. 5. Comparison of the model prediction and the experimental results for uniform (*a*) and concentrated (*b*) heating

situation is typical for a wide range of heat loads.

It should be noted that a good matching of experimental and calculation results takes place in the area of average and high heat loads. This points to the fact that the proposed model describes adequately heat processes in a flat evaporator and its computation module can be embedded in the integrated procedure of calculation of LHP working characteristics with such a type of an evaporator.

The results have shown that at a distributed heat supply a sufficiently uniform liquid evaporation takes place in the active zone, as is shown in Fig. 6 *a*. In this case such a picture is observed for the whole investigated range of heat loads from 20 to 900 W. It points to the fact that even at high heat loads the wick drying is not observed here. At a concentrated heating heat-transfer processes in the active zone proceed in a different way. The diagrams 6 *b* – 6 *d* demonstrates the transformation of an evaporating front at a heat load

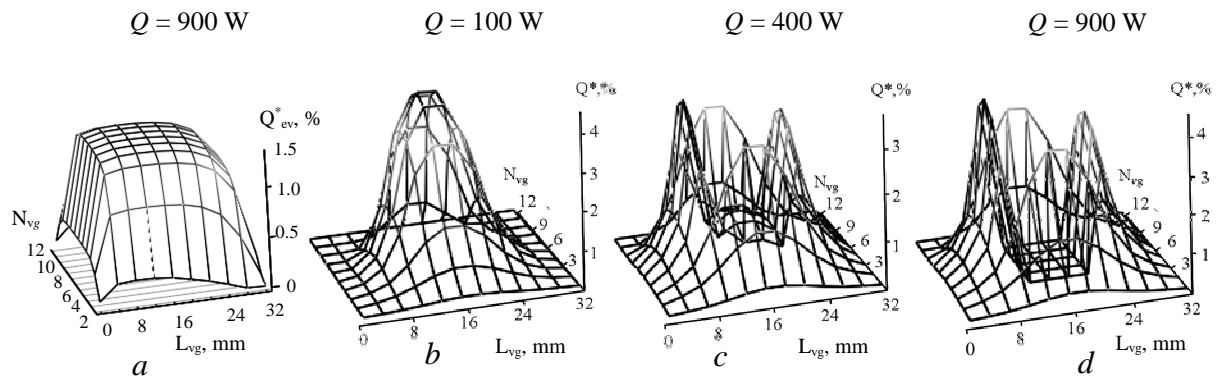


Fig. 6. Evaporation rate in the active zone at uniform (a) and concentrated (b, c, d)

increase. In this way Fig. 6, b shows that at low heat loads there is no wick drying. But at the same time a liquid evaporates intensively in the central part of the active zone. At a heat load of 400 W the evaporation intensity is reduced (Fig. 6 c). This is an indication feature of a partial wick drying under a heating spot. It is also seen that the evaporating front shifted in peripheral regions of the active zone. The further transformation of the evaporating front is presented in Fig. 5 d. At a heat load of 900 W a complete wick drying took place under the heater. There is no evaporation process in the central part of the "heating spot". In this case a significant increase of the evaporator thermal resistance is observed and the LHP operates on a higher temperature level but keeps the operability (see Fig. 5).

## CONCLUSION

A three-dimensional mathematical model has been developed for numerical simulation of a thermal state of the flat evaporator of a copper-water LHP. It takes into account the specific character of a one-sided heat load supply, the peculiarities of the configuration and geometric parameters of the evaporator and all its structural elements. The effect of a uniform and concentrated heat supply to the evaporator on the LHP's working temperature was investigated. Calculations have been made of evaporator temperature fields in the heat load range from 20 to 900 W. Comparative analysis of experimental data and results of calculation has shown that the model adequately describes thermal processes in the evaporator and may be used for analyzing the performance characteristics of LHPs.

The results obtained have demonstrated that with increasing heat load the rate of temperature rise in the heating zone exceeds the rate of its rise in the compensation chamber. The results have also shown that the evaporation processes in the LHP evaporator greatly depend on the heating spot area. At high local superheats a partial drying of a porous structure takes place under a heater, and at the same time the activation of an evaporation process is observed in the peripheral sections of the active zone.

## Acknowledgements

This work was supported by the Russian Foundation for Basic Research, Grant No. 11-08-00369-a.

## NOMENCLATURE

$c_p$	specific heat, J/(kg·K)
$B$	width, m
$D$	diameter, m
$G$	mass flow rate, kg/s;
$k$	thermal conductivity, W/(m·K)
$h$	latent heat of vaporization, J/kg
$Q$	heat load, W
$q$	heat flux, W/m <sup>2</sup>
$L$	length, m
$\dot{m}$	specific mass flow rate, kg/(s·m <sup>2</sup> );
$N$	serial number of vapor removal groove

P	pressure, Pa
$R^*$	specific thermal resistance $m^2$ , K/W
$R_p$	pore radius, m
$\alpha$	heat exchange coefficient, $W/(m^2 \cdot K)$
$\varepsilon$	porosity
$\rho$	density, $kg/m^3$
$\sigma$	surface tension, N/m

#### Subscripts

b	evaporator body (or wall)
cc	compensation chamber
cond	condensator
coll	vapor collector
ev	evaporation
evp	evaporator
ext	external
q	active zone
in	into, inlet
int	internal
l	liquid
tot	total
s	saturation
vl	vapor line
vg	vapor groove
w	wick

#### References

1. Maydanik Yu.F., Fershtater Yu.G. Theoretical basis and classification of loop heat pipes and capillary pumped loops // *Prep. of 10<sup>th</sup> Int. Heat Pipe Conference, Stuttgart*. 1997. Keynote lecture X-7.
2. Ku J. Operating characteristics of loop heat pipes // *SAE Paper 1999-01-2007*. 1999.
3. Chernysheva M.A., Vershinin S.V., Maydanik Yu.F. Operating temperature and distribution of a working fluid in LHP // *Int. J. of Heat and Mass Transfer*, 2007. Vol. 50, Issues 13–14. Pp. 2704–2713.
4. Fershtater Yu.G., Maydanik Yu.F. Analysis of the temperature field of the antigravitational heat pipe's capillary structure // *Eng.-Phys. J.*, 1986. Vol. 51, No. 2. Pp. 203-207 (in Russian).
5. Kiseev V.M., Nouroutdinov V.A., Pogorelov N.P. Analysis of maximal heat transfer capacity of capillary loops // *Prep. of 9<sup>th</sup> Int. Heat Pipe Conference, Albuquerque, USA*, 1995.
6. Maydanik Yu., Vershinin S. Development and investigation of copper-water LHP with high operating characteristics // *Heat Pipe Science and Technology*, 2010. Vol. 1, No.2. Pp. 151–162.
7. Joung W., Yu T., Lee J. Experimental studies on the operating characteristics of a flat bifacial evaporator // *Int. Journal of Heat and Mass Transfer*, 2010. Vol. 52. Pp. 276–285.
8. Maydanik Yu. Miniature loop heat pipes // *Proc. of 13<sup>th</sup> Int. Heat Pipe Conference, Shanghai, China*, 2004. Pp. 23–35.
9. Skripov V.P. *Metastable liquids*. N.Y. Halsted Press. 1974.
10. Altman E.I., Mukminova M.Ia., Smirnov H.F. The loop heat pipe evaporators theoretical analysis // *Proc. of the 12<sup>th</sup> Int. Heat Pipe Conference, Moscow, Russia*, 2002. Pp. 159–164.
11. Figus C., Le Bbray Y., Bories S., Prat M. Heat and mass transfer with phase change in a porous structure partially heated: continuum model and pore network simulations // *Int. Journal of Heat and Mass Transfer*. 1999. Vol. 42. Pp. 2557–2569.
12. Vershinin S.V., Fershtater Yu.G., Maydanik Yu.F. On the effect of contact thermal resistance on the heat exchange during evaporation from fine-pored capillary structures // *High temperature*. 1992. Vol. 30. Pp. 811–817.
13. Anderson D.A., Tannehill J.C., Pletcher R.H. *Computational fluid mechanics and heat transfer*, Vol.1 & 2, Hemisphere Publishing Corporation, New York, 1990.

## RESEARCH AND DEVELOPMENT ON PERFORMANCES OF LARGE-SIZED THERMOELECTRIC MODULE WITH HEAT PIPES

**L. I. Anatyshuk, L. N. Vikhor, Yu. Yu. Rozver**

Institute of Thermoelectricity, 1, Nauky Str., Chernivtsi, 58029, Ukraine  
Tel/Fax: +380372241917, e-mail: anatysh@inst.cv.ua

**B.M. Rassamakin, S.M. Hayrnasov, Yu. Ye. Nikolaienko**

National Technical University of Ukraine "Kiev Polytechnic Institute"  
Heat-and-power Engineering Department,  
6, Politekhnichna Str., Kyiv, 03056, Ukraine  
Tel/Fax: +380444068366, e-mail: office@lab-hp.kiev.ua

### Abstract

There are presented the experimental development results of large-size thermoelectric cooling module with heat pipes, which is capable to provide a thermal stabilization of electronic components of heightened power. The application of such assemblies of large-size modules and flat heat pipes allows us to meet the challenges of heat removal under increased heat flows and space limitedness for conventional heat-removing heat sinks placing. The construction and manufacturing technique of modules are optimized. The parameters analysis and characteristics of modules with heat pipes in different modes and heat removal conditions are performed. It is shown that it is reasonable to reduce heat pipes thermal resistance to the level of 0.05 K/W for the purpose of cooling efficiency increase.

### KEYWORDS

Heat pipe, thermoelectric module.

### INTRODUCTION

Applications of thermoelectric modules (TEM) to engineering of cooling chambers, air conditioning, automobile and domestic refrigerators are further promising. Their well known advantages over the other cooling facilities are as follows: temperature control at the temperature levels, which are below or above the ambient temperature values; possibility of alternation between cooling or heating functions absence of moving parts; noiseless, durable, and reliable operation; etc.). It's preferable for some working applications to use TEM with cold and hot plates of maximal size together with intensified heat transfer to their external sides, thus resulting in heightened cooling coefficient and performance [1–3]. At the same time, a number of design and technological tasks could appear while such TEMs development, and that is the evidence of the actuality of the problem on constructive and technological solution for the large-sized TEM designs.

Integration of several standard single stage TEMs into one unit and placing them between two flat Heat Pipes (HP) is one of the solutions for this problem. Due to the described TEMs design unit, heat transfer from its sides could be considerably intensified, heat source and heat sink areas of the plates and TEMs' radiators expanded.

The report is dealing with results on development of large-sized thermoelectric module (see Fig. 1) and experimental determination of its performances while the operation between the two heat pipes.

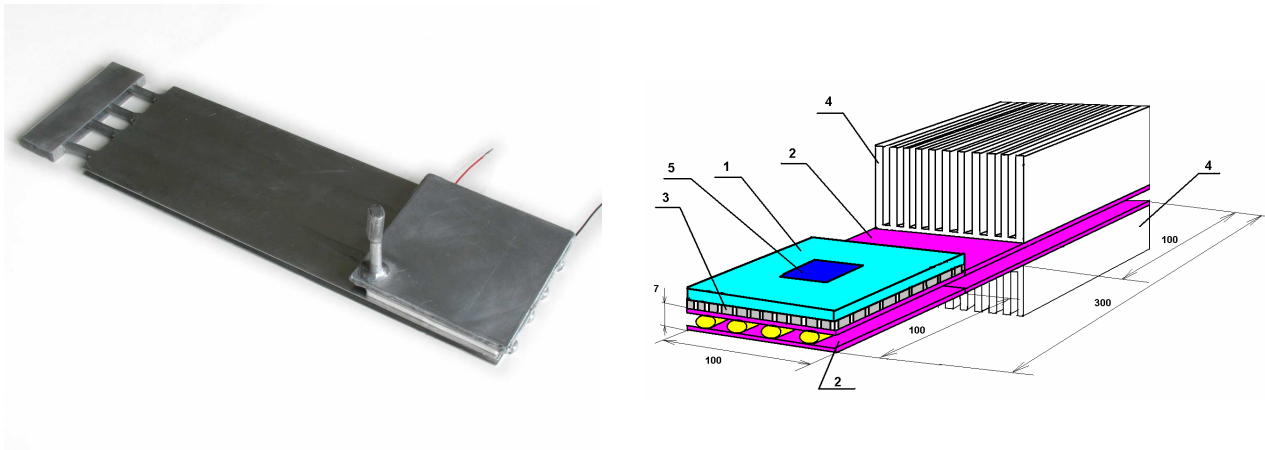


Fig. 1. Large-sized thermoelectric module between two flat heat pipes

## TECHNOLOGY FEATURES OF THE HEAT PIPES AND LARGE-SIZED COOLING MODULES

Two different aluminum flat heat pipes HP (1) and HP (2) have been developed: HP (1) serves as board for the cool sides of the TEMs unit (3) and HP (2) serves as a board for the hot sides of the TEMs unit (3). HP is a vapor chamber with specially grooved evaporation part in order to improve the heat transfer. HP's containers were made of aluminum alloys. HP (1) for cool TEMs' sides was made of AMЦ alloy, filled with acetone as a cooling agent and has 100×100×6 mm dimensions, HP (2) for hot TEMs' sides was made of АД31 alloy, filled with ammonia as a cooling agent and has 100×300×7 mm dimensions. Evaporation surface of HP (2) was of 100×100 mm dimensions and its condensation surface was of 100×200 mm dimensions. At that air and liquid cooled radiators (4) were placed to the part of condensation surface, having 100×100 mm dimensions. Owing to HP (1) application equal temperature values are ensured throughout its surface, wherever the cooled element (5) is placed on it and of whatever shape.

A special large-sized thermoelectric module based on Bi–Te materials have been designed [4] and developed. The module has the following construction:

- the number of thermoelements in a module  $n = 508$  couples of legs;
- the size of thermoelement legs: cross-sectional area 1.8×1.8 mm, leg height 1.5 mm;
- the legs are placed on the area 10×10 cm with the legs spaced apart 0.6 mm and divided into 4 segments with 16 rows, each section having 8 couples of legs;
- the legs in the segments are electrically connected in series, and segments in the module – in parallel.

A standard technology of the module assembly in an elastic matrix was used for large-sized thermoelectric module manufacturing. However, large dimensions of the module cause some peculiarities in the technology of its assembly. In order to overcome possible damaging effects of thermal expansion during thermal cycling the hot ceramic plate is divided into four equal sections with 0.6 – 0.7 mm gaps in between. Such structural solution allows to work with heat fluxes on the hot plane up to 650 – 700 W. In this case, the density of heat fluxes in the evaporation zone of the hot heat pipe must not exceed 12 W/cm<sup>2</sup>. To avoid the effect of condensed moisture on the module operation, it was sealed by means of a sealant with a low thermal conductivity.

To ensure a high-quality thermal contact between the heat pipes and corresponding planes of TEC, an accurate polishing of its surfaces in order to achieve flatness better than 0.01 mm on the module surface, was conducted.

The appearance of the large-sized module, manufactured by the described technology is shown in Fig. 2.

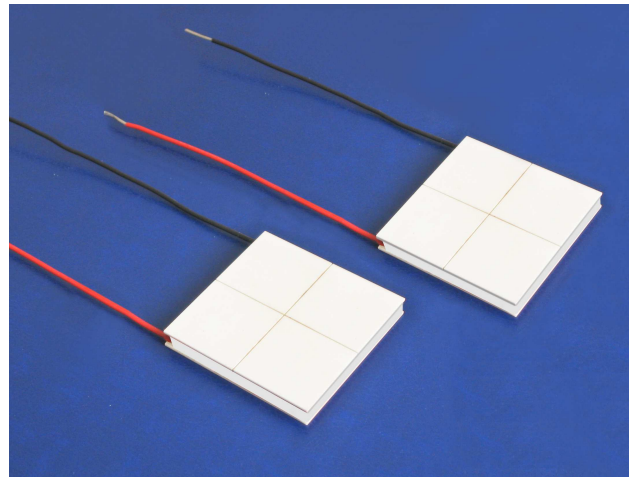


Fig. 2. Appearance of the large-sized thermoelectric cooling modules

The attachment of the heat pipes to the working surface of the module was conducted by using special heat conducting glues and clamping devices. The appearance of the module assembly with the heat pipes is shown in Fig. 1.

### EXPERIMENTAL STUDY OF CHARACTERISTICS OF THE MODULE WITH THE HEAT PIPES

To study the characteristics of the module with the heat pipes a special experimental setup has been developed. The scheme and appearance of the setup are given in Fig. 3.

The measuring equipment allows to study the parameters and characteristics of the module with the heat pipes in a water- and air flow-cooling conditions.

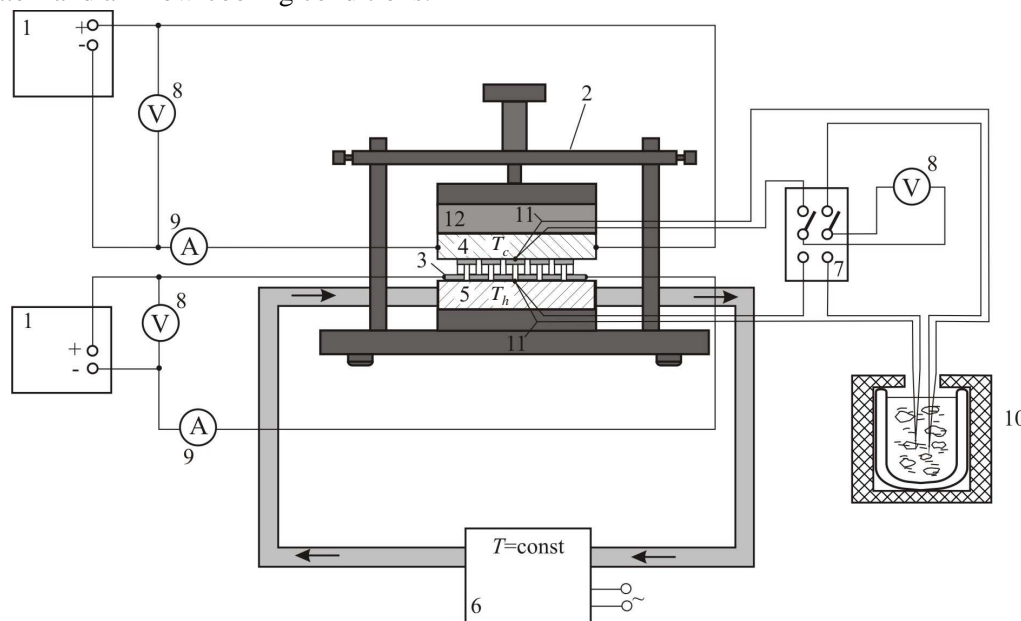


Fig. 3. Experimental setup for investigation of the thermoelectric modules:  
1 – power supply unit, 2 – mechanism for clamping, 3 – investigated cooling module (assembly with heat pipes), 4 – electric heater, 5 – heat exchanger, 6 – thermostat, 7 – switch, 8 – voltmeter, 9 – amperemeter, 10 – thermos (water-ice at 0 °C), 11 – differential thermocouple, 12 – the heat insulating plastic foam

The results of measuring basic characteristics of the large-sized module with the heat pipes during water-cooling of the "hot" heat pipe are shown:

Experimental characteristics of the module with the heat pipes  
at ambient temperature  $T_a = 27\text{ }^\circ\text{C}$

Maximum temperature difference $\Delta T_{\max}$ , K	49
Maximum cooling capacity $Q_{0\max}$ , W	260
Maximum supply current of the module $I_{\max}$ , A	11.5
Maximum voltage $U_{\max}$ , V	64
Operating mode with cooling capacity $Q_0$ , W	150
Supply current of the module $I$ , A	5
Voltage $U$ , V	29.6
Temperature difference $\Delta T$ , K	3
Coefficient of performance $\epsilon$	1.01
Temperature difference on the "cold" heat pipe, K	15
Temperature difference on the "hot" heat pipe, K	7.5

Comparison of the results of measuring the characteristics with their theoretically predicted values showed that the temperature drop on the cold heat pipe is twice as higher than a calculated value [5]. Thus, the experimental value of the thermal resistance of this pipe is set too high, which causes inconsistency of experimental characteristics of the module with the heat pipes and its computational indices [5].

## CONCLUSIONS

The possibility of further production of large-sized TEMs integrated with flat heat pipes was demonstrated by the developed prototypes and tests on their performances.

TEMs of this kind are able to provide thermal regimes for the objects with high heat-evolution level and could be widely applied to air conditioning, cooling of electronic equipment, boxes for medical vaccines, and other special devices.

The problem on heat remove from high thermal flows within the limited space could be solved by means of placing heat sinking radiators on the assemblies of large-sized TEMs combined with flat heat pipes.

It's expedient to work on HP's thermal resistance decrease to 0.05 K/W in order to upgrade further cooling assemblies of large-sized TEMs combined with HPs.

## References

1. Development, manufacturing and study of heat pipes for the cooling system with large-sized thermoelectric module / B.M. Rassamakin, S.M. Hayrnasov, Yu.Ye. Nikolaenko, V.K. Zaripov, Yu.Yu. Rozver // *Proc. of the XI Intern. Scientific and Practical Conf. "Modern Information and Electronic Technologies"*, Odessa, Ukraina. 2010. Vol. II. P. 33. (In Russian).
2. Thermoelectric modules on metal base and devices based on them // *Pribory*. 2002. No. 11. Pp. 16–17. (In Russian).
3. *Pat. RU 60271 U1, Russian Federation*. Thermoelectric modules / L.I. Anatyshuk (UA), Yu.Ye. Nikolaenko, (UA), A.L. Vainer (UA), T.Yu. Nikolaenko, (UA). Application 2005113031/22 of 28.04.2005. Published 10.01.2007, Bull. № 1. (In Russian).
4. Anatyshuk L.I., Vikhor L.N., Nikolaenko Yu.Ye., Rassamakin B.M., Rozver Yu. Yu. Simulation of large-sized thermoelectric cooling module with heat pipes // *J. of Thermoelectricity*. 2010. No. 3. Pp. 67–72.
5. Anatyshuk L.I., Vikhor L.N., Nikolaenko Yu.Ye., Rassamakin B.M., Rozver Yu. Yu. Large-sized thermoelectric cooling module with heat pipes // *J. of Thermoelectricity*. 2011. No. 1. Pp. 50–55.

## STEADY-STATE MODELING ANALYSIS OF CAPILLARY PUMPED LOOP FOR TERRESTRIAL APPLICATION

**L. Lachassagne, V. Ayel, C. Romestant, Y. Bertin**

Institut Pprime, Département Fluide, Thermique et Combustion, UPR 3346

1, avenue Clément Ader 86961 Futuroscope Chasseneuil Cedex, France

Phone: +33 5 49 49 81 32; Fax: +33 5 49 49 81 01

E-mail address: laurent.lachassagne@ensma.fr

### Abstract

The purpose of this study is to give an efficient steady-state modeling tool for Capillary Pumped Loops (CPL) working under gravity field. This modeling uses nodal method characterized by three variables: mass enthalpy, temperature and pressure; and one parameter: vapour quality. Thus, this modeling is divided into three networks (one for each variable) with strong couplings. The experimental setup used for the validation is a "Capillary Pumped Loop for Integrated Power" (CPLIP) filled with ethanol as working fluid. Tests for power applied from 500W up to 4000 W have allowed to validate the model, considering temperatures, pressure drops and mass flow rate as parameters. Some parametric studies are finally presented.

### KEYWORDS

Capillary pumped loop, steady-state modeling, nodal network, phase change, gravity.

### INTRODUCTION

For almost fifty years, Capillary Pumped Loops (CPL) and Loop Heat Pipes (LHP) have been developed and tested for space applications. Both can be divided into three major components: evaporator, where power is applied, condenser, where power is dissipated and reservoir. Two phenomena lead to fluid flow in these devices: mass transfer due to liquid evaporation and capillary pumping induced by the evaporator wick. It is consequently a challenge to adapt these devices and their dedicated modeling to applications in gravity field. Wang et al. [1] gave a good overview of whole modeling works done about CPLs and LHPs since the eighties. From an historical point of view, the first loop heat pipe model has been published by Dolgirev et al. [2] and was an analytical model based on the one-dimensional heat transfer equation in the wick. Since 1978, some modeling work about heat loops has been done to handle physical and mathematical complexity of loops behaviour. For instance, Kaya and Hoang [3] built a steady-state model of LHP based on energy balance equation for the loop. They completed their study with better thermal and hydraulic depicting of two-phase flow. Later, Chuang [4] introduces his own simulation code based on Hoang and Kaya analytical model. This model can predict LHP behaviour in case of adverse but also positive elevations, which was not previously possible. Finally, the last developments in heat loop steady-state modeling come from India with Adoni et al. [5] and France with Launay et al. [6]. Adoni et al. have developed a numerical code with four calculation algorithms using Newton-Raphson method. Their model works particularly in case of hard-fill reservoir and can predict either LHP or CPL steady state. The present study is a modeling approach based on enthalpy, pressure and temperature instead of only pressure and temperature like the major part of works named previously. This approach was presented at the 15<sup>th</sup> IHPC [7] and the present work will expose different parametric studies performed with this model.

### DESCRIPTION OF THE MODEL

The modeling approach of this study combines nodal method and CPL description with enthalpic, hydraulic and thermal networks. The CPL is divided into around 370 nodes which are located for major part in the condenser because of the model sensitivity in this area (Fig. 1). There are almost 100 nodes for the working fluid and the remaining nodes stand for the loop body.

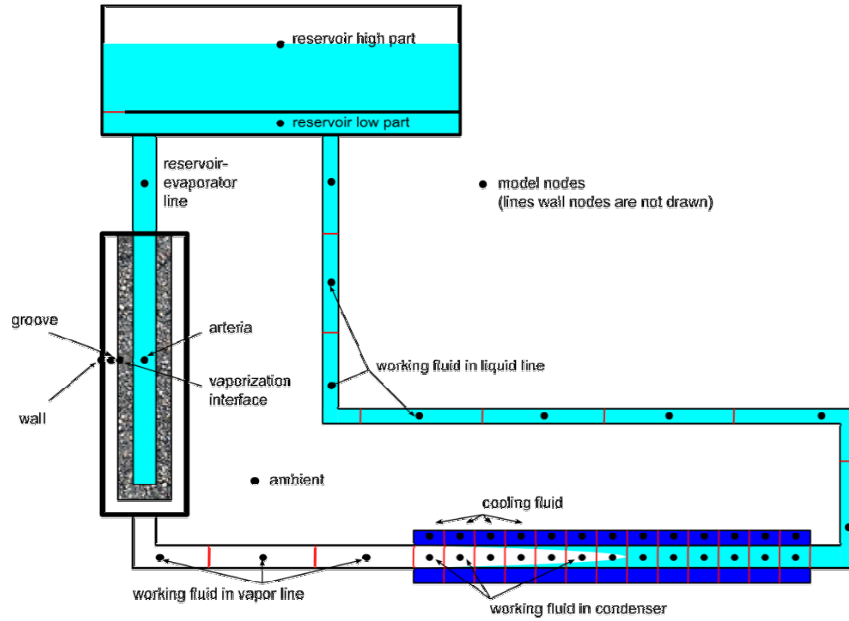


Fig. 1. Schematic view of CPL nodes

Commonly, the modeling approach combines a thermal network, where temperature nodes are calculated, coupled with an hydraulic network where pressure nodes are calculated. These networks are written according to thermal/electrical analogy. But temperature as only variable cannot take into account phase change phenomena. That is why this study introduces mass enthalpy of the node by replacing  $C_p T_i$  by  $h_i(T_i, P_i)$ , which leads to:

$$m_i \frac{dh_i(T_i, P_i)}{dt} = \dot{m}(h_{i-1} - h_i) + J_i, \text{ where } J_i = \sum_j G_{ij}(T_j - T_i) + \sum_k q_k. \quad (1)$$

In eq. (1),  $G_{ij}$  is the thermal conductance between node  $i$  and each adjoining node  $j$ . This conductance can be conductive or convective.  $q_k$  represents every other thermal fluxes. Mass flow rate in the loop  $\dot{m}$  is calculated thanks to the pressure network. Thus a new network is written with mass enthalpy calculation. An example of the three networks can be seen on Fig. 2.  $J_i$  is calculated from the thermal network. For one integration step, mass enthalpy is first calculated in enthalpic network such as pressure in hydraulic network (Figs. 2–3). Then, the temperature  $T = f(h, P)$  is fixed as boundary condition in the thermal network by means of a 2-D table implemented in the program. The new temperature values obtained are then used in pressure and enthalpic networks which lead to new values for mass enthalpy and pressure, etc... After some iterations, the converged values of  $h$ ,  $T$  and  $P$  are computed and the code proceeds to next integration step. Obviously, for steady-state simulations of this study, the left hand side of eq. (1) is null, which simplifies the networks writing as described in following parts. ESACAP software is used for simulations.

### Vapor quality and fluid thermophysical properties calculation

Here, the two-phase fluid is considered everywhere as a homogeneous liquid/vapor mixture. The major advantage of this method lies in the possibility of knowing the value of vapor quality  $x$  for each fluid node (eq. (2)). Thus, the fluid state (liquid, vapor or two-phase) is known in addition of temperature and pressure. Indeed, every node vapor quality is determined for each calculation step with mass enthalpy value:

$$\left\{ \begin{array}{l} x = 0 \text{ if } h \leq h_{liq,sat}, \\ x = \frac{h - h_{liq,sat}}{h_{vap,sat} - h_{liq,sat}} \text{ if } h_{liq,sat} \leq h \leq h_{vap,sat}, \\ x = 1 \text{ if } h \geq h_{vap,sat}. \end{array} \right. \quad (2)$$

The following hypothesis have been considered:

- The fluid physical properties function of mass enthalpy and pressure are defined in 2-D tables.
- Liquid and vapor are supposed incompressible.
- Two-phase fluid mixing is considered as a single phase fluid with adapted physical properties. For example, two-phase fluid density is a combination between liquid and vapor densities depending on vapor quality (eq. (3)). The same expression is used for fluid viscosity and thermal conductivity.

$$1/\rho_{diph} = (1-x)/\rho_{liq} + x/\rho_{vap} . \quad (3)$$

### Modeling of the condenser

The condenser of the CPL presented in the following part is a counter-current heat exchanger divided into 80 nodes for the working fluid. As shown in Fig. 2, each node has representation in enthalpic, thermal and hydraulic network. Thermal network describes the whole heat exchanger. Indeed, each fluid node  $T_i$  is surrounded by a node for inner wall  $T_{wint}$ , a secondary fluid (water-ethylene glycol mixture) node  $T_{seci}$ , a node for outer wall  $T_{wext}$  and finally the ambient temperature node  $T_{ext}$ . Every nodes are linked to each other by conductive ( $G_{cond}$ ) or convective ( $G_{conv}$ ) thermal conductances. In pressure network, conductances of pressure losses ( $GP_{pl}$ ) are functions of the flow regime, laminar or turbulent.

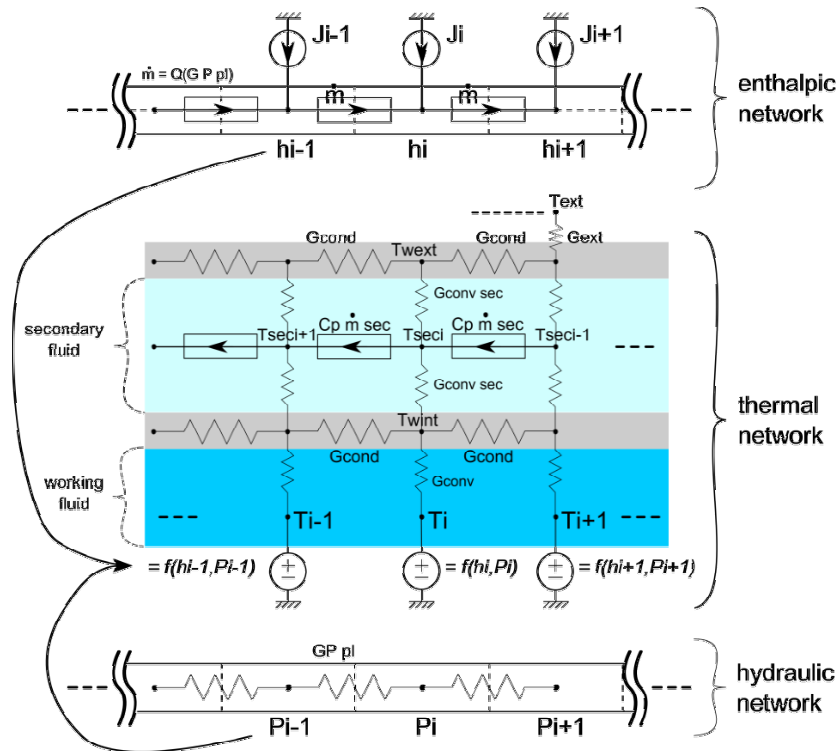


Fig. 2. Condenser networks

In condenser, the working fluid can flow under three phases: vapor, two-phase and liquid. Thus, the conductance  $G_{conv}$  depends on the node vapor quality (2). If  $x = 0$  or  $x = 1$ , the fluid is only liquid or vapor, then the heat transfer coefficient  $h_{conv}$  is only depending on the flow regime with liquid or vapor fluid properties. However, if  $0 \leq x \leq 1$ , there is two-phase flow in the node. The heat transfer coefficient is given by Shah correlation:

$$h_{diph} = 0.023 Re_l^{0.8} Pr_l^{0.4} k_l / D \left[ (1-x^{0.8}) + \frac{3.8 x^{0.76} (1-x)^{0.04}}{Pr_r^{0.38}} \right] . \quad (4)$$

The model also provides the length of the two-phase flow area  $L_{diph}$  in the condenser formed by each node with vapor quality  $x$  included between 0 and 1. Thus, the precision of  $L_{diph}$  computed is of the length of a condenser node.

Notice finally that comparison between modeling and experiment temperature at the condenser outlet has pointed out the necessity to adapt the heat transfer coefficient in subcooled area, due to particular geometry of the condenser presenting several U-bends [7], and weakness of flow patterns knowledge inside condenser.

### Modeling of transport lines

Transport lines modeling is similar to condenser one. Fig. 2 can be applied to vapor and liquid lines with a thermal network simplification. This approach gives possibility for this model to predict condensation also in vapor line or evaporation in liquid line. Moreover, as shown in figure 4 for the experimental loop, the reservoir is located above the condenser. This leads to gravitational pressure losses  $\Delta P_{grav}$  in the liquid line in addition to the frictional ones. A new conductance  $GP_{grav}$  is then added to  $GP_{losses}$  between two nodes  $i$  and  $i+1$  in the pressure network for liquid line only:

$$GP_{grav} = \frac{\dot{m}}{\rho_{liq} g (z_{i+1} - z_i)}. \quad (5)$$

### Modeling of the evaporator

The evaporator part of the model is detailed in Fig. 3. The fluid flowing through the evaporator is divided into three enthalpy nodes, one for the inlet  $h_{art}$ , one for the evaporation area  $h_{evap}$  and one for the grooves  $h_{groove}$ . The enthalpy  $h_{evap}$  is fixed for each iteration at the value of saturated vapor enthalpy as function of  $P_{evaph}$  which is computed in the pressure network.

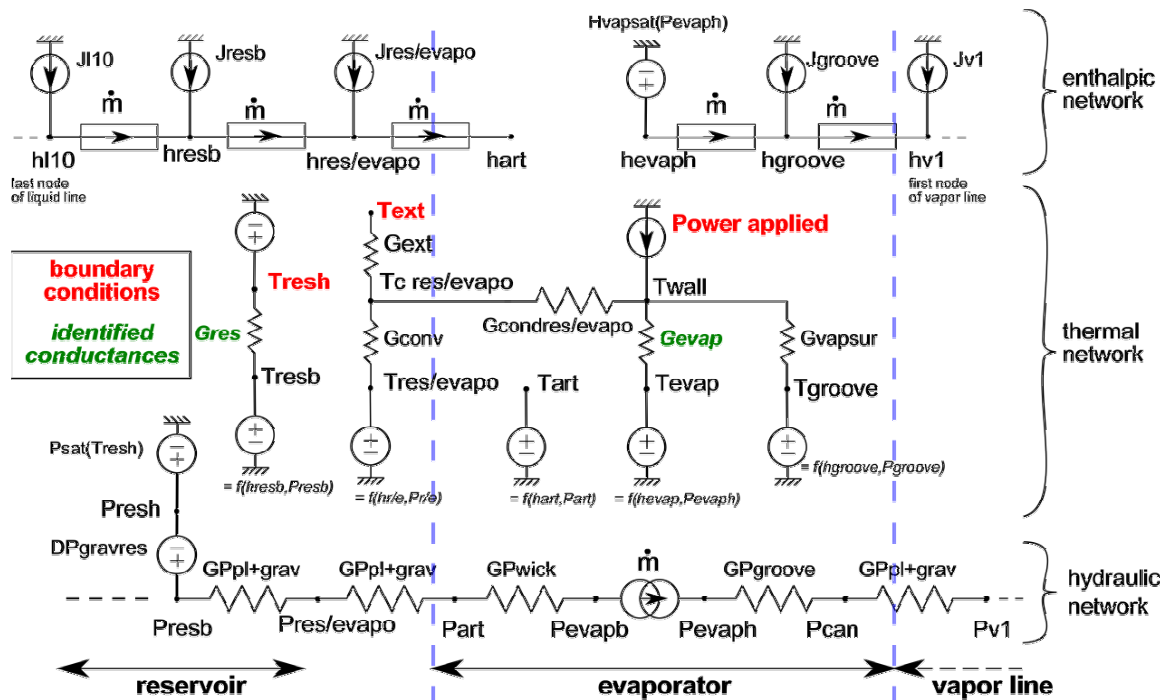


Fig. 3. Reservoir and evaporator networks

The node  $T_{wall}$  standing for evaporator body is linked to the others by two thermal conductances and receives an heating power input  $P$ . Conductance  $G_{evap}$  between wall and evaporation area is very hard to define due to geometrical complexity of the wick and phase change phenomena. That is the reason why this conductance has been experimentally identified as function of heat power applied and  $T_{resh}$ . The conductance  $G_{vapsup}$  stands for vapor superheating in grooves due to convective heat transfer. The mass flow rate  $\dot{m}$  is fixed in the hydraulic network with a current source between nodes  $P_{evapb}$  and  $P_{evaph}$ . Its value, given by eq.

(6), depends on the heat power of evaporation passing through conductance  $G_{evap}$  and of the heat power carried by sensible heat in the porous media.

$$\dot{m} = \frac{Q(G_{evap})}{h_{lv} + Cp(T_{evap} - T_{in})} \quad (6)$$

Pressure difference ( $P_{evaph} - P_{evapb}$ ) is also calculated. The model then provides the capillary pressure drop at the evaporation interface. This value can be compared with the maximal capillary pressure drop to determine if the evaporation interface get through the wick.

### Modeling of the reservoir

The CPL reservoir is divided into two nodes for the model (Figs. 1 and 3). The node “resb”, including the lower part of the reservoir, is supposed to be completely filled with liquid for each working point. The node “resh”, including the high part of the reservoir, is filled with two-phase fluid for each working point. These two conditions are verified by the loop mass filling. During tests, temperature of the reservoir higher part has been controlled by a PID regulator and set equal to a setpoint value  $T_{con}$ . In the model,  $T_{resh}$  is then consequently fixed at  $T_{con}$  in the thermal network. Thus, in hydraulic network,  $P_{resh} = P_{sat}(T_{con})$  is also fixed. Pressure in lower part of the reservoir  $P_{resb}$  depends on  $P_{resh}$  considering the gravity pressure drop due to liquid height in the reservoir. This height is given by a table function of liquid volume in the higher part of the reservoir. This table is an input for the model and takes into account the reservoir geometry. The mass balance in the loop is used to determine vapor volume fraction  $\alpha$  and then liquid volume in the higher part of the reservoir. In the model, mass is calculated for each fluid node depending on vapor quality  $x$ , two-phase fluid density and node volume. A thermal conductance  $G_{res}$  between the two parts of the reservoir is fitted with experimental results by ensuring heat balance in the reservoir. The node “resb” is then linked between two liquid line nodes in enthalpic, thermal and hydraulics networks.

### EXPERIMENTAL SETUP

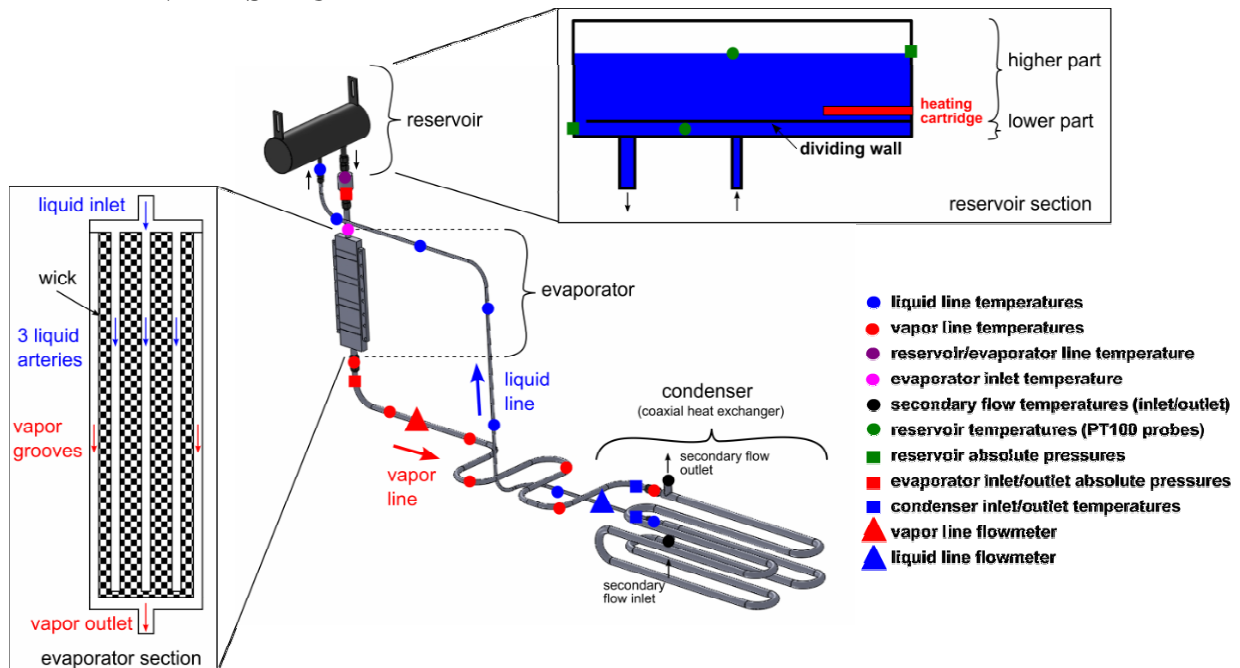


Fig. 4. Schematic view of the CPLIP

An experimental “capillary pumped loop for integrated power” (CPLIP) has been developed by EHP society -based in Belgium- for cooling high dissipative power electronics. The test-bench used for model validation has been presented elsewhere in [8]. It looks like a classical CPL with the separated reservoir, the

evaporator and the condenser (Fig. 4). However, here, the liquid flows through the lower part of the reservoir, situated above the evaporator, before entering this latter. As mentioned above, the diphasic part of the reservoir is controlled thanks to a PID regulator and is instrumented by a platinum thermal sensor and a GE druck PDCR3500 pressure sensor allowing verifying the saturated state  $P_{resh} = P_{sat}(T_{con})$ . It is separated from the lower part of the reservoir by a stainless steel plate. Except for the evaporator, the whole loop is made of stainless steel and the working fluid is ethanol.

The condenser of the test-bench is a 5 m long counter-current heat exchanger where ethanol flows in the inner tube (12 mm inner diameter) and the temperature controlled water/ethylen glycol mixture, cooled by a cryostat, flows in the external annular channel (between 14 mm and 17.3 mm diameters). The liquid -and vapor- lines are 1.92 -and 1.94 m- long with 6 -and 12 mm- inner diameters, respectively. Several T-type thermocouples of 0.1 mm diameter instrument different locations along the loop (liquid and vapor lines, reservoir, secondary fluid at the ends of the condenser, reservoir-evaporator line...).

The evaporator dimensions are of  $320 \times 81 \times 20 \text{ mm}^3$  and it includes a nickel porous wick. Sixteen cartridge heaters (of maximal power 6 kW) have been inserted in eight copper blocks, situated on one side of the evaporator. Finally, 32 T-type thermocouples of 0.5 mm diameter have been inserted between the copper blocks and the evaporator external body.

## MODEL VALIDATION

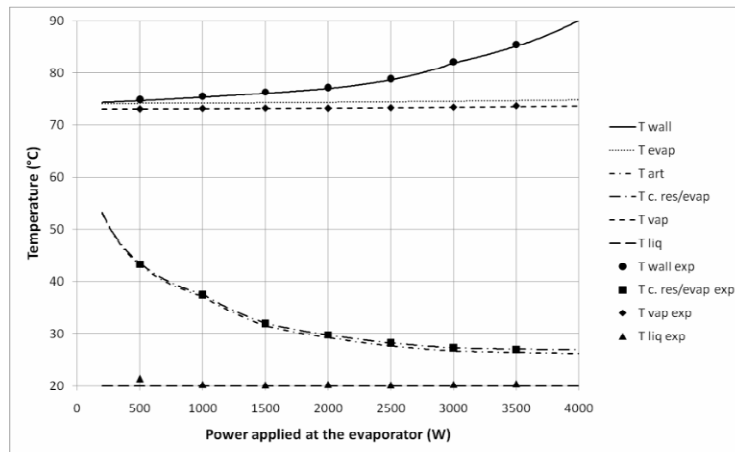


Fig. 5. Thermal validation of the model (reservoir 73 °C and condenser 20 °C)

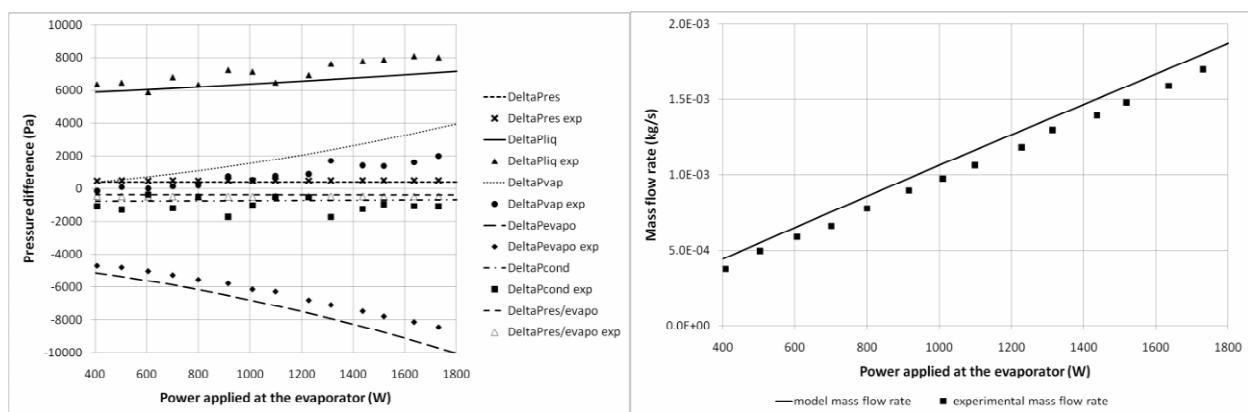


Fig. 6. Hydraulic validation of the model (reservoir 73 °C and condenser 20 °C)

The model has been validated by comparison with four experiments done with condenser secondary inlet temperatures of 5, 20, 30 and 40 °C. Heat power applied at the evaporator goes from 500 up to 4000 W for thermal validation and from 400 to 1800 W for hydraulic validation. Indeed, the insertion of flowmeters on the test-bench for hydraulic measurements has created additional pressures losses leading to a maximal heat

power decrease. Notice that the two thermal conductances *Gres* and *Gevap*, appearing in italic on Fig. 3, still need to be identified empirically for the tested heat power applied, as shown previously in [7]. Fig. 5 shows good agreement between modeling and experimental temperatures for the test with 20 °C at condenser. Same conclusion can be made for the three other secondary fluid temperatures tested.

Concerning the hydraulic CPLIP operation, Fig. 6 gathers the comparison between modeling and experiments for liquid mass flow rate and pressure differences in the CPLIP. The slight difference between measured mass flow rate on liquid line (Fig. 4) and calculated one is due to heat losses from evaporator and heating device to ambient (80 W measured for 1000 W applied at the evaporator). This model also predicts accurately pressure losses inside each loop component, except for vapor line, where pressure losses are overestimated. Note that some instabilities also appears at steady-state concerning condenser pressure losses. Finally, one can assume this model validated for thermal and hydraulic steady-state operation of the CPLIP.

## SENSITIVITY STUDY

Starting from this modeling approach, a sensitivity study to some critical design parameters has then been performed. The influence of these parameters on the evaporator wall temperature and on the capillary pressure drop are gathered in Table 1.

Table 1. Steady-state sensitivity study to some design parameters of the CPLIP

Parameter	Range	Influence on $T_{wall}$	Influence on $\Delta P_{cap,max}$ ( $\Delta P_{cap,max} \approx 10500$ pa)
Condenser position	[0 ; 0.6] (m)	up to 1.5°C $z_c \uparrow \rightarrow T_{wall} \downarrow$	up to 38% $\Delta P_{cap,max}$ $z_c \uparrow \rightarrow \Delta P_{cap} \downarrow$
Liquid line diameter < 10 mm > 10 mm	[4 ; 14] (mm)	negligible negligible	up to 20% $\Delta P_{cap,max}$ $d_{liq} \uparrow \rightarrow \Delta P_{cap} \downarrow$ negligible
Vapour line diameter < 14 mm > 14 mm	[8 ; 20] (mm)	up to 2.5°C $d_{vap} \uparrow \rightarrow T_{wall} \uparrow$ negligible	up to 95% $\Delta P_{cap,max}$ $d_{vap} \uparrow \rightarrow \Delta P_{cap} \downarrow$ negligible
Liquid line length	[1 ; 11] (m)	negligible	up to 24% $\Delta P_{cap,max}$ $L_{liq} \uparrow \rightarrow \Delta P_{cap} \uparrow$
Vapour line length	[1 ; 11] (m)	up to 2.5°C $L_{vap} \uparrow \rightarrow T_{wall} \uparrow$	up to 66% $\Delta P_{cap,max}$ $L_{vap} \uparrow \rightarrow \Delta P_{cap} \uparrow$
Wick permeability < $5 \times 10^{-13} \text{ m}^2$ > $5 \times 10^{-13} \text{ m}^2$	$[5 \times 10^{-14} ; 5 \times 10^{-11}]$ ( $\text{m}^2$ )	negligible negligible	up to 450% $\Delta P_{cap,max}$ $k \uparrow \rightarrow \Delta P_{cap} \downarrow$ up to 500 Pa
Heat transfer coefficient with ambient	[0 ; 1000] ( $\text{W} \cdot \text{m}^{-2} \cdot \text{K}^{-1}$ )	negligible	up to 7% $\Delta P_{cap,max}$ $h_{ext} \uparrow \rightarrow \Delta P_{cap} \uparrow$
Ambient temperature	[-20 ; 60] (°C)	negligible	up to 2% $\Delta P_{cap,max}$ $T_{ext} \uparrow \rightarrow \Delta P_{cap} \uparrow$
Fluid charge	[0.8 ; 2] (kg)	negligible	negligible

It appears clearly that the model sensitivity to each parameter mostly concerns hydraulic operation of this system. Parameters which impact directly pressure losses inside the loop (like condenser position or line dimensions) have a major influence on the capillary pressure drop. That is the reason why only these parameters, which have a very strong influence on pressure losses, can have a noticeable impact on the evaporator wall temperature due to thermo-hydraulic coupling linked to the conductance *Gevap*. Notice the particular case of porous wick permeability which has the greatest influence on capillary pressure drop but no influence on evaporator wall temperature. Indeed, at steady-state, capillary pressure drop will adapt (meniscus curve) to the amount of pressure losses between evaporator outlet and reservoir (reference point of the cycle) whatever the pressure difference between reservoir and vaporization interface is. This sensitivity study confirms that CPLIP operation is mastered by hydraulic couplings between the reservoir reference and other loop components, at least at steady-state.

## CONCLUSION

This study presents a steady-state model of capillary pumped loop taking gravity field into account. This model has been validated by a CPLIP experimental setup with ethanol as working fluid. At steady-state, temperatures are well predicted for the whole loop, such as mass flow rate and almost all components pressure differences. Some parametric studies has then been performed for steady-state operation, showing the importance of thermo-hydraulic couplings inside the CPLIP aimed at power electronics temperature regulation. Finally, in spite of two thermal conductances still to be identified by experiments and a lack of knowledge about condenser flow, we assume that this model has proven an efficient first design tool for the whole loop system.

## NOMENCLATURE

<i>Latin notations</i>		<i>q</i>	heat flux	(W)	<i>evapb</i>	below meniscus
$C_p$	heat mass ( $\text{J}\cdot\text{kg}^{-1}\text{K}^{-1}$ )	$Q$	branch flux	(W)	<i>evaph</i>	above meniscus
$D$	line diameter (m)	$Re$	Reynolds number		<i>grav</i>	gravity
$G$	conductance ( $\text{W}\cdot\text{K}^{-1}$ )	$T$	temperature (K)		<i>in</i>	inlet
$g$	gravity constant ( $\text{N}\cdot\text{kg}^{-1}$ )	$x$	vapor quality		$i,j,k$	nodes
$h_{lv}$	latent heat ( $\text{J}\cdot\text{kg}^{-1}$ )	$z$	node height (m)		$l,liq$	liquid
$h$	enthalpy ( $\text{J}\cdot\text{kg}^{-1}$ )	<i>Greek notations</i>			<i>lam</i>	laminar
$h$	heat transfer ( $\text{W}\cdot\text{m}^{-2}\text{K}^{-1}$ )	$\Delta$	difference		<i>res</i>	reservoir
$J$	node source (W)	$\rho$	density ( $\text{kg}\cdot\text{m}^{-3}$ )		<i>resb</i>	reservoir low part
$k$	Shah constant	<i>Subscripts</i>			<i>resh</i>	reservoir high part
$m$	mass (kg)	<i>con</i>	consign		<i>sat</i>	saturation
$\dot{m}$	mass flow rate ( $\text{kg}\cdot\text{s}^{-1}$ )	<i>cond</i>	condenser		<i>vap</i>	vapor
$P$	pressure (Pa)	<i>conv</i>	convection		<i>vapsup</i>	superheated vapor
$p_r$	critical pressure	<i>diph</i>	two-phase		<i>wall</i>	evaporator wall
$Pr$	Prandtl number	<i>evap</i>	evaporator			

## Acknowledgements

Our acknowledgements go to "Institut PPRIME" which has hosted this work in collaboration with PSA Peugeot-Citroën society among the sponsoring european project "Hiceps" (Highly integrated combustion electric propulsion system, <http://www.hi-ceps.eu/>). Our thanks also go to EHP society.

## References

1. Wang G., Mishkinis D., Nikanpour D. Capillary heat loop technology: Space applications and recent canadian activities // *Applied thermal engineering*. 2008. Vol. 28. Pp. 284–303.
2. Dolgirev Y., Gerasimov Y., Maidanik Y., Kiseev V. Calculation of a heat pipe with separate channels for vapour and liquid // *J. Eng. Phys. Thermophys.* 1978. Vol. 34. Pp. 988–994.
3. Kaya T., Hoang T.T. Mathematical modeling of loop heat pipes and experimental validation // *J. of Thermophysics and Heat Transfer*. 1999. Vol. 13. Pp. 314–320.
4. Chuang P.Y.A. *An improved steady-state model of loop heat pipes based on experimental and theoretical analyses* // PhD thesis, The Pennsylvania State University, 2003.
5. Adoni A., Ambirajan A., Jasvanth V., Kumar D. Thermohydraulic modeling of capillary pumped loop and loop heat pipe // *J. of Thermophysics and Heat Transfer*. 2007. Vol. 21. Pp. 410–421.
6. Launay S. Sartre V., Bonjour J. Analytical model for characterization of loop heat pipes // *J. of Thermophysics and Heat Transfer*. 2008. Vol. 22. Pp. 623–631.
7. Lachassagne L., Ayel V., Romestant C., Bertin Y. Steady-state modeling of capillary pumped loop for terrestrial application // *Proc. of 15th Intern. Heat Pipe Conf. (IHPC), Clemson, USA, 2010*.
8. Lachassagne L. *Développement expérimental et modélisation numérique d'une boucle diphasique en environnement gravitaire: application au refroidissement de composants d'électronique de puissance en contexte automobile* // PhD thesis, Ecole Nationale Supérieure de Mécanique et d'Aérotechnique, 2010.

## HEAT TRANSFER OF TWO-INTERACTING MICROJETS

**Jarosław Mikielawicz**

Institute of Fluid-Flow Machinery, Polish Academy of Science,  
80-952 Gdańsk, ul. Fiszerka 14, Poland  
Tel. +48 58 341 12 71, Fax: +48 58 341 61 44, email: jarekm@imp.gda.pl

**Dariusz Mikielawicz, Tomasz Muszyński**

Gdansk University of Technology, Faculty of Mechanical Engineering,  
80-233 Gdańsk, ul. Narutowicza 11/12, Poland  
Tel. +48 58 347 2254, Fax: +48 58 347 2816, e-mail: Dariusz.Mikielawicz@pg.gda.pl

### Abstract

The present paper paid particular attention to the flow and heat transfer performance for two microjets impinging upon the heated surface by means of experimental investigations. It has been demonstrated from the present study that the heat transfer performance for an array of the micro jets impinging onto the heated surface can be optimized with respect to the distance between the jets resulting in attenuation or augmentation in the impingement region, respectively, as compared with that onto the single one. The theoretical model enabling such calculation has also been postulated.

### KEYWORDS

Microjets, jet interaction, heat transfer.

### INTRODUCTION

In many industrial applications there are processes which require high heat fluxes removal. In addition there is also a demand for precise temperature control. Thermal management is in particular a constrain in cutting edge technologies. Development in every branch of industry is restrained due to problems with heat removal. Traditional methods of heat removal, like immersion cooling, are not only not effective enough but also to expensive. In some applications jet cooling is used, for example in steel and glass industry air jets are scrutinized to temper product after rolling. Recently in order to meet actual demands in microelectronics jet cooling has been applied.

Many work has been made in case of a single axisymmetric impinging jets. Experimental investigations of flow characteristics of confined and free jets were done by Garimella et al. [1]. Flow field was characterized to be highly dependent on nozzle geometry (nozzle length, diameter and height above impinged surface). Also dependence on Reynolds and Prandtl numbers was shown. Also many publications were devoted to examine heat distribution on cooled surface. Stagnation point Nusselt number was shown to be inversely proportional to jet diameter Mikielawicz et al. [2, 3].

There are many publications on impingement heat transfer of macroscale size jet arrays. Macroscale jets have been studied [4–10] with a variety of fluids and flow schemes and have been used to cool turbine blades and quench metals. Arrays of jets typically maintain a more consistent surface temperature and can cool larger areas than a single jet. Jet arrays have been studied [11–15] and require several parameters to define their geometry, which affect the heat transfer performance. Liquid crystal technique was used to visualize isotherms on plate cooled with array of round air jets, Goldstein et al. [4]. Mudawar et al. [5] studied the influence of outflow type from impinged surface, on local heat transfer coefficients. Although many experiments were conducted, only few correlations describing jet array dimensions on heat transfer characteristics were obtained. Results of existing relationships must be experimentally confirmed for smaller jet diameters.

However, one potentially more effective method that has not been extensively studied to date is microjet impingement cooling. Limited microscale studies have recently been conducted [11–15] to investigate the effects of scale on performance, including a potential scale enhancement. A previous study by the authors

[15] has shown that high ( $400,000 \text{ W}/(\text{m}^2\cdot\text{K})$ ) area-averaged heat transfer coefficients and heat fluxes exceeding  $1100 \text{ W}/\text{cm}^2$  can be attained with an array of single-phase water microjets. Boiling can be further used to enhance heat transfer and may allow even higher heat removal rates. Boiling jet studies have been performed [16, 17] but mostly with single jets.

This study presented experimental investigations into interaction of two-jets with the objective to find the most optimal pitch. A simple theoretical model of interaction for two such jets is also presented.

## EXPERIMENTAL SETUP

Present study shows results of steady state heat transfer experiments, conducted for forced convection regime. Fig. 1 shows the schematic diagram of the test section. It consisted of the probe, water supplying system, the measuring devices and DC power supply. Distilled water was fed to the nozzle from a water tank, which also serves as the pressure accumulator. The water pressure in the test section was raised by air compressor. Desired water flow rate was obtained by sustaining the constant pressure of water with a proper use of flow control valve. In order to reduce pressure drop necessary to create a steady laminar jet, nozzle was 2 mm long. Volumetric water flow rate was measured at inlet and outlet from the cooling chamber with a graduated flask. Also water tank was fitted with preliminary water heater, which allows to adjust water jet temperature. The distance between the nozzle exit and the cooled surface was fixed at 25 mm. Fig. 2 shows the cross-section of the probe.

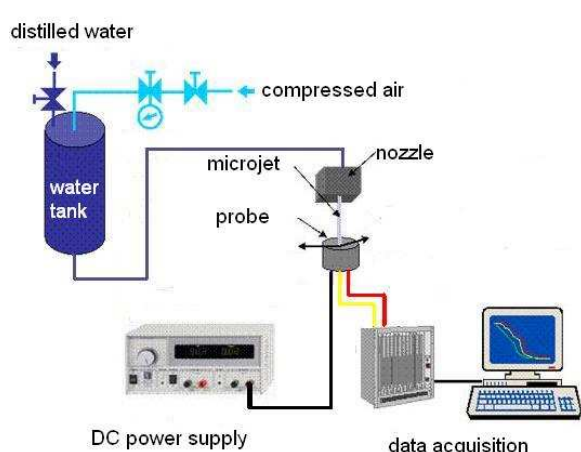


Fig. 1. The schematic diagram of test section

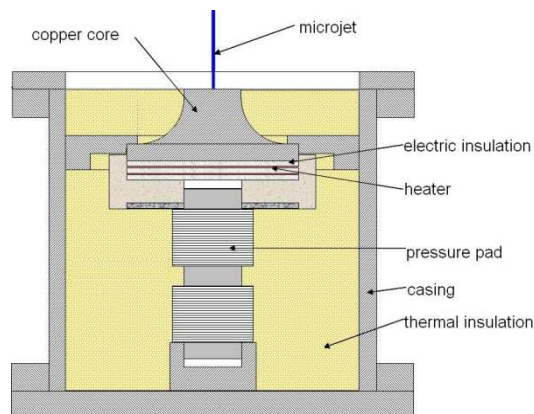


Fig. 2. The cross-section of the probe

The cooled surface was the copper truncated cone with top diameter 10 and 20 mm height. Water impingement surface was silver-plated, in order to prevent high temperature erosion. The radial distribution of surface temperature was determined with the aid of five T-type thermocouples, created from embedding  $50 \mu\text{m}$  thick constantan wire to copper core. Heat is supplied by a kanthal heater mounted at the bottom of a core. The whole set is thermally insulated and placed in the casing. Heater is powered by a DC power supply and the total power input is determined by measuring current intensity and voltage. Additional four K-type thermocouples are attached in copper rod axis. These thermocouples measure axial temperature gradient at the core of a heating block, and control the temperature of a heater. They are connected to a National Instruments data acquisition set. Signal from thermocouples was processed by LabVIEW application. Heater operating power values are precisely controlled and measured. The applied power losses through conduction into the insulation and radiation to the surroundings is accurately calculated and accounted for in all tests. Data are taken from a steady state measuring points in order to exclude heat capacity of the installation.

The jet nozzle module creates two microjets with  $0.107 \text{ mm}$  hydraulic diameter. Construction of module allows to moderate jet-to-jet spacing in range  $0.2 \div 10 \text{ mm}$ . Experimental data were obtained with four different jet spacing, namely:  $0.25, 1, 2, 3 \text{ mm}$ . Measurements were conducted in two series with constant water flow rate  $G = 7393$  and  $11320 \text{ kg}/(\text{m}^2\cdot\text{s})$ .

### THEORETICAL MODEL

In the paper presented is a model of interacting two liquid microjets with the objective to find the optimum distance between them. The optimum distance will result in a uniform heat removal from the surface. Heat transfer coefficients obtained while using single jet impingement may be represented as in Fig. 3. The distribution of heat transfer coefficient is not known in detail, but can be approximated using a simple bell-shape function, polynomial or a linear distribution. In order to simplify the proposed theoretical model, the distribution of heat transfer coefficient will be assumed linear, Fig. 4.

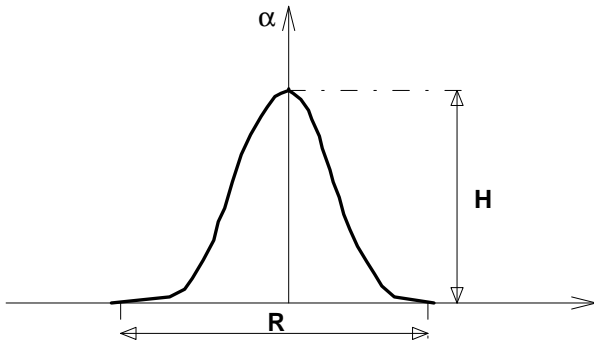


Fig. 3. Heat transfer coefficient distribution in case of single microjet impingement

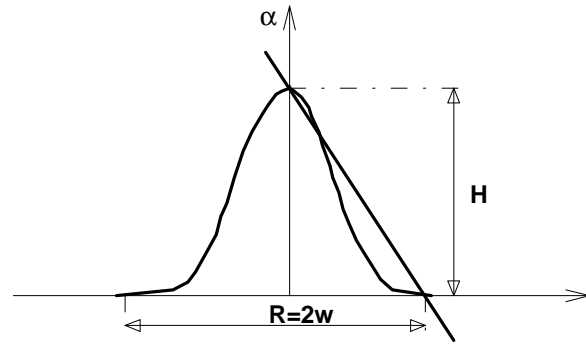


Fig. 4. Linear approximation of HTC on cooled surface

Linearized distribution of heat transfer coefficient has to obey two boundary conditions, namely for stagnation point ( $x = 0$ ) the heat transfer coefficient must reach maximum  $y = H$ , and at some distance from the stagnation point ( $x = w$ , see Fig. 4) the heat transfer coefficient tends to zero. This value can be determined from transformed energy balance equation, as presented below.

The radius of effective cooling  $R$  has been confirmed experimentally in the course of authors own experiment and approximated with the equation resulting from energy balance:

$$R = \sqrt{\frac{\dot{m}(r + c_p \Delta T)}{\pi q}} \quad (1)$$

A straight line can be fitted to the parametric form of the straight line, expressing variation of the heat transfer coefficient, expressed in the form:

$$\frac{y}{H} + \frac{x}{w} = 1. \quad (2)$$

In such case the distribution of heat transfer coefficient takes the form of linear variation from the maximum to zero, Fig. 5. When both sides of the jet are linearized and considered are two jets then the corresponding situation is shown in Fig. 6.

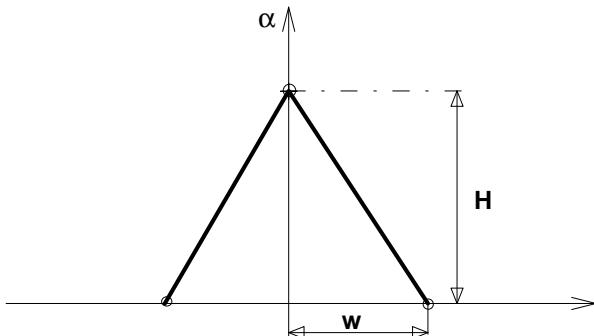


Fig. 5. Approximation of microjet by two straight lines

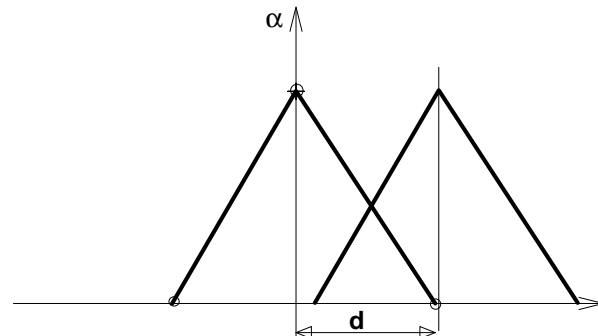


Fig. 6. Approximation of two microjets using the straight lines

Optimum jet-to-jet spacing will be sought using the superposition of interacting heat transfer coefficient distributions. The optimal value of spacing will correspond to a more or less equal distribution of superimposed heat transfer coefficients. The exact processes taking place at the boundary of interacting jets are not known, and definitely are not linear. Authors are aware of that flaw in the assumption. Superimposed heat transfer coefficient can be expressed as:

$$y = y_1 + y_2 = 2H - \frac{H}{w}(2x - d). \quad (3)$$

As we are looking for a solution in which the heat transfer coefficient will be constant over the cooled surface, thus the transformed equation (3) yields for the heat transfer coefficient:

$$H = 2H - \frac{H}{w}(2x - d). \quad (4)$$

Assuming that  $x = d$ , solution of equation (4) shows that the distance between the microjets should be equal to the radius of effective cooling:

$$d = w. \quad (5)$$

Equation (5) represents the simplest solution, for which we obtain the most uniform distribution of heat transfer coefficient on the impinged surface. Of course, approximated distribution of heat transfer coefficient can be performed using more complex functions.

## RESULTS

Experiments were conducted for free water microjets at atmospheric pressure. As the measurements took place under steady state convective heat transfer, for that reason the latent heat of evaporation in equation (2) is omitted. Water inlet temperature was kept constant throughout measurements at the level of  $T_f = 20^\circ\text{C}$ . In such case optimal jet-to-jet spacing depends on wall temperature and applied heat flux.

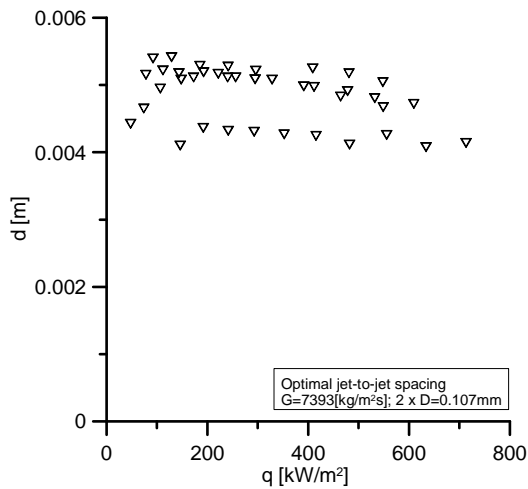


Fig. 7. Jet-to-jet spacing for experimentally obtained wall temperature and heat flux,  $G = 7393$

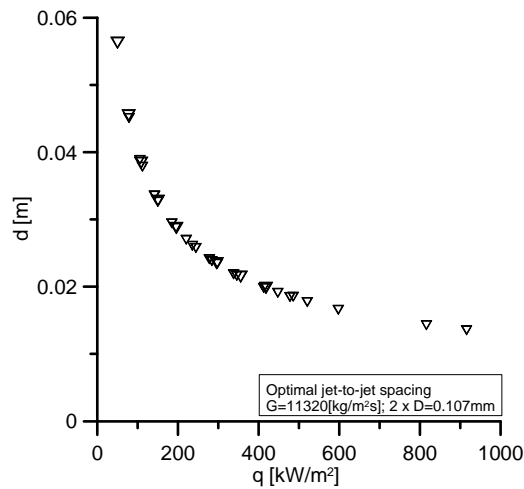


Fig. 8. Jet-to-jet spacing for experimentally obtained wall temperature and heat flux,  $G = 11320$

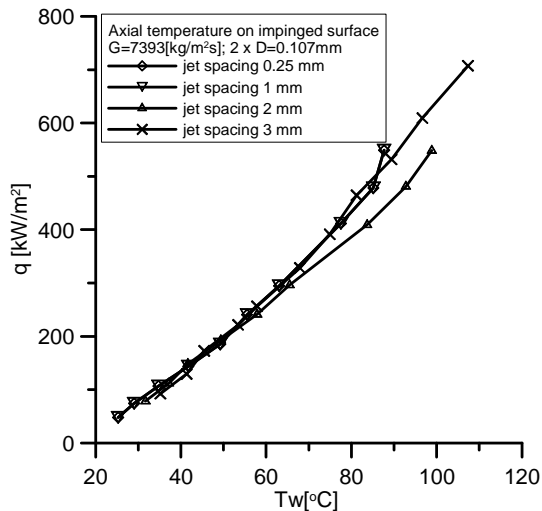


Fig. 9. Wall temperature vs heat flux, for different jet spacing,  $G = 7393$

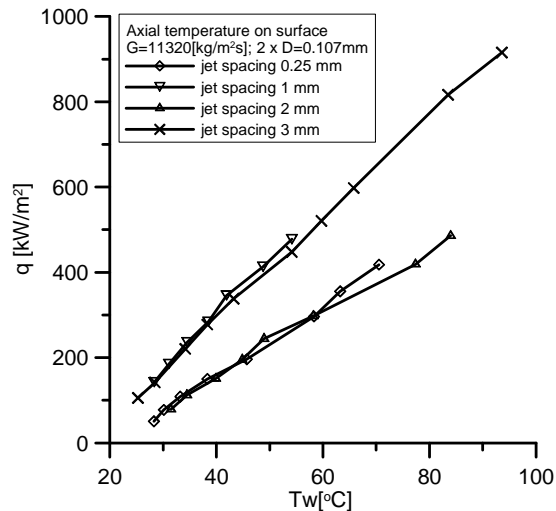


Fig. 10. Wall temperature vs heat flux, for different jet spacing,  $G = 11320$

Solution of eq. (2) for the whole range of experimental data ( $G = 7393\text{kg/m}^2\text{s}$ ) range gives almost a uniform value of radius of the jet coverage of  $d = 5\text{mm}$ . Fig. 7 presents calculated result in function of the heat flux. Results of measurements with water mass velocity  $G = 7393\text{ kg}/(\text{m}^2\text{s})$ , brings no conclusive results. The distributions obtained for several jet spacings almost overlap. Fig. 9 shows no influence between jet spacing and efficiency of cooling.

Different situation is observed in case of higher water mass velocity. Calculated optimal jet spacing tend to decrease asymptotically, with increased heat flux. This trend is shown in fig 10. Increasing heat flux tends to have a smaller impact on radial wall temperature in case of 2mm jet spacing. Temperature obtained in such setup is almost identical with 0.25mm jet spacing where two jets can be considered almost as a one jet of bigger diameter. Difference between series tends to increase with higher heat flux. Calculated jet spacing seems to be overestimated, but obtained tendency yields good agreement.

## CONCLUSIONS

In the paper presented have been theoretical and experimental studies of interacting two impinging microjets. Experimental investigations have been accomplished for two mass velocities in a wide range of heat flux variation. A simple analytical model of two interacting microjets was presented. Analysis of experimental findings indicate that the optimal spacing between jets varies with applied heat flux. The presented theoretical model takes that fact into account. Modifications and further development of the model of jet interaction will take place in course of further work.

## Acknowledgments

First two authors would like to appreciate the funding from a National Project POIG.01.01.02-00-016/08 *Model agroenergy complexes as an example of distributed cogeneration based on a local renewable energy sources*. Third author would like to appreciate the funding from the National Centre for Science research grant N512 455240 in years 2011–2013.

## References

1. Garimella S.V., Rice R.A., Confined and submerged liquid jet impingement heat-transfer // *J. of Heat Transfer*, 1995. Vol. 117. Pp. 871–877.
2. Mikielwicz D., Mikielwicz J., Analytical model of single microjet cooling of electronic equipment, *Proc. of 6<sup>th</sup> Int. ASME Conference ICNMM2008*, Darmstadt, Germany.
3. Mikielwicz D., Muszynski T., Experimental study of heat transfer intensification using microjets // *Int. Symp. on Conv. Heat and Mass Transfer in Sustainable Energy*, Hammamet, Tunisia, 2009.

4. Goldstein R. J., Timmers J. F., Visualisation of heat transfer from arrays of impinging jets // *Int. Journal of Heat Mass Transfer*. Vol. 25. Pp. 1857–1868.
5. Meyer M.T., Mudawar I. Single-phase and two-phase cooling with an array of rectangular jets // *Int. Journal of Heat Mass Transfer*, 2006. Vol. 49. Pp. 17–29.
6. Sung M.K., Mudawar I. Single-phase and two-phase heat transfer characteristics of low temperature hybrid micro-channel/micro-jet impingement cooling module // *Int. Journal of Heat Mass Transfer*. 2008. Vol. 51. Pp. 3882–3895.
7. Viskanta R. *Heat transfer to impinging isothermal gas and flame jets*, *Exp. Thermal Fluid Sci.* 6 (2) (1993) 111–134.
8. Webb B.W., Ma C.-F., *Single-phase liquid jet impingement heat transfer*, *Adv. Heat Transfer* 26 (1995) 105–217.
9. Womac D.J., Ramadhani S., Incropera F.P. Correlating equations for impingement cooling of small heat sources with single circular liquid jets // *J. Heat Transfer*. 1993. 115 (1). Pp. 106–116.
10. Chang C.T., Kojasoy G., Landis F., Downing S., Confined single- and multiple-jet impingement heat transfer – 1. Turbulent submerged liquid jets // *Int. J. Heat Mass Transfer*. 1995. Vol. 38. Pp. 833–842.
11. Robinson A.J., Schnitzler E. An experimental investigation of free and submerged miniature liquid jet array heat transfer // *Exp. Thermal Fluid Sci.* 2007. Vol. 32 (1). Pp. 1–13.
12. San J., Lai M. Optimum jet-to-jet spacing of heat transfer for staggered arrays of impinging air jets // *Int. Journal of Heat Mass Transfer*. 2001. Vol. 44. Pp. 3997–4007.
13. Michna G.J., Browne E.A., Peles Y., Jensen M.K. Single-phase microscale jet stagnation point heat transfer // *J. Heat Transfer*. 2009. 131, 111402.
14. Fabbri M., Dhir V.K. Optimized heat transfer for high power electronic cooling using arrays of microjets // *J. Heat Transfer*. 2005. Vol. 127 (7). Pp. 760–769.
15. Leland J.E., Ponnappan R., Klasing K.S. Experimental investigation of an air microjet array impingement cooling device // *J. Thermophys. Heat Transfer*. 2002. Vol. 16 (2). Pp. 187–192
16. Zhou D.W., Ma C.-F. Local jet impingement boiling heat transfer with R113 // *Int. Journal of Heat Mass Transfer*. 2004. Vol. 40. Pp. 539–549.
17. Omar A.M.T., Hamed M.S., Shoukri M., Modeling of nucleate boiling heat transfer under an impinging free jet // *Int. Journal of Heat and Mass Transfer*. 2009. Vol. 52. Pp. 5557–5566.

## EXPERIMENTAL AND THEORETICAL ANALYSIS OF DRYOUT IN ANNULAR FLOW

**Dariusz Mikielewicz, Michał Gliński, Jan Wajs**

Gdansk University of Technology  
Faculty of Mechanical Engineering  
Narutowicza 11/12, 80-952 Gdansk, Poland  
Tel: (+48) 58 347-22-54, E-mail: dmikiele@pg.gda.pl

### ABSTRACT

In the presented paper the experimental analysis of dryout in the small diameter channels is described. The investigations were carried out in vertical pipes of internal diameter equal to 1.15 mm and 2.3 mm. SES36 and R123 were considered as the test fluids. The modern experimental techniques were applied to record liquid film dryout on the wall, among the others the thermovisual camera. On the basis of experimental data a general correlation of critical heat flux was proposed. It shows good agreement with the data in the error band of 30%.

### KEYWORDS

Dryout, CHF, annular flow, flow boiling.

### INTRODUCTION

The phenomenon of liquid film dryout in an annular flow occurs for the medium and high vapor qualities, when the quite low values of heat flux are conducted to the wall. In the consequence of cooling liquid disappearance on the heated wall the mechanism of heat transfer is being changed. The sudden decrease of heat transfer coefficient and increase of wall temperature can be observed. In dependence on the supplied heat flux the temperature growth may exceed the melting temperature of heat exchanger wall. A burnout of the channel wall and the device failure can occur. Such phenomena are undesirable but may occur for example in boiling water reactors or steam generators, where water is the working medium.

In the case of low-boiling point fluids, so called freons, the film dryout is also observed, however it is not as negative as mentioned previously. It does not lead to very serious consequences, because the burnout temperature is not exceeded. Nevertheless, the heat exchanger becomes not efficient. Such kind of phenomena appear in the cooling and air-conditioning units and heat exchangers used to cool the surface, e.g. electronic chips, micro-channel heat sinks, Qu and Mudawar [1]. In the scientific literature plenty of research works connected with the liquid film dryout phenomena in the annular flow can be found. Mainly they report the investigations carried out in the conventional channels, however during the last years the phenomena occurring in the minichannels becomes the field of interest. Kandlikar [2] defined the minichannels as the channels for which the hydraulic diameter is not higher than 3 mm, for which the flow structures during boiling are different than in the case of conventional channels. It should be emphasized that in the minichannels the heat transfer coefficient is higher, which is connected with the turbulent flow, limited space for vapor bubble growth and also thinner boundary layer.

The analysis of film dryout phenomenon in the annular flow was carried out, Gliński [3]. The modern experimental technique – thermovisual camera was applied in measurements of wall temperature development. It enables fast and precise determination of the location of dryout occurrence on the channel wall. In this paper the results of studies in the channels of 1.15 and 2.3 mm diameter for two working media SES36 and R123 are presented. Experimental investigations were mainly concentrated on an influence of the flow velocity and supplied heat flux on the dryout in the flow, especially on the location of the liquid film dryout on the wall. Postulated also is empirical correlation of critical heat flux was proposed on the basis of experimental data. It is a modification of correlation presented by Katto and Ohno [4].

The main objective of the present study was to put more light into the dryout phenomena in annular flow in small diameter tubes. The additional aim of the Authors was to collect information about two low-boiling working fluids SES36 and R123 during dryout in minichannels ( $D < 3$  mm).

## EXPERIMENTAL INVESTIGATION

Two working media SES36 and R123 were used in the experimental analysis. In the atmospheric pressure SES36 boiling temperature is equal to  $36.7$  °C. This medium is new and from the authors point of view there is a lack of information related to its heat transfer efficiency. In the case of the atmospheric pressure R123 boiling temperature is equal to  $27.6$  °C.

The experiment was carried out on the test section, schematically presented in Fig. 1. In the test section upward flow boiling in smooth silver pipes is accomplished. The tube diameters are  $D = 1.15$  mm and  $2.3$  mm, while the tube length is about  $L = 38$  cm. Analyzed tube was placed in the thermal insulation to limit heat losses to the environment. The heat flux needed for the complete evaporation of medium in the test section was generated by low-voltage, high-current, AC power supply. It enabled to obtain the heat flux density up to  $600$  kW/m<sup>2</sup>. The temperature of medium at the inlet and outlet of test section was measured by thermocouples of K-type, while the pressure by Trafag 8253 manometers, which were controlled by Advantech acquisition system. The temperature field on the outside wall of channel and also location of the liquid film dryout in the flow were determined by the Thermovision A320 thermovisual camera of FlirSystems.

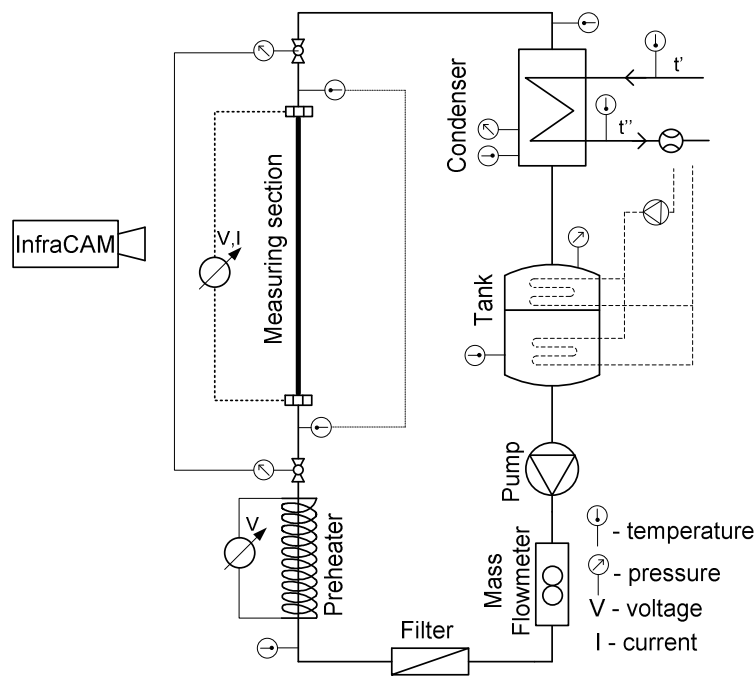


Fig. 1. Scheme of experimental setup

In Table 1 the range of investigated fluid parameters are listed.

Table 1. Range of fluids parameters used in investigations

Fluid	D, mm	G, kg/(m <sup>2</sup> ·s)	Q <sub>cr</sub> , kW/m <sup>2</sup>	P <sub>mean</sub> , bar	T <sub>sat</sub> , °C	x <sub>cr</sub> [-]	L, m
SES 36	1.15	300, 500, 700, 900	20 ÷ 100	1.1 ÷ 2	33 ÷ 70	0.86 ÷ 1.00	0.38
	2.3	300, 500, 700	25 ÷ 150	1.1 ÷ 1.9	37 ÷ 61	0.65 ÷ 1.00	0.375
R123	1.15	300, 500, 700, 900	23 ÷ 107	1.1 ÷ 2.1	23 ÷ 60	0.72 ÷ 1.00	0.385
	2.3	300, 500, 700	65 ÷ 150	1.3 ÷ 2.4	27 ÷ 67	0.75 ÷ 1.00	0.385

## RESULTS

The constant value of mass velocity  $G$  for one cycle of measurements was kept. By using the thermovisual camera the boiling front-line was observed with increasing supplied heat flux. It moved in the opposite direction in the comparison with the direction of medium flow in the channel. Figures 2 and 3 present the critical heat flux  $q_{cr}$  versus the critical length of the channel  $z_{cr}$  for chosen values of mass velocity  $G$  in the channel of 1.15 mm diameter for SES36 and R123 respectively. It can be observed that with increasing value of supplied heat flux the critical length  $z_{cr}$  decreases. It is connected with the rate of liquid evaporation on the film interface. The greater the heat flux is, the more intensive are the phenomena occurring in the annular flow and faster is the complete liquid evaporation. During the liquid film dryout phenomena the additional disturbance is coming from the entrainment and deposition rates of droplets in the flow. Similar tendency can be found in the case of 2.3 mm diameter channel, however it should be emphasized that the higher is velocity of medium, the larger is inclination of the lines.

In Fig. 4 and 5 dependence of the critical vapor quality on the critical heat flux is presented for two considered fluids. When the critical heat flux increases the critical vapor quality decreases with constant value of medium mass flux density.

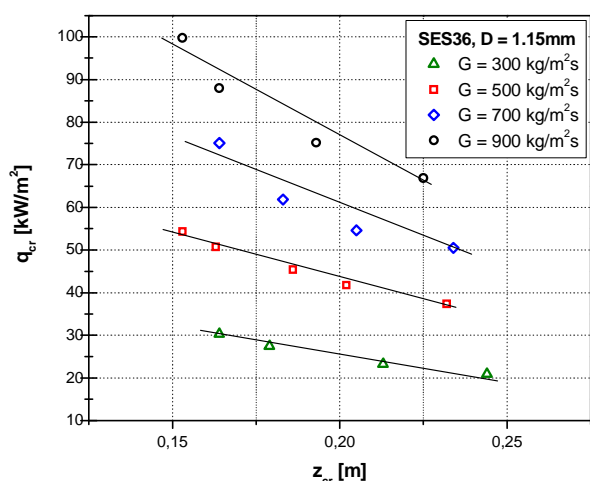


Fig. 2. Critical heat flux versus critical length of liquid film dryout in the channel of  $D = 1.15$  mm diameter for SES36

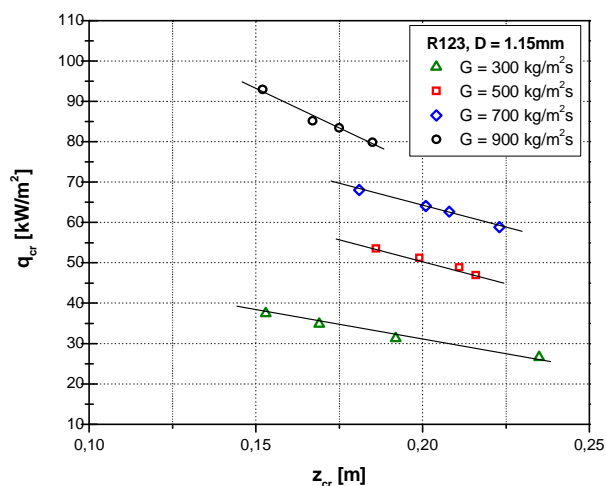


Fig. 3. Critical heat flux versus critical length of liquid film dryout in the channel of  $D = 1.15$  mm diameter for R123

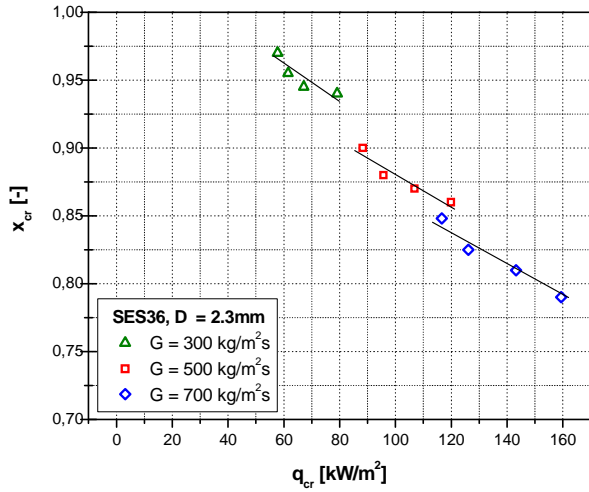


Fig. 4. Critical vapor quality versus critical heat flux in the channel of  $D = 2.3$  mm diameter for SES36

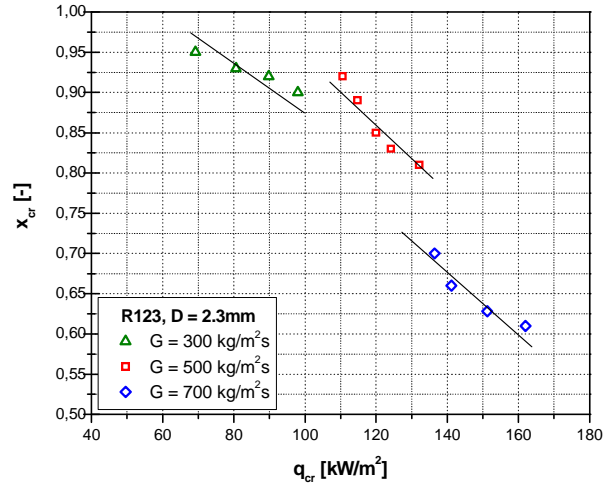


Fig. 5. Critical vapor quality versus critical heat flux in the channel of  $D = 2.3$  mm diameter for R123

The results for both fluids show that tendency and values of vapor quality are qualitatively similar, but they depend also on the medium velocity. The influence of fluid velocity on the critical vapor quality was examined and the results are presented in Fig. 6 and 7. The distinct decrease of critical vapor quality with increase of mass flux density  $G$  is observed. The influence of channel diameter was also considered. It was shown that the higher is the channel diameter the more intensive is decrease of critical vapor quality. It confirms the previous research accomplished by Wojtan and Thome [7] as well as Qi et al. [8].

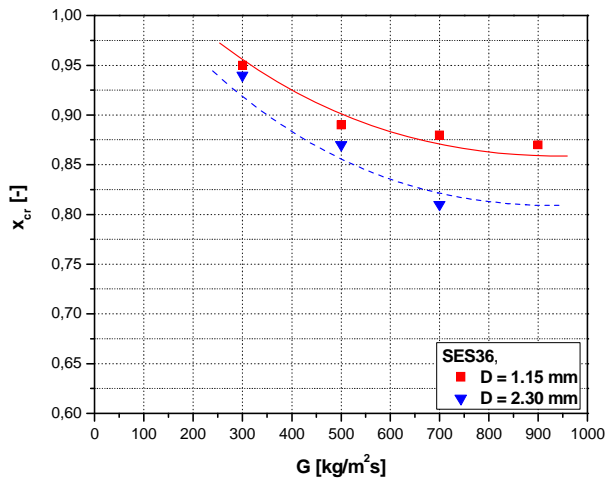


Fig. 6. The critical vapor quality versus the mass flux density for SES36

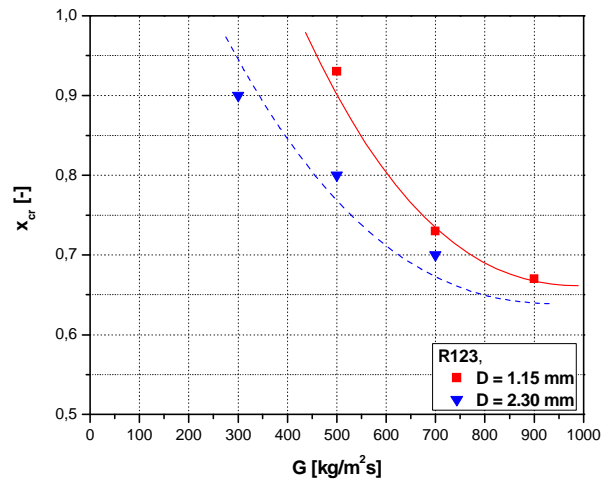


Fig. 7. The critical vapor quality versus the mass flux density for R123

In the basis of experimental results for two media considered in the paper (as well as R134a not reported here) the correlation describing the critical heat flux was proposed.

$$\frac{q_{cr}}{h_{lv}G} = 0.62 \left( \frac{\rho_v}{\rho_l} \right)^{-0.02} (We_{(D)})^{-0.05} \left( \frac{L}{D} \right)^{-1.17} \quad (1)$$

Equation (1) is the function of mass flux density  $G$ , the length of tube  $L$ , the channel diameter  $D$ , the Weber number and the working medium properties. Next the predictions obtained using equation (1) was compared

with the correlation proposed by Zhang et al. [9]. The mean square deviation (Fig. 8) was also calculated. It can be seen that 100% of experimental results are in the error band of  $\pm 30\%$  and 76% of results are in the range of  $\pm 15\%$ .

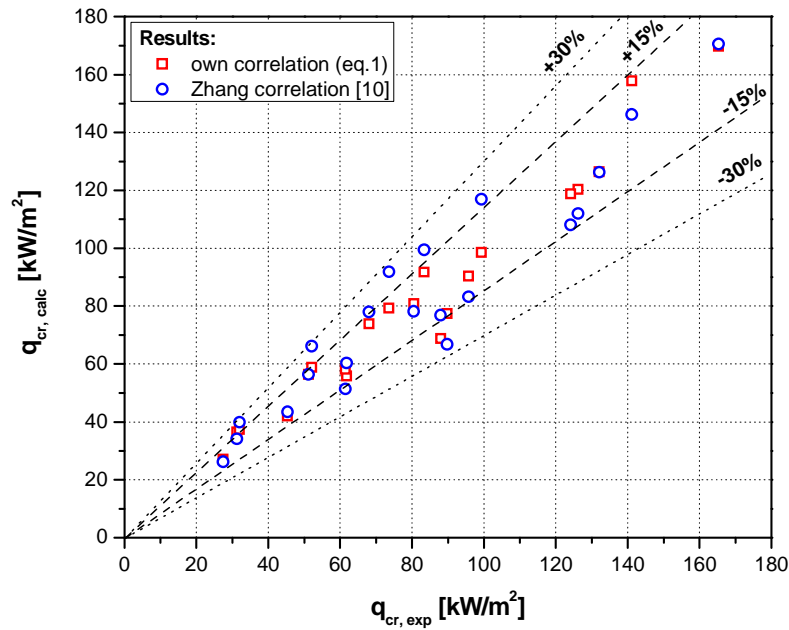


Fig. 8. Errors estimation of correlation (1) and proposed by Zhang et al. [9] in the basis of experimental data for SES36 and R123

## CONCLUSIONS

In this paper the experimental results of liquid film dryout on the channel wall was presented. The channel of two diameters  $D = 1.15$  and  $D = 2.3$  mm and two low-boiling point working fluids SES36 and R123 were investigated. The thermovisual camera was used in the experimental studies to record wall temperature distributions. It enables also precise determination of the boiling crisis location. The influence of supplied heat flux on the critical length and also critical vapor quality was demonstrated. It was observed that with an increase of supplied to the wall heat flux the critical length  $z_{cr}$  decreases and that with an increase of heat flux the critical vapor quality also decreases at constant value of medium mass flux. The influence of flow velocity on the values of critical vapor quality was also estimated and it was found that the critical vapor quality distinctly decreases with an increase in the mass flux density  $G$ . Additionally, the bigger is the channel diameter the more intensive is the decrease in critical vapor quality. In the basis of experimental data base the empirical correlation was proposed. It shows good compatibility in the error band of  $\pm 30\%$  for all results.

## Acknowledgement

The work has been carried out in the frame of the research projects of Ministry of Science and Higher Education No. 3T10B 003 30 and No. N513 3855 33

## References

1. Qu W., Mudawar I. Flow boiling heat transfer in two-phase micro channel heat sinks – II. Annular two-phase flow model // *Int. J. Heat and Mass Transfer*. 2003. Vol. 46. 2772–2784.

2. Kandlikar S. Critical heat flux in subcooled flow boiling – an assessment of current understanding and future directions for research // *Multiphase Science and Technology*. 2001. Vol. 13, No. 3. Pp. 207–232.
3. Gliński M. Badanie i modelowanie krytycznego strumienia ciepła w kanałach o małej średnicy // *PhD Thesis*, Gdańsk University of Technology, Faculty of Mechanical Engineering, Gdańsk, 2010.
4. Katto Y., Ohno H. An improved version of the generalized correlation of critical heat flux for the forced convection boiling in uniformly heated vertical tubes // *Int. J. Heat Mass Transfer*. 1984. Vol. 27. Pp. 1641–1648.
5. Okawa T., Kotani A., Kataoka I., Naito M. Prediction of the critical heat flux in annular regime in various vertical channels // *Nucl. Engng and Design*. 2004. Vol. 229. Pp. 223–236.
6. Mikielwicz D., Wajs J., Gliński M. Modelling of dryout process in annular flow with focus on entrainment // *XXVI National Heat Transfer Conf.*, Palermo, 2008.
7. Wojtan L., Revellin R., Thome J.R. Investigation of critical heat flux in single, uniformly heated microchannels // *Experimental Thermal and Fluid Science*. 2006. Vol. 30, Pp. 765–774.
8. Qi S.L., Zhang P., Wang R.Z., Xu L.X. Flow boiling of liquid nitrogen in micro-tubes: Part II – Heat transfer characteristics and critical heat flux // *Int. J. Heat Mass Transfer*. 2007. Vol. 50. Pp. 5017–5030.
9. Zhang W., Hibiki T., Mishima K., Mi Y. Correlation for critical heat flux for flow boiling of water in mini-channels // *Int. J. Heat Mass Transfer*. 2006. Vol. 49. Pp. 1058–1072.

# **MOISTURE CONTROL IN GAS DIFFUSION LAYER OF POLYMER ELECTROLYTE FUEL CELL: INVESTIGATION OF WATER DISTRIBUTION BY X-RAY RADIOGRAPHY AND OXYGEN DIFFUSIVITY MEASUREMENTS IN A NEW MICROPOROUS MEDIA**

**Yoshio UTAKA**

Division of Systems Research  
Yokohama National University  
Tokiwadai 79-5, Hodogaya-ku, Yokohama-shi  
Kanagawa 240-8501, Japan  
Tel. +81-45-339-3909/ Fax. +81-45-339-3909  
E-mail: utaka@ynu.ac.jp

**Ikunori HIROSE**

Corporate Monozukuri Innovation Center  
Olympus Corporation  
2-3, Kuboyama-cho, Hachioji-shi  
Tokyo 192-8512, Japan  
Tel.042-642-2642 /Fax.042-642-1044  
E-mail: ikunori\_hirose@ot.olympus.co.jp

**Yutaka TASAKI**

Advanced Materials Laboratory  
Nissan Research Center  
1, Natsushima-cho, Yokosuka-shi  
Kanagawa 237-8523, Japan  
Tel. +81-46-867-5225/ Fax. +81-46-865-5796  
E-mail: y-tasaki@mail.nissan.co.jp

## **Abstract**

The mass transfer characteristics of the gas diffusion layer (GDL) are closely related to the performance of polymer electrolyte fuel cells. This study investigates the configuration of a new GDL in which two porous media with different wettabilities are alternately arranged (hybrid GDL). The oxygen diffusivity characteristics with respect to water content (saturation) were measured using an experimental system that employs a galvanic oxygen sensor as an oxygen absorber. Furthermore, X-ray radiography was used to observe the internal water distribution in microporous media for GDL to elucidate the enhancement mechanisms of oxygen diffusivity of the new microporous media. It was possible to distinguish between voids and water in microporous media by using X-ray computer tomography. In addition, the water distributions in the new microporous media were visualized and the mechanisms for the high oxygen diffusivity of the hybrid structure of microporous media were clarified.

## **KEYWORDS**

Mass Transfer, Oxygen Diffusivity, Microporous Media, Wettability, Galvanic Battery, Gas Diffusion Layer X-Ray Radiography, Polymer Electrolyte Fuel Cell.

## **INTRODUCTION**

Polymer electrolyte fuel cells (PEFCs) are expected to be used as power sources for vehicles and as electric power supplies for domestic cogeneration systems because they can realize high efficiencies and have low environmental loads. Figure 1 shows a schematic diagram of the structure of a commonly used PEFC. The inner structure of a cell is called a membrane electrode assembly; it consists of two sets of a

catalyst layer (CL) and a gas diffusion layer (GDL), which are attached to both sides of an ion-exchange polymer electrolyte membrane (PEM) that is used as an electrolyte. Reduction, in which water is generated from oxygen and protons ( $H^+$ ), occurs on the anode side, while oxidation, in which hydrogen discharges electrons, occurs on the cathode side. The GDLs transport electrons from the CLs and conduct reaction heat to the separators. Particularly on the cathode side, a structure is required that permits generated water to be discharged to the gas channel and that simultaneously allows the reactant gas to diffuse in the opposite direction to the CL through the GDL.

Moisture management is very important for stable operation and for improving the performance of PEFCs. Consequently, the GDL has a remarkable effect on the cell characteristics. Flooding occurs due to the generation of excess water; it inhibits oxygen diffusion and is a limiting factor for high-density operation. Since water has a much higher resistance to oxygen transport than air, excess water interferes with oxygen diffusion paths. Consequently, the water distribution controls oxygen diffusion. For instance, cell performance is reduced when the oxygen diffusion resistance is very large since it results in insufficient oxygen being supplied for electricity generation even when the average water saturation in the pores is reduced by distributing water over a wider area perpendicular to the oxygen diffusion direction (see Fig. 2). Therefore, it is essential to remove excess moisture to prevent flooding. On the other hand, an adequate moisture content is required and the reactant gas is humidified because proton exchange occurs between the anode and the cathode due to the presence of hydrated protons in the polymer electrolyte membrane.

Thus, water control is critical in PEFCs since it is important to both remove water to enhance oxygen diffusion to the CL while ensuring that there is sufficient humidity for proton transport.

Various studies have examined the important role that the GDL plays in PEFCs. For example, Gurau et al. [1] investigated the effect of the wettabilities of various GDL media on PEFC performance. Narhe and Beysens [2] studied the effect of the contact angle of the GDL surface on PEFC performance. Yamada et al. [3] experimentally investigated using pressure drops to predict the occurrence of flooding. Benziger et al. [4] demonstrated that using two materials with different pore sizes is effective in improving PEFC performance. Par et al. [5] found that it was difficult to remove water from CLs employing two materials with different pore sizes. Utaka et al. [6–8] devised a method for measuring the oxygen diffusivity of a GDL containing moisture using an oxygen absorber, visualizing water behavior and they evaluated its gas diffusion characteristics.

Various studies have visualized water in porous media GDL by neutron radiography, X-ray radiography, and fluorescence microscopy and many experimental investigations of GDLs have been performed. However, to produce GDLs with even higher performances it is necessary to enhance water control in GDLs by using specially designed structures.

With the aim of enhancing fuel cell performance, the present study investigates the water distribution and behavior of a GDL with a novel configuration in which two porous media with different wettabilities are alternately arranged (we term this a hybrid GDL). Furthermore, the reason for the higher oxygen diffusivity of the hybrid GDL was clarified and the characteristics of the hybrid GDL were examined by visualizing internal water in the microporous media using X-rays.

## **GDL CONFIGURATION WITH A WETTABILITY DISTRIBUTION**

As mentioned above, the oxygen diffusion characteristics are determined by the behavior of water in the cathode-side GDL, which should provide a uniform supply of the reactant gas to the CL and remove water in the opposite direction. Factors that may affect water transport in the GDL include vapor generation by reactions that produce electricity and heat, pressure-driven vapor convection caused by a volume reduction on vapor condensation, vapor diffusion due to concentration gradients, and liquid movement caused by surface tension at liquid-vapor interfaces. In the present study, we consider the effect of substrate wettability on water behavior. We propose a novel GDL configuration that has a wettability distribution in the substrate with the aim of optimizing the water distribution and behavior.

Fig. 3 depicts the configuration and principle of the proposed GDL. In the proposed configuration, two different porous media with different wettabilities have a parallel, alternating arrangement. The two porous media have different liquid contact angles due to their different wettabilities. Liquid in the hydrophobic

medium is pulled toward the hydrophilic medium by the pressure difference generated in the liquid bridge between the two porous media. Consequently, continuous, empty pores form in the hydrophobic medium in the oxygen diffusion direction. It is thus possible to passively control the liquid behavior. By using such porous media with a wettability distribution, it should be possible to maintain oxygen diffusion paths in the hydrophobic medium near the interface between the two media even when the porous medium contains a certain amount of liquid. To manage water in the cell, it is desirable for there to be liquid in the hydrophilic medium and for oxygen diffusion paths to be maintained in the hydrophobic medium to achieve the conflicting goals of maintaining some water and ensuring adequate oxygen diffusion. Furthermore, using this hybrid configuration of two porous media it may be possible to control effective oxygen paths by varying the arrangement of the hydrophilic and hydrophobic media, including their sizes, pitches, and ratios.

The predicted improvement in the oxygen diffusion characteristics and the effectiveness of the configuration of the porous media in the presence of water were verified experimentally.

## EXPERIMENTAL SYSTEM AND PROCEDURES

### Oxygen diffusivity evaluation

Fig. 4 shows a schematic of the hybrid test piece used to evaluate the oxygen diffusion characteristics in the presence of moisture. The test piece consists of hydrophobic and hydrophilic porous media that are in close contact with each other and are parallel and alternately arranged. This test piece is installed in a polypropylene ring (inside diameter: 5 mm; thickness: 0.16 mm). Gaps between the test substrate and the inside of the ring are filled with silicone filler. Test pieces made from only the hydrophobic medium and from only the hydrophilic medium (we term these structures single configurations) were prepared for comparison. Thus, the combination of the hydrophobic and hydrophilic porous media was examined; the specifications is described below. The test pieces were 2.5 mm thick, whereas practical GDLs are generally about 0.2–0.4 mm thick. Such thick test pieces were used to facilitate experiments and to achieve stricter conditions for liquid movement because liquid distributions that more non-uniform in the oxygen diffusion direction can be generated in a thicker GDL.

Fig. 5 shows the system used for measuring the oxygen diffusivity, which employs an improved galvanic oxygen sensor and Fig. 6 shows the holder in which the test pieces were installed. The experimental system has been described in a previous study [6], so only a brief description is given here. The measurement is performed after fitting the holder used to fix the porous medium specimen to the cathode side of the galvanic battery. A small hole was drilled in the holder to allow air out, but it was closed off during measurements. A vacuum impregnation method [7], in which an evacuated leak-tight container containing the test material is dipped in pure water, was used to saturate the test porous material with water.

The effective oxygen diffusivity was measured by the method described in Ref. [6]. In this method, the oxygen consumption of the electrochemical reaction was calculated from the output electric current of the oxygen sensor using Eq. (1). Furthermore, the oxygen mass fraction of the battery side of the test material was determined using Eq. (2). The effective oxygen diffusion coefficient of the test substrate was calculated using Eq. (3), which assumes one-dimensional diffusion.

$$\dot{V} = 22.41 \times 10^{-3} \times \frac{I}{4F}, \quad (1)$$

$$\omega_1 = kI, \quad (2)$$

$$D = \frac{\dot{V}L}{A} \cdot \frac{1}{\ln\left(\frac{1-\omega_1}{1-\omega_0}\right)}. \quad (3)$$

### Visualization of water distribution by X-ray tomography

X-ray microtomography was employed to visualize water in the microporous media. The samples with moisture were set in a holder and the internal water behavior and voids in them were observed during evaporation. Figure 7 shows the X-ray tomography configuration. X-rays emitted from the cone-shaped

radiation source pass through the sample and reach the detector after being attenuated. Computed tomography can image the cross sections of samples containing moisture. The source-to-object distance and the source-to-image distance were adjusted to optimize the images. Figure 8 shows the configuration of the holder in which the hybrid GDL was inserted for tomography. Since the holder is made of 0.1-mm-thick acrylic, it is considered to have a negligible attenuation. A 0.16-mm-thick polypropylene ring and a silicone filler through which X-rays can pass without being attenuated, were used to set the sample in the holder. Vacuum impregnation was employed to impregnate samples with water. It involved evacuating all the air from a sample and then immersing the sample in pure water. X-ray tomography was performed on all three hybrid GDLs when the samples were undergoing the quasi-steady-state process of drying out.

### Test materials and measurement conditions

Table 1 lists the specifications of the test materials. A carbon paper that had been made hydrophobic by PTFE impregnation ( $CP_{NW}$ ) was used as hydrophobic porous materials. A carbon paper that had been made hydrophilic by coating with titanium oxide ( $CP_W$ ) was prepared as hydrophilic materials. The intended wettabilities of these materials were confirmed by performing capillary tests.

Table 2 shows the combinations of single test materials used for hybrid and single configurations. The two circles in far right column indicate the specifications for which X-ray tomography was performed. Measurements were performed for the  $CP_W$ – $CP_{NW}$  hybrid configurations based on the porous media shown in Table 1. In Table 2,  $(f_p)_w$  and  $(f_D)_w$  respectively denote the volume ratio of pores in hydrophilic media to the total pore volume and the ratio of the diffusion conductance in hydrophilic media to the total conductance in dry conditions (expressed by Eqs. (4) and (5), respectively). The effective oxygen diffusivities of single test materials were also measured using a similar method as that described above.

Table 1

Materials	Notation	Fiber Diameter mm	Pore Diameter mm	Porosity	Thickness mm	Density g/cm <sup>3</sup>
Carbonpaper (Non-wettable)	$CP_{NW}$	14	32	70%	0.38	0.48
Carbon paper(Wettable)	$CP_W$	14	32	70%	0.38	0.47

Table 2

Combination	Type	$t_w$ mm	$t_{NW}$ mm	$(f_p)_w$	$(f_D)_w$	CT
$CP_W$ – $CP_{NW}$	Single	$CP_W$		Wettable		
		$CP_{NW}$		Non-Wettable		○
	Hybrid	0.38	0.38	0.5	0.51	○
		0.76	0.76	0.5	0.51	

$$(f_p)_w = \frac{P_w t_w}{P_w t_w + P_{NW} t_{NW}}, \quad (4)$$

$$(f_D)_w = \frac{D_w t_w}{D_w t_w + D_{NW} t_{NW}}, \quad (5)$$

$CP_W$ – $CP_{NW}$  is a combination of hydrophilic- and hydrophobic-treated carbon papers. The periods of the hydrophobic and hydrophilic media were varied, but the oxygen diffusion conductance and pore volume ratios both remained approximately constant at 0.5. Since water vaporization occurred gradually under the measurement conditions, quasi-steady-state processes of the effective oxygen diffusion coefficient were realized after the test material was filled with water.

## EXPERIMENTAL RESULTS AND DISCUSSION

### $CP_W$ – $CP_{NW}$

Figure 9 shows the measurement results for the effective oxygen diffusivity for the combination  $CP_W$ – $CP_{NW}$ . The variation of the oxygen diffusivity ratio  $R_D = D/D_{dry}$  is shown as a function of the water saturation  $S_a$ . While  $R_D$  increases nonlinearly with decreasing saturation for the single configuration, an approximately linear variation is observed in the saturation range between approximately 70 and 0% and a higher oxygen diffusivity was achieved in the hybrid configuration. However, a relatively high oxygen diffusivity was measured for the single configuration of  $CP_{NW}$ .

Figure 10 shows tomography images of the combination of  $CP_W$ – $CP_{NW}$  in saturation range of 0 and 70%. Oxygen diffuses from the top to the bottom in the upper image of Fig. 10. The images also include the holder, ring, and filler around the samples. The lower image in Fig. 10 is a cross-sectional image. The darker regions in Fig. 10(a) indicate the microporous media, whereas the lighter regions and the dark colored regions indicate carbon fibers and voids, respectively. For the saturated condition of Fig. 10(b), most of the sample is light due to water filling the voids. Therefore, it is possible to distinguish regions filled with water and voids from the different colors since water and carbon fiber appear light whereas voids look dark.

Although it is difficult to distinguish carbon fibers and water in this case, comparison of the images for dry and wet conditions permits qualitative evaluation of void formation.

Figure 11 shows the tomography images for the drying process for a hybrid GDL with  $t_w = t_{nw} = 0.38$  mm (where  $t_w$  and  $t_{nw}$  indicate the thicknesses of wettable and non-wettable parts, respectively). In the tomography images of Fig. 11 (a), void formation starts from the wettability interface. In Fig. 11 (b), wettable regions filled with water appear light and voids, which preferentially form in the hydrophobic medium, appear dark. Consequently, the water distribution appears striped. The number of voids increases from Fig. 11(a) to Fig. 11(b). These images reveal that there is a binary distribution and oxygen can pass through voids in the diffusion direction. They also demonstrate that the hybrid GDL has improved oxygen diffusivity.

Figure 12 shows tomography images of  $CP_{NW}$  of single-structured laminated hydrophobic medium. The saturation decreases from the wet condition to the dry condition. Although the hydrophobic medium has an uneven water distribution, voids are preferentially formed at the interface of the laminated media and voids subsequently progress in the diffusion direction. Uneven hydrophobicity at the interface of laminated media might be why the  $CP_W$  of the single-structured laminated hydrophobic medium has a comparatively high oxygen diffusivity (although it is lower than that of the hybrid GDL).

Figures 13 shows the predicted wettability distributions for hydrophobic-treated carbon paper. The solid lines in the upper figures denote the interfaces between the two media, the dotted lines show the approximate liquid surfaces, and the arrows indicate the direction of liquid movement. The lower figures denote the wettability distributions corresponding to the upper figures. Since, as shown in the predicted wettability distribution, the hydrophobicity decreases toward the inner region from both surfaces due to the hydrophobic treatment, the liquid distribution was similar to that for the hybrid configuration.

## CONCLUSIONS

A new configuration of GDLs was proposed in which two porous media with different wettabilities are alternately arranged (the hybrid configuration). The effect of hybrid GDL was validated by comparing X-ray images and oxygen diffusivity with respect to the water content (saturation) was examined by measurements performed using an experimental system consisting of a galvanic oxygen sensor as the oxygen absorber.

The results are summarized below.

1. It is confirmed by X-ray tomography that void is formed in hydrophobic area in the vicinity of hydrophilic area by transferring water from hydrophobic area to hydrophilic area. This findings indicate that oxygen diffusivity improvement of hybrid GDL is derived from uneven water distribution.

2. The effect of the pitch (thickness) of the hydrophilic and hydrophobic media was examined experimentally and the oxygen diffusivity was found to increase with decreasing pitch under constant water saturation.

### Acknowledgments

This work was supported in part by a Grant-in-Aid for Scientific Research from the Japan Society for the Promotion of Science (JSPS), Japan [(B)(2)20360096], and by Funds for New Energy and Industrial Technology Development Organization (NEDO) Project (Strategic Development of PEFC Technologies for Practical Application/Development of Next-Generation Technology).

### NOMENCLATURE

- $A$  permeation area of porous specimen ( $= \pi d^2/4$ ),  $m^2$   
 $D_{O_2}$  effective oxygen diffusivity in porous specimen,  $m^2/s$   
 $F$  Faraday constant, C/mol  
 $I$  output current of oxygen sensor, A  
 $k$  characteristic constant of oxygen sensor, 1/A  
 $L$  thickness of porous specimen (holder length), m  
 $P$  porosity of porous medium  
 $S_a$  water saturation  
 $\dot{V}$  oxygen consumption rate of sensor,  $m^3/s$   
 $t$  width of hybrid test material, mm  
 $f_p$  average pore ratio  
 $f_D$  average diffusion conductance ratio

Greek symbols

- $\omega$  oxygen mass fraction

Subscripts

- NW hydrophobic component  
W hydrophilic component  
dry dry conditions  
0 ambient (atmospheric conditions)  
1 porous medium surface on the cathode side

### References

1. Gurau V., Bluemle M. J., De Castro E. S., Tsou Y.-M., Mann A. Jr., and Zawddzinski T. A. Jr. Characterization of Transport Properties in Gas Diffusion Layers for Proton Exchange Membrane Fuel Cells, I. Wettability (Internal Contact Angle to Water and Surface Energy of GDL Fibers) // *J. of Power Sources*. 2006. Vol. 160. Pp. 1156–1162.
2. Narhe R. D. and Beysens D. A. Water Condensation on a Super-hydrophobic Spike Surface. *Europhysics Letters*. 2006. Vol. 75, No.1. P.98.
3. Amada H., Hatanaka T., Murata H., and Morimoto Y. Measurement of Flooding in Gas Diffusion Layers of Polymer Electrolyte Fuel Cells with Conventional Flow Fields // *J. of The Electrochemical Society*. 2006. Vol. 159. Pp. A1748–A1754.
4. Benziger J., Nehlsen J., Blackwell D., Brennan T. and Itescu J. Water Flow in the Gas Diffusion Layers of PEM Fuel Cells // *J. of Membrane Science*. 2005. Vol. 261. Pp. 98–108.
5. Par G.-G., Sohn Y.-J., Yang T.-H., Yoon Y.-G., Lee W.-Y. and Kim C.-S. Effect of PTFE Content in the Gas Diffusion Media on the Performance of PEMFC // *J. of Power Sources*. 2004. Vol. 31. Pp. 182–187.
6. Utaka Y., Tasaki Y., Wang S., Ishiji T. and Uchikoshi S. Method of Measuring Oxygen Diffusivity in Microporous Media // *Int. J. of Heat and Mass Transfer*. 2009. Vol. 52. Pp. 3685–3692.

7. Utaka Y., Iwasaki D, Tasaki Y. and Wang S. Measurement of Effective Oxygen Diffusivity in Micro Porous Media with Moisture // Transactions of Japan Society of Mechanical Engineers, Series B. 2009. Vol. 75, No.757. Pp. 1822–1829.
8. Utaka Y., Hirose I, Tasaki Y., Characteristics of Oxygen Diffusivity and Water Distribution by X-ray Radiography in Microporous Media in Alternate Porous Layers of Different Wettability for Moisture Control in Gas Diffusion Layer of PEFC // Intern. J. of Hydrogen Energy, submitted.

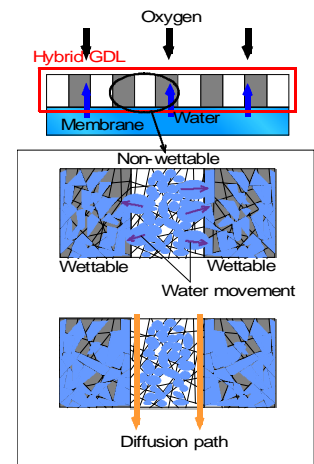
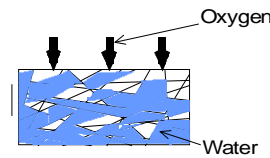
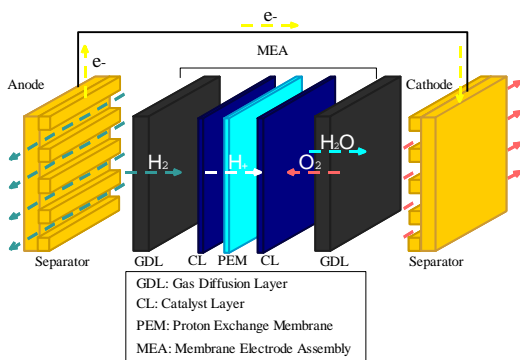


Fig. 1. Schematic of PEFC Fig. 2. Oxygen diffusion in GDL containing water Fig. 3. Configuration and principle of hybrid GDL

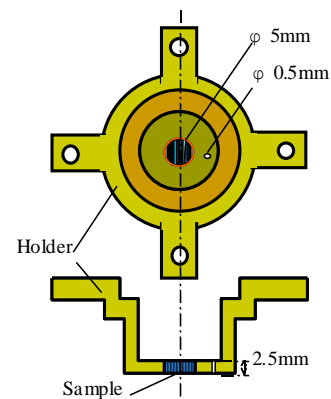
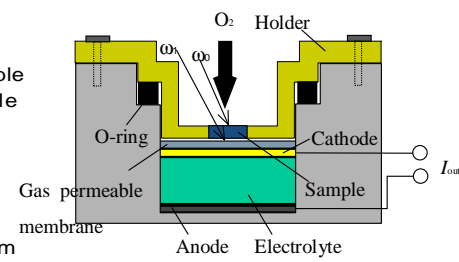
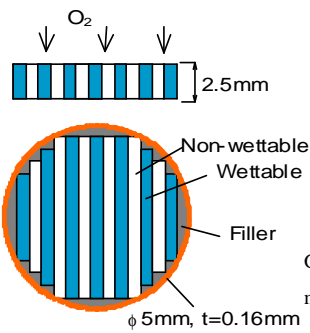


Fig. 4. Test piece of hybrid GDL Fig. 5. Configuration of experimental apparatus Fig. 6. Test piece holder

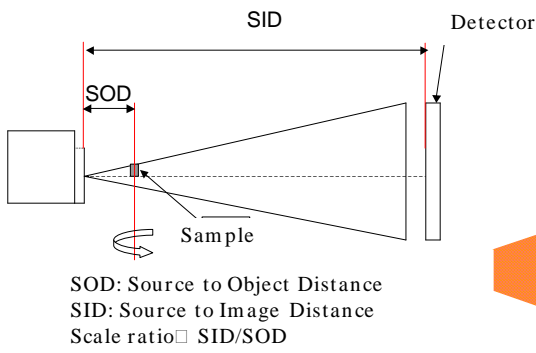


Fig. 7. Configuration of X-ray computed tomography system

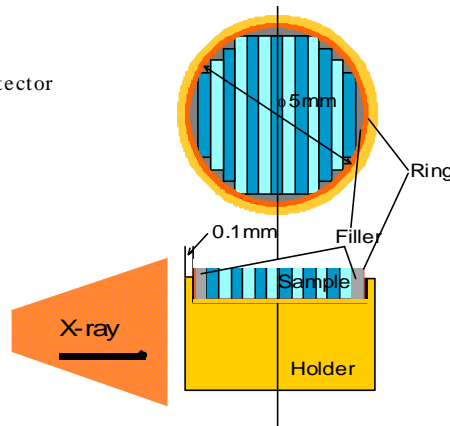


Fig. 8. Sample arrangements for computed tomography

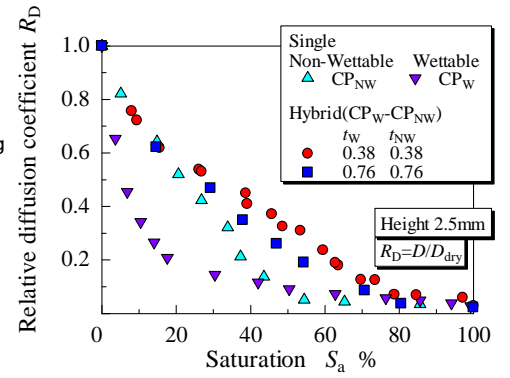


Fig. 9. Relative diffusion coefficient for combination

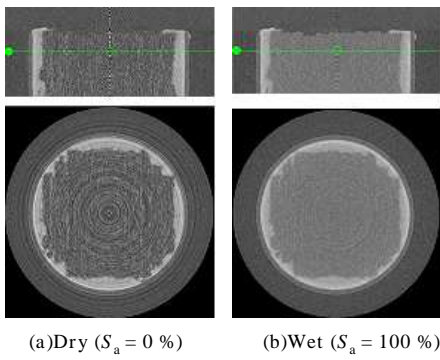


Fig. 10 X-ray computed tomography images for hybrid

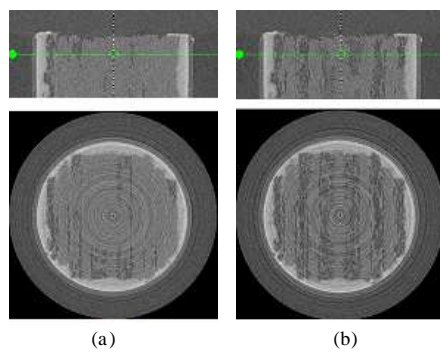


Fig. 11. X-ray computed tomography images for hybrid

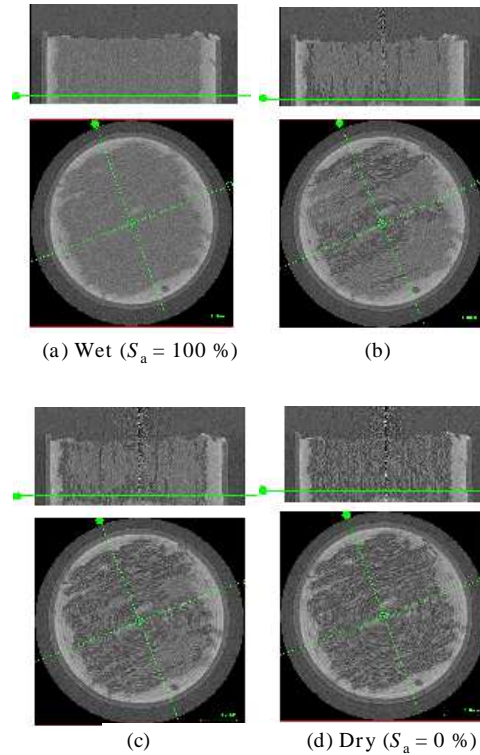


Fig. 12. X-ray computed tomography images for single  $CP_{NW}$

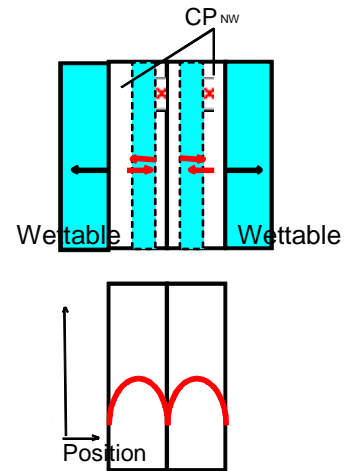


Fig. 13. Water displacement with wettability distribution

## NON INTRUSIVE MEASUREMENT OF THE MASS FLOW RATE INSIDE A CLOSED LOOP TWO-PHASE THERMOSYPHON

**Bruno Agostini, Eva Ferreira**  
ABB Ltd. Switzerland,  
Corporate Research,  
Segelhofstrasse 1K,  
5405 Daettwil, Switzerland  
Phone: +41 (0)58 586 80 42  
Telefax: +41 (0)58 586 40 06  
Bruno.agostini@ch.abb.com

### Abstract

Two-phase cooling is a promising technology for electronics cooling. It allows using dielectric fluids in passive systems and benefit from high heat transfer coefficients. Thermosyphons are a particularly interesting technology in the field of power electronics being entirely passive and simple equipments. Their performances are strongly related to the flow rate of the fluid inside the thermosyphon. In mini-channels thermosyphons liquid entrainment occurs so that flow rate is difficult to evaluate, hence the need for a non intrusive measurement method. For this purpose a mini-channel thermosyphon was manufactured out of borosilicate glass and equipped with a semi-transparent ITO layer as a direct current heating evaporator. It was illuminated by two lasers through the glass tube and the voltage from two photodiodes placed on the opposite side was measured. With an appropriate signal processing the maximal velocity was determined together with length and frequency of the vapor bubbles, the frequency of the thermosyphon cycle for several filling ratios and for various heating powers. From these measurements the total mass flow rate, the liquid mass flow rate, the gas mass flow rate, the void fraction, the vapor quality and the flow cycle frequency were calculated and compared to a thermosyphon simulation model developed at ABB.

### KEYWORDS

Two-phase cooling, thermosyphon, bubble velocity, laser, photodiode.

### INTRODUCTION

Thermosyphon cooling systems have been recognized to be beneficial for thermal management of electronics. The use of dielectric fluids and pumpless operation altogether with high heat transfer coefficients is an attractive combination for power electronics thermal management. In a state-of-the art Vasiliev [1] described the use of heat pipes for power semiconductors cooling, highlighting that it allows for higher power density. Thermosyphons using small channels are particularly appealing for their compactness and low material and fluid use. However, very few experimental data or models are available with the new dielectric fluids at the required working temperatures and channel diameters. Still, available studies on different thermosyphon configurations are helpful to outline some trends. Furthermore, small diameter channels allow taking advantage of the so called bubble pump effect to further increase the performances of the thermosyphon. This effect causes liquid plugs to be propelled in the channels and delay dry-out phenomena. This liquid pushing effect typically shows a maximum with heat load as shown by Delano [2]. An issue in such system is the flow instabilities, all the more so that the channel diameter decreases. Nayak *et al* [3] conducted a numerical study of boiling flow instability of a reactor thermosyphon system and showed that increasing the riser diameter, high power Type {II} instabilities disappear but a low power, low quality Type {I} instabilities appear. The effects of subcooling and riser length were also studied. The performances of a two-phase thermosyphon loop with a small diameter channel evaporator have been recently measured by Khodabandeh [4, 5]. The evaporator channels diameter ranged from 1.1 to 3.5 mm, but the riser had a diameter of 6.1 mm. The heat transfer coefficient was found to be strongly dependant on heat flux and the pressure drop to be adequately predicted by the homogeneous model. The influence of the filling ratio is also a crucial parameter. Ong and Haider-E-Alahi [6] investigated this effect on a R134a filled

thermosyphon and found that the performances increased with the filling ratio, reaching a maximum at about 0.8. Abou-Ziyan *et al* [7] found a maximal performance at a filling ratio of 0.5, also with a R134a filled thermosyphon. Furthermore they showed that vibrations could act against the boiling limit and extend the operating range of the thermosyphon. MacDonald *et al* [8] measured experimentally an optimum at 35% of filling ratio with refrigerant R11 in a large diameter tube two-phase thermosyphon and also showed with a numerical model that this optimum was strongly dependent on the respective lengths of the evaporator, riser and condenser. This last fact might explain why Ong and Haider-E-Alahi [6] and Abou-Ziyan *et al* [7], having different evaporator, riser and condenser lengths, found different optimal filling ratios. The Present study will highlight the effects of filling on mass flow and instabilities in the thermosyphon.

## EXPERIMENTAL SETUP

The principle of the thermosyphon and the experimental setup are shown in Fig. 1. The thermosyphon is filled with a low global warming potential fluid (Novec 649). At the bottom left of the system, an evaporator heats up the fluid beyond the onset of nucleate boiling thus generating vapor bubbles. Then, these elongated and confined bubbles grow, pushing upwards liquid plugs towards the condenser. The two-phase fluid then enters a Liebig condenser in which the vapor is condensed at constant temperature with a water flow at 25 °C. The condensate return to the evaporator by gravity and the cycle starts over.

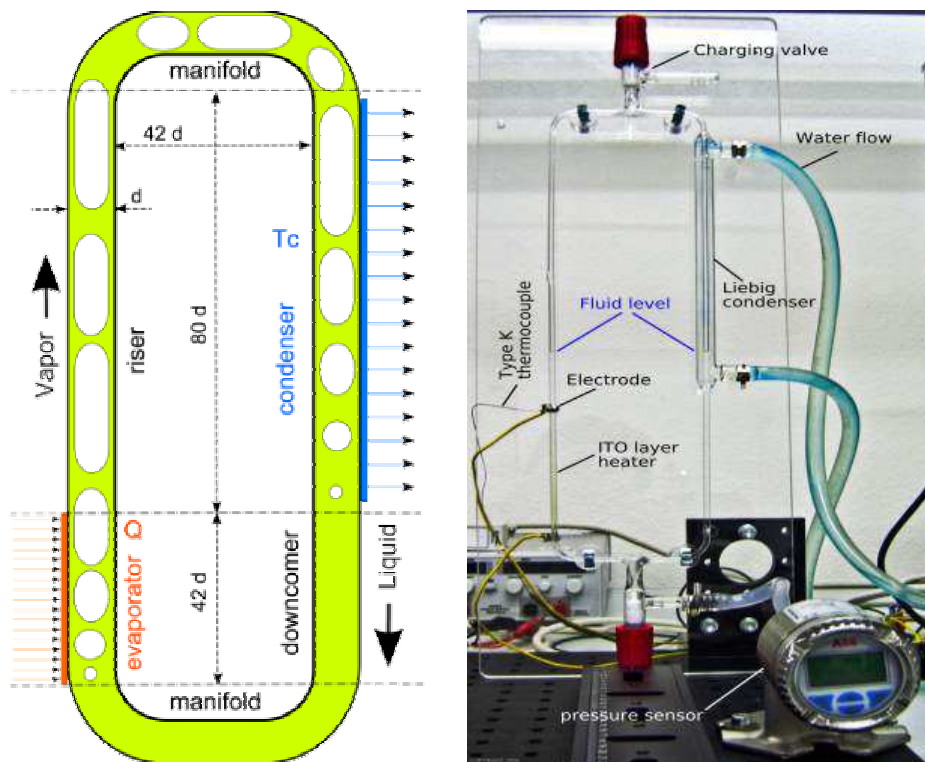


Fig. 1. Thermosyphon principle (left) and experimental setup (right)

The closed loop thermosyphon was manufactured out of 2.4 mm diameter borosilicate glass. The thermosyphon is equipped with a 100 nm semi-transparent Indium Titanium Oxide layer as a direct current heating evaporator. The internal pressure was measured through a valve on the bottom of the loop. A second valve at the top was used to change the filling of the thermosyphon. The electrical current was applied through two electrodes clamped on a silver padding which was applied on a 2.5 mm long section of the Indium Titanium Oxide layer at the bottom and top of the evaporator. A type K thermocouple soldered on the top electrode measured the temperature. The heating power was varied between 5 and 24 W. Two laser-

diode beams (1 mW @ 650 nm) were projected through the glass tube and focused with two lenses (focal length: 100 mm) as shown in Fig. 2. After crossing the tube, the laser beams were received by two photodiodes. The resulting voltage signals from the two diodes and the pressure sensor were recorded by a National Instruments SCXI acquisition system. Then, with an appropriate signal processing, it was possible to determine the maximum of the velocity, the length and the frequency of vapor bubbles, the frequency of the thermosyphon cycles for different filling and for several electrical power. The different instruments used for measurements and their accuracy is shown in table 1.

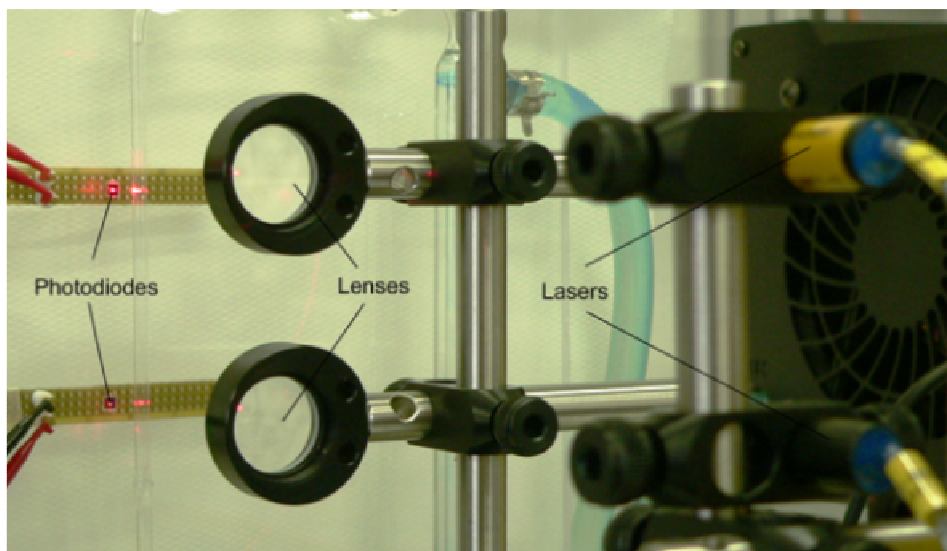


Fig. 2. Picture of the laser diodes arrangement

Table 1. Measuring devices and accuracy

Measurement	Device	Measured range	Accuracy	Unit
Power	Christ CPM138 wattmeter	5–35	0.05–0.35	W
Heater temperature	TC type K + JUMO dieco	24–73	±1.5	°C
Water temperature	Alman Reserator XT cooler	24–25	±1.5	°C
Pressure	ABB 261AS	44–207	±1	kPa

## MEASUREMENTS ANALYSIS METHOD

The difference in refractive index between liquid and vapor causes the laser beam angle of incidence to change with the passage of a liquid slug or vapor bubble in the tube, resulting in a drop in light intensity detected by the photodiode, thus recording a different voltage signal. The signal obtained using the cross-covariance is characterised by one high amplitude peak, which gives the time delay between the two signals, as shown in Fig. 3. Knowing the distance between the two lasers, it was possible to determine the maximum velocity of the bubbles and liquid slugs. Assuming the velocities of the bubbles and liquid slugs are the same, it is then possible to calculate the fluid mass flow rate. Different number acquisition points were used but beyond 15000 acquisition points there was no influence on the determination of the time delay. For the experiments, the duration of the acquisition chosen was 3–4 min. Measures could be repeated during a week within 5% of error for a same filling of the thermosyphon. The sampling rate was set at 10 kHz.

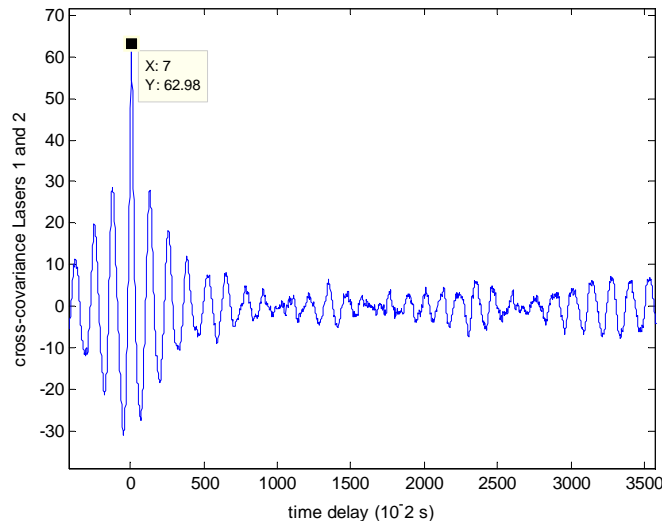


Fig. 3. Cross-covariance signal laser 1 and 2 versus time delay ( $10^{-2}$  s).

### LIMITS OF THE METHOD

This method showed two main limitations:

- coalescence phenomena can cause the signals of the first and second photodiode to be too different. The presence of the coalescence phenomena depends on the flow pattern, hence on the filling of the thermosyphon and the electrical power. This can also happen when a bubble is growing or when its length is decreasing. Backflow of the bubbles in the thermosyphon can also affect adversely the signal. Then a bubble would be counted twice by one of the photodiode.
- If the signal is perfectly periodic (period  $T$ ), the cross-covariance could indicate a time delay of  $(t+k\cdot T)$  because of the periodicity of the signals,  $k$  being an integer.

Because of these limitations, the distance between the two couple laser beams/photodiode had to be optimized. If the distance is too high, coalescence phenomena, growth or decrease in length of the bubbles will be detected by the photodiodes. If the signal is too periodic the distance between the two photodiodes should be lower than the flow velocity multiplied by the signal's period. But if this distance is too low, uncertainties will increase. A good compromise was a distance within 2 cm and 4.5 cm. The cross-covariance method is only applicable for a bubbly/slug flow and slug/semi-annular flow, thus measurements were impossible for a higher heating power than 15 W or for a less filling than 50%.

### CALCULATION OF BUBBLE VELOCITY

The void fraction depends on the length of the bubbles and on the length of the liquid plugs. If the instantaneous velocities of the vapor and of the liquid are the same (homogeneous model) and are equal to the velocity  $U$  given by the cross-covariance's method, the void fraction can be written as a function of the crossing time of the couple photodiode/laser beam by vapor bubbles  $T_g$  and by a liquid plugs  $T_l$ :

$$\varepsilon = \frac{U \cdot T_g}{(U \cdot T_g + U \cdot T_l)} \quad (1)$$

$$\varepsilon = \frac{T_g}{(T_g + T_l)}$$

The voltage signals  $V(t)$  from the two photodiodes detects the crossing of a couple photodiode/laser beam by a bubble or a liquid plug. For each voltage signal ( $V_1(t)$  for laser 1 and  $V_2(t)$  for laser 2, shown in Fig. 4 left), a voltage difference  $\Delta V_i(t)$ ,  $i=1$  or  $2$ , can be calculated:

$$\Delta V_i(t) = V_i(t) - V_i(t + \Delta t), \quad (2)$$

$\Delta t$  being the acquisition time step. This difference voltage is shown in Fig. 4 right and results in a peak each time the flow changes from liquid to vapor and inversely. In order count vapour bubbles and liquid slugs a peak detection threshold was chosen (dashed lines in Fig. 4 right). Thus, the time delay between a consecutive positive peak and negative peak, which is the time delay  $T_g$  between the front and back of a bubble can be calculated. The same method was applied to determine  $T_l$ . Finally, the void fractions  $\epsilon_1$  and  $\epsilon_2$  for the first and the second photodiode respectively and the average void fraction can be calculated. With the average fluid pressure vapor and liquid densities are known, hence the vapour quality is calculated.

If the threshold was too high, some peaks were not detected and there was insufficient information for calculations. If the threshold was too low, noise signal was considered similar to the peaks due to bubbles or drops. In this study, the ratio signal over noise was around 14. The best choice was 0.01 V. These threshold values were kept for each experimental set up.

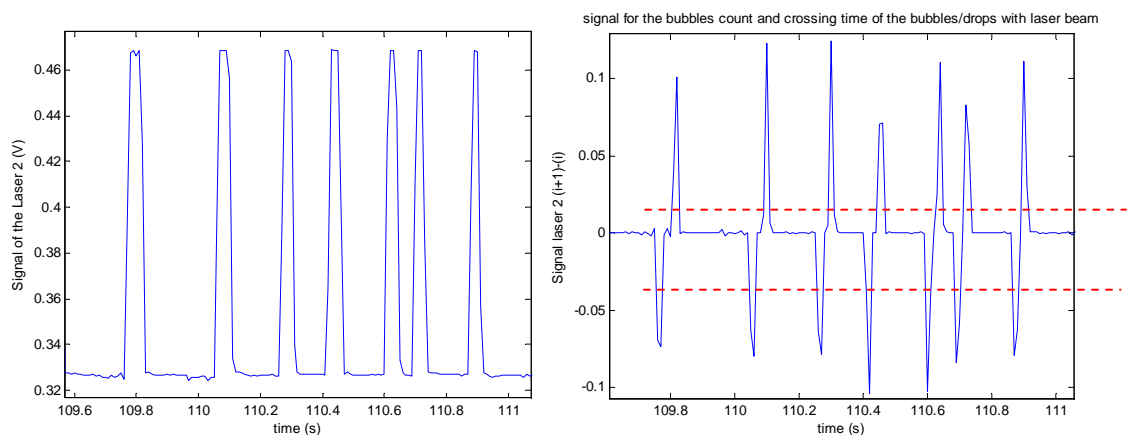


Fig. 4. Left: time series of the signal of the Laser 2 versus time (s). Right: threshold detection applied to the same signal

## PRESSURE MEASUREMENTS

The static pressure at the bottom of the thermosyphon was measured with a pressure transducer. The signal was periodic due to the cyclic behaviour of the thermosyphon. A Fast Fourier Transform gave the main frequencies of the pressure signal and the main frequencies of the couples photodiode/laser beam. As shown in Figs. 5 and 6 left, the same value of the cycle frequency was found for all the signals. This frequency increases with the electrical power. For example, frequencies for 80% filling are 0.4 Hz at 5 W and 1.2 Hz at 23 W. A fitting of the pressure signal confirmed the sinusoidal behaviour of the pressure as shown in Fig. 6 right.

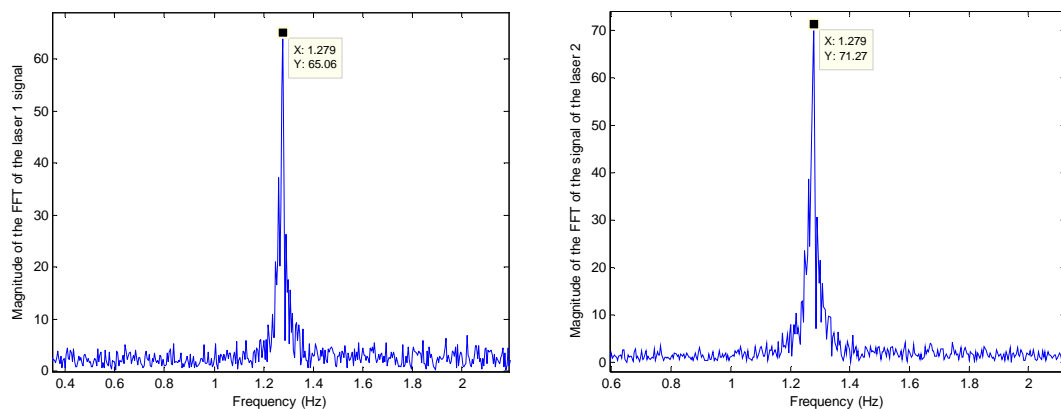


Fig. 5. Left: FFT of the Laser 1 signal. Right: FFT of the Laser 2 signal

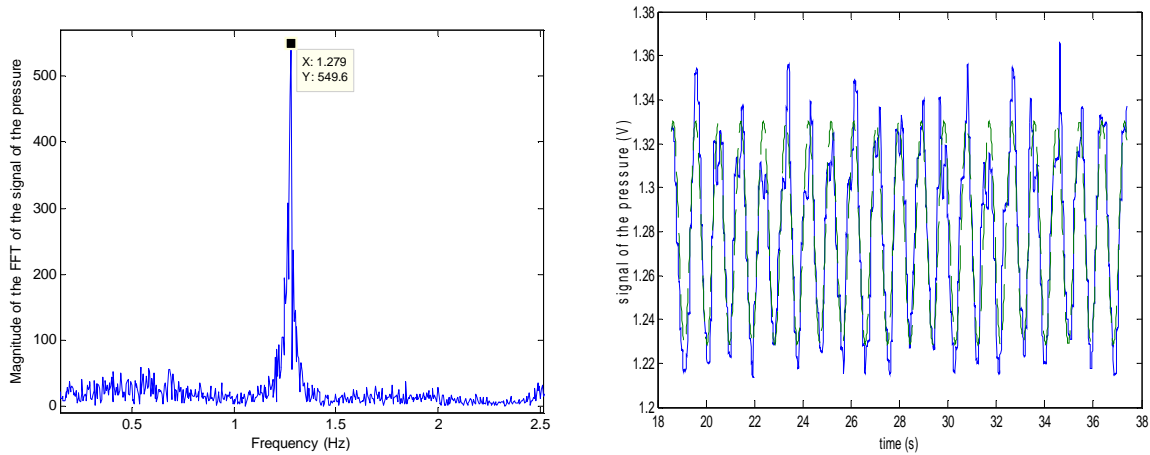


Fig. 6. Left: FFT of the pressure signal. Right: time series of pressure signal (V) and fit function; dashed line:  $1.52 + 0.04 \sin(6.73t + 1.7)$

## RESULTS

Fig. 7 shows the total mass flow rate versus the heating power for various fillings of the thermosyphon (left) and the total mass flow rate versus filling for various heating powers (right). As expected the mass flow increases to a maximum and decreases, both with power or with the thermosyphon filling. At 84% filling however the mass flow always increases with power, but it is suspected that a maximum would be reached at a higher power that was not possible to generate with the present setup.

A thermosyphon model based on the simultaneous solving of the three conservation equations with a minimization algorithm was presented by Agostini and Habert [9] and compared to the present measurements in Fig. 8. The agreement between simulations and measurements is quite dependant on the filling ratio, the best agreement being obtained for filing ratios favoring the elongated bubble flow regime. For low (52%) and high (80% not shown here) filling ratio the agreement is not as good as for 67%. However the trend and order of magnitude of the mass flow rate are adequately predicted by this simple one dimensional model.

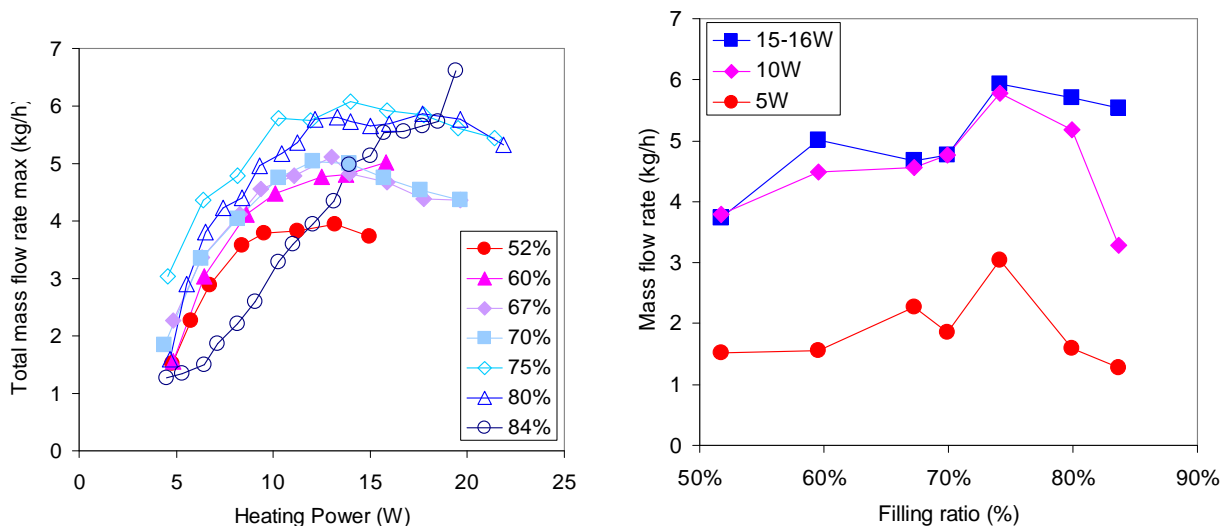


Fig. 7. Left: total mass flow rate maximum (kg/h) versus heating power (W). Right: total mass flow rate maximum (kg/h) versus filling (%)

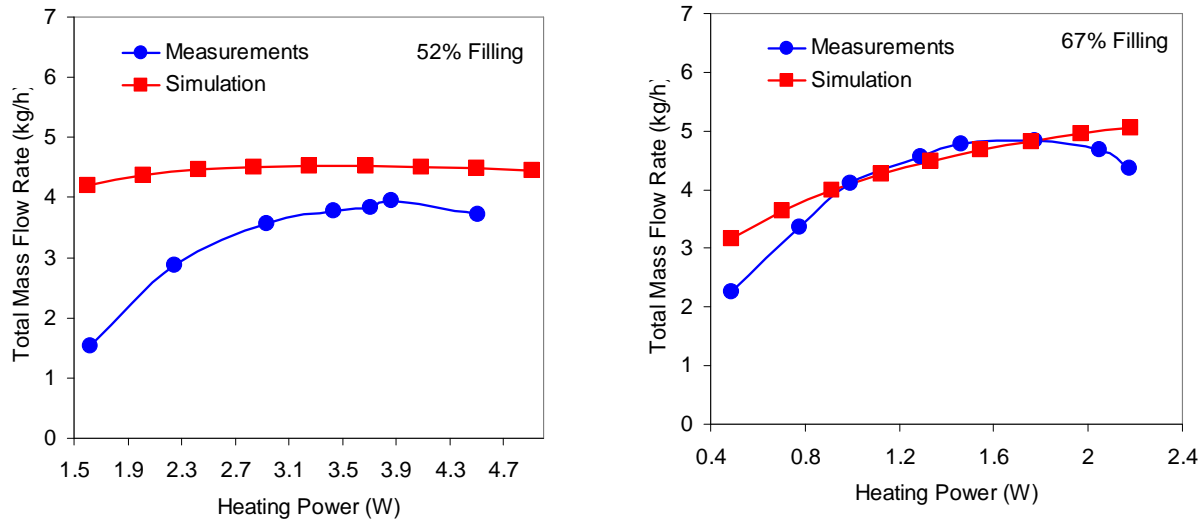


Fig. 8. Comparison between the experimental and the simulated total mass flow rates versus heating power for 52% (right) and 67% filling (left)

## CONCLUSIONS

A non intrusive optical mass flow measurement method for a transparent small channel thermosyphon was presented. Based on the use of two sets of laser beam and photodiodes, this method does not add any pressure drop to the system, but is limited to the elongated flow regime. These measurements showed that the mass flow exhibits a maximum with heat load and fluid filling ratio, which is expected in bubble pump systems. Furthermore the trend and order of magnitude of the mass flow rate were found to be adequately predicted by a one dimensional thermosyphon model based on the three conservations equations. The next step will be to measure the temperature distribution on the evaporator with an infrared camera et correlate it to the bubble frequency.

## NOMENCLATURE

$\epsilon$	Void fraction	(-)
$x$	Vapor quality	(-)
$T$	Thermosyphon cycle period	(s)
$T_{reg}$	Mean crossing time of bubbles	(s)
$T_1$	Mean crossing time of liquid slugs	(s)
$\Delta t$	Time delay between two acquisitions	(s)
$U_{gr}$	Velocity of the gas flow	(m/s)
$U_1$	Velocity of the liquid flow	(m/s)
$U$	Maximum velocity of the fluid	(m/s)
$V$	Voltage signal from the photodiode	(V)
$\Delta V$	Voltage difference	(V)

## References

1. Vasiliev L. L. State-of-the-art on heat pipe technology in the former soviet union // *Appl. Therm. Eng.* 1998. Vol. 18, No. 7. Pp. 507–551.
2. Delano N. *Design Analysis of the Einstein Refrigeration Cycle* // PhD thesis, Georgia Institute of Technology, June 1998.

3. Nayak A., Lathouwers D., van der Hagen T., Schrauwen F., Molenaar P., Rogers A. A numerical study of boiling flow instability of a reactor thermosyphon system // *Appl. Therm. Eng.* 2006. Vol. 26. Pp. 644–653.
4. Khodabandeh R. Heat transfer in the evaporator of an advanced two-phase thermosyphon loop // *Int. J. of Refrigeration*. 2008. Vol 28. Pp. 190–202.
5. Khodabandeh R., Pressure drop in riser and evaporator of an advanced two-phase thermosyphon loop // *Int. J. of Refrigeration*. 2005. Vol. 28. Pp. 725–734.
6. Ong K., Haider-E-Alahi M. Performance of a R-134-a-filled thermosyphon // *Appl. Therm. Eng.* 2003. Vol. 23. Pp. 2373–2381.
7. Nayak A., Lathouwers D., van der Hagen T., Schrauwen F., Molenaar P., Rogers A. A numerical study of boiling flow instability of a reactor thermosyphon system // *Appl. Therm. Eng.* 2006. Vol. 26. Pp. 644–653.
8. MacDonald T., Hwang K., Diccio R. Thermosyphon loop performance characteristics: Part 1. Experimental Study // *ASHRAE Trans.* 1997. Vol. 83. No. 2467. Pp. 250–259.
9. Agostini B., Habert M. Measurement of the performances of a transparent closed loop two-phase thermosyphon // *Proc. of the Advanced Computational Methods and Experiments in Heat Transfer XI*, WIT Press publishes leading books in Science and Technology, 2010. Pp. 227–235.

## TWO-PHASE FLOW IN MICROCHANNELS WITH VARIABLE CROSS SECTION AND ONE POROUS BOUNDING WALL

**A. Nouri-Borujerdi**

School of Mechanical Engineering  
Sharif University of Technology  
Azadi Avenue, Tehran, Iran  
anouri@sharif.edu

### Abstract

One-dimensional homogeneous adiabatic gas-liquid two-phase flow has been studied in a microchannel with a variable rectangular cross section. Liquid is injected through one porous side wall inside the channel under the assumption of hydrophobic condition to simulate water injection effects and developing mechanism of two-phase flow. The modeling and solution of the conservation equations provide velocity distribution of two-phase mixture, pressure drop, mass fraction and void fraction for different water injection rates. The results show that velocity and pressure drop significantly being perturbed when the water injection rate exceeds a critical value. This pressure drop is significant because of slug flow formation that fills a substantial portion of the microchannels cross section and act as a blockage to the air flow.

### KEYWORDS

Microchannel, two-phase flow, porous medium, liquid injection, numerical solution.

### INTRODUCTION

Fundamental flow characteristics problems encountered in the development and processing of microchannels have become a significant challenge for the design and control of these systems. Two-phase flow in microchannels finds applications in a variety of microfluidic flow systems such as bioengineering, compact heat exchanger for cooling systems of micro-electronic devices, high powered lasers and fuel cell. For instance, the performance of proton exchange membrane (PEM) fuel cell can be increased by using microchannels to improve the gas routing. However, they complicate water management particularly in terms of flooding. Because the agglomeration of liquid water on the interface of the catalyst layer and the gas diffusion layer limits the efficiency of the PEM fuel cells, [1-3]. When the cell is working at high current densities, the rate of liquid water production exceeds the rate at which water is removed from the catalyst layer. It is well established in the literature that the performance of the gas diffusion layer is enhanced by adding a microporous layer to it as a hydrophobic agent and using a gas diffusion layer with a larger pore size distribution.

Wang et al. [4] have observed the emergence, growth and detachment of liquid water droplet on the gas diffusion layer/gas channel interface. Recently, they [5] have measured the size of the droplet on the interface and find that liquid water can transport through the gas channel without interaction with channel wall at high gas velocity. He et al. [6] developed a two-fluid model for two-phase flows in PEM fuel cells to obtain liquid water droplet detachment diameter on the gas diffusion layer /channel interface. Their results show that a high contact angle and a low surface tension are advantageous for liquid water removal in the gas channel and the gas diffusion layer even though a low surface tension will lead to a low capillary force in the gas diffusion layer. Hidrovo et al. [7] presented an overview of the experimental work toward understanding of two-phase flow behavior in the microchannels. The greater scope of the work was to use the knowledge gained towards the development of strategies to improve water management. They concluded that under hydrophobic conditions the formation of slugs or blobs of size comparable to that of the microchannels greatly impeded the flow of air, especially at low pressure drops. On the other hands, liquid water affected under hydrophilic conditions was only noticeable at large injection rates ( $100 \mu\text{l}/\text{min}$ ). In contrast to their hydrophobic counterparts, two-phase flow in hydrophilic microchannels was characterized

by the formation of a thin film of liquid. Vigneron et al. [8] presented a theoretical model and a numerical simulation of a liquid-gas two-phase flow within a microchannel ( $50\mu m \times 500\mu m \times 2cm$ ) equipped with distributed liquid water injection through the side walls. The numerical results show that for small water injection rates ( $1-10\mu l/min$ ) the air flow velocity and pressure drop are not significantly perturbed by the presence of liquid water. But if water injection becomes important ( $10-100\mu l/min$ ) larger pressure drops are observed. Saisorn and Wongwises [9] studied experimentally adiabatic two-phase air-water flow characteristics, including the two-phase flow pattern as well as the void fraction and two-phase friction pressure drop in a circular microchannel, 320  $\mu m$ . The flow pattern map was developed from the observed flow patterns i.e., slug flow, throat annular flow, churn flow and annular-rivulet flow. The results showed that the void fraction data obtained by image analysis tended to correspond with the homogeneous flow model. They also calculated the friction multiplier and founded the multiplier data was depended on flow pattern as well as mass flux. Wongwises and Pipathattakul [10] measured void fraction in an inclined narrow annular channel having hydraulic diameter of 4.5 mm. Chung et al. [11] performed experiments on nitrogen-de-ionized water in a square channel with a hydraulic diameter of  $96\mu m$  and compared the results with those for a  $100\mu m$  circular tube employed by Kawahara et al. [12]. Similar results including pressure drop and void fraction data were obtained, regardless of the channel geometry. Hwang et al. [13] studied the two-phase ethanol- $CO_2$  flowing through a converging or diverging rectangular microchannels. Unlike previous works, they observed stratified and wavy stratified flows at the entrance of the converging microchannels. They found that the pressure drop in the diverging microchannels was substantially smaller than in the converging one. However, the two-phase frictional multiplier for both channels was independent of liquid flow rate. This result agreed with that obtained from nitrogen-water two-phase flow in circular microchannel carried out by Chung and Kawaji [14].

Very few studies have been directed towards understanding and modeling of the flow behavior in the microchannels with variable cross section under liquid injection from the wall. However, it is obvious that a comprehensive study is still lacking on the trends and parameters dominating the flow behavior in microchannels. Thus, the primary concerns of this work lie on the modeling of liquid injection induced two-phase flow. Furthermore, the effects of water injection in the flow rate-pressure drop relationship and volumetric void fraction characteristics are also treated under given flow conditions.

## MATHEMATICAL MODEL

A steady state one-dimensional homogeneous two-phase gas-liquid adiabatic flow in a rectangular microchannel ( $a \times b \times L$ ) is investigated, (Fig. 1). The height of the channel is variable and the wall thickness is  $t$  with one permeable boundary. The other boundaries are rigid and hydrophobic type. Under the hydrophobic condition, the liquid water phase forms slugs in the middle of the channel flow (unlike film formation in the hydrophilic case) and induces the air to flow around the slugs. This type of the flow pattern is equivalent to the slug flow and can be governed fairly by homogeneous model. The homogeneous assumption implies uniform mixing of the phases. Injection of water through the porous wall is assumed perpendicular to the channel axis. In a dimensionless form, the mass and momentum equations of the two-phase mixture are as follows.

$$\frac{\partial \rho^* u^* A^*}{\partial z^*} = \Gamma^* \quad (1)$$

$$\frac{\partial \rho^* A^* u^{*2}}{\partial z^*} = -A^* \frac{\partial P^*}{\partial z^*} - \frac{\tau_w p_w L}{\rho_i u_i^2 A_i} \quad (2)$$

where the above dimensionless parameters are defined as:

$$\rho^* = \rho/\rho_i, \quad u^* = u/u_i, \quad P^* = P/\rho_i u_i^2, \quad \Gamma^* = aL\Gamma/\dot{m}_i, \quad \dot{m}_i = \rho_i u_i A_i, \quad z^* = z/L, \quad A^* = \frac{A}{A_i} = \frac{ab}{ab_i} = \frac{b}{b_i}$$

$\Gamma$  is the liquid water injection rate per unit area ( $a \times L$ ) through the porous wall.  $A$  is the cross section area of the channel with width ( $a$ ) and height ( $b$ ).

If replace the wall shear stress in terms of the two phase friction pressure drop, the above equation changes as follows.

$$\frac{\partial \rho^* A^* u^{*2}}{\partial z^*} = -A^* \frac{\partial P^*}{\partial z^*} - \frac{f_{TP} P_w L \rho^* u^{*2}}{2A_i} \quad (3)$$

where,  $f_{TP}$  is the two phase friction factor.

With the assumption of  $\Gamma^*$  as a constant, integration of Eq. (1) under the boundary condition  $\rho^* u^* A^*(0) = 1$  is.

$$\rho^* u^* A^* = 1 + \Gamma^* z^* \quad (4)$$

The average density of the two-phase mixture is denoted by equality gas and liquid velocities as follows.

$$\rho^* = \alpha \rho_g^* + (1 - \alpha) \rho_f^* \quad (5)$$

Since the mass flow rate of the gas phase is constant through the channel, we get.

$$\rho_g u_g A_g = \rho_i u_i A_i \quad (6)$$

Because of the assumption of the homogeneous model,  $u_g = u$ , the gas void fraction can be obtained from the above equation as

$$\alpha = \frac{1}{\rho_g^* u^*} \quad (7)$$

Combining Eqs. (4, 5, 7), the gas density will be.

$$\rho_g^* = \frac{\rho_f^*}{1 + \rho_f^* u^* - \frac{1 + \Gamma^* z^*}{A^*}} \quad (8)$$

If the equation of state of the gas behaves like,  $P = Z \rho_g R_g T$ , its dimensionless form will be.

$$P^* = \rho_g^* P_i^* \quad (9)$$

where,  $Z$  is the compressibility factor and  $P^* = P / \rho_i u_i^2$ .

Inserting Eq. (8) into Eq. (9) and introducing the final result into Eq. (3), the homogeneous two-phase velocity will be.

$$\frac{du^*}{dz^*} = \frac{\frac{\rho_f^* P_i^*}{A^*} \left( \Gamma^* - \frac{1 + \Gamma^* z^*}{A^*} \frac{\partial A^*}{\partial z^*} \right) + \left[ 1 + \rho_f^* u^* - \frac{1 + \Gamma^* z^*}{A^*} \right]^2 \times \left[ \Gamma^* + \frac{f_{TP} P_w L}{2A_i} \times \frac{1 + \Gamma^* z^*}{A^*} \right] \times \frac{u^*}{A^*}}{\rho_f^{*2} P_i^* - \frac{1 + \Gamma^* z^*}{A^*} \left[ 1 + \rho_f^* u^* - \frac{1 + \Gamma^* z^*}{A^*} \right]^2} \quad (10)$$

**Constitutive Relations:**  $f_{TP}$  is assumed to be calculated based on the single friction factor for a rectangular channel. For a laminar developed flow and non-slip flow can be calculated closely by the following empirical equation provide by Shah and London [15] with short side  $a$ , long side  $b$ , and a channel aspect ratio defined as  $\eta = a/b$ .

$$f_{TP} Re_D = 24 \left( 1 - 1.3553\eta + 1.9467\eta^2 - 1.7012\eta^3 + 0.9564\eta^4 - 0.2537\eta^5 \right) \quad (11)$$

Hidrovo et al [7] claim that the value of C is higher than those predicted by theory for fully developed single phase flow in rectangular channels of aspect ratio 10:1, which is 85. Several factors contribute to this discrepancy including entrance length effects and the bends in U-shape among others, all of which lead to higher effective  $fRe$  values [16].  $Re_D = 4\dot{m} \rho^* u^* / \rho_w \mu_{TP}$  and  $D = 2ab / (a + b)$  is hydraulic diameter.

The form of the relationship between  $\mu_{TP}$  and the quality  $x$  is chosen by equation proposed by McAdams et al. [17] as:

$$\frac{1}{\mu_{TP}} = \frac{x}{\mu_g} + \frac{1-x}{\mu_f} \quad (12)$$

The mass fraction of the gas at any cross section of the channel is denoted by the ratio of the mass flow rate of the gas to that of the two-phase mixture as follows.

$$x = \frac{\rho_i u_i A_i}{\rho_i u_i A_i + a \Gamma z} = \frac{1}{1 + \Gamma^* z^*} \quad (13)$$

## SOLUTION PROCEDURE

To obtain the effect of the liquid injection on the velocity and pressure distribution of the two-phase mixture along the microchannel, Eq. (10) is first integrated numerically by the fourth order Runge-Kutta method under boundary conditions  $u^*(0) = 1$  and  $P^*(0) = P_i^*$  along the microchannel length in which  $P_i^* = P_i / \rho_i u_i^{*2}$ . Then the void fraction, gas density, pressure and mass fraction of the gas are calculated from Eqs. (7), (8), (9) and (13) respectively.

## RESULTS AND DISCUSSION

In this homogeneous adiabatic air-water two-phase flow, air enters a rectangular microchannel with a uniform velocity at the rate of  $\dot{m} = 0.06 \mu gr/s$ ,  $T_i = 293K$  and  $P_i = 0.2 MPa$ . Liquid water is injected through one porous side wall with a uniform distribution for different rates,  $\Gamma^* = aL\Gamma/\dot{m} = 0.1, 0.5, 1, 5, 10$ . The microchannels surface is assumed to be hydrophobic and its sizes are: width  $a = 50\mu m$ , depth  $b_i = 500\mu m$ , length  $L = 24mm$  with variable cross section as  $A^* = (1 - \gamma z^*)$  where  $\gamma = (b_i - b_o)/b_i$  (see Fig. 1).

Fig. 2 shows the non-dimensional velocity distribution along the microchannels for different liquid water injection rate through the porous wall. In this case  $\gamma = 0.5$ . This means that the outlet cross section has been decreased in half. The velocity trend is linear for small values of liquid injection up to  $\Gamma^* = 1$  but after that increases significantly. Fig. 3 illustrates the same function but for three different channel slopes,  $\gamma = 0, 0.5, 0.75$ , when  $\Gamma^* = 10$ . The figure explains that the variation of slope almost has no effect on the

velocity trend up to 40% of the channel length but after that increases sharply. Comparison between this figure with the previous one states that the effect of  $\gamma$  is more severe than that of  $\Gamma^*$ . Fig. 4 depicts the pressure variation against the channel length for different water injection rates. At low injection rate, the pressure variation is linear and the effective force is probably the frictional force and the inertial force has no significant effect, but at high injection rate both forces become important. Fig. 5 reports the pressure variation for different slopes of the channel. Similar to the velocity, the slope of the channel has more effect on pressure drop than that of the water injection rate especially near to the end region of the channel. For instance, when the exit cross section is one fourth of the inlet one,  $\gamma = 0.75$ , the exit pressure reaches about 82% of the inlet pressure.

Fig. 6 describes the mass fraction distribution along the channel for different liquid injection. The results show that for low liquid injection, the mass fraction drops linearly but it has exponential behavior at high rate of the liquid injection. On other hand, the most variation occurs at the entrance region of the channel. As Eq. (13) shows the mass fraction is independent of the channel slope, because the gas flow rate is constant and the liquid injection rate only depends on location. Fig. 7 plots the vapor void fraction as a function of location for  $\Gamma^* = 10$  and different channel slopes. In contrast to the mass fraction, the variation of the void fraction is distributed over the entire length. It is expected, liquid water blobs are formed in the middle of the microchannel and form a slug flow pattern. These water blobs fill a portion of the channel with the air flow around them and cause the void fraction changes. This flow structure allows us to choose a homogeneous model to understand more two-phase flow behavior in microchannels under different liquid water injection.

## CONCLUSIONS

This paper presents a numerical simulation of one-dimensional homogeneous adiabatic air-water two-phase flow in a rectangular microchannel with one boundary porous wall. The other walls are solid under hydrophobic conditions. We have assumed gas enters the microchannel with a uniform velocity and liquid water is injected through the porous side wall. The modeling and solution of the conservation equations provide two-phase velocity distribution and pressure drop for different water injection rates. It is expected the hydrophobic conditions help to the formation of liquid water blobs in the middle of the microchannel and form a slug flow pattern. The present results show that pressure drop and velocity enhance sharply when the water injection rate exceeds a critical value. This pressure drop is significant because of slug flow formation that fills a substantial portion of the microchannels cross section and act as a blockage to the air flow.

## NOMENCLATURE

$A$	cross section area, (m <sup>2</sup> )
$a$	channel width, (m)
$b$	channel height, (m)
$D$	channel diameter, (m)
$f$	friction coefficient
$L$	channel length, (m)
$\dot{m}$	mass flow rate, (kg/s)
$P$	pressure, (Pa)
$R$	gas constant, (kJ/kg.K)
$Re$	Reynolds number, ( $\rho u D / \mu$ )
$u$	velocity, (m/s)

$T$	Temperature, (K)
$x$	vapor mass fraction
$z$	compressibility factor, coordinate system, (m)

### Greek Symbols

$\alpha$	void fraction
$\gamma$	slope of channel
$\mu$	viscosity, (kg/m.s)
$\Gamma$	injection of liquid per unit area, (kg/m <sup>2</sup> .s)
$\vartheta$	specific volume
$\rho$	density, (kg/m <sup>3</sup> )

### Subscripts

$f$	liquid
$g$	gas
$i$	inlet
$o$	outlet
$TP$	two-phase
$w$	wall

### Superscripts

*	Dimensionless
---	---------------

## References

1. Tuber K., Pocza D., Hebling C., Visualization of water buildup in the cathode of a transparent PEM fuel cell // *J. Power Sources*, 2003. 124. Pp. 403–414.
2. Hakenjos A., Muenter H., Wittstadt U., Hebling C., APEM fuel cell for combined measurement of current and temperature distribution and flow field flooding // *J. Power Sources*, 2004. 131. Pp. 213–216.
3. Sinha P.K., Halleck P., Wang C.Y., Quantification of liquid water saturation in a PEM fuel cell diffusion medium using X-ray microtomography // *Electrochem. Solid- State Lett.*, 2006, 9, A344-A348.
4. Yang X.G., Zhang F.Y., Lubawy A.L., Wang C.Y., Visualization of liquid water transport in a PEFC // *Electrochem. Solid-State Lett.*, 2004, 7, A408-A411.
5. Zhang F.Y., Yang X.G., Wang C.Y., Liquid water removal from a polymer electrolyte fuel cell // *J. Electrochem. Soc.*, 2006, 153, pp. A225-A232.
6. He G., Ming P., Zhao Z., Abudula A., Xiao Y., A two-fluid model for two-phase flow in PEMFCs // *J. Power Sources*, 2007, 163, pp.864-873.
7. Hidrovo, C.H., Wang, F., Lee, E.S., Vigneron, S., Steinbrenner, J.E., Paidipati, J.V., Kramer, T.A., Eaton, J.K., Goodson, K.E., Experimental investigation and visualization of two-phase flow and water transport in microchannels // *ASME Int. Mechanical Engineering Congress and RD&D Expo, Anaheim, California, USA*, Nov. 13-19, 2004.
8. Vigneron S., Hidrovo, C.H., Wang, F., Lee, E., Steinbrenner, J.E., Kramer, T.A., Eaton, J.K., Goodson, K.E., 1-D homogeneous modeling of microchannels two-phase flow with distributed liquid water injection from walls // *ASME Int. Mechanical Engineering Conference, Anaheim, California, USA*, 2004. Pp.13–19.
9. Saisorn, S., Wongwises, S., Flow pattern, void fraction and pressure drop of two-phase air-water flow in a horizontal circular microchannels // *Experimental Thermal and Fluid Science*, 2008, 32. Pp. 748–760.
10. Wongwises, S., Pipathattakul, M., Flow pattern, pressure drop and void fraction of two-phase gas-liquid flow in an inclined narrow annular channel // *Experimental Thermal and Fluid Science*, 2006, 30. Pp. 345–54.
11. Chung, P.M.Y., Kawaji, M., Kawahara, A., Shibata, Y., Two-phase flow through square and circular

microchannels: effects of channel geometry// *J. Fluid Engineering Transaction, ASME*, 2004, 126. Pp. 546–552.

12. Kawahara, A., Chung, P.M.Y., Kawaji, M., Investigation of two-phase flow pattern, void fraction and pressure drop in a microchannels// *Int. J. Multiphase Flow*, 2002, 28. Pp. 1411–1435.

13. Hwang, J.J., Tseng, F.G. Pan, C., Ethanol- $CO_2$  two-phase flow in diverging and converging microchannels// *Int. J. Multiphase Flow*, 2005, 31. Pp. 548–570.

14. Chung, P.M.Y., Kawaji, M., The effect of channel diameter on adiabatic two-phase flow characteristics in microchannels// *Int. J. Multiphase Flow*, 2004, 30. Pp. 735–761.

15. Shah, R.K., London, A.L., *Laminar flow forced convection in ducts*, Supplement I to advances in heat transfer, New York, Academic press, 1978.

16. Shah, R.K., London, A.L., A correction for laminar hydrodynamic entry length solution for circular and noncircular ducts, // *J. of Fluid Engineering*, 1978, 100. Pp. 177–179.

17. McAdams, W.H., Woods, W.K. and Bryan, R.L., //Vaporization Inside Horizontal Tubes-II-Benzene-Oil Mixture, *Trans. ASME*, 64, 1942. Pp. 193.

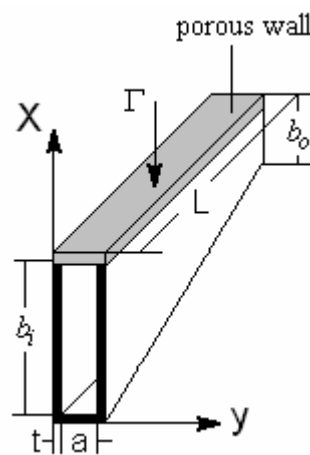


Fig. 1 Schematic diagram of the microchannel with variable cross section

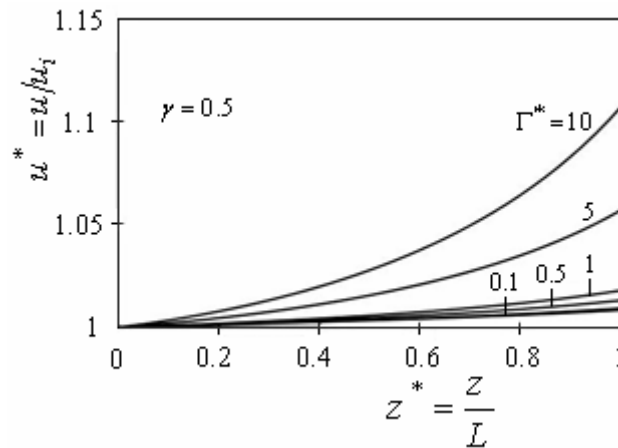


Fig. 2. Velocity distribution along the channel for different liquid injection

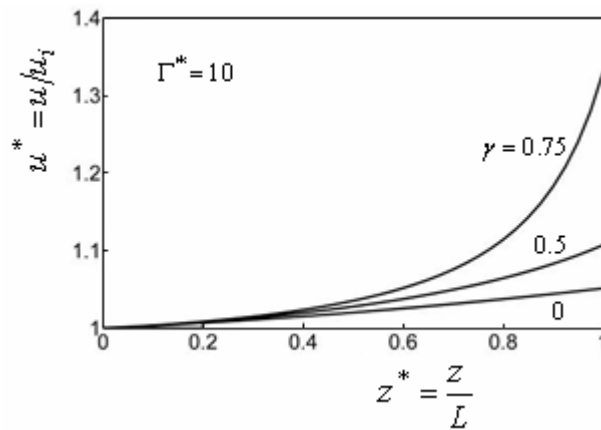


Fig. 3. Velocity distribution along the channel for different cross sections

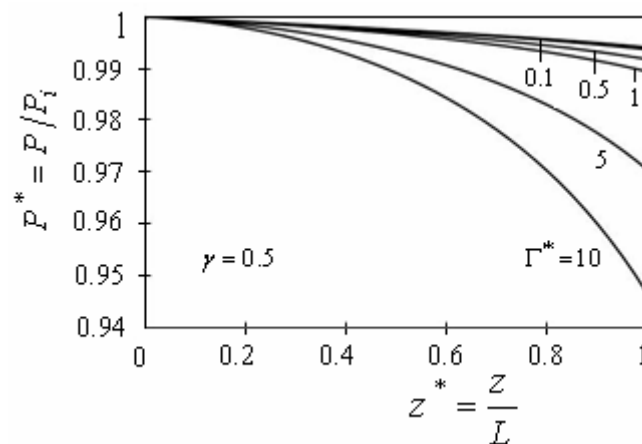


Fig. 4. Pressure distribution along the channel for different liquid injection

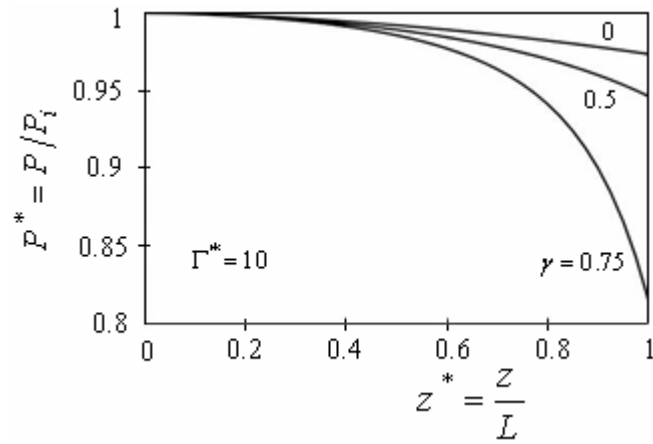


Fig. 5. Pressure distribution along the channel for different cross sections

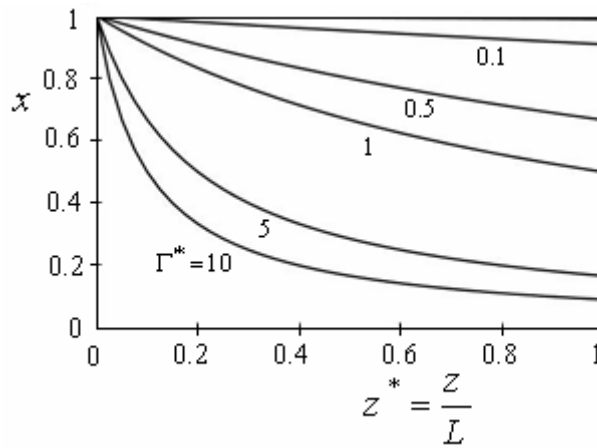


Fig. 6. Mass fraction distribution along the channel for different liquid injection

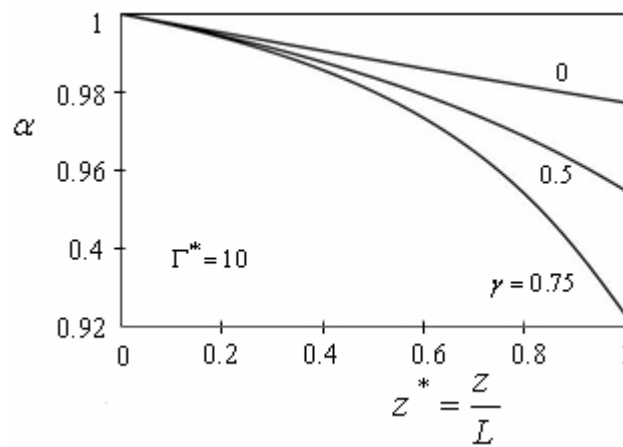


Fig. 7. Void fraction distribution along the channel for different cross sections

## VISUALIZATION OF A LOOP HEAT PIPE USING NEUTRON RADIOGRAPHY

**Atsushi Okamoto, Ryuta Hatakenaka**

Thermal Systems Group, Aerospace Research and Development Directorate

Japan Aerospace Exploration Agency

2-1-1 Sengen, Tsukuba, Ibraki, 305-8505, Japan

Tel: +81-50-3362-2132, Fax: +81-29-868-5969. E-mail: okamoto.atsushi@jaxa.jp

**Masahide Murakami**

Department of System and Information Engineering

University of Tsukuba

1-1-1 Tennodai, Tsukuba, Ibarki, 305-8571, Japna

Tel: +81-29-853-7366, Fax: +81-29-853-5207, E-mail: murakami@kz.tsukuba.ac.jp

### Abstract

It has recently become difficult to meet the increasing thermal control requirement of spacecraft with existing thermal control devices. A loop heat pipe (LHP) is an effective method to satisfy the requirement. JAXA has been developing a small LHP for space application. As part of the development and to better understand LHP operation, visualization of the working fluid using neutron radiography was conducted. As a result, much significant information, such as the behavior of the liquid at start-up and dryout behavior in the primary wick, was observed. This information contributes greatly to the improvement of LHP design and the establishment of a numerical simulation model.

### KEYWORDS

Loop heat pipe, Neutron Radiography, Visualization, Thermal Control, Heat transfer, Space.

### INTRODUCTION

It has recently become difficult to meet the increasing thermal control requirement of spacecraft with existing thermal control devices. A loop heat pipe (LHP) is an effective method to satisfy the requirement. An LHP is a two phase heat transfer device that utilizes the evaporation and condensation of a working fluid to transfer heat and capillary force to circulate the fluid [1–4]. Fig. 1 shows a schematic of an LHP. It consists of an evaporator, a vapor transport line, a condenser, a liquid transport line, and a reservoir (also called a compensation chamber or a hydro-accumulator). The evaporator contains a porous wick that develops a capillary force to circulate the fluid. The operating principle of the LHP is as follows: As heat load is applied to the evaporator, the working fluid is vaporized and a meniscus is formed at the vapor/liquid interface in the evaporator wick. The meniscus develops capillary force and the capillary force circulates the working fluid. The vapor enters the condenser through the vapor line and condenses in the condenser by dissipating the heat to the heat sink. The liquid is subcooled and goes back to the evaporator through the liquid line and bayonet tube. The excess liquid is stored in the reservoir. The LHP can transport much heat for a long distance against gravity and has many other excellent characteristics, such as high controllability of operating temperature and a shutdown function. Due to its excellent characteristics, the LHP has gained great acceptance as an essential thermal control device

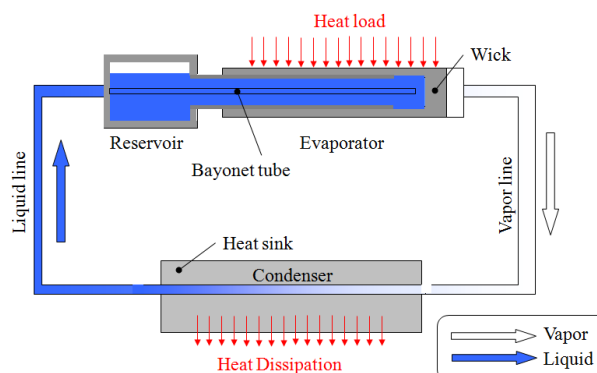


Fig. 1. Schematic of a loop heat pipe

among spacecraft thermal engineers and is being applied to many U.S., Russian, and European satellites [5–8]. A double-condenser-type LHP was used on the Monitor of All-sky X-ray Image (MAXI) in the Japanese Experiment Module (JEM) on the International Space Station (ISS), but it was not manufactured in Japan [9]. Although research and development of an LHP has been conducted for a long time in Japan, a Japanese LHP has not yet been employed in a practical mission. Two types of LHP are under development: One is a normal LHP and the other is a Reservoir Embedded LHP (RELHP). In the RELHP, a reservoir is not connected to the evaporator, and the wick core is used as the reservoir. The RELHP is in the space demonstration phase and an on-orbit experiment of an RELHP-based deployable radiator is being conducted [10–15]. Meanwhile, the normal LHP, in which the reservoir is connected to the evaporator, is in the laboratory experiment phase. As part of the development and to better understand LHP operation, visualization of the working fluid using neutron radiography was conducted. This paper describes the visualization test of the LHP using neutron radiography. This work was supported by radiation applications and the basic nuclear technologies transfer program of the Japanese Ministry of Education, Culture, Sports, Science and Technology.

## DESCRIPTION OF TEST PROGRAM

### Visualization Test

The objectives of the visualization test were to (i) observe the behavior of the working fluid in steady and transient state operation, (ii) use the visualization results to further our understanding of LHP operation, and (iii) improve hardware design and the numerical simulation model. Neutron radiography was employed to visualize the LHP. Neutron imaging is ideal for the visualization of liquid in metal containers since most metals are nearly transparent to neutron beam, while liquid has high neutron attenuation. That is, liquid and vapor can be easily distinguished because liquid (working fluid) appears dark on the images and metal (evaporator casing and tube) appears light on the image. The neutron beam facility at the research reactor JRR-3 in the JAEA (Japan Atomic Energy Agency) Tokai Research and Development Center was utilized for this test. Figure 2 shows the experiment setup. The neutron flux of this facility is  $1.5 \times 10^8$   $1/(\text{cm}^2 \cdot \text{s})$  and the beam size is  $255 \times 305$   $\text{mm}^2$ . The neutron beam that comes from the reactor core is scattered and absorbed by the liquid phase of the working fluid while it passes through the LHP envelope portion and the vapor phase. The neutron beam that passes through the LHP hits the converter and the part hit by the neutron beam emits a faint light. The light emitted from the converter is diffracted by mirrors and photographed by a cooled CCD camera.

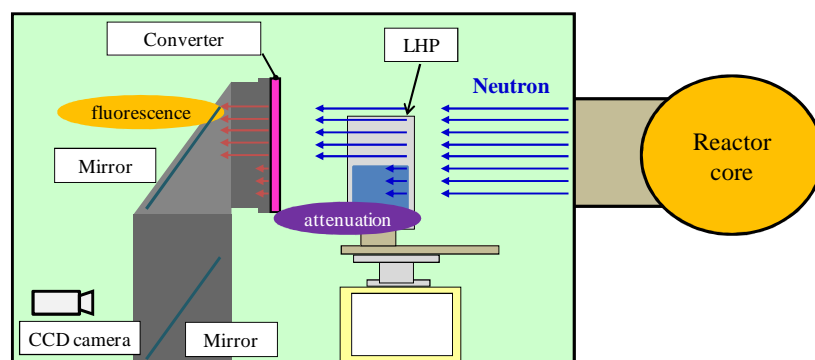


Fig. 2. Experiment set-up of visualization test

### Loop Heat Pipe

Fig. 4 shows a picture of the LHP used in the visualization test. It consists of an evaporator, a vapor line, a condenser, a liquid line, and a reservoir. The evaporator casing is made of aluminum and houses a stainless steel wick with a pore radius of 2.8  $\mu\text{m}$ . Ceramic heaters capable of delivering 400 W are attached to the evaporator casing to provide heat load to the evaporator. The vapor line and liquid line, each 1000-mm long, are made of stainless tubes with an O. D. of 3.17 mm. The condenser is made of stainless steel tube of 3.17 mm in O. D. x 500 mm in L. A cold plate is attached to the condenser pipe by soldering. Fluorinert (FC-3283, Sumitomo 3M Limited) was used as a coolant for the cold plate because it is nearly transparent to the neutron beam. It is cooled and circulated by a chiller. The reservoir is 7.6 mm in I. D. x 35 mm in L. The LHP does not have a secondary wick. The piping layout is arranged so that the entire LHP matches the converter size. The LHP is wrapped with ceramic wool, which has low neutron attenuation, for the purpose of thermal insulation. Water is used as a working fluid in the visualization test. Although water and stainless steel are not compatible, the reason why water is chosen as a working fluid is that it has high attenuation and high-contrast images can be obtained. In order to avoid the influence of NCG (Non Condensable Gas), test is conducted just after water is charged. The LHP major design parameters are summarized in Table 1. The location of the thermocouples and the heaters is shown in Fig. 5. Test was conducted at two different orientations as shown in Fig. 6.

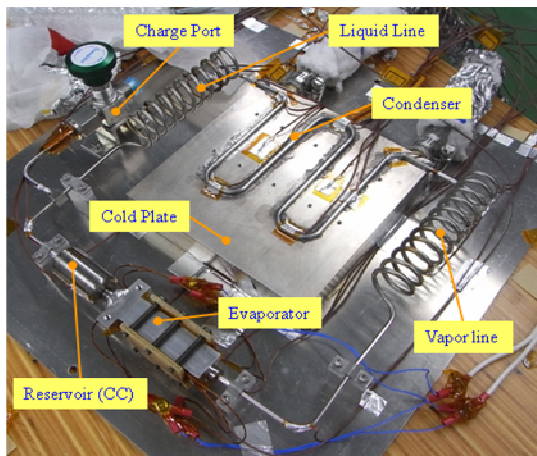


Fig. 4. LHP for visualization test

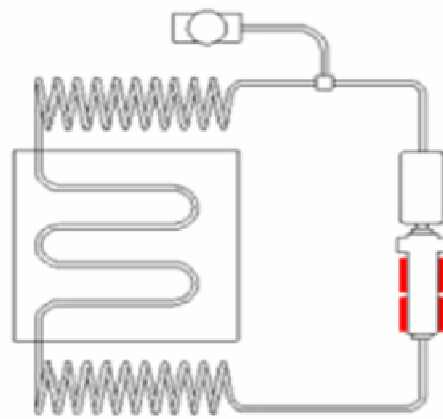


Fig. 5. Location of thermo-couples and heaters

Table 1. Major Design Parameters of the LHP

Evaporator	Size	18.6 x 18.6 x 76.5 mm
	Material	A5052
Wick (primary)	Size	O. D. 12.6 mm, I. D. 6 mm, L = 60 mm
	Pore Radius	2.8 $\mu\text{m}$
	Porosity	40%
	Material	SUS304
Vapor Grooves	Size	1.0 mm H. x 1.5 mm W
	Number of Axial Grooves	18
Vapor Line	Size	3.17 mm O. D. x 1000 mm L
	Material	Stainless Steel
Condenser	Size	3.17 mm O. D. x 500 mm L
	Material	Stainless Steel
Liquid Line	Size	3.17 mm O. D. x 1000 mm L
	Material	Stainless Steel
Reservoir	Size	7.6 mm I. D. x 35 mm L
	Material	Stainless Steel
Bayonet Tube	Size	1.58 mm O. D.
	Material	Stainless Steel
Working Fluid		Water

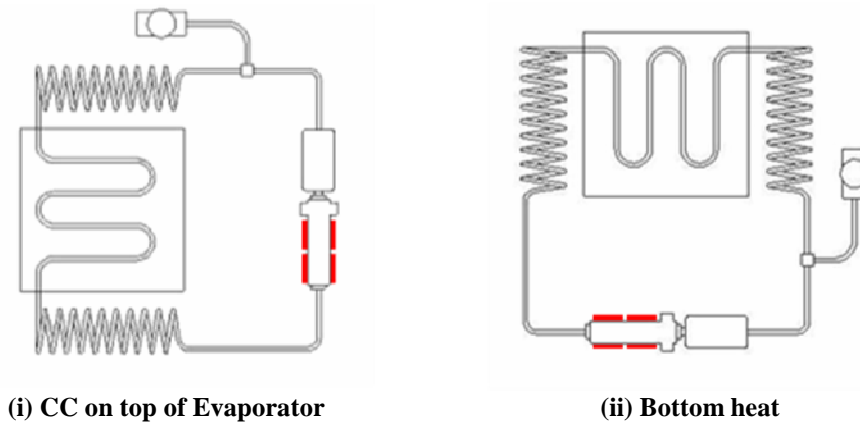


Fig. 6. LHP orientations and imaging area

## EXPERIMENTAL RESULTS

A comprehensive series of tests was performed to characterize thermal performance under steady and transient states. Fig. 7 and 8 show the neutron radiographic images at a vertical orientation with CC on top of the evaporator (Fig. 6 (i)). Fig. 7 shows the image of empty LHP and Fig. 8 shows the image when the LHP is working at steady state. In this paper, the behavior of the liquid in steady state and in dryout at bottom heat (Fig. 6(ii)) are described.

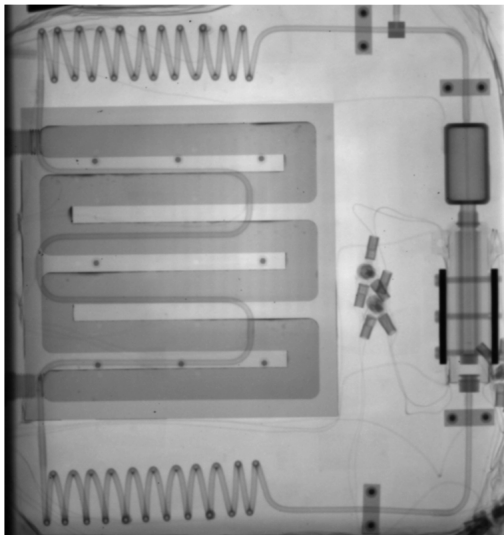


Fig. 7. Neutron radiographic image of the LHP without working fluid

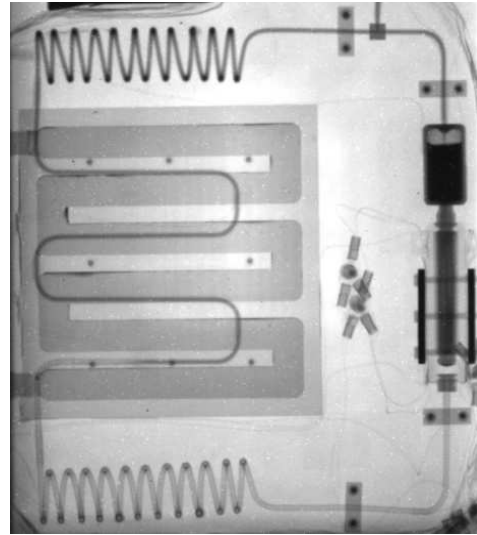


Fig. 8. Neutron radiographic image of the LHP with working fluid

### Behavior of Liquid in Steady State

The variation of liquid distribution in the evaporator under steady state at bottom heat with a heat load was examined with the aid of visualization by neutron radiography. The heat load was increased stepwise from 40 to 120 W. The LHP successfully started up at 40 W and operated stably at every heat load, as shown in Fig. 9. Visualization images of the evaporator when the LHP was operating under steady state at each heat load are shown in Fig. 10. When the LHP was operating at 40 W, the liquid gathered in the left half of the wick core and the vapor occupied the remaining space, as shown in Fig. 10 *a*. It is seen that a meniscus was formed in the wick core. This meniscus helps supply liquid to the upper side of the primary wick in 1-g. It is also believed that another meniscus might be formed at the exit of the connection tube, which connects the evaporator and the reservoir. This is because the liquid level in the reservoir was higher than the height of the connection tube. When the LHP was operating at 60, 80, and 120 W, the liquid in the

wick core gathered only on the lower side due to gravity, and the liquid amount varied with heat load, as shown in Fig. 10 *b*, *c*, and *d*. In these cases, the wick core and the reservoir were hydraulically connected with liquid through the connection tube, that is, liquid was supplied to the wick core from the reservoir. This is very important for LHP operation because the LHP adjusts the necessary liquid amount from the reservoir during transient state. In addition, if vapor generates in the wick core, the vapor must flow to the reservoir or be compensated by the subcooled liquid or liquid supplied from the reservoir. It is interesting, however, to note that the liquid in the wick core gathered only on the lower side due to gravity. In such a situation, the primary wick has to carry the liquid against the gravity to the upper side where the heat load is applied. Since this causes an increase of the pressure drop of the system, a device such as a secondary wick is necessary to prevent it.

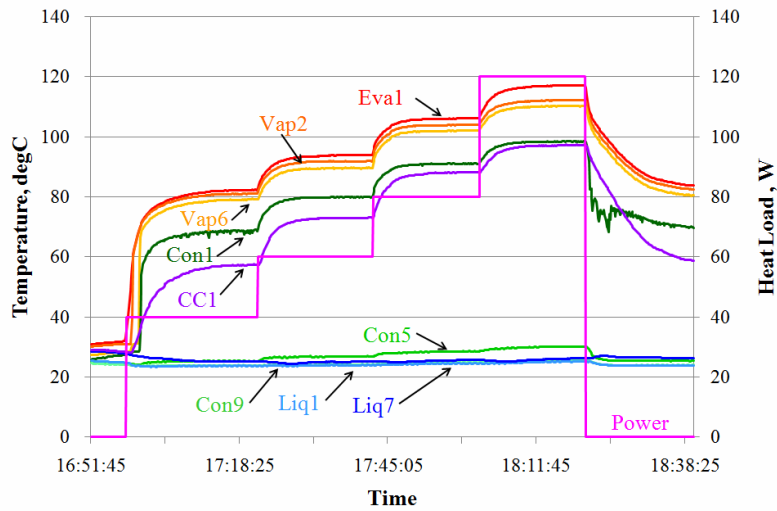


Fig. 9. Temperature history of LHP in visualization test

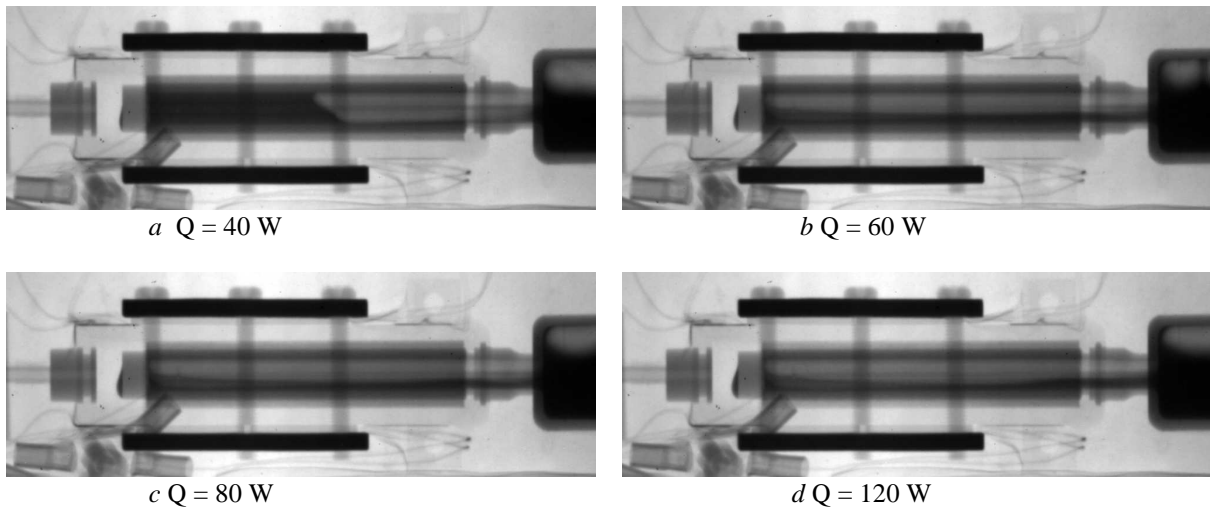


Fig. 10. Neutron radiographic image of the LHP evaporator (Bottom heat,  $Q = 40$  W, 60, 80, 120)

### Behavior of Liquid in Dryout

As described previously, the LHP operated stably at 120 W in the bottom heat when the heat load was increased stepwise from 40 W. However, the LHP failed during start-up when the heat load of 120 W was suddenly applied to the evaporator at bottom heat, resulting in dryout. The transient variations of liquid distribution in the evaporator were successfully visualized by neutron radiography. Fig. 11 shows the time variations of the temperatures of the LHP during start-up failure in the case of a heat load of 120 W at bottom heat. Fig. 12 shows neutron radiographic images indicating the distribution of liquid in the evaporator. Image a) shows the distribution of liquid before heating, where the vapor line and the vapor grooves were filled with liquid. When the heat load of 120 W was applied, the liquid in the vapor grooves rapidly evaporated and the vapor flowed through the vapor line, as shown in image b. The returning liquid wetted the end of the primary wick and the amount of liquid in the primary wick core increased, as shown in Fig. 12 b, c, and d. It is found from Fig. 11 that the vapor front passed over the condenser inlet right after the heating started. The excess liquid was stored in the reservoir and the liquid level in the reservoir became higher than that in the primary wick at Fig. 12 c. At that time, the liquid in the wick core gathered in the lower side of the core. However, the liquid amount in the wick core began to decrease and to localize near the end of the wick core, as shown in Fig. 12 d. It can be seen from the images that the liquid level in the reservoir was higher than that in the wick core. It is believed that a meniscus formed at the exit of the connection tube between the evaporator and the reservoir because the gap thickness between the inner surface of the connection tube and the outer surface of the bayonet tube is narrow enough to form one. Then the high-pressure vapor in the wick core interrupted the liquid supply from the reservoir at the meniscus and the liquid disappeared in the wick core at Fig. 12 e. At the same time, the temperature rising rate of the evaporator increased. Finally, partial dryout began in the middle of the primary wick at Fig. 12 f. Because the heaters are attached near the middle of the evaporator and the liquid is supplied at both ends of the evaporator from the bayonet tube and the reservoir, the middle of the primary wick is more susceptible to dryout. It is found from Fig. 11 that the temperature of the evaporator (Eva1) increased and the temperature of the condenser (Con1) decreased at 19:51, which indicates that the generation of vapor in the evaporator decreased due to the liquid shortage in the primary wick. The dryout area in the primary wick expanded with the lapse of time, and the evaporator temperature continued to increase. At Fig. 12 g, a larger portion of the primary wick was dried out, while the end of the primary wick was still wet with the returning liquid from the bayonet tube. As the evaporator temperature reached over 150 °C, the heater turned off for the sake of safety at 19:52. After heating was stopped, the high-pressure vapor remained in the primary wick core, interrupting liquid supply from the reservoir, as shown in Fig. 12 h. When the evaporator temperature sufficiently decreased, the liquid entered the wick core from the reservoir and saturation of the primary wick began. It is concluded from this result that sufficient hydraulic connection through installation of a device such as a secondary wick between the primary wick core and the reservoir is necessary for stable operation of the LHP.

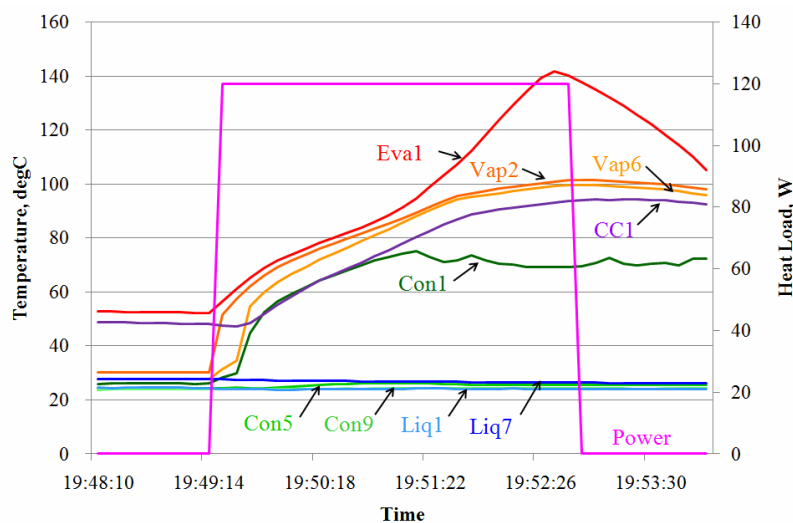


Fig. 11. Failed start-up in visualization test

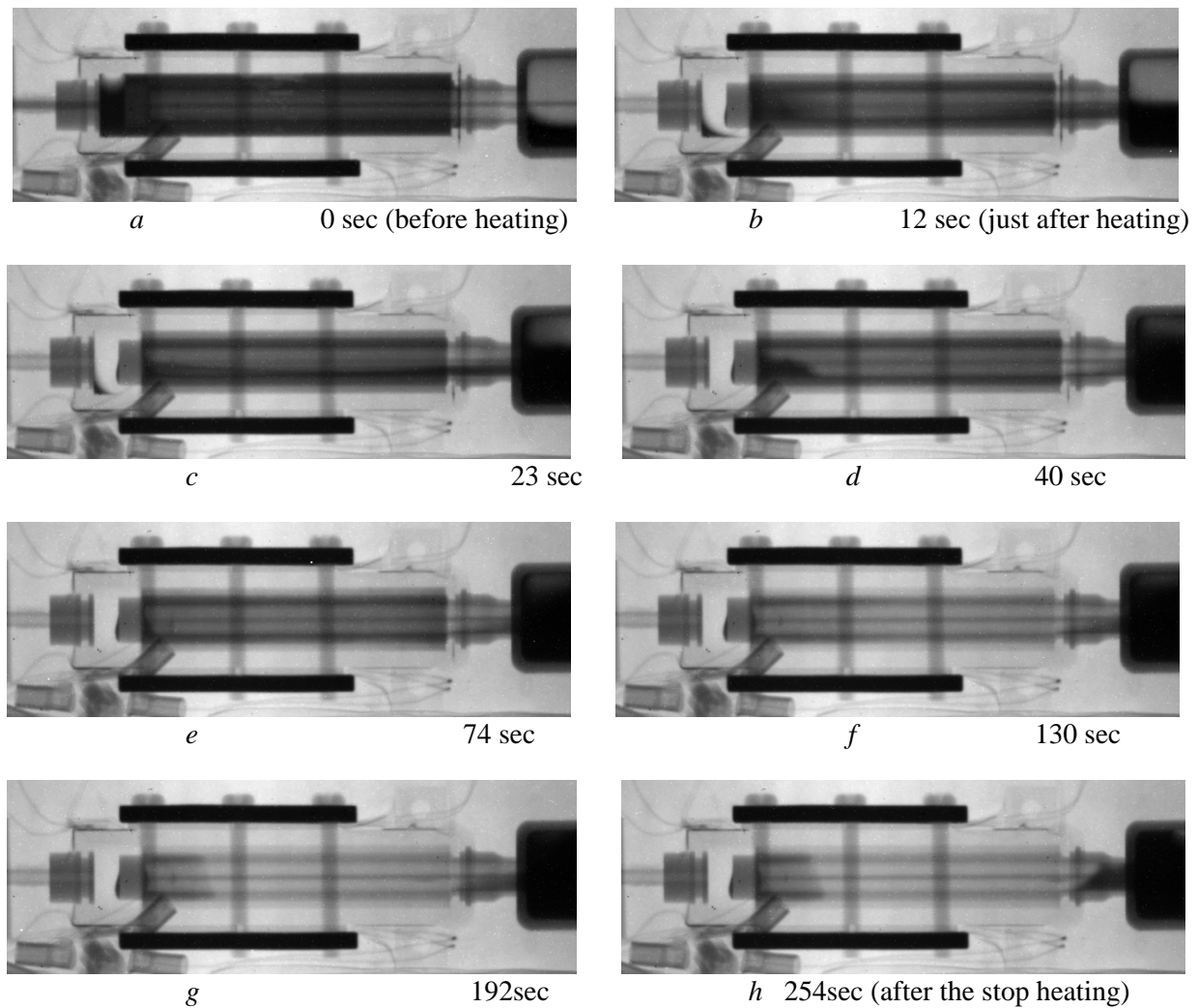


Fig. 12. Neutron radiographic image of the LHP evaporator (Bottom heat,  $Q = 120$  W)

## CONCLUSIONS

Visualization of the working fluid of the LHP in steady state and transient state operation was conducted to further our understanding of LHP operation. As a result, much significant information, such as the behavior of the liquid at start-up and dryout behavior in the primary wick was observed. This information is very useful since it is difficult to get from temperature data. The information contributes greatly to the improvement of LHP design and the establishment of a numerical simulation model.

### References

1. Ku J. Operating Characteristics of Loop Heat Pipes // *SAE Paper* No.1999-01-2007, 1999.
2. Maidanik Y. F and Fershtater Y. G. Theoretical Basis and Classification of Loop Heat Pipes and Capillary Pumped Loops // *Proc. 10<sup>th</sup> Intern. Heat Pipe Conf.*, X-7. Pp.1–15, 1997.
3. Kaya T. and Hoang T. T. Mathematical Modeling of Loop Heat Pipes and Experimental Validation // *J. of Thermophysics and Heat Transfer*. 1999. Vol.13, No.3, July-September.
4. Hoang T.T. and Ku J. Heat and Mass Transfer in Loop Heat Pipes // *Proc. of 2003 ASME Summer Heat Transfer Conf.*, July 21–23, 2003, Las Vegas, Nevada, USA
5. Oost S., Dubois M., Bedaert G., Moschetti B. and Amidies M. High Performance Capillary Loop, Operation Mapping and Applications on STENTOR // *SAE Paper*. 1996. No.961565.
6. Bodendieck F., Schllit R., Romberg O., Goncharov K., Buz V, and Hildebrand U. Precision Temperature Control with a Loop Heat Pipe // *SAE Paper*. 2005. No.2005-01-2938.
7. Douglas D., Ku J. and Kaya T. Testing of the Geoscience Laser Altimeter System (GLAS) Prototype Loop Heat Pipe // *AIAA Paper*. 1998. No.98-1587.
8. Grob E.W. System Accommodation of Propylene Loop Heat Pipes for the Geoscience Laser Altimeter System (GLAS) Instrument // *SAE Paper*. 2001. No.2001-01-2263.
9. Nagai H. and Ueno S. Performance Evaluation of Double-condenser Loop Heat Pipe onboard Monitor of All-sky X-ray Image (MAXI) in Thermal Vacuum Testing // *SAE Paper*. 2005. No.2005-01-2939.
10. Ogushi T., Murakami M., Yao A., Okamoto T., and Masumoto H. Heat Transfer Performance of Flexible Looped Heat Pipe // *Proc. of 10<sup>th</sup> IHPC*. 1997. Pp.1–6.
11. Ogushi T., Yao A., Xu J., Masumoto H., and Kawaji M. Heat Transfer Characteristic of Flexible Looped Heat Pipe under Micro-gravity Condition // *Proc. of 11<sup>th</sup> IHPC*. 1999. Pp.1–6.
12. Ogushi T., Haga S., Ishikawa H., Yao A., Miyasaka A., and Noda H. Mathematical Modeling for Predicting Steady State and Transient Characteristics of Reservoir Embedded Looped Heat Pipe (RELHP) // *SAE Paper*. 2001. No.2001-01-2239.
13. Ishikawa H., Yao A., Ogushi T., Haga S., Miyasaka A., and Noda H. Development of Loop Heat Pipe Deployable Radiator for Use on Engineering Test Satellite VIII (ETS-VIII) // *SAE Paper*. 2001. No.2001-01-2341.
14. Kawasaki H., Yabe T., Okamoto A., Ishikawa H., Nomura T., and Saito Y. Characteristics of Reservoir Embedded Loop Heat Pipe in an Orbital Environment in the First Year // *SAE Paper*. 2009. No.2009-01-2518.
15. Kawasaki H., Noda H., Yabe T., Ishikawa H., Nomura T., and Saito Y. Characteristics of Reservoir Embedded Loop Heat Pipe in Deployable Radiator on ETS-VIII at Beginning of the Experiment under Orbital Environment // *AIAA Paper*. 2008. No.08-3926.

## MINIATURE LOOP HEAT PIPES WITH NONINVERTED MENISCUS POWDER CAPILLARY STRUCTURE

**Victar V. Maziuk, Viachaslau V. Doktorau\*, Alexander F. Ilyushchanka,**  
Powder Metallurgy Institute, Platonov str., 41, 220005, Minsk, Belarus  
E-mail: slaslasla@tut.by

**Vladislav N. Murzin, Valery P. Radchenko**  
2 JSC "Radiofizika", Geroev Panfilovtsev str., 10, Moscow, Russia,  
vnmurzin@mail.ru

### Abstract

Miniature loop heat pipes (MLHP) use evaporators with inverted meniscus. This design requires using capillary structure with relatively high thermal resistance to avoid vaporization in compensation camber. MLHP with noninverted meniscus concept allows using capillary structure with high thermal conductivity (such as copper powder capillary structure). Results of calculation based on developed model shown, that design of MLHP with noninverted meniscus provides more efficient heat exchange at evaporation comparing to standard loop heat pipes. Experimental test of manufactured MLHP with noninverted meniscus shown that own thermal resistance of evaporator with noninverted meniscus is significantly less than own thermal resistance of evaporators with inverted meniscus.

### KEYWORDS

Loop heat pipe, inverted meniscus, noninverted meniscus, capillary structure, heat transfer.

### INTRODUCTION

Rapid technique development creates new requirements to provide heat regimes, which can't be satisfied by heat pipes (HP) of conventional design. One of mentioned requirements is the necessity to provide a HP operation in the mass forces field in the case of quite great heat transfer distance. In mentioned conditions the most complex problem to be solved is heat transfer in antigravitational regime when working fluid returning into evaporation zone is in direct opposition to the gravitation force. The same situation may be also appears due to inertial overloads in moving objects. Physical aspect of operation limits in these cases is condition of the great increasing of hydraulic resistance and relative low magnitude of capillary pressure. Effective great distance heat transfer at any HP orientation in the gravitational field is provided by loop HP (LHP) [1]. The basic physical and design principles of LHP concept are give in the following.

1. Renunciation of displacement of capillary structure along the full length of heat transfer providing hydraulic connection between source and sink of heat, that takes place in conventional HP. Capillary structure is displaced mainly in the heat receiving zone, so the path of liquid moving inside capillary structure is just about several millimeters and it serves as capillary pump and heat plug.

2. Using capillary structure of quite small pore size 0.1–10  $\mu\text{m}$ , which allows creating great capillary pressure.

3. Both the transport channels for vapor and liquid are divided in space.

4. Evaporation zone is organized by inverted meniscus principle; it is means that heat and liquid flux are directed opposite to each other in the evaporation zone.

5. Maximally close dislocation of capillary structure vapor generation zone and heat receiving surface. Vapor removal is realized by special system of channels.

6. Strongly determined relationship between inner volumes of LHP constructive elements.

7. Liquid overcooling in condenser.

8. The presence of a reservoir (hydroaccumulator or compensation chamber) for liquid heat carrier.

Usually LHPs have a cylindrical evaporator with diameter from 12 up to 28 mm. The vapor and liquid channels length may achieve 10 m and more. The absence of capillary structure in mentioned channels

---

\* Corresponding author

allows them to be flexible and accept required shape. Another important LHPs advantage is low sensibility to the orientation with respect to gravity.

To spread the field of LHP application, for example for electronics and personal computers cooling it is necessary to make a miniaturization of heat removing equipment. It is quite a complex problem because evaporator diameter decreasing leads to limits connected with LHP operation principles. At the same times for mentioned LHP application it is necessary to use evaporator of diameter about 6 mm and vapor and liquid channel of 1–2 mm one. The ability of such equipments creation is shown in [1] where LHP with active zone length less than 40 mm are considered as MLHP. They may overcome HP of traditional constructions if heat transfer distance is about 0.3–0.5 m and it is necessary to provide effective operation at any orientation in gravity or if it is necessary to provide flexible or complex connection between heat source and heat sink.

In the work [2] it is reported about producing and investigations of a MLHP with cylindrical evaporator (diameter 9 mm, active length 65 mm) and flat one (active diameter 25.6 mm) Maximal heat transfer capacity with 0.4 m length were 130 W for water and 90 W for acetone as the working fluid.

In the work [3] a MLHP is described with cylindrical evaporator of 5–6 mm diameter and 0.2–0.25 m effective length which were developed for electronics cooling and have thermal transfer capacity of 80 Wt at any orientation relative to gravity. Own thermal resistance of MLHP is 0.3–0.5 K/W. In the work [4] the possibility to use such MLHP for cooling notebook PC without cooler is shown. However it is admitted that the cost of mentioned systems is quite large and a problem is posed to develop cheaper but not less effective systems of electronics cooling on the base of miniature LHPs.

In the work [5] MLHPs with titanium and nickel capillary structure were investigated. The best evaporator thermal resistance was 0.15 K/W at horizontal orientation of MLHP. But it should be accented that in [5] capillary structure consisted from 4 parts: biporous nickel layer, monoporous nickel layer, titanium layer and secondary wick. Apparently described construction is much expensive than for example uniform copper structure.

So a conclusion may be made that there are some problems to be solved in the field of contemporary electronics cooling with MLHP. So HPs of conventional design can't provide increasing requirements by cooling heat-generating equipments whereas MLHPs owing to necessary parameters are too expensive for wide application. Consequently developing of cheap in serial manufacturing MLHP with high effective heat conductivity for cooling contemporary electronic equipment is very important problem to be solved.

## **MINIATURE LOOP HEAT PIPES WITH NONINVERTED MENISCUS CONCEPT**

As a rule all tested in presence cooling systems based on MLHP use evaporators (diameter about 6 mm) of the same design that LHP of lager size (with inverted meniscus). It means that thermal resistance of such cooling systems maintains quite large. However, relatively small sizes of PC components allow avoiding the inverted meniscus principle, arrangement of longitudinal motion and evaporation of liquid in LHP evaporator by the scheme of conventional HP (with noninverted meniscus) [6, 7]. By this way it is possible to use materials with high heat conductivity such as copper for evaporator case and capillary structure. It leads to essential decreasing of evaporator thermal resistance.

The LHP evaporator case may be both cylindrical and flat. The simplest flat evaporator design performing noninverted meniscus principle is shown in Fig. 1.

Capillary structure consists from two parts. The thicker part totally overlays space inside the case dividing compensation chamber and vapor channel and serving as a hydraulic and heat plug. Thin part of capillary structure is displaced at the case wall and serves for liquid distribution overall the heat receiving surface and for effective heat exchange due to liquid evaporation from porous space.

Photo of the MLHP is given in Fig. 2.

The concept of MLHP with noninverted meniscus uses just items 1, 3, 6, 7 and 8 from those mentioned above. As for pore size (item 2) its area may be wider (up to 100  $\mu\text{m}$ ) due to small hydraulic resistance of capillary structure. Thickness of the capillary structure layer is not more than this providing required liquid heat carrier flow. Minimum thickness of the capillary structure layer provides approach of vapor generation zone to heat receiving surface.

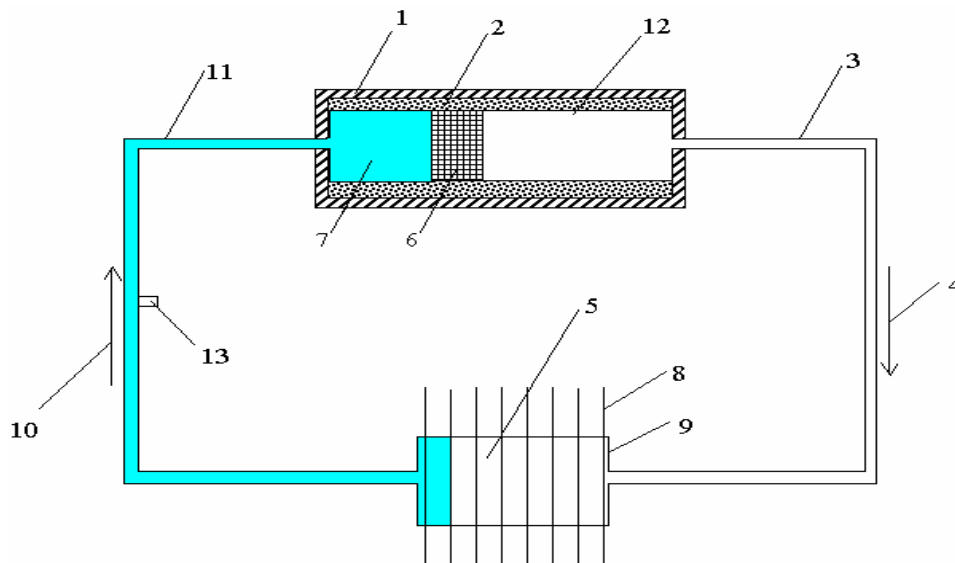


Fig. 1. Loop heat pipes with noninverted meniscus: 1 – evaporator; 2 – capillary structure; 3 – vapor line; 4 – vapor direction; 5 – condensation zone; 6 – plug; 7 – compensation chamber; 8 – sink; 9 – condenser; 10 – liquid direction; 11 – liquid line; 12 – evaporation zone; 13 – appendix

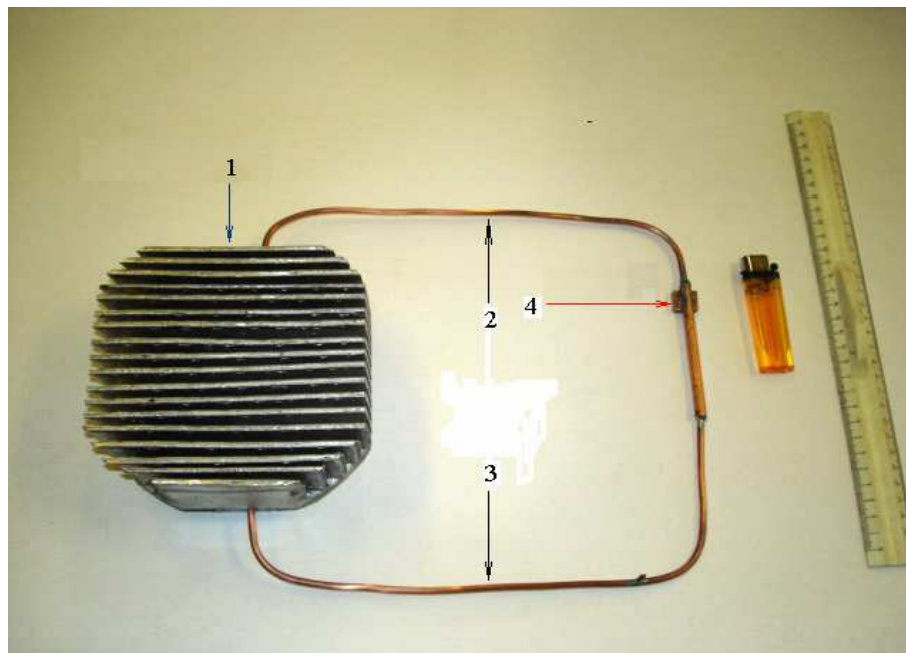


Fig. 2 Loop heat pipe: 1 – heat sink, 2 – vapor line, 3 – liquid line, 4 – evaporation zone

### OPERATING CHARACTERISTICS OF EVAPORATOR

Theoretical analyze of evaporator operation may be carried out using physical model with following assumptions:

- structure parameters of capillary structure porous powder material are constant along the MLHP,
- MLHP operates in the regime of evaporation,
- the heat flux density is constant over the evaporation zone surface,
- the operating temperature is the temperature of vapor saturation in vapor channel,

- there are no heat sources and heat sinks in vapor phase,
- liquid flow in capillary structure is laminar and may be described by Darcy's law,
- friction forces at the vapor-liquid interface are negligible comparing with friction forces inside capillary structure,
- the problem is considered as one-dimensional.

There are some well-known correlations between MLHP parameters, which are necessary for MLHP operation calculation. But as for MLHP with noninverted meniscus there are some features in mentioned correlations. One of well-known correlations is pressure correlation. It states that capillary pressure  $p_c$  must be greater than pressure drop over the loop. To provide a stable MLHP with noninverted meniscus operation capillary structure should be totally wetted because even a small dryout may lead to essential liquid penetration decreasing. In case of MLHP with noninverted meniscus pressure correlation may be written as following:

$$\frac{4\sigma}{d} = \rho_l gh + \frac{Q_{\max} v_l l_{ef}}{kLS_{cs}} + \frac{8v_v l_v Q_{\max}}{L\pi R^4} + \frac{Q_{\max} \delta_{cs}}{S_{hf} \lambda_{cs}} \frac{dp}{dT} \Big|_{T_v}, \quad (1)$$

where  $\sigma$  is liquid surface tension,  $d$  – mean hydraulic pore size,  $\rho_l$  – liquid density,  $g$  – gravity acceleration,  $h$  – vertical distance between evaporator and condenser,  $Q_{\max}$  – maximum heat transfer capability,  $v_l$  and  $v_v$  – kinematics viscosity of liquid and vapor,  $l_{ef}$  – effective liquid path in capillary structure,  $k$  – capillary structure permeability,  $L$  – latent evaporation heat,  $S_{cs}$  – cross section area of capillary structure excluding a plug,  $l_v$  – vapor line length,  $R$  – vapor line radius,  $\delta_{cs}$  – thickness of capillary structure layer,  $\lambda_{cs}$  – effective heat conductivity of capillary structure,  $S_{hf}$  – area of heat flux in capillary structure,  $T_v$  – temperature of saturated vapor over the evaporation surface.

So for maximum heat transfer capability one can get using Clapeyron – Clausius equation:

$$Q_{\max} = \frac{\frac{4\sigma}{d} - \rho_l gh}{\frac{v_l l_{ef}}{kLS_{cs}} + \frac{8v_v l_v}{L\pi R^4} + \frac{\delta_{cs}}{S_{hf} \lambda_{cs}} \frac{L\rho_v}{T_v}}, \quad (2)$$

where  $\rho_v$  is vapor density.

Another aspect of MLHP with noninverted meniscus is connected with parasitic heat flux. It is directed into compensation chamber and may lead to liquid boiling there. Temperature difference between evaporating and adsorbing surface of capillary structure shouldn't be less than temperature difference connecting pressure drop over the loop except capillary structure. Using Clapeyron – Clausius equation the greatest parasitic heat flux may be written as following:

$$Q_{par.\max} = Q_{\max} \frac{c_l}{L} \left[ T_v - T_{ocl} - \frac{T_v}{L\rho_v} \left( \rho_l gh + \frac{8v_v l_v Q_{\max}}{L\pi R^4} \right) \right] \quad (3)$$

where  $c_l$  is specific heat capacity of liquid,  $T_{ocl}$  - temperature of overcooled liquid.

The minimum required cross-section area of capillary structure providing distribution of liquid flow overall evaporation surface at maximum heat transfer is equal:

$$S_{cs} = \frac{Q_{\max} l_{ef} v_l}{kL(p_c - \Delta p_o)}, \quad (4)$$

where  $\Delta p_o$  is pressure drop over the loop except capillary structure and  $p_c$  is capillary pressure.

If width of capillary structure is  $a$  then its minimum thickness corresponding to minimum required cross-section area is equal  $\delta_{cs}=S_{cs}/a$ . At transfer heat power  $Q_{\max}$  the temperature differential across capillary structure of length  $l_{cs}$  is determined by relation:

$$\Delta T_{cs} = \frac{Q_{\max} \delta_{cs}}{\lambda_{cs} a l_{cs}}, \quad (5)$$

and temperature differential across wall of evaporator frame – by relation:

$$\Delta T_c = \frac{Q_{\max} \delta_c}{\lambda_c a l_{cs}}, \quad (6)$$

where  $\delta_c$  is the thickness,  $\lambda_c$  - heat conductivity of frame wall.

For own thermal resistance  $R_e$  of evaporator with noninverted meniscus at maximum heat load, determined by relation:

$$R_e = \frac{\Delta T_{cs} + \Delta T_c}{Q_{\max}}, \quad (7)$$

one can get from relations (4)–(7):

$$R_e = \frac{1}{a l_{cs}} \left( \frac{Q_{\max} l_{ef} \mu_l}{k \rho_l L a \lambda_{cs} (p_c - \Delta p_o)} + \frac{\delta_c}{\lambda_c} \right). \quad (8)$$

At large enough heat conductivity of case the second item in relation (8) is small, thus own thermal resistance of evaporator is about proportional to assigned heat flux and can be minimized by means of selection of capillary structure optimal parameters.

In a similar manner the relation for own thermal resistance of evaporator having cylindrical shape at maximum heat load may be obtained as following:

$$R_e' = \frac{1}{2\pi l_{cs}} \left( \frac{\ln \frac{d_c}{d_2}}{\lambda_c} - \frac{\ln \sqrt{1 - \frac{4Q_{\max} l_{ef} \nu_l}{\pi d_2^2 k L (p_c - \Delta p_o)}}}{\lambda_{cs}} \right), \quad (9)$$

where  $d_2$  is the inner diameter of evaporator case.

Dependence of the evaporator thermal resistance on transferred heat power calculated according to equation (9) is shown in Fig. 3 (copper powder capillary structure of optimized thickness has average pore size  $33 \mu\text{m}$ ,  $k = 1.45 \cdot 10^{-11} \text{ m}^2$ ,  $p_c = 7500 \text{ Pa}$ ,  $\Delta p_o = p_c/2$ ,  $l_{cs} = 6 \text{ cm}$ ,  $d_c = 6 \text{ mm}$ ,  $d_2 = 5 \text{ mm}$ ,  $\lambda_c = 380 \text{ W/(m}\cdot\text{K)}$ ,  $l_{ef} = 3 \text{ cm}$ ,  $\lambda_{cs} = 40 \text{ W/(m}\cdot\text{K)}$ , thermal physical properties of water as heat carrier are taken at  $60 \text{ }^\circ\text{C}$ ). As one can see, evaporator design of MLHP with noninverted meniscus provides efficient heat exchange at evaporation - thermal resistance of the evaporator is less in order comparing to evaporators with inverted meniscus [3, 5].

## EXPERIMENTAL INVESTIGATION

There was manufactured and tested a MLHP with noninverted meniscus intended as CPU heat remover. Its parameters were following:  $R = 1.5 \text{ mm}$ ,  $l_v = 0.45 \text{ m}$ ,  $d = 20 \mu\text{m}$ ,  $l_{cs} = 35 \text{ mm}$ ,  $\delta_{cs} = 1 \text{ mm}$ . Evaporator case had a cylindrical shape with outer diameter  $7 \text{ mm}$  and wall thickness  $0.5 \text{ mm}$ . Both evaporator and capillary structure were made of copper. Water was used as heat carrier liquid. There was measured temperature difference  $T_1 - T_2$  between cylindrical surface of evaporator case and surface of vapor line at evaporator outlet.

Result of MLHP test in horizontal position is shown in Fig. 3.

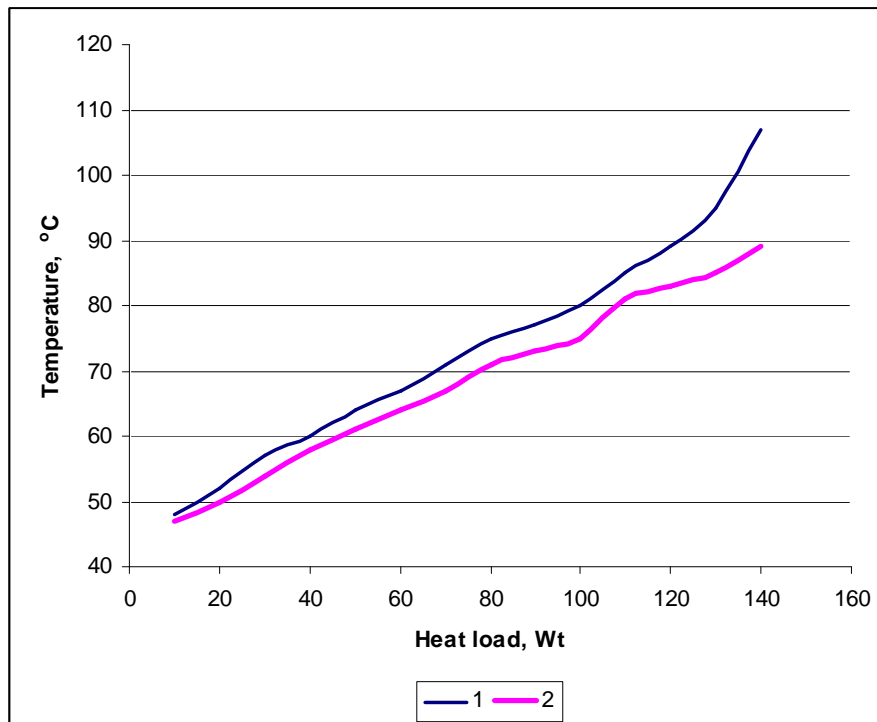


Fig. 3. MLHP test results: 1 – temperature of the evaporator frame, 2 – temperature of the vapor

The experimental values of own thermal resistance of evaporator in heat transfer range up to 120 W is about 0.05 K/W, what is significantly less than own thermal resistance of evaporators with inverted meniscus [3–5]. Additionally it should be noted that described MLHP with noninverted meniscus had extremely small heat input surface (order of 1 cm<sup>2</sup>) in comparison with MLHP with inverted meniscus. For instance in [5] MLHP with inverted meniscus had heat input surface equal 10 cm<sup>2</sup> and thermal resistance about 0.15 K/W. Consequently MLHP with noninverted meniscus is able to remove heat fluxes with much greater density than MLHP with inverted meniscus.

## CONCLUSION

Concept of miniature heat pipes with noninverted meniscus is formulated. Relations for main operation characteristic of MLHP with noninverted meniscus are obtained. Experimental test of MLHP with noninverted meniscus shown that own thermal resistance of evaporator with noninverted meniscus is significantly less than own thermal resistance of evaporators with inverted meniscus. Additionally MLHP with noninverted meniscus is able to remove heat fluxes with much greater density than MLHP with inverted meniscus.

## References

1. Maidanik Yu.F. State-of-the-art of CPL and LHP technology // *Proc. of the 11th Intern. Heat Pipe Conf., Tokyo, 1999*. Pp. 19–30.
2. Kiseev V., Belonogov A. Miniature heat transport systems with loop heat pipes // *Proc. of 4th Minsk Intern. Seminar "Heat Pipes, Heat Pumps, Refrigerators"*, Minsk, 2000. Pp. 15–22.
3. Pastukhov V.G., Maidanik Yu.F., Vershinin C.V., Korukov M.A. Miniature loop heat pipes for electronics cooling // *Proc. of 12th Intern. Heat Pipe Conf., Moscow, 2002*. Pp. 373–378.
4. Chang C.S., Huang B.J., Maidanik Yu.F. Feasibility study of a mini LHP for CPU cooling of a notebook PC // *Proc. of 12th Intern. Heat Pipe Conf., Moscow, 2002*. Pp. 390–393.
5. Chernysheva M.A., Vershinin C.V., Maidanik Yu.F. Development and test result of loop heat pipes with a flat evaporator // *Proc. of 12th Intern. Heat Pipe Conf., Moscow, 2002*. Pp. 134–139.
6. Gerasimov Ju.F., Maidanik Ju.F., Dolgirev Ju.V. Some results of investigation of low temperature heat pipes operating against gravity field // *Ing.-Phys. J.* 1976. Vol. XXX, No. 4. Pp. 581–586 (*in Russian*).
7. *Pat. 6533029A US*. Non-inverted meniscus loop heat pipe/capillary pumped loop evaporator / L. Fred; 2003.
8. Kreith F., Black W. Z. *Basic Heat Transfer*. Harper and Row Publishers, New York, 1980.

## DEVELOPMENT AND USING OF LONG-LENGTH COMPOSITE TWO-PHASE HEAT PIPES

**R. M. Bayasan, A. D. Lobanov, T. V. Bayasan, M. A. Lobanov**

"Inter Heat Pipe" Corporation  
117463, Paustovskogo street, 4, k.86, Moscow, Russia  
+7 (499) 724 4450; asanov.imr@yandex.ru

**S. I. Golubin**

"VNIIGAS" Institute  
142717, Razvilka, Moscow, Russia  
+7 (926) 228 1883; sgolubin@bk.ru

**G. P. Pustovoit**

Faculty of Geology  
Moscow State University  
119992, Leninskie Gory, Moscow, Russia  
+7 (495) 939 4920; egc@geol.msu.ru

### Abstract

Construction on saline permafrost soils is an actual engineering problem. Its solution would be impossible without soils thermal control and thermal stabilization for preventing dangerous cryogenic processes and their negative consequences concerned with violations of permafrost temperature conditions. The adequate technique for soils thermal stabilization is two-phase heat pipes also called thermal stabilizers (TS). The paper presents thermotechnical calculations results and efficiency evaluation for new TS type. Thermal stabilizers DOU-1 designed by "Inter Heat Pipe" Corp. have vertical or horizontal composite evaporators with the length up to 40 m. They permit thermal stabilization of permafrost under buildings and structures up to 80 m in width as well as deep freezing and cooling of soils. DOU-1 have been used at oil and gas field on Yamal peninsula.

### KEYWORDS

Thermal stabilization, two-phase heat pipes, permafrost, saline soils, construction, reliability.

### INTRODUCTION

Engineering structures reliability control is the actual problem of civil and industrial engineering in the northern and eastern regions of Russia where permafrost soils are prevailing. Permafrost soils temperature control is needed to prevent dangerous cryogenic processes and their negative consequences concerned with violations of permafrost temperature conditions. The development of thermal stabilization technique is an important scientific and practical problem. Seasonal cooling units i.e. two-phase heat pipes also called thermal stabilizers (TS) designed and manufactured by "Inter Heat Pipe" Corp. (TMD-4, TMD-5, TMD-5M, TSG-6 etc.) are widely used at different objects in Western and Eastern Siberia, Yakutia, Chukotka and other permafrost regions [1–4]. However these single-sectional thermal stabilizers (all their types and modifications) have maximal length 12 m that determined by manufacturing, transportation and installation conditions. This fact constricts range of application for permafrost thermal stabilization.

For thermal stabilization of soils at bases of buildings and structures with great dimensions, wellheads and shaft collars as well as for creation of frozen walls and dam cores with the depth about tens of meters we have set a problem to design a long-length TS. This device has to be in complete factory readiness with thermal-physic properties similar to ordinary single-sectional TS. In addition it has to be convenient to transportation and installation under close conditions of permafrost zone.

These requirements and further investigations lead to opinion that a long-length TS has to be composed of several sections – individual two-phase heat pipes. Note that the knowledge of thermal-physic processes inside a single two-phase heat pipe is not enough for design of composite TS. First of all the effective heat transfer has to be provided between adjacent heat pipes, i.e. in zones of adjoined heat pipes overlay. Secondly for each section of composite TS the amount of heat carrier should be precisely specified because of the length of "pool" in overlay zones (in evaporation zone) should be minimal as such "pool" disables a part of condensation zone for adjoined section (heat pipe).

## OVERALL PERFORMANCE

To solve the above problems we have performed investigations and testing of heat carrier film-type flowing inside sections of vertical and slightly inclined (almost horizontal) composite TS. The results permit to specify the amount of heat carrier for each section taking into account boundary conditions change during the active (cold) season. The length of adjoined heat pipes overlay zones (zones for heat transfer between sections) may be found from the next proportion:

$$\frac{L_{n,n-1}}{L_{n+1,n}} = \frac{K(N-n+1)}{N-n},$$

where  $K$  – coefficient depending on heat pipe body material,  $0.6 \leq K \leq 1.0$ ;  $N$  – the amount of sections in the composite TS;  $n$  – section number,  $2 \leq n \leq N-1$ ;  $L_{n,n-1}$  – the length of heat transfer zone between sections number  $n$  and  $(n-1)$ ;  $L_{n+1,n}$  – the length of heat transfer zone between sections number  $(n+1)$  and  $n$ .

If a composite TS consists of cylindrical (tubular) sections then intermediate insertion units with high thermal conductivity should be used at the contacts between sections. The task has been solved about tolerance for insertion unit diameter that would provide effective heat transfer at minimal use of heat-conducting lubricant.

Our research showed that the optimal choice of section type for composite TS is well known and widely used thermal stabilizers TMD-5 [1, 2]. These devices have efficient cold productivity and flat temperature gradient along evaporators. They are manufactured from aluminum alloy and they have  $\Omega$ -shape evaporator cross-section because an aluminum plate is welded to the tube to increase its cooling surface and rigidity. This shape is rather important for the effective adjunction of adjoined sections. We have designed and tested the connecting unit for  $\Omega$ -shape sections providing temperature drop at the most 0.2 centigrade.

Advantages related to aluminum include minor mass (e.g. 7.3 kg at the length of 6.2 m), high thermal conductivity and no need for an anticorrosive coating. The specific internal features of the TMD-5, decrease the turn-on time to 0.8–2.5 hours compared with 8–12 hours for steel TS. That is why during autumn and spring when freezing air temperatures are experienced only at night, steel TS have insufficient time to operate efficiently, whereas fast-response TMD-5 do. As a result, the active running time increases by 1–1.5 months per year.

As a result of our research and testing we have developed and manufactured the long-length composite TS called DOU-1 (it is Russian abbreviation for "long-length cooling unit") where TMD-5 plays a part of individual sections. There are two types of DOU-1: linear type for vertical disposition and L-shape type for slightly inclined (almost horizontal) disposition. In the last case the first section (condenser with the first evaporator) has L-shape, and the rest evaporator sections have linear shape. These constructions have been patented.

## DESIGN, CALCULATIONS AND RESULTS

On the basis of DOU-1 we have developed innovation engineering solutions for thermal stabilization of saline permafrost soils under buildings and engineering structures with "floors on the ground" at Bovanenkovo oil and gas field on Yamal peninsula. Yamal is located in the north of Western Siberia and is characterized by rigorous climate and continuous permafrost with the average temperature about -4.5...-5.0

centigrade. Soils are mainly saline, and so their phase transfer temperature is shifted to the range  $-1.5 \dots -2.5$  centigrade and lower. This fact essentially decreases bearing capacity of foundations [5, 6], especially for heat-releasing buildings and structures.

For instance, warm parking should provide suitable entrance and exit without ramps, and so floors on the ground have been projected. This design results in heat release into the soils, permafrost thawing, differential settlement and foundations deforming. Note that the last may be caused by frost heave as well. So, foundation soils needs for engineering maintenance and thermal stabilization. As heat-releasing buildings and structures may have width up to 50 m and more, ordinary TS types (up to 12 m in length) are inapplicable and long-length thermal stabilizer DOU-1 is now the unique solution.

In the first place a building thermal effect on foundation soils has to be evaluated, and then optimization problem about thermal stabilization may be set. For this purpose mathematical simulation of soils temperature fields has been used with the help of the computer program "HEAT" developed at the chair of geocryology in Moscow State University. This program realizes finite-difference method for Stephen's problem (thermal conductivity equation with phase transitions).

The model for simulation of building thermal effect on foundation soils is illustrated by Fig. 1. The building (warm parking, 48 m in width,  $+20$  centigrade inside) should be founded on the ground with thermal insulation (foamed polyurethane or polystyrene, 100 mm in thickness) and pile foundation (pile length is 11 m). Only a half of the building is shown at fig. 1 because of symmetry. Air temperature outside of building and snow cover parameters have been obtained from meteorological data. Permafrost soils at the base of the building are medium saline and strongly saline with high ice content and phase transfer temperature up to  $-2.2$  centigrade.

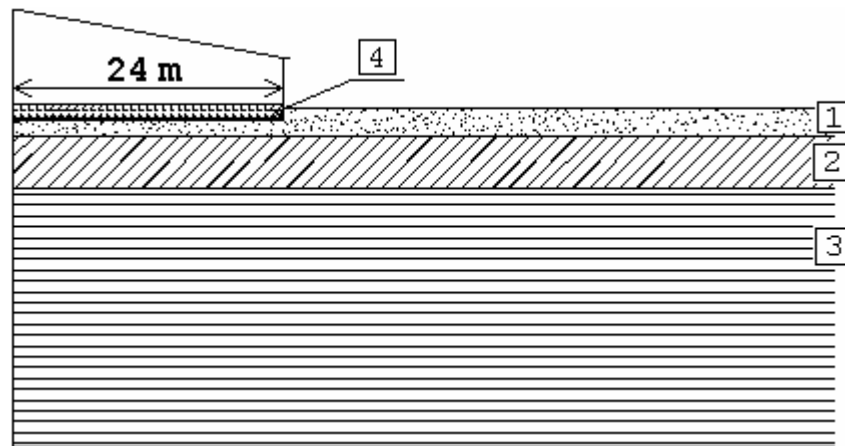


Fig. 1. Scheme for simulation of building thermal effect on foundation soils:  
1 – sand, 2 – saline loam, 3 – saline clay, 4 – floor with thermal insulation

The diagram (Fig. 2) presents calculation results. They show that during 15 years permafrost thawing will reach 6 m under building border and 8.5 m under its center. As a result 55...80% of pile length will be located inside thawed waterlogged ground. It will lead to abrupt decrease of bearing capacity and to unacceptable deformations (and probably to building destruction). Thermal insulation increase cannot prevent permafrost thawing – it may simply decrease thawing rate. Active thermal stabilization by horizontal cooling system is needed here, and DOU-1 is now the only device for this system design at so wide building (48 m).

We have suggested using DOU-1 horizontal type (Fig. 3) where the first section has L-shape: condenser is disposed vertically whereas evaporator is slightly inclined ( $1 \dots 2$  degrees to horizon). Two important geometrical parameters have been determined by calculation: the depth of TS location ( $1.0 \dots 1.2$  m) and TS-to-TS spacing (the distance between neighbour TS,  $2.8 \dots 3.0$  m). Note that DOU-1 may be installed into

previously laid pipes, and so their installation may be performed even after an object has been built as well as simultaneously with building. Installation do not require special equipment (lift crane, etc.) because of each section of DOU-1 weighs at the most 12 kg and has up to 10 m in length.

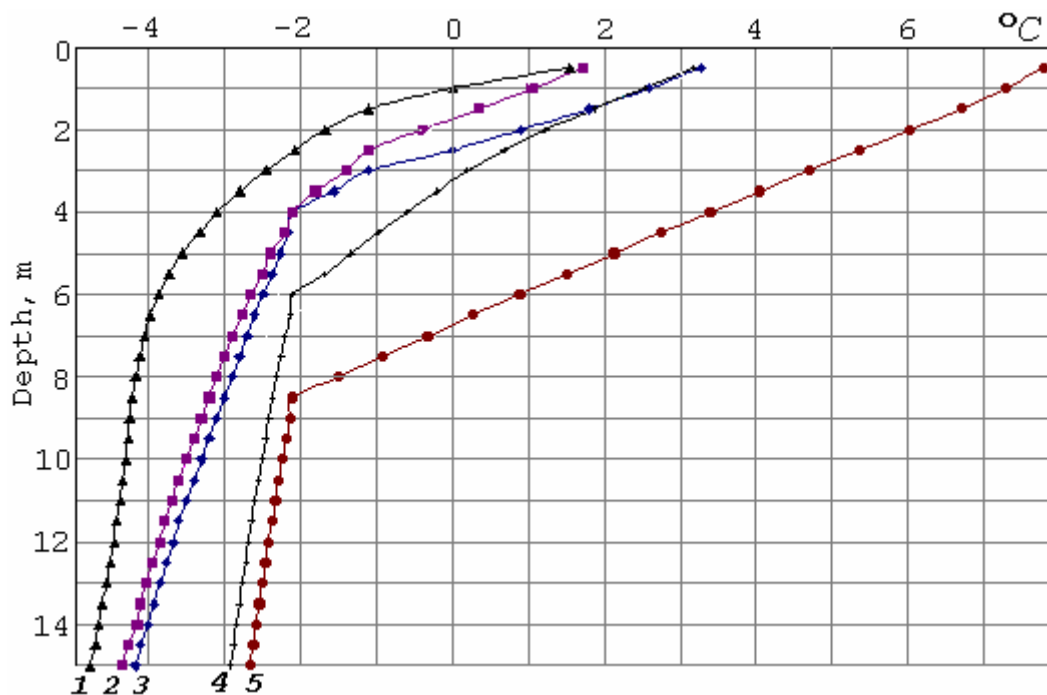


Fig. 2. Soil temperature at the end of warm season (Oct. 1): under natural condition (1); under the building border (2) and center (3) without DOU-1 after 5 years; the same after 15 years: border (4) and center (5)

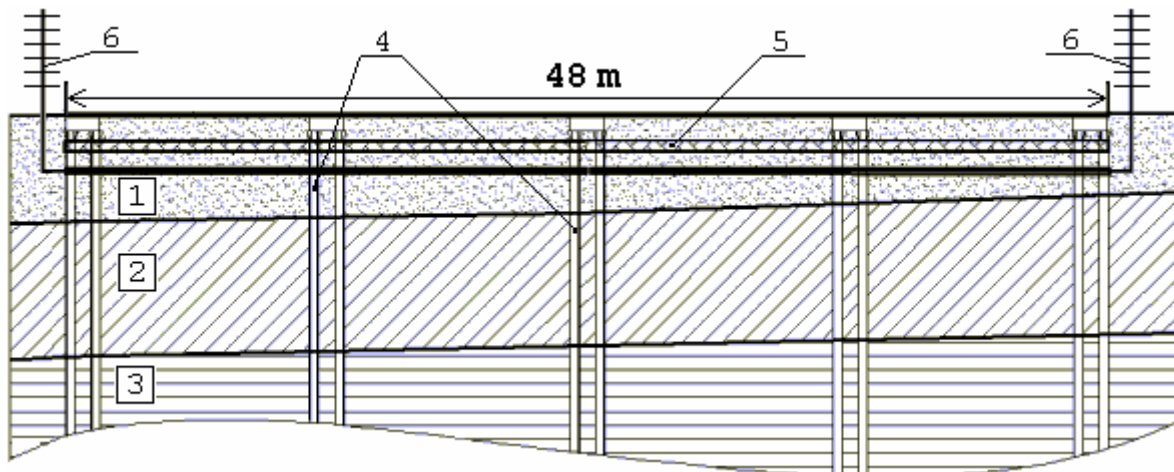


Fig. 3. The building foundation design with DOU-1 horizontal type: 1 – sand, 2 – saline loam, 3 – saline clay, 4 – piles, 5 – thermal insulation, 6 – DOU-1.

Thermal interaction between soils, building, cooling system and atmosphere have been simulated by means of the above-mentioned program "HEAT". The results (Fig. 4) show that DOU-1 operation retains

soil temperature below -4 centigrade during the first year and afterwards temperature decrease progresses. So, bearing capacity of pile foundation will be provided as well as thawing and deformation will be eliminated. This design has undergone examination by experts and has been realized at Bovanenkovo oil and gas field on Yamal peninsula (Fig. 5).

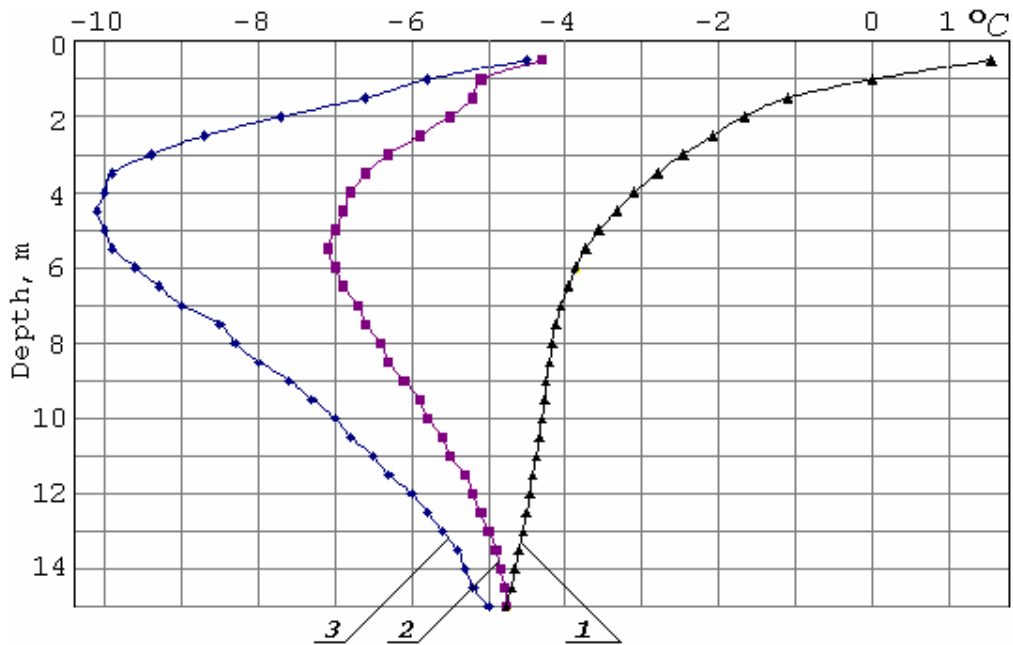


Fig. 4. Soil temperature at the end of warm season (Oct. 1): under natural condition (1); under the building border (2) and center (3) after 1 year of DOU-1 operation



Fig. 5. Backfilling of installed horizontal DOU-1 at the building construction on Yamal peninsula

## CONCLUSIONS

Construction on saline permafrost soils is impossible without soils thermal control and stabilization for preventing dangerous cryogenic processes and their negative consequences concerned with violations of permafrost temperature conditions. The adequate technique for soils thermal stabilization is two-phase TS. Long-length thermal stabilizers DOU-1 have been designed and used by "Inter Heat Pipe" Corp. They are composed of several sections – individual two-phase heat pipes of TMD-5 type, and they permit thermal stabilization of permafrost under buildings and structures up to 80 m in width as well as deep freezing and cooling of soils. A single section weighs at the most 12 kg and its length is up to 10 m, so transportation has no problems and installation do not require special equipment (lift crane, etc.). Complete factory readiness guarantees high quality and reliability of DOU-1 in contrast to some TS types being made and filled with heat carrier at field condition. For horizontal cooling system design DOU-1 may be installed with the spacing about 3 m – this is enough for joining of neighbour frozen zones. DOU-1 application at oil and gas field on Yamal peninsula seems to be successful.

## References

1. Bayasan R.M., Korotchenko A.G., Pustovoi G.P. Foundation stability on permafrost: probability, determinism and new technique // *Soil mechanics and foundation engineering*. 2002. No. 5. Pp. 26–31.
2. Bayasan R.M., Korotchenko A.G., Lobanov A.D., Pustovoi G.P. Technique for thermal stabilization of soils at bases of structures in permafrost regions // *J. of Glaciology and Geocryology*. 2004. Vol. 26 (suppl. Aug.). Pp. 201–206.
3. Bayasan R.M., Korotchenko A.G., Pustovoi G.P., Volkov N.G. Use of two-phase heat pipes with the enlarged heat-exchange surface for thermal stabilization of permafrost soils at the bases of structures // *Appl. Therm. Eng.* 2008. Vol. 28. No. 4. Pp. 274–277.
4. Bayasan R.M., Golubin S.I., Pustovoi G.P., Proshina T.V., Korotchenko A.G. Optimization of engineering solutions for thermal stabilization of saline permafrost soils at bases of structures by means of two-phase heat pipes // *Proc. of 7th Minsk Intern. Seminar "Heat Pipes, Heat Pumps, Refrigerators, Power Sources"*, Minsk, Belarus, 2008. Pp. 367–370.
5. Roman L.T. *Frozen ground mechanics*, MAIK "Science/Interperiodicals", Moscow, 2002. – 426 p.
6. Broushkov A.V. *Saline frozen grounds of Arctic shore, their origin and properties*, Moscow State University, Moscow, 1998. – 332 p.

## PERFORMANCE OF GEOTHERMAL HEAT PIPE USING PROPANE

**Thomas Grab, Thomas Storch, Sebastian Braune, Ulrich Gross,**  
Institute of Thermal Engineering, Technische Universität Bergakademie Freiberg  
09596 Freiberg, Germany  
Tel. 0049-3731-393185; fax 0049-3731-393963; e-mail: thomas.grab@iwtt.tu-freiberg.de

**Steffen Wagner**  
Institute of Drilling Technology and Fluid Mining, Technische Universität Bergakademie Freiberg  
09596 Freiberg, Germany

### Abstract

Approximately 48% of the heat pumps installed in Germany are combined with geothermal heat exchangers. Geothermal heat can be extracted by standard heat exchangers such as U-tubes or coaxial tubes, where a fluid is circulated by a pump. A more effective way is using the heat pipe principle where a fluid with a low boiling temperature (e.g. Propane) is circulated through the heat exchanger. A combination of both types of heat exchangers can be very effective for heating and cooling as the heat is stored in the ground and helps the underground temperature to regenerate much faster.

On the property of the TU Bergakademie Freiberg an energy park has been installed where a heat pump system based on seven geothermal heat pipes combined with seven geothermal brine tubes is currently in evaluation. The present work contribution is focused on the operating performance of this heating and cooling system. The experimental plant is equipped with various measuring devices including a fibre-optical sensor fixed outside of the tubes. The present paper reports the effect of various operating parameters on these temperature profiles along the tubes together with pressure and temperature measurements at selected locations on the heat pump system, and finally its power consumption. The amount of extracted and introduced energy per day will be presented, leading to conclusions for an effective operating regime.

The operation of geothermal heat pipes proved to be effective, there is however some need for further optimization, for example the evaluation of measured data shows, that film spreading cannot be expected along the whole tube.

### KEYWORDS

Geothermal heat pipe, Two phase closed thermosiphon, Propane, Cooling and heating, Geothermal energy.

### INTRODUCTION

Household and water heating account for 33% of the overall German energy consumption [1]. In times of increasing fossil fuel prices, the German government has ambitious efforts to increase the use of energy efficient technologies from renewable energy sources. Besides improving domestic household insulation, the use of energy efficient technologies can reduce the costs of heating and also reduce the emission of greenhouse gases such as carbon dioxide. The use of shallow geothermal energy technology enables reduction in the primary energy consumption of heating by approximately 35 to 45% compared with oil and gas condensing boilers [2].

The use of energy stored in the ground for heating is a promising alternative to fossil fuels, which is also interesting for private users. Particularly in newly built residential properties and office buildings, the use of geothermal heating systems is increasing. Approximately 23,000 geothermal heat pumps were installed in German households in 2010 [3].

Geothermal heat exchangers for heat extraction can be classified as open or closed systems.

In an **open system** it is possible to use the heat source medium itself for heating. The heat transfer medium, for example groundwater is pumped out of the reservoir to the surface and cooled down. The water is pumped back to the reservoir through an injection well where the geothermal heat can be absorbed from the surrounding rock again.

In a **closed system**, heat is absorbed from the ground by horizontal or vertical geothermal heat exchangers, where the heat transfer fluid is circulating and not in direct contact with the surrounding rock. The heat is transferred by convection and conduction from the surrounding rock to the circulating fluid. Horizontal heat collectors, vertical heat exchangers and heat exchangers installed in ground connected concrete parts of a building are examples of a closed system [4].

Geothermal heat can be extracted by circulating a fluid (e.g. water-glycol mixtures) inside tubes or by film evaporation of fluids with low evaporation temperatures (e.g. Propane or CO<sub>2</sub> [5, 6]) inside tubes. Because of the different working principles one can classify the closed systems into two technologies:

- conventional brine tube (BT)
  - single or double U-tubes,
  - coaxial tubes.
- geothermal heat pipes (HP).

To use geothermal energy for heating, it is necessary to run a heat pump in order to lift the temperature level from the ground (8–3 °C) to an advantageous temperature level for household heating (35–55 °C). Most geothermal heating systems in Germany are based on standard heat exchangers such as U-tubes or coaxial tubes. An advantage of conventional brine tubes is the ability to use them for heating and cooling. Ground coupled heat pipes can be only used for heating, however they enable a more effective way of extracting energy and no electricity is needed for circulation of the heat carrier fluid, this can increase the performance for a single household heating system by 15 to 20 % [7].

Ground coupled heat pipes consist of a long vertical tube (normally 60 to 200 m long). The tubes are commonly made of steel and welded together from single bore tubes or corrugated tubes. The tubes are closed and pressurized when they are installed and cemented into the ground. At the top end of the tube a heat exchanger (condenser), which is connected to a heat pump on the secondary site, is supplying condensate to the fluid distributor where a fluid film on the inside of the heat pipe wall is generated, Fig. 1. The cold liquid flows down the tube due to gravity and cools the surrounding rock by evaporation. Due to

condensation of the propane vapor in the heat exchanger, the pressure decreases and vapor is transported upwards inside the tube. The released latent heat of condensation enthalpy is used to evaporate the refrigerant in the heat pump cycle. For the heat transport inside the tube no additional introduced energy is required.

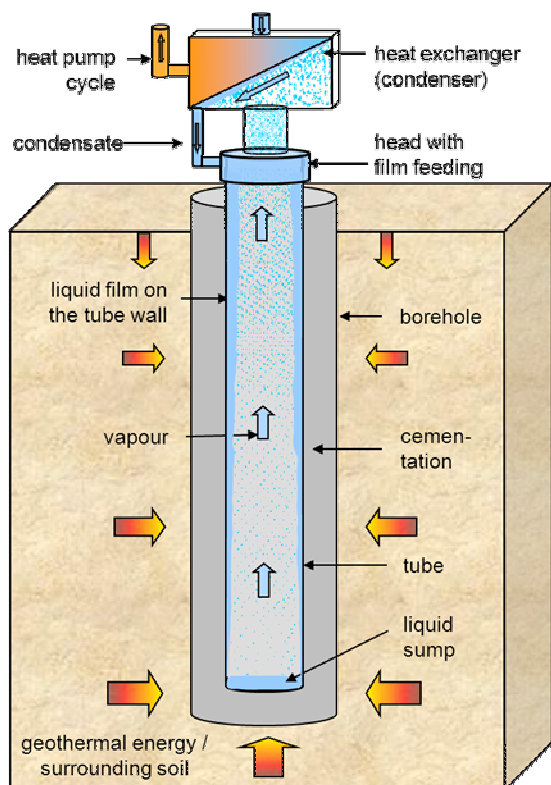


Fig. 1: Construction and operating mode of a geothermal heat pipe

### Geothermal heat pump system "Reiche Zeche"

One example of an operating geothermal propane heat pipe is situated in Freiberg in Germany where an energy park has been installed at the Technische Universität Bergakademie Freiberg. Freiberg is situated in the eastern part of the German state Saxony where the climatic zone can be described as a low mountain range climate. A reliable and efficient system is necessary to provide heat for households particularly during winter, when temperatures can drop significantly below zero.

The park consists of several renewable energy sources including four heat pumps based on seven geothermal heat pipes (HP 1-7) which have been used for heating a laboratory building since 2007. The depth of the boreholes varies between 85.0 and 95.5 m. Each

of the boreholes has a diameter of 140 mm and a distance of 6 m between each other.

After drilling the boreholes it was discovered that the first 20 m of the boreholes are almost vertical, as the depth increased, the inclination increased to approximately 12° from the vertical. This results in an average inclination of 8° over the entire borehole.

Two heat pipes are connected to each heat pump except for one heat pump that has a single heat pipe connected. All heat pipes (inner diameter 53 mm) are combined with an additional coaxial or U-tube geothermal heat exchanger for cooling (BT 1-7). The working fluid of the heat pipes is propane and a water-glycol mixture is used for the conventional brine tubes. The heating and cooling cycles are separate and currently not designed for simultaneous heating and cooling. The geothermal power plant of the "Reiche Zeche" is special in its combination of two different working principles in one plant. As mentioned previously the geothermal cooling system consists on seven conventional brine tubes and was projected to have a cooling capacity of 5 kW each. Two of the brine tubes are made as U-tubes (HDPE, High Density Polyethylene) and the remaining five are constructed as coaxial tubes (steel). If cooling is required, all the brine-tubes operate simultaneously. In the brine tubes of the cooling cycle, heat is transferred from the laboratories to the water-glycol mixture. The mixture is circulated by a pump through the brine pipes and cooled down by transferring heat to the ground.

It is noted that the geothermal heat pipes are placed at an old mining area, so that the first 20 m of the ground are made of loose rock deposit. Deeper than 20 m, solid rock in the form of gneiss is present. Because of the previous mining no groundwater and thus no ice formation during extended heat extraction periods is expected.

## DESIGN AND FUNCTION

For the scientific evaluation of the heat pump system, extensive measuring devices were installed. The main part of the measurement equipment is installed at the heat pipes and at the heat pumps, Fig. 2. Furthermore, the cooling cycle and the heating system are equipped with measurement sensors too.

The measuring equipment includes the following components:

Heat pump cycle: temperature measurement devices (thermocouples),  
electricity meter for each heat pump,  
pressure measurement (high and low pressure).

Heat pipe cycle: temperature measurement (thermocouples) for vapor and condensate,  
1 x fibre optical temperature measurement (FOM) along the heat pipes in the  
ground (spatial resolution 0.5 m; measurement accuracy  $\pm 0.3$  K, length 1200 m),  
pressure measurement device at each heat pipe (propane vapor).

Heating cycle: heat meter.

Cooling pipe cycle: temperature measurement (thermocouples) at pipeinlet and outlet,  
heat meter.

The FOM cable is attached as a loop on the outside of the heat pipe to measure the temperature along the whole tube. Therefore it is possible to measure the temperature profile along the tube during different operating regimes or regeneration of the surrounding rock with the entering cable arm and the outgoing cable arm. Approximately 1,500 m of FOM cable were installed. In Fig. 3 a temperature profile of a heat pipe in passive (blue line) and operating (green line) status is shown. The temperature jump at the base of the heat pipe can be explained by the FOM cable undercutting its minimum bending radius. At the head of the heat

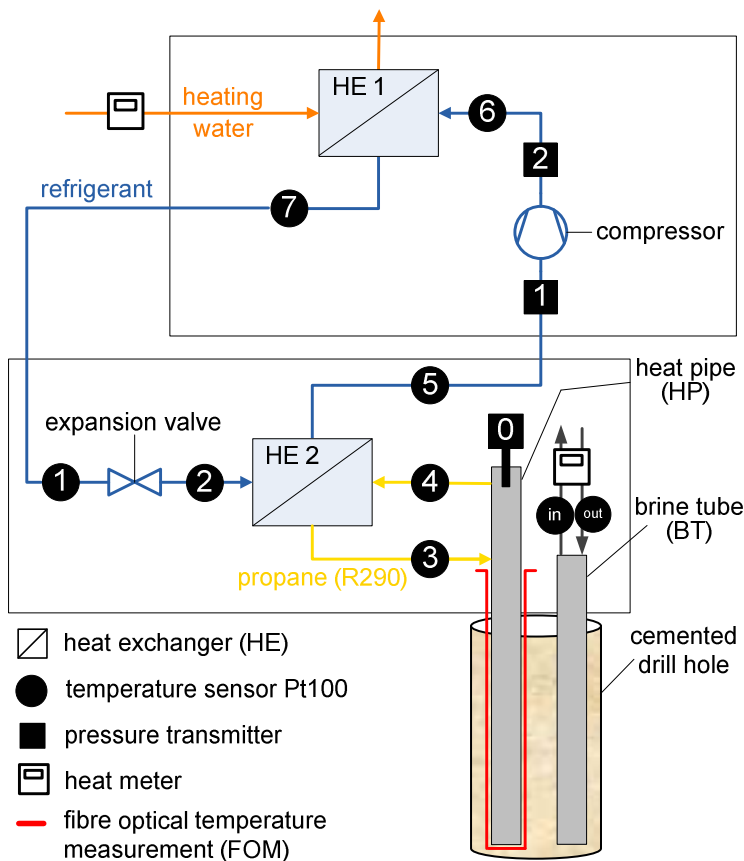


Fig. 2. Schematic representation of the installed measuring equipment for each heat pipe and heat pump

operation. The smaller temperature discontinuity can be explained by the connection of the FOM to the tube and the surrounding rock. A propane rivulet instead of a fully wetted tube is expected to result in a temperature discontinuity too.

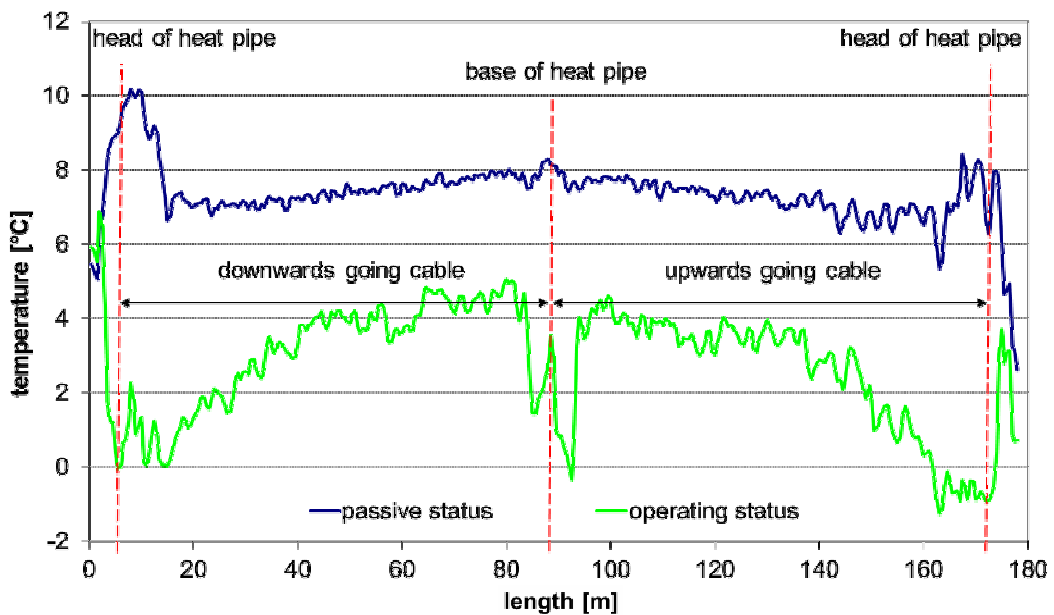


Fig. 3. Typical temperature profile created by the fiber optical temperature measurement

pipe the FOM cable is connected via a special connector with another FOM cable to form one long measuring device. These connectors influence the signal and thereby a temperature jump occurs. For further consideration of the FOM temperatures it is very important to define the initial conditions. All heat pipes displayed a constant ground temperature between 7 to 8 °C after a long regeneration time, and if there was no heat introduced through the brine tubes. It was observed that the underground temperature increases with depth by approximately 1 K along the length of the pipe. During passive status the temperature at the head of the pipe is slightly increased due to the environmental influence (air).

During operation status when heat is extracted from the ground, a distinct lowering of temperature followed by an asymptotic increase in temperature is observed with increased depth. The base of the heat pipe (~90 m depth) shows a low temperature which can be interpreted as representing the sump, where a large amount of the heat energy is extracted, particularly at the beginning of an

## Operation conditions

To find the optimized settings for running a geothermal heat pipe it is very important to know the working parameters and have a detailed strategy prior to installation. However, discontinuity due to geology or installation can only be defined by experimental tests. Therefore different tests have been performed to simulate a long term use. One heat pipe was operated for approximately 9 days and 7 hours without interruption. In Fig. 4 the temperature profile along the tube at 50 m and the propane pressure for different operating times are shown.

Even though it is known that a real static condition with a ground coupled heat pipe cannot be achieved in this timescale, the results of the long term test show an almost static condition. The temperature at a depth of 50m and the propane pressure are almost constant after 192 h of operating.

The results show that the temperature in the first 25 m of the heat pipe is below 0 °C after 24 h of operation. This can be explained by the fact that the first 20 m of the ground are made of rock deposit from the mining period, therefore the thermal conductivity and capacity is less than that of solid rock. Furthermore the first 20 m are almost vertical whereby a better film efficiency is expected compared to the deeper pipe sections where rivulets may occur. If the whole inner surface of the tube cannot be used for evaporation, heat must be extracted out of the sump which has an undisturbed rock temperature at the beginning of the experiment (0 h). Visual observation inside a working heat pipe using a camera indicated that the sump can be used as a temporary heat source as well [8]. In alternating time intervals the sump erupts and provides additional energy for the heat pipe cycle, as a result, the sump is cooling down and shows lower temperatures than the deeper sections of the heat pipe.

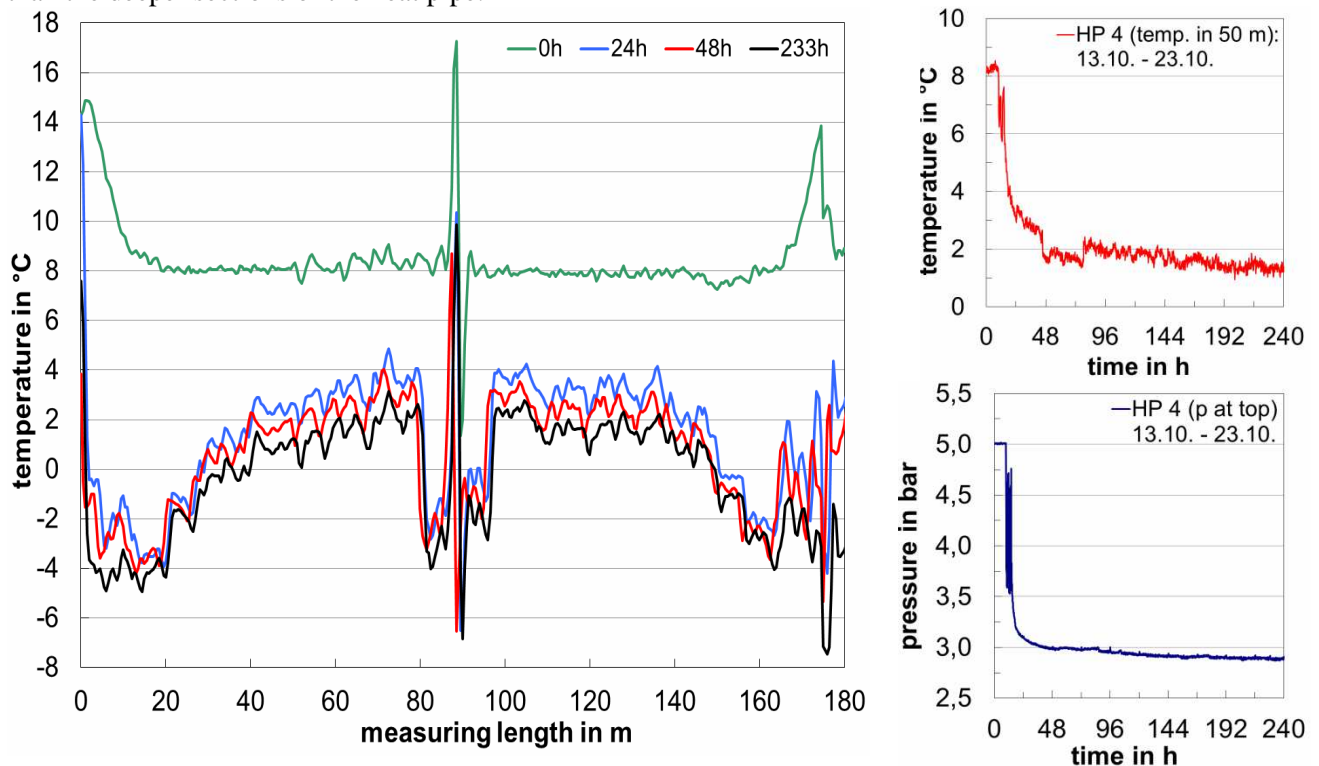


Fig. 4. Temperature and propane pressure profile during a long term test of 233 h (13.10–23.10)

Care was taken during the experiment that similar initial conditions were used, so it was possible to reproduce the temperature profile along a heat pipe after 24 h of running time across several experiments. The regeneration of the heat pipe (HP 6) was observed, which can be seen in Fig. 5. The temperature at a depth of 50 m after 24 h is approximately 2.4 °C and recovers within 6 h to approximately 7 °C, this fast regeneration can be explained to some extent by the self-circulation inside the heat pipe even if the heat sink at the top end is turned off. This will be substantiated in further experiments by visual observation.

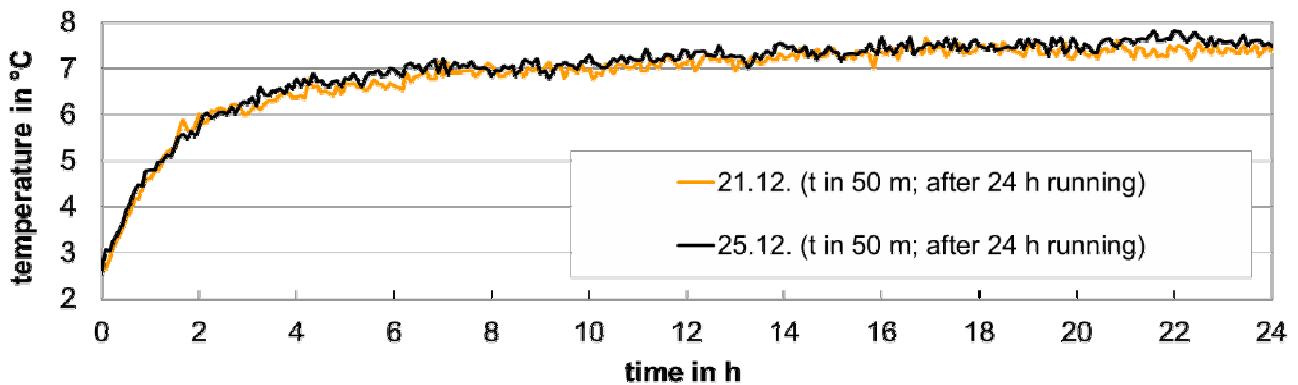


Fig. 5. Temperature regeneration at a depth of 50 m after 24 h of operating (HP6, without heat introduction through the brine tube)

**Interaction between heating and cooling mode**

The unique construction of the power plant, consisting of heat pipes for heating and brine tubes for cooling, enables to analyze the influence of both working modes relative to each other. Particularly during summer it is often necessary to cool during the day and heat during the night.

Fig. 6 shows the temperature profile of brine tubes which consist of 2 U-tubes and 2 coaxial-tubes. It is noted that the temperature profile presented has been measured with an FOM cable fixed to the heat pipes and not to the brine tubes, as such the temperatures can only be considered approximate values. On the basis of the temperature measurements, it was observed that the brine tubes all operate consistently, as the change in temperature per unit time is similar. Furthermore, it was discovered that the remaining difference in temperature between the single tubes after a 5h regeneration, can also be determined while operating. The U-tubes (BT 2 and 3) show a constant increase in temperature as the depth increases in comparison with the coaxial-tubes which show a V-profile, where the upper parts of the ground are more heated than the lower parts.

For each day and month the introduced and extracted energy was measured and a coefficient of performance (COP) was calculated. The COP is calculated by dividing the use (heating or cooling energy) by the costs (electric power) of the power plant.

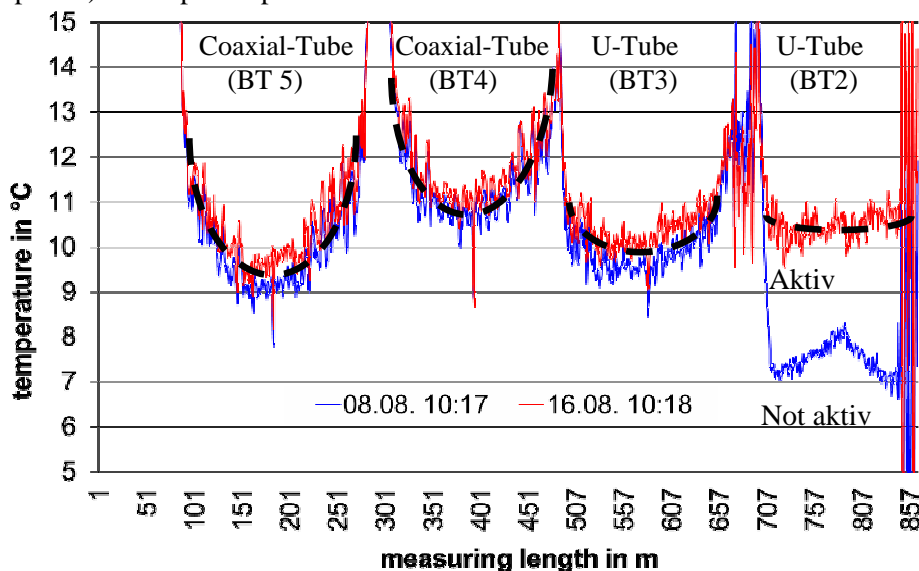


Fig. 6. Temperature profile during cooling mode for brine tubes (U-Tubes and Coaxial-Tubes), comparison of the temperature profile before and after activating BT2

Therefore, the introduced heat (use) to the ground and the brine pump performance (costs) was observed for the cooling mode. To evaluate the efficiency of the heating cycle, the extracted heat (use) was compared to the energy used for the heat pump (costs). It was demonstrated that with increased heating; resulting in cooling down the ground, the cooling mode became very efficient. During the summer, the COP varied between 24 to 38 which is a very good result. A COP (long term) for the ground coupled heat pipe cannot be presented, as the power plant is an experimental rick and constant long term parameters cannot be established. Using the ground for cooling and as a very large heat buffer, represents a very efficient method for cooling buildings and processes. The enhanced recovery of the ground by cooling after a heating cycle is very important for long term use and this increases the COP of the ground coupled heat pump. Also, the heat pipe can provide a low temperature heat sink for refrigeration applications which operate below 0 °C, which is rarely achieved by brine tubes.

To illustrate the heating and cooling cycle, Fig. 7 shows operating conditions of the power plant from 2009 to 2010. It is observed that heating is necessary for most of the year. The figure also shows that the recovery of the underground temperature at a depth of 50m is supported during summer.

## RESULTS AND DISCUSSION

The combination of cooling and heating during the summer months produces a significantly better performance of the ground coupled heat pump and in addition an improved recovery of the ground. Due to higher underground temperatures, the heat source for the heat pump provides a more efficient temperature level, which results in a higher COP. A long term storing of heat during summer months is conceivable, even if this cannot be verified, due to the load cycle changes between cooling and heating. The temperature profile created by a coaxial tube during cooling appears to align with the temperature profile of a heat pipe better than a U-tube profile. This can be explained by the fact that the heat pipe extracts the heat energy from the upper part of the bore hole at the beginning of the cycle.

Because of the difficulty of generating vertical boreholes, it is assumed that most of the heat pipes have an inclination angle. As such, a fully wetted inner side of the heat pipe cannot always be assumed. This needs to be proved in further visual observations. While cooling the ground from the top down, the sump also needs to provide heat for the heat pump, this behavior was observed while investigating the temperature profile along the heat pipes.

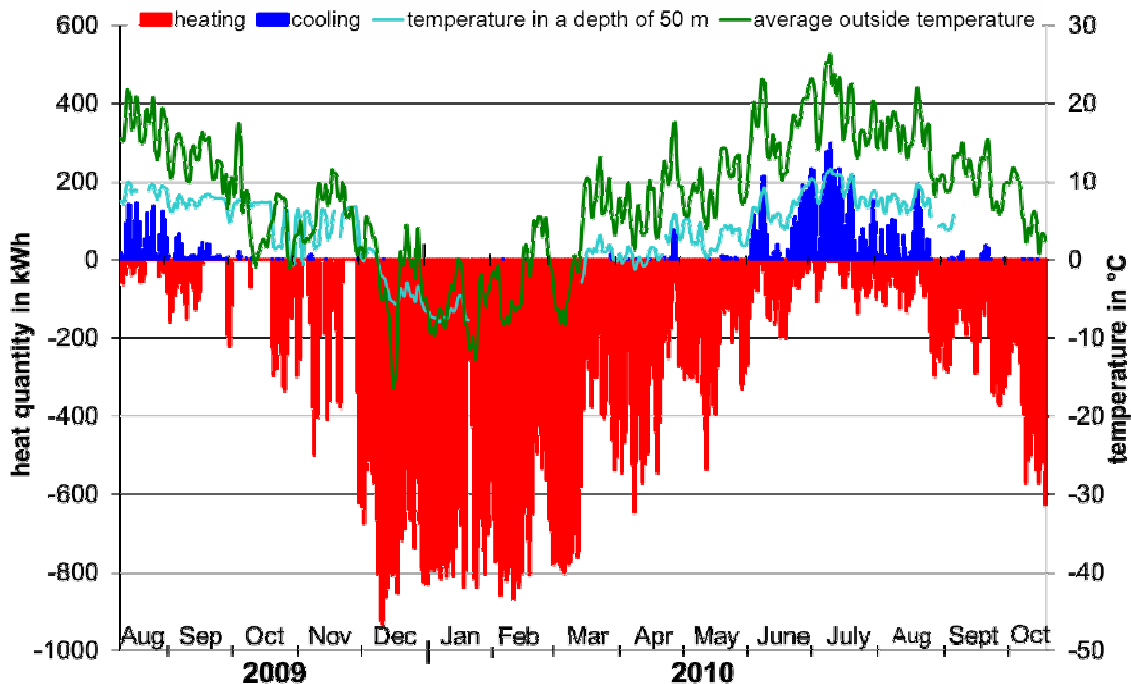


Fig. 7. Introduced and extracted energy to the subsurface at the geothermal power plant, in combination with the outside surface temperature and the temperature at a depth of 50 m

## Acknowledgement

We would like to thank Mr. H. Fischer, Mr. A. Wahl and the staff of BLZ Geotechnik Service GmbH for their instrumentation support and all the students who worked on this project. Furthermore, we would like to thank the "SIB Chemnitz" for its cooperation and the foundation "Technische Universität Bergakademie Freiberg" for their financial support.

## References

1. Kaltschmitt M., Streicher W., Wiese A., Renewable Energy -Technology and Environment Economics, Springer-Verlag, 2007//
2. Verein Deutscher Ingenieure, Thermal use of the underground – fundamentals, approvals, environmental aspects, VDI 4640 Part 2, 2010.
3. Bundesverband Wärmepumpen e.V., Heizen mit Wärmepumpen – klimafreundlich, zukunftssicher, wartungsarm, 15.01,2011, Berlin, [http://www.waermepumpe.de/fileadmin/grafik/pdf/Flyer-Broschueren/BWP\\_Endkundenbrosch %C3%BCre\\_web.pdf](http://www.waermepumpe.de/fileadmin/grafik/pdf/Flyer-Broschueren/BWP_Endkundenbrosch%C3%BCre_web.pdf)
4. Kaltschmitt M., Huenges E. & Wolff H. Energie aus Erdwärme, Deutscher Verlag für Grundstoffindustrie, 1. Auflage, 1999, Stuttgart.
5. Kruse H., Rüssmann H., Novel CO<sub>2</sub>-Heat Pipe as earth probe for heat pumps without auxiliary pumping energy // *Proc. 8<sup>th</sup> IEA Heat Pumps Conf.*, 2005, Las Vegas.
6. Wagner R. Einsatz von geothermischen Phasenwechselfonden im Wohnungsbau, *bbr Fachmagazin für Brunnen- und Leitungsbau – Sonderheft Oberflächennahe Geothermie*, 2010.
7. Ochsner K. Carbon dioxide heat pipe in conjunction with a dround source heat pump (GSHP) // *Appl. Therm. Eng.* 2008. Vol. 28. Pp. 2077–2082.
8. Storch T., Grab T., Zieger C., Schreiter S., Kupka M., Gross U., Wagner R.M. Visual observations inside a geothermal heat pipe // *Proc. of VIII Minsk Intern. Seminar "Heat Pipes, Heat Pumps, Refrigerators, Power Sources"*, Minsk, Belarus, September 12–15, 2011.

## THE NEW CONCEPT OF CAPILLARY FORCES DRIVEN EVAPORATOR WITH APPLICATION TO WASTE HEAT RECOVERY

**Dariusz Mikielewicz, Paweł Szymański, Jan Wajs**

Gdansk University of Technology, Faculty of Mechanical Engineering,  
80-233 Gdańsk, ul. Narutowicza 11/12, Poland

Tel. +48 58 347 2254, Fax: +48 58 347 2816, e-mail: Dariusz.Mikielewicz@pg.gda.pl

**Jarosław Mikielewicz, Eugeniusz Ihnatowicz**

Institute of Fluid-Flow Machinery, Polish Academy of Science,  
80-952 Gdańsk, ul. Fiszerza 14, Poland

Tel. +48 58 341 12 71, Fax: +48 58 341 61 44, email: jarekm@imp.gda.pl

### Abstract

In the paper presented are studies on the possibility of application of loop heat pipes concept to a modern design of evaporator for waste heat recovery. The potential application of such evaporator is for example a domestic micro CHP. One of the problems in the micro CHP is excessive demand for pumping power. The design under scrutiny here helps in overcoming that issue. In the proposed evaporator there is a possibility of reducing the demand for pumping power as the evaporator will produce the extra pressure effect due to capillary forces. In such case the circulation pump operates only to compensate the pressure drop due to friction losses and the wick covers the demand for overcoming the pressure drop in the expansion device. Out of 14 tested fluids 3 were selected for further scrutiny, namely ethanol, water and ammonia. It has been assumed that the fluid should work in the evaporator at temperature of 160 °C. The results of surface tension distributions with respect to temperature have been presented in figures. Preliminary analysis of the results indicates water as having the best potential, however taking into account all issues it can be said that the best effect is obtained using ethanol.

### KEYWORDS

Loop heat pipe, capillary forces, waste heat recovery

### INTRODUCTION

The new promising direction of modern energy development are applications to recover waste heat. One of such examples that could in future supplement the centralized energy sector is dispersed energy sector, in which is produced electrical energy in cogeneration with heat. The primary components of micro CHP operating according to the Clausius-Rankine cycle are as follows (Fig. 1): boiler (evaporator), expansion machine (steam turbine), condenser, electrical generator and circulation pump. A new concept of micro CHP requires solving a number of new problems, such as the choice of an appropriate working fluid and other issues [1], namely the development of compact heat exchangers. Another issue is that the pumping power in such cycle is excessive, and available for that purpose circulation pumps expensive. Using capillary forces for pumping a working fluid in the Clausius-Rankine cycle is a new idea, that allows to reduce or even eliminate the device pumping the working fluid in such cycle.

The research proposes a new concept of evaporator, namely the shell and tube recuperator made of a set of tubes containing wicks, where by means of capillary forces the operation of circulation pump is aided. The possibility of such application were already analyzed in the authors earlier paper [3]. It is additionally possible to exploit the gravity force to support operation of a circulation pump by placing the evaporator below the condenser and creating the thermosyphon loop. Usage of kinetic energy of vapour, generated at the evaporator of the Loop Heat Pipe – device similar to micro CHP, were analyzed only in a few papers (e.g. [4, 5]). Interesting results were obtained. However, the efficiency of LHP combined with the impulse turbine was rather low, at maximum few percent. The present research analyzes the cycle similar to LHP cycle supported by a circulation pump allowing to create a large enthalpy drop in micro CHP expander. This allows for the use of the reaction turbine.

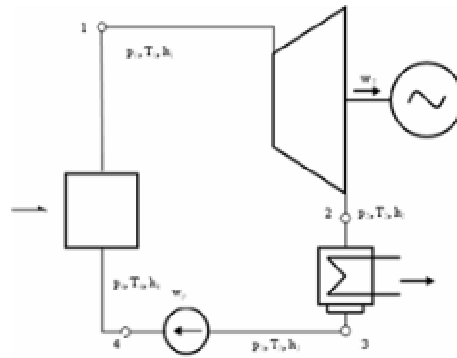


Fig. 1. Scheme of micro CHP working according to the Clausius-Rankine cycle

## THEORETICAL MODEL OF EVAPORATOR WITH TUBES HAVING WICK

To take the advantage of capillary forces for pumping the working fluid, it is assumed that evaporator will be a shell and tube recuperator, in which tubes will be made of sintered metal powder in the form of a porous tubular wick. Porous material will transport the working fluid from the inner to outer surface of the wick, from where it will be evaporated and transported further to turbine. To apply the wick, it requires a bit larger than a standard tube diameters in mini-tubes recuperator. The use of wick will cause a reduction of pressure difference at the pump pumping a working fluid. The collector that feeds a working fluid to recuperator-evaporator tubes will additionally serve as a chamber compensating volume of fluid working the cycle. The evaporator of low boiling fluid that heats a working fluid up to saturation temperature will be made as micro channel recuperator, to increase the compactness of the envisaged micro CHP. Structural scheme of this cycle is shown at Fig. 2.

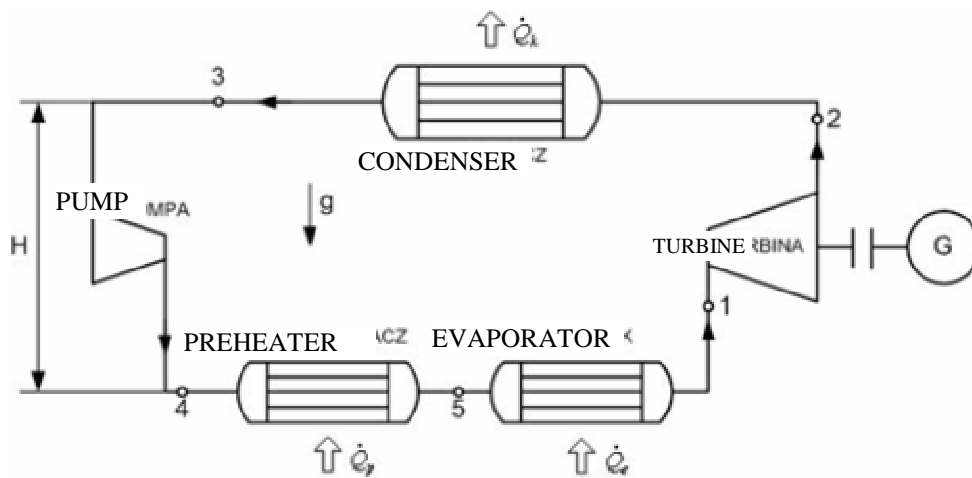


Fig. 2. Structural scheme of the cycle

Energy balance of the Clausius-Rankine cycle, based on the first law of thermodynamics provides the relation:

$$\dot{Q}_p + \dot{Q}_e = \dot{W} - \dot{Q}_c, \quad (1)$$

where  $\dot{Q}_p = \dot{m}(h_5 - h_4)$  is heat supplied to the preheater,  $\dot{Q}_e = \dot{m}(h_1 - h_5)$  is heat supplied to evaporator,  $\dot{W} = \dot{W}_T - \dot{W}_p$  is net work of cycle, taking into account the work used to drive the pump,  $\dot{Q}_c = \dot{m}(h_2 - h_3)$  is heat dissipated in the condenser.

The following assumptions are made to analyse the ORC cycle:

1. Liquid and vapor legs are insulated

2. In evaporator a complete evaporation of the liquid takes place, similarly as in the condenser where complete vapor condensation of working fluid (low boiling fluid) is present,

3. The demand for heat discharged by cooling water in the condenser is known. The model of condenser was developed in [6] and hence the flow rate of water cooling the condenser and flow rate of working fluid is known.

4. The pressure drop of two-phase working fluid condensing in the condenser is known.

Schematic of evaporator element (single tube) is presented in Fig. 3.

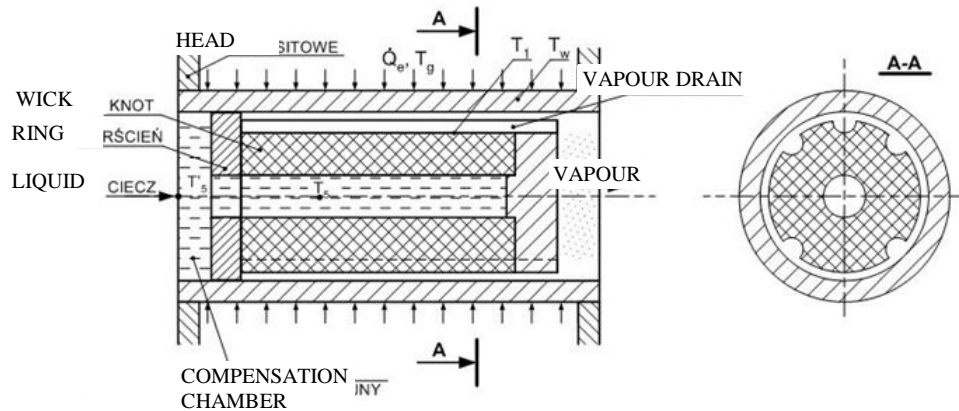


Fig. 3. Schematic of the tube of evaporator

The pressure balance in the cycle yields:

$$\Delta p_p + \Delta p_c + \Delta p_g \geq \Sigma \Delta p_i + \Delta p_T. \quad (2)$$

The left side of the equation represents the driving pressure respectively for the pump, capillary forces and gravity. The right side of the equation represents the pressure drop caused by friction in all parts of the cycle and the pressure drop in the turbine. Assuming that the increase of the pressure in the pump compensates the pressure drop in the turbine, it can be assumed that the positive pressure increase created in the cycle will overcome the friction losses in all elements of the cycle. Due this fact, the large power savings are projected. When the preheater is placed below the condenser (the best at the lowest point of the cycle) the gravity force creates the thermosyphon that supports the pump. Assuming that the liquid and vapor lines have the same length  $H$ , approximately equal to the difference in height between condenser and evaporator it is obtained:

$$\Delta p_g = gH(\rho_l - \rho_v). \quad (3)$$

Maximum pressure difference, caused by the capillary forces in the wick is:

$$\Delta p_c = \frac{2\sigma}{r_p} \quad (4)$$

where  $\sigma$  is surface tension,  $r_p$  is radius of a single pore in the porous material. Pressure drop for the two phase flow in the liquid and vapor lines are calculated by the formula:

$$\Delta p_i = f \frac{1}{2} \rho_i u^2 \frac{l}{d_h} \quad (5)$$

The coefficient of friction  $f$  for laminar flow is:

$$f = 64/Re \quad \text{for} \quad Re \leq 2200 \quad (6)$$

and for turbulent flow:

$$f = 0.316Re^{-0.25} \quad \text{for} \quad 2200 < Re < 10\,000. \quad (7)$$

Pressure drop in the wick is determined by [3]:

$$\Delta p_w = \frac{\mu_1 \dot{m}_r}{\rho_1 K \pi d_w}, \quad (8)$$

where  $K$  is the permeability of wick,  $m_r$  is radial flow rate in the single pipe with wick.

Energy balance for the cycle results from (1). The heat supplied to the cycle is determined by:

$$\dot{Q}_d = \dot{Q}_p + \dot{Q}_e. \quad (9)$$

The heat value is known as the heat dissipated in the condenser is known and the approximate work of the turbine and pump obtained by the thermodynamic calculations with given maximum pressure in the cycle is also known.

The heat supplied by the preheater can be determined from:

$$\dot{Q}_p = \dot{m} c_p (T_5 - T_4). \quad (10)$$

The heat supplied to evaporator  $\dot{Q}_e$  is used to evaporate the working fluid with mass flow rate  $m$ , to heat the fluid in the wick as a result of fluid flow and radial heat transfer  $\dot{Q}_{wi1}$ , and to heat the fluid at the compensation chamber (collector) as a result of heat transfer along the tube wall and along the wick  $\dot{Q}_w + \dot{Q}_{wi2}$  and radial heat transfer of the wick  $Q_{wi1}$ .

$$\dot{Q}_e = \dot{Q}_w + \dot{Q}_{wi1} + \dot{Q}_{wi2} + \dot{m} h_{lv} = \dot{Q}_d - \dot{m} c_p (T_5 - T_4). \quad (11)$$

According to (11) each element of the equation has the following interpretation:

$$\dot{Q}_w = \frac{\lambda_m A_w}{l_{eff}} (T_w - T_5), \quad (12a)$$

$$\dot{Q}_{wi1} = G_{wick} (T_1 - T_5), \quad (12b)$$

$$\dot{Q}_{wi2} = \frac{\lambda_{wi} A_{wi}}{l_{eff}} (T_1 - T_5). \quad (12c)$$

It can be assumed that approximately  $T_w = T_1$ . Then from the above simultaneous equations can be determined the temperature to which the fluid is heated at the preheater:

$$T_5 = \frac{\dot{Q}_d - \dot{m} h_{lv} + \dot{m} c_p T_4 - R T_1}{\dot{m} c_p - R}, \quad (13)$$

$$\text{where } R = \frac{\lambda_m A_w}{l_{eff}} + \frac{\lambda_{wi} A_{wi}}{l_{eff}} + G_{wick}.$$

The radial heat transfer of the porous material  $G_{wick}$  can be determined from the heat balance of the wick. It can be determined by the procedure described below.

## FLUID FLOW THROUGH THE WICK

The wick construction must ensure adequate strength to be able to transfer the capillary pressure difference and to provide the greatest possible temperature difference between fluid temperature, which roughly corresponds the saturation temperature difference between the evaporator and condenser.

It is assumed that the thickness of the annular porous layer is small comparing to diameter of wick. It allows to propose a heat transfer model similar to the one of heat transfer through a flat wall, Fig. 4. It is also assumed that the fluid flow through the pores is laminar and the fluid is in thermal equilibrium with a porous wick. Then, the energy equation yields:

$$\rho_1 c_p u_y \varepsilon \frac{dT}{dy} = \lambda_e \frac{d^2 T}{dy^2}, \quad (14)$$

$$\text{where } u_y = \frac{\dot{m}}{\rho_1 A \varepsilon} \text{ and } \lambda_{\min} = \lambda_1 \varepsilon, \lambda_{\max} = \lambda_s (1 - \varepsilon) \text{ and } \lambda_e = \lambda_{\min}^{0.5} \lambda_{\max}^{0.5}.$$

Boundary conditions for equation (14) are as follows:

$$\text{for } y=0 \quad T = T_5 \text{ and for } y=\delta \quad T = T_1 \quad (15)$$

By solving (14) with conditions (15) we obtain:

$$T = \frac{C_1}{\eta} e^{\eta y} + C_2, \quad (16)$$

$$\text{where } \eta = \frac{\dot{m}_r c_p}{\lambda_e A}.$$

Integral constants  $C_1$  and  $C_2$  are:

$$C_1 = \frac{\eta(T_5 - T_1)}{1 - e^{\eta\delta}}, \quad (17a)$$

$$C_2 = T_5 - \frac{C_1}{\eta}. \quad (17b)$$

Radial heat transfer in the porous material is determined from the heat balance condition for the wick:

$$G_{wick} = \frac{\lambda_e A}{T_5 - T_1} \frac{dT}{dy} = \frac{\lambda_e A}{1 - e^{\eta\delta}} \eta e^{\eta y}. \quad (18)$$

As it is shown at the formula (18) the heat transfer in radial direction is caused not only by the thermal conductivity, but also by a radial fluid flow. From the temperature of two phase layer results a saturation pressure. Saturated vapour is directed to turbine where is expanding to the saturation pressure corresponding to ambient temperature in the condenser.

## CALCULATIONS

The 14 different working fluid, that can be used in a ORC cycle were examined to create a maximum capillary pressure drop. These were: ethanol, ammonia, 123, toluene, water, R365mfc, R141b, R245ca, R134a, R245fa, R236ea, perfluoropentane  $C_5F_{12}$ , R227ea, RC318. It was assumed that fluids should work in evaporator at temperature 160 °C, and the condensation process take place at temperature 50 °C. The results of dependence of surface tension temperature for selected fluids are shown in Fig. 4. The obtained data analysis show that water have the greatest potential to create the capillary pressure difference. Unfortunately other considered thermodynamics criteria in those temperature range disqualify this fluid.

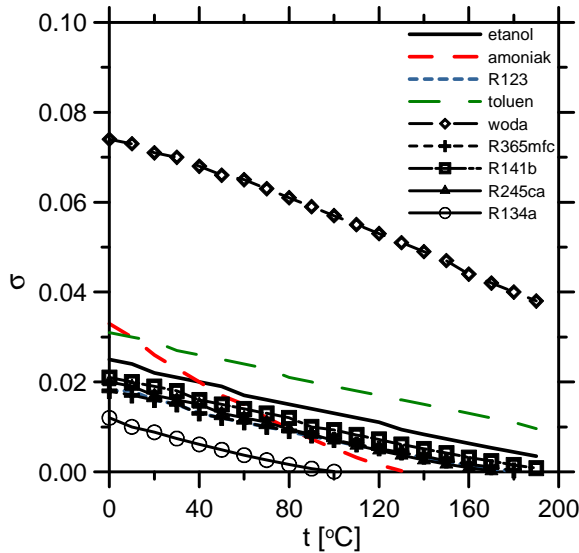


Fig. 4. Distribution of surface tension for different fluids in function of temperature

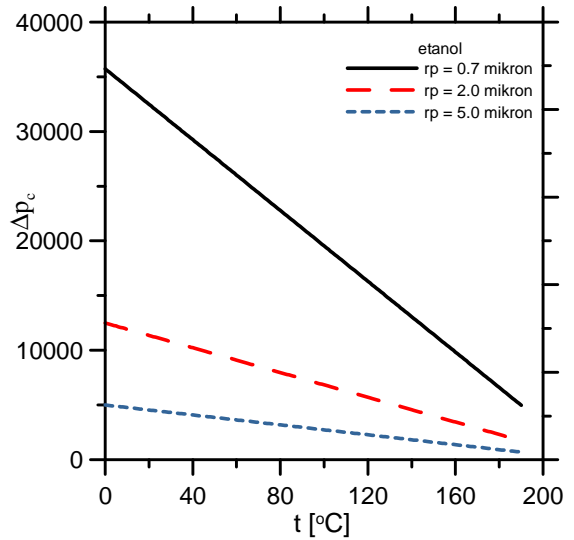


Fig. 5. Distribution of available capillary pressure drop for ethanol

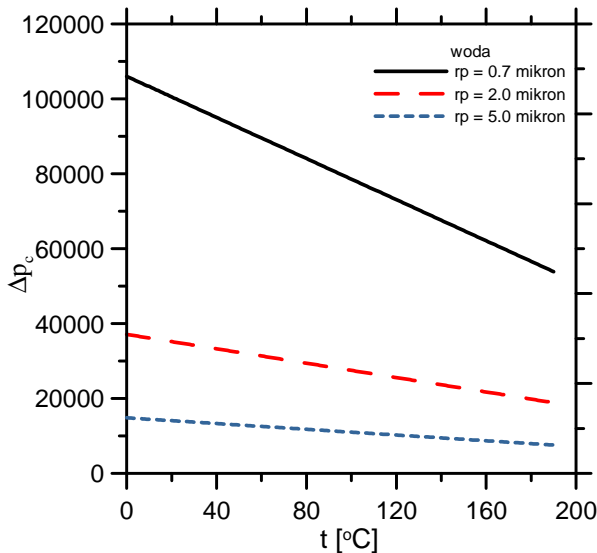


Fig. 6. Distribution of available capillary pressure drop for water

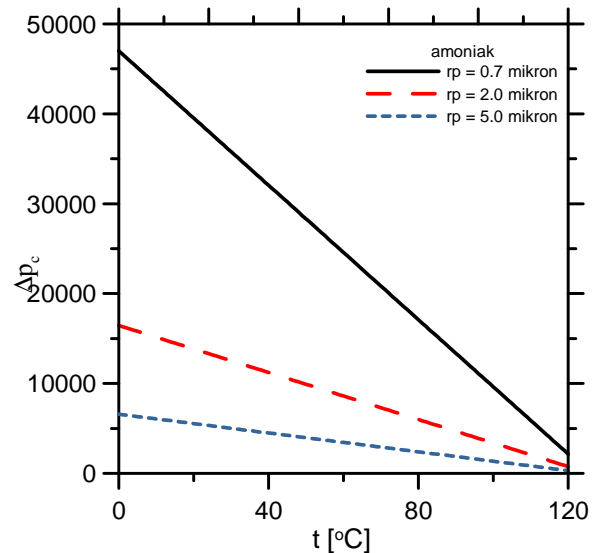


Fig. 7. Distribution of available capillary pressure drop for ammonia

Another attractive working fluid is toluene, and then ammonia and ethanol. Ammonia would be a good fluid to use, but at a lower temperature range. Among CFCs examined, all behave similar, and clearly different from the rest of the fluids is R134a. In a next step assumed three different pores sizes of the wick material, respectively  $r_p = 0.7, 2, 5\mu\text{m}$ . The obtained results of pressure drop for the three liquids,

respectively ethanol, water, ammonia are shown in Fig. 5–7. Reducing the active pore surface significantly increase capillary pressure difference possible to use. Ethanol represents the greatest capillary pressure difference at analyzed temperature range.

In the next step is determined the appropriate pressure drop possible to obtain in the laboratory facility. The following values for each parameter selected in micro CHP diagram (Figure 1) have been set for calculations:

- Enthalpy before the turbine ( $t = 160\text{ }^{\circ}\text{C}$ ),  $h_1 = 1365.6\text{ kJ/kg}$
- Isentropic enthalpy after the turbine ( $t = 50\text{ }^{\circ}\text{C}$ ),  $h_{2s} = 1141.7\text{ kJ/kg}$
- Turbine efficiency  $\eta = 0.8$
- Enthalpy after the turbine  $h_2 = 1186\text{ kJ/kg}$
- Enthalpy of saturated liquid at  $t = 50\text{ }^{\circ}\text{C}$ ,  $h_3 = 328.67\text{ kJ/kg}$
- Enthalpy in circulation pump,  $h_4 = 330.27\text{ kJ/kg}$
- Mass flow rate of the working fluid,  $\dot{m} = Q_{skr}/(h_2 - h_3)$
- Heat supplied to evaporator,  $Q_d = \dot{m}((h_1 - h_2) + (h_2 - h_3) + (h_4 - h_3))$
- The internal diameter of the tube inside evaporator,  $d_{par} = 0.006\text{ m}$
- The diameter of the channel supplying fluid to evaporator,  $d_{ciecz} = 0.01\text{ m}$
- The diameter of the channel removing fluid from evaporator,  $d_{para} = 0.0375\text{ m}$
- The radial thickness of the wick layer,  $\delta_{wick} = d_{par}/2$
- Length of liquid and vapour lines,  $L = 1\text{ m}$
- The porosity of the wick,  $\varepsilon = 0.6$
- The length of evaporator tube,  $L_{par} = 0.5\text{ m}$
- The length of condenser tube,  $L_{skr} = 0.3\text{ m}$
- Effective length of wick,  $L_{eff} = 0.6L_{par}$
- The temperature before the preheater,  $T_4 = 50\text{ }^{\circ}\text{C}$
- The temperature after evaporator,  $T_1 = 160\text{ }^{\circ}\text{C}$
- The wall thickness of evaporator casing,  $\delta_w = 0.003\text{ m}$
- Pore diameter,  $r_p = 2 \cdot 10^{-6}\text{ m}$
- The heat transfer coefficient of the wick material,  $\lambda_{wick} = 5\text{ W}/(\text{m}\cdot\text{K})$

The physical properties of ethanol were taken from the program Refprop 9 for condensing temperature of  $50\text{ }^{\circ}\text{C}$  and temperature of  $150\text{ }^{\circ}\text{C}$ . In the first stage of the calculation, it is assumed that the pressure increase in the circulation pump is equal to a pressure drop in the expansion machine, that corresponds to the ideal cycle conditions without pressure loss. Equation (2) follows that the friction must be balanced by the capillary pressure in the wick and the buoyancy pressure in the gravity field. To calculate the pressure drop in the wick (8) we must determine the fluid flow rate through a single tube of evaporator. The total flow rate due to the heat balance of the condenser (1) working at the ORC cycle. The number of tubes in the evaporator can be estimated from the amount of heat exchanged in the evaporator, which results from the cycle energy balance and the average temperature difference between heating fluid and the fluid working in the cycle and estimation of heat transfer coefficient. Further, dividing the total flow rate by the number of tubes is obtained, the fluid flow rate that flow through a single wick and pressure drop in the wick. Other pressure drops caused by the energy dissipation are calculated by assuming the appropriate channel diameters. The calculations were carried out using the MATHCAD software. With proper selection of the wick pores, and by locating the condenser below the evaporator, it is possible to balance the driving pressures to pressure drops (2). Then pump overcomes the pressure drop coming from the expansion machine. This is illustrated by this calculation example.

The energy balance of the preheater and evaporator allows to calculate the temperature to which the fluid must be heated in the preheater.

## CONCLUSIONS

As the result of calculations of heat exchanger supported by a capillary forces, it can be concluded that the use of wick at evaporator significantly saves power required for fluid circulation in ORC cycle. In this case, only the circulation pump works to compensate the pressure drop caused by friction of fluid, and the wick cover the power demand needed to overcome the pressure drop in the expansion machine. We are dealing with the power savings of pump that drives a cycle. The best result of application of the wick and thermosyphon forces to obtain such working conditions, in which it is possible to cover all the pressure drops in the system (without the pump).

Preheater heats to a lower temperature than in a cycle with evaporator without a wick. The new temperature results from the heat balance of the evaporator and the preheater. In the performed calculations, the temperature is lower by about 17°C from that at which it would be needed to obtain, if as there was no wick. Such situation leads to a reduction of the dimensions of preheater, by using the larger diameter of tubes in evaporator (and its larger dimensions). However, we results the energy savings by using low-power pump.

Pressure drop in the inlet and outlet collectors is different for a smaller number of tubes than for larger number of them. This issue requires a separate analysis, because the intake of collector space serves as a compensation chamber in the cycle. As a result of the heat supply to the cycle the volume occupied by the working fluid is changed. The change in fluid volume is compensated by the volume of the collector intake.

## Acknowledgments

First three authors would like to appreciate the funding from the Ministry for Science and Higher Education research grant №512 479539 in years 2010–2013. Last two authors appreciate funding from Ministry for Science and Higher Education research grant R 06 011 03 in years 2007–2010 and a National Project POIG.01.01.02-00-016/08 *Model agroenergy complexes as an example of distributed cogeneration based on a local renewable energy sources*.

## References

1. Mikielewicz D., Mikielewicz J. Cogenerative micro power plants – a new direction for development of power engineering? *Archives of Thermodynamics*. 2008. Vol. 29(4). Pp. 109–132.
2. Mikielewicz J., Mikielewicz D. Comparative study of selected fluids for use in supercritical Organic Rankine Cycles // *Archives of Thermodynamics*. 2009. Vol. 30(2). Pp. 3–15.
3. Mikielewicz D., Mikielewicz J., Ichnatowicz E. Analiza możliwości wykorzystania sił grawitacji oraz kapilarnych do przetłaczania cieczy przez wymiennik minikanalowy // *IMP PAN internal report*, 2009.
4. Akbarzadeh A., Johnson P., Nguen T., Mochizuki M., Mashiko M., Sauciuc I., Kusaba S., Suzuki H. Formulation and analysis of the heat pipe turbine for production of Power from renewable resources // *Appl. Thermal Eng.* 2001. Vol. 21. Pp. 1551–1563.
5. Ziapour B.M. Performance analysis of an enhanced thermosyphon Rankine cycle using impulse turbine // *Energy*. 2009. Vol. 34. Pp. 1636–1641.
6. Mikielewicz J., Mikielewicz D. Algorytm obliczeń mini wymienników ciepła typu kanalikowego dla obiegu mikrośilowni // *IMP PAN internal report*, 2009.

## VISUAL OBSERVATIONS INSIDE A GEOTHERMAL HEAT PIPE

**Th. Storch, Th. Grab, Chr. Zieger, St. Schreiter, M. Kupka, U. Gross**

Institute of Thermal Engineering, Technische Universität Bergakademie Freiberg  
Gustav-Zeuner-Strasse 7; 09599 Freiberg, Germany

Phone: +49-(0)3731-393185; fax +49-(0)3731-393963; E-mail: thomas.storch@iwtt.tu-freiberg.de

**R. M. Wagner**

BLZ Geotechnik Service GmbH

Industriepark Str. A Nr. 1; 39245 Gommern, Germany

Phone: +49-(0)39200-7020; E-mail: wagner@blz-geotechnik.de

### Abstract

The efficiency of geothermal heat pipes depends, e.g., on the wetted inner tube surface due to the principle of falling film evaporation. To achieve a high evaporation rate a nearly closed liquid film down to the lower end of the pipe is required. No standard measurement technique is available to investigate the processes inside a geothermal heat pipe more in detail, especially the falling liquid film, so visual observations are necessary. To provide visual observations of the inner processes inside a geothermal heat pipe operated with propane, a special pressure lock system for the heat pipe's head was developed. Therewith a miniature camera can enter the heat pipe's section for the visual observations. The test setup with the pressure locks (gland nuts) are presented in detail as well as the first surprising results from visual observations of the starting process with focus on wetted areas and the liquid pool.

### KEYWORDS

Geothermal plant, Heat pipe, Thermosyphon, Evaporation, Falling film, Visual Observation, Heat Pump.

### INTRODUCTION

Increasing prizes for fossil fuels indicate the need for alternative and sustainable energy resources for cooling and heating of buildings. In Germany, e.g., 33% of the final energy consumption is used for room heating applications [1].

Shallow geothermal energy is obtained at depths of up to 400 meters, and it is usable as energy source for cooling and heating of buildings. There exist various closed systems of borehole heat exchangers, like geothermal u-tubes, coaxial tubes, heat pipes and energy piles. For heating applications ground heat pumps are necessary to increase the temperature level up to the required heating temperature [2].

In the past heat pipes in general have been widely investigated. The first applications for extracting heat from the ground by means of heat pipes were used for freezing ground to stabilize pipeline and railway fundaments, e.g. [3]. Furthermore geothermal heat pipes research has been done on the field of heating highways and bridges, e.g. [4, 5].

Nowadays heat pipes are an alternative solution for geothermal energy use for heating applications. Thereby the heat pipe mechanism transfers heat very efficiently compared to other techniques which can be a big motivation for users, e.g. house owners, see [6] and [7]. The efficiency in heat pipes depends, e.g., on the wetted inner tube surface due to the principle of falling film evaporation. To achieve a high evaporation rate a nearly closed liquid film down to the lower end of the pipe is required. The liquid film spreading depends on several properties of the heat pipe (see also [8]) like pipe material, surface roughness, inclination angle, length as well as the operating regime.

The mechanism of geothermal heat pipes is strongly connected with falling film evaporation and condensation. Hence formation and structure of falling liquid films have been studied by various experimental methods in the past few years. An overview of the numerous publications has been given by Philipp et al. (2006) [9]. Various characteristic wave shapes have been presented based on visual observations of water and isopropanol liquid films flowing down inside vertical tubes under isothermal conditions [10].

This paper deals with visualization of falling film flow inside a geothermal heat pipe, operated with propane as the working fluid. To provide the visual observations a special pressure lock for the head of the heat pipe was developed where a miniature camera can enter the heat pipe section. The test setup will be presented in detail subsequently as well as the first results from visual observations of the starting process with focus on wetted areas and the liquid pool.

## EXPERIMENTAL

For the visual investigations of the falling film inside a geothermal heat pipe a new heat pipe was installed. Therefore a borehole of approximately 145 mm in diameter and a depth of 95 m was drilled. The heat pipe consists of outside coated (against corrosion) steel pipes welded every 6 m with an inner diameter of 53 mm and a total length of about 92.2 m (incl. probe head with heat exchanger, see Fig. 1).

A chamber for a miniature camera with a special pressure lock system for installation on the flange of the heat pipe's head was developed, pretested and built.

### Experimental test plant

The head of the heat pipe was especially adapted for the research project. Therefore it consists of standard equipment like plate heat exchanger, thermostatic expansion valve from heat pump cycle and a flange as well as extra equipment as a flow meter for propane and a ball valve. The head is situated in an inspection chamber, see Fig. 1.

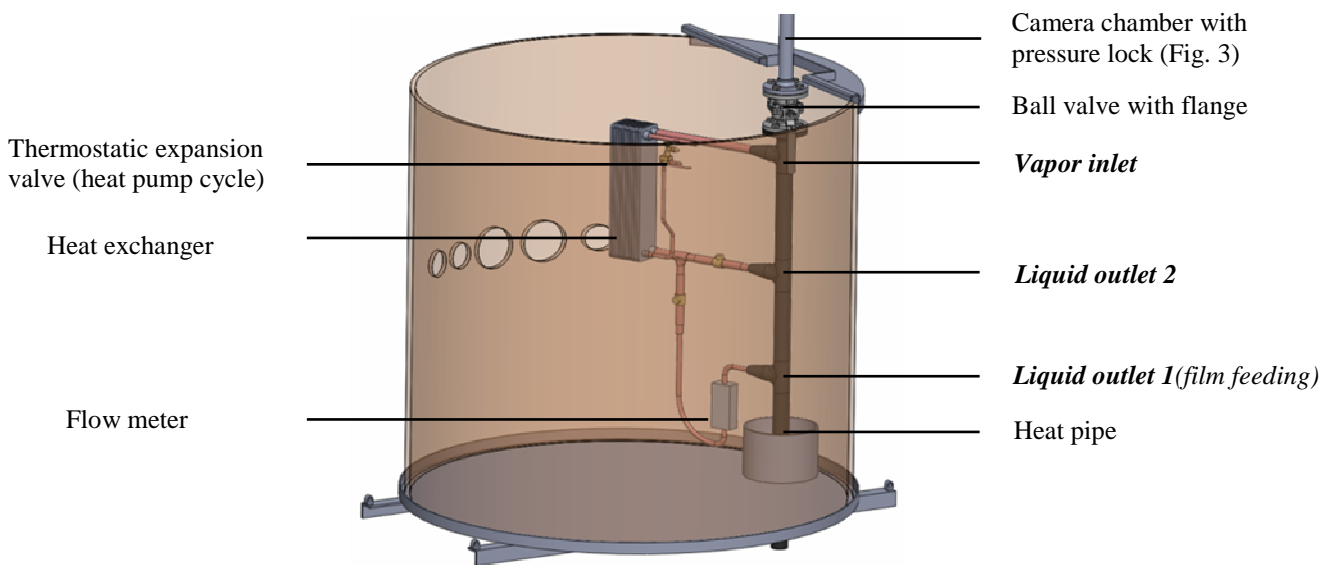


Fig. 1. Inspection chamber with the head of heat pipe, connection to camera chamber and pressure locks

The test plant with heat pipe is connected to a heat pump cycle which is furthermore equipped with extensive measurement technique, such as a distributed fibre-optical temperature sensing system (DTS), several temperature sensors and pressure transmitter, see Fig. 2. The DTS enables long-time checking and a monitoring during the experimental investigations.

In the heat pipe cycle a flow meter is installed (see Fig. 1) to measure the volume flow rate of the circulating liquefied propane. Therewith the heat extracted from the ground could be calculated and the system efficiency could be checked, whereby the system can be adapted if necessary.

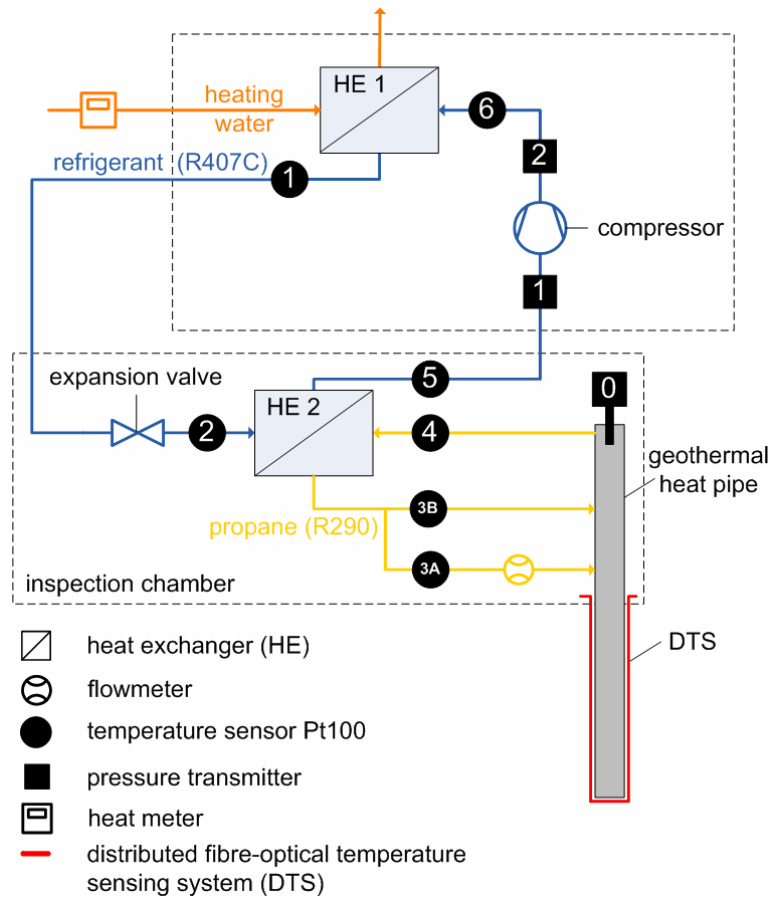


Fig. 2. Cycles and instrumentation of the test plant

To provide visual observations with a miniature camera inside the geothermal heat pipe during operation an access with integrated pressure maintenance had to be developed. It has to be mentioned, that a lot of sealing compounds and especially a lot of plastics are not resistant in propane atmosphere for a longer period. Due to that the lifting jack of the miniature camera is situated outside of the propane atmosphere. Therefore a pressure lock system (two gland nuts) for cable bushing, similar to some which are used for investigations of deep gas caverns, were constructed and pretested with propane, see also Fig. 4 A–C. Furthermore one example for the sealing used and an open gland nut with three sealing rings is shown in Fig. 3. One pressure lock consists of several gland nut sealing layers composed of three sealing rings with different diameter, see Fig. 3B.

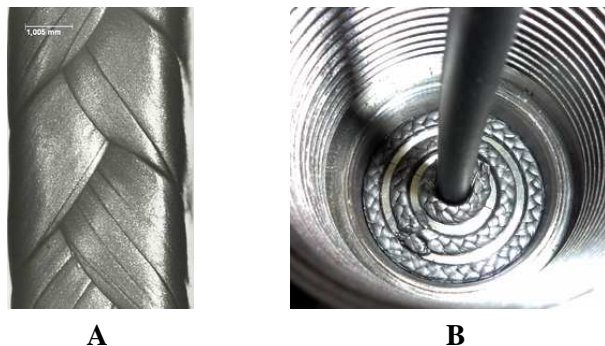


Fig. 3. Gland nut sealing material (A); gland nut with three sealing rings (B)

Fig. 4A shows a schematic drawing of the installed pipe work for steady pressure maintenance. In Fig. 4B the two pressure locks with the intermediate pressure chamber are shown. A photo of the whole pressure locks setup with implemented camera cable is shown in Fig. 4C.

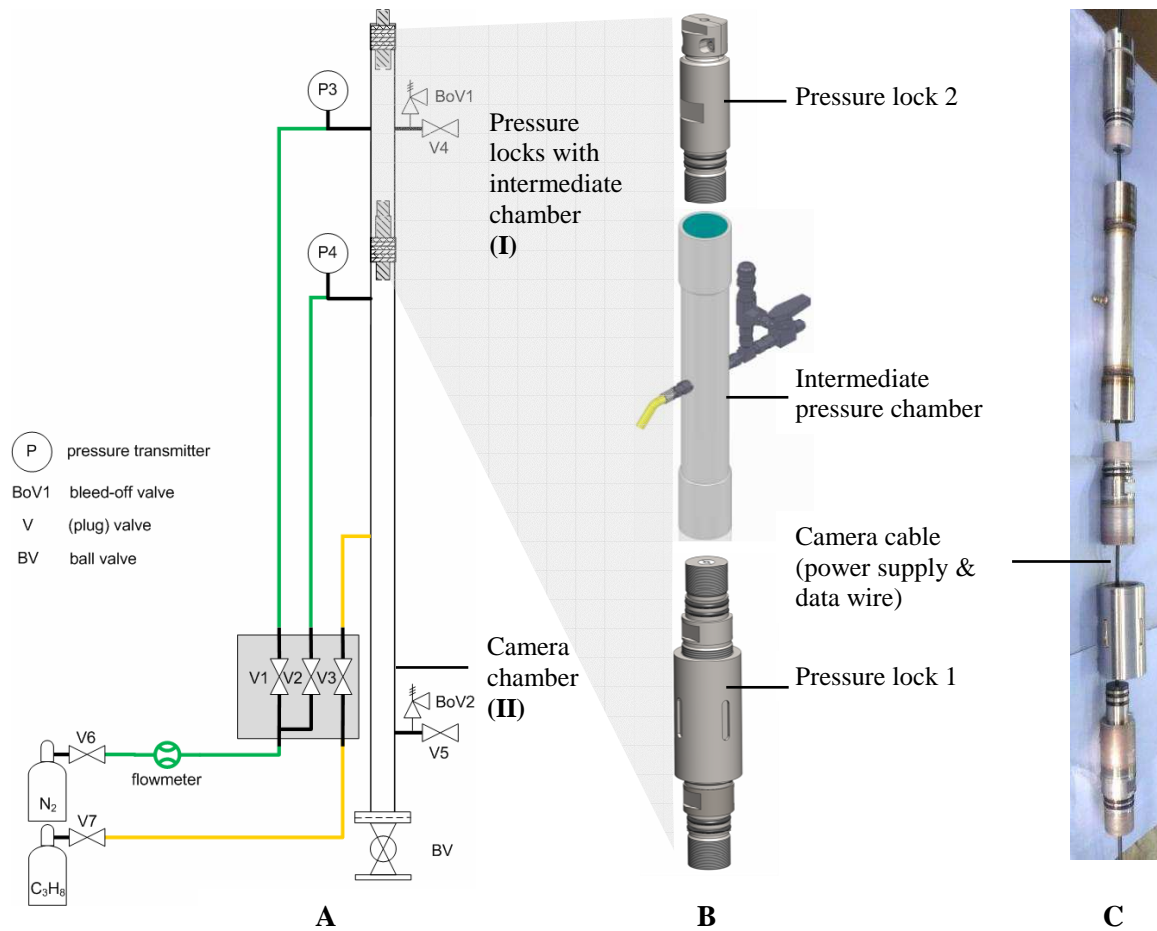


Fig. 4. Schematic drawing of developed pressure locks with camera chamber and pipe-work (A); constructed pressure locks (B); photo of setup with camera cable (C)

For the visual observations a special miniature camera made of stainless steel with an outer diameter and total length of about 17 mm and 65 mm, respectively, an  $82^\circ$  field of view and up to 20 bar pressure-proof was chosen, see Fig. 5. For illumination LED's are implemented placed uniformly around the camera head. Furthermore a bush (hollow cylinder) made of stainless steel is used to protect the miniature camera and its lens from mechanical impact (Fig. 5C). The camera is centralized by three flexible longer and above three stiffly spacers who are situated every  $120^\circ$  over the circumference per layer (Fig. 5C).

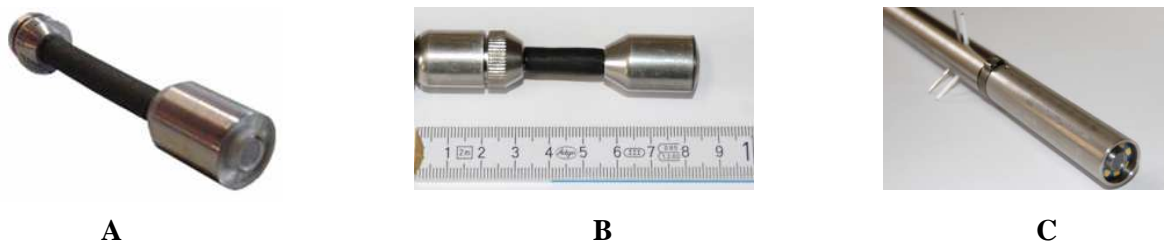


Fig. 5. Miniature camera (A) & (B) (*mincam GmbH*); camera with metal bush and centralizer (C)

### Experimental Procedure

Before starting a visual observation inside the heat pipe the camera chamber (Fig. 4A, (II)) has to be evacuated, whereby the ball valve with flange is locked. So it's ensured that no inert gases can enter the heat pipe's section. Afterwards the camera chamber is filled with gaseous propane. Parallel the intermediate pressure chamber (Fig. 4A, (I)) gets filled with nitrogen at lower constant pressure level (approx. 0.5 bar below) than the heat pipe for having a counter pressure to the propane pressure to avoid that:

- propane is emitted and the heat pipe's function is affected,
- nitrogen enters the heat pipe.

Before the pressure locks were tested, the whole system (welded seams, connections, etc.) was checked to exclude leakages. Afterwards first brief function tests of the pressure lock system were done, whereby at the beginning predefined excess pressures were adjusted and in the following measured, see also Fig. 6:

- camera chamber (Fig. 4A, (II)): start: 5.85 bar  
end: 5.70 bar
- intermediate pressure chamber (Fig. 4A, (I)): start: 3.60 bar  
end: 5.35 bar.

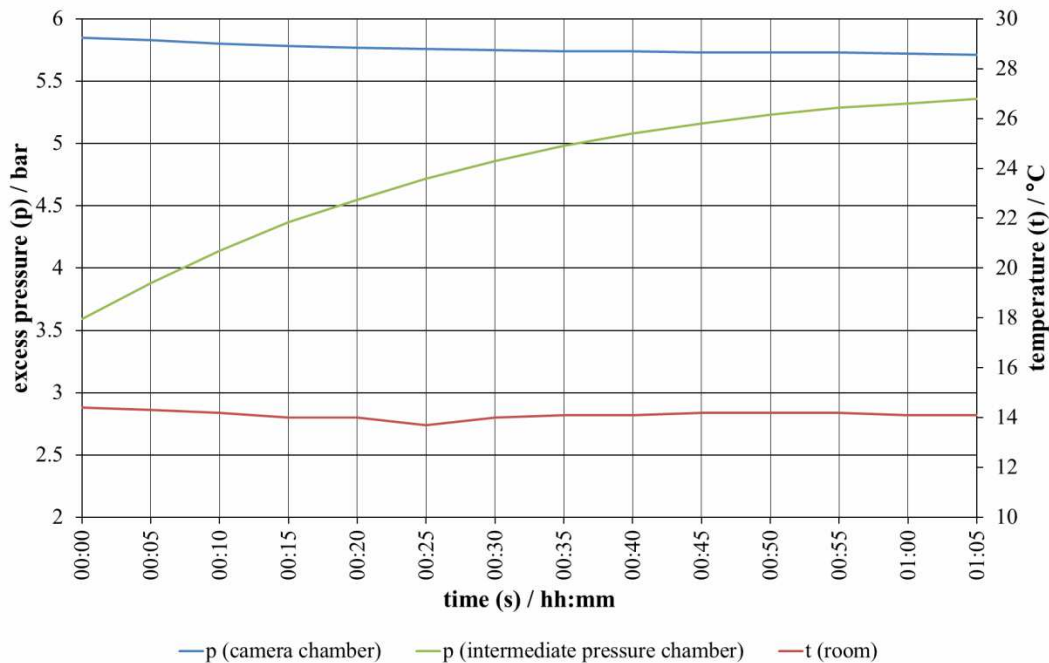


Fig. 6. Pressure – time plot of first brief function test (pressure locks)

In Fig. 6 the matching between the two measured pressures over time is clearly visible. The pressure lock 1 (Fig. 4B) seems to be a poor packing. Due to the low volume of the intermediate chamber the pressure increases shortly after filling. Further tests showed that the pressure lock 2 (Fig. 4B) is much better so that the combination of both locks is sufficient for the visual investigations.

### RESULTS AND DISCUSSION

During the first visual observations the main aim was to observe the start-up process next to the liquid inlet and the liquid pool. In the next figures 7–10 the starting process will be described, beginning with liquid inlet (after heat exchanger).

### Film Feeding

After start of the heat pump system the saturated propane vapor rise to the heat pumps head and condenses. Before liquid distribution on the heat pipes inner surface the first liquefied propane is accumulated due to a liquid baffle plate which is installed at the outlet of the heat exchanger. After approximately two minutes a rivulet starts flowing in the heat pipe (Fig. 7), increasing more and more.



Fig. 7. Liquid film inlet after few minutes of heat pump start

### Liquid Pool

The starting process with the view on a wetted area and the liquid pool is shown chronological in Fig. 8 and 9. In general it is difficult to visualize changing processes with few numbers of frames, wherefore a series of minimum three pictures are used in the next figures. In Fig. 8 (1a) the situation before heat pump start is shown. A sixth of the inner pipes area is wetted. With the start of the heat pump system the wetted area decreases rapidly in few seconds, Fig. 8 (1b)–(2b), until a total dry surface is visible, Fig. 8 (2c). During this process the liquid pool starts surface evaporation with the transition to pool boiling – visible in Fig. 8 (1c) – (2c), whereby the surface becomes cumulative billowy.

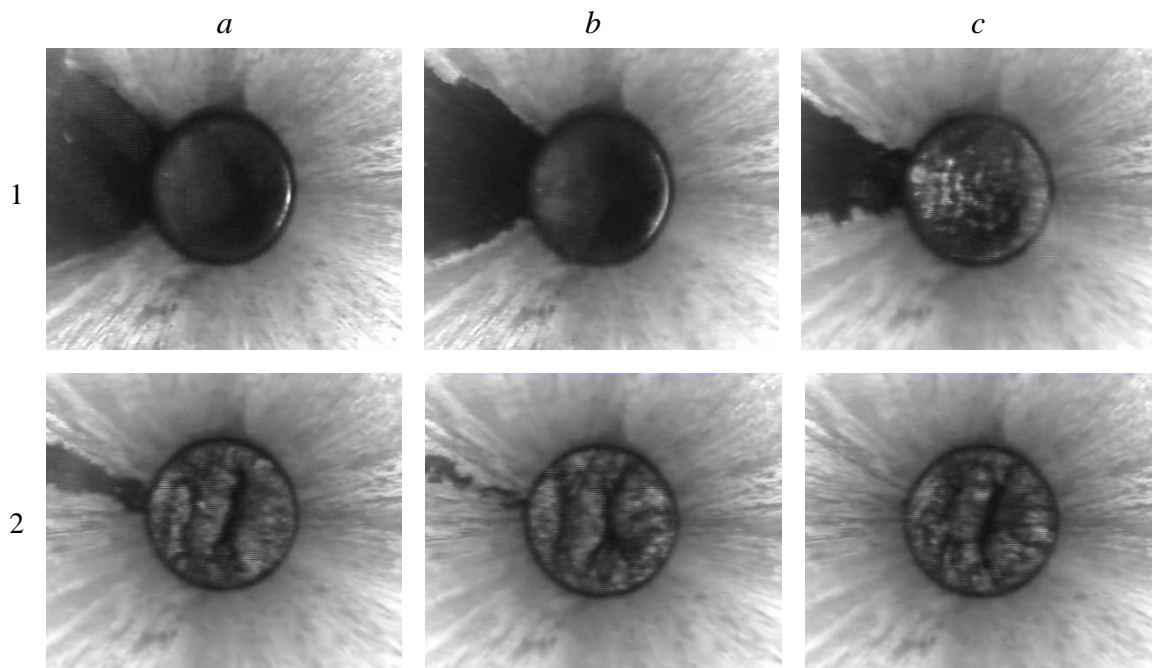


Fig. 8. Heat pump off - wetted area with propane liquid pool - (1a); heat pump on – surface: dry out – pool: starts surface evaporation transition to pool boiling (1b) – (2c); 86.5 m depth

After complete surface dry out the intensity of pool boiling increases and culminates in an eruptive rising of pool level (from 86.7 to ca. 85.6 depth) due to bubble flow and churn flow. Thereby nebulous vapor is visible (Fig. 10A). This state is time-limited and the pool level decreases in depth (depth of camera position increases) and the bubble activity drops, whereby the wetted pipe surface dries out again, see Fig. 9B. Afterwards the liquid pool becomes completely smooth without any bubble activity, compare Fig. 9C. In the first investigations this starting process could be observed several times.

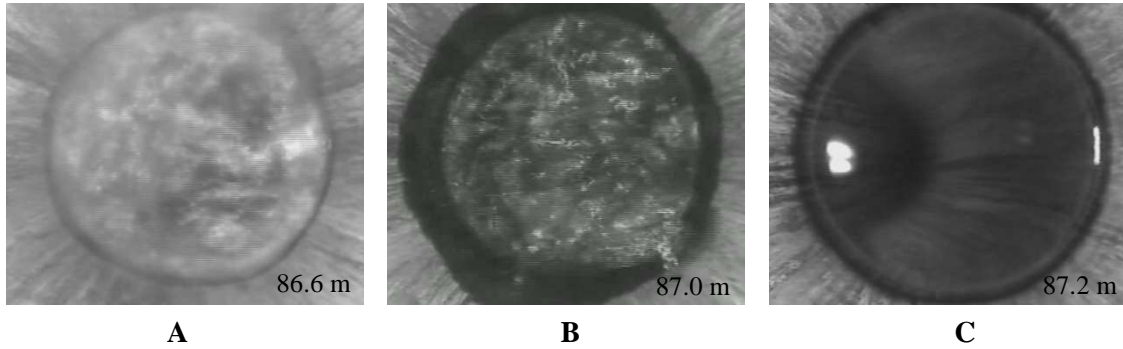


Fig. 9. View on propane liquid pool (chronological order after Fig. 8): eruptive pool boiling (A); shrinking pool level & boiling (B); smooth liquid pool (C)

A longer period after heat pump start a liquid film comes in the focus of the camera which stayed next to the pool level, Fig. 10 (1a–2c). The liquid film front is attended by a nebulous vapor which seems to flow downwards with the liquid film (Fig. 10 (1a–1c)). Temporally the liquid film becomes visible downstream and the nebulous vapor seems to stagnate and getting more and more transparent until it’s only visible directly next to the liquid film surface and the rivulet edges, compare Fig. 10 (1c–2c).

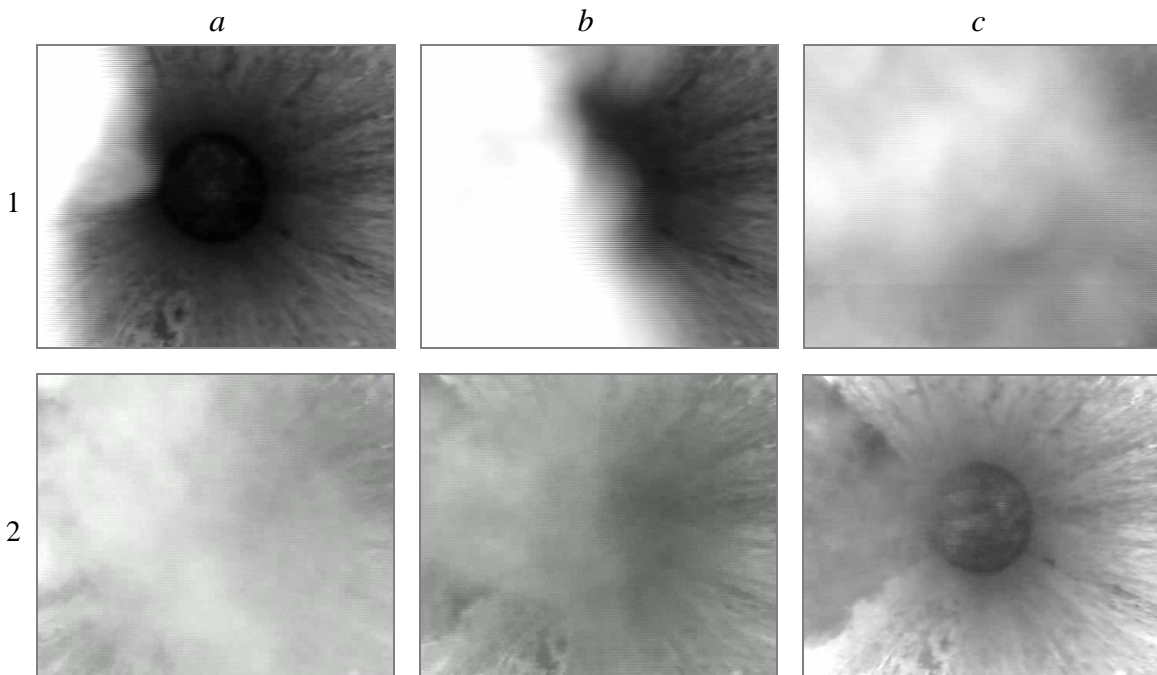


Fig. 10. View in pipe with arriving liquid film with nebulous vapor (chronological order 1a–2c)

Further investigations are concentrated on the time-dependent liquid distribution along the heat pipe length, the liquid inlet and the liquid pool characteristics in comparison to heat output and temperature profile. In the future some changes in heat pump technic overhead are planned to allow further interesting investigations.

### Acknowledgement

We want to thank Mr. H. Fischer and Mr. A. Wahl for their instrumentation support, the staff of BLZ Geotechnik Service GmbH for realizing the test rig and Mr. Braune and Mr. Weickert for their work in this project. Furthermore we thank the Foundation "Technische Universität Bergakademie Freiberg" and the "SIB Chemnitz" for the good cooperation.

This research project is supported by the *Federal Ministry of Economics and Technology* on the basis of a decision by the German Bundestag. The author is funded by the European Union and the federal state Saxony, Germany.

Supported by:



on the basis of a decision  
by the German Bundestag

### References

1. Kaltschmitt M., Streicher W., Wiese A. *Renewable Energy – Technology, and Environment Economics*, Springer-Verlag, 2007.
2. Verein Deutscher Ingenieure. VDI 4640. Part 2. *Thermal use of the underground – fundamentals, approvals, environmental aspects*, 2010.
3. Vasiliev L. L., Vaaz S.L., Grakovich, L.P., Sedelkin V.M, Heat transfer studies for heat pipe cooling and freezing ground: *Advances in Heat Pipe Technology* / Eds. D. A. Reay, Pergamon Press, Oxford, 1981. Pp. 63–71.
4. Tanaka O., Yamakaga H., Ogushi T., Murakami M., Tanaka Y., Snow melting using heat pipes: *Advances in Heat Pipe Technology* / Eds. D. A. Reay, Pergamon Press, Oxford, 1981. Pp. 11–23.
5. Nydahl J.E, Pell K., Lee R., Bridge deck heating with ground-coupled heat pipes: analysis and design // *ASHRAE Transactions*. 1987. Vol. 93 (1). Pp. 939–958.
6. Storch Th., Grab Th., Wagner St., Gross U. Evaluierung einer Geothermieanlage mit Direktverdampfer sonden // *Der Geothermiekongress 2010*, Karlsruhe, Germany, 2010.
7. Ochsner K. Carbon dioxide heat pipe in conjunction with a ground source heat pump (GSHP) // *Appl. Therm. Eng.* 2008. Vol. 28 (16). Pp. 2077–2082.
8. Weickert T., Grab Th, Storch Th, Gross U. Investigations regarding the wetting behaviour of propane on the surfaces of geothermal heat pipes // *Proc. of 8th Minsk Intern. Seminar "Heat Pipes, Heat Pumps, Refrigerators, Power Sources"*, Minsk, Belarus, 2011.
9. Philipp Ch., Doeg A., Tellefsen, Kufaas S., Groß U. Wave characteristics of liquid films – correlation of heat transfer data with visual observations // *Proc. of 13th Intern. Heat Transfer Conference, Sydney, Australia*, 2006, CD-ROM, ISBN 1-56700-226-9.
10. Gross U., Storch Th., Philipp Ch., Doeg A. Wave frequency of falling liquid films and its effect on reflux condensation in vertical tubes // *Int. J. Multiphase Flow*. 2009. Vol. 35 (4), Pp. 398–409.

## FULL-SCALE THERMAL VACUUM TESTS OF BELAUSIAN SPACECRAFT

**A. Gutkin, A. Chobitko**

Institute of Electromechanics  
11, Panfilova st., Istra, Moscow region, 143500, Russia  
Tel/Fax: +7 495 2545375; e-mail: fvniem@istranet.ru

**K. Goncharov, A. Kochetkov, K. Dorofeev**

The Heat Pipe Centre, Lavochkin Association,  
24, Leningradskaya st., Khimki, Moscow region, 141400, Russia,  
Tel/Fax: +7 495 5736374; e mail: heatpipe@laspace.ru

**A. Shnip**

A. Luikov Heat & Mass Transfer Institute  
15, P. Brovki st., Minsk, 220072, Belarus

### INTRODUCTION

Thermal control system (TCS) of the Belarusian spacecraft is developed on the basis of axial grooved heat pipes (AGHP). The TCS includes thermal honeycomb panels with embedded AGHPs in them with outer diameter of 12.5 mm (Fig. 1), the angular AGHPs with outer diameter of 8 mm (Fig. 2) and "II-shaped" AGHPs with outer diameter of 12.5 mm (Fig. 2).

Angular AGHPs divert the heat from the honeycomb panels towards the body radiator of the spacecraft. The four collector "II-shaped" HPs bind honeycomb panels together for leveling temperature distribution.

The thermal vacuum comprehensive tests (TVT) of the spacecraft are the most important and responsible stage during the land thermal vacuum adjustment. Carrying out the thermal vacuum tests in land conditions is one of the major factors providing spacecraft normal functioning in regular operation conditions.

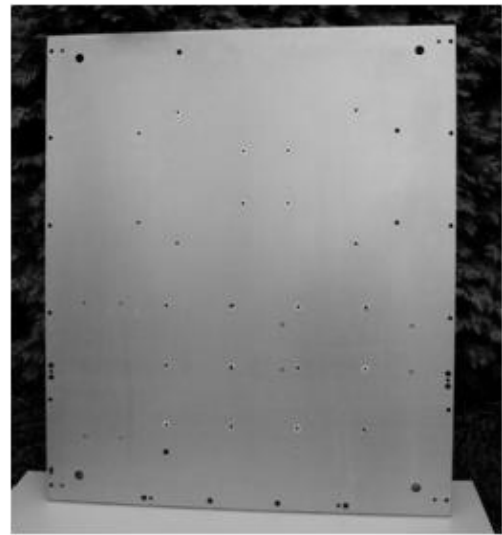
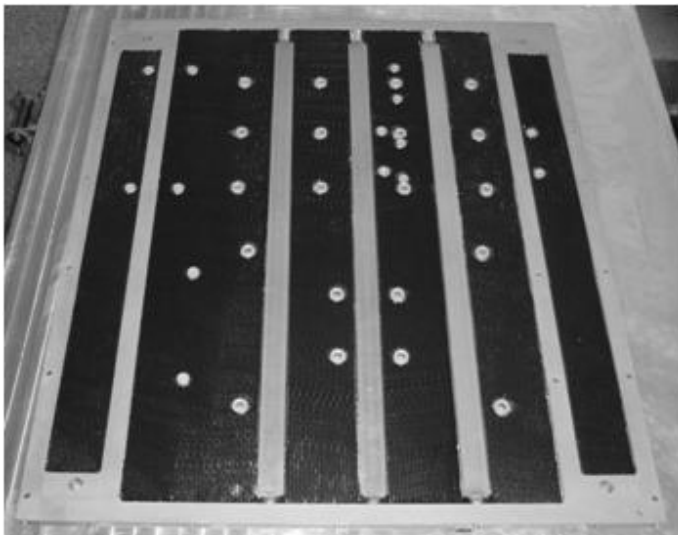


Fig. 1. The honeycomb panels with embedded HPs



Fig. 2. The angular and the "II-shaped" HPs

During the tests there was carried out: the TCS functionality check similar to the real operational conditions; construction temperature fields were investigated; the TCS efficiency on different thermal loadings was determined; the onboard equipment was checked with the help of the telemetry data received by the measuring and computing complex. The necessary TCS improvements can be made and the admission of the spacecraft to the flight tests can be received by the results of thermal vacuum tests.

The TCS efficiency tests were made by means of the unit temperature change in the course of tests.

## 1. FUNCTIONING CONDITIONS OF THE SPACECRAFT DURING THE ORBITAL OPERATION. EXTERNAL INFLUENCES IMITATION TESTS OF THE SPACECRAFT

In the course of regular operation the spacecraft is exposed to influence of the space vacuum, the "cold black" outer space and the external sources of radiation.

Because of the absorption and reflection of thermal radiation selective character (depends on wave length), it is necessary to consider the process of the radiant heat exchange of the spacecraft surfaces in two ranges of a spectrum: short-wave (sunlight) and long-wave (the own radiation of the Earth and the elements of the spacecraft).

The basic source of the external thermal influence on the spacecraft is the thermal flow of the direct sunlight. The reflected sunlight flow from the Earth and the own Earth's radiation flow is received by the spacecraft along with the direct Sun radiation. The flows reradiation between the construction elements external surfaces take place in the course of regular spacecraft operation. So, for example, the spacecraft is set in the vacuum chamber without the solar battery, which shades the radiating surface on 6%. This fact is necessary to consider with a correction of the thermal mathematical model of the spacecraft in the conditions of heat transfer of the vacuum chamber.

The choice of the external influences imitation means on the spacecraft is insignificant. In the case of the simulator of sunlight (SS) usage during tests, the spacecraft should perform difficult rotation around the SS. The thermal control system (TCS) of the spacecraft as a whole consists of 39 axial grooved heat pipes which can't operate at a rotation in gravity.

The thermal exposure on the test unit during the TVT was reproduced by the means of infra-red simulators (IRS) in the vacuum chamber. Thus, for imitation of the short-wave sunlight the recalculation of a flow value according to a parity of  $A_s$  and  $\epsilon$  values of the perceivable surfaces is made.

The modeling of the space vacuum influence and the "cold black" outer space was created by the bench systems of the vacuum chamber. The pressure at which it is possible to neglect the convective heat transfer and the molecular heat conductivity was made in the vacuum chamber. Such thermal flows for the given conditions make up less than 1 % from a radiation heat transfer.

The imitation of an unlimited outer space and the full absorption of thermal radiation of the tested unit were provided with a necessary parity of volumes of the unit and the working volume of the chamber, the IRS "transparency" for the surfaces thermal radiation of the unit and the cooling of the vacuum chamber screens by the liquid nitrogen to the temperature not above minus  $(190 \pm 5)$  °C along with the thermo-optical characteristics of the screens surfaces not less than 0.9.

## 2. THE IR FLOW INFLUENCE PECULIARITIES ON THE SPACECRAFT SURFACE

Meshed IRS mounted over the spacecraft surfaces were used as external influences emulators. There were used 22 IRS placed on the unit at thermal vacuum tests.

The heat flow sensors mounted between the IRS and the surface of the unit were used to determine the value of the heat flow falling on the spacecraft's surface.

At imitation of falling flows on separate assemblage units of the spacecraft, for example, on assemblage of the star sensors that have radiators with a different coverings: one has the "solar reflector" type (K208Sr;  $A_s \leq 0.12$ ;  $\varepsilon \geq 0.85$ ) and the other has absorbing covering ( $A_s = 0.92$ ;  $\varepsilon = 0.92$  internal surfaces of a blends), it is necessary to mount the IRS over each of these surfaces. Considering the interference of the IRS, it is impossible to satisfy this condition. There were used two IRS mounted in parallel to the entrance gate planes of the blends at carrying out the thermal vacuum tests. In this case the radiation surfaces absorbed the heat flow exceeding demanded in 0.85/0.12 times. This fact was taken into consideration at carrying out the conductive bond correction between the star sensors assemblage and the body of the spacecraft.

The solar radiation doesn't reach the internal surfaces of the lenses and the sensible device head in natural operation conditions. Because of the directivity of the solar radiation, it is completely absorbed by the blends.

The diffuse IRS flow had the direct influence on the equipment internal surfaces of the lenses and on the sensible device head in the conditions of heat exchange in the thermal vacuum chamber. When the equipment and the star sensors assemblage with the body of the spacecraft conductive bond correction was held, the heat flow from the IRS was considered as an internal heat emission

## 3. THE TEST UNIT. THE SPACECRAFT'S BODY HEAT PIPES FUNCTIONING PECULIARITIES

The preproduction model of the spacecraft was used as the test unit. The model consists of the service platform module and the equipment monoblock (Fig. 3). The service platform module is based on the body of the spacecraft that has the form of a rectangular parallelepiped with dimensions of  $(750 \times 750 \times 900)$  mm. The body facets were made with the honeycomb panels. Each honeycomb panel has three embedded axial grooved heat pipes inside. The embedded heat pipes of the panels " $\pm Y$ ", " $\pm Z$ " are located horizontally in the thermal vacuum chamber. The embedded heat pipes of the panels " $\pm X$ " are located in vertical position. Twelve angular HPs realize the conductive link between the panels " $\pm Y$ ,  $\pm X$ "

The radiator of the service platform and the honeycomb panel " $+Y$ " is located at the top part of the vacuum chamber. Angular HPs divert the heat from the honeycomb panels " $-Y$ ,  $\pm X$ " towards the body radiator of the spacecraft. The heat from the honeycomb panels " $\pm Z$ " is diverted by four collector "II-shaped" HPs.

All heat evolving devices of the service module are mounted on the panel embedded HPs.

The equipment placed on vertically located honeycomb panels " $\pm X$ ", are located on the zones of the HPs that are partially or completely free from the working fluid.

The additional HP with the radiator are mounted on the propulsion system to decrease the honeycomb panel " $-X$ " thermal load.

For the operability assurance of the HP, the technological analog of the device was used during the tests.

The special technological heat removal device was used for the vertically located HPs start-up and for making positive temperature difference between embedded HPs of the honeycomb panels " $\pm Y$ " ( $(T^- - Y^- - T^+ + Y^+) > 0$ ).

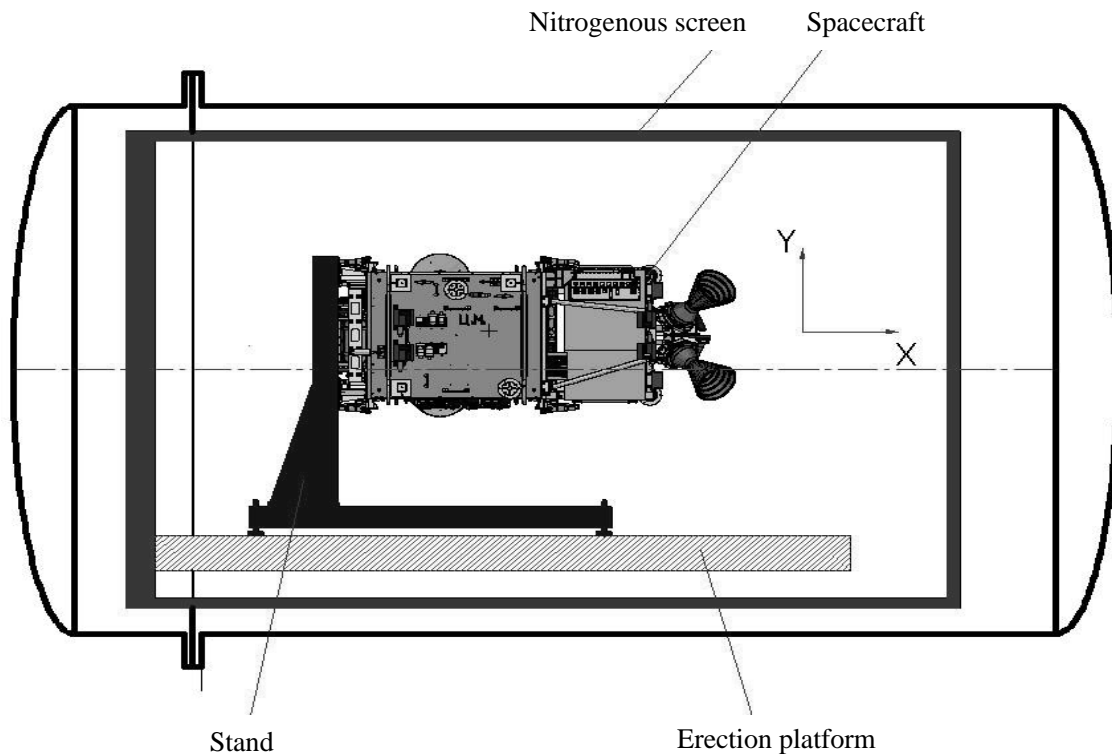


Fig. 3. Arrangement of the spacecraft in the vacuum chamber

The heat removal device was mounted on the collector HPs with the modified geometry for the purpose of returning of the working fluid to the evaporation zone, and for the electric heating unit installation in the zones of contact with the embedded HPs of the honeycomb panel “-Y”. The electric heating unit’s power corresponded to the power of the absorbed flows of the radiant surface.

The equipment has self-contained TCS. The equipment is heat-insulated from the spacecraft conductive and radiative heat exchange.

The isotherm of the surveying system lenses is reached by mounting of the electric heating units on the blends, an instrumental frame, focal blocks and the thermal covering placing on all external contour, except for the radiators and the lens aperture.

The electric heating units are commutated by the electronics block which is a part of the service module of the spacecraft. The electronics block provided the elements of the surveying systems with temperature maintenance on two levels of temperature with an error of  $\pm 1$  °C.

The heat divert from the focal blocks to the survey equipment radiators was realized by the four axial grooved heat pipes. The HPs evaporation zones were positioned below the condensation zones. The HPs were functioning in the thermosyphon mode. The heat transfer from the on-board information system to the radiator was carried out by conductive heat exchange.

The test unit was mounted in the vacuum chamber on a special technological support. The four-section security electric heating unit was mounted in four zones of fastening of the unit to the support-farm. The power of each section is 70 W. The security electric heating unit prevented the conductive heat exchange between the test unit and the support-farm.

By means of a special farm, the IRS emitters were mounted over the surfaces of the spacecraft. Thermal flow sensors were mounted between the IRS emitters and the spacecraft’s surfaces by means of their own arms.

The monitoring of a thermal mode was carried out by the regular telemetry system sensors and by the additional sensors mounted on the technological device of heat removal, the chemical battery, the central part of the radiator and the surface of the security electric heating unit. The regular telemetry system sensors

indications were received by the measuring and computing complex of the spacecraft. The additional sensors data was received by MIC-036.

The management of the spacecraft was made with the help of the measuring and computing complex. For the detailed functioning analysis of: the accessory power system, the motion control system, the special-purpose information radio link, the correcting propulsion system the corresponding checkout gear was used. The tests were carried out with use of the testing programs developed for each stage of tests.

#### 4. THE RESULTS OF THE THERMAL VACUUM TESTS

The technological heat removal device was activated before the thermal vacuum tests began. The device functioning was monitored by the sensors: TS1, TS3 – of the first branch; TS2, TS4 – of the second branch. The start of the HPs device is shown in Fig. 4. The difference of the first branch sensors didn't exceed 1.5 °C, whereas the second branch temperature difference didn't exceed 0.5 °C.

The results for the two main thermal vacuum test stages:

- the standby state (a life support state) of the spacecraft in a "cold" conditions of external heat exchange.
- the spacecraft operation mode in a "hot" conditions of external heat exchange

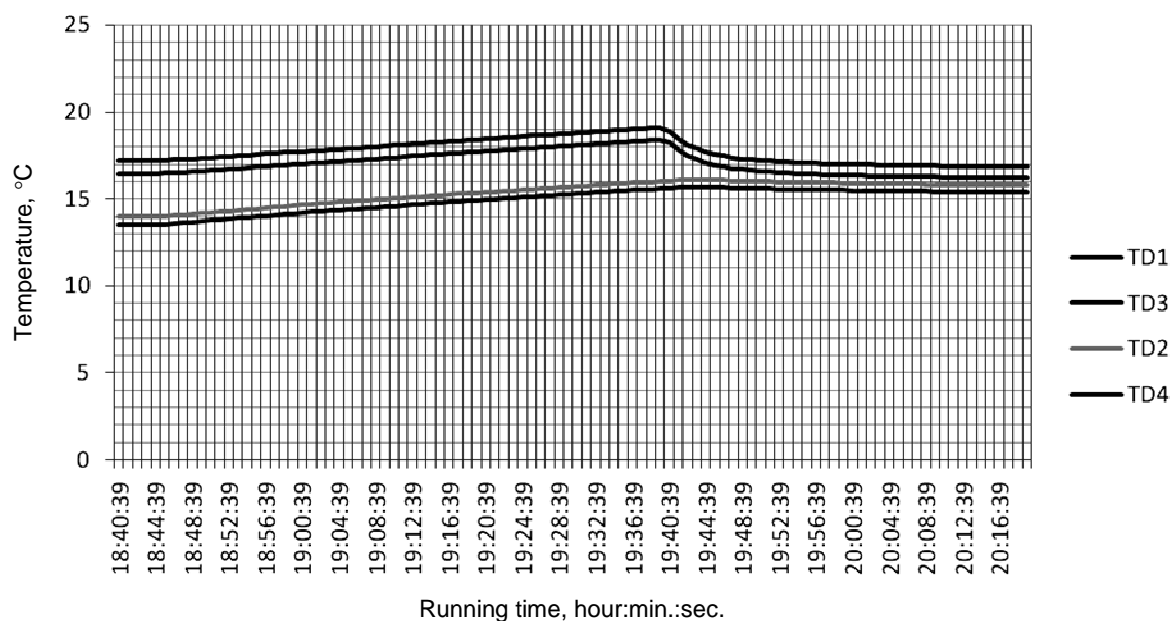


Fig. 4. The technological heat removal device start-up before carrying out the TVT

The standby state of the spacecraft in a "cold" conditions of external heat exchange. The incident fluxes corresponding to the regular operation conditions of the spacecraft were set by the IRS. At these conditions an angle between the plane of an orbit and a direction on the Sun equals minus 8 degrees.

In this case the spacecraft has the minimal light illumination of an orbit (the maximum shadow site of a coil). The charge of the chemical battery was made only on the lighted part of a coil. Heat emission of the spacecraft in a standby state was 171.5 W + 34 W (technological heat removal device electric heating units) = 205.5 W. The honeycomb panels heat distribution in this case: the panel "+Z" 6.4 W; the panel "-Z" 46.0 W; the panel "+X" 55.0 W; the panel "-X" 17.5 W; the panel "+Y" 46.6 W; the panel "-Y" 34 W.

The duration of tests was defined by the time that was spent by the spacecraft to reach the steady-state (quasisteady state) thermal mode. The temperature curve of the body panel embedded heat pipes of the spacecraft is shown in Fig. 5. The thermal steady-state mode on the honeycomb panels with the permanent heat emission has been recorded during 5 hours (~3 coils). The honeycomb panel "+X" had varying thermal emission. Such thermal emission is due to the work of equipment, simulating typical perturbation on the motion control system.

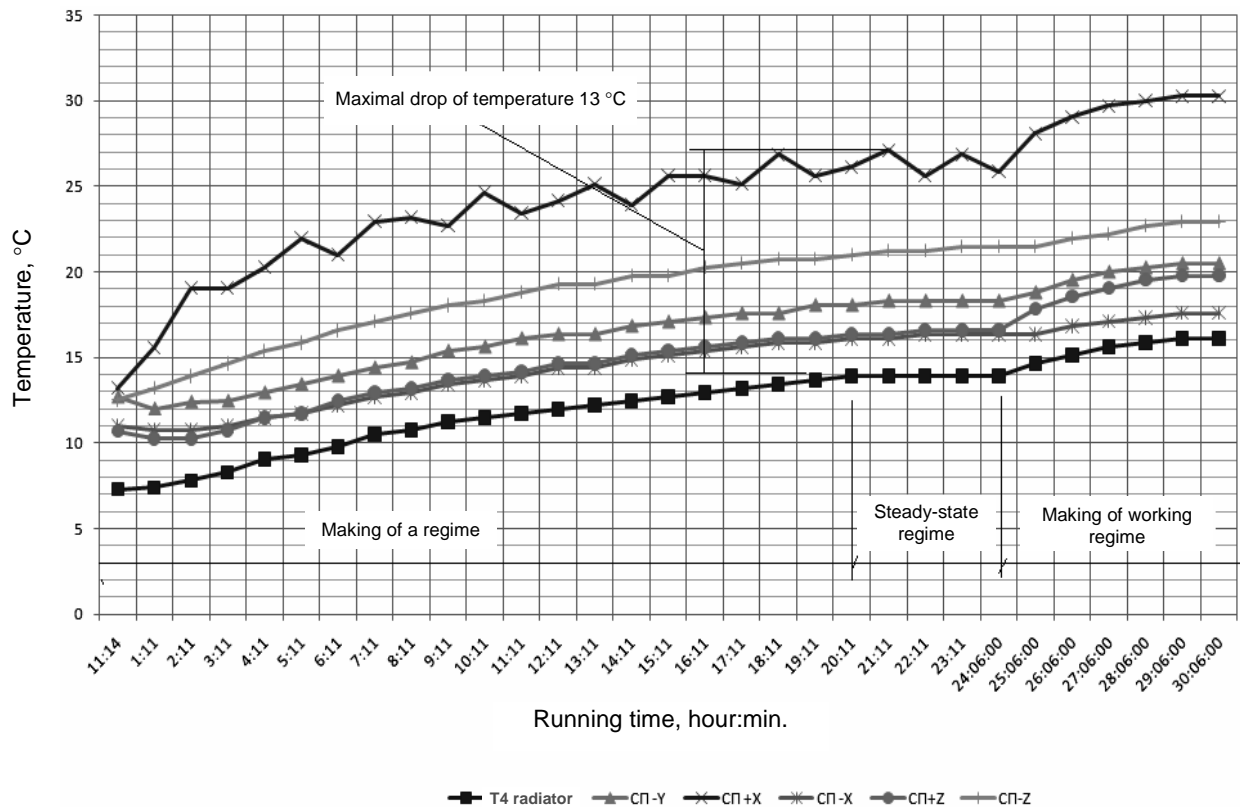


Fig. 5. Experimental data. The spacecraft standby state in a “cold” conditions of external heat exchange

The honeycomb panel “+X” had varying thermal emission. Such thermal emission is due to the work of equipment, simulating typical perturbation on the motion control system. The spacecraft’s radiating surface temperature makes 14 °C in case of the thermal standby-state conditions. The settled temperature difference between the honeycomb panels “±Y” is approximately ~4 °C. This proves the functioning of the technological heat removal device that provides the start-up of the embedded heat pipes of the panels “±X” and heat removal from the panels “±Z” to the radiating surface of the spacecraft.

The maximal temperature difference on the spacecraft body between the honeycomb panels “+X”, “+Y” is 13 °C. The heat transfer from the panel “+X” to the panel “+Y” has been realized as a consecutive chain: the embedded HP of the honeycomb panel “+X” – thermal resistance in the contact of embedded HP of the honeycomb panel “+X” and the angular HP – the angular HP – thermal resistance in the contact of angular HP and embedded HP of the panel “+Y” – the embedded HP of the panel “+Y”.

The heat transfer of the similar branch between the panel “+X” and panel “-Y” didn’t take place because the angular HP’s evaporation zones were above the condensation zones. The predicted temperature drop in a regular operation conditions will make 8 °C.

The thermal vacuum tests important problem is the mathematical model thermal correction. The experimental and calculated temperature values of the embedded HPs of the panels “±Y” in the stationary-state conditions are shown in Fig. 6. The calculated temperature values were obtained at following heat conduction values in the thermal vacuum chamber:

- consecutive heat transfer between the panels “±X” and panel “+Y” as well as between the panel “-Y” and panel “-X” (the heat transfer scheme in this case is: embedded HP – angular HP – embedded HP) makes 1.4 W/degree;
- consecutive heat transfer between the panels “±Z” and panel “+Y” as well as between the panel “-Y” and panel “+Z” (the heat transfer scheme in this case is: embedded HP – the HP of the technological heat removal device – embedded HP) makes 3.3 W/degree.

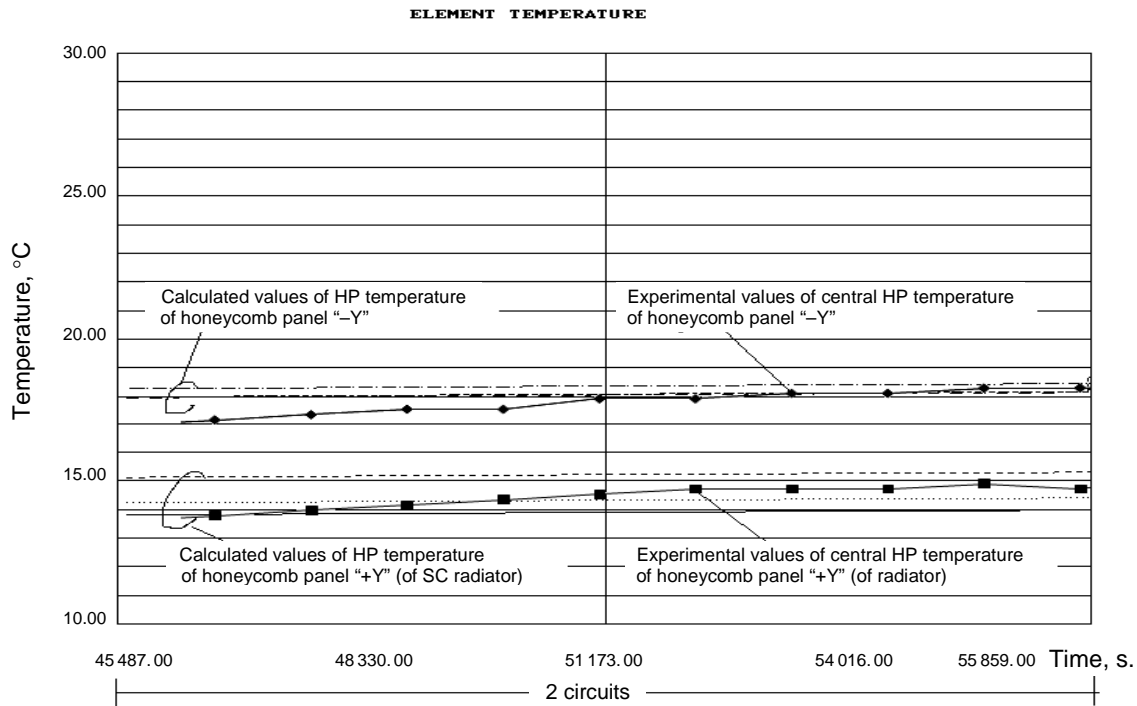


Fig. 6. The standby state of the spacecraft in a "cold" conditions of external heat exchange. The experimental and calculation temperature values of the honeycomb panels "±Y" comparison

The spacecraft operation mode in a "hot" conditions of external heat exchange. The incident fluxes corresponding to the regular operation conditions of the spacecraft were set by the IRS. At these conditions an angle between the plane of an orbit and a direction on the Sun equals minus 18 degrees. The spacecraft's radiating surface temperature makes 17 °C in case of the thermal standby-state conditions. The settled temperature of the honeycomb panel "+X" makes 30.5 °C (Fig. 5). The charge of the chemical battery was made only on the lighted part of a coil.

The thermal load of the spacecraft's body in operation conditions differs from the thermal emission of the standby state. The difference makes the value of the RLCI equipment thermal emission. All RLCI equipment except for the informational streams generation block (ISG) is located at the panel "-Y". The RLCI operating time doesn't exceed 700 sec in a coil. The thermal emission of the honeycomb panel "-Y" is increased on the value of 174 W during the radio-communication contact. And thermal emission of the honeycomb panel "+X" is increased on 20 W. The main mode of the RLCI is the two information transfer channels simultaneous switching on. This is essential for realizing complete equipment information transfer during the communication session. The power amplifiers (PA) are the most heat-stressed elements of the RLCI. The PAs are reserved in each channel of the RLCI. The thermal emission of the activated PA is 62 W.

The activation control chart of the RLCI at the thermal vacuum tests is shown on Fig. 7. The control chart provides for: simultaneous activation of two of two channels, the information transferred through the checkout gear of the RLCI detailed analysis, the two channels of the main and reserve half-sets consecutive activation. The sections of facing sheets of the honeycomb panel "-Y", located between embedded HPs with mounted PAs are the most heat-stressed elements of the panel. The temperature reached 30.5 °C on thermal sensors T30–T33. This exceeded the embedded HP's temperature by 6–7 °C. When RLCI stopped working the temperature of the radiation surface has made 19 °C and the temperature of the panel "+X" has made 32 °C.

Temperature of the elements of the honeycomb panel on the simultaneous channels activation mode, the calculation results for the simultaneous activation of both channels for 700 sec are given in Fig. 8.

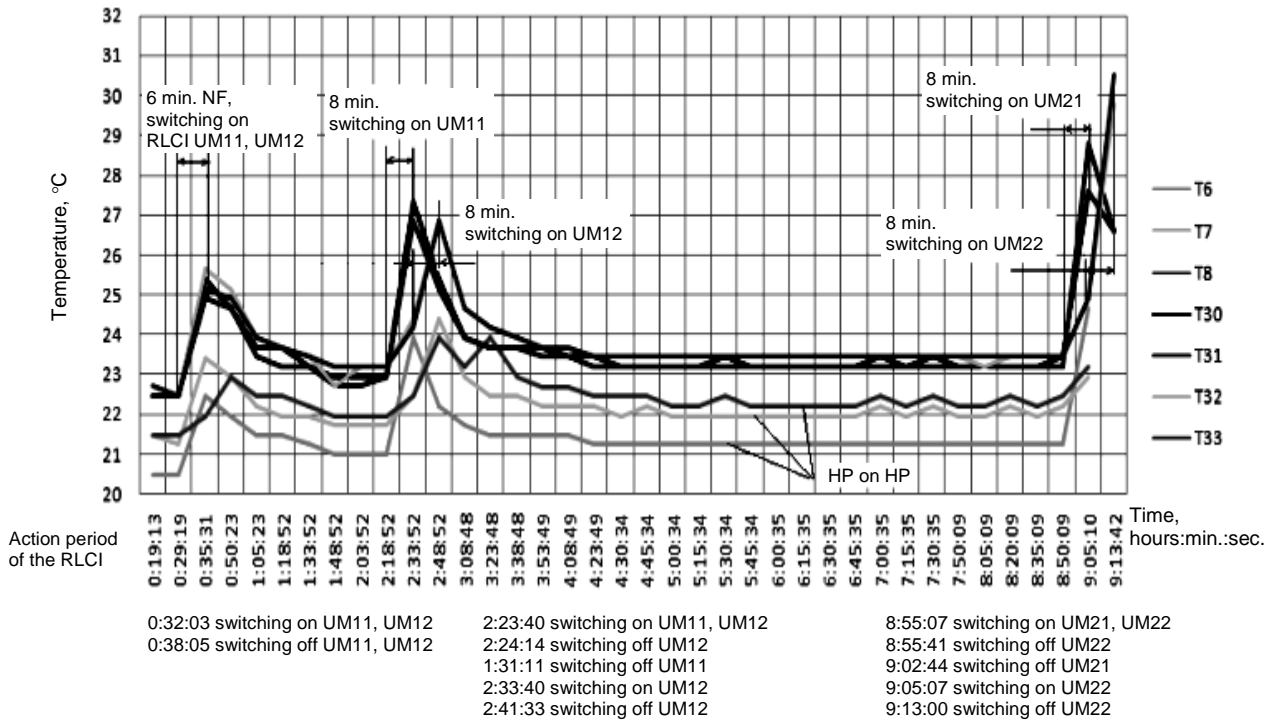


Fig. 7. The spacecraft operation mode in a "hot" conditions of external heat exchange. The RLCI activation

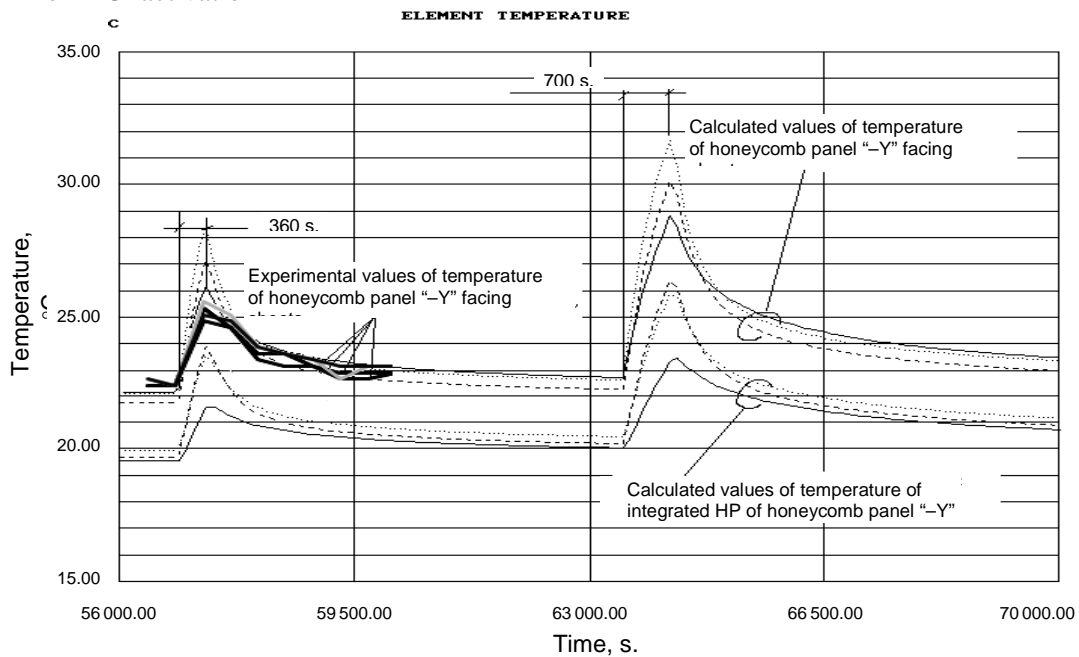


Fig. 8. The spacecraft operation mode in a "hot" conditions of external heat exchange. Experimental and calculation temperature values of the honeycomb panel "-Y" during the RLCI work

## 5. CONCLUSION

The thermal vacuum comprehensive tests of the preproduction model of Belorussian spacecraft with the close to regular operation conditions were carried out.

The correctness of the TCS chosen scheme on the basis of axial grooved heat pipes is proven.

The spacecraft's draft proposal in case of temperature maintenance of the honeycomb panels in range of 0–40 °C are experimentally confirmed. The calculated and corrected by the results of TVT temperature range of the spacecraft makes 10–28 °C.

The work logic of the electric heating units control block is experimentally verified.

## **THERMAL CONTROL OF LOOP HEAT PIPE WITH PRESSURE REGULATING VALVE**

**D. Mishkinis, A. Kulakov, F. Romera, C. Gregori, A. Torres**

IberEspacio Tecnología Aeroespacial

Magallanes 3, 4A, Madrid, 28010, Spain

Phone/Fax: +34.91.309.80.00, E-mails: dm@iberespacio.es, akd@iberespacio.es

### **Abstract**

Innovative approach to regulate operation temperature of LHP with two-way valve is discussed. Comparison with traditional three-way bypass valve is done. It was investigated that two-way valve design provides better ability of thermal control as traditional three-way design and has significant advantages. Some examples of two-way valve application is presented.

Heat transfer limitation of LHP with PRV was verified. Both modes of PRV application demonstrated practically the same maximum heat transfer rate of LHP. It was also obtained that maximum heat transfer capacity of LHP with valve is higher than for LHP without valve.

Start up ability of LHP with and without PRV was compared. It was found that PRV can facilitate start up.

### **KEY WORDS**

Loop Heat Pipe, Pressure Regulating Valve, Two-way Regulation Mode, Spacecraft Thermal Control.

### **INTRODUCTION**

Loop heat pipes (LHP) are widely used for thermal control of spacecraft electronic equipment. For a number of satellite operational scenarios the temperature of LHP condenser can decrease significantly. That causes the lowering of LHP evaporator temperature and therefore temperature of the LHP controlled equipment. Thus, onboard equipment temperature can decrease below an acceptable value. To prevent the equipment overcooling the pressure regulating valve (PRV) can be used. Other fields of pressure regulating valve applications are precise temperature control of satellite equipment and "thermal switch" for Lunar and Mars rovers [1]. PRV has feedback from vapor temperature of LHP and can keep the temperature of the equipment at required level. This method of temperature control has a number of advantages in comparison with other techniques [2].

### **TWO-WAY AND THREE-WAY PRESSURE REGULATING VALVE DESIGN AND OPERATION PRINCIPLE COMPARISON**

Usually three-way valves are used for LHP to redistribute vapor flow between main LHP loop included condenser and bypass line linked vapor line and compensation chamber. Thus, the incorporation of a 3-way regulating valve in vapor line was proposed in the process of an ESA Two-Phase experiment (In-orbit Technology Demonstration Program aboard Space Shuttle STS-60, February 1994) [3].) TPX is a scaled-down capillary pumped two-phase ammonia system with multichannel condensers, vapor quality sensors (VQS) and a controllable 3-way valve (Fig. 1). One of TPX objectives was the in-orbit calibration of the vapor quality sensors, by adjusting the 3-way Controllable Valve, mixing the by-passed vapor with liquid leaving the condenser.

The idea to use by-passed vapor for heating of the LHP compensation chamber or liquid line and finally, for the control of equipment temperature with the help of a 3-way pressure regulated valve (Fig. 2), was proposed by Lavochkin/TAIS and successfully realized in a number of onboard thermal control systems, including Russian Mars Rover application [4-6]. The same approach (3-way valve) was originally pre-selected for European Mars Exploration Program and a prototype has been extensively tested [7-9]. It was found that for certain combinations of condenser temperature and input power, the temperature oscillations (in the range of several degrees) are possible due to the gravity effect. It has a minor influence on LHP

thermal switch functional performance. Detailed explanation of this phenomenon has been presented in [10]. However, in case of regulation temperature being very low (below  $-20^{\circ}\text{C}$ ) the oscillation amplitudes can reach ten degrees and even higher.

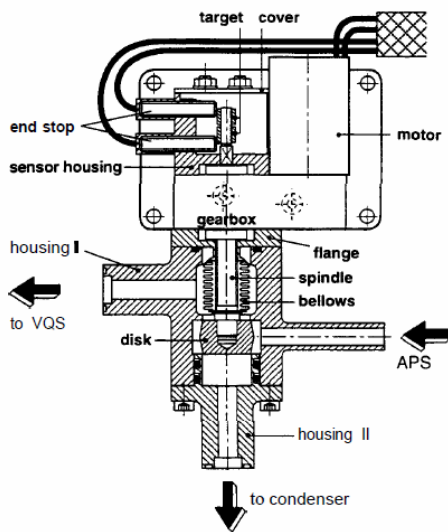


Fig. 1. TPX 3-way valve [5]

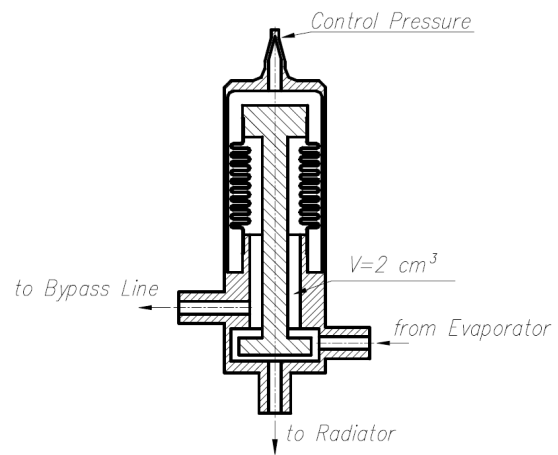


Fig. 2. Lavochkin/TAIS 3-way valve [6]

Comprehensive description and analysis of PRV operation can be found in [10].

However the main drawback of the 3-way regulating valve is the following: in case of even a very small vapor flow leakage into the bypass line, the performance (conductance) of the LHP will degrade, particularly for the operational regimes when the bypass line is closed and the two-phase loop is working as a regular LHP without the valve. It means that possibility of heat source overheating above an acceptable limit exists, since temperature difference between the evaporator and the condenser increases. It is also difficult to guarantee the total leakage absence since the typical material for evaporator capillary structures is metallic powder and the particles of the powder can appear and migrate in the loop during LHP operation. These particles can deposit on the valve stem and seats and cause the vapor leak into the bypass. Actually, the leakage in the bypass line produces the same effect as a parasitic heat leak from the evaporator into the compensation chamber: difficult start-up, low LHP thermal conductance, instabilities at transient regimes, etc.

To overcome the above noted drawbacks of the 3-way regulating valve, a new method of evaporator temperature control is proposed [11]. In fact, this approach simplifies the current design of the 3-way regulating valve up to a two-way regulating valve and eliminates the necessity of the bypass line (Fig. 1, 2). Two-way valve has only one input and one output (Fig. 3). Other elements are the same as for the 3-way valve.

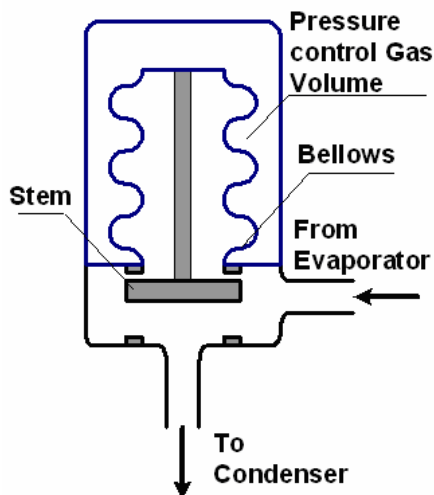


Fig. 3. Two-way pressure regulating valve

However, the law of valve regulation is different. Since LHP is evaporating- condensing heat transfer device, it operates around vapor-liquid saturation line. The increase of pressure drop of the external loop of LHP (the drop between vapor and liquid sides of evaporator porous structure) leads to the corresponding increase of temperature difference between evaporator and condenser. This effect is used in case of two-way regulating valve LHP.

The two-way valve is able to adjust automatically the hydraulic resistance of the circuit by adjusting the hydraulic resistance of the vapor transport line. The two-way regulating valve acts on the hydraulic resistance of the

vapor line by means of acting on the fluid flow through it, by changing the cross section of the line, thus varying the LHP external pressure difference. In this way, the temperature of the evaporator is maintained close to constant and is independent of the condenser temperature.

### THREE-WAY AND TWO-WAY VALVES OPERATION COMPARISON

#### Experimental LHP description

Miniature LHP (MLHP) equipped with pressure regulating valve was designed, manufactured and tested [12] to characterize the LHP performance. Special investigation was performed with objectives to compare and verify operation of LHP with 3-way and 2-way valves and to find limitations of LHP operated with regulating valves of two types. This LHP is shown in Fig. 4. The PRV is installed on top of the evaporator saddle.

Main dimensions are shown in Table 1. Wick properties of the MLHP are presented in Table 2. PRV set point is 4°C and regulation point 12°C. The difference between Set and Regulation points is discussed in [10].



Fig. 4. Mini-LHP with PRV

Table 1: MLHP main dimensions

Component	Length (mm)	Diameter (mm)
Evaporator	55	12
Condenser	300	2
Reservoir	30	16
Vapor Line	700	3
Liquid Line	700	2

Table 2. Wick properties of the MLHP

Characteristics	LHP-SS
Wick Material	Stainless Steel
Porous diameter ( $\mu\text{m}$ )	3.5
Porosity (%)	70
Permeability ( $\text{m}^2$ )	6.5E-13

#### Test description

MLHP has been tested in accordance to the measurement plan shown in Fig. 5.

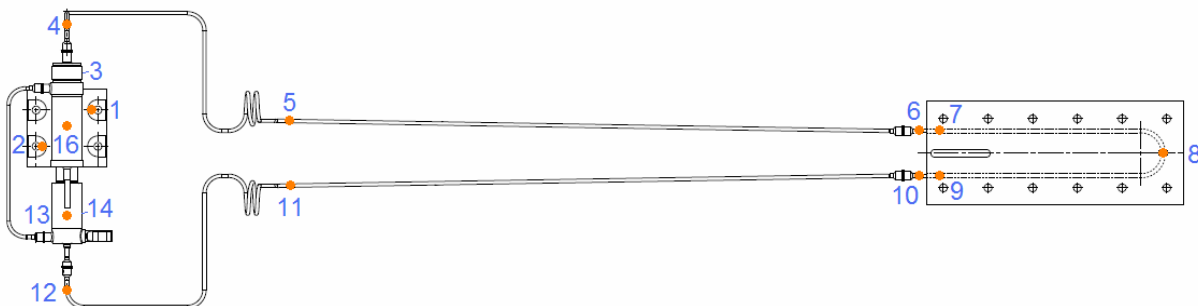


Fig. 5. Mini-LHP Measurement Plan

The condenser plate was set in contact with the cold plate of the chiller. The evaporator saddle was attached to the saddle of the cartridge heater (which provides the power dissipated by the MLHP). During

ambient tests MLHP was thermally isolated. T-type thermocouples were used to monitor of MLHP temperatures. A photograph of MLHP on test bench can be seen in the Figure 4.

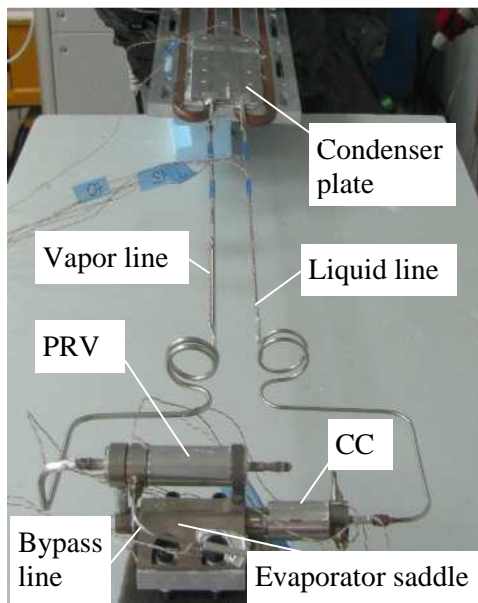


Fig. 6. MLHP on the test bench

Performance tests were carried out for different LHP configurations. Initially the MLHP was tested as it was manufactured: with 3-way valve. Then bypass line was pinched to change mode of operation to 2-way valve. Pressure of argon inside the valve remained the same that led to moving of temperature of regulation to set point temperature. To verify influence of temperature of PRV regulation on maximum heat transfer capability several special tests were performed. Argon reservoir of the PRV was connected to cylinder with argon with ability to regulate argon pressure. Finally, argon was removed completely from the valve to have the MLHP operated like a LHP without valve.

PRV can operate only when natural operation temperature (which LHP could have without PRV) is less than temperature of regulation. Let's consider such conditions as Cold case. Conditions when PRV is beyond regulation can be considered as Hot case.

During tests cold plate temperature maintained constant with step-wise increment of power.

### Test results

During the tests chiller was set to the minimum allowable temperature to verify operation of the regulating valve. LHP regulation by PRV continued up to dry-out event.

The MLHP with 3-way valve mode and with 2-way valve mode sustained practically the same power: up to about 300W (Figs. 7 and 8). As it was expected temperature of regulation for 2-way valve (Set point) was below than for 3-way valve (Regulation point). The MLHP demonstrated same conductance during Cold case tests.

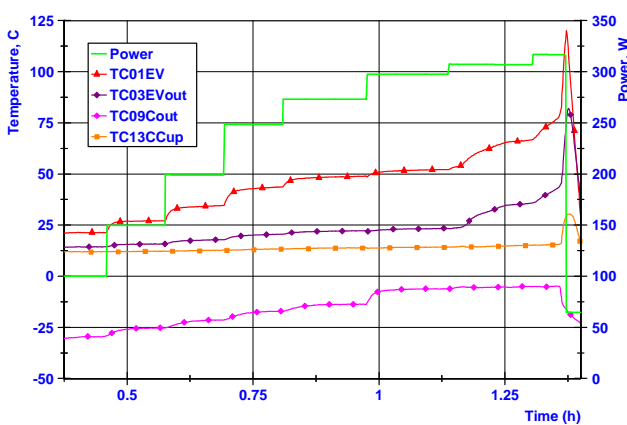


Fig. 7. Maximum performance test of MLHP with 3-way valve. Sink at cold case

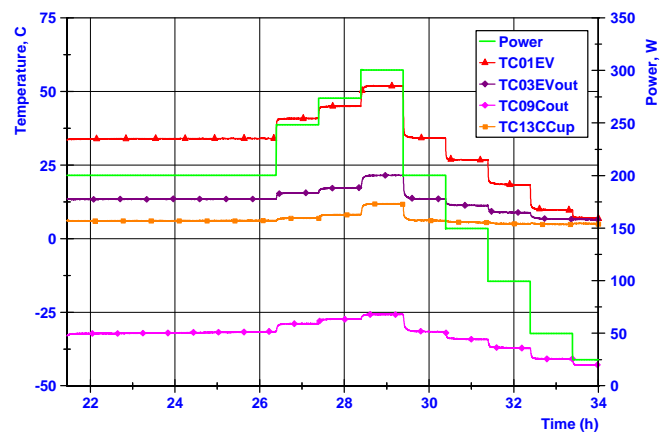


Fig. 8. Maximum performance test of MLHP with 2-way valve. Sink at cold case

For comparison purposes the MLHP was tested without valve control (when argon was removed). In this case the MLHP operated as usual LHP without any regulation. Test showed that maximum heat transfer capability was reduced significantly for the same sink conditions (Fig. 9). The MLHP could transfer only 200W despite the absence of the PRV operation which introduces additional hydraulic resistance to the loop.

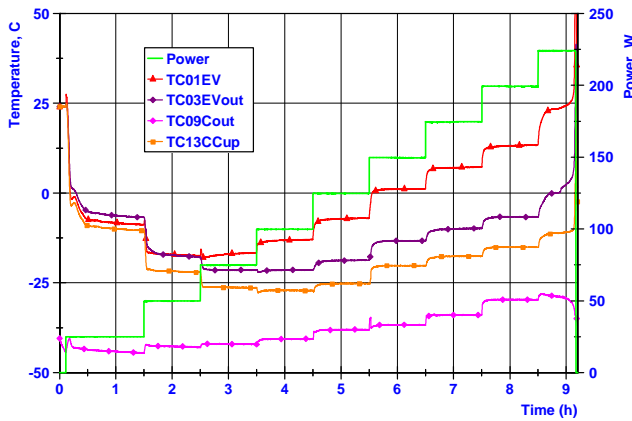


Fig. 9. Maximum performance test of MLHP without valve. Sink at cold case

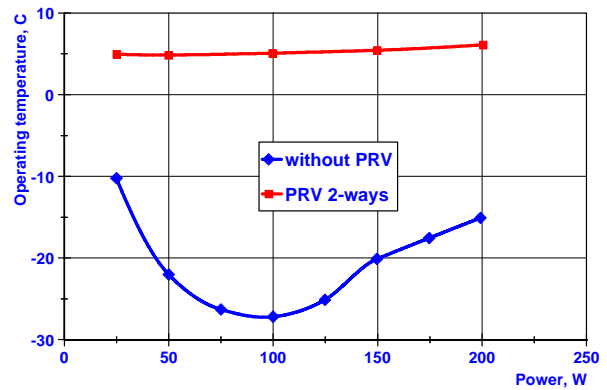


Fig. 10. Comparison of operating temperature for MLHP without and with PRV

Comparison of operating temperature for different modes of LHP operation is shown in Fig. 10. Decreasing of maximum capability of the MLHP without valve becomes logical taking into account that operational temperature of the MLHP decreased. On the other hand, there is no significant difference between two PRV designs from point of view of maximum heat transfer capacity of LHP. Difference between them is that if three-way valve controls temperature at regulation point, corresponded to upper position of stem inside the valve, two-way valve regulates at set point, corresponded to lower position of the stem (for the same pressure of argon). This difference is several degrees of Celsius and for real applications can be adjusted on the step of charging of PRV with inert back pressure gas (argon).

Different type of maximum performance test is shown in Fig. 11. It was conducted at constant applied power (273W) with decreasing of argon pressure inside valve. For this test the charging tube of PRV was open and back pressure gas reservoir of the PRV was connected through pressure regulator to argon cylinder. The MLHP could transfer heat up to decreasing of operating temperature till 0 °C that showed again general tendency of decreasing of transferred power with decreasing of operation temperature.

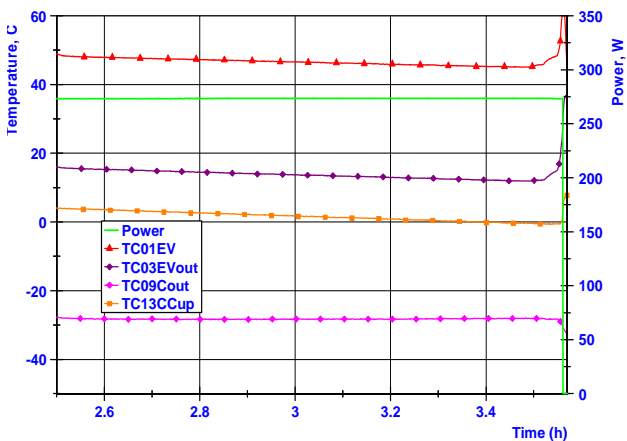


Fig. 11. Maximum performance test of MLHP with 2-way valve. Sink at cold case. Power 273W is applied constantly. Argon pressure was decreased to decrease valve set point from 4 °C to 0°C (dry-out)

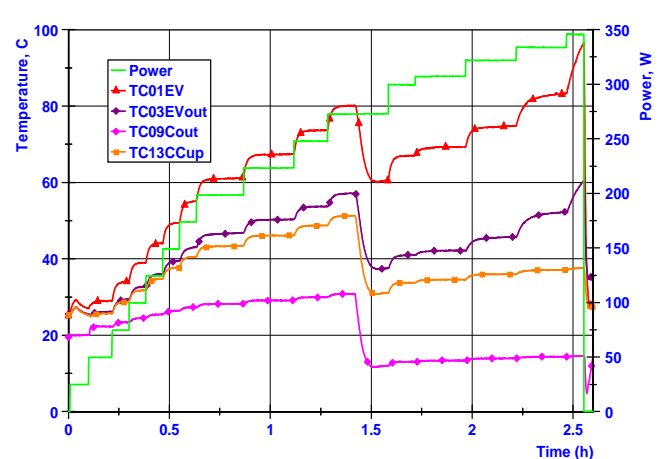


Fig. 12. Maximum performance test of MLHP without valve. Sink at hot case

In Figs. 12 and 13 maximum performance tests for "hot case" without valve and with valve are shown. The LHP demonstrated similar performance for both cases because at hot case the valve does not operate for the PRV set point.

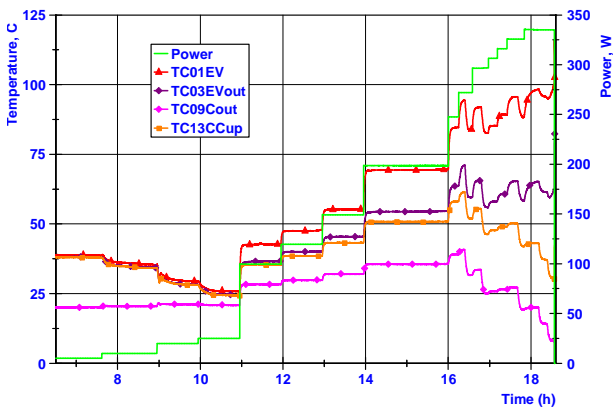


Fig. 13. Maximum performance test of MLHP with 3-way valve. Sink at hot case

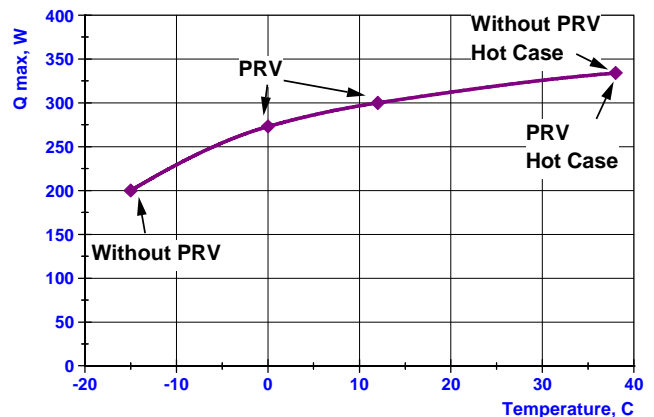


Fig. 14. Comparison of maximum heat transfer rate  $Q_{max}$  of MLHP vs. operating temperature

In Fig. 14 summary of performed tests is represented. Similar data was obtained for MLHP with PRV, both 3 or 2-way type. For the highest temperatures of tests similar data was obtained for LHP with and without PRV because at this temperature level PRV is beyond regulation and operates like LHP without valve.

From point of view of maximum value of  $Q_{max}$  optimal set point of PRV exists, that is logical taking into account Figure of merit which has maximum for every working fluid and  $Q_{max}$  is increased up to the certain level with increasing of set point and operation temperature and then is decreased.

Taking into account obtained test results we can conclude that maximum heat transfer rate of LHP depends on operation temperature which, in turn, influences the pressure drop along LHP and does not depend on the nature of the drop. It can be a "natural" pressure drop in LHP without valve, pressure drop introduced by PRV or caused by hydrostatic height or even by non-condensable gas presence. Thermal and hydraulic balance exists in compensation chamber because operation cycle of LHP is near saturation curve of working fluid. The balance finally determines overall temperature drop of LHP. Both internal and external heat flows between outer and inner surfaces of wick influence the thermal balance: along main contour of LHP and across the wick. Thus, heat leak across wick (and conditions in the evaporator core and compensation chamber) is proportional to external pressure drop  $\Delta P_{LHP} + \Delta P_{PRV} + \rho gh$ .

Therefore, mechanism of PRV operation in 3-way and 2-way modes can be considered as similar. In the same operation conditions (temperatures of condenser and evaporator are the same) LHP should be in the same hydro-mechanical and thermal equilibrium. LHP is a device, operating temperature of which is driven by temperature of compensation chamber. Due to operation of valve LHP has the same pressure drop and thermal state of compensation chamber. The difference between two PRV designs is in character of adjusting of compensation chamber state. In case of 3-way valve direct vapor flow exists through bypass line to compensation chamber. For 2-way valve increased heat leak from evaporator core to compensation chamber plays the same role: while pressure drop along of LHP had been increased heat leak from evaporator core to compensation chamber increased to adjust LHP operation temperature level. We can conclude that heat flow through bypass line and heat leak from evaporator core are the same and valve introduces the same pressure drop in both modes of operation (when argon pressure adjusted to have the same temperature of regulation). Therefore it can be considered that from point of view of thermo- and hydrodynamics LHP operates in the same regime for both modes.

## LHP WITH 2-WAY VALVE FOR PLANETARY ROVERS

Because of their characteristics, the LHPs are particularly suitable to control the temperature of the electronics and equipments inside the rovers, which are designed for planetary exploration missions and they operate in gravity fields [1,13]. The temperature control of the rovers is rather challenging because of the extreme environmental conditions. Usually, to control the temperatures of the equipments, it is enough to remove some power to keep the temperatures below a maximum allowable limit. However, in these applications, the night temperatures can be very low and it is necessary to prevent the electronics from overcooling. Such temperature control can be organized by different methods [13]. Specifically for the rover missions the passive control techniques are preferable since during the night only batteries power is available. Therefore pressure regulating valve was integrated in the LHP design to provide the device a thermal switch function. This element does not require any power and allows to dissipate the heat from the rover electronic equipment through the radiators in nominal conditions, but also thermally decouple the electronics from the outside cold temperatures when needed.

A propylene MLHP equipped with a regulating valve has been designed for Mars Rover applications in the frame of the ExoMars project [14]. This breadboard is based on a previous prototype developed for the ESA TRP "Passive Variable Thermal-Conductance Device (PVTCD) for Mars Rover Applications" [7]. Nevertheless, in the current application the thermal requirements have been modified according to the updated EXOMARS needs, and there are important differences in terms of dissipated power and temperature control set point. The new power range is from 5 W to 25 W and the required set point has been decreased up to  $-30\text{ }^{\circ}\text{C}$ . To provide an accurate temperature control for these new conditions, a two-way pressure regulating valve has been proposed. This novel design has demonstrated its precise temperature control as well as its capability to avoid oscillations and back flow at low power regimes.

### LHP with 2-way Valve Design

A general view of one of the mini LHPs developed for the Rover applications is provided in Fig. 15. It consists of one evaporator, one compensation chamber, one condenser, two transport lines and one 2-way pressure regulating valve located in the vapor line. The selected working fluid is propylene to avoid the freezing in the condenser during the Mars night cold temperatures (according to the specification the radiator temperature can reach  $-120^{\circ}\text{C}$ ). The main characteristics of the design are shown in Tables 3 and 4.

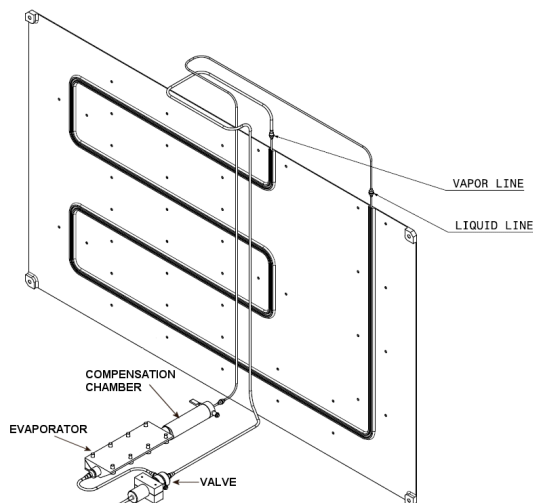


Fig. 15. Mini LHP schematic

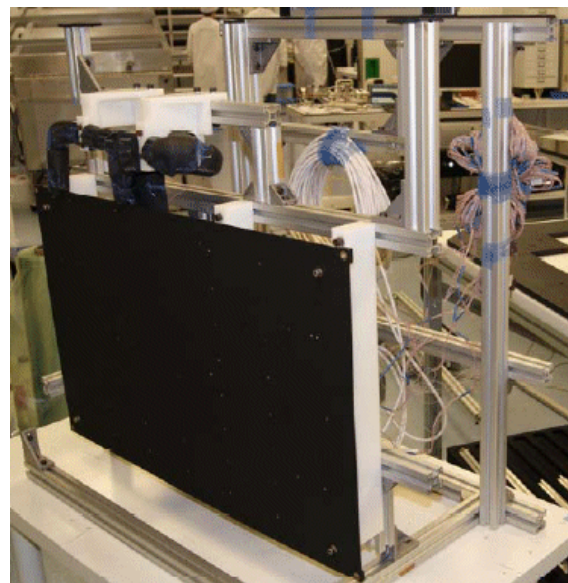


Fig. 16 Mini LHP test set up: radiator panel view

Table 3. MLHP main dimensions

Component	Length (mm)	Diameter (mm)
Evaporator	130	12
Condenser	2340	2
Reservoir	75	19
Vapor Line	1160	3
Liquid Line	970	2

Table 4. Design characteristics of the MLHP

Characteristics	LHP-SS
Wick Material	Stainless Steel
Porous diameter ( $\mu\text{m}$ )	3.4
Porosity (%)	65
Valve set point	-30 °C

### LHP with 2-way Valve Test Set Up

The LHP is tested in nominal orientation as it is presented in Fig. 16. The evaporator saddle is bolted to the saddle of the cartridge heater, which provides the power to be dissipated by the LHP. Additionally, a start up heater is glued to the evaporator saddle to provide extra power to facilitate the start up. Then, the LHP is instrumented with thermocouples type T according to the measurement plan shown in Figs. 17 and 18.

To reduce the heat exchanged with the environment and between the different components, each LHP component (excepting the condenser plate) is isolated separately by Armaflex elastomeric foam. Additionally, to reduce the influence of the forced convection of the climatic chamber, the subassembly evaporator, compensation chamber and valve is covered by plastic, closing the possible inlets. The photo of the set-up can be found in Fig. 16. Finally, the LHP is introduced in the climatic chamber.

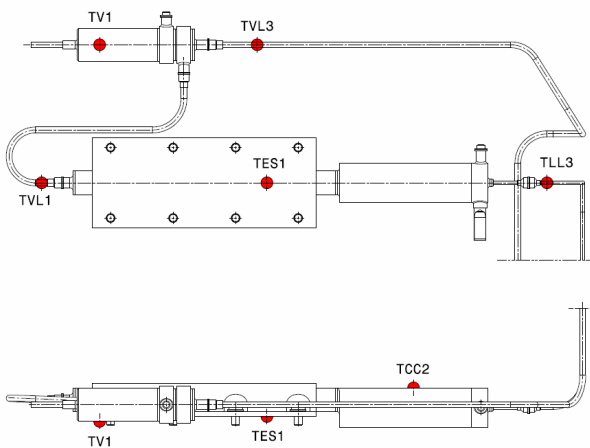


Fig. 17. Evaporator block measurement plan

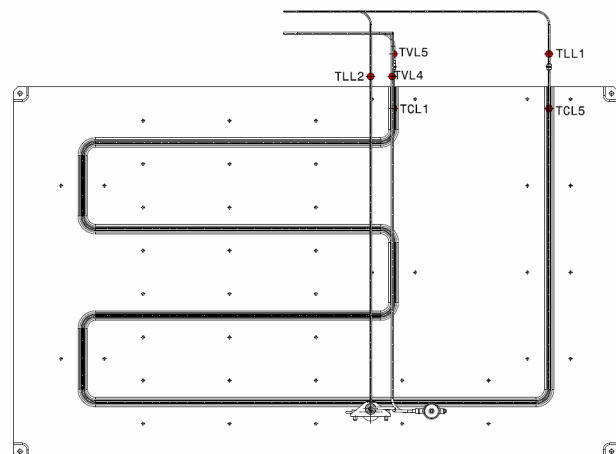


Fig. 18. Condenser measurement plan

## THERMAL SWITCH TEMPERATURE CONTROL: RESULTS & DISCUSSION

### Valve Tests

The objective of these tests is to verify the valve behavior and to check the LHP regulation capability. In this way, two different kind of tests have been carried out. In the first ones the chamber temperature is fixed and the applied power on the cartridge heater is cycled. Then the power is fixed and the chamber temperature is cycled. The results obtained in these conditions are presented below:

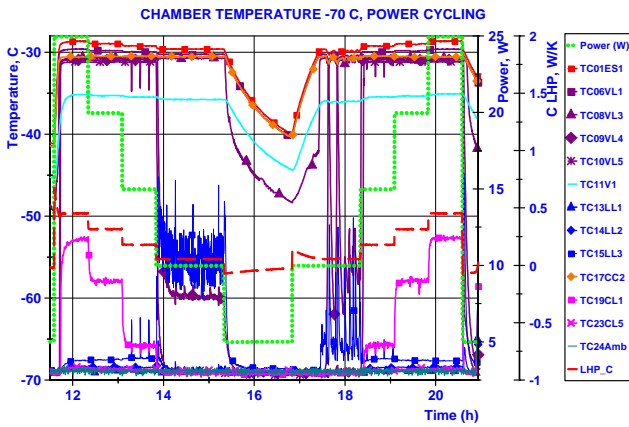


Fig. 19. Valve test results – Chamber T = -70 °C, power cycling

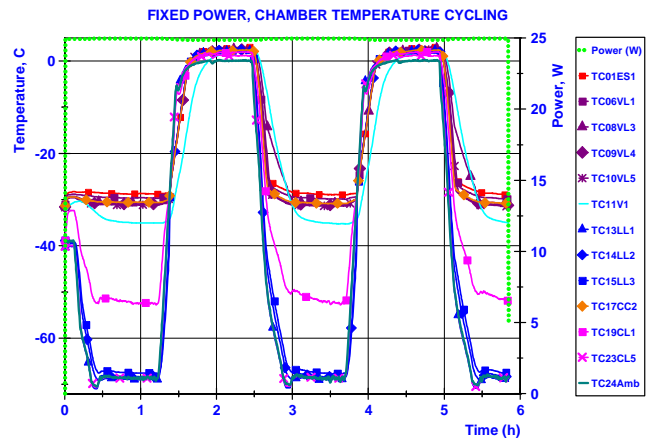


Fig. 20. Valve test results – Chamber temperature cycling

For a chamber temperature of -70 °C (Fig. 19), the LHP is regulating correctly, very close to the required set point for almost all the power levels. In fact, the compensation chamber temperature is regulated around -31 °C for powers higher or equal to 10 W. When the power applied is 5 W, practically all the power is leaked to the ambient and the net power introduced in the LHP is not enough to keep the LHP operating. Therefore, the LHP shuts down and the temperatures decrease due to the leakages to the ambient. The big number of cycles tested demonstrates the repeatability of the results and the proper behavior of the LHP as a temperature control device.

In these conditions, when the valve is regulating the temperatures, the obtained values of the LHP thermal conductance vary from 0.05 W/K to 0.45 W/K depending on the power applied. When the LHP is stopped for a power of 5 W, the LHP thermal conductances decrease to negative values since the total power applied is leaked to the ambient.

Then the chamber temperature is increased and set to -40 °C. The LHP is regulating at the specified set point (-30 °C) for the whole power range and the good repeatability of the results is demonstrated.

When the valve is controlling the temperature of LHP, the path to the condenser is not completely closed, and a small flow is still circulating through the LHP. Since the operational conditions for this chamber temperature are more favorable than in the previous test, the obtained LHP thermal conductances are higher, and they are within 2.25 W/K and 0.25 W/K.

Afterwards, the power is fixed and the chamber temperature is cycled between 0 °C and -70 °C. To test the LHP behavior in the whole power range, two extreme power levels are fixed: 25 W and 5 W.

As shown by the results presented in Fig. 20, for a fixed power of 25 W, the LHP operates as expected without regulation for a chamber temperature of 0 °C. For a chamber temperature of -70 °C, the valve controls the temperature around the required set point (the compensation chamber temperature is about -31°C).

For an applied power of 5 W, practically all the power is leaked to the ambient when the chamber temperature is -70 °C. In these conditions, the LHP stops and the temperatures are cooled due to the heat exchanged with the ambient. When the chamber temperature is increased to 0 °C, the condenser temperatures increase quicker than the evaporator ones. Therefore, the time needed to reach a start up is large and this event is achieved at the very end of the power step.

The thermal conductances calculated in steady conditions for a power of 25 W is 0.5 W/K for -70 °C. The obtained value is low when the valve is regulating and decoupling the evaporator from the condenser. Additionally, the value calculated when the LHP is working without regulation is 16 W/K, which is a high value considering the low power applied.

When the applied power is 5 W, the LHP thermal conductance becomes negative (LHP stops) because all the applied power is leaked to the ambient. Since there is not enough time to reach steady conditions for a chamber temperature of 0 °C, the thermal conductance could not be estimated.

## Start Up Tests

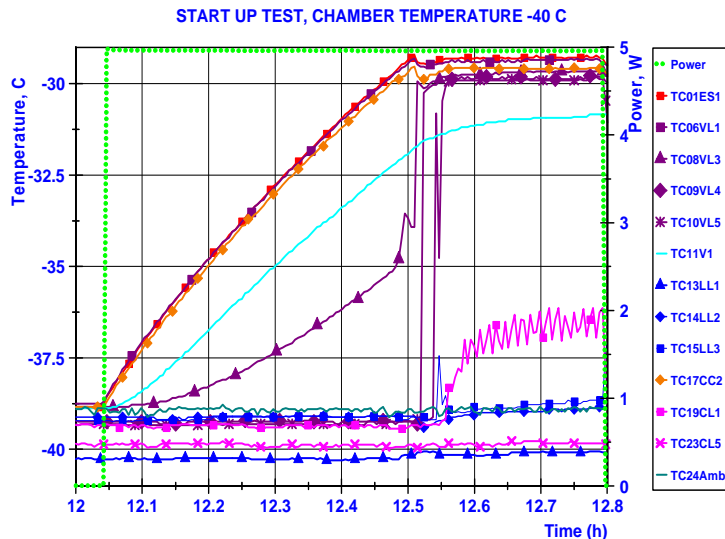


Fig. 21. Start up test results - Chamber T = -40 °C

The main objective of these tests was to determine what is the minimum power needed to reach a successful start up in cold conditions. Since the LHP is not perfectly insulated and there are some thermal leaks to the ambient, the estimated coupling of 0.2 W/K is considered to calculate the net power introduced in the LHP and, consequently, to establish the minimum start up power. The power is applied on the start up heater and the chamber temperature is set to two different values: -40 °C and -70 °C. Moreover, several

attempts are performed to demonstrate a minimum of 3 consecutive successful start ups.

For a chamber temperature of -40 °C, the leakages to ambient are about 2 W. Therefore, a total power of 5 W is applied to the start up heater to demonstrate that the LHP is able to start up with only 3 W.

Five consecutive successful start ups have been achieved in these conditions. As it is shown in the detailed graph (Fig. 21), as soon as the temperatures cross the valve set point (-30 °C), a successful start up is reached and a non overshoot is observed. Moreover, the results demonstrate a reliable and repeatable behavior of the LHP. Regarding to the LHP thermal conductance, the calculated values are around 0.3 W/K for steady conditions when the LHP is operating.

Then the chamber temperature is decreased to -70 °C. In this case, the leakages to ambient are around 8 W. A total power of 10 W is applied to the evaporator saddle to check if there is a successful start up with a minimum power of 2 W in this worse scenario.

According to the results, four consecutive successful start ups have been achieved in these conditions. In the first two attempts, the time with the power applied is not enough to verify the steady conditions. For this reason, in the next steps this application time has been increased significantly. As it can be verified in the detailed plot of the third attempt, as soon as the temperatures cross the valve set point (-30 °C), a successful start up is reached and a non overshoot is observed. Again, the test results demonstrate a reliable and repeatable behavior of the LHP even for this worst case. Finally the LHP thermal conductance calculated in these conditions are about 0.1 W/K. It has to be mentioned that a 2-way valve facilitates the start-up from cold conditions since vapor is generating in vapor line entrance before the start-up event and all vapor removing grooves are filled by vapor and "waiting" the opening of the valve.

Ambient performances test shows a high thermal conductance of the LHP for the low power range typical of the electronics inside Mars/Lunar rovers [14].

One more particularity of LHP with 2-way valve was observed: pressure oscillations appeared in LHP with 3-way valve due to gravity effect was not seen for 2-way valve. For example, oscillatory behavior has been found in a LHP with PRV designed and manufactured for a Mars rover application by IberEspacio [7-10].

Additional information regarding the LHP testing can be found in [14].

## OVERALL COMPARISON OF DIFFERENT METHODS OF REGULATION OF LHP

In general LHP with two-way valve has demonstrated outstanding performance and excellent capability of temperature control. The new design of pressure regulating valve allows to eliminate such undesirable effects as gravity caused temperature oscillations and instability of start up and operation at low power regimes, to increase the system reliability and precision of temperature control. Comparison of this method of LHP control with traditional and the most used 3-way valve and with heater on compensation chamber is presented in Table 5.

Table 5. Comparison of different methods of regulation of LHP operation temperature level

Method of control	2-way valve	3-way valve	Heater on compensation chamber
Reliability	5	4	5
Necessity of active control	No	No	Yes
Power consumption	No	No	Yes
Simplicity of design	5	4	4 (Electronic device for control is needed)
Redundancy	Yes	No	Yes
Remarks		Temperature oscillations in gravity. Instability of start up and operation at low power and low temperature regimes	Complex algorithm of regulation Sensitivity to transients** [15]

\* Additional valve can be installed in the loop to increase system reliability.

\*\* According to [15] it is not easy to provide reliable algorithm of temperature control of compensation chamber. LHP can stop operation if rate of change of control power is higher than rate of change of evaporator power. The control heater power level should be low enough to avoid an undesirable shut down of LHP, and on the other hand it should be high enough to be able compensate subcooling if returning fluid is relatively cold.

## CONCLUSION

Mini LHP equipped with pressure regulating valve was designed, manufactured and tested to compare two-way and three-way valve design and verify LHP heat transfer limitations. To investigate particularities of two-way valve operation, especially at low temperature of regulation, an extensive test campaign has been performed on the propylene mini LHP developed for rovers applications.

The new concept of two-way pressure regulating valve allows to perform precise temperature control at low power and low temperature levels, to increase reliability and temperature stability of the system, and to eliminate the drawbacks of three-way valves such temperature oscillations caused by gravity.

Both types of PRV design demonstrated practically the same maximum heat transfer rate of LHP. Moreover, it was found, that heat transfer capability of LHP with PRV becomes higher than "natural operated" LHP without PRV. Optimal temperature set point of PRV exists, providing maximum of heat transfer performance.

The specific valve performance verification test campaign has been carried out to demonstrate the regulation capability of the LHP at a set point of -30 °C. For all the conditions the valve regulates correctly the temperature around set point value. Additionally, when the net power applied directly to the LHP is too small to keep the LHP operating, the LHP shuts down and the evaporator and the condenser are completely thermally decoupled.

Moreover, several start-up tests have been performed considering the worst environmental scenarios. Even in these conditions, the LHP start up capability has been demonstrated for a power so small as 2 W. Therefore we can conclude that the presence of this two-way valve facilitates the start up in cold conditions.

The ambient performances test shows a high thermal conductance of the LHP for the low power range typical of the electronics inside Mars/Lunar rovers.

The results obtained from these tests prove the suitability of the propylene mini LHP with novel two-way valve to the Planet Exploration Programs needs, and demonstrates the capability of these devices to control the temperature of the equipments and electronics.

## Nomenclature

<i>EV</i>	– Evaporator	<i>g</i>	– gravitation acceleration
<i>LHP</i>	– Loop Heat Pipes	<i>h</i>	– liquid column height
<i>PRV</i>	– Pressure Regulating Valve	<i>P</i>	– pressure
<i>PVTCD</i>	– Passive Variable Thermal Conductance Device.	$\Delta P$	– pressure drop
<i>SS</i>	– Stainless Steel	<i>T</i>	– temperature
<i>TPX</i>	– Two-Phase experiment	$\rho$	– liquid density.
<i>TRP</i>	– Technological Research Program.		

## Indexes

LHP – loop heat pipe  
max – maximum

PRV – pressure regulating valve  
w – wick.

## References

1. Anderson W.G., Hartenstine J.R., Walker K.L. and Farmer J. T. Variable Thermal Conductance Link for Lunar Landers and Rovers // *IECEC 2010, 8th Annual International Energy Conversion Engineering Conference*, Nashville, Tennessee, USA, July, 2010, – 10 p.
2. Kaya T. and Mishkinis D. Accurate Temperature Control Using Heat Pipes // *International Review of Mechanical Engineering (I.R.E.M.E.)*. 2008. Vol. 1. n. 1– 7 p.
3. Delil A.A.M., Dubois M. and Supper W. The European Two-Phase eXperiments TPX I & II // *Proceedings of the Xth International Heat Pipe Conference*, Stuttgart, Germany, 21–25 September 1997.
4. Goncharov K., Kochetkov A., Buz V. Development of Loop Heat Pipe with Pressure Regulator // *Int. Two-Phase Thermal Control Technology Workshop*, LA, USA, March 7th–9th, 2005.
5. Goncharov K.A., Kozmine D.E., Smirnov F.Yu., Nikitkin M.N., Fershtater Yu.G., Maidanik Yu.F. Loop Heat Pipes for Space Mission Mars 96 // *Proceedings of International Seminar and Workshop "Heat Pipes, Heat Pumps, Refrigerators"*, Minsk, Belarus, September 12–15, 1995.
6. Goncharov K. Orlov A., Tarabrin A., M. Gottero, V. Perotto, S. Tavera G. P. Zoppo. 1500 W Deployable Radiator with Loop Heat Pipe // *Proceedings of the 31<sup>th</sup> International Conference on Environmental Systems*, SAE Paper 01ICES-68, Orlando, Florida, USA. July 9–12, 2001.
7. Mishkinis D., Gregori C., Romera F. and Torres A. Development of Propylene LHP for European Mars Rover Applications // *Heat Pipe Science and Technology International Journal*. 2010. Vol. 1, Issue 1. Pp. 19–46.
8. Molina M., Franzoso A., Bursi A., Romera F., and Barbagallo G. A Heat Switch for European Mars Rover // *Proceedings of the 38<sup>th</sup> International Conference on Environmental Systems*, SAE Paper 2008-01-2153, 2008.
9. Molina M., Franzoso A., Romera F., and Barbagallo G. Thermal Testing of a Heat Switch for European Mars Rover // *Proceedings of the 39<sup>th</sup> International Conference on Environmental Systems*, SAE Paper 2009-01-2573, 2009.
10. Romera F., Mishkinis D., Kulakov A., Torres A. Control of LHP operation temperature by a pressure regulating valve // *15th International Heat Pipe Conference*, Clemson, USA, April 25-30, 2010.
11. *Patent application PCT/ES2010/070677 21/10/2010*. Dispositivo de Control Térmico Regulado por Presión / Mishkinis D., Torres A., 2010.
12. Mishkinis D., Kulakov A., Turrion E., Radkov A., Torres A. Application of Peltier Element in Loop Heat Pipes // *40th International Conference on Environmental Systems*, AIAA paper 2010-6004, 15p.
13. Bugby D. C., Farmer J. T., O'Conno B. F., Wirzburge M. J., Abel E. D., and Stouffer C. J., Two-Phase Thermal Switching System for a Small, Extended Duration Lunar Surface Science Platform // *SPESIF Conference*, 23-26 Feb 2010.
14. Mishkinis D., Gregori C., Huidobro D., and Torres A. Low Power and Low Temperature LHP for Thermal Control of Rovers // *41th International Conference on Environmental Systems*, Marriott Portland Downtown Waterfront Portland, Oregon, USA, 17 - 21 Jul 2011. 12 p. (to be presented).
15. Kaya T., Baker Ch., Ku J. Comparison of Thermal Performance Characteristics of Ammonia and Propylene Loop Heat Pipes // SAE paper 2000-01-2406, *International Conference On Environmental Systems*, July 2000.

## THE STUDY OF HEAT PIPES IN DEVELOPMENTS OF TsSKB – PROGRESS

**Kitaev A.I, Nikolaev V.A, Gavrilova E.S.**

Department 1600

TsSKB – PROGRESS

Zemetsa st., 18, Samara, Russia, 443009,

Tel: (846) 955-13-61, Fax: (846) 992-65-18, E-mail: csdb@samtel.ru

### **Absrtact**

Now practically on all space vehicles of out working of "TSSKB-PROGRESS" those or other types of a heat pipes are applied. On small-sized SV last out workings the space vehicles thermal control system consists only of the heat pipes and a film heaters. Thus the heat pipes on some products provide the thermostatic control of external elements located in a free space («the Resource - P»), on a products "Maksat", "Stork", "Open space" the heat pipes are built in the structure of thermopanel and provide the thermostatic control of onboard equipment, on other products the heat pipes are used as radiating radiators. In the present materials conditions of carrying out and results of thermopanel heat tests with the built in the heat pipes are resulted. Tests were gone out on experimental installation "TSSKB-PROGRESS". The purpose of the thermal tests was the definition of a temperature field on a thermopanel's surface in the established thermal mode for specification of mathematical thermal model of the thermopanel and the product as a whole. Working out of the thermopanel design documentation and taking place of the heat pipes on them has been executed in conformity by the thermal calculations by "TSSKB-PROGRESS" forces with the account work cyclogrammes of onboard equipment and the trajectory of the product movement. The thermopanel manufacturing was cheking by "Tais". In the article the received schedules of change of temperatures on a thermopanel surface; differences of temperatures on the thermopanel in a direction of the heat pipes; differences of temperatures on width of the thermopanel between the surface of the thermopanel and the heat pipe; the general difference of temperatures on the whole thermopanel are presented. Experiments were made at two thermopanel positions: horizontal and vertical. The comparative analysis of the received values is given. The received differences confirm the carried out the calculations and working capacity of the heat pipes as a part of the thermopanels. The received results are recommended to be used at carrying out and the analysis of the results of thermovacuum tests of the product as a whole.

### **KEYWORDS**

Heat pipes, thermal panels, thermal vacuum test.

Nowadays different types of heat pipes are used almost in all spacecraft developed by TsSKB - Progress. The last developed Aist, Prostor small spacecraft are equipped with a thermal control system consisting of heat pipes and film heaters. The heat pipes provide thermal control of the Resource - P spacecraft's external elements exposed to the open space.

Thermal tests are an essential stage in preparing thermal panels with integrated heat pipes, basic elements of a thermal control system.

Thermal panels can be made as multilayered structures having embedded elements for onboard equipment mounting and heat pipes with sealed cavities filled with the ammonia. Thermal panels with heat pipes inside are structures, which perform the double function: on the one hand, onboard equipment is fastened on the honeycomb (during the tests - heat load simulator as an electrical heater) and on another hand, withdrawal of thermal energy is realized from thermal panel emitting surface (function of radiator) to environment. Such structure of thermal panel mast brings up the thermal control of onboard equipment.

Terms and results of honeycombs with integrated heat pipes thermal tests are presented in the paper.

The tests were carried out in accordance with the test program at experimental equipment, in which heat pipes were placed in compliance with thermal design and design specifications.

The test venue – the experimental site of TsSKB - Progress.

Thermal tests were aimed at the determination of the thermal field at thermal panel surface with steady thermal conditions for adjustment of thermal panel engine heat model and the whole product.

The test purposes were:

- the determination of the temperature drop lengthwise of the thermal panel along heat pipes direct axis (TT);
- the determination of the temperature drop width way of the thermal panel between thermal panel surface and heat pipes.

Research terms:

- air temperature -  $21,4 \pm 1$  °C;
- atmospheric pressure –  $101 \pm 2$  kPa;
- air humidity -  $35 \pm 10$  %.

Thermal tests of the SHM (special-purpose hardware module) thermal panels were carried out on a prototype product, consisting of:

- thermal panels 1113-0 и 1114-0;
- electrical heaters, which were used as heat load simulators at thermal panel nonfunctional surface above the heat pipe (TT);
- thermal panel surface heat insulation placed on the thermal panel operating surface and on the nonfunctional surface along the lower edge within 250 mm with the electrical heaters
- temperature sensors, mounting on the thermal panels;
- on-board cabling.

Layouts of electrical heaters and temperature sensors on thermal panels 1113-0 и 1114-0 are given on pictures 1-4.

Each panel was tested in horizontal and vertical position.

Heat-removing was realized to environment without the forced blow-off.

Total capacity value feeding to the electrical heaters of each thermal panel during the tests was 60, 120, 180, 240 and 300 Wt.

During the each test mode the same capacity was fed to each electrical heater. Input power had increased to the next value after temperature stable mode reaching. Mode was considered as stable when the temperature parameters were not changed more than  $\pm 1$  °C during 30 minutes.

Periodicity of data acquisition from all sensing ports was no less than one time per 60 seconds.

Horizontal positioning check of the prototype product was done with the KO-1M optical quadrant.

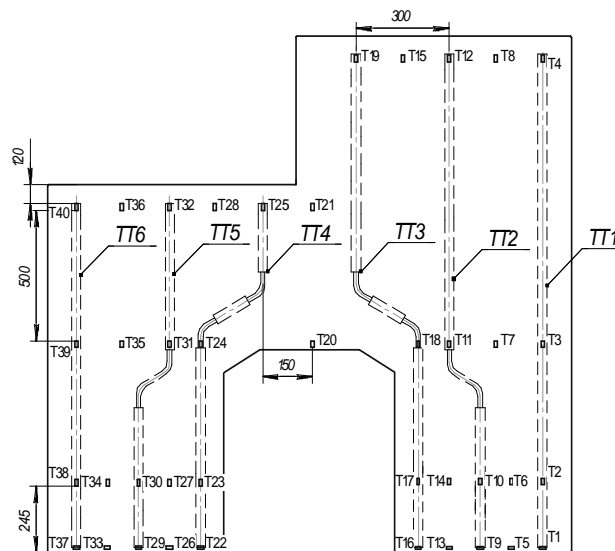


Fig. 1. Layout of the temperature sensors on Panel 1113

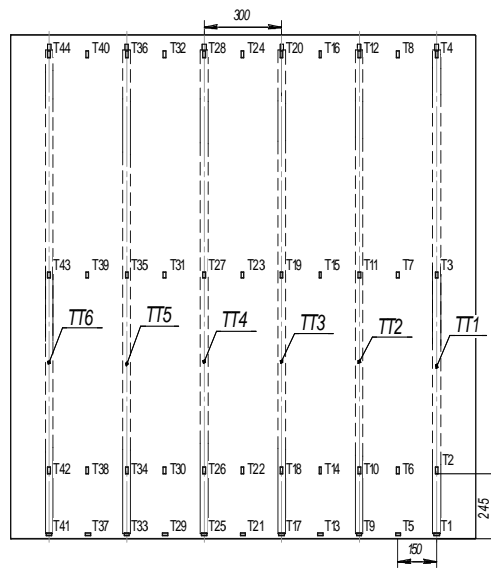


Fig. 2. Layout of the temperature sensors on Panel 1114

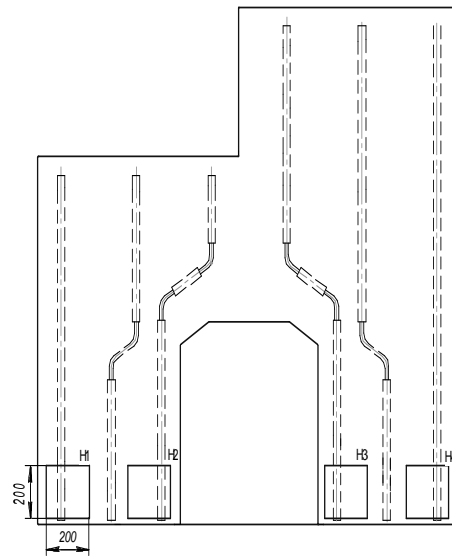


Fig. 3. Layout of the electrical heaters on the outer side of Panel 1113-0

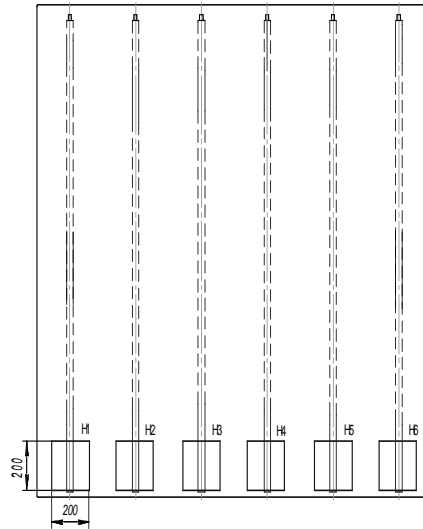


Fig. 4. Layout of the electrical heaters on the outer side of Panel 1114-0

In the course of tests, using actual values of temperatures, the following thermal conditions characteristics were determined:

- temperatures on thermal panel surfaces;
- temperature drops on thermal panel along the heat pipes;
- temperature drops width way of the panel between thermal panel surface and heat pipes.
- total temperature drop on whole thermal panel

The temperature drop on the thermal panel along heat pipes direct axis (TT) was determined as a temperature difference above heat pipe in the electrical heater mounting area and condensation zone of heat pipe.

Temperature drop at the thermo panel between thermal panel surface and heat pipe was determined as a temperature difference above heat pipe and between heat pipes in the evaporation zone, condensation zone and at middle level of heat pipe.

Total temperature drop at the whole thermal panel was determined as the difference of maximal and minimal thermal panel temperature, received during the tests.

Temperature curves at the thermal panel surface with horizontal and vertical position are given at the pictures 3, 4.

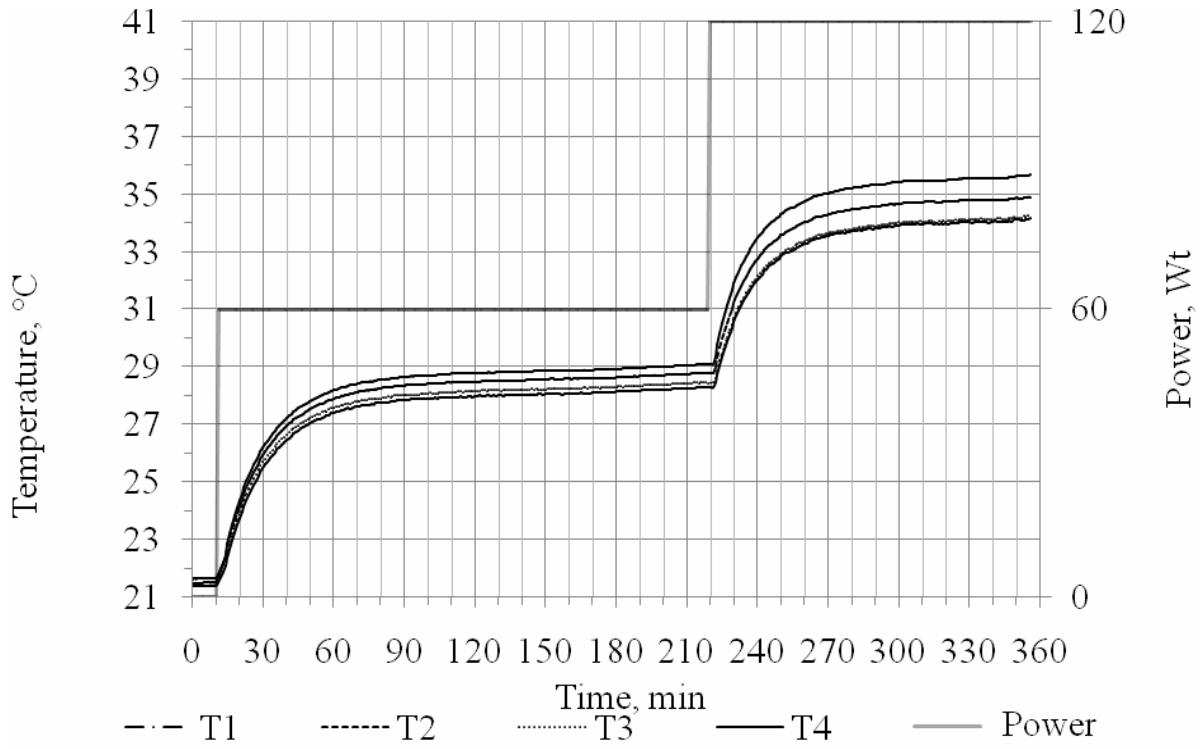


Fig. 5. Thermal panel 1113 temperature variation with horizontal position

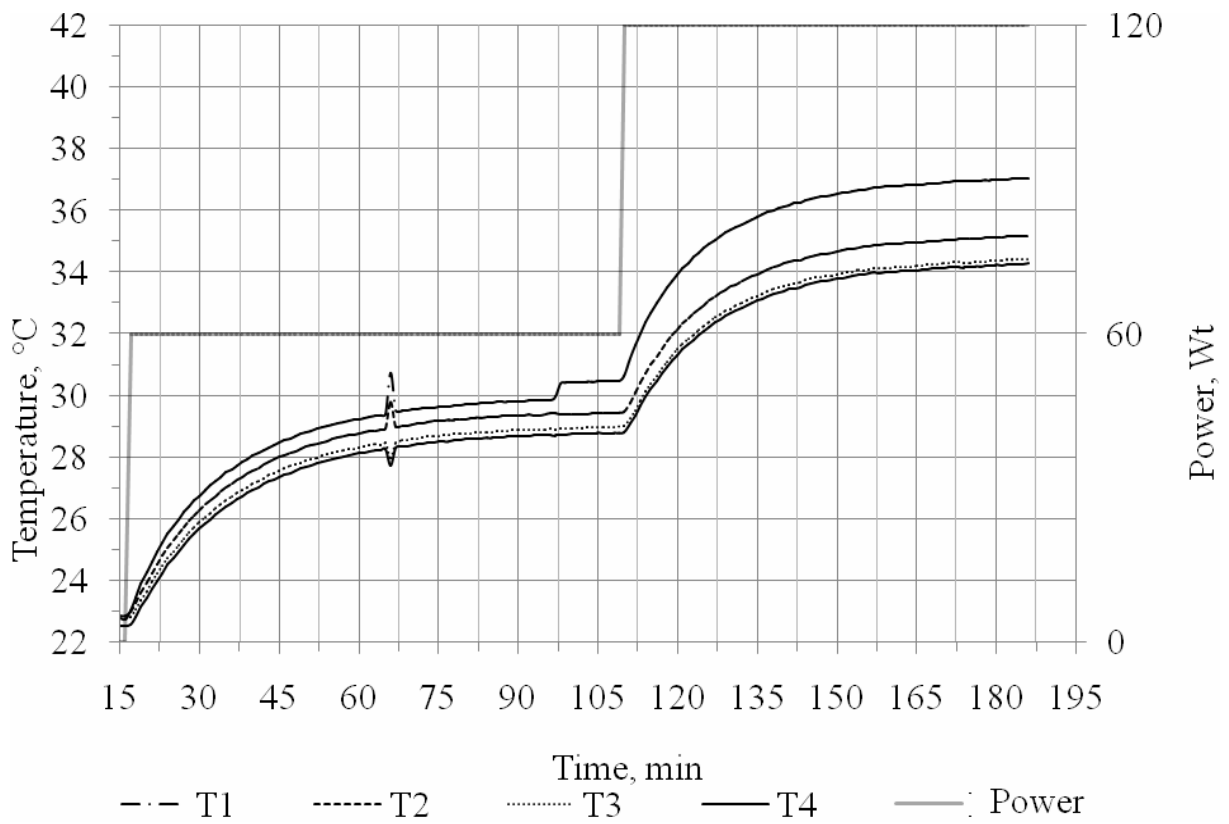


Fig. 6. Thermal panel 1113 temperature variation with vertical position

Heat pipes thermal resistance of panel 1113 for horizontal position is in the range from 0,008 to 0,016 K/Wt, for vertical position from 0,012 to 0,072 K/Wt.

Heat pipes thermal resistance of panel 1114 for horizontal position is in the range from 0,011 to 0,170 K/Wt, for vertical position from 0,011 to 0,084 K/Wt.

Temperature drops measured during the tests with horizontal position of the thermal panel along the heat pipes direct axis are not more than 3,08 °C for the thermal panel 1113 and 5,08 °C for the thermal panel 1114.

Temperature drops along the heat pipes direct axis with vertical position are not more than 3,57 °C for the thermal panel 1113 and 6,73 °C for the thermal panel 1114.

The drops received during the tests, confirm the executed accounts and the operability of heat pipes within thermal panels.

Temperature drops on thermal panel surface with its horizontal position measured during the tests are near 75 % from the meaning of the drop with vertical position, while the heat pipes are working in the thermosyphon mode, with the evaporation zone situated down the condensation zone.

Identified differences are recommended to be used with in analyzing the results of the thermal vacuum testing of the product, because the heat pipes characteristics under standard zero gravity operational conditions are close to those under gravity conditions with horizontal positioning of heat pipes. The vertical position of heat pipes in the thermal panels is envisaged during the thermal vacuum test.

## IMPROVEMENT OF HEAT AND MASS TRANSFER PARAMETERS IN HEAT PIPE EVAPORATORS WITH POROUS COATING OF CAPILLARY GROOVES

**L.L.Vasiliev, L.P.Grakovich, M.I.Rabetsky**

A. V. Luikov Heat and Mass Transfer Institute, National Academy of Sciences of Belarus  
Minsk, Republic of Belarus

Tel.: +375-17-284-21-33; E-mail: leonard\_vasiliev@rambler.ru

**D.V. Tulin**

S. A. Lavochkin Scientific Production Association  
Moscow, Russian Federation

### Abstract

Comparative studies of the heat transfer coefficients of the evaporators with three types of capillary grooves were conducted. The parameters of the evaporators with smooth capillary grooves and capillary grooves having porous coating of walls with a thickness of 50  $\mu\text{m}$ . The regimes of both evaporation and boiling of heat carrier (ammonia) were provided in the experiments. Within the entire studied range of temperatures and heat loads the heat transfer coefficients of all types of evaporators with the porous coating are 1.3–1.8 times higher than of similar evaporators with a smooth surface of capillary grooves.

### KEYWORDS

Heat pipe, capillary-porous coating, evaporation, capillary grooves, heat transfer coefficient.

### INTRODUCTION

It is known that the coefficients of heat transfer on evaporation in thin liquid films greatly exceed the coefficients on liquid evaporation and pool boiling. Capillary-porous coatings are often used for creation and maintenance of thin liquid films. Porous materials have received the widest recognition in heat pipes where a capillary structure provides not only heat transfer enhancement but also transportation of liquid into the evaporation zone. In heat pipes intended for the support systems of temperature regimes in spacecrafts the capillary structures in the form of capillary grooves have received wide acceptance. The properties of these structures and heat pipes employing them have been studied rather adequately and modern improvement of them is in optimization of shapes and dimensions of capillary grooves depending of the purpose and specific conditions of exploitation. At the same time, though capillary grooves possess indisputable advantages, they present certain restrictions in evaporation and boiling of liquid that are related to the special features of heat transfer in the grooves. The possibility of coating the groove surface with an additional thin (25–100  $\mu\text{m}$ ) porous layer forms next stage of heat transfer enhancement. The authors of [1–3] showed both theoretically and experimentally that deposition of a porous coating on the groove surface positively affects the heat transfer coefficient. This related to the specifics of liquid evaporation from the capillary groove.

At present the model of liquid evaporation predominantly in a very limited zone of a transient thin film of the liquid meniscus in the groove is the proved evaporation model [4, 5]. It is shown in these works that the intensity of evaporation is not high in the region of the main meniscus (large thickness of the layer of low-thermal-conductivity liquid) and in the zone of an equilibrium film (large effect of surface intermolecular interactions).

A mean intensity of evaporation in the capillary groove can be increased by increasing the surface area of the groove edge where a rather thin liquid film is constantly maintained. A uniformly wetted rather large surface area can be created by thin capillary-porous coating on the inner surface of the groove edge and its crest. It is evident that the coating thickness must be much smaller than the characteristic dimensions of capillary grooves for capillary transport of liquid along the groove not to be limited. The porous coating

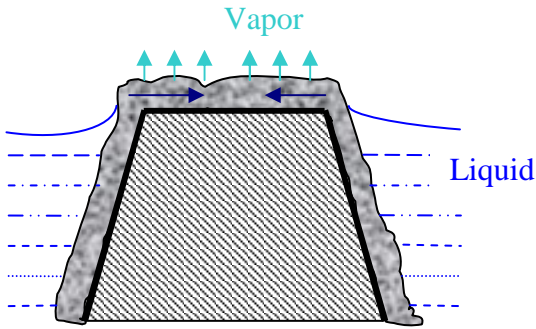


Fig. 1. Schematic of liquid evaporation in a capillary groove with porous coating

from the surfaces of liquid menisci open to the vapor channel. It exists at small heat loads. The second regime (can be identified as boiling) takes place with a further increase of the fed heat flux when vapor forms on a smooth surface of the edge in the form of bubbles and goes to the vapor channel through the porous layer. Vapor bubbles can also form in the pores inside the coating. In both cases, in the stationary regime vapor, as a rule, is removed through stationary channels that are formed in largest macropores of the coating. Vapor generated inside smaller pores (of micro and nano size) of the coating also gets into these channels. It is presented in Fig. 2.

thickness and permeability should provide the necessary flow rate of the evaporating liquid. The mechanism of evaporation from the groove with a capillary-porous coating is shown in Fig. 1. This method of heat transfer enhancement was first suggested and experimentally checked in [1, 2] and later confirmed in [3].

Porous coating uniformly spreads liquid over the volume. In this case, the whole surface of the groove edge beyond the zone of the main meniscus in the groove turns to be wetted uniformly and the area of effective evaporation can increase manifold (Fig. 1).

Evaporative heat transfer in a porous layer can occur in two regimes. The first regime is represented by evaporation

from the surfaces of liquid menisci open to the vapor channel. It exists at small heat loads. The second regime (can be identified as boiling) takes place with a further increase of the fed heat flux when vapor forms on a smooth surface of the edge in the form of bubbles and goes to the vapor channel through the porous layer. Vapor bubbles can also form in the pores inside the coating. In both cases, in the stationary regime vapor, as a rule, is removed through stationary channels that are formed in largest macropores of the coating. Vapor generated inside smaller pores (of micro and nano size) of the coating also gets into these channels. It is presented in Fig. 2.

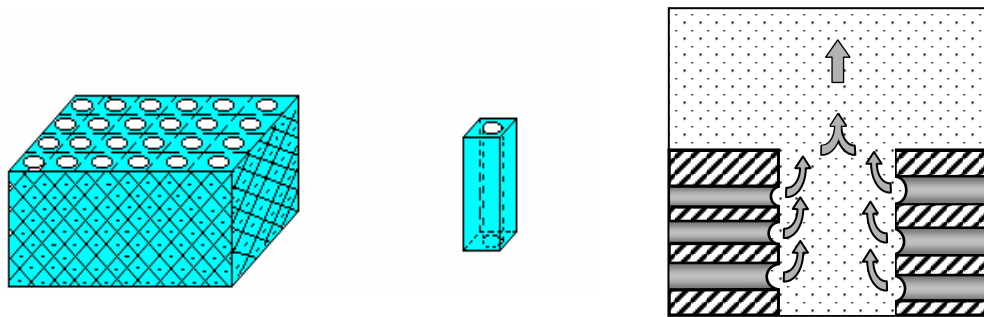


Fig. 2. Model of transfer in a porous structure

## EXPERIMENTAL RESULTS

Heat flux that can be removed from the porous layer of certain thickness and length can be determined by the familiar expression:

$$q = \frac{\frac{2\sigma \cos \theta}{R_p} - \rho_l g L \sin \varphi}{\left( \frac{\mu_l}{\rho_l K A_w} + \frac{1}{n_{\max}} \frac{8\mu_v \delta_v}{\rho_v r_v^4 L} \right) \frac{L A_e}{h_{fg}}}$$

Capillary transport of liquid in thin coatings with a microporous structure can become an appreciable factor that limits heat removal. A maximum curvature of the meniscus is determined by the dimensions of used particles. For a fin with a rather wide edge or in the case of liquid meniscus deepening in the channel the capillary potential of the coating may turn to be insufficient. In this case, a portion of the edge surface beyond the zone of the main meniscus can be dried and the effect of the porous coating decreases. The capillary structure used in the experiments is shown in Fig. 3. It is manufactured from the aluminum oxide particles by a special technology. Figure 4 shows the calculated dependences of maximum heat fluxes that can be removed from one crest of the groove edge, when the groove is wetted completely, depending on the liquid (ammonia) temperature. It is assumed that the main meniscus of the liquid lies at the groove base.

The experimental studies were aimed at obtaining quantitative dependences of the heat transfer parameters in evaporation and boiling for the surfaces with capillary grooves of different shape and at determining the extent to which these parameters are affected by thin capillary coatings (50-100  $\mu\text{m}$ ). The supplied power and temperatures of the heating surface and vapor were measured in the experiments. The characteristics of capillary grooves are presented in Table 1.

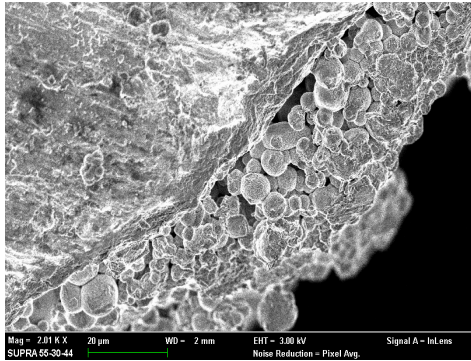


Fig. 3. Sample of a porous coating of the surface

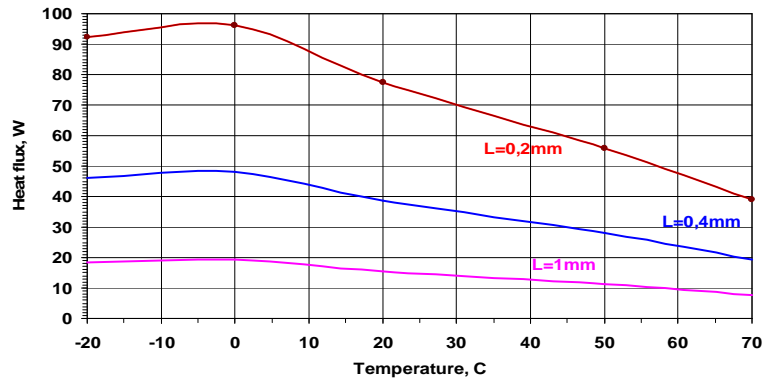


Fig. 4. Heat flux removed from one edge of the capillary groove with porous coating as a function of temperature.  $L$  is the edge width, mm; temperature of ammonia vapor  $-20^{\circ}\text{C}$

Since the investigations were applied to heat pipes, the evaporators had a cylindrical shape.

Table 1. Characteristics of the studied capillary grooves

Structure designation	Groove type	Groove depth, mm	Edge width at the crest, mm	Porous coating thickness, $\mu\text{m}$
S-1		2	0.54	
S-1-1		2	0.54	50
S-2		2	1	
S-2-1		2	1	50
S-3		1.3	0.36	
S-3-1		1.3	0.36	50

In Figs. 5–7, we compare the heat transfer coefficients for the surfaces of types S1, S2, and S3 as a function of heat carrier (ammonia) temperature. The evaporative heat transfer was maintained in the experiments.

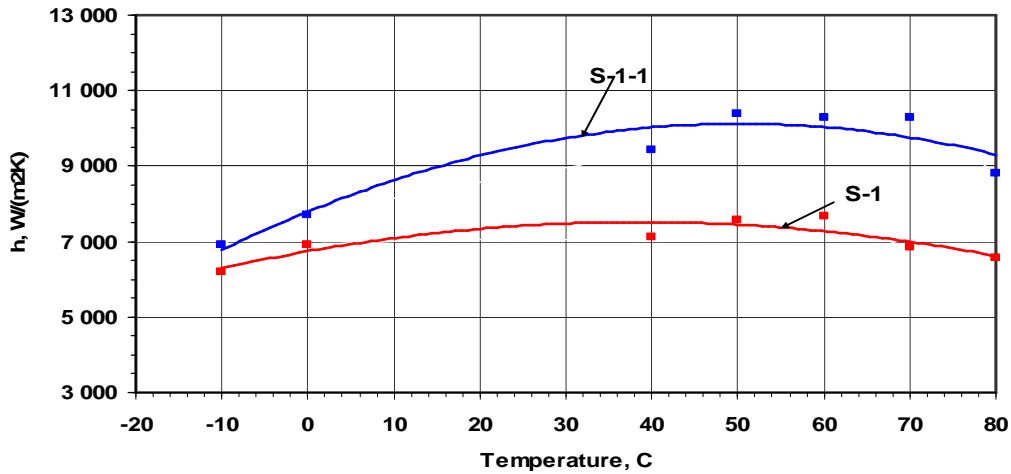


Fig. 5. Heat transfer coefficients of ammonia for the S1 surface as a function of temperature

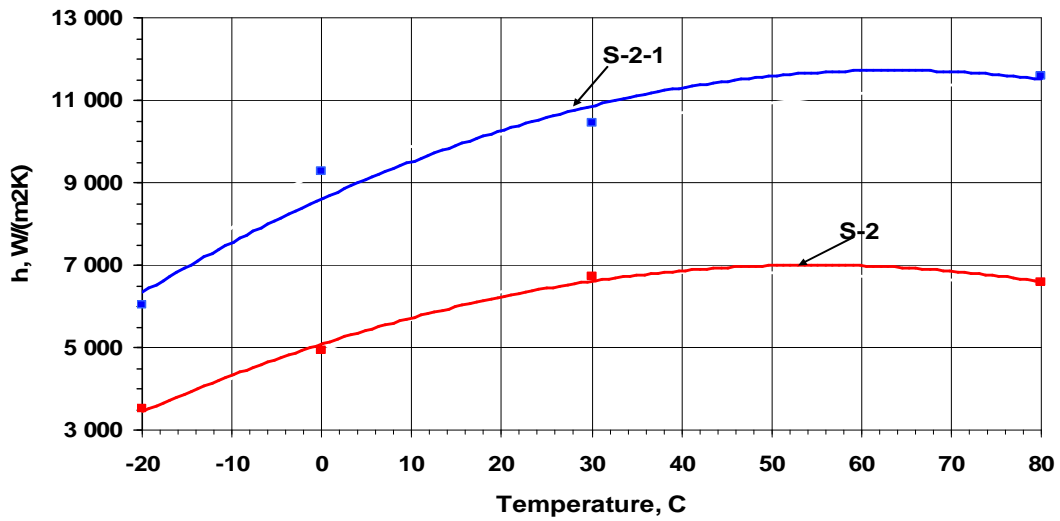


Fig. 6. Heat transfer coefficients of ammonia for the S2 surface as a function of temperature

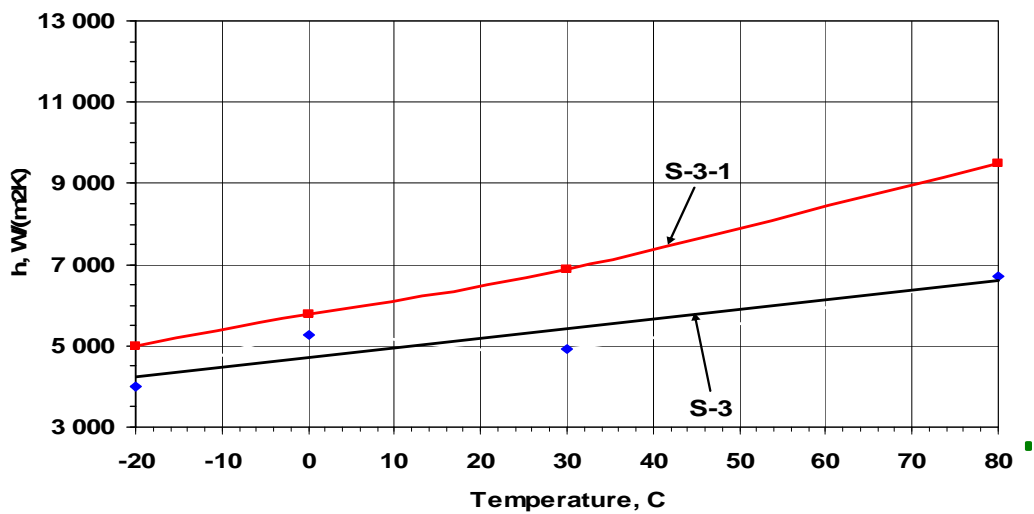


Fig. 7. Heat transfer coefficients of ammonia for the S3 surface as a function of temperature

An appreciable increase in the heat transfer coefficients is noted for all the surfaces tested after deposition of capillary grooves. For grooves of different shapes and dimensions this increase is within the range of 1.3–1.6 times. As should be expected, the highest increase of the heat transfer coefficient is observed on the S2 surface. As has been already mentioned, the level of heat transfer enhancement depends on the degree of an increase of the wetted surface of the groove edge. This increase is the highest for the S2 surface for which the portion of the total area occupied by the crests of edges is the largest and amounts to about 0.6. For S1 surfaces it is 0.43 and for S3 surfaces it equals 0.33. Moreover, as has been already stated, meniscus deepening, which results in an increase in the evaporation surface, is possible for the S2 surface. These data are in agreement with those given in [3].

As an example, Fig. 8 gives the dependences of the heat transfer coefficients for the S2 surface within the entire studied range of heat loads. Gradually, the degree of enhancement decreases with an increase in the heat load. In our opinion, this is explained by boiling-up of the heat carrier and blocking of a portion of the surface by vapor channels.

As has been already mentioned, with appreciable heat fluxes stable channels are formed in the macropores of the porous coating for escape of vapor generated in evaporation and boiling. Vapor enters from smaller pores with micro and nano dimensions as shown in Fig. 2. A portion of the surface occupied by vapor channels does not take part in heat transfer. Indirectly this follows from the data presented in Fig. 8. Using the model suggested in [6] we can estimate the portion of this surface. Figure 9 presents the results of calculations for the S1-1 surface. Since the calculation technique is constructed on evaporation in a non-flooded porous coating, as the heat transfer surface area we take only the area of the edges crests of capillary grooves with the porous coating. As is seen from Fig. 9, the character of the dependence changes already with the portion of the surface occupied by vapor channels equal to about 0.1.

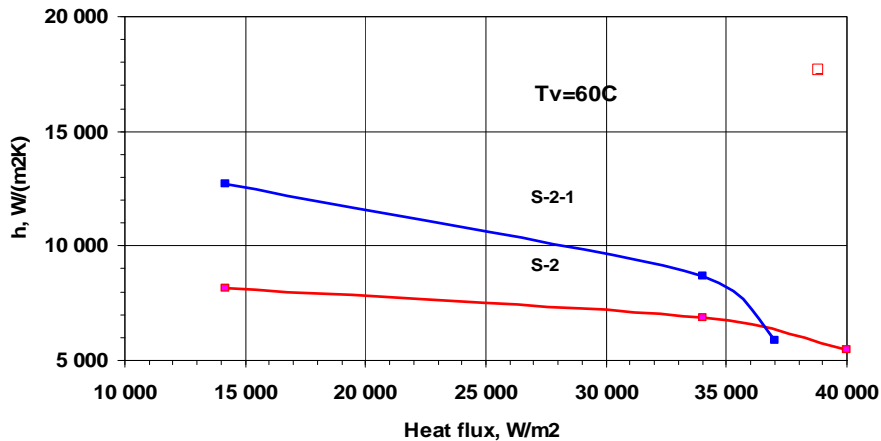


Fig. 8. Heat transfer coefficients as a function of heat load for the S2 surface  
Vapor temperature 60°C

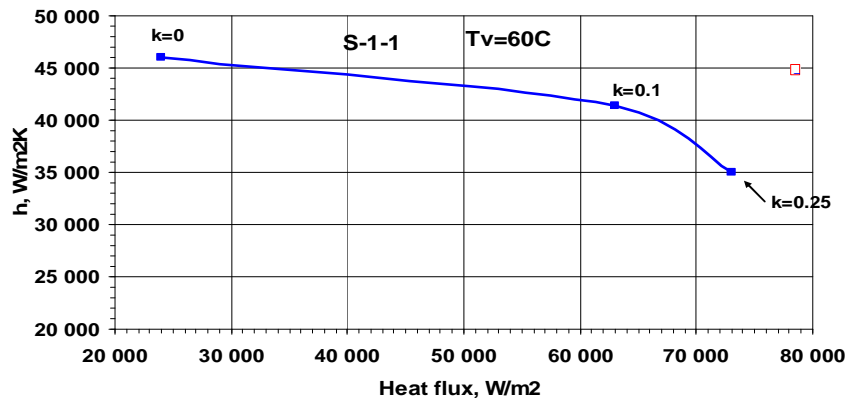


Fig. 9. Heat transfer coefficients as a function of heat flux for the S1-1 surface,  
 $k$  is the portion of the heating surface occupied by vapor channels

Capillary coatings formed from micro- and nanoparticles enhance heat transfer not only in the regime of formation of a thin liquid film but also when they are flooded. In this case, coating particles play the role of additional and stable centers of vapor generation which do not require high superheating of the surface. To prove this, we conducted the experiments with plane evaporators having grooves of triangular profile, depth 0.5 mm, and pitch 1 mm; both grooves and edges have a porous coating of aluminum oxide particles. The particle size ranges from 5 to 7  $\mu\text{m}$  and the coating thickness is 20–30  $\mu\text{m}$ . The size of pores in the porous layer is 0.1–2  $\mu\text{m}$ . The coating porosity is of about 50%. The heat carrier is propane.

The results of experiments with the heat carrier level being maintained 2 mm higher than the crests of capillary grooves are given in Fig. 10. As in previous cases, the heat transfer coefficients for the surfaces with a porous coating are noticeably higher than for the surfaces with smooth capillary grooves. As for the heat transfer coefficients with the liquid level 5 mm above the crests of capillary grooves edges, they are similar to those presented in Fig. 5.

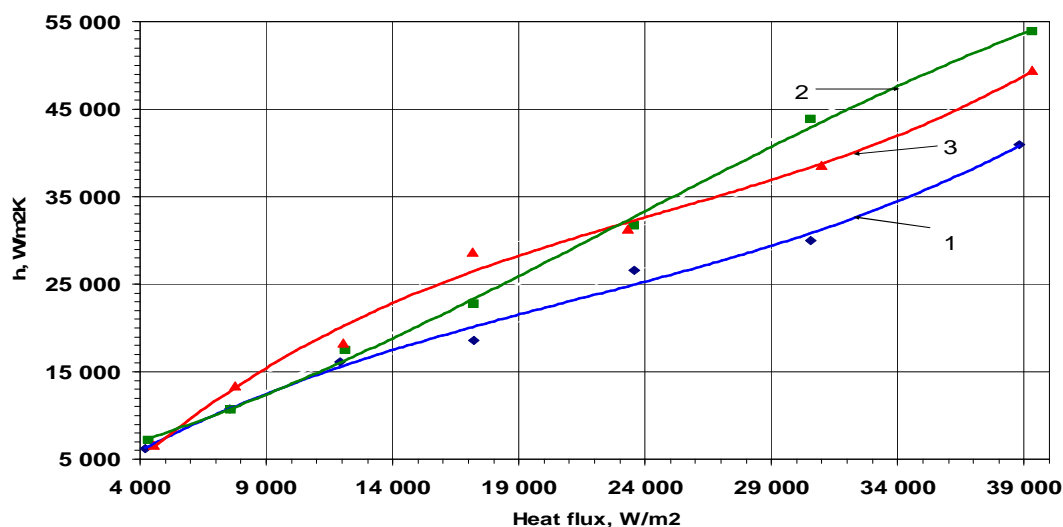


Fig. 10. Heat transfer coefficients as a function of the density of the supplied heat flux for evaporation surfaces with smooth capillary grooves (1) and with porous coating (2, 3). The heat carrier level is 2 mm above the crests of capillary grooves

## CONCLUSIONS

Comparative studies of the heat transfer coefficients of the evaporators with three types of capillary grooves were conducted. The parameters of the evaporators with smooth capillary grooves and capillary grooves having porous coating of walls with a thickness of 50  $\mu\text{m}$ . The regimes of both evaporation and boiling of heat carrier (ammonia) were provided in the experiments.

Within the entire studied range of temperatures and heat loads the heat transfer coefficients of all types of evaporators with the porous coating are 1.3–1.8 times higher than of similar evaporators with a smooth surface of capillary grooves.

On determining the required parameters of the porous coating one should, along with the structural characteristics, take into account the geometry and dimensions of capillary grooves and temperature and heat load of the evaporator.

The change in the height of the liquid level above the surface of edges of capillary grooves does not result in appreciable changes of the heat transfer coefficient.

### References

1. Vasiliev L. L., Khrustalev D. K., Grakovich, L. P. *Heat Pipes in the Systems with Renewable Energy Sources*, Nauka i Tekhnika Press, Minsk, 1988 (*in Russian*).
2. Khrustalev D. K., Denisevich S. V., Heat transfer in evaporation and condensation in a heat pipe with a combined capillary-porous structure: *Heat Pipes with Capillary-Porous Structures* / HTMI, Minsk, 1986. Pp. 39–50 (*in Russian*).
3. Wang J., Catton I. Enhanced evaporation heat transfer in triangular grooves covered with a thin porous layer // *J. Appl. Thermal Eng.* 2001. Vol. 21. Pp. 1721–1737.
4. Khrustalev D., Faghri A. Heat transfer during evaporation on capillary grooved structures of heat pipes // *J. Heat Transfer.* 1995. Vol. 117. Pp. 740–747.
5. Ma H. B., Peterson G. P. The interline heat transfer of evaporating thin film along a micro grooved surface // *ASME J. Heat Transfer.* 1996. Vol. 118. Pp. 747–755.
6. Wang J., Catton I. Vaporization heat transfer in biporous wicks of heat pipe evaporators // *Proc. 13 Int. Heat Pipe Conf. "Heat Pipe Theory and Applications," Shanghai, China, 2004.* Pp. 96–104.

## REGULATIVE CHARACTERISTICS OF THERMAL CONTROL SYSTEMS ON THE BASE OF VCHP AT VARIABLE HEAT GENERATION AND EXTERNAL HEAT EXCHANGE CONDITIONS

**Volodymyr M. Baturkin**

Heat Pipe Laboratory, Heat and Power Engineering Faculty  
National Technical University of Ukraine "Kyiv Polytechnic Institute"  
Pr. Peremogy, 37, 03056, Kyiv, Ukraine  
+38044-4068087, baturkinvm@mail.ru

### Abstract

The paper is devoted to decision of the scientific-applied problem of creation of the high-efficiency thermal control systems (TCS) of scientific space apparatus, operating in non hermetical compartments, with the use of heat pipes (HP) of variable conductance (VCHP), executing the functions of transport of heat, control of the temperature of devices by maintenance of thermal balance in the system «mounting place of device in a spacecraft (SC) – device – space environment» on the required temperature level. Heat balance equations are the basis for definition of thermal parameters of TCS elements: heat pipe, radiator, thermal insulation, flexible elements, low conductance supports, cables, contact resistances, providing function of passive TCS.

Proposed conceptions of TCS do not foreseen subsidiary electric power consumption of spacecraft and they are based on the use of own heat generation of scientific devices, or heat of subsidiary sources such as sun, providing stabilization of device temperature at the level of 290 K. Such approach is experimentally tested for the groups of scientific devices: for separate electronic cards (with mass of 0.3 kg), autonomous electronic unit (mass to 5 kg) and device panel of SC compartment (mass – 60 kg) at the change of own heat generation ration 1:10, temperatures of SC 253...323 K and illumination by external sources (sun, planet) to 270 W/m<sup>2</sup>.

### KEYWORDS

Thermal control systems, heat pipe, heat transfer models, heat exchange research, testing, application, scientific devices, space research.

### INTRODUCTION

Intensive investigation of heat mass transfer process in variable conductance heat pipes (VCHP) with non condensing gas (NCG) is conducted in many scientific centers of the world [1–12]. Such activity has created sufficient base ground for sequent introducing of this self controlling heat transfer instrument into complex thermal control systems (TCS) for space application [13–19].

The integration of VCHP into passive thermal control system for space electronics foresees the solution of the following tasks: joined design of heat pipe and electronic unit, thermal design of heat pipe, additional elements of thermal schemes such as insulation, heat conductive lines to provide the positive thermal balance of system – quantity of generated and incoming heat is enough to compensate the all type of heat leak. The thermal attachment of system to mounting place or to surroundings will produce dominant influence of these boundary temperatures and positive effect of system operation can be lost.

The conceptions of different extent of VCHP integration into electronic equipment, described in the literature, could be conditionally summarized [17]:

- Heat pipes operate with single part or element of electronic device;
- Heat pipes provide thermal stability of electronic block surface;
- Heat pipes are incorporated into electronic plates;
- Heat pipes create the thermal network between devices;
- Heat pipes act as isothermal shell of electronic device.

Above-mentioned constructive conceptions are shown on Fig. 1.

The application of every scheme is defined by concrete exploitation conditions and usually requires complex preliminary analysis. Some remarks to the characterization of these schemes are:

a) heat pipes, providing the thermal regime of separate element or part of device. Heat pipes have limited sizes of surface thermal interface with heat-generating element or part of device. The thermal mode of the whole device is provided by other TCS;

b) heat pipes, providing the thermal mode of single device. Thermal pipes have limited sizes of surface thermal interface with a block. TCS supports the thermal regime of device in the whole;

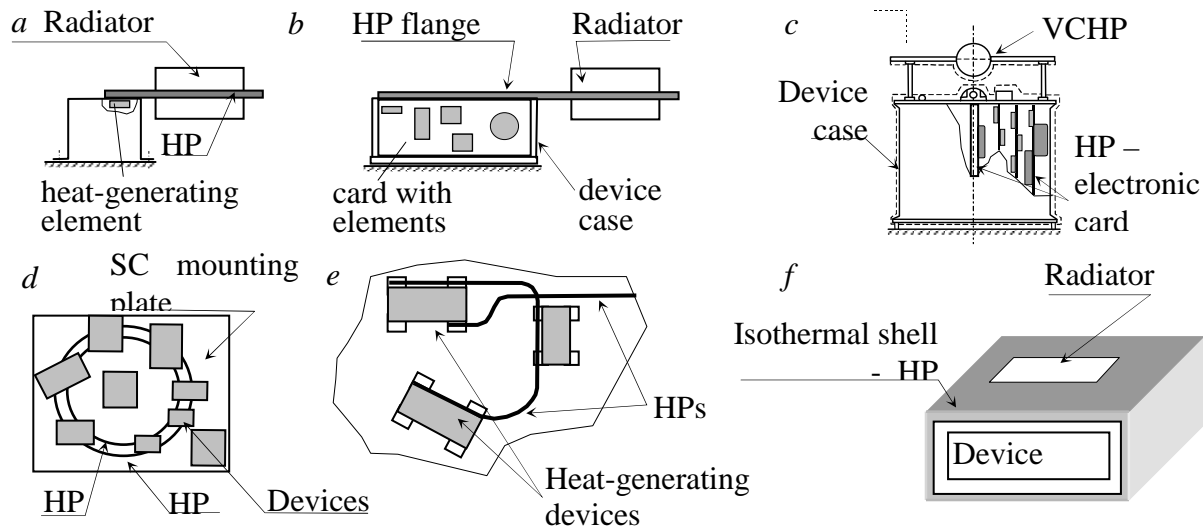


Fig. 1. Integration of HP for cooling and temperature regulation of individual elements (a), thermal interface surface of device (b), elements, located on electronic plate (c), group of instruments with heat exchange via mounting plate (d) or directly (e), and with creation of isothermal shell (f)

c) heat pipes, being a part of electronic device construction or electronic plate, are assembled as a component of electronic equipment. TCS on the basis of HP provides the thermal mode of device;

d) heat pipes which are mounted in a landing surface, create an isothermal surface for setting of devices and equipment. The thermal mode of device is provided by the additional thermal checking system or system on the basis of heat pipes;

e) heat pipes form a thermal network for direct exchange by thermal energy between parts of object or devices. The thermal mode of devices is provided by joint work of TCS of every device or centralized system on the basis of HP;

f) heat pipes support isothermality of container (shells, surfaces), which a device is in. The thermal regime of device is provided by system on the HP basis or combination with active control (heater or thermobattery), regulator, source of electrical energy).

## ELABORATION OF THERMAL CONTROL PRINCIPLES AND THEIR VERIFICATION

At the second level of integration for stabilization of the temperature of device case, which contains electronic cards, the TCS is offered with VCHP, functioning due to heat generation of device  $Q_{dev}$ . On the basis of joint analysis of heat exchange in the system "SC – device – TCS — space environment" (Fig. 2.) and VCHP regulative characteristics the following terms are proposed for consideration:

a) heat flux, transferred by VCHP  $Q_{VCHP}$  must be inside of the limits  $Q_{min} \dots Q_{max}$ , defined by the physical processes of heat transfer in VCHP;

b) components of the device thermal balance, which include a heat exchange with the mounting place ( $Q_{dev-mp}$ ) and to external environment ( $Q_{dev-o}$ ), at the minimal and maximal values of  $T_{dev}$ ,  $T_{mp}$ ,  $T_o$  are within the following limits  $Q_{min} < (Q_{dev,min} - Q_{dev-mp} - Q_{dev-o})$  and  $Q_{max} > (Q_{dev,max} + |Q_{dev-mp}| + |Q_{dev-o}|)$ ;

c) choice of radiator area ( $F_{rad}$ ) and its thermal efficiency  $\eta_{rad}$  should provide the condition  $\eta_{rad}\epsilon_{rad}F_{rad}\sigma(T_{v,max}^4 - T_{o1,max}^4) \geq (Q_{dev,max} + |Q_{dev-mp}| + |Q_{dev-o}| + |Q_{dev-rad}| + Q_{ab,max})$ ;

d) the change of vapor temperature  $T_v$  is conditioned by thermodynamics of moving of gas plug in the ranges of  $T_{v,min} \geq (T_{dev,min} - Q_{dev,min}R_{dev-v})$  and  $T_{v,max} \leq (T_{dev,max} - Q_{dev,max}R_{dev-v})$ , where  $R_{dev-v}$  – thermal resistance of "device – vapor of VCHP in evaporation zone".

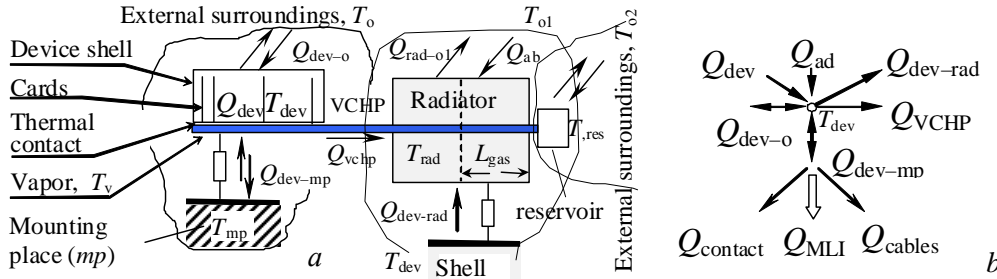


Fig. 2. Principle of TCS operation with use of VCHP: a – scheme of TCS with device; b – distribution of heat fluxes for device

Components of the heat flux  $Q_{dev-mp}$  are proportional  $(T_{dev} - T_{mp})$  и  $(T_{dev}^4 - T_{mp}^4)$ , and components of  $Q_{dev-o}$  are proportional to  $(T_{dev} - T_o)$  и  $(T_{dev}^4 - T_o^4)$ .

The offered principle of temperature regulation was experimentally approved in the model of autonomous electronic device (Fig. 3). For the conditions of circular orbit with the attitude  $h = 300$  km at the orientation of radiator plane along the velocity vector of SC the following boundary conditions have been postulated: absorbed heat flux by flat surface  $q_{ab} = Q_{ab}/F_{rad} = 120...270$  W/m<sup>2</sup> ( $T_{eff} = 230...273$  K); temperatures of mounting places  $T_{mp} = 253 ... 323$  K and heat generation of device  $Q_{dev} = 2...13$  W.

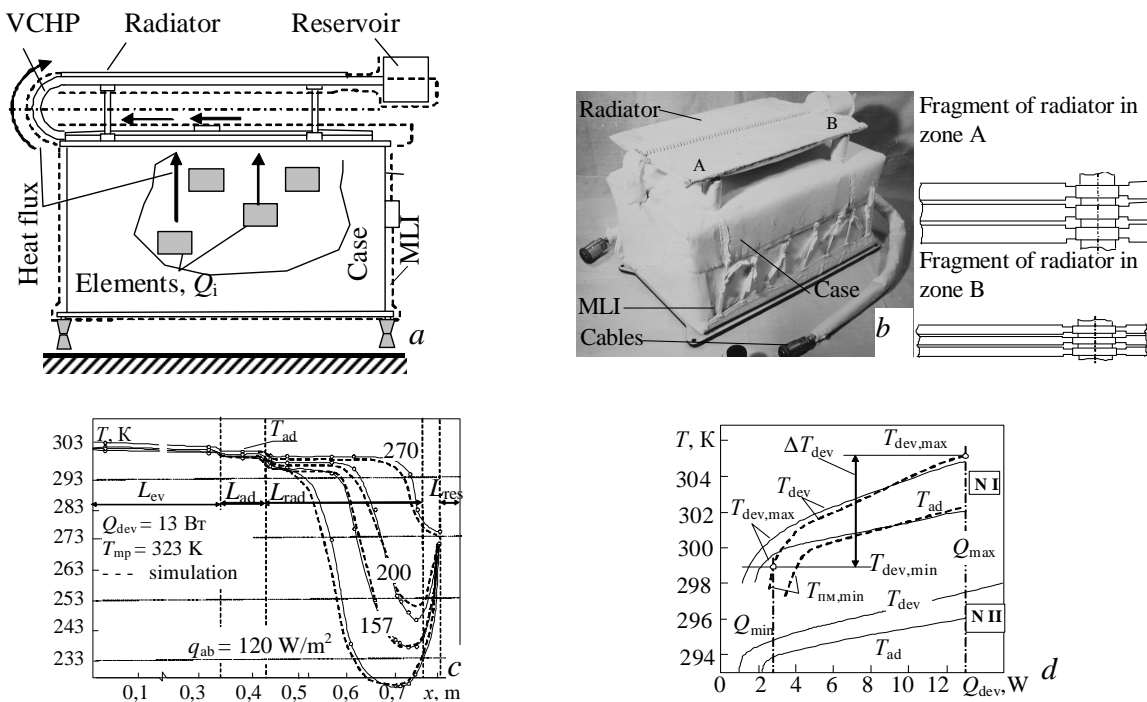


Fig. 3. Autonomous electronic device with TCS (a) and its appearance (b), distribution of temperatures on the length of VCHP at the change of absorbed heat flux  $q_{ab}$  (c) and dependence of temperatures of device case  $T_{dev}$  and transport zone ( $T_{ad}$ ) on device heat generation  $Q_{dev}$  at  $T_{mp,min} = 253$  K and  $T_{mp,max} = 323$  K in the mode of reservoir temperature  $T_{res} = const$  for modifications of TCS NI and NII (d). MLI – multilayer insulation

Under these conditions the level of stabilization of device case temperature  $T_{dev}$  is  $293 \pm 10$  K in the passive mode ( $T_{res} = f(q_{ab})$ ) and  $302 \pm 3$  K in the semipassive mode ( $T_{res} = const$ ). Optimization of heat exchange in the TCS elements (supports, MLI, cables and VCHP case) has enabled to begin regulation of the device temperature at  $Q_{dev,min} = 1,5 \dots 2,5$  W.

On identical conditions the traditional passive system could control the device temperature in the range of 253 ... 323 K, and the active system (heater controlled system) provides stabilization of the temperature at the level of  $(293 \pm 10)$  K at additional energy of regulator heater  $Q_{reg} = 15$  W.

The third levels of HP integration, which is based on the design of two-stage TCS, foresees directly setting of electronic elements on an isothermal substrate (IS) – flat HP, temperature of which, in its turn, is regulated by TCS on VCHP basis (Fig. 4).

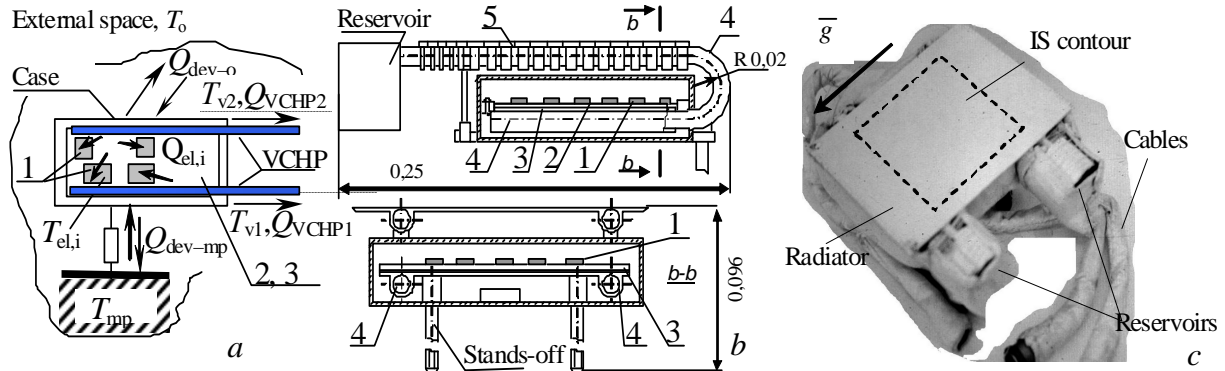


Fig. 4. Principle of electronic elements cooling in autonomous electronic block with isothermal substrate (a), layout of TCS (b): 1 – heat-generating elements; 2 – electronic printed circuit board (PCB); 3 – isothermal substrate – HP; 4 – VCHP; 5 – radiator

An electronic PCB ( $0.18 \times 0.13$  m) has 25 heat-generating elements with correlation of heat generation  $Q_{el,max}/Q_{el,min} = 10:1$ . Obligatory requirements for the previous scheme were complemented with the equalization for the vapour temperature of IS  $T_{v,IS}$ . As the regulation of elements temperature is provided by two parallel operating VCHP with a general radiator, the temperatures of heat-generating elements  $T_{el,i}$  are connected to the temperature  $T_{v,IS}$ , and this temperature is related to the VCHP vapor temperatures

$$T_{v,IS} = (\Sigma Q_{el,i} + T_{v1}/R_{IS-VCHP1} + T_{v2}/R_{IS-VCHP2}) / (1/R_{IS-VCHP1} + 1/R_{IS-VCHP2}). \quad (1)$$

The temperature  $T_{v,IS}$  is stabilized due to constancy or small rise of  $T_{v1}$ ,  $T_{v2}$  at the passive regulation, or their reduction with increase of  $(Q_{VCHP1} + Q_{VCHP2})$  at the active regulation of reservoir temperature  $T_{res}$ .

For the execution of thermal vacuum researches of device and enhancement of location of elements on the PCB an additional requirement to the construction of capillary structure of flat IS – HP is its ability to operate at any orientation, even when the vector of gravity lies in the plane of IS, and geometrical exceeding of heating zone above condensation zone  $\Delta z$  reaches 0.18 m. At this position of IS the temperature of elements  $T_{el,i}$  and  $T_{v,IS}$  are saved at the same level as at horizontal position ( $\Delta z = 0$ ), and change of the orientation of elements from above or from below in the horizontal plane of IS does not influence on their temperature (Fig. 5).

Experimental investigations have shown that the range of maintenance of temperature of PCB elements in the passive mode is  $(296 \pm 10)$  K for not heat-generating elements ( $T_{ev,VCHP}$ ),  $(313 \pm 25)$  K – for elements with heat generation of  $0.1Q_{IS}$  and flux density  $q_{el} = 12$  W/m<sup>2</sup> ( $T_{el,max}$ ) and  $(301 \pm 13)$  K – for elements with heat generation of  $0.011Q_{IS}$  and heat density up to  $q_{el} = 6$  W/m<sup>2</sup> ( $T_{el,min}$ ). These data were obtained at the change of  $T_{mp}$  in the range of 253 ... 323 K, total heat generation of IS  $Q_{IS} = 1 \dots 8$  W and at  $q_{ab} = 140 \dots 280$  W/m<sup>2</sup> (the last corresponds  $T_{eff}$  of radiator and reservoir within the limits of 233...273 K). The design of PCB with TCS has passed complete mechanical tests, imitating transport and starting loadings,

that confirmed the rightness of the chosen structural-technological decisions for the thermal elements of TCS.

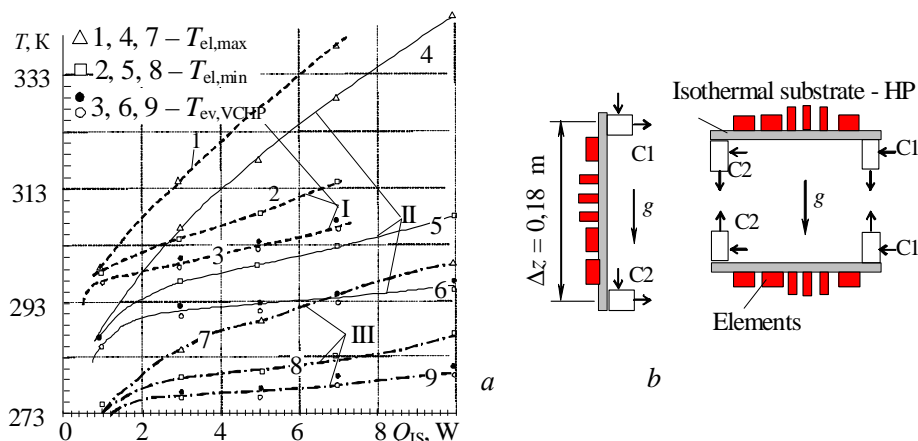


Fig. 5. Temperature dependence of the electronic elements  $T_{el}$  and the VCHP heating zone  $T_{ev}$  on power  $Q_{Is}$  at three levels of external heat disturbances  $T_{eff} = 273 K$  (I),  $233 K$  (II),  $213 K$  (III) (a) and the orientation of the isothermal substrate atn its autonomous investigation with its cooling by two coolers C1 and C2 (b)

For scientific devices which do not have own heat generation ( $Q_{dev} = 0$ ) but require the narrowing of exploitation temperature range the use of classic passive TCSs and their combinations is problematic for the maintenance of device temperature  $T_{dev}$  inside of the range of  $280...300 K$  at wide change of solar constant, for example, during the cruise phase "Earth – Mars" in the conditions of SC energy deficit (Fig. 6, a) [18]. For such cases conception of integration of passive heating element – absorber of sun radiation heat for functioning of TCS (heat  $Q_{s,ab}$ ) and VCHP, which compensates the changes of both external and internal characteristics of heat exchange of device with a space environment and SC is first offered (Fig. 6, b, c).

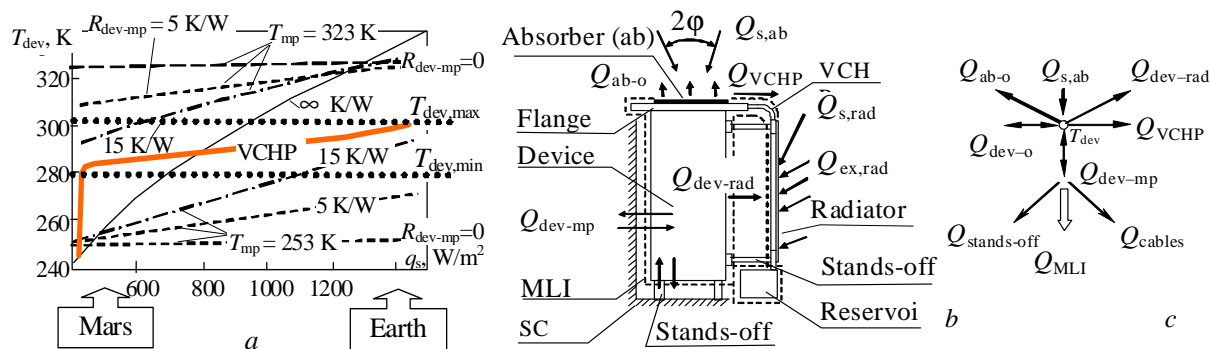


Fig. 6. Temperature of device at the use of traditional passive TCS (at  $R_{dev-mp} = 0 K/W$ , and at  $R_{dev-mp} = 5, 15$  and  $\infty K/W$ ) and TCS with VCHP at the change of  $T_{mp} = 253 ... 323 K$  and solar sun constant  $q_s = 500...1400 W/m^2$  (a); proposed principle of temperature regulation with VCHP (b) and heat balance (c)

The device and radiator heat balance must be supported in all range of initial parameters:  $q_s$  ( $q_{s,max}/q_{s,min} = 2.8$ ), angle  $\varphi = \pm 20^\circ$  at the maneuvers of SC,  $T_{mp} = 253...323 K$ , the masses of device  $5...15 kg$ , sizes to  $0.3 \times 0,2 \times 0,5 m$  and thermal resistance  $R_{dev-mp} > 15 K/W$  at the temperature level of device  $T_{dev} = 298 K$ :

$$Q_{VCHP} = -\epsilon_{ab} F_{ab} \sigma (T_{ab}^4 - T_o^4) + \alpha_{s,ab} F_{ab} q_s \cos(\varphi) + (T_{mp} - T_{dev}) / R_{mp-dev} \geq Q_{min}; \quad (2)$$

$$Q_{VCHP} + (T_{dev} - T_{rad}) / R_{dev-rad} + \alpha_{s,rad} F_{rad} q_s \sin(\varphi) + Q_{ext,rad} < \epsilon_{rad} F_{rad} \sigma \eta_{rad} (T_{rad}^4 - T_o^4), \quad (3)$$

where  $F_{ab}$ ,  $F_{rad}$  – the area of absorber and radiator of VCHP;  $R_{dev-rad}$  – thermal resistance of "device – VCHP radiator",  $Q_{ex,rad}$  – absorbed additional heat flux.

On the basis of these equations the density of absorbed by radiator flux has been defined as  $q_{ab,rad} = 18 \dots 240 \text{ W/m}^2$ , heat flux passed via VCHP  $Q_{VCHP} = 1 \dots 14.5 \text{ W}$ , and the parameters of VCHP are also estimated. For elaboration of engineering model the followings scientific-technological tasks were decided: development of absorber with  $\alpha_{s,ab} > 0.95$  and  $\epsilon_{ab} < 0.18$ ; background and verification of methods of diminishing of sizes of VCHP reservoirs, minimization of heat exchange through stands-off, via MLI and the integration of two VCHP in the joint radiator. The proposed thermal conception of the device temperature control was realized in the model of TCS (Fig. 7 a). At operation on the Earth orbit at  $\varphi = 0^\circ$  and variation of  $T_{mp}$  from 253 to 323 K the passive TCS provides  $T_{dev} = 296 \dots 299 \text{ K}$ , and for the Mars orbit is in the range of  $T_{dev}$  from 289 to 292.5 K (Fig. 7 b).

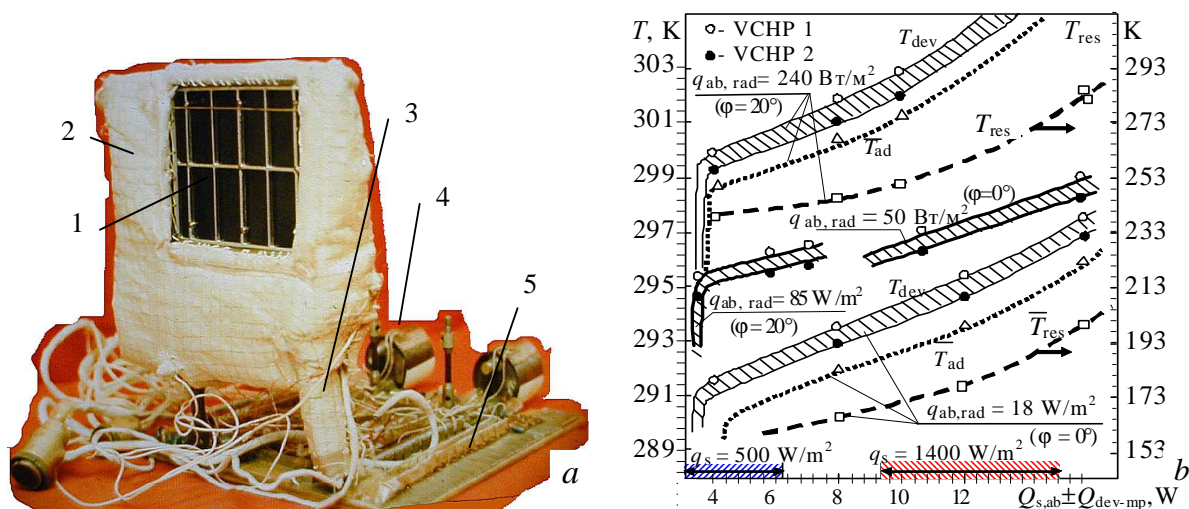


Fig. 7. Passive thermal control system for devices without power generation (a) and regulative characteristics of system as function of temperatures of device, adiabatic zone and reservoir on power transferred (b): 1 – solar absorber; 2 – flange with MLI; 3 – VCHP; 4 – reservoir; 5 – radiator

At the change of angle  $\varphi$  to  $20^\circ$  (at SC maneuvers) the range of  $T_{dev}$  for the Earth orbit is increased to 299 ... 305 K, and for the Mars orbit to 295 ... 296.5 K. For further improvements of thermal control characteristics at  $q_s < 700 \text{ W/m}^2$  the increasing of absorber surface valid for one occasion only was offered.

The next stage of VCHP introduction into spacecraft design deals with elaboration of thermal and mechanical conception of isothermal device compartment. Here the two-level TCS system is proposed: four device panels form the device compartment. Every panel has distributed network of aluminium axially grooved heat pipes with thermal interface to VCHP. The last is used for temperature regulation of devices mounting places (Fig. 7). The design of mounting panel is an all-metal structure, made of alloy of AMГ6 or Д16 without inner honeycomb structure. It was fabricated by milling (without press equipment), that gives substantially larger mobility at construction of the whole compartment, saving the mass and thermal parameters of panels. Thermal network in panels and method of integration of HP and shells allows to warm or cool arbitrarily located devices and transport heat into the area of heat exchange with VCHP. Every device panel had  $0.8 \text{ m}^2$  surfaces for the two-sided arbitrary mounting of devices with heat generation to 60 W. The mass of panel with HPs made 7 kg.

In the design an ancillary thermal energy source (with mass of 2.5 kg) is foreseen, that allows TCS to be independent of the heat generation value of devices at different operating modes. The range of the temperature control of panel is  $(289 \pm 14) \text{ K}$  at the variation of heat generation of devices  $Q_{dev} = 0 \dots 60 \text{ W}$  (Fig. 8). At the density of heat generation  $5 \text{ kW/m}^2$  nonisothermality of panel on length of 0.75 m did not exceed 2 K. This principle has been applied in the design of device compartment of space laboratory "Regata" (developer of laboratory – Institute of Space Researches of Russian Academy of SCIENCES,

Russia) which should conduct the scientific researches in interplanetary space, moving due to pressure of sun beams [19].

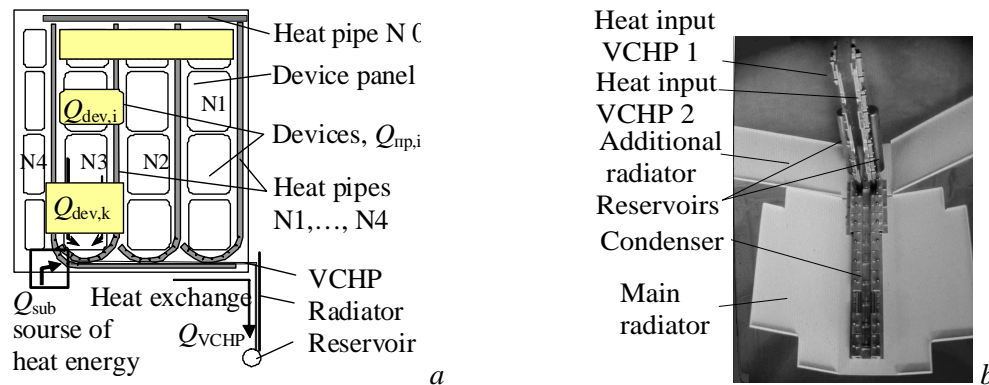


Fig. 8. Concept of isothermal panel with regulative temperature (a) and scheme of VCHP (b)

## CONCLUSION

It was experimentally proved that for devices with heat generation  $Q_{dev}$  relative to the mass up to 3.3 W/kg (up to 950 W/m<sup>3</sup>) limits of temperature stabilization of the contact surfaces of electronic PCB are 298 ... 305 K in semi-passive mode (at the constant temperature of the reservoir with non-condensable gas) and 283 ... 313 K in a passive mode (without any additional energy sources). These data are attributed to the following thermal disturbances: thermal unit ( $Q_{dev,min} / Q_{dev,max} = 1.5 \dots 13$  W), external heat absorption flux ( $q_{ab,min} / q_{ab,max} = 120 \dots 270$  W/m<sup>2</sup>) and the temperature of mounting places  $T_{mp,min} / T_{mp,max} = 253 \dots 323$  K.

The concept of two-level TCS system for electronic elements of the printed board circuit is proposed. The flat heat pipe, which could operate at any orientation relative to gravity, is the base for element layout and attached VCHP – for temperature control. The resulting circuit design significantly narrows the range of element temperatures: for non heat-generating elements up to 296±10 K and for heat-generating elements to (313±25) K, with variable heat load, temperature of mounting place and external thermal disturbances.

Theoretical basis of heat transfer inside of the TCS with VCHP has been formulated for the case of devices temperature stabilization, which do not have own heat generation, by the use of solar energy. The achievement of the device temperature stabilization in the range of 289 ... 305 K (at the passive control) under external disturbances, which include changes of solar constant on the Earth orbit to Mars orbit, the temperature change of device mounting places within 253 ... 323 K and change of the orientation of the spacecraft relative to the sun as a result of maneuvers in a cone of ±20 °, is theoretically predicted and experimentally confirmed.

The design of the isothermal panel for the device compartment combines the functions of mechanical fastening of devices, their cooling / heating and redistribution of thermal energy, providing isothermallity of devices less than 5 K on the in the temperature of device mounting places of 9288±13) K when the heat generation is within 0 ... 60 W. Four such panels create the frame of payload compartment of small space laboratory.

## Acknowledgment

The participation in the 8-th Minsk International Seminar “Heat Pipes, Heat Pumps, Refrigerators, Power Sources” was supported by Institute for Space Systems (DLR) in the frame of AGREEMENT ON SCIENTIFIC COLLABORATION No. 3.030 between NTUU “KPI” (Ukraine) and Institute for Space Systems (Germany).

Practical implementation of thermal control system on VCHP basis was conducted due to the cooperation with Special Design Bureau of Institute of Space Research of Russian Academy of Sciences (Frunze) and with Institute of Space Research of Russian Academy of Sciences (Moscow).

### References

1. Bienert W. B., Brennan P. J., Kirkpatrick J. P. Feedback controlled variable conductance heat pipes // *AIAA Paper*. 1971. No. 421. Pp. 1–11.
2. Marcus B. D. *Theory and Design of Variable Conductance Heat Pipes* // Report NASA CR – 2018, TRW Systems Group, April 1972. – 238 p.
3. Groll M., Hage M. Development of an electrical feedback controlled variable conductance heat pipes for space applications // *AIAA Paper*. 1974. No. 752. Pp. 1–7.
4. Vasiliev L. L., Konev S. V. Controlled heat pipes // *Eng.-Phys. J. (Inzhenerno-Fizichesky Zhurnal)*. 1977. Vol. 32, No. 5. Pp. 920–938 (in Russian).
5. Galaktionov V. V., Shalya O. M. Two-dimensional problem of heat and mass transfer in the field of a vapour and gas front of a gas-controlled heat pipe // *Heat and Mass Transfer and Apparatuses. Books of Sci. Proc.* Iss. 268. Moscow Power Engineering Institute, Moscow. 1975. Pp. 121–128 (in Russian).
6. Shekrladze I. G., et al. On the issue of an analysis of temperature regimes of a gas-controlled heat pipe operation // *Thermal Physics of High Temperatures (Teplofizika Vysokih Temperatur)*. 1976. Vol. 14, No. 5. Pp. 1126–1129 (in Russian).
7. Delil A. A. M. van der Vooren J. Uniaxial model for gas-loaded variable conductance heat pipe performance in the inertial flow regime. *Advances in Heat Pipe Technology* // *Proc. of 4<sup>th</sup> Intern. Heat Pipe Conf.*, London, United Kingdom, 1981. Pp. 359–372.
8. Furukawa M. *Analytical Studies for Temperature Predictions and Control with Emphasis on Space Application*, TKU-80604, National Space Development Agency of Japan, 1983. – 163 p.
9. Dulnev G. N., Belyakov A. P. *Heat Pipes in Electronic Systems of a Temperature Stabilization*, Radio i Svyaz, Moscow, 1998. – 96 p. (in Russian).
10. Antoniuk D. Generalized modelling of steady state and transient behaviour of variable conductance heat pipes // *Proc. of AIAA 22<sup>nd</sup> Thermophysics Conf., Honolulu HI, USA*, 1987. – 8 p.
11. Semena M. G., Baturkin V. M., Rassamakin B. M., Grechina N. K. Analytical and experimental study of operating characteristics of low temperature variable thermal resistance heat pipes // *Proc. of 7<sup>th</sup> Intern. Heat Pipe Conf.*, Minsk, Belarus, 1990. Vol. 1: Fundamental and Experimental Studies. Pp. 525–532.
12. Edom A. *Development and Dynamic Study of a Space Radiator Integrating Multiple Gas-Loaded Heat Pipes* // Thesis for the obtaining of the degree of doctor in mechanical engineering, Federal university of Santa Catarina, Brasil, 2001. – 195 p.
13. Kirkpatrick J. P. Marcus B. D. A Variable conductance heat pipe/radiator for the lunar surface magnetometer // *AIAA Paper*. 1972. No. 27. Pp. 1–9.
14. Mock P. R., Marcus E. A., Edelman B. D. Communications technology satellite – a variable conductance heat pipe application // *Proc. of AIAA/ASME Thermophysics and Heat Transfer Conf.*, Boston MA, USA, 1974. Pp. 743–749.
15. Savage C. J., Aalders B. G. M., Kreeb H. A Variable conductance heat pipe radiator for MAROTS-type communications spacecraft // *J. of Spacecraft*. 1979. Vol. 16, No. 3. Pp. 176–180.
16. Lanteri A., Henning B. Tele-X antenna module thermal control // *Proc. of 3<sup>rd</sup> Europ. Symp. on Space Thermal Control and Life Support Systems, Noordwijk, The Netherlands*, 1988. Vol. 2. Pp. 319–326.
17. Baturkin V. Passive thermal control systems on heat pipes for space application and terrestrial technology: *PTC-03 Short Course on Passive Thermal Control* / Int. Center for Heat and Mass Transfer, Begell house Inc., New York, 2003. Pp. 83–137.
18. Baturkin V. M., Grechina N. K., Mockalenko O. P., Schoda K. N. Passive thermosate system with application of gas-filled heat pipes and thermal energy of solar radiation // *Proc. of 4<sup>th</sup> Europ. Sympos. on Space Environmental and Control Systems*, Florence, Italy, 1991. Pp. 769–774.
19. Baturkin V. M., Grechina N. K., Zhuk S. K. Component of thermocontrol system on the basis of heat pipes for scientific device compartment of small space laboratory "REGATA" // *Proc. of 8<sup>th</sup> Int. Heat Pipe Conf.*, Beijing, China, 1992. – 12 p.

## COMBINED SATELLITE THERMAL CONTROL SUBSYSTEM BASED ON THE HEAT PIPES AND ACTIVE FLUID LOOP

Alexander A. Rudko, Evgeniy V. Yurtaev, Valeriy V. Dvirniy  
JSC "Academician M.F. Reshetnev "Information Satellite Systems"  
Zheleznogorsk, Russia

This report describes the combined thermal control subsystem based on the heat pipes and the fluid loop. It presents the results of optimization of the fluid loop and the heat pipe/fluid loop thermal interface configuration verified by satellite ground tests.

This report also provides the comparison between the satellite thermal control subsystem based on the heat pipes only and the combined thermal control subsystem based on the heat pipes and the fluid loop.

Modern satellites manufactured by JSC "Academician M.F. Reshetnev "Information Satellite Systems" are based on the satellite platforms of non-pressurized design.

GEO-satellite has a module design and consists of two modules (Service and Payload module). Modules are of the rectangular parallelepiped shape; they are made of honeycomb panels. Most of heat dissipating equipment is accommodated within the volume of modules' equipment bays on the inner skins of honeycomb panels. (Figure 1).

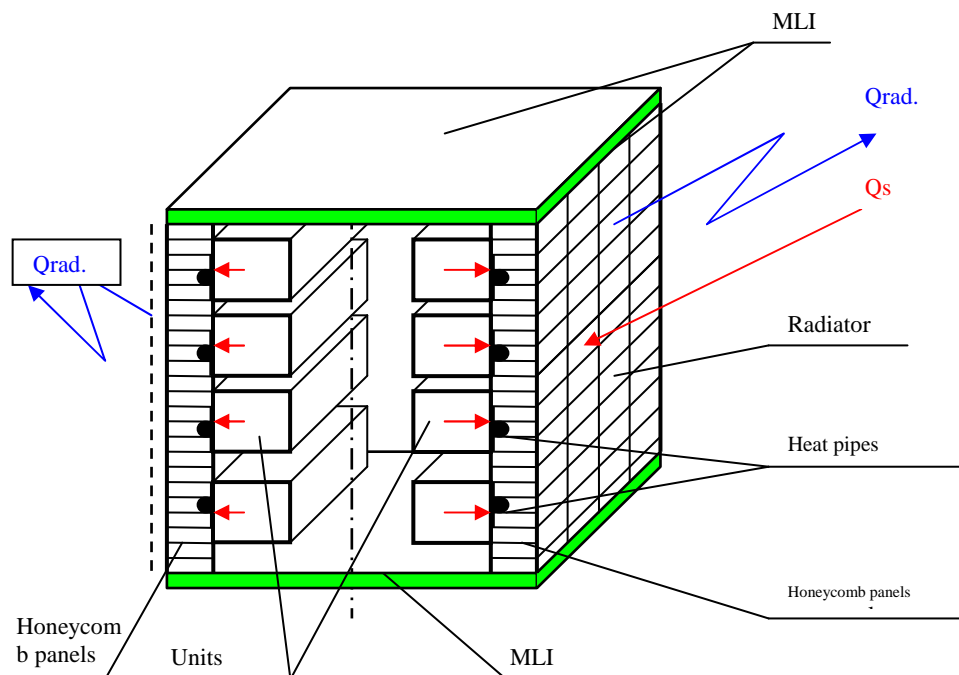


Fig. 1. Non-pressurized design SC TCS thermal scheme

In order to ensure the satellite thermal mode, the heat shall be emitted to the outer space from the outer skins of the honeycomb panels. The heat from the equipment is transferred through the heat pipes on the internal skin and then it is transferred from the internal to the external skin through the honeycomb filler by means of thermal conductivity, which radiates into space.

On the geostationary satellites, the heat dissipating equipment is located mainly on the North and South panels since these panels are less subjected to the solar radiation (North and South panels are parallel to the orbit plane, the normal to North panel is directed towards the North pole and the South panel normal is directed towards the South pole).

Nevertheless, the three-axis stabilization of a satellite in the geostationary orbit predetermines the fact that its North and South panels will be sequentially affected by the solar flux during about half a year; thus, the effectiveness of one of the radiating surfaces is reduced.

At the satellite design stage, a lot of attention is paid to the accommodation of the equipment installed on the panels with the heat pipes.

In order to create comfortable temperature conditions and make effective use of radiators, it is advisable to accommodate the heat dissipating equipment uniformly along the entire radiator surface. Nevertheless, to ensure the required RF performances, the active elements of the repeater output section are usually concentrated in the proximity of antenna feeds. As a result, the areas with concentrated heat dissipation appear on the equipment panels and non-uniform distribution of heat dissipation between the North and South panels.

A network of heat pipes routed on the equipment panel in mutually perpendicular direction is employed to transfer heat from such zones and distribute it over the whole equipment panel area (radiating surface) in American and European satellites. The equipment is installed on the two-shelf heat pipes and attached to the honeycomb panels. The presence of heat pipe network does not allow conducting ground thermal balance tests with the Spacecraft in vertical position.

At present moment European and American space agencies are developing combined thermal control systems employing the fluid loop for high power Spacecrafts.

Equipment thermal control for the current Spacecrafts developed by JSC "ISS" is ensured by application of parallel heat pipes embedded into the honeycomb panels on the equipment side and a double fluid loop installed on the honeycomb panel perpendicularly to the direction of the heat pipes. Diagram of the thermal interface between the Fluid loop and Heat pipes is given in Figure 2.

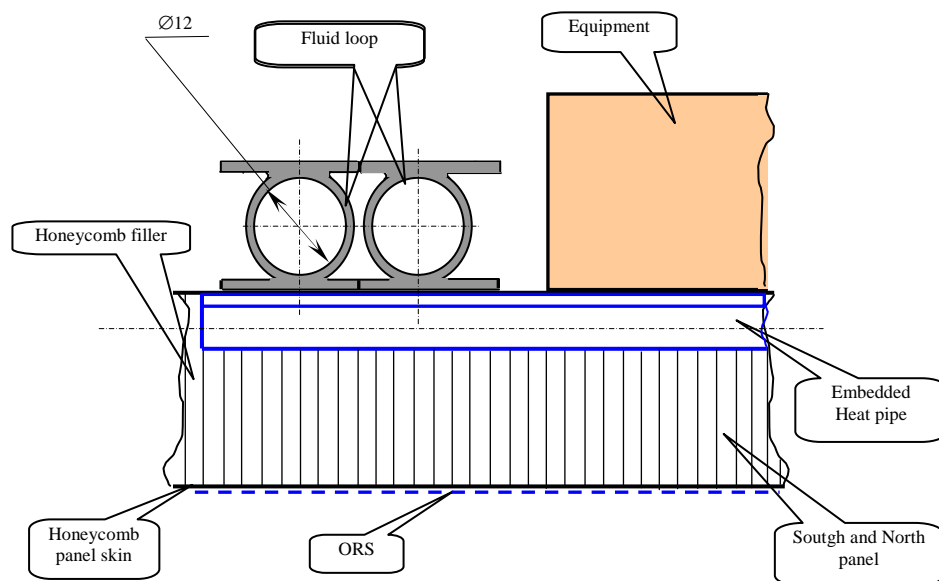


Fig. 2. Scheme of thermal interface between Fluid loop and Heat pipes

The fluid loop ensures:

- heat transfer in the direction perpendicular to the heat pipes;
- transfer of a portion of absorbed solar flux between South and North panels which ensures optimal usage of the available radiating surfaces;
- possibility of ground thermal balance test implementation with the Spacecraft in vertical and horizontal position;
- allocation of equipment with the heat flux density more than  $3\text{W}/\text{cm}^2$  over the fluid loop.

Transfer of the solar flux absorbed by illuminated panel to the non-illuminated panel has significant impact on the temperature of the radiating surfaces. The calculated temperatures of illuminated ( $T_{ill}$ ) and non-illuminated ( $T_{non}$ ) panels are given in Figure 3 depending on ratio of the solar flux transferred by fluid

loop to the flux absorbed by the illuminated panel  $K=Q_{fl}/Q_{sol}$  ( $Q_{fl}$  is a solar flux transferred by the fluid loop to the non-illuminated panel,  $W$ ;  $Q_{sol}$  – is a solar flux absorbed by the illuminated panel,  $W$ ).

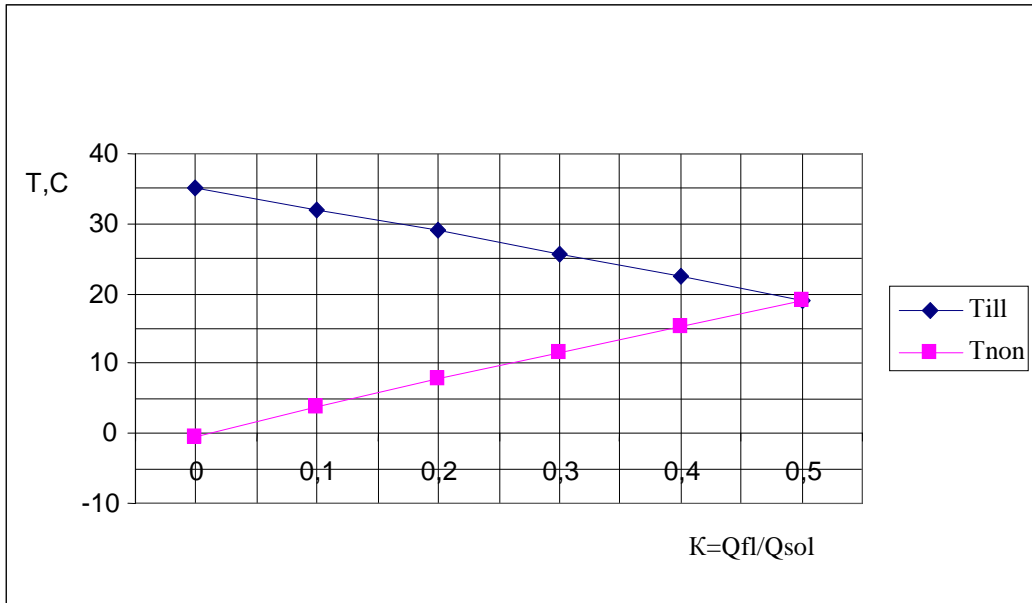


Fig. 3. Illuminated and non-illuminated panels calculated temperatures

Simultaneous application of a large number of heat pipes (over 100) and a fluid loop in TCS requires calculation and experimental activities to be carried out in order to investigate the issues related with thermal interface "heat pipe - fluid loop" and optimization of fluid loop configuration. Necessary to investigate dependency of the equipment temperature: heat transfer coefficient in the fluid loop, length and total area of contact between fluid loop and heat pipes, heat transfer coefficient in interface zone "heat pipe - fluid loop".

At present moment is developed thermal mathematical model and conducted thermal analysis of combined TCS with heat pipes and fluid loop. Spacecraft with the combined TCS is passes the ground thermal balance tests.

Thermal model takes into account the following types of heat exchange and processes:

- Conductive coupling inside the panel with account for heat pipes;
- Conductive coupling between the fluid loop and heat pipes;
- Conductive coupling between the fluid loop and panel skin;
- Conductive coupling between the equipment and panel skin;
- External radiative coupling;
- Internal radiative coupling;
- External heat fluxes on the orbit;
- Heat transfer by the heat fluid.

Thermal model consists of 923 nodes. Thermal model subdivision into nodes is given in Figure 4.

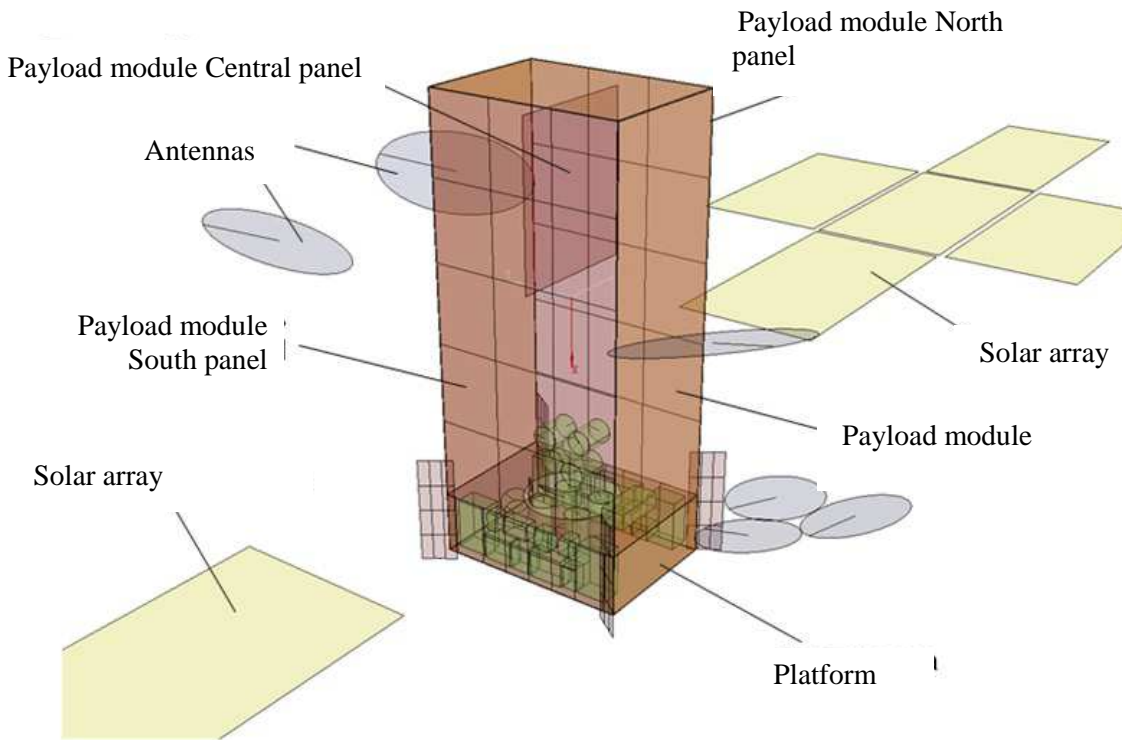


Fig. 4. Thermal model subdivision into nodes

The coolant flow direction in double fluid loop is given in Figure 5.

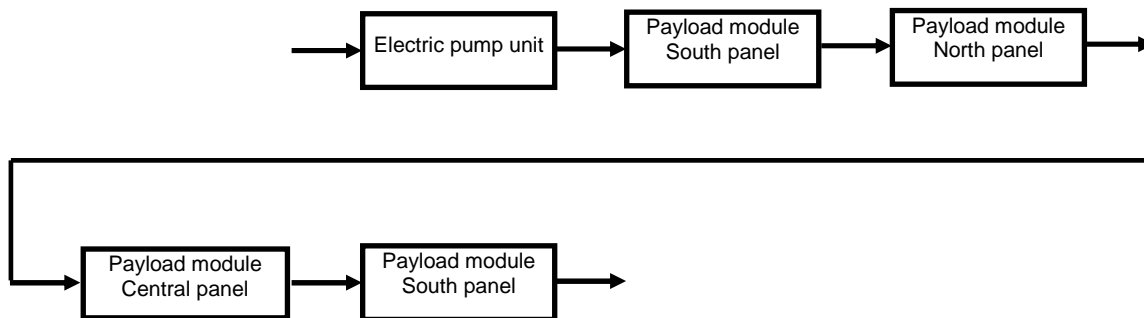


Fig. 5. The coolant flow direction in double fluid loop

Heat exchange between the equipment and fluid loop (heat pipes) is calculated according to the formula 1 and 2:

– Conductive coupling (fluid loop (heat pipe) – panel skin)

$$GL1 = K_{ef} \times L, \quad (1)$$

where  $L$  – contact length;

$K_{ef}$  – heat transfer coefficient;

– Conductive coupling (equipment – panel skin): the equipment is installed through the filler

$$GL2 = H \times S, \quad (2)$$

where  $S$  – contact area;

$H$  – coupling coefficient.

Calculated values of temperature drop between the panels are given in Table 1.

Table 1. Temperature drop calculated values

Period	North panel temperature, °C	South panel temperature, °C	Transferred heat flux, W
Summer Solstice	24	21	741,4
Winter Solstice	21,5	24,2	762,9
equinox	minus 0,5	minus 0,5	0

Thermal model calculation results related to: temperature drop between illuminated and non-illuminated panels; heat flux transferred from the illuminated panel to the non-illuminated ; temperature drop with respect to panel height are well compliant with the preliminary results of thermal balance tests.

Combined TCS with heat pipes and fluid loop has a number of advantages in comparison to TCS based on heat pipes. Comparison results are given in Table 2.

Table 2. Comparison of two TCS types

Performance	Thermal control subsystem	
	with heat pipes and fluid loop	only with heat pipes
1. Portion of heat flux absorbed by the illuminated panel transferred by fluid loop, %	41	-
2 The requirement position SC during ground and thermal balance tests	Any position: horizontal or vertical	only Vertical
3. Thermal control of equipment outside North or South panel	Centralized, by means of a liquid loop	Autonomous
4. Possibility of equipment thermal control with the heat flux density in the contact area more than 3 W/cm <sup>2</sup> .	Possible, by means of installation on the fluid loop	Problematic
5. Conventional surface area ratio to the area of TCS with heat pipes	~0,8	1,0

## CONCLUSION

1. Combined TCS with heat pipes and fluid loop are being developed at present moment for GEO-satellites with big heat dissipation (> 5000 W).
2. Combined TCS with heat pipes and fluid loop has a number of advantages in comparison to TCS having only heat pipes.
3. Developed thermal mathematical model and conducted thermal analysis. The results are confirmed by the ground tests.
4. Conducted settlement of experimental work of "heat pipe - fluid loop - honeycomb panel" thermal interface are being carried out.

## IN-FLIGHT EXPERIENCE OF HEAT PIPE BASED THERMAL CONTROL SYSTEM FOR GEOSTATIONARY ORBITING SERVICE MODULE

Tulin D. V., Tulin I. D., Serov G. P., Shabarchin A. F.

Lavochkin Association, 141400 Russia, Moscow region, Khimki, Leningradskaya 24  
[ival@laspace.ru](mailto:ival@laspace.ru)

In this paper there will be discussed some payload thermal control system in-flight operating results of the meteorological geostationary satellite since 21 January 2011. The satellite overview is presented on Fig. 1.

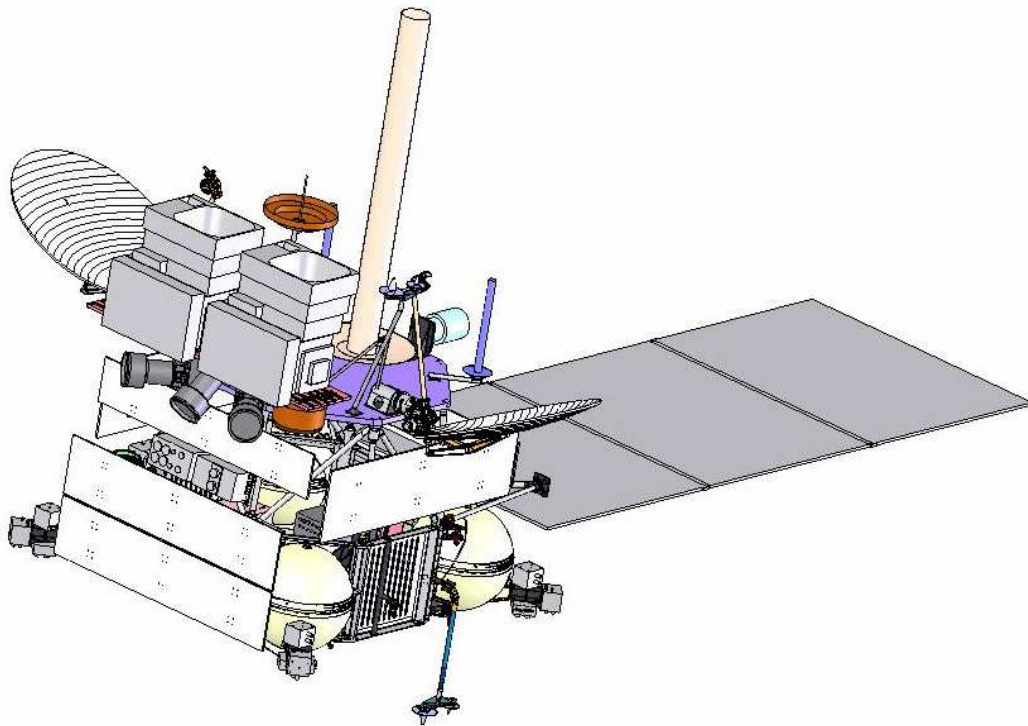


Fig. 1

Satellite main parts are as follows:

- target equipment complex;
- complex of the service systems

All equipment of the satellite is designed for operation in outer space without keeping it in the sealed gas filled container.

The satellite thermal control system (TCS) designed as a complex of autonomous thermal control subsystems providing temperature regime of separate spacecraft parts. It allows to conduct thermal vacuum tests fragmentarily. Thermal interference of these spacecraft fragment is insignificant and could be estimated.

The most of service equipment located on the thermal honeycomb panel (THP). The THP has plane octagon shape and located inside the basic module framework. The THP design represents honeycomb panel with embedded axial grooved heat pipes.

The heat power generated in the THP equipment is rejected by axial grooved heat pipes, collector heat pipes and then by LHP to the operating surface of the radiation heat exchanger (RHE) from which it is radiated to environment

The TCS includes two heat pipe based RHEs, which radiating areas orientated in following way: "-Z"-axis the first one and "+Z"-axis the second. The service systems THP (THP CS) "+X"-axis view is presented on Fig. 2.

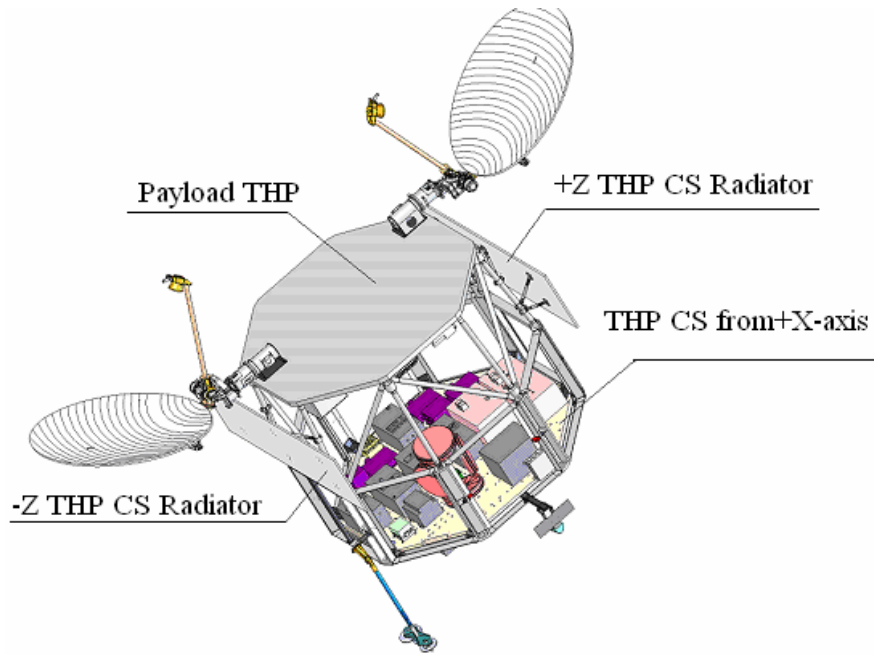


Fig. 2

Some part of THP CS surface ( $0,81 \text{ m}^2$ ) from the "-X"-axis direction with low absorption coefficient covering is not covered with MLI and serves as additional radiator. The service systems THP CS "-X"-axis view is presented on Fig. 3.

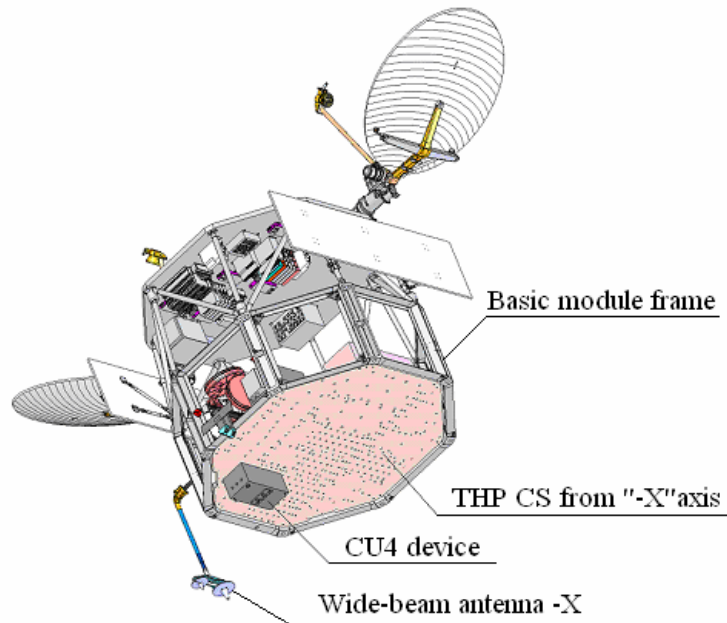


Fig. 3

During the geostationary orbiting the satellite has two orientation modes: standby mode and operating mode.

In standby mode the satellite "-X"-axis is solar oriented and while the "-X" radiator is always sunlit, the "+X" radiator is always in the shadow.

In operating mode the satellite "+X"-axis is Earth oriented and "-Z" and "+Z" oriented radiators are sunlit by turns.

In this paper there will be given the results of in-flight temperature measurements in standby and operating orientation modes and in different service systems TCS modes. The comparison of in-flight, estimated and experimental issues will be also presented.

## CONDENSATION PROCESSES AT SURFACE TENSION FORCES ACTION FOR SPACE APPLICATION

**Vasily Buz,**  
TAIS Ltd

Ap.122, Akademika Koroleva Street 72/2, Odessa 65122, Ukraine  
Tel (+38 0482) 427677; E-mail:buz@farlep.net

**Konstantin Goncharov**  
TAIS Ltd

Khimky, Moscow region, Russia  
Tel (+7 495) 5736374; E-mail tais@heatpipe.ru

**Henry Smirnov**

Odessa Academy of Food Technology  
Kanatnaya Street 112, Odessa 65039, Ukraine  
Tel (+38 0482) 402344; E-mail: [g.smirnov@e-mail.ua](mailto:g.smirnov@e-mail.ua)

### Abstract

The film-wise condensation mathematical models at considerable influences of surface tension forces are offered. The cases of immovable vapor condensation on surface and moving vapor condensation in channel are considered. With use of these models the condensation process accounts results in various conditions are received. In considered cases the influence of surface tension forces reduce to existence of heat exchange intensity maximum. The analysis of the physical reasons of liquid slugs formation in the LHP condenser is carried out. The model of formation of liquid slugs, model of the hydrodynamic phenomena at full vapor condensation taking into account formation of liquid slugs are presented. The model for hydrodynamic and heat exchange calculation at full vapor condensation in the pipe is proposed, results of calculations and their analysis are presented.

### KEYWORDS

Condensation, heat exchange, pulsation, modeling, loop heat pipe.

### INTRODUCTION

Being present in literature of recommendation for calculation heat exchange at the vapor film condensation are received, as a rule, for conditions, when surface tension forces influence is insignificant. In the cases majority the surface tension forces is small in comparison with weight forces and the vapor dynamic action, therefore the recommended dependences, permit with accuracy sufficient for engineering calculations to define the heat transfer coefficient. At the same time, at condensation on profiled surfaces, in channels of small sizes, role of forces of surface tension becomes considerable, and in some cases - determining. At the rational organization of condensation process with surface tension forces help it is possible to achieve of heat transfer coefficient considerable increase, as, for example it is shown by Rifert and Trocoz [1], Vasiliev et al [2].

The role of surface tension forces is especially important for condensers of board equipment two-phase thermal control systems because small gravitation and strict requirements of compactness.

At full vapor condensation in the channel liquid slugs can be formed. Mechanisms of these slugs formation are not studied. It is considered to be, that slugs are formed as a result of waves merge on the liquid films surface. Formation of slugs is not only influences heat exchange at condensation, but also leads to occurrence of considerable pulsations of pressure. Last fact can be especially important for LHP with low capillary pressure.

Despite of a significant amount of the publications devoted to problems of condensation inside pipes, today there are distinctions in recommendations on solution dependences. Solutions by recommendations of different authors differ in two - three times. It is connected first of all by that the majority of dependences are received on the basis of experimental results generalization, contain errors, which are applicable in a narrow range of parameters change. Published results of researches concern the area of vapor turbulent flow and turbulent flow of liquid film on the pipe wall. In the LHP condensers a turbulent flow zone of vapor and liquid film is usually small, or it is absolutely absent. Besides, the feature for process of condensation in small diameter pipes is essential influence of a surface tension forces. It is not taken into account in the majority of existing settlement models.

## IMMOVABLE VAPOR CONDENSATION

### Heat exchange processes modeling on single flat element of condenser

Schematic of the considered condensing process is presented on Figure 1. It was assumed that film flow is one-dimensional and forms under the action of suction in A-A section and weight force, liquid subcooling was not taken into account. For case, when weight force is insignificant, a system of dimensionless equations was proposed by Buz and Smirnov [3]. With taking into account of weight forces this system have a next view

$$P' = \text{Re}^2 \left( 2 \frac{\text{Re}'}{\text{Re}} + \frac{\Delta'}{\Delta} \right) + \frac{3 \text{Re}}{\Delta^2} - \text{Ga} \cdot \sin \gamma, \quad (1)$$

$$\Delta'' = A \sqrt{1 + \Delta'^2} \left[ P - \frac{\rho_l}{\rho_v} (\text{Re}' \Delta + \text{Re} \Delta')^2 \right], \quad (2)$$

$$\text{Re}' = \frac{K}{\Delta^2} - \frac{\text{Re} \Delta'}{\Delta}, \quad (3)$$

$$K'' = \frac{BK}{\Delta} \quad (4)$$

Here  $X = \frac{x}{l}$ ;  $\Delta = \frac{\delta_l}{l}$ ;  $Nu = \frac{\bar{\alpha} l}{\lambda}$ ;  $\text{Re} = \frac{\bar{u}_l l}{\nu_l}$ ;  $\text{Ga} = \frac{g l^3}{\nu^2}$ ;  $A = \frac{\rho_l \nu_l^2}{\sigma l}$ ;  $B = \frac{\lambda_l l}{\lambda_w \delta_w}$ ;  $K = \frac{\lambda (t_s - t_w)}{\rho v r}$ ;

$$P = \frac{(p_s - p_l) l^2}{\nu_l^2 \rho_l}; \quad P' = \frac{dP}{dX}; \quad \text{Re}' = \frac{d \text{Re}}{dX}; \quad \Delta' = \frac{d\Delta}{dX}; \quad \Delta'' = \frac{d^2 \Delta}{dX^2}; \quad K'' = \frac{d^2 K}{dX^2}.$$

Equations (1) and (2) present the law of conservation of momentum along the  $x$  and  $y$  axis, correspondingly; equation (3) is a combined equation of energy, continuity and heat transfer; equation (4) presents heat transfer in the rib.

Different variants of boundary conditions combination determine the variety of (1)-(4) equations system solutions. Some examples of such combinations are presented here for the most simple case of isothermal condensing surface (if  $B = 0$ , equation (4) can be excluded from the consideration).  
1) Calculation case when the left side of condensing section adjoins the thermal isolated surface totally submerged by liquid:

$$\text{if } X = 0 \quad \text{then} \quad \text{Re} = 0; \Delta' = 0; P = 0 \quad (5)$$

$$\text{if } X = 1 \quad \text{then} \quad P = P_1 \quad (6)$$

2) Calculation case when there is a symmetry at the left border and at the right border, as a result of design

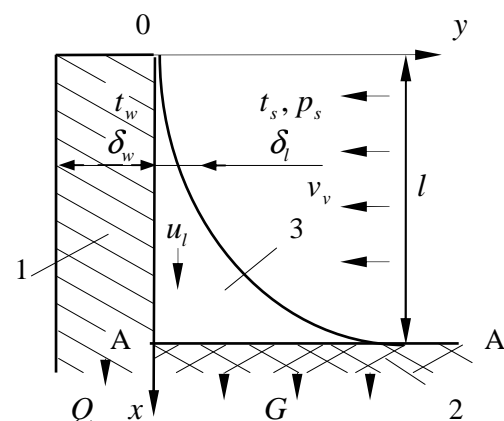


Fig. 1. Schematic of film condensing process in case of liquid suction: 1 - heat removing rib; 2 - porous structure; 3 - liquid film

peculiarities  $\Delta_1$  is a fixed value and does not depend on  $P_1$ :

$$\text{if } X = 0 \text{ then } Re = 0; \quad \Delta' = 0 \quad (7)$$

$$\text{if } X = 1 \text{ then } \Delta = \Delta_1; \quad P = P_1 \quad (8)$$

3) Calculation case of symmetry or total submerging of perpendicular walls:

$$\text{if } X = 0 \text{ then } Re = 0; \quad \Delta' = 0 \quad (9)$$

$$\text{if } X = 1 \text{ then } \Delta' = \infty; \quad P = P_1 \quad (10)$$

4) Calculation case of condensing on the ribbed surface element:

$$\text{if } X = 0 \text{ then } Re = 0; \quad \Delta = \varepsilon, \quad (11)$$

$$\text{if } X = 1 - \Delta \cdot \Delta': \quad \Delta' = tg(\pi/2 - \beta/2); \quad P = P_1 \quad (12)$$

The results of numerical solution of (1)-(3) equations system for isothermal condensing surface ( $B = 0$ ) at boundary conditions mentioned above following. Film condensing with suction of liquid is characterized by considerable and non-monotonous change of pressure gradient  $P'$  along the liquid film. Assumption that  $P'$  has constant value along  $X$  axis made by some authors is not correct for all cases. Dependence of the average intensity of heat exchange  $Nu$  on the suction intensity  $P_1$  testifies that there is some maximum of heat removal intensity (Figure 2). Considerable difference is also observed in values of integral characteristic of heat ex-change -  $Nu$  number for different boundary conditions.

Calculation results for different condensation device on the above mentioned model are presented in report [4]. Some of them and other are presented below.

### External task of condensing on the surface with triangle ribs and liquid suction along grooves between ribs

Schematic of process is presented on Figure 3. Saturated vapor is over the ribbed surface, heat is rejected from the bottom surface of the wall. Condensed liquid flows along axis  $x$  from the top of rib to its foot. Then liquid moves along the groove between ribs (along axis  $z$ ). Gravity influence is negligible, liquid is moving under the pressure action. Minimum pressure in liquid film will be at the point of pumping out (at  $z = z_f$ ), maximum pressure will be at the top of rib. While liquid moving, pressure in liquid film decreases because of friction. It is assumed that liquid rate along axis  $z$  on the side surface of rib is negligible in comparison with its rate along axis  $x$ . As regards the triangle groove, rate vector component directed along axis  $z$  will be of main importance.

Task of condensing on rib surface corresponds to one of the tasks described in previous chapter (variant  $d$ , boundary conditions (11), (12)). For definition of the complete model for considered process, it is necessary to solve this task together with task of liquid flow at variable mass flow along triangle groove between ribs (along axis  $Z$ ) to the point of pumping out. For this case, there is drawn following dimensionless equation from equation of continuity:

$$\frac{d Re_z}{dZ} = \frac{Re_f tg(\beta/2)}{\Delta_f L^2} - \frac{2 Re_z}{\Delta_f} \frac{d\Delta_f}{dZ} \quad (13)$$

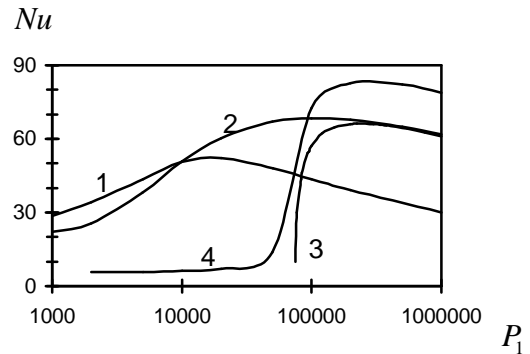


Fig. 2. Dependency of average heat exchange intensity parameter,  $Nu$ , when film condensing on intensity of liquid suction,  $P_1$ , at  $B=0$ ,  $Ga=0$ ,  $K=0.001$ ,  $A=0.00002$  and different boundary conditions: 1 - (5), (6); 2 - (7), (8); 3 - (9), (10); 4 - (11), (12)

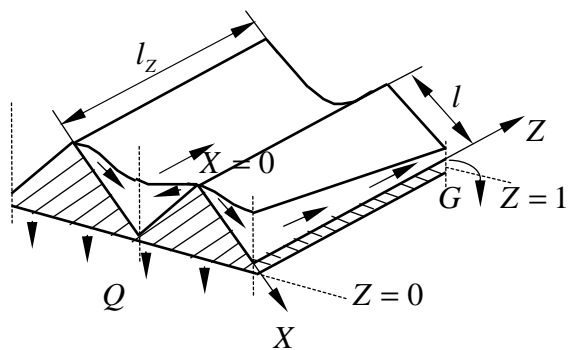


Fig. 3. Schematic of condensing on ribbed surface in case of liquid removal along grooves between ribs.

Here index  $f$  concern the liquid film parameters at  $X = X_f$ ;

$$Re_z = \frac{\rho_l w l}{\mu_l}; Z = z / l_z; L = l / l_z; \beta - \text{angle}$$

at the bottom of groove;  $w$  - average rate along axis  $z$  at free space of liquid flow cross section.

Assuming that the liquid flow is laminar, following dimensionless equation can be drawn from Darcy equation:

$$\frac{dP_f}{dZ} = \frac{C}{8} \frac{(1 + \operatorname{tg} \beta / 2)^2 Re_z}{\Delta_f^2} \quad (14)$$

Mathematical model of considered process for case of isothermal condensing surface contains equations (1)-(3) with boundary conditions (11), (12) and equations (13), (14) with boundary conditions (15):

$$\begin{aligned} \text{if } Z = 0 \quad Re_z &= 0; \\ \text{if } Z = 1 \quad P_f &= P_{f1}, \quad \Delta = \Delta_{f1} \end{aligned} \quad (15)$$

Examples of calculation results for conditions presented on Figure 3 are shown on Figures 4 and 5. Difference of curve is conditioned by different  $P_f$  values in each cross section because of hydraulic losses when liquid moving along groove between ribs. As it can be seen from Figure 5, these losses (along axis  $Z$ ) has considerably non-linear change dependency. This non-linear characteristic is conditioned, firstly, by increase of liquid mass flow along axis  $Z$  and, secondly, by decrease of cross section area because of surface tension forces action. As a result of difference in distribution among cross sections, average Nusselt number along section is also changing along axis  $Z$ . This curve has a maximum characteristic for condensing in case of liquid film suction (see Figure 2).

### Modeling of condensation in heat pipes with axial grooves.

Liquid films one-dimensional flow in cross section of thermal pipe on surface rib in groove for liquid removal is considered. The dynamic action of vapor on liquid film was not taken into account. The accounts were conducted for following conditions:  $Ga = 0$ ;  $A = 3 \cdot 10^{-6}$ ;  $K = 3 \cdot 10^{-3}$ ;  $L = 0,4$ ;  $\rho_l / \rho_v = 91$ . The received film thickness distributions are submitted on Figure 6. The accounts show, that at small

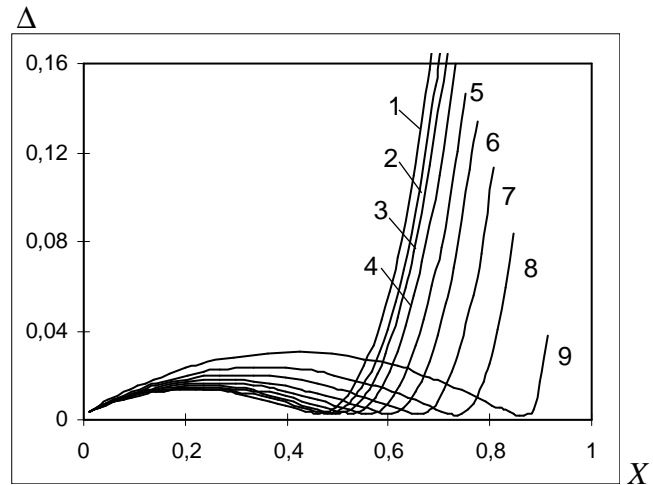


Fig. 4. Distribution of liquid film thickness along condensing surface for different cross sections  $Z$ : 1 - 0,1; 2 - 0,3; 3 - 0,4; 4 - 0,5; 5 - 0,6; 6 - 0,7; 7 - 0,8; 8 - 0,9; 9 - 1 ( $B = 0$ ,  $Ga = 0$ ,  $K = 0,001$ ,  $A = 2 \cdot 10^{-5}$ ,  $P_{Z=1} = 9 \cdot 10^4$ ,  $\beta = \pi / 2$ ).

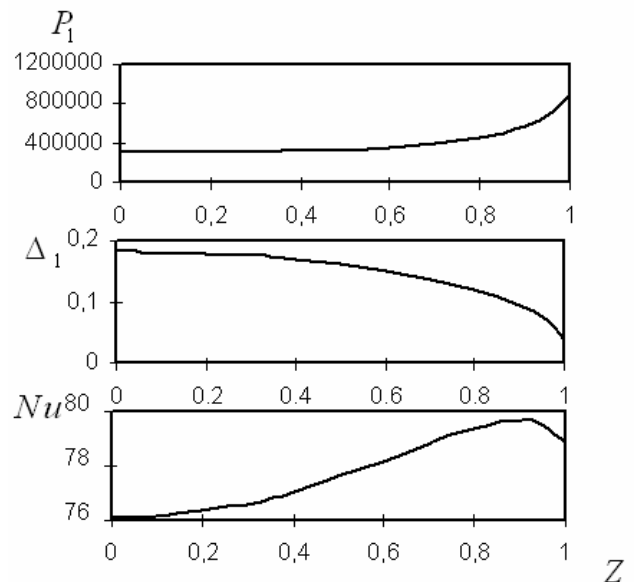


Fig. 5. Change of dimensionless pressure  $P_1$ , liquid film thickness at the rib foot  $\Delta_1$  and average (along rib contour) Nusselt number along channel for liquid removal at  $B=0$ ,  $Ga = 0$ ,  $K = 0,001$ ,  $A = 2 \cdot 10^{-5}$ ,  $P_{Z=1} = 9 \cdot 10^4$ ,  $\beta = \pi / 2$ .

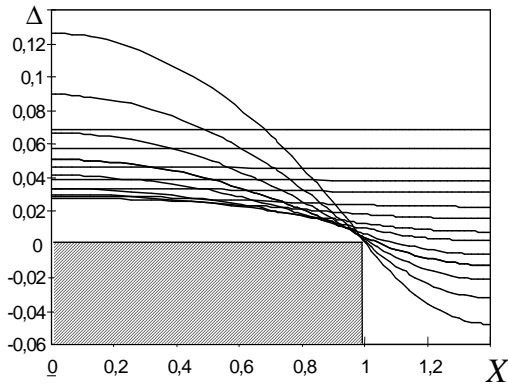


Fig. 6. Liquid film thickness distribution on cross section of heat pipe with axial grooves by different pressure difference between vapor and liquid in groove

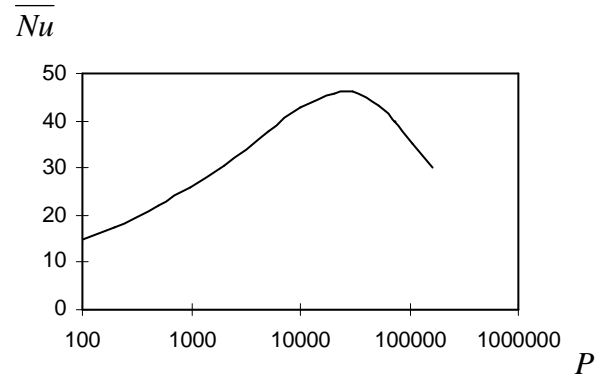


Fig. 7. Dependency of average Nusselt number from dimensionless pressure difference between vapor and liquid in the groove.

difference of pressure between vapor and liquid in groove the uniform liquid distribution on heat pipe perimeter is observed. At increase liquid suction and growth of pressure difference is formed meniscus in groove zone. At that the average thickness of film in the beginning decreases, and then increases. The consequence of it is the existence of maximum in dependence of average Nusselt number from dimensionless pressure difference (see Figure 7).

## MODELING OF CONDENSATION IN LHP

### Experimental researches

1. Researches of condensation processes in LHP with the transparent condenser are carried out. LHP evaporator 800 Watt was used in experimental installation. The LHP working fluid was purity water. Capillary pressure of evaporator was about 1 Bar. The condenser was made from quartz glass tube with internal diameter of 4 mm. The full length of the condenser was 8,5 meters. Condenser cooling medium was air. Operating modes LHP were observed which the device steadily worked of one hour and more. Next phenomena of LHP working were visually fixed:

2. The liquid film is not visible on a main part of the condenser (60%), because it has a very small thickness. About 90% of condenser length there content a separate flow of a liquid film near the pipe wall and vapor in a stream kernel. On last third part of condenser in the bottom part of a horizontal pipe the liquid stream was observed. The thickness of a liquid layer monotonously increases along the condenser.

3. Liquid slugs were formed on distance 0.2 - 0.5 meters from the end of condenser. The period of their formation was from 2 till 6 seconds in the dependent of power. (See Fig.8). Periodic changing of condenser length connected with thermal-hydraulic fluctuations in the loop. Injections of the

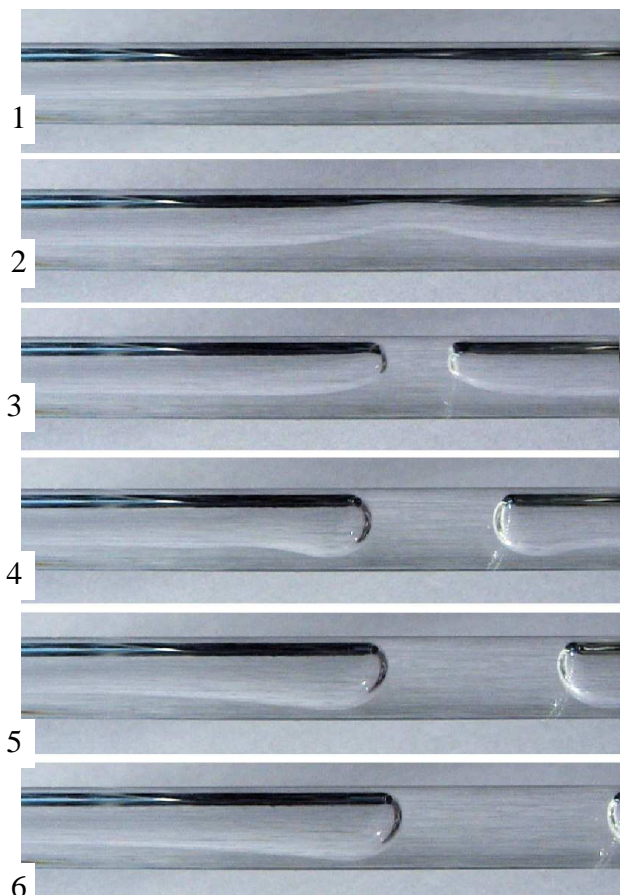


Fig. 8. Liquid slug formation and evolution

overcooled liquid to compensation chamber are opening the condenser. The last reduce condensate overcooling and after return the process. The period of 20 seconds is a time of passage by a liquid from the condenser to compensation chamber.

4. After formations of a liquid slug its speed of movement is great, movement is hardly distinguishable, further the speed is slowing down practically to zero at the moment of achievement by a slug in the end of condenser.

5. Periodically moving of a liquid slug to the end of condenser with period about of 20 seconds and amplitude about of 0.5 meters was observed. Condenser babbles closing occurs slowly, but opening - quickly.

6. The vapor (gas) bubbles with length from 2 to 5 millimeters (depending on loading) were remained in the condensers end. Near of the condensers end its size is decreasing. The distance between bubbles was 10 to 20 millimeters. Temperature in this zone was essentially below the saturation temperature.

7. Bubbles decreased in sizes after formation liquid slugs. In the beginning length of the bubbles was 50 - 100 millimeters. Bubbles moving after formation, it decrease in sizes and disappear completely on distance 0,7 - 1 meter from the end of condenser.

8. At the moment of formation of a liquid slug there was sharp moving of a liquid meniscus against general stream on 1-2 mm. After that the meniscus came back to an initial position and moved with general stream.

9. Liquid slugs at the moment of its formation have length about 15 mm (at  $t_s = 65^{\circ}\text{C}$ ). At the moment, when has come the following slug (through 3-4 sec.) the first one increased to 25 mm of length. The maximum liquid film thickness was observed approximately in 0.25 m from liquid slug meniscus. The liquid film thickness increased in the beginning slowly and then with escalating speed. Finally came to very fast formation of a liquid slug. This process was visible especially well at small heat power and saturation temperature 60 - 70 $^{\circ}\text{C}$ . Period between slug's formations was approximately of 6 seconds. The thickness of liquid film is decreased near to a meniscus of slug (see photo on fig. 8). The length of a liquid slugs was increasing at the moment of it movement. Difficult processes occur on the last 10% of condenser length. The speed of vapor become small in this zone and the essential role in liquid removing is played by its movement to a liquid slug. But such mechanism of liquid removing is effective only near to meniscus. This movement is accompanied by mechanical displacement by slug of a liquid from walls. Such mechanism can play the important role in the micro gravitation.

### Vapor dynamic action modeling

Liquid film flow modeling in the channel at full vapor condensation was presented in [4]. The example of calculation result for liquid film distribution is showing on fig. 9 for steady state mode.

As well as in experimentation, surface tension forces are important on the last 10% of condenser length. Vapor dynamic action on liquid film is already small at the distance of 80% condenser length and longitudinal action of surface tension forces is small yet. As show the experiments, liquid slugs creation takes place in the pipe. Liquid slugs generate the pulsation of pressure and liquid flow velocity. Such pressure pulsations can be approximately equal by capillary pressure value. In experiments [6] with water vapor condensation at the temperature of 120 $^{\circ}\text{C}$  pressure pulsation of 100 kPa have been observed. Modeling and determination of amplitude and frequency of pulsation in LHP is of great interest.

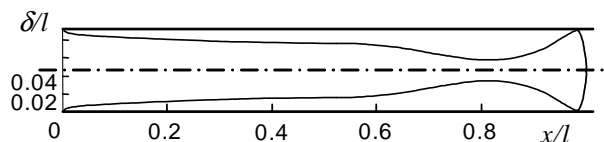


Fig. 9. Liquid film distribution in accordance with presented model [4]

### Modeling of a liquid slugs formation

Some motionless volume of a liquid is considered in the round channel for liquid slugs formation in case of action surface tension only [6,7]. Suppose that a liquid volume will take one of two forms presented on fig. 10.

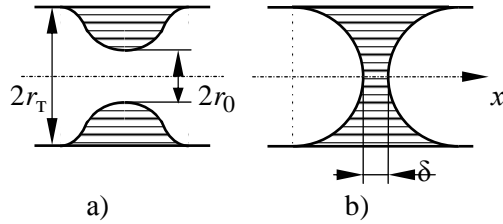


Fig. 10. Liquid configuration

In case of the form (fig. 10a) two components of a surface tension operate together. The first is defined by longitudinal curvature and operates from an axis to a wall, second is defined by curvature in cross-section and operates to a pipe axis. Modeling and calculations result show (fig. 11), that at volume of a liquid more than some critical value in the form (fig. 10a) becomes impossible and there is a spontaneous transformed to the second configuration (fig. 10b).

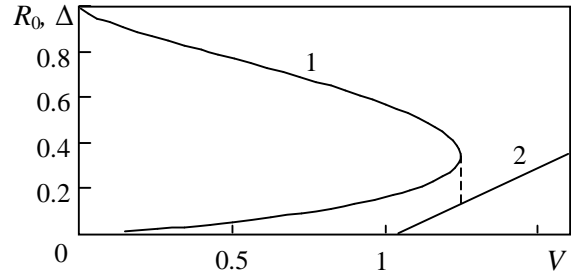


Fig. 11. Liquid volume parameters in the pipe.

1 –  $R_0 \equiv r_0/r_T = f(V)$  (for case fig.3a);

2 –  $\Delta \equiv \delta/r_T = f(V)$  (for case fig.3b)

### 3.4. Dynamic modeling of full vapor condensation

One-dimensional model of pulsation phenomena at full vapor condensation in a pipe proposed below (fig. 12). The model content the equation of liquid slug movement (1), the material balance equations of liquid slug 2 (2), of vapor bubble 3 (3), of vapor volume 1 (4), of liquid film on a pipe wall in a zone of a vapor bubble 3 (5), the equation of thermal balance of a wall (6) and the equations of a fluid properties on the saturation line.

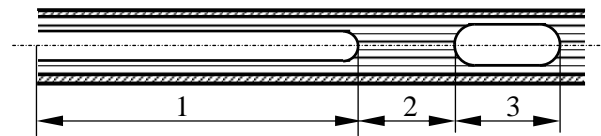


Fig. 12. Condensation with liquid slug

$$\frac{d(m_2 w_2)}{d\tau} = (p_1 - p_3) \omega_3 - \xi \frac{l_2 \rho' w_2^2}{2d}, \quad (16)$$

$$\frac{dm_2}{d\tau} = -\rho' \omega_3' \frac{dz}{d\tau}, \quad (17)$$

$$\frac{dm_3''}{d\tau} = -\frac{q_3 l_3}{r}, \quad (18)$$

$$\frac{dm_1}{d\tau} = G - \frac{q_1 l_1}{r}, \quad (19)$$

$$\rho' \pi (d - 2\delta_3') \frac{d\delta_3'}{d\tau} = \frac{q_3}{r}, \quad (20)$$

$$\rho_w c_w \omega_w \frac{dt_w}{d\tau} = q_3 - \alpha_0 (t_w - t_0) \pi (d + 2\delta_w) \quad (21)$$

Where the weights of liquid slug  $m_2 = \rho' l_2 \omega_2$ , its velocity  $w_2 = \frac{dz_2}{d\tau}$ , weights center coordinate  $z_2 = l_3 + l_2/2$ , linear density of heat flow at condensation vapor bubble  $q_3 = \lambda'(t_3 - t_w) \pi d / \delta_3'$ , area of cross section and whole of channel  $\omega_2 = \pi d^2 / 4$ . The numerical index indicate the appropriate zone number on figure 12.

The modeling calculation results present on fig. 13.

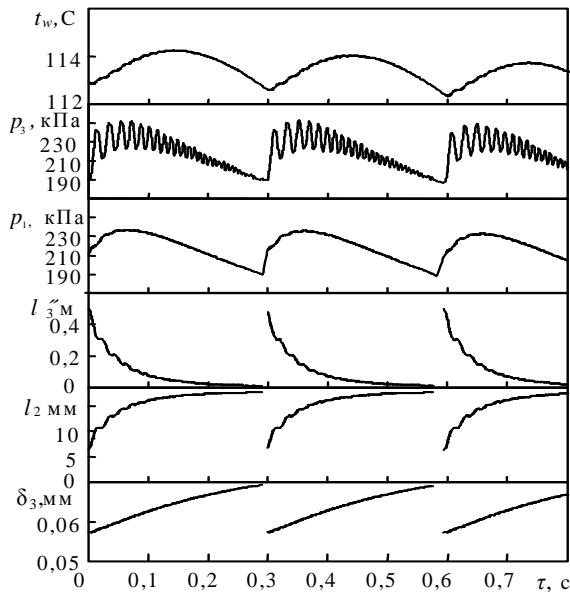


Fig. 13. The liquid slugs formation modeling results

pipe wall temperature in vapor bubble zone  $t_w$ ,  
 pressure in vapor bubble  $p_3$ ,  
 pressure in front of liquid slug  $p_1$ ,  
 vapor bubble length  $l_3$ ,  
 liquid slug length  $l_2$ ,  
 liquid film thickness in vapor bubble zone  $\delta_3$ .

Pressure pulsations are generating not at the moment of vapor bubble full condensation, but at the moment of liquid slug formation;

Formation of liquid slug occurs not as a result of the waves phenomena, but action of surface tension forces at critical liquid volume.

The offered model allows determined the pulsation phenomena in the LHP condenser.

## Nomenclature

$c$  - specific heat capacity, J/kg K;  
 $d$  - diameter, m;  
 $G$  - mass flow rate, kg/sec;  
 $g$  - gravitational acceleration, m/s<sup>2</sup>  
 $h$  - height of flat slot, m  
 $l$  - length, m  
 $m$  - mass, kg;  
 $p$  - pressure, Pa  
 $q$  - heat flow, W/m<sup>2</sup>;  
 $R$  - radius, m;  
 $r$  - latent heat, J/kg  
 $t$  - temperature, °C  
 $u$  - velocity, m/s  
 $x, y, z$  - coordinate, m;  
 $\alpha$  - heat transfer factor, W/(m<sup>2</sup> K)

The calculation results are good corresponding with experiments results [6]. The calculation results shows the amplitude of pressure pulsations till 60 kPa for  $p_3$  and till 40 kPa for  $p_1$ . that correspond to experiments data [6]. As well as experiments, it is observed two characteristic frequencies of fluctuations of pressure. From diagrams follows, that low-frequency pulsations have frequency of 3 Hz, and high-frequency at the moment of a liquid slug formation of 40 Hz. Last frequency with reduction of fluctuations amplitude is increasing. It corresponds to results of experiments [6].

Results of calculations on this model are correlating with results of experiments and allow to correct physical representations about mechanisms of pulsating phenomena:

1. Pressure pulsations are generating not at the moment of vapor bubble full condensation, but at the moment of liquid slug formation;
2. Formation of liquid slug occurs not as a result of the waves phenomena, but action of surface tension forces at critical liquid volume.

## CONCLUSIONS

The carried out experimental and modeling researches open mechanisms of liquid flow in the condenser channel.

$\beta$  - apex rib angle  
 $\gamma$  - inclination  
 $\delta$  - thickness, m  
 $\lambda$  - heat conductivity, W/(m K)  
 $\nu$  - kinematic viscosity, m<sup>2</sup>/s  
 $\rho$  - density, kg/m<sup>3</sup>  
 $\sigma$  - surface tension, N/m  
 $\tau$  - time, sec;  
 $\omega$  - cross-section area, m<sup>2</sup>;

**Indexes:**

' ,  $l$  - liquid;  
" ,  $v$  - vapor;  
s - saturation;  
 $w$  - wall;  
1 - fluid stream before liquid slug;  
2 - liquid slug;  
3 - vapor bubble;

**References**

1. Rifert V.G., Trocoz Ya.Ye. Heat transfer during static vapor film condensation on the profiled surface // *Energetic and Transport*. 1987. No. 6. Pp. 92–101 (in Russian).
2. Vasiliev L.L., Khrustalev D.K., Kulakov A.C., Prochorov Yu.M., Surguchev G.V. High-efficient condensers with capillary channels adv. in heat pipe science and technology // *Proc. of the 8th Int. Heat Pipe Conference, Beijing, China*, 1994. Pp. 254–263.
3. Buz V.N., Smirnov H.F. The film-wise condensation on the finned surfaces and with artificial suction in space conditions // *The Physics of Heat Transfer in Boiling and Condensation. Proc. of the Int. Symp. of the Physics of Heat Transfer in Boiling and Condensation, Moscow, Russia*, 1997. Pp. 545–549.
4. Smirnov H.F., Buz V.N., Goncharov K.A.. Intensification of heat exchange in two-phase loop condensers of space application // *Proc. of the 10th Int. Heat Pipe Conference, Stuttgart, Germany*, 1997. A1-1.
5. Buz V.N., Goncharov K.A. Hydrodynamics and heat exchange at full vapor condensation in channels of the small sizes // *Physical Bases of Experimental and Mathematical Modeling of Gas Dynamic Processes and Heat Exchange in Power Engineering. XIII a School-Seminar, St. Petersburg, Russia*, 2001. Vol. 1 Pp. 381–384.
6. Fiodorov V.A., Milman O.O. *Heat hydraulic auto fluctuations and instability in heat exchange systems with a two phase flow*, MPEI Publishing, Moscow, 1998.
7. Buz V.N. Modeling of thermo-hydraulic auto fluctuations at full vapor condensation inside direct pipes // *J. of Heat Power Engineering*. 2001. No. 5. Pp. 44–48.

## EXPERIMENTAL STUDY OF THE THERMAL RESISTANCES IN THE UNIT, INCLUDING TWO AXIAL HEAT PIPES JOINED TO EACH OTHER

**Konstantin A. Goncharov, Aleksey J. Kochetkov**

The Heat Pipe Centre Lavochkin Association,  
24, Leningradskaya st., Khimki, Moscow region, 141400, Russia,  
Tel/Fax: +7 495 5736374; Email: heatpipe@laspace.ru

**Victor A. Antonov, Kirill A. Dorofeev**

TAIS Ltd., Khimky, Moscow region, Russia  
Tel/Fax: +7 495 5736374; Email: tais@heatpipe.ru

### INTRODUCTION

Modern spacecrafts have the following main features: the non-sealed compartments and structures; usage of a many honeycomb panels and the axial grooved heat pipes. The thermal honeycomb panel structure includes internal axial grooved heat pipes. The "TAIS" Co Ltd. has accumulated the great experience in the axial grooved heat pipes design, manufacturing and testing of the various sizes of axial grooved heat pipes.

The temperature field equalization on the panel surface is important and actual task of the thermal panel design. The problem is often solved by use of the collector AGHP mounted on the heat panel surface perpendicular to the panel internal heat pipes. The AGHP provides the heat power redistribution between the panel internal heat pipes. The valid data on the internal and collector heat pipes interface is the most important component of the spacecraft thermal control system design process.

### THE TEST UNIT

The experimental assembly consisting two AGHPs cross joint is produced for the test devoted to the joint interface thermal resistance.

The unit consists of the two AGHP and aluminum plate inserted between them. Both AGHPs are produced from the same aluminum profile of 12.5 mm diameter (the AGHP cross-section is presented in the Fig. 1). The AGHP1 length is 818mm and the AGHP2 length is 643 mm. The plate was produced from the 7075 aluminum alloy. Its thickness is 0,5 mm. The plate size is 140×140 mm. The ammonia of high purity was used as the AGHPs heat fluid.

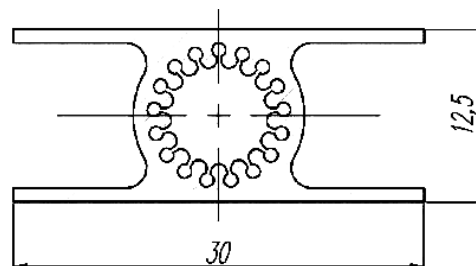


Fig. 1. The AGHP section

The AGHPs are joined in cross direction between each other and to the aluminum plate with the heat-conducting polymerizing paste. The paste coefficient of heat conductivity is  $\lambda = 2.0 \text{ W/m}^2$ . The paste layer thickness is from 0.01 up to 0.05 mm. The AGHP arrangement is shown in the Fig. 2.

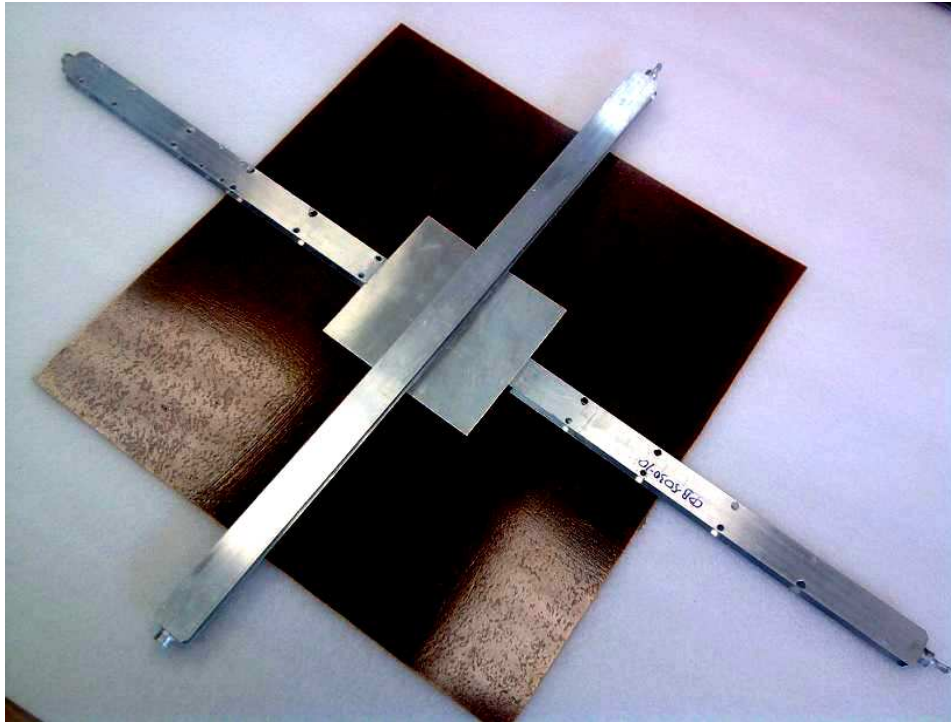


Fig. 2. The AGHP experimental assemble

The AGHPs assembly cross-section in the contact area is presented in the Fig. 3.

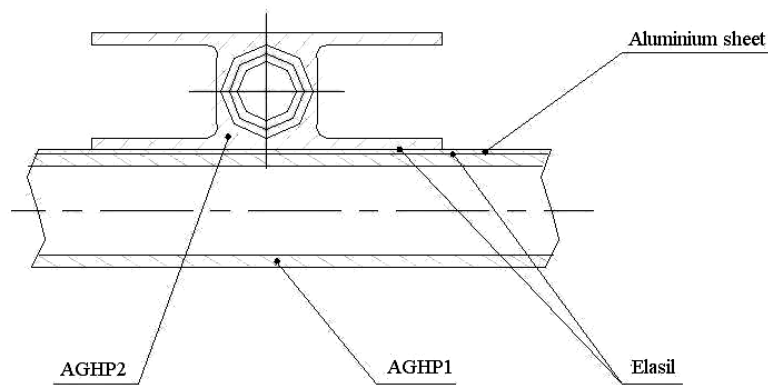


Fig. 3. The AGHPs assembly cross-section in the contact area

Length of the AGHP1 and AGHP2 heating and cooling zone is 200 mm. The zones are located out of the aluminum plate. The heat power up to 100W is supplied by the facility heater. The heat power is dissipated by the liquid nitrogen cooler (see Fig. 4).

The testing was performed on the two typical positions of the AGHP assembly location. At the first case the heater was mounted at the AGHP2 top. The AGHP2 was mounted on the aluminum plate. The AGHP1 was mounted on the plate bottom. The cooler was mounted in the AGHP1 bottom. Such heater and cooler arrangement provides better heat exchange comparing to the real heat exchange observed in space at the zero-gravity condition.

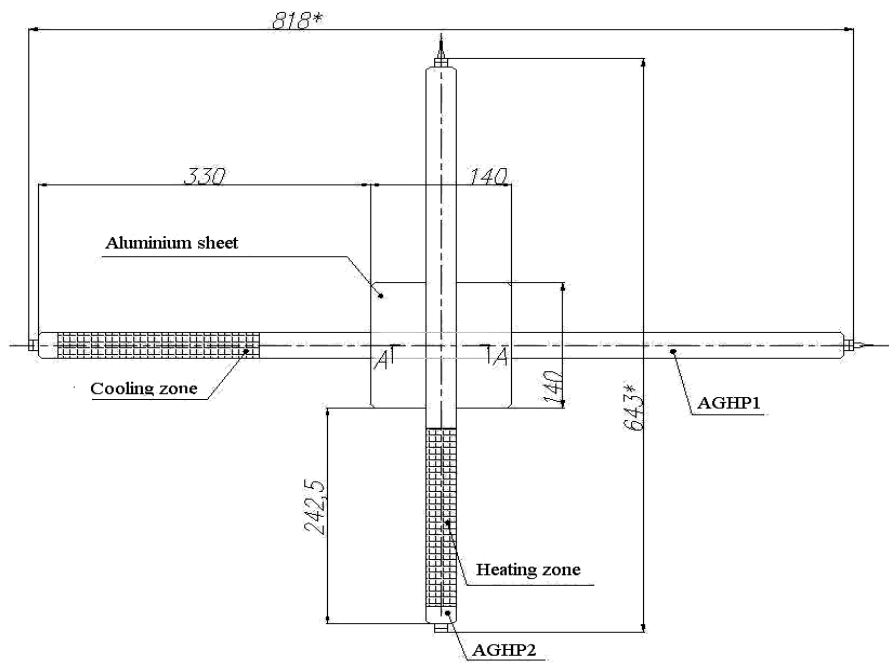


Fig. 4. The test facility

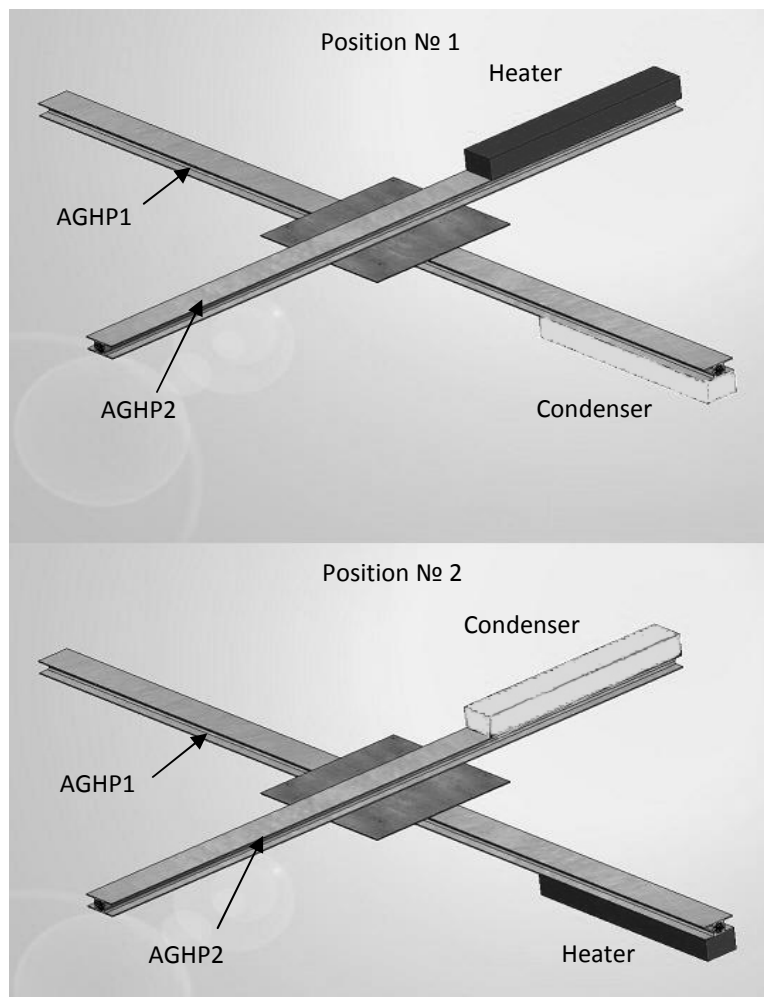


Fig. 5. The heater and cooler arrangements

At the Position 2 while the construction remained the same the heater was mounted at the AGHP1 bottom and the cooler was located at the top of the AGHP2. The heat exchange of the Position 2 is comparatively weaker than the real heat exchange in the zero-g condition.

The heater and cooler arrangements for the Positions 1 and 2 are presented in the Fig. 5.

The test was performed for 3 thermal modes. Each mode was defined by the temperature in the transportation zone of the colder AGHP (the one with the condenser). The following temperature values were selected for the test: minus 20 °C, plus 20 °C, plus 40 °C.

The test was started at the heater initial power 10 W. After the AGHP1 and AGHP2 stationary mode achievement the heat load was increased with step 10 W. In case when the temperature difference between the AGHP2 heating zone and AGHP1 cooling zone has exceeded 20 °C the test was stopped and the next thermal mode has been begun.

The temperature values were measured by the thermocouple sensors. The measurement tolerance was  $\pm 0.3$  °C. Each heat pipe surface was divided into several zones. Each zone was provided with 4 thermocouples. The thermocouples placing scheme is presented in the Fig. 6.

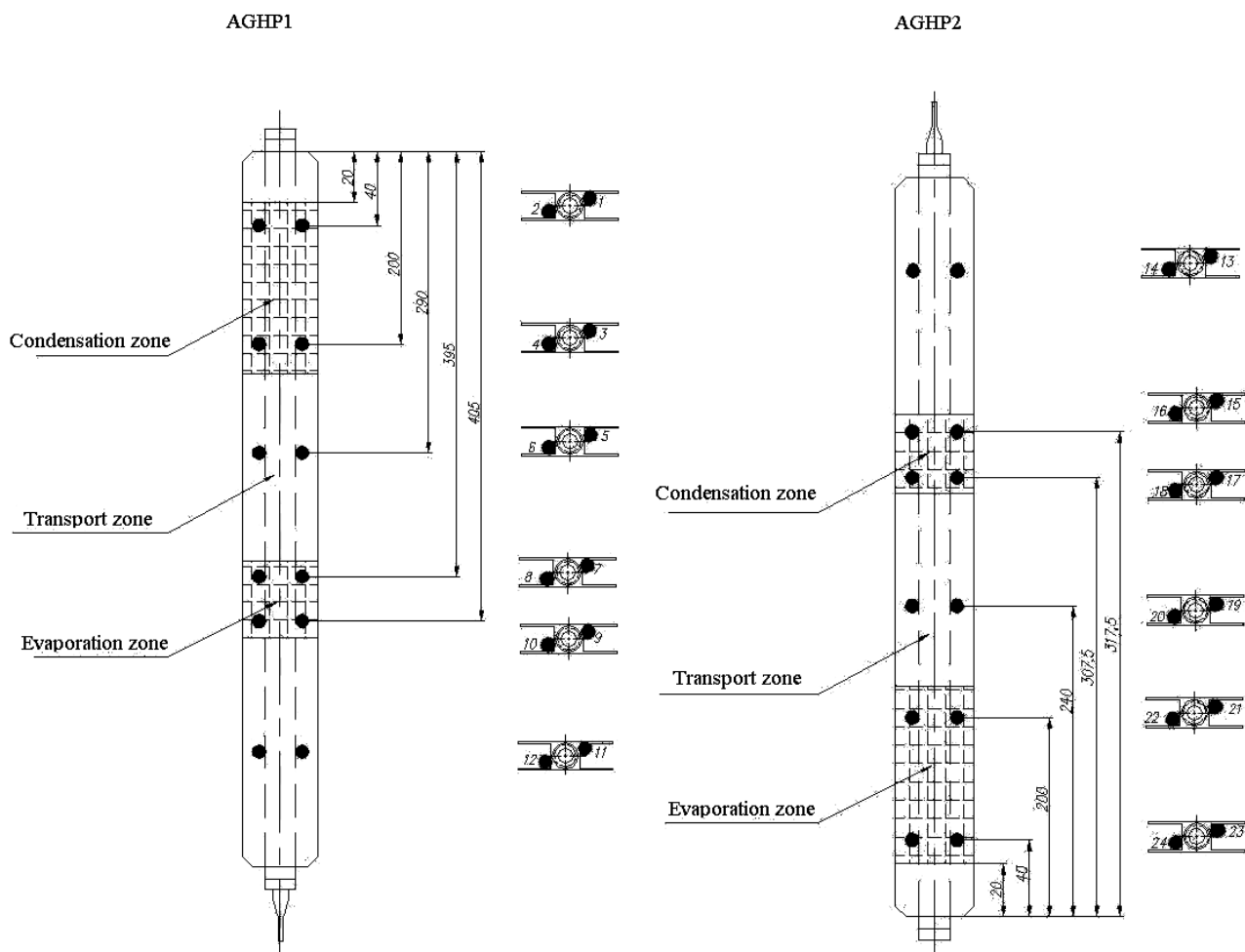


Fig.6. Thermocouple sensors placing scheme

The test was performed at the atmospheric test facility. The tested unit was mounted on the turntable with the supports through the heat insulation gaskets (Fig. 7) and was covered with the heat-insulating mats.

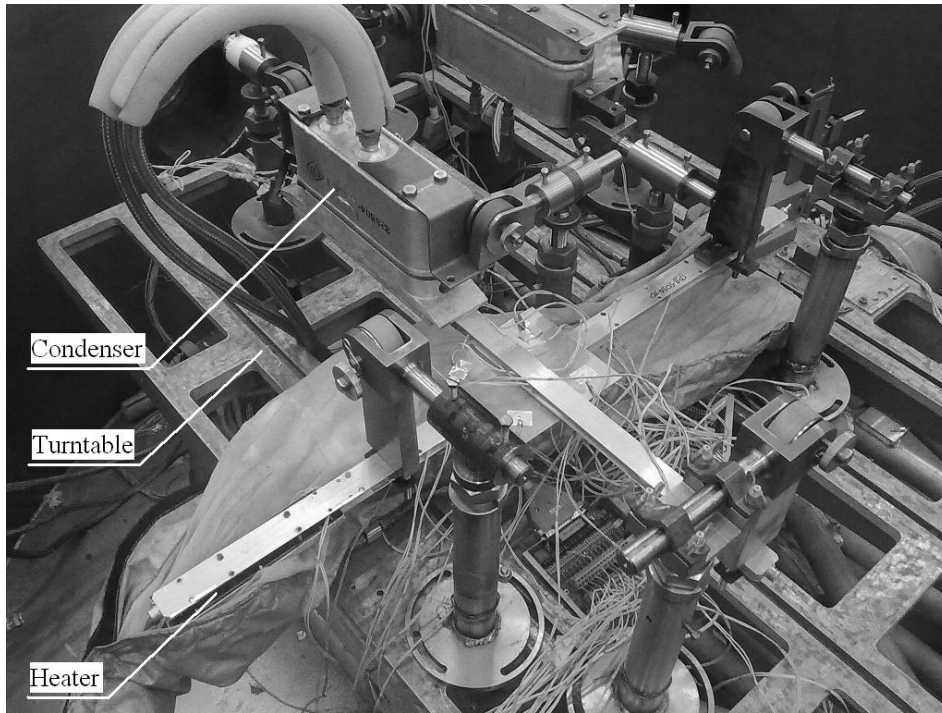


Fig. 7. The Experimental Facility

### THE METHOD OF THE AGHP THERMAL RESISTANCE AND HEAT DISSIPATION FACTOR DETERMINATION

The thermal resistance is a very important thermal engineering parameter used for the spacecraft TCS design. It shows the temperature gradient of the heat flux propagation in the studying structural element. The valid analytical value of the thermal resistance can be received only for the simplest structures. Therefore the thermal resistance of the tested unit was calculated as the temperature difference at the specified section of the AGHP, related to the transmitted heat power.

The thermal resistance along the AGHP:

$$R_{AGHP} = \frac{(T_{vap.av.} - T_{cond.av.})}{Q_{AGHP}}, \quad (1)$$

where  $T_{vap.av.}$  – the average temperature in the AGHP evaporation area,  $T_{cond.av.}$  – the average temperature in the AGHP condensing area,  $Q_{AGHP}$  – the heat power, transmitted by the AGHP, W.

The thermal resistance between the AGHP1 vapor and AGHP2 vapor in the contact area:

$$R_x = \frac{(T_{cond.av.AGHP2} - T_{vap.av.AGHP1})}{Q_{AGHP}}, \quad (2)$$

where  $T_{vap.av. AGHP1}$  – the average temperature in the AGHP1 contact area,  $T_{cond.av. AGHP2}$  – the average temperature in the AGHP2 contact area,  $Q_{AGHP}$  – the heat power, transmitted by the AGHP, W.

### THE TEST RESULTS

The test results include the stationary operational mode for all operational temperature values (minus 20 °C, plus 20 °C, plus 40 °C). The thermocouple sensor indications were recorded for each mode and the maximal AGHP powers at the given temperature differences were determined. The Figs. 8, 9 present the tested unit temperatures distributions on the thermocouple sensor indications for the thermal mode plus 20°C in both positions.

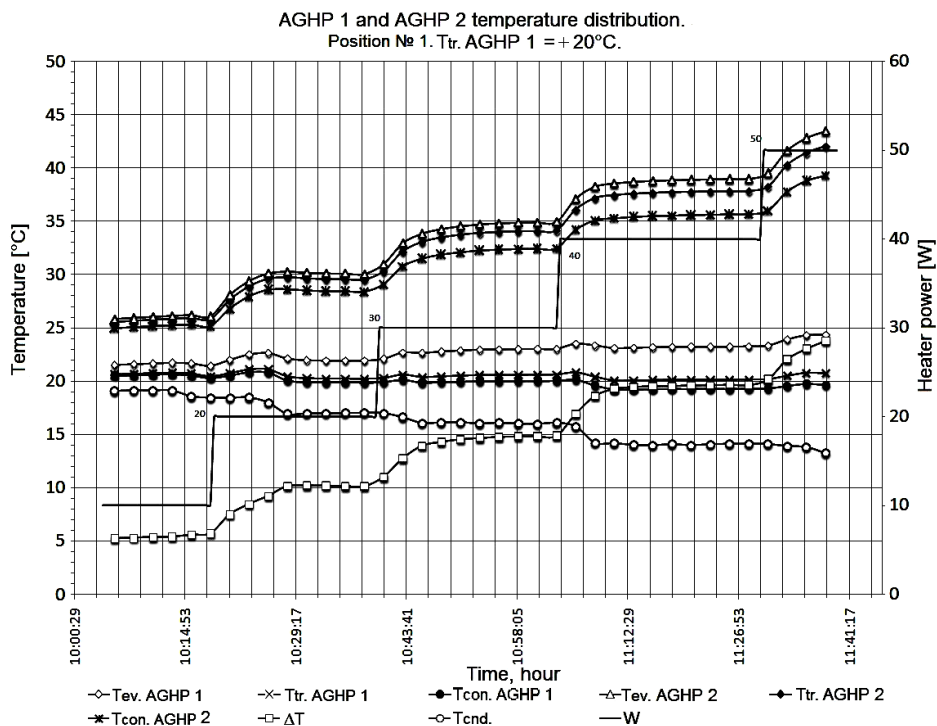


Fig. 8. The temperature distribution for Position 1 on the mode plus 20°C

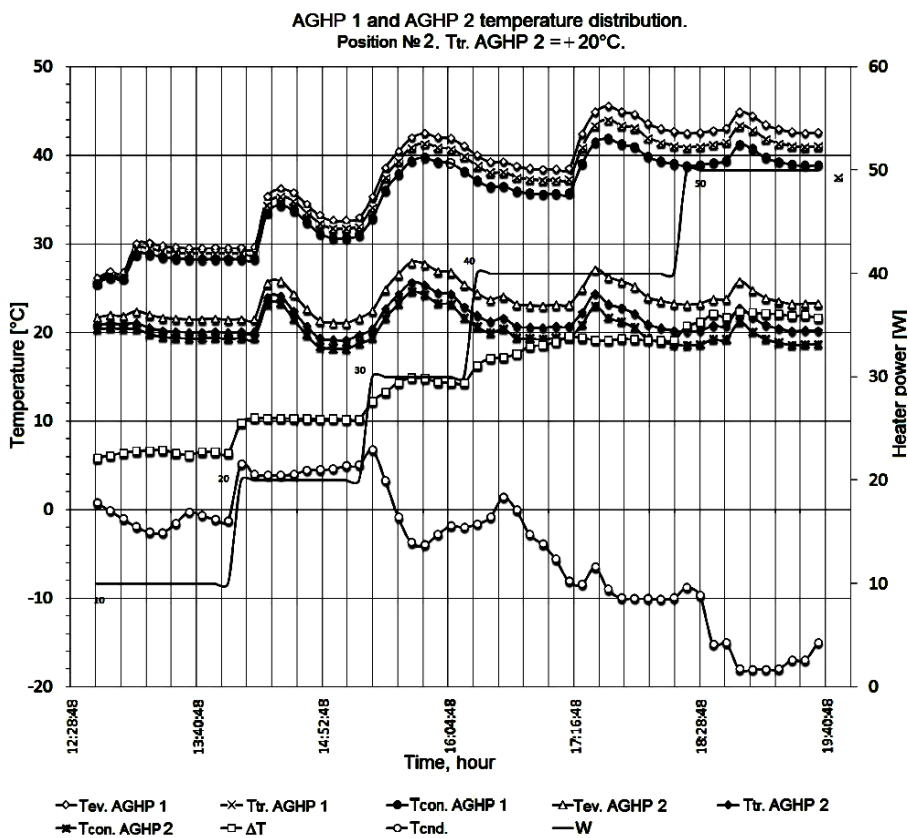


Fig. 9. The temperature distribution for Position 2 on the mode plus 20 °C

The given test mode monitoring was performed with the thermocouples of the cold AGHP1 transport zone. The test result analysis shows that during all thermal modes and various power values the AGHP

stationary operational mode has been achieved. At that the temperature difference between the heat input zone and heat dissipation zone was not more than 23 °C (Figs. 8, 9) at the power not more than 50 W.

The temperature jumps of all thermocouple sensors are stipulated by the heater input power increase. The required thermal mode in this case was restored by the heat fluid rate regulation.

Analysis of the AGHP thermal resistance calculated values for different temperature modes, and the experimental curve analysis (presented in the Figs. 8, 9) shows the following. External heat flows are typical for the temperature mode minus 20 °C. Therefore the received thermal resistance values exceed the real values. The mode plus 40 °C is presented with heat dissipations and the thermal resistance values are lower than real values. Most valid from the practical point of view is the thermal resistance value for the mode plus 20 °C. In this case the temperature of testing was corresponded to the ambient temperature and therefore the heat inputs and heat dissipations were minimum.

Based on the test results the following thermal resistance values for the Position 1 were received (the heat input was provided from the unit top and the heat output was provided from the bottom of the unit):

$$\begin{aligned} R_{av,AGHP1} &= 0,097 \text{ K/W}; \\ R_{av,AGHP2} &= 0,078 \text{ K/W}; \\ R_{av,x} &= 0,313 \text{ K/W}. \end{aligned}$$

For the Position 2 the received values are the following (the heat input was provided from the bottom of unit and the heat output was provided from the top of the unit):

$$\begin{aligned} R_{av,AGHP1} &= 0,066 \text{ K/W}; \\ R_{av,AGHP2} &= 0,1 \text{ K/W}; \\ R_{av,x} &= 0,332 \text{ K/W}. \end{aligned}$$

Calculated as the test data processing results the AGHP average thermal resistance in the contact area in Position 1 differs from the AGHP average thermal resistance in the contact area of Position 2 (Figs. 10, 11) insignificantly (the difference is 6%). At that the considered thermal model of the heater and cooler position (see Fig. 5) provides the better heat exchange than the real heat exchange in the zero-g space environment. The thermal model of Position 2 provides heat exchange worse than the real heat exchange in the zero-g space environment. So the real thermal resistance value in the zero-g space environment will be in the range between the two above mentioned values of the thermal resistances  $R_{av,x}$ .

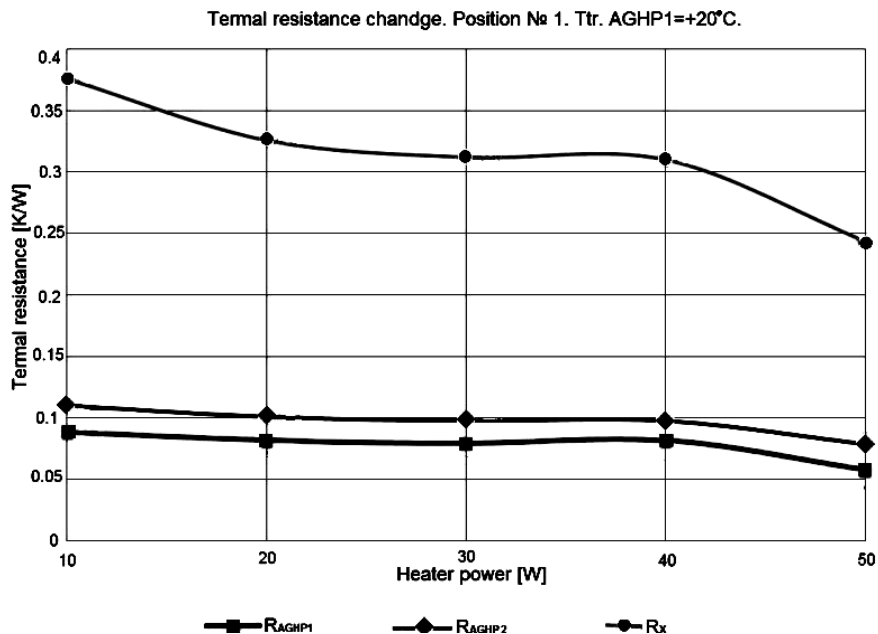


Fig. 10. The AGHP1 and the AGHP2 cross joint thermal resistance depending on the heat input Position 1. Mode – plus 20 °C

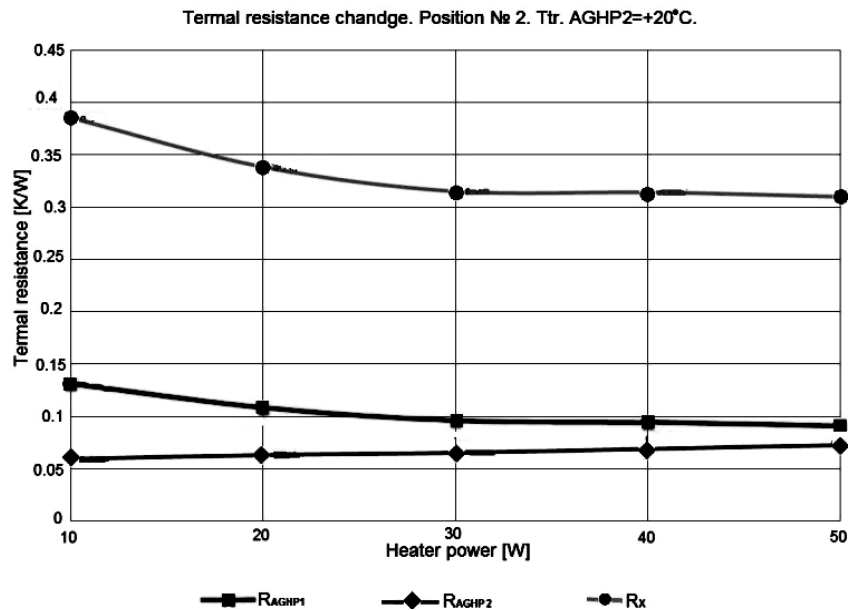


Fig. 11. The AGHP1 and the AGHP2 cross joint thermal resistance depending on the heat input. Position 2. Mode – plus 20 °C

## CONCLUSION

Based on the test results the thermal resistance of the unit containing the AGHPs (of 12,5mm diameter) cross joint could be accepted as 0,33K/W.

## References

1. Chi S. W. *Heat Pipe. Theory and Practice*, Hemisphere Publishing Corporation, Washington – London, 1976.
2. Goncharov K. A., Barantsevich V. L., Orlov A. A. *Experience of Development of Heat Pipes Applied in Russian Spacecrafts*.
3. Isachenko V. P., Sukomel A. S., Osipova V. A. *Heat Transmission (Teploperedacha)*, 3<sup>rd</sup> ed, Moscow, 1975 (in Russian).
4. Vargaftik N. B. *Handbook Regarding of Gases and Liquids Thermophysical Properties*, Nauka. Glavnaya Redaktsiya Fiziko-Matematicheskoi Literatury, Moscow, 1971 (in Russian).
5. Dunn P., Reay D. *Heat Pipes*, Energia Publisher, Moscow, 1979 (in Russian). Original: Dunn P.D., Reay D.A.. *Heat Pipes.*, Pergamon Press, Oxford, New York, Toronto, Sydney, Paris, Braunschweig, 1976.
6. Bogdanov S. N., Ivanov O. P., Kupriianova A. V. *Refrigerating Engineering. Properties of Materials: Handbook*, Agropromizdat Press, Moscow, 1985 (in Russian).
7. Ivanovsky M.N., Sorokin V.P., Iagodkin I.V. *Physical Basics of Heat Pipes*, Atomizdat Press, Moscow, 1978 (in Russian).
8. Bazhan P.I., Kanevets G.E., Selivestrov V.M. *Handbook on Heat Exchange Apparatus*, Mashinostroenie Press, Moscow, 1989 (in Russian).

## TWO-PHASE SYSTEMS FOR LIGHT-EMITTING DIODES COOLING

**Valery M. Kiseev, Dmitry S. Aminev, Victor G. Cherkashin and Radislav M. Murzin**

Ural State University, Department of Thermophysics and Surface Phenomena

Lenin av. 51, 620083, Ekaterinburg, Russia,

Phone: (+7) 343-261-6775, Fax: (+7) 343-261-6778

e-mail: Valery.Kiseev@usu.ru

### Abstract

Extensive development of the light-emitting diode (LED) devices on the basis of LED matrix offers capabilities to occupy LED an increasingly important place for the street and industrial lighting as more reliable and energy-efficient. However, there are not enough experimental data on the optimization of the cooling systems for LED devices. Traditionally, the cooling systems for LED devices are designed with even pitch of LED locations on the radiator's surface. By the increase of LED power the radiator's surface and the distance between the LED locations grows correspondingly. It results in the increase of a mass and size the LED device.

This paper presents some designs of two-phase thermal control systems for the LED cooling on the basis of conventional thermosyphon (TS), loop thermosyphon (LTS) and heat pipe (HP) and studies the experimental data, which were investigated for the two-phase systems considering the gravity influence. The presented results include:

- Some designs of the two-phase systems for the LED cooling.
- Start-up characteristics by low, high and intermediate powers.
- Power cycling (monotonic and random) and sink temperature cycling behavior.
- Temperature drop and temperature oscillations.

### KEYWORDS

Two-phase thermal control system, conventional thermosyphon, loop thermosyphon, heat pipe, LED lamp, radiator, working fluid, heat transfer.

### INTRODUCTION

The main attractive quality of LED devices is its high level of luminous efficiency in comparison to alternative light sources. Therefore, employing LED technology may result in different economic and social effects. The most important effect among others is a considerable reduction in electrical energy consumption, used for illumination purposes, which, according to different estimations, is about 18–20% of overall produced electricity. The comparison of available light sources is presented in Table 1.

Table 1. Characteristics of light sources

Light source type (LS)	luminous efficiency of LS, lm/W	Efficiency of lamps with respective LS, lm/W	Life time, hours
Glow lamp	8–13	6–10	1 000
halogen lamp	16–37	12–20	50–6 000
Compact luminous tube lamp	50–70	35–50	6 000–15000
metal-halide lamp	60–100	<40	6 000–10 000
luminous tube lamp	60–100	55–70	15 000–32000
Semiconductor LED (Cree XR-E)	100–110	90–100	>50 000
Sodium high-pressure lamp	90–130	<50	15 000–32000

Although LED lamps are more than 50 times as expensive as bright white lamps and about 7 times as expensive as compact luminous lamps, the price has been decreasing for the last years. Assuming that the characteristics improve and the price reduces, it is predicted that within few years LED sources will be used in the majority of lighting systems.

However, some of the factors that prevent LED from wide application should be taken into account. Thus, diode's parameters are very sensitive to working temperature, applied voltage, current etc. For example, when the temperature of a diode is more than 80 °C the luminous efficiency reduces, while at 120 °C the one tends to zero. Moreover, the lifetime decreases significantly. In order to deal with all mentioned problems it is required to develop and employ an efficient method of heat removing, i.e. the new LEDs or LED matrices which possess the maximal heat diffusion ability are needed.

Similar problems with thermal control exist in other fields such as space and aircraft industry, semiconductor industry, etc. In order to deal with these problems two-phase thermal control systems – heat pipes and devices based on them are often used [2–4].

Therefore, the goal of this work was to develop and study cooling technologies of the LED matrixes that have the output more than 30 W using effective heat sinks – loop heat pipes[5–7], including the most simple of them: loop thermosyphons and conventional thermosyphons [8–11].

## DEVELOPMENT AND STUDY OF TWO-PHASE THERMOSYPHONS FOR LED MATRICES COOLING

### The schematic diagram of loop two-phase thermosyphon (LTS)

The schematic diagram of loop two-phase thermosyphon is shown in Fig. 1. When voltage is applied on diode 2 it begins to glow and produces heat energy, which then is passed through substrate 9 to the liquid located at liquid cavity 7 of evaporator 1. Depending on the density of heat flux, the liquid boils or evaporate and becomes vapor, consuming latent heat of vaporization. During this process the vapor's pressure in a vapor cavity 8 is higher than the one in condenser because of the temperature difference between them, so the vapor travels through the vapor line 3 to the condenser 4, where it condenses with release of latent heat of condensation and becomes a liquid. Then the released heat is transferred to the condenser 4 and eventually by means of the radiator 6 to the environment. The liquid, influenced by gravity or capillary forces, drains through liquid line 5 back into the liquid cavity 7 and, therefore, encloses the evaporation-condensation heat transfer cycle.

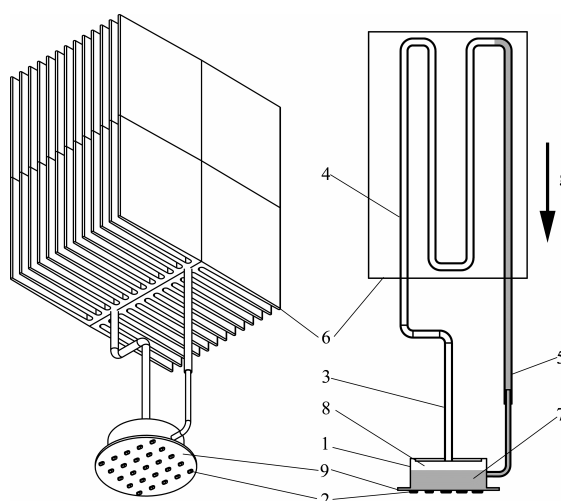


Fig 1. The schematic diagram of loop two-phase thermosyphon (LTS) for LED cooling:  
1 – evaporator, 2 – diodes; 3 – vapor line; 4 – condenser; 5 – liquid line; 6 – radiator;  
7 – liquid cavity of evaporator; 8 – vapor cavity of evaporator; 9 – LED matrix

The proposed LTS design allows to transform the heat energy from light emitting diodes compactly situated on metal substrate, which has smaller size than the radiator, as well as, it allows to spatially separate the heat input and output. The lack of moving parts as well as the benefits mentioned above positively affect LED devices, allowing easily arrange the radiator at places with the most intensive heat transfer and where natural or forced convection takes place. This results in lower power consumption, illumination efficient increase of LED matrix and lifetime expansion alongside the overall rise of reliability.

The Fig. 2 shows the photograph of developed experimental LTS for cooling LED matrices (on the left) and the LED matrix with 20 to 40 diodes (Osram, Germany) located on the aluminum plate, which is 1.7 mm in thickness and 80 mm in the diameter (on the right). To reduce the number of light emitting diodes and correspondingly the overall price of the device, the nominal load per diode has been increased up to 3.6 W, whereas in most cases 1 Watt per diode is used. The reduction of luminous efficiency, caused by the increase of nominal load from 0.35 A to 1 A, were about 14% of the nominal.

The evaporation chamber of the studied LTS was made of copper, tablet-shaped with 60 mm inner diameter and 25 mm wall thickness respectively. The vapor line and the coil condenser (4 loops with step 25 mm) were made of copper tube with inner diameter of 4, 1 mm thickness. For the condenser line a copper 2x0.5 mm tube was used.

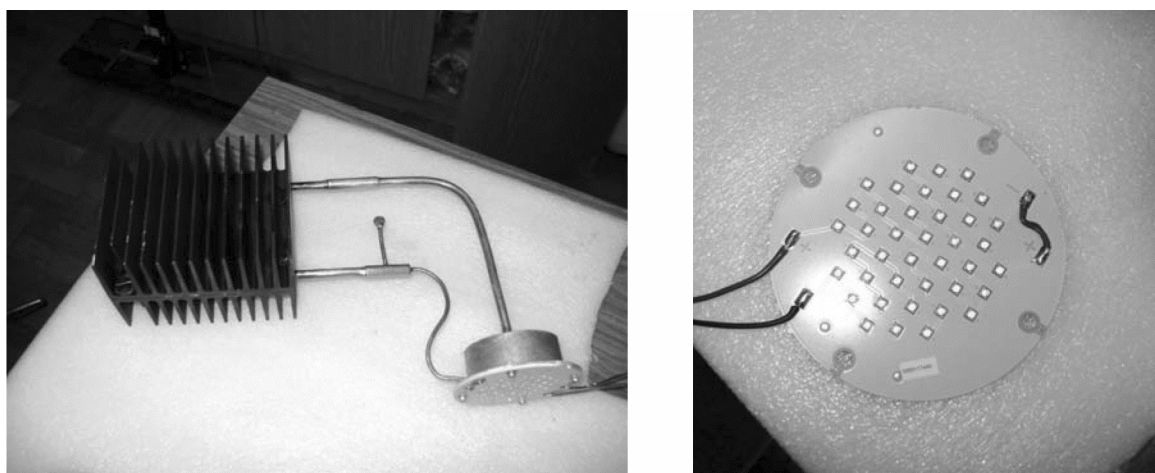


Fig. 2. Loop thermosyphon (LTS No. 1) with LED matrix (on the right)

The radiator 6 is composed of two standard finned radiators, which are 125x98 mm and 125x196 mm with the fin's length of 39 mm and 46 mm for LTS No. 1 and LTS No. 2 respectively. The total finned surface of radiator was 0.20 m<sup>2</sup> for the LTS No.1 and 0.48 m<sup>2</sup> for the LTS No. 1 respectively. On the finless surfaces of radiators the grooves for the coil condenser were made. Two halves of the radiator with applied thermal interface were fastened together by bolts this way that the coil condenser was between the halves, inside the radiator as it is shown in Fig. 1.

The material of LTS No. 2's radiator is aluminum. In order to test thermal characteristics of heat-conducting composite plastic with thermal conductivity of 8 W/(m ·K ) [12] (Teplostok T6-E5-7, SpecPlast-M ltd, Russia), the comparison of the aluminum radiator and the radiator made of the plastic have been conducted. The dimensional parameters of the radiators were the same.

### The schematic diagram of the conventional two-phase thermosyphon (CTS)

The schematic diagram of the conventional two-phase thermosyphon is presented in Fig. 3. The illuminating device works in the following way. When voltage is applied on diodes 4, they begin to glow and produce heat energy, which then is passed through the substrate 3 to the liquid 2 located at the bottom part of chamber 1. Depending on the density of heat flux, the liquid boils or evaporate and becomes vapor, consuming latent heat of vaporization that for most liquids exceeds the thermal conductivity for hundred times. After that, the vapor travels to the above part of the chamber 1, where it condenses and becomes a liquid with release of latent heat of condensation, which is then transferred to environment by means of the

radiator 5. The originated condensate 6 drains on the inner wall surface back into the bottom part of chamber 1, thereby enclosing the evaporation-condensation heat transfer cycle.

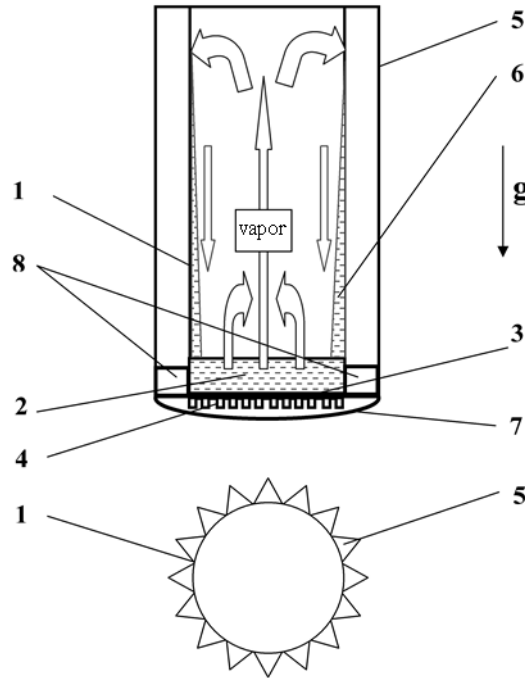


Fig. 3. The schematic diagram of conventional thermosyphon (CTS):  
1 – evacuated hermetic chamber – two-phase closed thermosyphon,  
2 – working fluid, 3 – heat-conductive metal substrate, 4 – LEDs, 5  
– radiator’s fins, 6 – condensate , 7 – optically transparent cover, 8 –  
power supply with functional sensors

The heat-transfer system, from which the air has been evacuated, is filled by working fluid that has the freezing point lower than the lowest climatic temperature specific for a region. For instance, in south regions, where the air temperature in winter time is not lower than  $+5^{\circ}\text{C}$ , pure distilled water might be selected as a working fluid, while for the northern regions, where the air temperature could possibly be below  $+5^{\circ}\text{C}$ , the working fluid might be methanol, acetone and ethanol, the freezing temperature of those are below  $-60^{\circ}\text{C}$ .

The proposed CTS design allows to transform the heat energy from light emitting diodes compactly situated on metal substrate, which has smaller size than the radiator, as well as to spatially separate the heat input and output. The lack of moving parts as well as the benefits mentioned above positively affect LED devices, allowing easily arrange the radiator at places with the most intensive heat transfer and where natural or forced convection takes place. This results in lower power consumption, illumination efficient increase of LED matrix and lifetime expansion alongside the overall rise of reliability. The Fig. 2 shows the photograph of developed experimental CTS for cooling LED matrices and the LED matrix with 20 to 40 diodes (Osram, Germany) located on the aluminum plate, which is 1.7 mm in thickness and 80 mm in the diameter. To reduce the number of light emitting diodes and correspondingly the overall price of the device, the nominal load per diode has been increased up to 3.6 W, whereas in most cases 1 Watt per diode is used. The reduction of luminous efficiency, caused by the increase of nominal load from 0.35 A to 1 A, were about 14% of the nominal.

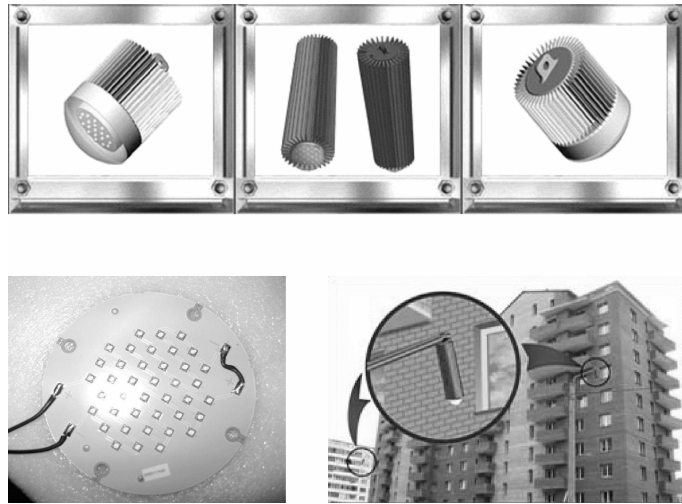


Fig. 4. The conventional thermosyphon with LED matrix and the LED matrix (left-bottom)

### EXPERIMENTAL APPARATUS AND PROCEDURE

The experimental setup was designed to measure temperature on different points of thermosyphon versus nominal power load  $N$  applied directly to LED matrix or versus a heat load  $Q$ . The local temperatures on LTS characteristic points were measured by thermocouples or the infrared imager (Fluke Ti32). Thermocouples were located as follows. One thermocouple was placed on the heat input zone, on the middle part of the LED matrix or on the middle part of the evaporator's shell between an electric heater and the evaporator (label  $T_h$ ). Two thermocouples were mounted on the vapor line and the liquid line, one on the outlet of the evaporator (label  $T_v$ ) and one on the inlet of the evaporator (label  $T_l$ ) respectively. The environmental temperature  $T_{env}$  was measured as well. All thermocouples were connected to data acquisition system (Owen TRM-148).

The experimental LED illuminating device based on a conventional thermosyphon and the locations of thermocouples is shown in Fig. 5. For this series of experiments the device were made of aluminum and the total external surface for heat exchange with environment was  $S_p = (0.336 \pm 0.004) \text{ m}^2$ , while the CTS's mass was  $m_{cts} = (2.40 \pm 0.05) \text{ kg}$ .

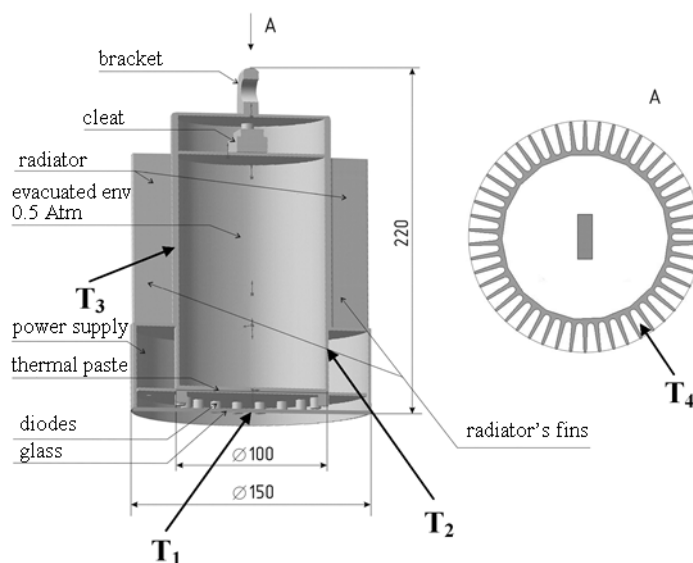


Fig. 5. Experimental LED illumination device and the thermocouples' locations

## RESULTS AND DISCUSSION

The fig. 6 represents a typical experimental curve for LTS No. 2 with water as a working fluid. From the graph it is seen, that under a low heat load the oscillations of measured temperature with the magnitude up to 3–4 degrees occur. However, the magnitude considerably decreases with a rise of the heat load.

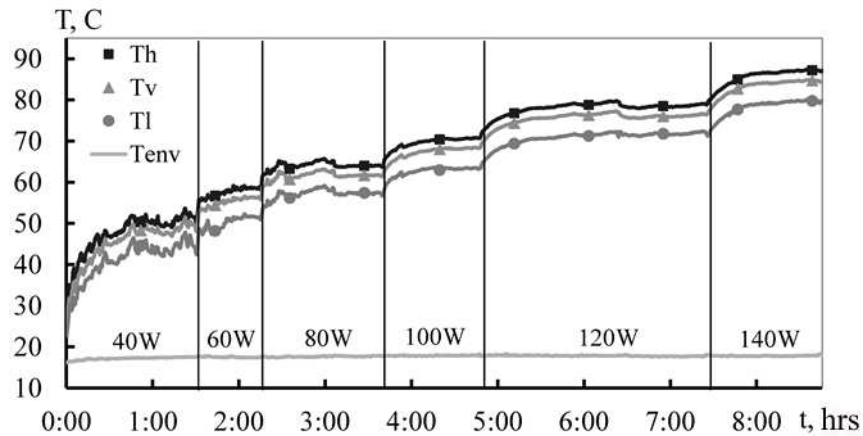


Fig. 6. Working temperatures ( $T$ ) of LTS No. 2 (working fluid - water) for various heat loads ( $Q$ )

One of the goals of this work was to compare the thermal characteristic of heat conductive plastic against the ones of traditional materials, such as aluminum. To do so, two geometrically identical radiators, one of the plastic and the other of traditional aluminum, were made. The Fig. 7 below shows the results of the comparison.

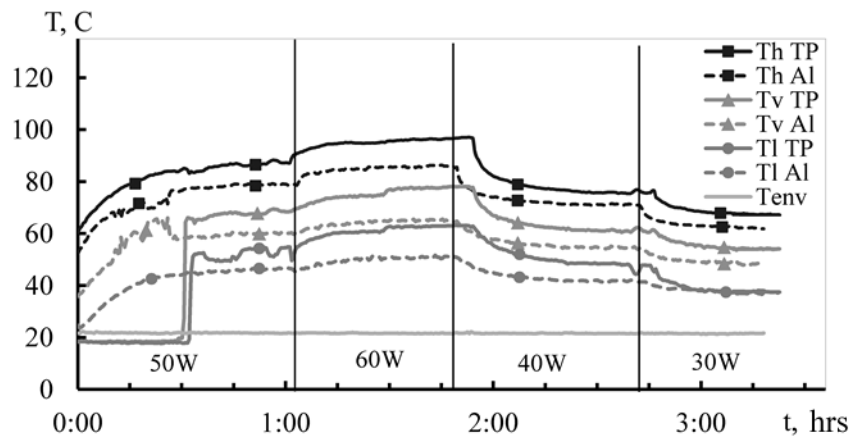


Fig. 7. Working parameters for LTS No. 1. Comparison of aluminum (Al) radiator and heat-conductive plastic (TP) radiator.

From the data above it is followed that the heat conductive plastic, having a relatively low thermal conductivity of 8 W/(m K) compared to aluminum and its alloys (220 – 180 W/(m K)), is suitable for heat sink within a natural convection condition. During this series of experiments, when the aluminum radiator was replaced by the TP radiator, the temperature on heat input zone increased by 4–8 per cent depending on the heat load (other conditions were kept the same).

The Fig. 8 represents the results of test for the conventional thermosyphon with acetone as a working fluid depending on an input power. In addition, a possibility to employ water as a working fluid, supposing its chemical compatibility with thermosyphon's materials and the ability to work under temperatures below 0 °C, is of interest as water is non-toxic and easy-to-work with.

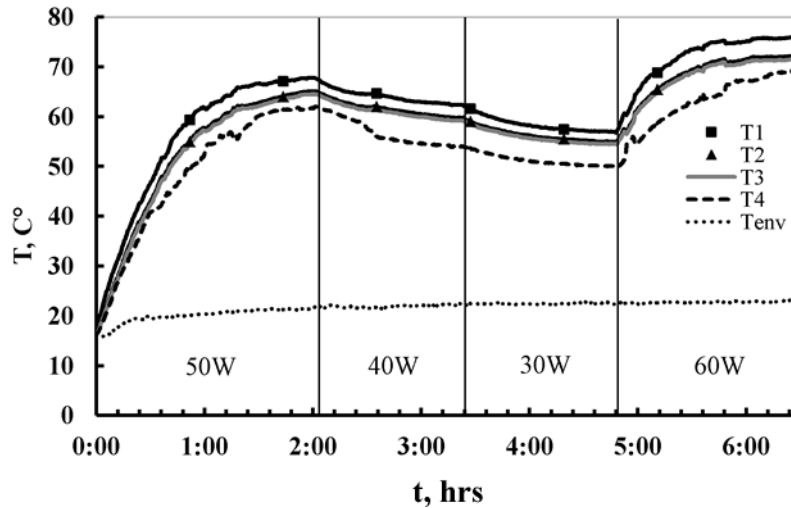


Fig. 8. The temperature field as a function of time and power. Working fluid – acetone

Below, in Fig. 9 a typical experimental dependence of the heat zone temperature on time  $t$  is shown. In this experiment the working fluid was frozen and the heat load on thermosyphon  $Q$  was 50 W. When the temperatures are about 0 °C the phase transition "ice-water" occurs, which is seen as a small step on the curve. Then, with the rise of temperatures the device's working regime changes to the normal two-phase one.

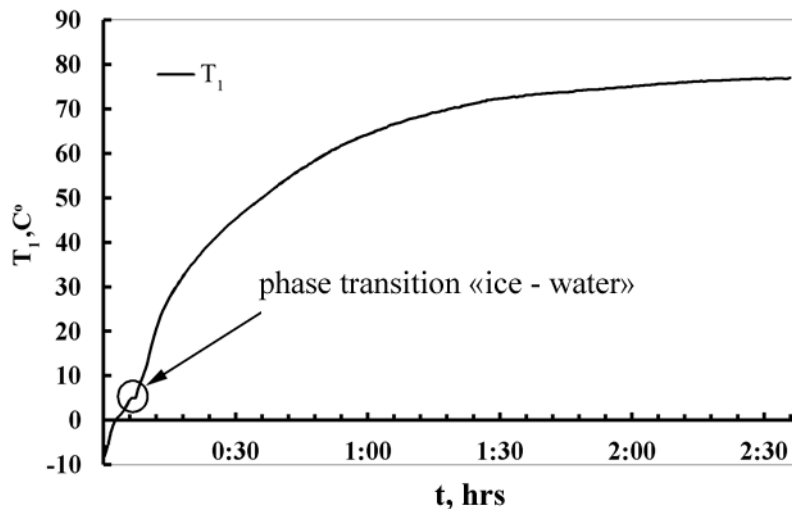


Fig. 9. Startup diagram  $T_1 = f(t)$  from frozen state of working fluid (water) under nominal heat load  $Q = 50$  W and the environmental air temperature  $T_{env} = (24 \pm 1)$  °C

This study has shown that all working parameters of thermosyphon filled with water remained the same for both normal conditions and when the phase transitions occurred. Additionally, no mechanical damages or

changes in the geometry of the thermosyphon were observed. This can be explained by a relatively small portion of the water in the internal volume of the device, about 2.5 per cent of the volume. Considering all the factors, water may be recommended as a working fluid for two-phase thermosyphons; however, some of limits such as chemical compatibility, relatively small volume of liquid, should be taken into account.

## CONCLUSIONS

1. A thermal control system for LED cooling based on the loop thermosyphons has been proposed. The complex study of loop thermosyphons has been performed and it has been showed that these systems might be applied in the LED devices cooling.

2. A thermal control system for LED cooling based on the conventional thermosyphons has been proposed. The complex study of conventional thermosyphons with flat end heat input has been performed and it has been showed that these systems might be applied in the LED devices cooling.

3. The comparative analysis of aluminum radiators and heat-conductive plastics has been performed. It was showed that the heat conductive plastics, low-cost, low-weight and easy-to-process material, have a great potential in thermal applications.

4. Using of thermosyphons allowed to raise the nominal load per diode to 3.5 W by increasing the current to 1 A, while the reduction of luminous efficiency was no more than 14%.

## References

1. Staroverov K. Cooling systems for LED // *Novosti Elektroniki*. 2008. Vol. 17. Pp. 21–23 (*In Russian*).
2. Dan P., Ray D. *Heat Pipes*. Moscow: Energia, 1979 (*in Russian*).
3. Voronin V. G., Revyakin A. V., Sasin V. Ya. et al. *Low-Temperature Heat Pipes for Aircrafts*. Moscow: Mashinostroenie, 1976 (*in Russian*).
4. Faghri A. *Heat Pipe Science and Technology*. Taylor & Francis, New-York, 1995.
5. Gerasimov Yu. F., Maydanik Yu. F, Shegolev G. T., Filippov G. A., Starikov L. G., Kiseev V. M., Dolgirev Yu. E. Low temperature heat pipes with separated channels for vapor and liquid // *Inzhenerno-Fizicheskii Zhurnal*. 1975. Vol. 28, No. 6. P. 957 (*in Russian*).
6. Maydanik Yu. F. Loop heat pipes // *Applied Thermal Engineering*. 2005. Vol. 25. P. 635.
7. Kiseev V. M., Vlassov V. V., Muraoka I. Optimization of capillary structures for inverted meniscus evaporators of loop heat pipes and heat switches // *Int. J. of Heat and Mass Transfer*. 2010. Vol. 53. P. 2143.
8. Pioro A. S., Pioro I. L. *Two-Phase Thermosyphons and its Applications in Industry*. Kiev. Nukova Dumka, 1988. 131 p. (*in Russian*).
9. Kiseev V. M., Pogorelov N. P., Menkin L. I. The study on two-phase thermosyphon application for mock-up fuel elements temperature regime modeling // *Proc. of the 8<sup>th</sup> IHPC, Beijing*, 1992. P. 673.
10. Kiseev V. M. *Physics of Heat Transfer Systems*. Ekaterinburg: Publisher of the Ural State University, 2006 (*in Russian*).
11. *Pat. 100587. RU*. LED illuminating device / V. M. Kiseev, R. M. Murzin; 2010.
12. Krivatkin A., Sakunenko Yu. Heat conductive plastics – challenge to aluminum // *Solid-State Lightning*. 2010. Vol 1. P. 54 (*in Russian*).

## A NEW EXPRESSION FOR SONIC LIMITATION IN HEAT PIPES

**R. Bertossi, C. Romestant, V. Ayel, Y. Bertin**

Institut P' (UPR CNRS 3346) CNRS - ENSMA - Université de Poitiers

Département Fluides, Thermique, Combustion

1, Av. Clément Ader BP 40109 86961 Futuroscope CHASSENEUIL Cedex, France

Tel: +33 5 49 49 81 32/ Fax: +33 5 49 49 81 01; e-mail: remi.bertossi@let.ensma.fr

### Abstract

Sonic limitation can interfere with the operating of heat pipes when vapour velocity reaches too high a level: a shock wave can consequently be generated and block vapour flow. This paper presents a detailed description of the known physical phenomena interfering with vapour flow and involving this limitation. It will be followed by a discussion on previous models predicting this limitation. To conclude, a new and original approach, considering vapour at saturation state all along the heat pipe, will be presented and lead to a new expression of this limitation, which will be compared with previous ones.

### KEYWORDS

Sonic limitation, analytical study, vapour, heat pipes.

### INTRODUCTION

The functioning of heat pipes is highly dependent on their operational limitations. Indeed, maximal performances are limited by their operating conditions. Five types of limitations are classically defined. Fig. 1 represents the operating domain of heat pipes as a function of the different limitations that can possibly interfere. These limitations are conditioned by the thermophysical properties of the working fluid and are also directly linked to fluid flow characteristics.

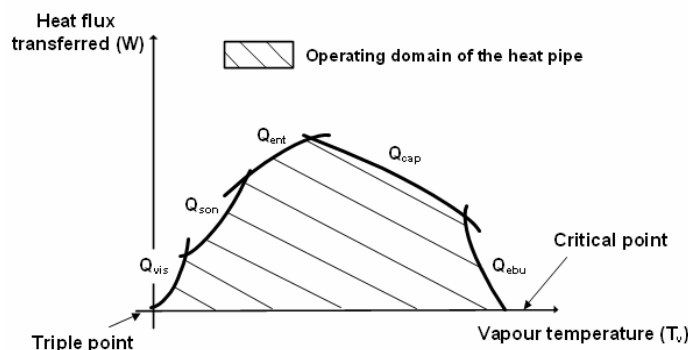


Fig. 1. The different operating limitations interfering with heat pipe functioning

Operating limitations can be divided into two main categories: some involve liquid flow and the others pertain to vapour flow. The latter correspond to viscous and sonic limitations. The first ( $Q_{vis}$ ) occurs in viscous flows for which the temperature is quite close to triple point (Fig. 1); the second ( $Q_{son}$ ) corresponds to flows that have attained the speed of sound and generally appears under low vapour temperatures. In macro heat pipes, variations in liquid film thickness along the heat pipe do not affect the vapour phase section. Consequently, it is possible to determine the maximal capacity of heat transfer through a pipe with regard to specific operational limitations, with vapour flow alone being taken into account.

This paper presents a description of the physical phenomena interfering with vapour flow when the sonic limitation is reached. Based on original hypotheses, analytical expression of the maximal heat flux induced by this limitation will be presented at the end of this paper.

## DESCRIPTION OF THE KNOWN PHYSICAL PHENOMENA

In Fig. 1, the sonic limitation appears only after appearance of the viscous limitation for increasing temperatures. It occurs when vapour velocity is high enough to reach the speed of sound. A shock wave can then be generated and block the vapour flow, thereby preventing transmission of the heat flux from the evaporator into the condenser. Compressibility effects and pressure losses due to the motion of the molecules have also got to be taken into account. In this paper, elementary physical hypotheses will be used to study the different possible vapour flow behaviours; a model for vapour flow will subsequently be adopted and used to obtain a simple expression of sonic limitation.

Let us assume the flow to be 1D; the maximal flux, which is attained when vapour velocity is equal to the speed of sound  $U_s$  and can be expressed as a function of the latter:  $Q_{son} = \rho_v U_s \frac{\pi}{4} D_v^2 h_{lv}$ . Given that the reference temperature is taken in the adiabatic zone, one easily obtains the following expression:

$$Q_{son} = \frac{\pi}{4} D_v^2 h_{lv,a} \rho_{v,a} \sqrt{\gamma_g T_{v,a}}, \quad (1)$$

where  $U_s = \sqrt{\gamma_g T_{v,a}}$  and "a" refers to the adiabatic section, where the temperature is assumed to be constant if the viscous losses are not taken into account.

Mass flow is given by the classical relation:  $\dot{m}_v = \rho_v U_v S_v$ . Differentiating the previous equation, one obtains:

$$\frac{d\dot{m}_v}{\dot{m}_v} = \frac{d\rho_v}{\rho_v} + \frac{dU_v}{U_v} + \frac{dS_v}{S_v} \quad (2)$$

Density  $\rho_v$  and velocity  $U_v$  are classically linked by a thermodynamic relation. Consequently, evolution of the couple  $(\rho_v, U_v)$  is a function of the variation of the section and of mass flow. Considering evolution of this couple with respect to Eq. (2), an increase of relative mass flow induces an equivalent decrease of the section. So, vapour flow in a constant section of a pipe ( $dS_v = 0$ ) with matter injection ( $d\dot{m}_v > 0$ ) shows exactly the same behaviour as in cases of constant mass flow ( $d\dot{m}_v = 0$ ) in a convergent nozzle ( $dS_v < 0$ ). The equivalence is illustrated on Fig. 2. In the same way, vapour flow with condensation and no variation of the section is comparable to constant mass flow with increasing section (cf. [1]).

For isentropic ideal gas flow, Candel [2], for example, has shown that when the speed of sound is reached in a nozzle throat, speed and subsequently mass flow attain a maximal value. By analogy with flows in a nozzle, in heat pipes, the sonic limitation corresponds to the heat flux transferred when maximal mass flow is attained at the end of evaporator, that is to say when the vapour reaches the speed of sound.

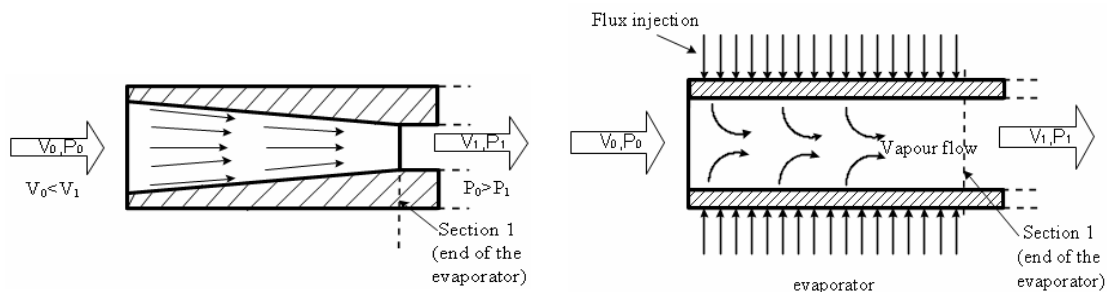


Fig. 2. Compressible vapour flow: equivalence between a convergent nozzle and an evaporator with constant section

**In most studies concerning heat pipes, the vapour is assumed to be an ideal gas.** Consequently, for a reversible and adiabatic flow, one may suppose that the vapour phase, at the evaporator, follows the

behaviour of an ideal gas in a convergent nozzle. This approach has been widely used [1, 3, 4]. For a 1D vapour flow, neglecting the viscous forces, a momentum balance for the whole evaporator (with a constant section) gives:  $P_{v,0} = P_{v,1} + \rho_{v,1} V_{v,1}^2$ . In the previous equation, "0" refers to the entrance of the evaporator ( $z = 0$ ) with a null velocity, and "1" refers to the "sonic throat" where velocity is maximal (at the entrance to the adiabatic zone).

Expressing vapour velocity as a function of the speed of sound and using the relation of ideal gas law, the relation (3) is then obtained:

$$\frac{P_{v,0}}{P_{v,1}} = 1 + \gamma Ma_1^2. \quad (3)$$

Sonic limitation can be estimated when the velocity is equal to the speed of sound at the end of the evaporator ( $Ma_1 = 1$ ), that is to say:

$$\frac{P_{v,0}}{P_{v,1}} = 1 + \gamma. \quad (4)$$

## DISCUSSION ON THE EXISTING APPROACHES

In Eq. (1), the major difficulty lies in the values to be assigned to  $h_{lv,a}$ ,  $\rho_{v,a}$  and  $T_{v,a}$  in the adiabatic zone. The following two approaches involve isothermal and isentropic evolutions of the vapour flow between the evaporator and the adiabatic zone.

### Isothermal model

Busse [5] has studied an isothermal vapour flow, considering the vapour as an ideal gas. Using Eq. (1), with this hypothesis, the following expression for the sonic limitation ( $Q_{son,isot}$ ) can be found:

$$Q_{son,isot} = \frac{\pi}{4} D_v^2 h_{lv,a,isot} \rho_{v,a,isot} \sqrt{\gamma r_g T_{v,0}}, \quad (5)$$

where "0" refers to the entrance to the evaporator.

Assuming that the vapour is at saturation state at the entrance to the evaporator, that the evolution of the pressure along the evaporator is considered as isentropic (given by Eq. (4)), and using the ideal gas law, one finally obtains:

$$Q_{son,isot} = \frac{\pi}{4} D_v^2 h_{lv,a,isot} (1 + \gamma) P_{v,0,sat} \sqrt{\frac{\gamma}{r_g T_{v,0,sat}}}. \quad (6)$$

The model's weakness derives from the fact that temperature evolution is assumed to be constant, even though it is generally admitted that along heat pipes, vapour temperature may evolve to some extent. Due to the thermophysical properties of the fluids, such evolution may modify the results obtained with the model, which has consequently been deemed somewhat unrealistic; that is one reason why alternative approaches have been developed.

### Isentropic model

In the more widely used isentropic model [1, 3, 4], the evolution of pressure along the evaporator is once again given by relation (4) and the vapour is still considered as an ideal gas. By analogy with Eq. (4), for an isentropic flow, an energy balance for the whole evaporator gives:

$$\frac{T_{v,0}}{T_{v,1}} = 1 + \frac{\gamma-1}{2} Ma_1^2 \quad (7)$$

And, if  $Ma_1 = 1$ , the following relation is obtained:

$$\frac{T_{v,0}}{T_{v,1}} = \frac{\gamma+1}{2}. \quad (8)$$

Using the general expression of  $Q_{son}$  (Eq. (1)) and the ideal gas law, the following expression can be obtained:

$$Q_{son,isen} = \frac{\pi}{4} D_v^2 h_{lv,a,isen} \frac{P_{v,a,isen}}{\sqrt{T_{v,a,isen}}} \sqrt{\frac{\gamma}{r_g}}. \quad (9)$$

Assuming that the vapour is at saturation state at the entrance to the evaporator, and using relations (4) and (8), one finds:

$$Q_{son,isen} = \frac{\pi}{4} D_v^2 h_{lv,a,isen} \frac{P_{v,0,sat}(1+\gamma)}{\sqrt{T_{v,0,sat}}} \sqrt{\frac{1+\gamma}{2}} \sqrt{\frac{\gamma}{r_g}}. \quad (10)$$

But, if the hypothesis of an ideal gas flow in a convergent nozzle is taken classically into account, the vapour phase cannot be considered to be at saturation state all along the heat pipe. Moreover, on the phase diagram, an isentropic evolution from point "0" in the saturation curve necessarily leads to a working point in the throat (point referred to as "1") that is situated in the liquid phase (cf. Fig. 3); as a result, the hypothesis of an isentropic flow with an operating point at saturation conditions likewise appears to be unrealistic.

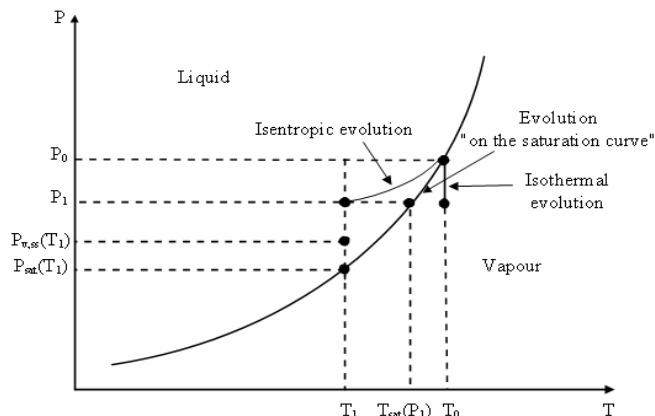


Fig. 3. Relative position of the reference points with regard to sonic limitation

However, Carey [6] has shown that while a supersaturation state is conceivable for the vapour, a limitation exists beyond which droplet condensation can be triggered. Based on kinetic analysis of the

droplets growing in the vapour phase and comparing the theory with experimental results, Carey obtained the following relation:

$$\frac{P_{v,ss}(T_v)}{P_{sat}(T_v)} = e^{\left( \frac{E^* \sqrt{-\ln J^*}}{2\sqrt{E^* + (-\ln J^*)^{3/2}}} \right)} \quad (11)$$

with:  $E^* = \frac{16\pi\sigma^3}{3k_B\rho_l r_g^2 T_v^3}$  and  $J^* = J \frac{M\rho_l}{N_A} \sqrt{\frac{\pi M}{2\sigma N_A}} \left( \frac{r_g T_v}{P_{sat}(T_v)} \right)$ ,  $J = 10^6 \text{ m}^{-3} \cdot \text{s}^{-1}$ : flux of droplets number per unit of volume, obtained through experimental results.

Table 1 Numerical applications for evolution of the vapour phase at the evaporator

Fluid	Initial point		"Sonic throat"		Saturation		Supersaturation Eq. (11)		
	$T_0$	$P_0$	$T_1$ Eq.(8)	$P_1$ Eq.(4)	$T_{sat}(P_1)$	$P_{sat}(T_1)$	$-\ln(J^*)$	$E^*$	$P_{v,ss}(T_1)$
Water	40	7370	-12	3100	23	-	-	-	-
Water	60	19920	4.5	8300	42	840	55.8	103	3150
Methanol	0	4050	-45.5	1690	-13	127	52.4	30.7	270
Sodium	427	95.1	310	40	377	4	42.0	3.05	5

Temperatures in °C, Pressures in Pa,  $J^*$  and  $E^*$  dimensionless

Eq. (11) determines the maximal supersaturation pressure that can be admitted in the vapour phase for a given temperature  $T_v$ . Table 1 gathers numerical applications that locate the reference points of the vapour flow when the Mach number is equal to 1 at the end of the evaporator, taking an initial operating point at saturation state. The different characteristic points are represented on Fig. 3, assuming that the vapour phase reaches the speed of sound at the throat: considering an isentropic evolution, the pressure at the throat  $P_1$  always highly exceeds the maximal pressure of supersaturation  $P_{v,ss}(T_1)$ . As a result, **appearance of droplets in the vapour phase inevitably occurs when the flow velocity at the end of the evaporator is sonic**. Consequently, the vapour cannot remain at supersaturation state. This hypothesis is confirmed by the presence of liquid in the interface: since it represents a condensation zone, the interface is necessarily close to the saturation state.

The vapour flow can no longer be considered as isentropic. Given this conclusion, vapour flow behaviour has been modified, and a new model has been built into the study.

## NEW HYPOTHESES FOR PREDICTION OF SONIC LIMITATION

In this case it is assumed that vapour flow follows the saturation curve of the working fluid: it is supposed to be saturated and dry all along the heat pipe. From this original hypothesis, a new expression of the sonic limitation may be proposed.

### New expression of the sonic limitation

Firstly, evolution of the thermophysical properties  $P$ ,  $T$  and  $\rho$  on the saturation curve does not follow the ideal gas law. However, the ratio  $r_g = P(T_{sat})/\rho(T_{sat})T_{sat}$  does not significantly vary for temperatures close to the triple point, and  $r_g$  can be approximated, in a first approach, as a constant. Fig. 4 confronts evolution of the ratio  $r_g$  with the specific gas constant,  $r_{specific}$ , defined as  $R/M_{gas}$ , as a function of  $(T - T_{TP})$ ,  $T_{TP}$  being the temperature at the triple point. The curves are drawn with regard to three fluids: water, methanol and sodium. For the latter, the data close to the triple point are missing so the curves have been obtained for temperatures relatively far from the triple point. For methanol and water, the ratio  $r_g/r_{specific}$  is particularly close to unity up until  $(T - T_{TP}) \approx 100$  K and decreases for greater temperature differences. For sodium, the ratio is particularly close to unity for  $(T - T_{TP}) \approx 220$  K and decreases for greater temperature differences. One can suppose that in cases where  $(T - T_{TP}) \leq 220$  K, the ratio remains close to 1.

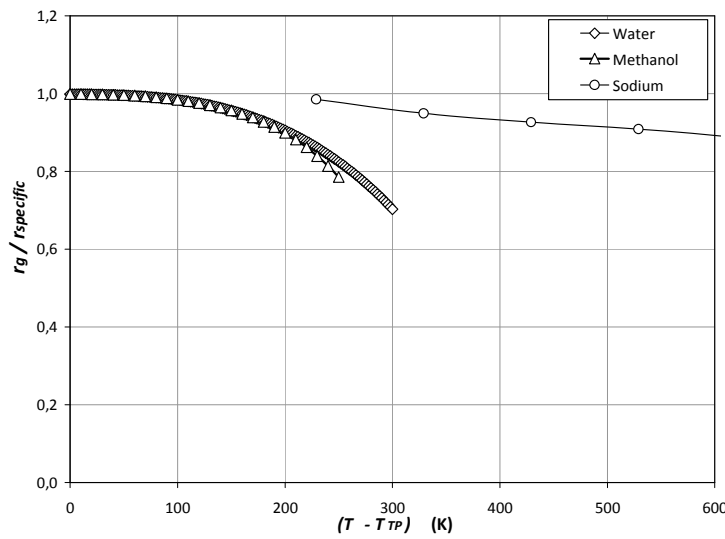


Fig. 4. Evolution of the ratio  $r_g/r_{specific}$  as a function of  $T-T_p$ .

For the three fluids, the approximation  $r_g/r_{specific} \approx 1$  is no longer valid when temperature increases on the saturation curve because of the pressure increase and on account of the irreversible phenomena associated with molecular shocks. If the vapour is assumed to be at saturation state all along the heat pipe, integrating the Clausius-Clapeyron equation between sections "1" and "0", and using the ideal gas law ( $r_g = P(T_{sat})/\rho(T_{sat})T_{sat}$ ), the relation (12) is obtained:

$$\frac{P_{v,0,sat}}{P_{v,1,sat}} = e^{\frac{h_{lv,sat}}{r_g} \left( \frac{1}{T_{v,1,sat}} - \frac{1}{T_{v,0,sat}} \right)}. \quad (12)$$

Starting from this, using Eq. (1) and the previous approximation concerning  $r_g$ , one finally obtains:

$$Q_{son,sat} = \frac{\pi}{4} D_v^2 h_{lv,a,sat} \frac{P_{v,a,sat}}{\sqrt{T_{v,a,iat}}} \sqrt{\frac{\gamma}{r_g}}. \quad (13)$$

Assuming that pressure evolution along the evaporator is given by Eqs. (4) and (12), one finally obtains:

$$Q_{son,sat} = \frac{\pi}{4} D_v^2 h_{lv,a,sat} (1 + \gamma) P_{v,0,sat} \sqrt{\frac{\gamma}{r_g T_{v,0,sat}}} \frac{1}{\sqrt{1 - r_g / h_{lv,a,sat} T_{v,a,sat} \ln(1 + \gamma)}}. \quad (14)$$

### Comparison of the different expressions of the sonic limitation

First, let us determine the ratio between the sonic limitation in the case of an isentropic flow ( $Q_{son,isen}$ ) and in the case of a saturated vapour flow ( $Q_{son,sat}$ ). Using Eqs. (10) and (14), the following relation is obtained:

$$Q_{son,sat} / Q_{son,isen} = \sqrt{2 / \left( (1 + \gamma) \left( 1 - \frac{r_g T_{v,a,sat}}{h_{lv,a,sat}} \ln(1 + \gamma) \right) \right)}. \quad (15)$$

To evaluate this ratio, the latent heat of phase change  $h_{lv}$  is considered to be constant and equal to  $h_{lv,a,sat}$  because, for temperatures close to the triple point, it does not significantly vary. This ratio is close to 1: in general, it is included in the interval **[0.9;1]**, as can be seen on Fig. 5 on curves drawn with white items.

In the same way, the sonic limitation  $Q_{son,sat}$  can be compared to the sonic limitation obtained when considering an isothermal vapour flow ( $Q_{son,isot}$ ), using relations (6) and (14):

$$Q_{son,sat} / Q_{son,isot} = \left( 1 - r_g T_{v,a,sat} \ln(1 + \gamma) / h_{lv,a,sat} \right)^{-1}. \quad (16)$$

This ratio typically varies from **1** to **1.04** for temperatures close to the triple point, as seen on Fig. 5, on curves drawn with black items.

Our model is consequently situated in between the isentropic model and the isothermal one.

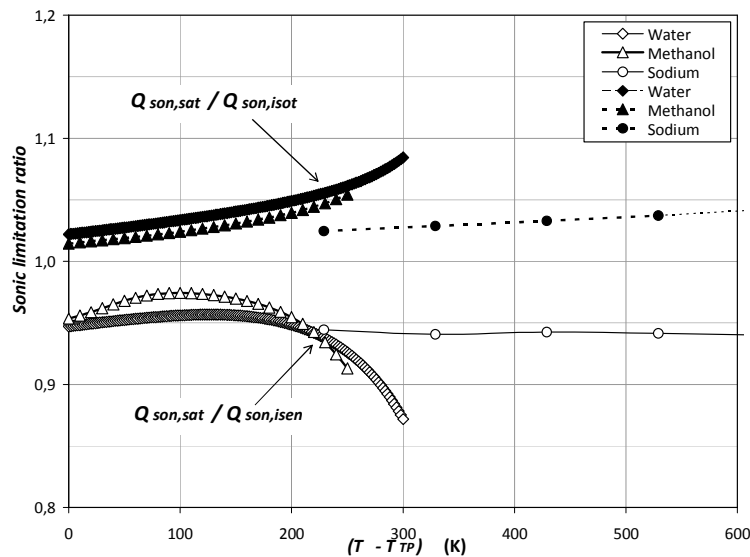


Fig. 5. Evolution of the sonic limitation ratio as a function of  $(T - T_p)$

In previous experimental work, the results obtained by Gagneux [7] on a sodium heat pipe showed satisfactory agreement with Busse's model (Eq. (6)). However, the measurements are not accurate enough to differentiate the three models under study. Moreover, a "diphasic" vapour flow model (vapour phase containing liquid droplets) made by Levy [8] gave results particularly close to those obtained by Busse, and which appear to confirm the validity of the numerical values obtained in the paper. As far as we know, there

is not enough experimental data to conclusively validate our model. However, as the isothermal and the isentropic models present hypotheses that may be questionable (even if they produce results that are close to experimental data), our intermediate model, which takes into account a vapour flow at saturation state, seems to be adoptable.

## CONCLUSION

In this paper, an original analysis about sonic limitation has been presented. It shows that the classical approaches may be contestable, even though they yield results in general conformity with the experimental data. A new approach has been proposed: the vapour is assumed to be at the saturation state all along the heat pipe. In conclusion, a new expression of sonic limitation has been obtained and compared with those obtained through previous models.

That said, the present model has yet to be fully validated, and only through additional experiments will it be possible to provide convincing evidence that one process is markedly more realistic than the others that have been proposed. In any event, it should be noted that for temperatures close to the triple point, the results gathered from the different approaches preclude any errors exceeding 5%.

## NOMENCLATURE

<i>Latin notations</i>		$U$	$x$ -axis velocity (m/s)	eb	ebullition
$D$	diameter (m)	$V$	velocity (m/s)	eff	effective
$g$	gravity constant (m/s <sup>2</sup> )	$y, z$	coordinate (m)	ent	entrainment
$h_{lv}$	latent heat (J/kg)	<i>Greek Symbols</i>		isen	isentropic
$L$	heat pipe length (m)	$\gamma$	isentropic coefficient	isot	isothermal
$Ma$	Mach number	$\mu$	dynamic viscosity (Pa.s)	l	liquid
$\dot{m}$	mass flow (kg/s)	$\rho$	density (kg/m <sup>3</sup> )	sat	saturation
$P$	pressure (Pa)	$\sigma$	surface tension (N/m)	son	sonic
$Q$	heat flux (W)	<i>Subscripts</i>		ss	supersaturation
$r$	radius (m)	a	adiabatic	v	vapour
$r_g$	specific gas constant (J/kg·K)	c	condenser	w	wall
$T$	temperature (K)	cap	capillary		
		e	evaporator		

## Acknowledgements

The authors wish to thank the “Institut PPRIME” and the French Ministry of Research for their financial support. Jeffrey Arsham, a professional translator, has thoroughly reviewed the written English.

## References

1. Deverall J.E., Kemme J.E., Florschuetz L.W. Sonic limitation and startup problems of heat pipes, Los Alamos scientific laboratory, report LA-4518, 1970.
2. Candel S. *Mécanique des Fluides*, Dunod Université, Paris, 1990. Chapter 8.
3. Faghri A. *Heat pipe science and technology*, Taylor and Francis, New York, 1995. Chapter 4.
4. Peterson G.P. *Heat Pipes: modeling testing and applications*, Wiley and Sons Inc, New York, 1994.
5. Busse C.A. Theory of the ultimate heat transfer limit of cylindrical heat pipes // *Int. J. of Heat and Mass Transfer*, 1973, Vol.16 Pp. 169–185.
6. Carey V.P. *Liquid-Vapor change phenomena : An introduction to the thermophysics of vaporization and condensation process in heat transfer equipment*, Taylor and Francis, New York, 1992, Chapter 5.
7. Gagneux P. *Contribution à l'étude des caloducs à sodium* // PhD Thesis, Université de Poitiers, LET, ENSMA, 1979.
8. Levy E.K. Theoretical investigation of heat pipes operating at low vapor pressures // *ASME Aviation Space Conference*, 1968. Pp. 671–676.